THE UNIVERSITY *of* EDINBURGH

Spectroscopic Monitoring of Long-term AGN Transients: Threading the Micro-needle.

Alastair G Bruce

Doctor of Philosophy
The University of Edinburgh
June 2018

"I may not have gone where I intended to go, but I think I have ended up where I needed to be."

Douglas Adams

Lay Summary

Active galactic nuclei (AGN) are extreme objects. The most luminous class of AGN, also known as quasars, can produce enough energy to outshine entire galaxies of stars. This happens in a volume of space not much bigger than our own solar system. To power such a monster requires a supermassive black hole, an object so dense that light cannot escape it and with a mass of more than a million Suns. These behemoths are known to exist at the center of most galaxies. By definition they don't emit light but if any matter falls onto them this gives them the potential to liberate huge amounts of energy before the material finally reaches the central black hole.

We are confident that for an AGN to be able to radiate efficiently, an accretion disc of matter must be present. In addition, when examining the specific wavelengths of light emitted from these objects via spectroscopy, we know there must be fast-moving clouds of material nearby and, in some objects, dense obscuring material further out. However, the exact shape and structure of these inner regions is beyond the resolution limit of modern telescopes, leaving many unanswered questions. Additionally, all AGN are known to be variable, displaying a characteristic 'flickering' behaviour which can provide us with additional clues.

A sample of AGN have been discovered which are behaving unusually. Rather than simply flickering, they are instead varying slowly and smoothly over periods of years and changing brightness by factors of several. In this thesis I will be analysing the light curves and spectra of these transients as they evolve. I will also be exploring the possibility that the changes seen in these objects may not be intrinsic to the AGN themselves. Rather they may be getting 'lensed' by a massive object, such as a star, crossing our line of sight. This is a consequence of the fact that massive objects can bend the path of light passing nearby and can lead to the amplification of distant sources. If true, these events may be giving us a unique opportunity to probe the inner-most regions of these enigmatic AGN.

Abstract

All active galactic nuclei (AGN) are known to vary in the rest-frame UV/optical. Typical variations are on the order of 30% or so and are stochastic in nature. Therefore, the discovery of a number of extreme AGN transients, which are smoothly evolving on year-long timescales and by a factor of four or more, is surprising and necessitates further analysis. Are these objects simply at the extreme end of the variability distribution seen in normal quasars or is there another mechanism which can explain their atypical behaviour? The primary focus for this work is on the possibility that a number of these extreme AGN transients are actually rare, high-amplitude microlensing events, caused by intervening stellar mass object(s). Not only do the microlensing models provide an explanation for the observed variability but they also allow constraints to be placed on the morphology of the emitting regions of the AGN, namely the accretion disc and broad line region (BLR).

These transients have been monitored both photometrically and spectroscopically, since their discovery. The majority of spectroscopic observations have been conducted using the William Herschel Telescope. At time of writing (Sept. 2017), there are now 64 confirmed AGN and 235 individual spectra. The spectral reduction pipeline, calibration and initial measurements are described in Chapter 2. This chapter also details the microlensing models and procedures used in interpreting both the light curve information and spectral measurements. This includes: a comprehensive treatment of the simple point-source/point-lens model; quantitative point-lens models which allow for the use of extended sources; and also an initial exploration into more complex lensing morphologies involving multiple lensing objects and/or an external shear.

Chapter 3 details the results of the spectroscopic monitoring campaign for the entire transient sample. A general classification scheme is developed which allows for a comparison of the evolutionary trends seen in objects exhibiting similar

behaviour. A subset of transient AGN, the most extreme objects in the sample, is also discussed in detail, with a particular focus on the evolution of the continuum, line fluxes and equivalent widths.

Chapter 4 details the results of the analysis of four key targets, selected for their suitability in addressing the microlensing hypothesis. For two targets the point-source point-lens model performs very well. Lens parameters for these objects are presented and in one particular case, the data is sufficient to allow constraints to be placed on the size of various components comprising the broad line region.

Chapter 5 expands the microlensing analysis to include the entire AGN transient sample. Approximately 10% of objects are well matched by a simple point-source, point-lens microlensing model. In other objects, evidence is seen which requires a more complex lensing scenario to adequately explain. In one class of objects there is also evidence that the accretion disc is being resolved by the lens.

Chapter 6 revisits a notable flare seen in an AGN which lies behind M31. The analysis reaffirms that this event is well described by a simple microlensing model and provides an independent estimate that the most probable location for the lens is within M31 itself.

Declaration

I declare that this thesis was composed by myself, that the work contained herein is my own except where explicitly stated otherwise in the text, and that this work has not been submitted for any other degree or professional qualification except as specified.

Parts of this work (primarily Section 2.5 and Chapter 4) have been published in Bruce A., Lawrence A., MacLeod C., Elvis M., Ward M.J., Collinson J.S., Gezari S., Marshall P.J., Lam M.C., Kotak R., Inserra C., Polshaw J., Kaiser N., Kudritzki R-P., Magnier E.A., Waters C., 2017, MNRAS, 467, 1259.

(*Alastair G Bruce, June 2018*)

Acknowledgements

Heartfelt thanks to my Mum and Dad for always being there for me, my siblings and siblings-in-law for putting up with me and my Gran fer the banter. You guys rock.

I'd like to thank my supervisor, Prof. Andy Lawrence, for keeping me sane and insane in equal measure. It's been a pleasure sir.

Of the plucky band of Edinburgh-based collaborators I'd like to thank Chelsea MacLeod for always being in a good mood, Nic Ross for lifting mine and David Homan for being the mostly sensible one.

William and Martin, it's been an honour and a privilege not knowing enough about too many things with you guys over the years.

Cheers to Nathalie for putting up with my inability to 'finance' and to Paula for much needed moral support.

Thanks to my office chums Cass, Derek, Marco, Rosie, Sam, Vanessa and the twa Davids. There will be whisky for you all.

Thanks also to the finest of collaborators Martin W, James, Daniel, Martin E, Phil and Suvi.

A thousand thanks to Edinburgh University for awarding me the PCDS scholarship and my mentor Catherine for allowing me to 'break the data'.

At the IfA I'd like to thank Ken, Philip, Beth and Jim in particular and also Tania, Olivia and co. next door. I really appreciate all the support.

And Trish, I wouldn't have made it without you.

Cheers ya'll.

Contents

Lay Summary iii

Abstract v

Declaration vii

Acknowledgements ix

Contents xi

List of Figures xv

List of Tables xxiii

1 Introduction 1
- 1.1 AGN summary . . . 2
- 1.2 The accretion disc . . . 5
- 1.3 The BLR . . . 7
- 1.4 AGN variability . . . 10
  - 1.4.1 Extreme variables . . . 11
  - 1.4.2 Searching for extreme transients . . . 14
- 1.5 AGN microlensing . . . 16
  - 1.5.1 Microlensing introduction . . . 16
- 1.6 Thesis outline . . . 23

2 Observations, data reduction and modelling 25
- 2.1 Photometric observations . . . 26
  - 2.1.1 SDSS . . . 26
  - 2.1.2 Pan-STARRS . . . 26
  - 2.1.3 Liverpool Telescope . . . 27
  - 2.1.4 CRTS . . . 28
  - 2.1.5 Broad-band filter approximation and light curves . . . 28
  - 2.1.6 PS1 transient sample . . . 29
- 2.2 Spectroscopic observations . . . 29
  - 2.2.1 WHT . . . 29
  - 2.2.2 MMT . . . 31
  - 2.2.3 SDSS/BOSS . . . 31
- 2.3 Spectroscopic reduction pipeline . . . 33

2.3.1 Pipeline overview . . . 33
2.3.2 Bias correction and flat-fielding . . . 36
2.3.3 Cosmic-ray removal . . . 37
2.3.4 Aperture extraction . . . 38
2.3.5 Wavelength calibration . . . 39
2.3.6 Flux calibration and combining . . . 40
2.3.7 Error-map generation . . . 45
2.4 PS1-A AGN transient sample . . . 45
2.4.1 Re-scaling spectroscopic epochs . . . 47
2.4.2 De-reddening and composite model fitting . . . 48
2.5 Microlensing models and analysis techniques . . . 50
2.5.1 Point-source point-lens model . . . 50
2.5.2 Extended sources . . . 53
2.5.3 Chang-Refsdal models and beyond . . . 55

3 Spectral evolution of 64 long-term AGN transients 59
3.1 Introduction . . . 59
3.2 Outline . . . 59
3.3 Global results . . . 63
3.4 Subsample definitions . . . 71
3.5 Subsample spectral evolution . . . 74
3.5.1 Spectral evolution: 'Simple' . . . 75
3.5.2 Spectral evolution: 'Rounded' . . . 75
3.5.3 Spectral evolution: 'Dipper' . . . 78
3.5.4 Spectral evolution: 'Double' . . . 82
3.6 Detailed spectral evolution: 'Prime' . . . 83
3.6.1 J084305 . . . 83
3.6.2 J094511 . . . 86
3.6.3 J103837 . . . 87
3.6.4 J105502 . . . 89
3.6.5 J110805 . . . 89
3.6.6 J133004 . . . 89
3.6.7 J142232 . . . 92
3.6.8 J150210 . . . 94
3.6.9 J175610 . . . 94
3.6.10 J223210 . . . 96
3.6.11 Summary . . . 97

4 Spectroscopic analysis of four 'hypervariable' AGN: A microneedle in the haystack? 101
4.1 Introduction . . . 102
4.2 Observations . . . 103
4.2.1 Target selection criteria . . . 103
4.2.2 Photometry . . . 104
4.2.3 Spectroscopy . . . 105
4.3 Spectroscopic results . . . 107
4.3.1 J084305 . . . 108

4.3.2 J094511 . . . 112
4.3.3 J142232 . . . 113
4.3.4 J103837 . . . 114
4.4 Microlensing models: techniques . . . 116
4.5 Microlensing models: results . . . 116
4.5.1 Point-source point-lens model . . . 116
4.5.2 Extended source models . . . 118
4.5.3 Lensing plus external shear . . . 122
4.6 Discussion . . . 125
4.6.1 Continuum variability . . . 125
4.6.2 Accretion disc: point-source or extended? . . . 127
4.6.3 BLR . . . 128
4.6.4 Lensing system . . . 130
4.6.5 Future work . . . 132
4.7 Conclusions . . . 133
4.8 Supplementary data . . . 134

5 AGN transients under a simple lens: full sample analysis 141
5.1 Introduction . . . 141
5.2 Refining the simple microlensing analysis . . . 142
5.3 Results of comprehensive analysis . . . 144
5.4 Discussion of the six best performing simple objects . . . 146
5.4.1 J083714 . . . 146
5.4.2 J083544 . . . 147
5.4.3 J084305 . . . 148
5.4.4 J235635 . . . 148
5.4.5 J164740 . . . 151
5.4.6 J143531 . . . 153
5.5 Simple microlensing: notable failures . . . 153
5.5.1 J105502 . . . 155
5.5.2 J111547 . . . 155
5.5.3 J155427 . . . 157
5.5.4 J094511: not as simple as first thought . . . 158
5.6 Extended source under a point-lens: J155427 case study . . . 160
5.7 Extended source under a complex lens . . . 164
5.8 Next steps . . . 165

6 Sharov 21: the remarkable AGN flare 167
6.1 Introduction . . . 167
6.2 Sharov 21: simple microlensing MCMC results . . . 168
6.3 Discussion . . . 170

7 Summary and conclusion 179
7.1 PS1 'slow-blue' AGN transient sample . . . 179
7.1.1 Sharov 21 . . . 181
7.2 Future work . . . 182

A Spectra **185**

B Light curves **251**

C StarsightVR **285**
C.1 Introduction 285
C.2 'StarsightVR' 285
C.3 Update: September 2017 289

Bibliography **291**

List of Figures

(1.1) Type-I SED reproduced from Richards et al. (2006) which includes useful power-law slopes for comparison. 3
(1.2) Type-I UV-optical composite spectrum of 718 quasars from the Large Bright Quasar Survey, reproduced from Francis et al. (1991). 4
(1.3) A changing look AGN, from Seyfert 1-1.8. Note the disappearance of Hβ and reduction in UV continuum over a period of several years. Reproduced from Shappee et al. (2014). 14
(1.4) Schematic of a gravitational lens system. Reproduced from Meylan et al. (2006). 18
(1.5) The left panel shows a binary caustic for two equal masses with separation $\theta_{\rm E}$ and four different tracks for an extended source of radius $\theta = 0.05\,\theta_{\rm E}$. The right panel shows the corresponding light curve, offset by one magnitude for clarity. Reproduced from Wambsganss (2006). 18
(1.6) Two independently generated microlensing magnification maps giving a comparison of varying optical depth while keeping the external shear and smooth matter fraction constant ($\gamma = 0.1$, $s = 0.0$). Left: $\kappa = 0.1$, Right: $\kappa = 0.6$. Magnification maps reproduced from the GERLUMPH database (Vernardos et al., 2015). 20
(1.7) An example of the magnification maps and source path used to reproduce the observed light curves for each quasar image in the Einstein Cross: Q2237+0305. Reproduced from Kochanek (2004). 21
(1.8) An illustration of chromatic microlensing due to a caustic crossing event for an accretion disc with a radial emission profile. The longer wavelength radiation rises faster but peaks lower and later than the shorter wavelength. Here ξ is a measure of the distance from the centre of the disc to the caustic as a ratio of the disc size. Reproduced from Mosquera et al. (2009). 22

(2.1) Raw, full-length images obtained for target J223210 on 9/9/13. Blue arm on top, red arm below. 34
(2.2) Normalized flat fields generated from the calibration observations on 9/9/13. Blue arm on top, red arm below. 34
(2.3) Bias-corrected, flat-fielded, cosmic-ray subtracted images for target J223210 on 9/9/13. Blue arm on top, red arm below. . . 34

(2.4) Zoomed portion of the raw spectra obtained for target J223210 on 9/9/13. Blue arm on top, red arm below. Note the sky lines, cosmic ray hits and evidence for narrow-line emission in the red-arm AGN trace (right of center). 35
(2.5) Zoomed portion of the master bias frames generated from the calibration images obtained on 9/9/13. Blue arm on top, red arm below. Note the additional structure in the red arm bias, the result of a problematic bias frame in this region which was not excluded before combining. With a combined total of 20 bias frames, the overall effect is very slight. 36
(2.6) Zoomed portion of the normalized flat fields generated from the observations on 9/9/13. Blue arm on top, red arm below. In this region of the spectra, the red arm is relatively featureless whereas there is some notable structure in the blue. 37
(2.7) Zoomed portion of the bias-corrected, flat-fielded, cosmic-ray extracted images for target J223210 on 9/9/13. Blue arm on top, red arm below. 38
(2.8) Sensfunc produced for one of the standards on 9/9/13. Note the sharp decline in the function at the inner 'wings'. The wavelength ranges used for the red/blue arms and inner wings are as follows: 3100-5100Å(blue curve); 4900-5350Å(green); 5250-5700Å(yellow); 5500-10600Å(red). The grey shaded areas are less certain due to the lack of available standard star data in this region. 42
(2.9) Final combined spectrum for target J223210 on 9/9/13. The vertical lines indicate the location of prominent telluric features. The dip seen in Hβ is due to a cosmic ray hit that has not been subtracted particularly well. 44
(2.10) A test of the validity of an error map produced using the error combination script. Plotted in red are the residuals to a continuum-subtracted region of featureless spectrum for target J142232 on 23/4/15 (average of 4x1800s exposures). In green is a normal distribution with a width equal to the mean sigma in the generated error map for this same region. The two appear to agree well. 46
(2.11) Example scaling fit to target J094511. The spectral epochs in red are the estimated LT g-band magnitudes. Those in green are the rescaling points to the cubic spline fit to the LT light curve shown. 48
(2.12) Example of the fitting process for target J094511. The components include the following: power-law (green), Gaussian line fits (magenta), convolved iron template (cyan) and overall best fit (red). 49
(2.13) Example simple microlensing light curves showing the expected magnification vs timescale for various impact parameters. Reproduced from Wambsganss (2006). 52

(2.14) Plot of the Chang-Refsdal shear parameter, γ, against total galaxy mass for selected star-galaxy distances. Here, the lens redshift is assumed to be 0.2 and the source redshift 1. 57

(3.1) Example of fit to the Hβ region obtained for target J014139 on 22/10/16. Line and continuum components are shown as green solid/dashed lines respectively, the Fe contribution is in cyan and the complete fit is shown in red. This includes a two-component fit for the Hβ line and the discontinuity near HeII$_{4686}$ at $\sim$ 7600Å is due to a telluric mask. 61
(3.2) Distribution of various parameters for the PS1 AGN transient sample. See Section 3.2 for more information. 65
(3.3) Derived black-hole mass vs bolometric luminosity for the entire sample. The points are coloured to reflect the slope of the measured power-law fit in the UV. Every spectral epoch is plotted and data for individual AGN are linked via a grey line. 66
(3.4) Selection of the 'Prime' subsample based on significant spectroscopic changes over the duration of the observing campaign. . . 72
(3.5) Light curve for J105502 including SDSS, CRTS, DVO, LT data. An example of the 'Simple' subsample. Figure credit: CM . . . 72
(3.6) Light curve for J155427 including SDSS, CRTS, DVO, LT data. An example of the 'Rounded' subsample. Figure credit: CM . . 73
(3.7) Light curve for J223210 including SDSS, CRTS, DVO, LT data. An example of the 'Dipper' subsample. Figure credit: CM . . . 73
(3.8) Light curve for J150042 including SDSS, CRTS, DVO, LT data. An example of the 'Double' subsample. Figure credit: CM . . . 74
(3.9) Rest-frame equivalent widths plotted against the monochromatic continuum luminosity at 1450Å . Trend lines are shown for $f_{\rm line} \propto f_{\rm cont}^{\alpha}$ for given values of α. 76
(3.10) Power-law slopes from the UV and optical regions plotted against the monochromatic continuum luminosity at 1450Å 77
(3.11) Rest-frame equivalent widths plotted against the monochromatic continuum luminosity at 1450Å . Trend lines are shown for $f_{\rm line} \propto f_{\rm cont}^{\alpha}$ for given values of α. 79
(3.12) Power-law slopes from the UV and optical regions plotted against the monochromatic continuum luminosity at 1450Å 80
(3.13) Rest-frame equivalent widths plotted against the monochromatic continuum luminosity at 1450Å . Trend lines are shown for $f_{\rm line} \propto f_{\rm cont}^{\alpha}$ for given values of α. 81
(3.14) Power-law slopes from the UV and optical regions plotted against the monochromatic continuum luminosity at 1450Å 82
(3.15) Rest-frame equivalent widths plotted against the monochromatic continuum luminosity at 1450Å . Trend lines are shown for $f_{\rm line} \propto f_{\rm cont}^{\alpha}$ for given values of α. 84
(3.16) Power-law slopes from the UV and optical regions plotted against the monochromatic continuum luminosity at 1450Å 85

(3.17) Evolution of various parameters in the 'Prime' subsample. Top row: continuum values (f_{3000}, f_{5000}) and Fe template scaling relative to the maximum epoch and power-law slopes - cyan: UV, magenta: Optical. Bottom/middle rows: Line fluxes/FWHM/EW (blue/red/green) relative to the maximum epoch. 86

(3.18) Evolution of various parameters in the 'Prime' subsample. Top row: continuum values (f_{3000}, f_{5000}) and Fe template scaling relative to the maximum epoch and power-law slopes - cyan: UV, magenta: Optical. Bottom/middle rows: Line fluxes/FWHM/EW (blue/red/green) relative to the maximum epoch. 87

(3.19) Evolution of various parameters in the 'Prime' subsample. Top row: continuum values (f_{3000}, f_{5000}) and Fe template scaling relative to the maximum epoch and power-law slopes - cyan: UV, magenta: Optical. Bottom/middle rows: Line fluxes/FWHM/EW (blue/red/green) relative to the maximum epoch. 88

(3.20) Evolution of various parameters in the 'Prime' subsample. Top row: continuum values (f_{3000}, f_{5000}) and Fe template scaling relative to the maximum epoch and power-law slopes - cyan: UV, magenta: Optical. Bottom/middle rows: Line fluxes/FWHM/EW (blue/red/green) relative to the maximum epoch. 90

(3.21) Evolution of various parameters in the 'Prime' subsample. Top row: continuum values (f_{3000}, f_{5000}) and Fe template scaling relative to the maximum epoch and power-law slopes - cyan: UV, magenta: Optical. Bottom/middle rows: Line fluxes/FWHM/EW (blue/red/green) relative to the maximum epoch. 91

(3.22) Evolution of various parameters in the 'Prime' subsample. Top row: continuum values (f_{3000}, f_{5000}) and Fe template scaling relative to the maximum epoch and power-law slopes - cyan: UV, magenta: Optical. Bottom/middle rows: Line fluxes/FWHM/EW (blue/red/green) relative to the maximum epoch. 92

(3.23) Evolution of various parameters in the 'Prime' subsample. Top row: continuum values (f_{3000}, f_{5000}) and Fe template scaling relative to the maximum epoch and power-law slopes - cyan: UV, magenta: Optical. Bottom/middle rows: Line fluxes/FWHM/EW (blue/red/green) relative to the maximum epoch. 93

(3.24) Evolution of various parameters in the 'Prime' subsample. Top row: continuum values (f_{3000}, f_{5000}) and Fe template scaling relative to the maximum epoch and power-law slopes - cyan: UV, magenta: Optical. Bottom/middle rows: Line fluxes/FWHM/EW (blue/red/green) relative to the maximum epoch. 95

(3.25) Evolution of various parameters in the 'Prime' subsample. Top row: continuum values (f_{3000}, f_{5000}) and Fe template scaling relative to the maximum epoch and power-law slopes - cyan: UV, magenta: Optical. Bottom/middle rows: Line fluxes/FWHM/EW (blue/red/green) relative to the maximum epoch. 96

(3.26) Evolution of various parameters in the 'Prime' subsample. Top row: continuum values (f_{3000}, f_{5000}) and Fe template scaling relative to the maximum epoch and power-law slopes - cyan: UV, magenta: Optical. Bottom/middle rows: Line fluxes/FWHM/EW (blue/red/green) relative to the maximum epoch. 97

(4.1) Left-hand panels: composite light curves for each target including spectral epochs. The open circles show the raw spectral magnitudes before rescaling as per Section 4.2.3 and the green circles show the rescaled values. CRTS data have offsets of +0.1/0.1/0.4/0.2 mag, respectively. The extended tails on the error bars for J084305 and J094511 reflect the errors used in the microlensing analysis. Right-hand panels: relative fluxes of the various measured spectral components. For the first three targets, the fourth panel shows the CIII]/MgII ratio. For J103837, the two Gaussian components used in the fit (broad and wide) are displayed. Asterisks denote less reliable values as noted in the text. The green dashed line reflects the continuum under CIII] in each case. 109

(4.2) Left-hand panels: velocity offsets for the centre of the measured line profiles for each target assuming rest-frame wavelengths, in Å, of the following: CIV(1549); CIII](1909); MgII(2800); [OII](3727); H β/[OIII](4861/5007). The AGN systemic redshift/velocity is determined from the median of the [OII] centres. In the case of J142232, due to a lack of observed narrow lines, MgII has been used. The error bars in this case only reflect the uncertainty in the measured line centre and omit the additional systemic velocity uncertainty. The FWHM of CIV for J142232 is not shown as this value was tied to that of CIII] in the fitting process. Right-hand panels: FWHM of the measured line profiles for each target. 110

(4.3) Left-hand panels: CIII] and MgII profiles for each object. For J103837, the profile is truncated due to the blue arm cut-off. Right-hand panels: additional emission line profiles measured in the fitting process. For clarity, all plots, barring those for [OII], have had a median filter applied. 111

(4.4) Fourth spectral epoch for J142232 highlighting the narrow absorption features seen. These are consistent with MgII/FeII absorption at a lower redshift or possibly an outflow intrinsic to the AGN. A similar MgII/FeII feature is seen nearer the blue wing of the MgII broad line though in this case only the MgII doublet is readily visible. 114

(4.5) Third spectral epoch for J103837 highlighting the narrow absorption feature. It is consistent with an MgII doublet at a lower redshift than the AGN. 115

(4.6) Extended source model light curves for J084305. The grey data are the original photometry points and the vertical lines are the spectral epochs. The source sizes are listed in Table 4.6. The dashed line represents the AGN base flux. 120
(4.7) Evolution of extended model fluxes relative to the first spectral epoch. Overplotted are the spectroscopic measurements of CIII] and MgII. The source sizes are listed in Table 4.7. 121
(4.8) Chang-Refsdal lens model light curves for J142232. The grey data are the original photometry points, the darker points are the LT epochs. The source sizes are listed in Table 4.9. The dashed line represents the AGN base flux. 124
(4.9) Magnification map and source/track to produce the thin-disc light curve shown in Fig. 4.8. 124
(4.10) Spectra for J084305 as produced by my reduction pipeline. They have been scaled to our microlensing model (4.5.1) and are corrected for Milky Way reddening. The red lines show the best-fitting models from the fitting process. 135
(4.11) Spectra for J094511 as produced by my reduction pipeline. They have been scaled to our microlensing model (4.5.1) and are corrected for Milky Way reddening. The red lines show the best-fitting models from the fitting process. 135
(4.12) Spectra for J142232 as produced by my reduction pipeline. They have been scaled to our LT data (4.2.3) and are corrected for Milky Way reddening. The red lines show the best-fitting models from the fitting process. Inset is a zoomed region of the central portion of the fourth epoch to highlight the absorption complex. 136
(4.13) Spectra for J103837 as produced by my reduction pipeline. They have been scaled to our LT data (4.2.3) and are corrected for Milky Way reddening. The red lines show the best-fitting models from the fitting process. 136
(4.14) Corner plot from the MCMC analysis showing the one- and two-dimensional posterior probability distributions for J084305. . . . 138
(4.15) Corner plot from the MCMC analysis showing the one- and two-dimensional posterior probability distributions for J094511. . . . 139

(5.1) Top: Simple microlensing model for J083714. Full parameter constraints are displayed in Table 5.3. Also displayed are the ranking parameters described in Section 5.3. Bottom: Residuals to the fit with the highlighted region reflecting the location of the data points corresponding to the ranking parameter r. . . . 147
(5.2) Top: Simple microlensing model for J083544. Full parameter constraints are displayed in Table 5.4. Also displayed are the ranking parameters described in Section 5.3. Bottom: Residuals to the fit with the highlighted region reflecting the location of the data points corresponding to the ranking parameter r. . . . 149

(5.3) Top: Simple microlensing model for J084305. Full parameter constraints are displayed in Table 5.5. Also displayed are the ranking parameters described in Section 5.3. Bottom: Residuals to the fit with the highlighted region reflecting the location of the data points corresponding to the ranking parameter r. . . . 150

(5.4) Top: Simple microlensing model for J235635. Full parameter constraints are displayed in Table 5.6. Also displayed are the ranking parameters described in Section 5.3. Bottom: Residuals to the fit with the highlighted region reflecting the location of the data points corresponding to the ranking parameter r. . . . 151

(5.5) Top: Simple microlensing model for J164740. Full parameter constraints are displayed in Table 5.7. Also displayed are the ranking parameters described in Section 5.3. Bottom: Residuals to the fit with the highlighted region reflecting the location of the data points corresponding to the ranking parameter r. . . . 152

(5.6) Top: Simple microlensing model for J143531. Full parameter constraints are displayed in Table 5.8. Also displayed are the ranking parameters described in Section 5.3. Bottom: Residuals to the fit with the highlighted region reflecting the location of the data points corresponding to the ranking parameter r. . . . 154

(5.7) Top: Simple microlensing model for J105502. Full parameter constraints are displayed in Table 5.9. Also displayed are the ranking parameters described in Section 5.3. Bottom: Residuals to the fit with the highlighted region reflecting the location of the data points corresponding to the ranking parameter r. . . . 156

(5.8) Top: Simple microlensing model for J111547. Full parameter constraints are displayed in Table 5.10. Also displayed are the ranking parameters described in Section 5.3. Bottom: Residuals to the fit with the highlighted region reflecting the location of the data points corresponding to the ranking parameter r. . . . 157

(5.9) Top: Simple microlensing model for J155427. Full parameter constraints are displayed in Table 5.11. Also displayed are the ranking parameters described in Section 5.3. Bottom: Residuals to the fit with the highlighted region reflecting the location of the data points corresponding to the ranking parameter r. . . . 159

(5.10) Top: Simple microlensing model for J094511. Full parameter constraints are displayed in Table 5.12. Also displayed are the ranking parameters described in Section 5.3. Bottom: Residuals to the fit with the highlighted region reflecting the location of the data points corresponding to the ranking parameter r. . . . 160

(5.11) Light curve for J155427 and model fit obtained from the low-resolution MCMC microlensing analysis. 162

(5.12) Corner plot from the low-resolution MCMC microlensing analysis for J155427. 163

(6.1) MCMC walker plot for Sharov21 which failed to converge. Each panel shows one of the parameters used in the model. Left, from top to bottom: z_d, M_l, $v \perp$, y_0. Right, from top to bottom: t_0, F_s, F_b. Units as per Table 6.1 169
(6.2) MCMC walker plot for Sharov21 which performs better than the previous attempt. Each panel shows one of the parameters used in the model. Left, from top to bottom: $\log(z_d)$, M_l, $v \perp$, y_0. Right, from top to bottom: t_0, F_s, F_b. Units as per Table 6.1 . . 171
(6.3) Corner plot for the successful MCMC run for Sharov21. Note that the values for the lens redshift are in $\log(z_d)$. 172
(6.4) Full light curve and residuals to the microlensing fit for Sharov 21, using the data supplied by Meusinger et al. (2010). Fit parameters, as defined in Chapter 5, are also displayed. 173
(6.5) Zoomed-in portion of the light curve for Sharov 21 showing the main transient event and residuals to the microlensing fit. Fit parameters, as defined in Chapter 5, are also displayed. 174
(6.6) PHAT colour composites for Sharov21, highlighted with a red cross. Left: ACS/WFC F814W/F475W; right: ACS/WFC F160W/F110W. The cutouts are approximately 10 arcseconds across. 175
(6.7) Sharov 21 location, with respect to 'Brick 08' in the PHAT survey, marked with a red cross. North is up, East is left. The projected size is $\sim 1.5\,\mathrm{kpc} \times 3\,\mathrm{kpc}$ ($\sim 6.6' \times 13'$). 176

(C.1) A single Oculus Rift DK2 headset running StarsightVR. 286

List of Tables

(1.1) Reverberation mapping result for NGC 5548 taken from Peterson (2008). Lags are relative to the UV continuum at ~ 1350 Å and $F_{\rm var}$ is the variability amplitude as an rms fractional variation, corrected for measurement uncertainties. 8

(2.1) WHT observation nights and number of target spectra obtained for the PS1-A sample and other targets (O), respectively. Also noted are the nights for which I was present as an observer. . . . 32

(2.2) Spectroscopic epochs for the PS1-A sample currently available from SDSS/BOSS. 33

(2.3) Free parameters in the simple microlensing model. 51

3.1 A selection of observed and derived parameters for all targets. (1-4) Target Identifier, position and no. of spectral epochs. (5) Milky Way extinction values. (6) Mean redshift. (7) SDSS earliest g-band epoch minus the LT peak g-band epoch. (8)/(9) Max/min values for the monochromatic luminosity. (10)/(11) Max/min values for MgII rest-frame equivalent width. (12) Minimum black hole mass. (13) Minimum bolometric luminosity. (14) Maximum Eddington fraction ($L_{\rm bol}/L_{\rm Edd}$). Two targets are missing data, J025633, which has a near-featureless spectrum and J154404, the highest redshift target in the sample, with no reliable MgII detection. 68

(4.1) Summary of the target selection criteria noted in Section 4.2.1 . 104

(4.2) Details of the spectral observations carried out for the objects listed here. The airmass values reflect the mean airmass over the duration of the observation(s). Magnitudes estimates are approximations based on the LT photometry. Seeing estimates reflect the range in measured full width at half maximum (FWHM) of the central region of the blue arm trace for each image. 106

(4.3) Information on the targets in this section. The A_V values are those obtained from Schlafly & Finkbeiner (2011) assuming an R_V of 3.1. 107

(4.4) Parameter estimates obtained from the MCMC analysis, including the Einstein radius in the source plane, for J084305. The model using these marginalized parameters, assuming a negligible background flux, produces a fit to the data with a reduced chi-squared value of 0.69 and has an Einstein radius of 12.1 light-days. Parameter definitions are as per Table 2.3. 117

(4.5) Parameter estimates obtained from the MCMC analysis, including the Einstein radius in the source plane, for J094511. The model using these marginalised parameters, assuming a negligible background flux, produces a fit to the data with a reduced chi-squared value of 1.14 and has an Einstein radius of 12.8 light-days. Parameter definitions are as per Table 2.3. 118

(4.6) Empirical estimates for the accretion-disc sizes for J084305, calculated as per Section 2.5.2. 119

(4.7) Estimated CIII] and MgII sizes for J084305. They have been determined from the spectroscopic data as per Section 4.5.2. The errors here reflect the fitting process only. 120

(4.8) Empirical estimates for the accretion-disc sizes for J094511, calculated as per Section 2.5.2. 122

(4.9) Empirical estimates for the accretion-disc sizes for J142232, calculated as per Section 2.5.2. 123

(4.10) Damped-random-walk parameters obtained for J084305 and J094511. The values have been computed for the observed data and the residuals after subtraction of the microlensing model. . . 126

(4.11) Data table. (1) Scaling correction factor applied to the spectrum as described in 4.2.3. (2) Power law slope from the fit given by Eq. 2.1. (3) Observed AGN monochromatic continuum flux at rest-frame 3000Å calculated from the power-law fit to the UV region. (4) AGN monochromatic continuum luminosity derived from (2). (5)/(6)/(7) Line centre, sigma and total line flux from the Gaussian fit to MgII in the observed frame. For J103837 the values are from the narrower of the two broad MgII components. (8) Black hole mass calculated using the McLure & Dunlop (2004) relation. Errors are from the fitting process only. 137

(5.1) Comparison between parameter estimates from the simple microlensing MCMC results for target J084305. The analysis for this chapter included the latest photometry and updated priors as detailed in Section 5.2 143

5.2 Parameters used for ranking the resulting MCMC best-fit simple microlensing models for the entire AGN transient sample, sorted by χ^2_ν. This includes J025633 with no confirmed redshift (assumed $z = 1$ in the analysis). Parameter definition as per Section 5.3 with favoured simple microlensing candidates in bold. [1]Objects originally classified as per Chapter 3 but excluded from that analysis due to an insufficient sampling of spectroscopic epochs. [2]NVSS detections, i.e. radio-loud objects. 145
(5.3) Parameter constraints from the MCMC analysis for J083714. . . 148
(5.4) Parameter constraints from the MCMC analysis for J083544. . . 148
(5.5) Parameter constraints from the MCMC analysis for J084305. . . 149
(5.6) Parameter constraints from the MCMC analysis for J235635 . . 152
(5.7) Parameter constraints from the MCMC analysis for J164740. . . 153
(5.8) Parameter constraints from the MCMC analysis for J143531. . . 153
(5.9) Parameter constraints from the MCMC analysis for J105502. . . 156
(5.10) Parameter constraints from the MCMC analysis for J111547. . . 158
(5.11) Parameter constraints from the MCMC analysis for J155427. . . 158
(5.12) Parameter constraints from the MCMC analysis for J094511. . . 161

(6.1) Parameter constraints for the Sharov21 event from the simple microlensing MCMC analysis. 170

Chapter 1

Introduction

Since their discovery, Active Galactic Nuclei (AGN) have been the focus of a large amount of research effort in the astronomical community. Efforts to produce a unified model of AGN that describe their myriad observational properties have come a long way but there are a number of uncertainties which still remain (Peterson, 1997; Lawrence, 2012; Netzer, 2015).

The focus for this thesis is on the variability of these enigmatic objects, particularly rare, high-amplitude events. This endeavor began with the serendipitous discovery of a number of high-amplitude, slowly evolving optical transients that spectroscopic follow-up revealed to be AGN (Lawrence et al., 2016). The observed changes in magnitude are at the extreme end of the scale for AGN and offer up clues as to the underlying physical processes involved. In addition to analysing the spectral evolution of this sample, I will also focus on microlensing as one of the possible explanations for the observed variability. That is, the apparent increase in flux of a distant source due to an intervening stellar-mass object crossing near to the line of sight (Wambsganss et al., 1990; Chang & Refsdal, 1984). This can even, in some cases, allow constraints to be placed on the sizes of the emitting regions involved.

Given the wide scope of the ongoing research surrounding AGN, it is prudent to give a brief summary of these objects before focusing on topics which are pertinent to this thesis. Key areas of research are the observational constraints on the morphology and kinematics of the accretion disc and broad line region (BLR) and the variability typically associated with these regions. I will also favour the UV/optical regions of the AGN spectrum as these are the primary wavelengths

available to me from the photometric/spectroscopic monitoring campaign.

1.1 AGN summary

The earliest systematic study of nuclear activity in galaxies was that of Seyfert (1943). Since then, this lower-luminosity class of AGN, where the host galaxy is clearly resolved, have been referred to as Seyfert galaxies. Their more luminous counterparts, the point-source-like quasars, were not confirmed to lie at cosmological distances until a watershed moment in 1963 (Schmidt, 1963; Greenstein, 1963; Hazard et al., 1963; Oke, 1963). It is now generally accepted that accretion onto a central supermassive black hole is what powers these luminous objects which can sometimes outshine their host galaxy by factors of ~ 100.

A defining feature of AGN is that they display broad spectral energy distributions (SEDs) with significant output from the X-ray to sub-mmm and also radio in the case of radio-loud objects (approximately 10% of the AGN population). In addition, type-I AGN display prominent broad emission lines with typical velocity widths $\sim 10,000\,\mathrm{km\,s^{-1}}$ at FWHM. Type-II AGN do not display prominent broad lines or a strong optical-UV continuum. The difference is thought to be due to obscuration of the central source. However, the presence of a BLR can still be revealed through spectropolarimetry (Antonucci & Miller, 1985). Prominent narrow emission lines, such as those seen in HII regions (Balmer lines,[OII],[OIII] etc.), are seen in both type-I and type-II AGN with typical velocity widths $\sim 500\mathrm{km\,s^{-1}}$. Type-I AGN are also variable, showing typical continuum fluctuations in the optical of around $\sim$ 30% which increases as observations move further into the UV. This variability occurs on both short ($\sim$days) and long ($\sim$years) timescales and will be discussed in a later section.

Further subdivisions are possible. Some type-II AGN, rather than being obscured, may not host any broad line region at all and are referred to as 'true' type-II AGN (eg. Tran (2003)). It is possible to characterise an AGN by its accretion efficiency giving rise to 'radiative mode' and 'jet mode' definitions (Heckman & Best, 2014). In the latter case the accretion disc is not radiating efficiently. The presence of jets, and their orientation relative to the observer, also play an important role. If the jet is aligned near to the line of sight, significant non-thermal emission, likely synchrotron radiation, can dominate spectral observations. These jet-dominated

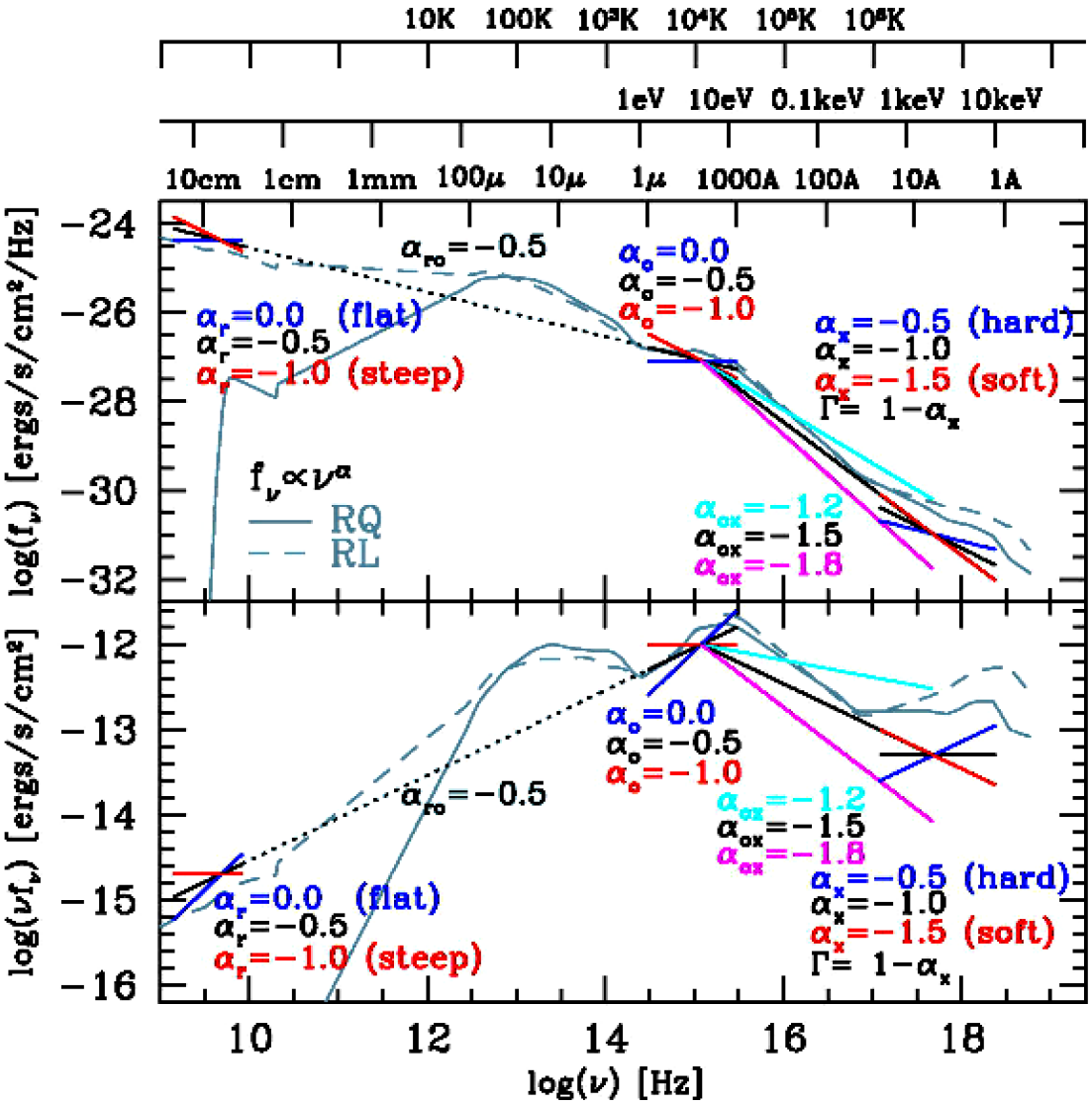

Figure 1.1 *Type-I SED reproduced from Richards et al. (2006) which includes useful power-law slopes for comparison.*

AGN are also significantly more variable and are known as blazars. A key blazar sub-type, termed a BL Lac object, is notable for spectra which display a near-featureless continuum.

The majority of AGN in this thesis can be considered type-I, radiative mode, radio-quiet objects so I will concentrate the discussion in this area. However, six targets from the sample ($\sim 9\%$), do have a viable cross-match in the NRAO VLA Sky Survey (NVSS) (Condon et al., 1998) making these candidates for radio-loud AGN.

Figure 1.1, taken from Richards et al. (2006) shows a typical type-I SED and power-law slopes of the form $F_\nu \propto \nu^\alpha$. The three key features are the X-ray

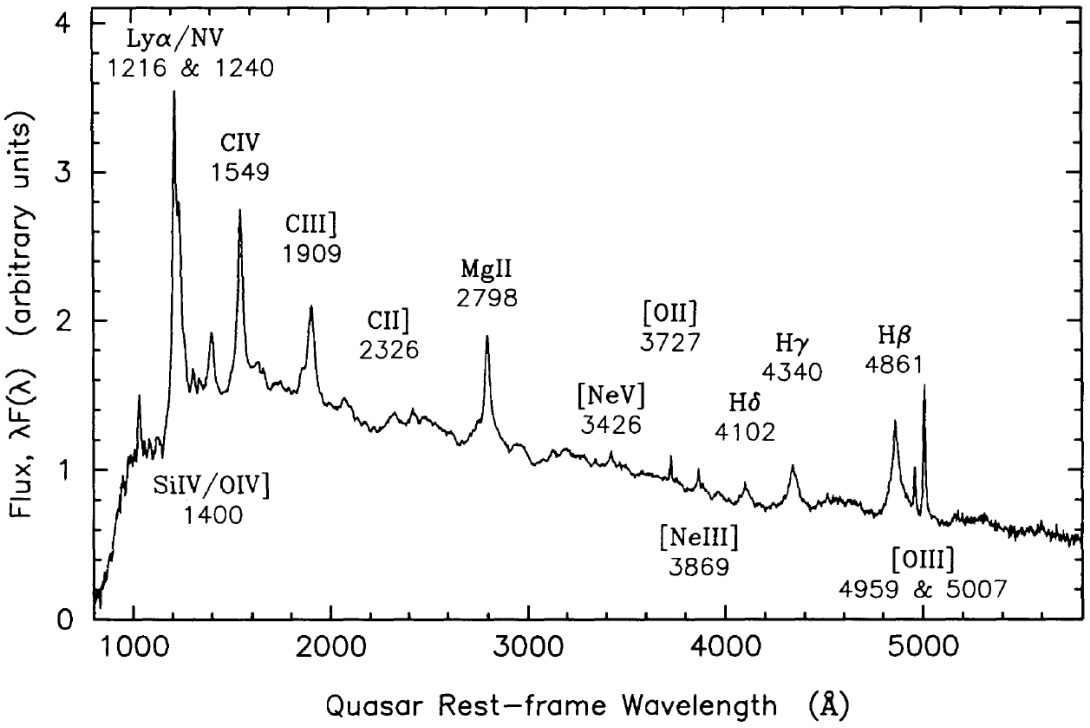

Figure 1.2 *Type-I UV-optical composite spectrum of 718 quasars from the Large Bright Quasar Survey, reproduced from Francis et al. (1991).*

peak, the 'big blue bump' in the optical-UV and the IR-peak redward of the $1\,\mu$m minimum. It should be noted that the exact shape of the big blue bump, blueward of the Lyman limit (13.6 eV), is not well constrained. This is due to the presence of neutral hydrogen in galaxies which effectively makes them opaque to these ionizing photons. Figure 1.2, taken from Francis et al. (1991), shows a composite UV-optical spectrum where the broad emission lines are very clear and are superimposed on a strong continuum which peaks in the UV. Also seen are some prominent narrow lines.

It had long been suspected that the nuclear activity in galaxies has a common origin which has led, over time, to the development of a 'unified model' for AGN (Burbidge et al., 1963; Lawrence, 1987; Antonucci, 1993). Such a treatment allows for the myriad range of observed AGN sub-classes but depends only on a few key parameters. The general picture is that all AGN are driven by accretion onto a central supermassive black hole. Key variables are then the black-hole mass, accretion rate and inclination relative to the observer but all are comprised of essentially the same physical components. These, in approximate order of increasing radius, are: the accreting black hole and X-ray corona; accretion disc; broad-line-region clouds; obscuring dusty 'torus'; narrow-line region. A

simple consequence of geometry (and possible presence of a jet) can thus allow an observer to see many different configurations of the same phenomenon. While this goes some way towards explaining observations, many questions remain, chief among them the nature of the dusty torus, perhaps more accurately described as a clumpy obscuring medium. The current state of the unified interpretation is considered in detail in Netzer (2015).

Further reading on the subject of AGN can be found in the following: Peterson (1997) and Netzer (2013).

1.2 The accretion disc

The central source of an AGN is very likely to be a supermassive black hole that generates prodigious amounts of energy through accretion. It is generally agreed that for the efficient generation of energy, which is required for high luminosity AGN, there must be an accretion disc present. This accretion disc provides a mechanism for the transport of angular momentum outwards whilst allowing the infalling gas to radiate away some of the liberated energy before finally being accreted onto the black hole. The accretion efficiency η is defined as $L = \eta \dot{M} c^2$ and is $\gtrsim 0.01$ in the case of type-I AGN with a typical value thought to be ~ 0.1 or greater (Soltan, 1982; Yu & Tremaine, 2002; Elvis et al., 2002). Another useful concept is the Eddington luminosity L_{E}. This defines the maximum luminosity of an AGN powered by spherical accretion, i.e. before the outward radiation force exceeds the inward gravitational force, as $L_{\mathrm{E}} = 4\pi G c m_{\mathrm{p}} / \sigma_{\mathrm{e}}$. A radius scale which will be of use is the Schwarschild radius $R_{\mathrm{S}} = 2GM/c^2$. A full relativistic treatment shows that around a non-rotating black hole, the inner-most stable circular orbit (ISCO) lies at a distance of $\sim 3\, R_{\mathrm{S}}$. This provides an estimate for the inner edge of the accretion disc. If the black hole spin is taken into account this radius generally decreases and the potential efficiency increases (Netzer, 2013).

The archetypal model for accretion discs around AGN is that of the standard or α disc model (Shakura & Sunyaev, 1973; Pringle & Rees, 1972; Novikov & Thorne, 1973; Frank et al., 2002). It describes a geometrically thin ($H/r < 0.1$), optically thick disc rotating at $\simeq$ Keplerian velocity with a blackbody emission profile that varies with distance from the inner edge of the disc, with $T \propto r^{-3/4}$ ($r \gg r_{\mathrm{in}}$). The radial velocity of the in-falling material is much less than the orbital velocity. The disc is likely turbulent and an α coefficient is used to parametrise the unknowns

relating to the gas dynamics, relating the viscosity in the disc to the local sound speed and scale-height of the accretion disc. The peak emission is expected at radii of $\sim 5\,R_{\rm S}$ and the model only applies to steady-state discs.

This model is lacking in several important respects, many of which are summarised in Koratkar & Blaes (1999) and Lawrence (2012). Peterson (2008) notes that it is a gross oversimplification as it significantly under-predicts the X-ray emission and the prediction of $F_\nu \propto \nu^{1/3}$ in the UV-optical is also not what is observed. In addition, observations of near-simultaneous variability in the UV-optical become hard to explain if the emission peaks at different disc radii for different wavelengths. Blaes (2007) notes that this is due to a lack of reprocessing in the model. For example, the X-ray emission is seen to vary on smaller timescales than the UV-optical which suggests a smaller emitting region, possibly outwith the disc itself. A hot X-ray corona outwith the disc could have a significant effect on the SED due to scattering/heating but the conditions for the formation of such a corona are still unknown (Netzer, 2013). One other problem concerns the observed peak in the SED at $\sim 1100\,\text{Å}$ which implies a peak disc temperature which is cooler than that predicted by the thin disc model (Lawrence, 2012). In the X-ray regime accretion disc models, which take into account the opacity of the inner disc, can provide SED fits and a possible explanation for the origin of the soft X-ray excess and harder power-law tail seen in AGN (Done et al., 2012). The soft excess appears to diminish in importance as the accretion rate increases.

The outer edge of the accretion disc is difficult to define but a natural outer boundary would be where the vertical component of gravity due to the black hole becomes less than the self-gravity of the material, causing it to form clumps (Netzer, 2013). Simple variability arguments, which assume that fluctuations in disc emission cannot propagate faster than the speed of light, also place an upper limit on the disc size. If the disc is too large, any fluctuations would be smoothed out on a disc-crossing timescale. Estimates for the outer boundary are on the order $\sim 1000\,R_{\rm S}$ (Malkan, 1983). This is too small to be directly resolved but there have been some interesting attempts to measure the size of the accretion disc via gravitational microlensing. Results from Morgan et al. (2010) indicate that the thin disc theory prediction for the scaling relationship $R \propto M_{\rm BH}^{2/3}$ agrees with their observations. However, standard thin disc models also predict a radial temperature profile of $T \propto r^{-3/4}$. In the case of the Morgan et al. (2010) microlensing size estimates, a disc with this temperature profile would appear

more luminous than observed for these objects. This leads to a prediction that the accretion disc requires a flatter temperature profile to reconcile these two size estimates. It appears as if accretion disc sizes based on a $T \propto r^{-3/4}$ temperature profile are around a factor of four smaller than actually observed. Microlensing as a method of constraining individual AGN parameters will be discussed in greater detail below.

It is worth noting that the standard disc model works well for stellar mass black holes (Blaes, 2007). More advanced numerical simulations which take magnetic fields, relativistic effects, time dependent parameters and reprocessing into account are not yet able to reproduce all of the observed AGN spectral features. Lawrence (2012) summarises many of the known problems relating to the standard accretion disc interpretation, particularly the observed 'universal' UV peak. Many of the observational issues could be resolved by having a combination of an accretion disc and also a reprocessing medium at radii of $\sim 30\,\mathrm{R_S}$ in the form of dense, fast-moving clouds. The true peak in the SED may lie in the EUV part of the spectrum and the observed peak may instead be 'false', relating instead to blurred emission lines from these clouds. Whilst the model is only preliminary, clouds at a large range of radii from the central source may be a common feature in AGN. There are also possible issues regarding the interpretation of observed lags in NGC 5548. Gardner & Done (2017) show that the observed lags are not simply the light-travel time for either X-ray or FUV reprocessing but rather may be due to changes in the vertical disc structure.

1.3 The BLR

The broad line region (BLR) is the photoionised region responsible for the line emission seen in type-I spectra and is not well understood, particularly in regard to the kinematics of the region. Early estimates for the size of the the BLR (eg. Bahcall & Kozlovsky (1969)) were based on photoionisation equilibrium calculations, with some assumptions regarding densities which allowed for semi-forbidden lines such as CIII]. More recent reverberation mapping (RM) results, from observations of changes in emission line flux, show the BLR to be significantly more compact than these early predictions (Peterson et al., 1985). With RM, a technique first proposed by Blandford & McKee (1982), the cross-correlation between the continuum and emission line light curves confirmed that the BLR is radially stratified, with the higher-ionisation lines originating nearer

Feature	$F_{\rm var}$	Lag (days)
UV continuum	0.321	-
Optical continuum	0.117	$0.6^{+1.5}_{-1.5}$
HeII λ1640	0.344	$3.8^{+1.7}_{-1.8}$
NV λ1240	0.411	$4.6^{+3.2}_{-2.7}$
HeII λ4686	0.052	$7.8^{+3.2}_{-3.0}$
CIV λ1549	0.136	$9.8^{+1.9}_{-1.5}$
Lyα λ1215	0.169	$10.5^{+2.1}_{-1.9}$
SiIV λ1400	0.185	$12.3^{+3.4}_{-3.0}$
Hβ λ4861	0.091	$19.7^{+1.5}_{-1.5}$
CIII] λ1909	0.130	$27.9^{+5.5}_{-3.3}$

Table 1.1 *Reverberation mapping result for NGC 5548 taken from Peterson (2008). Lags are relative to the UV continuum at* $\sim 1350\,\AA$ *and* $F_{\rm var}$ *is the variability amplitude as an rms fractional variation, corrected for measurement uncertainties.*

to the central source. Table 1.1, taken from Peterson (2008), shows the results of one RM study. These estimates assume that the continuum can be treated as a point source and that the dominant timescale is the light travel time which is much longer than the recombination time and much shorter than the dynamical time. Estimates for the radius of the BLR are of the order $\sim 1000\,R_{\rm S}$ and it may even be a natural extension of the outer accretion disc (Gaskell, 2008).

The widths of the emission lines are usually within a factor of ~ 2 of each other and, given that the distances determined by RM change by a factor of ~ 10 (see table 1.1), this requires a range of emission from different radii to explain the observed profiles. There are three key factors to consider. The first is whether the emitting clouds are situated at a narrow range of radii or are distributed throughout the region. The latter case is termed the locally optimally emitting cloud (LOC) model (Baldwin et al., 1995; Korista & Goad, 2000). A second factor is the longevity of the clouds. If not contained by self-gravity or external gas/magnetic pressure then they would likely be destroyed on a sound-crossing timescale and would require replenishing. Indeed, this may help to explain some of the observed variability in AGN (Lawrence, 2012). A third factor is the consideration of winds which might alter the observed line profiles due to motion along the line of sight which is not due to gravitationally bound material. RM studies have seen signs of infalling material (Gaskell, 2008) and blue-shifted absorption features in the UV/X-ray indicate there is at least some outflowing component but there is the freedom for many possible configurations. It is worth noting that in some earlier RM studies there was no detectable lag in the response

of the optical FeII lines to continuum changes (Peterson, 2008), and possibly also for MgII, indicating that these lower ionisation lines are emitted over a large range of radii. More recently reliable MgII lags have been detected in a number of AGN (Shen et al., 2016).

One important observation regarding the BLR is that the relative strength of BLR emission with respect to the continuum is anti-correlated with luminosity. This is commonly referred to as the Baldwin effect (Baldwin, 1977; Zhang et al., 2013). This describes observations of increasing line equivalent width with decreasing AGN luminosity and is observed for many BLR line species, including some narrow lines. There may be a number of explanations for this effect, perhaps due to changes in covering factor, accretion rate, ionising continuum or BLR morphology. A nonlinear BLR response to continuum changes can also manifest as an intrinsic Baldwin effect in individual AGN.

Unfortunately, there are currently no well-defined constraints on the kinematics of the BLR. There are a number of indications that it may display a flattened structure rather than random orbital motions and in some cases shows signs of infalling material (Grier et al., 2013) but this remains to be shown conclusively. There are also indications from microlensing studies that some BLR line species may require multiple components, i.e. physically distinct regions, to reproduce observations (Sluse et al., 2011). This may take the form of an inner disc-shaped region and outer spherical component.

If the regions responsible for the broad lines are assumed to be virialised then they become a useful tool for deriving the mass of the accreting black hole from single epoch spectroscopy using an empirically derived relationship. These radius-luminosity relationships are typically calibrated using low redshift reverberation mapped AGN, where the stellar dynamics allow a check on the derived black hole masses. From Shen & Liu (2012), single epoch estimates using the width of both the Balmer and MgII lines appear to give consistent black hole masses with the scatter, at best $\sim$ 0.3 dex, increasing for lines further into the UV region. This is in part due to the systemic offsets observed in some of these lines, possibly the result of a dynamic, wind-based component. Recently the SDSS reverberation mapping campaign has begun to increase the number of reliable lags for MgII at redshifts greater than 0.3 (Shen et al., 2016). Campaigns such as this are designed to ultimately provide hundreds of lags as opposed to most earlier RM campaigns which have focused on individual objects. It is interesting to note that the measured lags can also vary during individual RM campaigns, an

indication that material further from the ionising source responds most strongly to continuum variations or perhaps a sign of the BLR physically 'breathing' in response to those changes (De Rosa et al., 2015).

1.4 AGN variability

As has been mentioned above, type-I AGN are variable objects on both short and long timescales. Typically the amplitude of the variation will increase with time and also increases at shorter wavelengths. A number of studies have now been performed to help quantify the variability of the observed AGN population. The excellent coverage of the Sloan Digital Sky Survey (SDSS), particularly the stripe 82 quasars where there is better time-sampling, has been particularly fruitful. MacLeod et al. (2010, 2012) uses a statistical model to characterise the variability seen in the SDSS quasar sample. The model in question, which provides a satisfactory description of AGN variability, is commonly termed a damped random walk (DRW). The variability is quantified using a structure function (SF) which is the rms magnitude difference as a function of time lag between measurements. In the case of MacLeod et al. (2010), they conclude that SF_∞, i.e. the variability seen on the longest timescales, is anti-correlated with luminosity and rest-frame wavelength and correlated with $M_{\rm BH}$. These results are borne out in other similar studies (de Vries et al., 2005; Morganson et al., 2014). What is less clear is the evidence for a turnover in the structure function at the longest timescales. Above a characteristic timescale τ, the SF for the DRW would be expected to flatten to a constant value but the observational evidence for this is not conclusive. The variability studies also show that AGN with lower $L/L_{\rm E}$ rates are more variable. It should also be noted that when modeling AGN light curves with a DRW the survey length may not be sufficient to reliably derive AGN parameters (Kozłowski, 2017).

The nature of the underlying mechanism for AGN variability is still very much an open question. It appears that some reprocessing of the X-ray and/or UV primary emission is required to explain observations showing a tight correlation between some continuum bands, on light-travel timescales, but not all observations agree. In the case of NGC 5548, which has been the subject of many multi-band monitoring surveys (Clavel et al., 1991; Korista et al., 1995), the UV and optical continuum variability appears to be strongly correlated. (Korista et al., 1995) notes that the lag between the UV and optical is $<$ 1 lt-day. Similar to

reverberation mapping of the broad line region, these lags can then be used to infer the size of the accretion disc. Broadly speaking, the prediction that longer wavelength emission peaks at greater radii appears to be borne out by observations (Edelson et al., 2015; Fausnaugh et al., 2016). This also appears to be the case in an analysis of the continuum lags for a sample of 200 AGN (Jiang et al., 2017) though they note a number of objects with no reliable lag detections or show 'out-of-order' variation. Some of these may be due to contamination in one or more bands. These lag detections seem to agree with the standard disc prediction that the observed lags are proportional to $\lambda^{4/3}$ but also give estimates for a larger accretion disc size than the standard model. This is also in agreement with a number of microlensing studies, which will be discussed in the next section. Given that the X-rays appear to only correlate weakly with the UV continuum, and in some cases lag behind, the reprocessing is still not clearly understood. Recent results for NGC 5548 imply that a simple reprocessing model is not enough to reconcile the observed X-ray/UV/optical lags (Gardner & Done, 2017). This also appears to be the case in recent observations of NGC 4151 (Edelson et al., 2017).

1.4.1 Extreme variables

On the subject of more extreme variability, MacLeod et al. (2012) note that the probability of an AGN exhibiting a change in magnitude of $\Delta m > 2$, relatively typical of our sample, is less than 1 in 10,000. Average rms fluctuations over longer timescales are on the order of ~ 0.3 mag. One slight drawback is that magnitude changes of $|\Delta m > 3|$ were excluded from this analysis to prevent issues due to poor photometry in the SDSS sample. It may be possible that some genuinely high-amplitude transients were excluded in this way. In general, the DRW model appears to perform well on shorter timescales but there may be issues with extrapolating accurate DRW parameters if the duration of the light curve is $\leq 10 \times \tau$ (Kozłowski, 2017). That being said, it is clear that changes in magnitude of $\Delta m > 2$ are rare in AGN but not impossible.

Sharov 21

One of the clearest examples of an extreme AGN transient event was that observed in M31 in 1992. Over the course of ~ 1 yr Sharov et al. (1998) observed a bright

blue transient and initially attributed it to an extreme nova projected near M31. Follow-up spectroscopy by Meusinger et al. (2010) later confirmed that this event was actually a background AGN at the much greater redshift of $z = 2.109$. The AGN is $21'$, or $\sim 4.8\,\mathrm{kpc}$, from the centre of M31. They carefully reconstructed observational data from a number of telescopes and surveys to provide a light curve for this target with a very long baseline. The time-sampling is not always ideal but it is clear that the transient event looks to be isolated with regards to the AGN background level and only a modest intrinsic scatter of $\sim 0.2\,\mathrm{mag}$ was seen at other epochs. The event peaked at $\Delta m_{\mathrm{B}} \approx 3.3\,\mathrm{mag}$ and the light-curve displayed a near-symmetric profile with a more rapid rise to peak and total duration of $\sim 2\,\mathrm{yr}$.

Meusinger et al. (2010) looked at two possible explanations for the large change in magnitude observed. The first was that the background AGN was magnified due to a microlensing event caused by a lens in M31. They reason this is the more unlikely explanation due to the fact that the optical depth, and hence probability, to microlensing based on the surface mass density of M31 is too low. Their second possible explanation was a tidal disruption event (TDE). This is seen if a star wanders close enough to a supermassive black hole such that the tidal forces are sufficient to disrupt it, leading to some fraction of the material being accreted by the black hole. For these events a UV-optical flare is predicted with a characteristic timescale and luminosity that scales with the mass of the star (see next section also). They note that they require at least a $10\,\mathrm{M}_{\odot}$ star to account for the profile and that current theoretical models for TDEs are based on quiescent black holes rather than AGN. It is uncertain what would happen due to the effects of the AGN accretion disc but their model requires that the perihelion of the star must approach to around $3\,R_{\mathrm{S}}$ which implies there may be a significant effect.

This event will be considered in greater detail in Chapter 6.

Tidal disruption events

Tidal Disruption Events (TDEs) are a catch-all term used to describe the optical transient associated with the disruption of a star which wanders too close to a black hole (Gezari et al., 2012; Arcavi et al., 2014; Chornock et al., 2014). The tidal forces are great enough that the star may be fully disrupted or simply lose a portion of its outer envelope. The disruption and accretion of this stellar envelope

produces an optical flare which peaks rapidly and decays at a slower rate. This decay rate is sometimes assumed to be $\propto t^{-5/3}$ though this need not always be the case (Guillochon & Ramirez-Ruiz, 2013). Spectra taken during these events can be featureless or show supernova-like P-Cygni absorption profiles. They can also sometimes show broad emission features. The lack of significant colour evolution of these events from the initial blue flare is used to disfavour a supernova origin for these events.

The TDE candidate of Gezari et al. (2012) was the first to have well-sampled photometric data on the rise. The observations confirmed that the flare was very blue at the start, decayed on a timescale of months and displayed signatures of broad helium lines at a redshift of $z = 0.17$. The possibility that there might be contamination from a weak AGN is dismissed due to the fact that no narrow lines were present in the spectrum. However, there remains the possibility that a background AGN at the greater redshift of $z \sim 0.96$, if it were being microlensed, might in fact be responsible for the observed lines. CIII] λ1909 and MgII λ2800 would then provide an adequate explanation for the He features to within 10 Å (see Fig.1, Gezari et al. (2012)). The lack of narrow emission lines could then be due to the fact that they are not as prominent in this region of the spectrum, [OII] 3727 would be visible at ~ 6237 Å but may be intrinsically weak. This is all quite speculative but their spectra and light-curves are qualitatively similar to the confirmed AGN transients in this thesis.

'Changing look' AGN

Some AGN, in addition to photometric variability, can display significant changes in their spectra over extended periods. If there are two or more widely spaced spectral epochs available, it is possible to identify a subset of highly variable AGN known as 'changing-look' AGN. That is, over time, an appearance/disappearance of the some or all of the broad lines, particularly the Balmer lines, leading to a change in classification from type I<>II. Intermediate stages such as type 1.8/1.9 (no broad Hβ but broad Hα) are also sometimes used. These changes have been known about for some time, with the early examples being from nearby, and hence lower luminosity, AGN (Khachikian & Weedman, 1971; Aretxaga et al., 1999; Shappee et al., 2014). More recently, similar spectroscopic changes have been seen in a number of higher luminosity objects and the availability of wide-field spectroscopic survey data has enabled a more systematic search (LaMassa

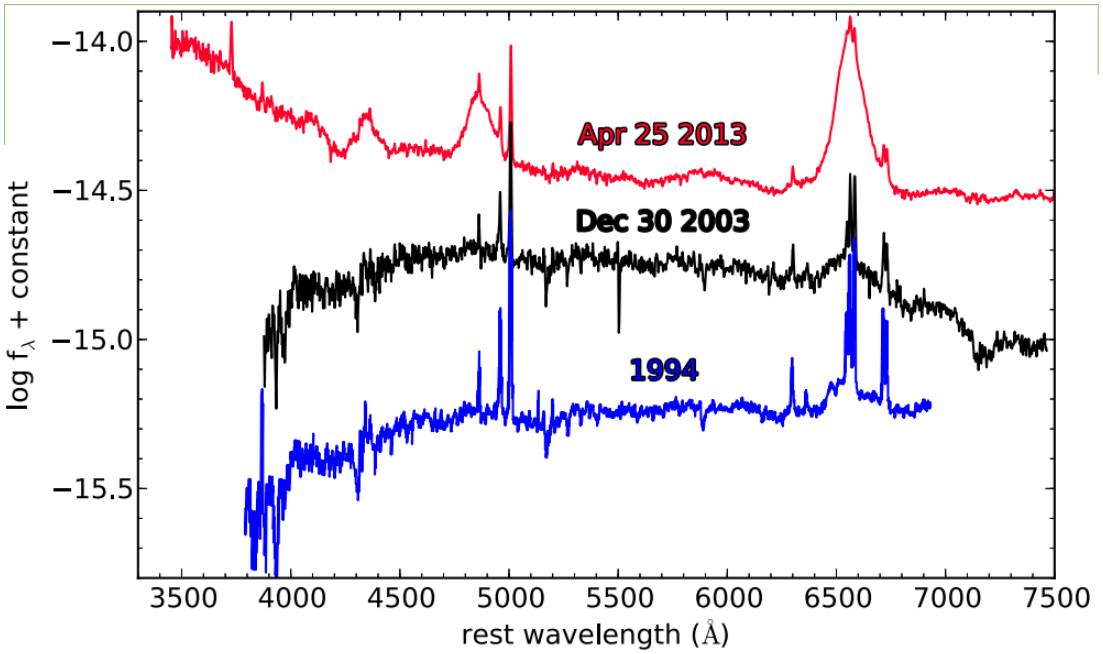

Figure 1.3 *A changing look AGN, from Seyfert 1-1.8. Note the disappearance of Hβ and reduction in UV continuum over a period of several years. Reproduced from Shappee et al. (2014).*

et al., 2015; MacLeod et al., 2016; Runnoe et al., 2016).

These spectral changes are usually accompanied by a substantial change in the light curve, though the term 'changing look' tends to be reserved for objects displaying BLR changes in addition to photometric variability. The mechanism behind this variability is not understood but is currently thought to be connected to a change in accretion rate. Another possibility is that they are due to obscuration events, perhaps caused by a dust-cloud in close proximity to the source. The dynamical timescale for such an obscuration event could be on the order required for these objects but this does not appear to provide a satisfactory explanation for the changes seen in the both continuum and BLR (MacLeod et al., 2016). It remains to be seen whether, over time, all AGN are capable of exhibiting this type of behaviour.

1.4.2 Searching for extreme transients

The study of general AGN variability tends to involve either focused observation campaigns on single objects or ensemble data from wide-field surveys. The cadence of wide-field surveys such as SDSS (with the exception of stripe-82), is typically less than ideal for transient identification. The focus with most

dedicated transient surveys, in addition to locating new solar system bodies, tends to be on supernovae and/or tidal disruption events, i.e. those with fast-rises and slower decay, and typical timescales on the order of ∼months. However, any systematic searches for optical transients will, in general, also include extremely variable AGN in the sample. Some notable examples are the Palomar Transient Factory (PTF, Law et al. (2009)), the All Sky Automated Survey for SuperNovae (ASAS-SN, Holoien et al. (2017)) and Time Domain Spectroscopic Survey (TDSS, Ruan et al. (2016)) which actually includes repeat visits on variable quasars as part of its remit.

The Pan-STARRS 3π survey (Magnier et al., 2013) has proved to be an excellent all-purpose resource and it is this data which is primarily responsible for identifying the AGN transients described in this thesis. The transient identification was carried out via the Faint Galaxy Supernova Search (FGSS) run by QUB[1] (Inserra et al., 2013). This work included a search tailored towards the detection of tidal disruption event candidates around quiescent black holes. The nightly data from Pan-STARRS was cross-matched with sources within the SDSS DR7 (Abazajian et al., 2009) footprint in order to identify any new transients. Selection as a possible TDE candidate required that a PS1 object be coincident with an SDSS 'galaxy' (within 0.5") and to display at least a 1.5 mag change in any given filter vs the SDSS epoch. Additional magnitude constraints required that the PS1 object be brighter than magnitude 20 and the SDSS object be within the magnitude range 18-23 in any given filter. This resulted in several thousand candidate events per month which were eye-balled to remove false positives and identify the most promising candidates for follow-up photometry/spectroscopy.

The comparison of the Pan-STARRS sources with those in SDSS (instead of the delayed PS1 year 1 source catalogue) was somewhat serendipitous as it transpires that approximately two-thirds of the flagged TDE candidates were, in fact, slowly evolving type-I AGN transients. In Lawrence et al. (2016), which also provides further details on the selection criteria and follow-up photometry, these are referred to as the 'slow-blue', and/or 'hypervariable', AGN transients, ie. type-I AGN displaying a relatively smooth factor ~ 10 increase in brightness over a timescale of ~ 10 years. Since this work was carried out a number of additional AGN transients have been confirmed. The complete 'PS1-A' AGN transient sample, which forms the basis for this thesis, will be detailed in Chapter 2.

[1]Queen's University Belfast

A notable recent paper has also identified a number of long-term AGN transients in data taken with the Catalina Real-time Transient Survey (Graham et al., 2017). Many of these are similar to the transients in this thesis. Of the single-peaked events, there does not appear to be a preference for a fast-rise, slow-decay over a slow-rise, fast decay. This strongly suggests that many of these transients cannot be due to tidal disruption events as these would be expected to exhibit a fast rise and $t^{-5/3}$ decay. Also, the timescales for many of these events would require a significant amount of energy to be released from a TDE, requiring a large accretion efficiency or suitably massive disrupted star to power them. However, the possibility of a long-lasting TDE with a shallow decay cannot be completely ruled out (Lin et al., 2017).

1.5 AGN microlensing

1.5.1 Microlensing introduction

In the context of these AGN transients it is essential to look at the effects of gravitational microlensing as a possible explanation. There is an excellent review on the subject (Wambsganss, 2006). The term microlensing can be used to describe a transient event where a distant source is amplified due to a point-mass-like object(s) crossing the line of sight relative to an observer. In the case of AGN microlensing this may be due to a star(s) in a foreground galaxy. The magnification induced by microlensing can be significant and the timescale for an event is expected to be similar to that observed in our transients.

In brief, microlensing refers to the magnification of a background source due to an intervening stellar- or planetary-mass lens. The physics is the same as that observed in galaxy-scale strong lenses except that the multiple image separation is only on the order of μarcsec and the timescale for the events is much faster. These events can have typical durations on the order of days to weeks for stellar sources in the galactic neighborhood or even years in the case of AGN. The characteristic timescale for simple models is given by the Einstein time $t_{\rm E} = D_{\rm d}\theta_{\rm E}/v_{\perp}$ which involves the distance to the lens, the transverse velocity of the source relative to the lens and the Einstein radius

$$\theta_{\rm E} = \left(\frac{4{\rm G}M}{{\rm c}^2}\frac{D_{\rm ds}}{D_{\rm d}D_{\rm s}}\right)^{1/2} \tag{1.1}$$

where $D_{\rm d}$, $D_{\rm s}$ and $D_{\rm ds}$ are the angular diameter distances to the lens, source and from lens to source respectively. The simplest microlensing model is for that of a point-mass lens. The full general relativistic treatment can be avoided as long as the impact parameter η, which subtends an angle β (see Fig. 1.4), for the source is much greater than the Schwarschild radius of the lens. The normalised impact parameter is given by $y = \beta\,/\theta_{\rm E}$ and the point-mass approximation breaks down as $y \to 0$. Assuming the motion of the source relative to the lens is in a straight line then the trajectory can be represented as

$$y(t) = \sqrt{y_0^2 + \left(\frac{t - t_0}{t_{\rm E}}\right)^2} \tag{1.2}$$

where t_0 is the time at which the separation is at the minimum value y_0. The total magnification is given by

$$\mu = \frac{y^2 + 2}{y\sqrt{y^2 + 4}} \tag{1.3}$$

and this can be used in conjunction with eq. 1.2 and the baseline source flux $F_{\rm s}$ to construct a light curve for the event. There is a degeneracy between these parameters that allows multiple fits to the same light-curve if the mass and lens distance are not fixed for any assumed transverse velocity.

Another useful model is that for a 'binary' lens where the presence of a second mass considerably increases the complexity of the microlensing profile. The central-point degeneracy at $y = 0$ in the previous model instead gives way to caustics in the source plane which map to critical curves in the lens plane. The critical curves represent the points at which the magnification of the lensed images reaches a maximum. In the case of the point-mass the critical curve is simply a ring of radius $\theta_{\rm E}$. In the binary case, as the source crosses a caustic there will be a corresponding peak in the light-curve as well as the creation/destruction of a pair of lensed images. A caustic-crossing event produces a notable spike in light-curve and the minimum magnification is higher for the source when inside the region defined by the caustic. This can produce a very specific light curve profile, an example of which is seen in fig. 1.5.

In cosmological microlensing, in addition to the primary lens object(s), there may be the presence of an external shear caused by a matter distribution, i.e. lens galaxy, near to the line of sight (Chang & Refsdal, 1984). If the effect is strong this creates a notable smearing effect on the caustics in the magnification map.

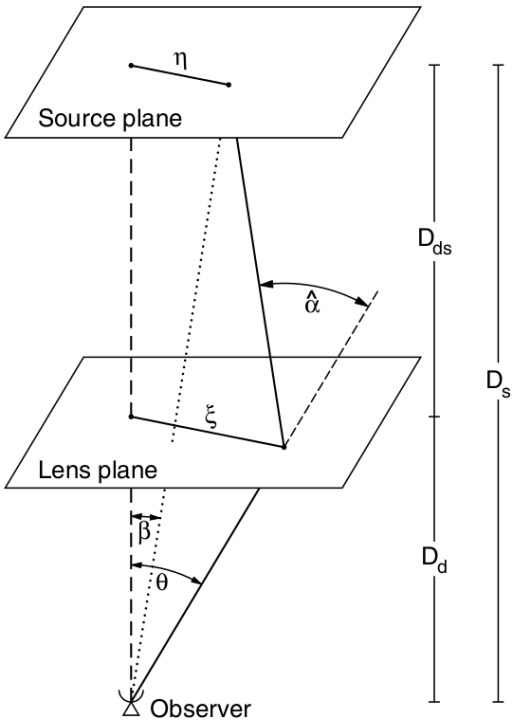

Figure 1.4 *Schematic of a gravitational lens system. Reproduced from Meylan et al. (2006).*

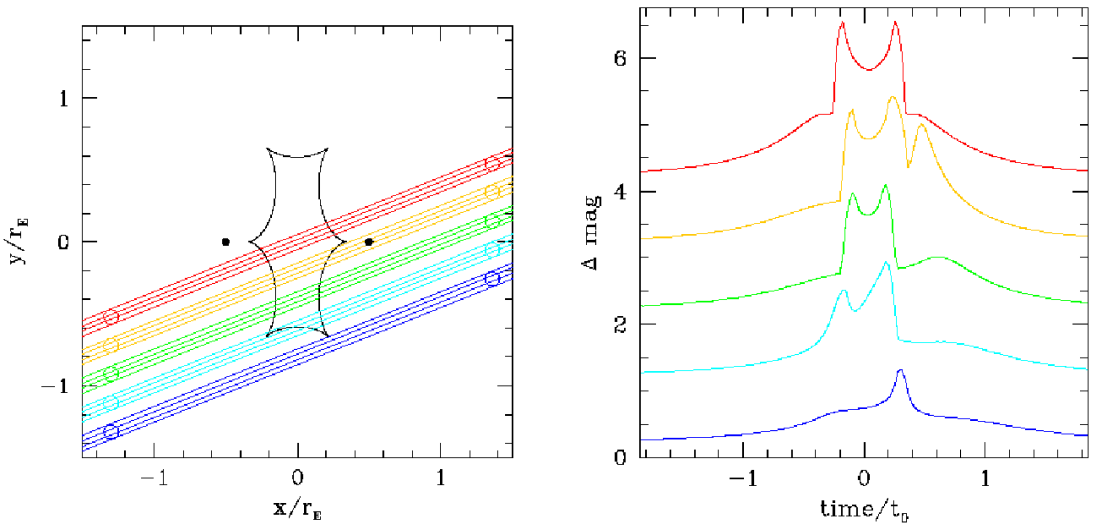

Figure 1.5 *The left panel shows a binary caustic for two equal masses with separation $\theta_{\rm E}$ and four different tracks for an extended source of radius $\theta = 0.05\,\theta_{\rm E}$. The right panel shows the corresponding light curve, offset by one magnitude for clarity. Reproduced from Wambsganss (2006).*

Regions where microlensing causes demagnification are also not uncommon. It should be noted that most, if not all, AGN microlensing studies to date have focused on multiply-imaged, strong-lensed quasars. In these cases a massive lens galaxy provides a significant macro-lensing potential resulting in two or more images of a distant quasar, one notable example being the 'Einstein Cross'. Each individual image will also be subject to microlensing effects which are not correlated. The main advantage with these objects is that, after accounting for a time-delay at each image, the intrinsic quasar variability can be corrected for, leaving the microlensing signal at each. The main disadvantage is that the inferred microlensing magnification maps are typically very complex due to the presence of a significant amount of shear and expected surface mass density of stars. This increases the uncertainty in the modelling but also lowers the probability that there will be isolated regions of very high magnification in the maps, particularly if the source is extended (Wambsganss et al., 1990; Wambsganss, 1992). The microlensing seen in these objects could reasonably be described as a low level flickering but observations are nonetheless very useful as will be seen.

In contrast to the complex magnification maps seen in multiply-imaged AGN, a small lens-host galaxy, with low surface-mass density, could give rise to isolated regions of high amplification, rather than a dense caustic network. This may provide a reasonable explanation for the transients discussed in this thesis. In these cases, the optical depth to microlensing, and frequency of observed events, would also be lower. Figure 1.6 shows a comparison of magnification maps with differing optical depths as an example of this where the parameters κ, γ, s are the convergence, external shear and smooth matter fraction respectively. The radial extent of the accretion disc with respect to these maps can dramatically alter the resulting light curve (smoothing increases with radius) but in the example with lower optical depth, the prospect of seeing an isolated, high-amplitude 'single-peaked' event is perhaps more likely.

Another important consideration in microlensing is the possibility of observing colour changes. Normally for a point-source the microlensing light curve would be achromatic but if an extended source has a surface brightness distribution that varies with wavelength then colour changes may be observed. In the case of the AGN inner-regions this could prove important as it is expected that shorter-wavelength emission peaks at smaller radii, so the observed light curve may exhibit colour changes during the microlensing event. Similarly, emission lines from the BLR may display changes as a result of the lensing event if the region is

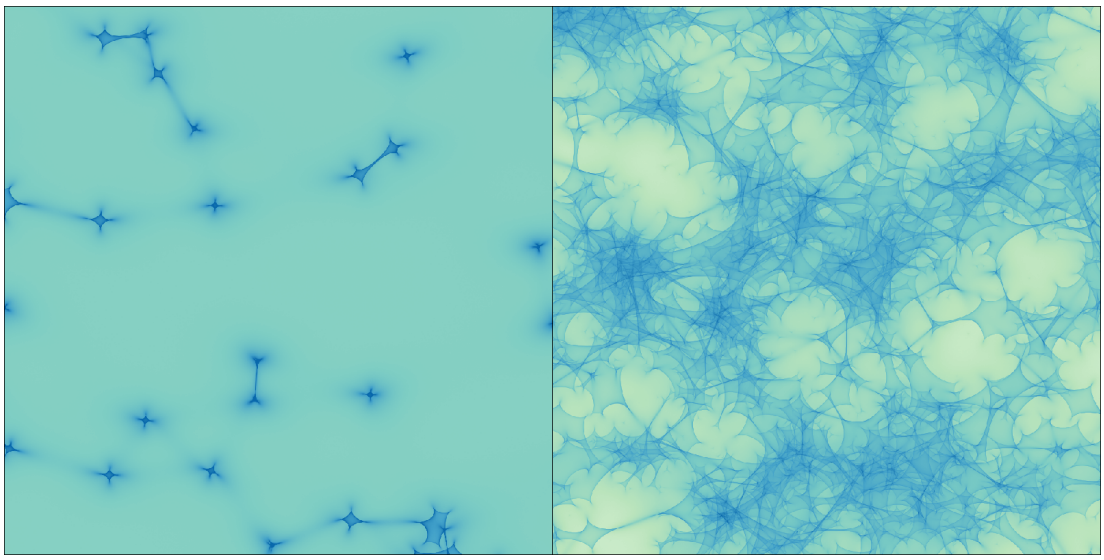

Figure 1.6 *Two independently generated microlensing magnification maps giving a comparison of varying optical depth while keeping the external shear and smooth matter fraction constant ($\gamma = 0.1$, $s = 0.0$). Left: $\kappa = 0.1$, Right: $\kappa = 0.6$. Magnification maps reproduced from the GERLUMPH database (Vernardos et al., 2015).*

sufficiently small with respect to the lens footprint. For example, a disc-shaped morphology may give rise to enhancements on the blue/red wings of the line as the lens tracks across the source. This may provide very valuable information on the structure of the inner-regions that would otherwise be unavailable due to the extremely small angular sizes of these objects. Unfortunately, chromatic changes would also be expected from an intrinsic brightening of the central source but the two effects may be distinguishable. In a point-lens case, if the AGN accretion disc is small relative to the Einstein angle of the lens (ie $< 0.01\,\theta_{\rm E}$ these effects will be negligible. As an example, for an AGN at $z = 1.0$ and lens at $z = 0.2$, a distance of $25\,R_{\rm S}$ corresponds to $0.01\,\theta_{\rm E}$ for a $10^8\,{\rm M}_\odot$ black hole and $1\,{\rm M}_\odot$ lens.

The potential application of microlensing in the study of AGN has been known about for some time (Paczynski, 1986) but given that the timescales are typically a factor of 10 longer than events local to our own galaxy, and event rates were expected to be low, it took until the turn of the century for this idea to gain traction. Kochanek (2004) was among the first to simultaneously fit a number of parameters regarding the source and lens configuration in the 'Einstein Cross' multiply-imaged quasar. Their method is computationally intensive but has shown that the radius for the emitting region, allowing for some simplifying assumptions such as a face-on disc, appears to be consistent with that expected from standard disc theory. Mosquera et al. (2009) also reported the detection

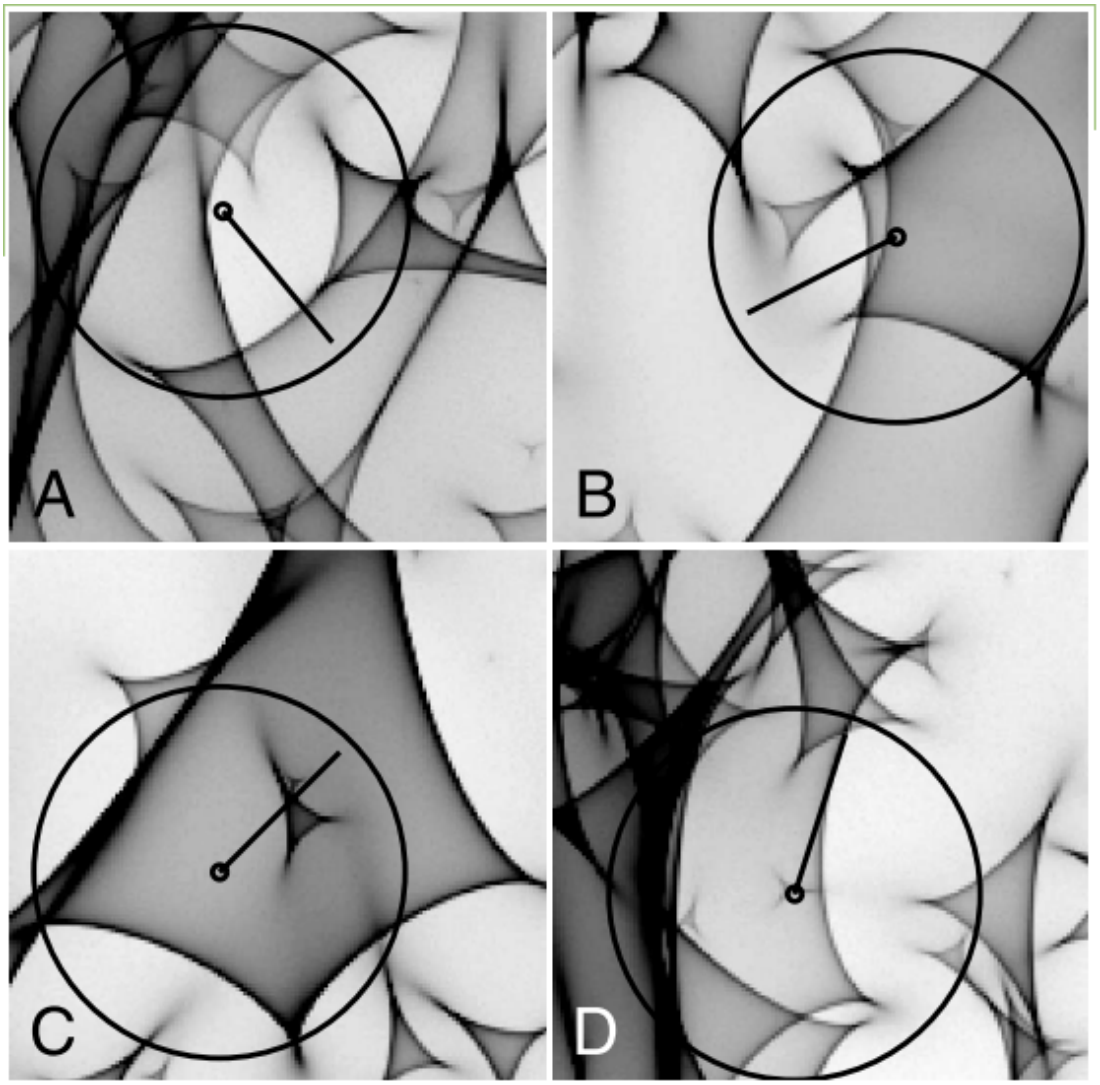

Figure 1.7 *An example of the magnification maps and source path used to reproduce the observed light curves for each quasar image in the Einstein Cross: Q2237+0305. Reproduced from Kochanek (2004).*

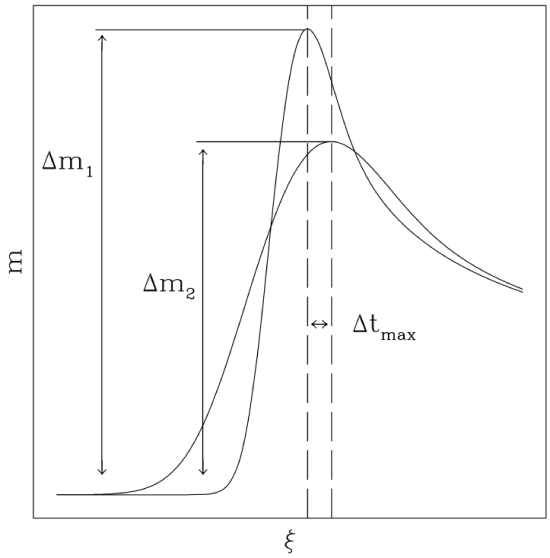

Figure 1.8 *An illustration of chromatic microlensing due to a caustic crossing event for an accretion disc with a radial emission profile. The longer wavelength radiation rises faster but peaks lower and later than the shorter wavelength. Here ξ is a measure of the distance from the centre of the disc to the caustic as a ratio of the disc size. Reproduced from Mosquera et al. (2009).*

of chromatic microlensing in the Einstein Cross. They model a simple caustic crossing event and the predicted effects are shown in fig. 1.8. If, as expected, the accretion disc has a radial emission profile the shorter wavelength radiation will undergo greater magnification and evolve on a shorter timescale than the longer wavelength light. There is also a delay between the observed peaks. Their analysis is consistent with the radial profile $r \propto \lambda^{3/4}$ expected from simple thin disc models but they note that there are other reasonable fits to the data. These results appear to be consistent with standard disc theory but there are also a number of studies which find that standard accretion disc sizes seem to be too small by a factor of ~ 4 (Pooley et al., 2007; Floyd et al., 2009; Morgan et al., 2010; Mosquera & Kochanek, 2011).

After careful deconvolution of the long-term spectral data for the Einstein Cross, a similar treatment has also yielded constraints on the size of the CIV/CIII] emitting regions in this object (Sluse et al., 2011). As the Einstein Cross has a lens galaxy at a comparatively low redshift, the time-delays between images are < 1 day making this a particularly fruitful object for microlensing studies. The CASTLES database now lists approximately 100 multiply-imaged systems and many of these systems, including key lens/AGN parameters, are detailed in Mosquera & Kochanek (2011). The number of microlensing studies of individual

objects is also increasing (Poindexter et al., 2008; Dai et al., 2010; Mosquera et al., 2013; Blackburne et al., 2014, 2015). Constraints on the size of the X-ray emitting regions sometimes disagree as to whether or not the hard X-rays are more compact than the soft. This appears to be due to the amount of reprocessing seen in individual objects.

When these results are taken in context, there has been a growing consensus that the size of the accretion disc is larger than implied by the standard disc model. The analysis of 'flux anomalies', the predicted vs observed fluxes seen in quasar images in optical/X-ray which are also likely due to microlensing, allowed Pooley et al. (2007) to conclude that the emitting regions must be larger than predicted by a factor ∼3-30. Other studies taking into account several multiply-imaged systems with microlensing data have yielded similar results (Morgan et al., 2010; Jiménez-Vicente et al., 2014; Chartas et al., 2016). In general, it appears as if the accretion disc temperature profile is flatter than $T \propto r^{3/4}$, an important result.

Where do the 'slow-blue' AGN transients in this thesis fit into the picture? At present, there are no indications of any massive lens galaxies or multiple images. It is possible that the lens galaxies are small and/or that any image splitting is thus far unresolved at the ∼0.5" limit. Nonetheless, the timescales and smooth variations seen in a number of these objects do appear to fit a microlensing profile. If this is true, these objects may be in a different regime to their multiply-imaged cousins. The loss of the ability to extract the intrinsic AGN variability from each image may be offset by the fact that the absence of any significant macrolensing might yield a simpler modelling process.

1.6 Thesis outline

The work contained herein focuses on two key areas with respect to these AGN transients. The first is on the large amount of spectroscopic data available from the transient monitoring campaign. At the time of writing there are 235 individual spectral epochs spread across 64 targets. I have been responsible for the construction and implementation of a robust reduction pipeline for this data, which is detailed in Chapter 2. The reduced spectra have been measured in a systematic manner to provide continuum fluxes, line profiles and a large number of derived parameter estimates for these objects. A classification scheme, related to the transient light curve profiles, allows a broad characterisation of these

transients and I compare and contrast their spectroscopic evolution in Chapter 3. I also provide a detailed analysis of the evolution of the most variable objects in the sample. This includes continuum fluxes, BLR and NLR equivalent widths, spectral indices and various other spectroscopic parameters.

The second key area of my research is on the light curves for these transients, particularly with respect to the exploration of the microlensing hypothesis. In Chapter 4 I select a small subset of candidate objects with which to focus on and use an MCMC analysis (with additional technical details in Chapter 2) to provide quantitative fits to the data. The detection of differential changes in BLR vs continuum flux, when taken in context with the microlensing models, also allows me to place constraints on the size of some BLR components. Chapter 5 takes the simple microlensing model and applies it across the whole sample using the most recent light curve data available. In approximately 10% of cases, the light curves for these transients do appear to be well described by the simple model. In other objects, the failure of the simple model does not rule out microlensing but rather provides evidence for a more complex lens configuration. The difficulties in accurately modelling such complex scenarios are also discussed. I also provide an example fit to a light curve where the accretion disc is potentially being resolved by the lens. Finally, Chapter 6 revisits the notable AGN flare seen behind M31 as a possible microlensing event.

As to the underlying cause of these AGN transients, this work primarily focuses on the microlensing scenario. I have been able to demonstrate that this can provide a reasonable explanation to the data in a number of cases, but microlensing is unlikely to be the sole explanation for every object in the sample. Other possibilities, including tidal disruption events, are briefly considered but I have attempted to remain agnostic with respect to other scenarios. This is, in part, due to a lack of existing models which can adequately describe extreme AGN/CLQ variability. For instance, there are currently no known examples (with the possible exception of the M31 flare) of a TDE candidate around a luminous AGN, i.e. with extant accretion disc, meaning the challenge of modelling these events is considerable. The longer timescales seen for these AGN transients also appear to be at odds with the known population of TDEs thus far. The discussions around these alternative scenarios are thus kept to a minimum but it is hoped that the spectroscopic observations reported herein may still provide illumination as to the true nature of some of these events.

Chapter 2

Observations, data reduction and modelling

A significant amount of my time was invested in the creation of a robust data reduction pipeline for the spectroscopic observations undertaken with the William Herschel Telescope (WHT). It was also a primary task for me to ensure that all data taken with the WHT was reduced in a similar fashion, including any archival data taken prior to commencement of the PhD. This chapter provides details of the observations taken and the reduction pipeline itself. For completeness, there will also be a brief description of other observational data used in this project. This chapter will also describe the techniques used to obtain accurate spectroscopic measurements from the reduced data. In addition, I will outline the MCMC analysis techniques used in exploring the simple point-lens, point-source microlensing model with regard to the light curve for some of the single-peaked slow-blue transients. There will also be information on the techniques employed to explore extended source models and more complex lensing configurations. Some of this work is published in Bruce et al. (2017).

Additional publications for which I was present as an observer, or have contributed spectroscopic reductions are: Lawrence et al. (2016), Collinson (2016), Kankare (2017), Watson et al. (2016), Kankare et al. (2015) and Fraser et al. (2014).

2.1 Photometric observations

2.1.1 SDSS

The earliest photometric epochs for the majority of the slow-blue transients comes from the Sloan Digital Sky Survey (SDSS) (Ahn et al., 2012). Typically these will be the *cmodel* magnitudes, which should provide a reliable estimate for an extended object in a single band, and also agree with the Point Spread Function (PSF) magnitudes for stars. The current Sloan data release is DR12, though it should be noted that the photometric solutions are not expected to have evolved post-DR9, from which the SDSS photometry in this work is primarily derived. The SDSS survey observes in five filters: $u_{\rm SDSS}$, $g_{\rm SDSS}$, $r_{\rm SDSS}$, $i_{\rm SDSS}$ and $z_{\rm SDSS}$.

2.1.2 Pan-STARRS

The Panoramic Survey Telescope and Rapid Response System (Pan-STARRS), (Magnier et al., 2013; Schlafly et al., 2012; Tonry et al., 2012), 3π Steradian Survey data was used, initially to identify candidate transient events. A team at Queen's University Belfast (QUB) ingested the nightly data for comparison with the earlier SDSS footprint. This work was part of the Faint Galaxy Supernova Survey (FGSS) which, as the name suggests, was primarily aimed at searching for supernovae. In addition to this, a search was also designed to look for tidal disruption event candidates but, as mentioned in Section 1.4.2, serendipitously turned up the 'slow-blue' AGN transients which are studied in this thesis. Additional photometric epochs from Pan-STARRS assisted in classification of the light curve for any flagged events. Magnitudes are typically PSF magnitudes and it will be noted from which repository the Pan-STARRS data is sourced in the appropriate sections.

The Pan-STARRS filters, $g_{\rm P1}$, $r_{\rm P1}$, $i_{\rm P1}$, $z_{\rm P1}$ and $y_{\rm P1}$ are similar to those in SDSS but not identical. The Pan-STARRS images are processed via the image processing pipeline (IPP) and the data, provided by the Pan-STARRS consortium, are available through both the DVO and PSPS databases. Finkbeiner et al. (2016) show that the Pan-STARRS and SDSS photometric systems are consistent to within ± 9 mmag though there is also a colour term to take into account. For main sequence stars with $g_{\rm P1} - i_{\rm P1} \leq 0.6$ the transformation between

filters $g_{\rm SDSS} - g_{\rm P1} \leq 0.1$ (Finkbeiner et al., 2016). The filter approximations will be discussed further below. The IPP has evolved over the duration of this project, from PV1.2 to PV3 and the most recent, publicly available, 'DR1' release, which does not currently include individual detections.

2.1.3 Liverpool Telescope

The Liverpool Telescope (LT) is a 2m, fully robotic telescope situated on the island of La Palma and operated by Liverpool John Moore's University (Steele et al., 2004). It has proven crucial in characterizing the light curves of the slow-blue transients and provides much better sampling than the Pan-STARRS survey. After the initial PS1 transient identification, those which passed the quality-control steps would be ingested into the LT programme for follow-up observations. The cadence, exposure times and filter selection were also adjusted as required. Observations were carried out in u, g and r with the filters assumed to be a close approximation to those in SDSS. Two cameras, first RATCAM and gradually switching to IO:O, were used with a field-of-view of approximately 4.6'/10.2' respectively. This was sufficient to provide a number of reference stars allowing for calibration on non-transparent nights.

The scheduling of observations and reduction of the LT light curves, after bias subtraction, flat-fielding and astrometric reduction by the LT pipeline, has been handled entirely by Prof Andy Lawrence (AL), though I was involved in the proposal stages and target priority discussions. The LT light curves are aperture magnitudes, generated using a 2" aperture and several SDSS DR7 reference stars in frame. The seeing typically varied between 0.7-2" and the data was not used if the seeing was greater than 2". The initial cadence on targets was every few days and was then lowered according to how fast the object was changing. Exposure times were 100s in g/r and 400s in u for targets with $g \leq 20$ giving $\sim$5% photometry in all bands. For fainter targets, exposure times were 200s in g/r and 400s in u, with u being discontinued as deemed necessary. Monitoring of the current AGN sample high priority targets is still ongoing.

2.1.4 CRTS

Data from the Catalina Real-time Transient Survey (CRTS) (Drake et al., 2009) provides us with long-baseline photometry for a number of the slow-blue objects. The CRTS survey consists of data from up to three separate telescopes, the 0.7m Catalina Schmidt (Arizona, USA), the 1.5m Mt. Lemmon (Arizona, USA) and 0.5m Uppsala Schmidt (Siding Spring, Australia). The observations span the approximate period 2005-2013. No filters are used in this survey meaning colour terms may be significant. The publicly available data are aperture magnitudes (extracted via Sextractor) and calibrated to an approximate V-band zero-point. The CRTS data allows us to see the pre-Pan-STARRS evolution in many of our objects.

2.1.5 Broad-band filter approximation and light curves

Generally, I make the assumption that the differences between the $g_{\rm SDSS}$, $g_{\rm P1}$ and $g_{\rm LT}$ filters can be neglected and designate magnitudes as simply g. This approximation should be reasonable given that the photometric uncertainty is expected to be dominated by intrinsic AGN variability, typically ~ 0.2 mag or greater. For the PS1 data, no g-band correction has been applied thus far as this is likely to be less than 0.1 mag for the majority of objects in the sample. For the CRTS data, colour effects will likely be significant due to the clear filter in use. Typically this data is only used to inform our understanding of the longer term behaviour of the light curve. For the microlensing models, magnitude-to-flux conversions are performed assuming an effective wavelength of 4770 Å.

The photometric data outlined above are the primary source of light curve information used throughout this thesis. At time of writing (Sep 2017), I have also endeavored to add g-band data from other available sources so that the light curves display all available data. This includes an attempt to correct the CRTS data based on the SDSS colours. These up-to-date light curves can be found in Appendix B.

2.1.6 PS1 transient sample

The initial PS1 transient sample obtained from the FGSS transient identification process is summarised in Lawrence et al. (2016). As already mentioned in Section 1.4.2, this was the result of a systematic search for TDEs around quiescent black holes. This sample contains those transients with a minimum of three LT photometry points as of May 2013 and consists of: 35 previously unknown AGN; 8 probable AGN; 16 known/probable SNe; 6 radio sources (3 of which were known AGN); 4 emission line stars and 7 of unknown classification.

Since this work was carried out, the number of spectroscopically confirmed AGN transients has risen to 64. It is these 64 targets which comprise the AGN-only transient sample used throughout this thesis, hereby referred to as the 'PS1-A' AGN transient sample and summarised in Section 2.4. No new targets have been added to the PS1-A sample since July 2014.

2.2 Spectroscopic observations

2.2.1 WHT

The William Herschel Telescope is a 4.2m optical/near-IR telescope located at the Observatorio del Roque de los Muchachos on the island of La Palma in the Canary Islands. It is currently run by the Isaac Newton Group of Telescopes and sits at an altitude of 2344m. The observing conditions on La Palma are generally good, though there is a tendency to lose more nights to adverse weather in the winter months. In summer, dust blown in from the Sahara, known locally as 'Calima', can cause additional problems.

The WHT is the primary source of spectroscopic data for the PS1-A transients. For the spectroscopic data presented in this thesis, there have been 43 nights on the telescope, some full, some as part of a shared night, and some as service time, which have involved at least one object in the PS1-A catalogue. The number of individual WHT spectroscopic epochs now totals 217 for the AGN transients and all of this data has been reduced, by myself, using the same software pipeline I have developed. In addition, there are 115 supplementary spectra, which have been reduced in a similar fashion, that are not part of the main AGN catalogue.

Many of these objects are supernovae, which were observed when classifying the larger Pan-STARRS transient candidates. Other targets include: stellar contaminants; other AGN of interest and TDE candidates which have warranted additional attention. At time of writing (Sep 2017) the spectroscopic observations have continued but, to allow time for analysis, the cutoff for the spectroscopic data presented here is Feb 2017.

After an initial WHT epoch confirmed a type-I AGN transient, each target was then scheduled for follow-up spectroscopy as the observing time allowed. This is in addition to continued photometric monitoring with the LT. The spectroscopic cadence on each target is somewhat arbitrary, primarily determined by the allocation of telescope time each semester, typically several nights per year. Observations began apace in mid-2013 (though 3 targets also have pre-2013 WHT data) and have continued into 2017. Before an observing run, each target would have a priority assigned which was dependent on several factors, the two most important being the time since the last spectral epoch and the behavior of the light curve over the previous several months. For example, an erratic target would be assigned a lower priority than one showing a smooth but sudden decline in flux. These priorities were then used when making scheduling decisions for the upcoming observing run.

All of the spectral observations were conducted using the Intermediate dispersion Spectrograph and Imaging System (ISIS) long-slit spectrograph with the following configuration. The 5300 dichroic was used along with the R158B/R300B grating in the red/blue arms, respectively, along with the GG495 order sorting filter in the red arm. Typically 2× binning in the spatial direction was used to improve the signal-to-noise ratio (SNR) along with a narrow CCD window to reduce disk usage and readout times. In later observations, this was relaxed to simply make use of the default CCD window. This set-up gives a spectral resolution of $R \sim$1500 at 5200 Å in the blue and $R \sim$1000 at 7200 Å in the red for a slit width of 1 arcsec and total coverage $\sim$ 3100–10600 Å.

Exposure times on science targets were typically in 1800s 'shots', with the number of shots on target based on the latest LT g-band photometry. This would range from: 1x shot at $g < 20$; 2x shots for $20 \leq g \leq 20.5$ and 4x shots for $g > 20.5$. Individual shots were reduced separately and combined in the final part of the pipeline. Table 2.1 details the number of science spectra obtained for each observation night on the WHT. In all, I have been present as an observer on seven separate occasions, sometimes also helping inexperienced WHT observers

become acquainted with the instrument. For all observation runs since August 2013, I have taken a lead role in the observation planning and target selection processes.

Typically, calibration images were taken at the start of each night including bias frames, lamp flats and CuNe/Ar arc-lamp images. These were obtained using a script, originally developed by the QUB supernova group, which automatically obtains the required images, subject to a cursory glance to ensure the script was successful. It can sometimes be desirable to take additional calibration images when on target. This can help address changes in the instrument due to flexure or environmental factors though it does take up valuable time. It was decided early on that the expected improvement in wavelength calibration was not enough to justify losing one or more science observations per night, especially given that the observations are at a relatively low spectral resolution. Additionally, during the reduction stage, it was possible to make use of observed sky lines to try to correct for any instrument flexure. Spectroscopic standard stars were imaged at $\sim$2h intervals throughout the night though this cadence was not always possible. Observations were carried out at the parallactic angle unless otherwise noted.

2.2.2 MMT

A small number of targets were observed, 18 in total, with the blue arm spectrograph on the 6.5m MMT situated on Mount Hopkins, Arizona on the 9th & 10th March 2015. Here, the $300\,\mathrm{g\,mm^{-1}}$ grating was used with $2\times$ binning in the spatial direction. A filter wheel issue meant that no order-sorting filter was used and some observations suffered due to poor observing conditions. Remote observations were primarily carried out by a colleague, Dr Chelsea MacLeod (CM), though I assisted in the planning and proposal stages. The data for the MMT was also processed by myself, using a modified version of the WHT reduction pipeline.

2.2.3 SDSS/BOSS

SDSS spectroscopic epochs are available for some of the PS1-A sample, primarily from the Baryon Oscillation Spectroscopic Survey (BOSS). The focus for this thesis is solely on the WHT spectroscopy but the available epochs are noted in

Table 2.1 *WHT observation nights and number of target spectra obtained for the PS1-A sample and other targets (O), respectively. Also noted are the nights for which I was present as an observer.*

Date	MJD	#PS1-A	#O	Observer?
21/12/11	55916	1	10	
02/03/12	55988	2	13	
21/09/12	56191	1	9	
09/02/13	56332	3	5	
10/02/13	56333	4	3	
11/02/13	56334	6	3	
12/02/13	56335	2	6	
30/03/13	56381	5	3	
31/03/13	56382	9	2	
30/04/13	56412	2		
14/05/13	56426	2	5	
15/05/13	56427	6	1	
09/06/13	56452	4		
10/06/13	56453	5	2	
07/08/13	56511	8		y
08/08/13	56512	8	1	y
09/09/13	56544	8	1	y
10/09/13	56545	4	4	y
03/12/13	56363	3	1	y
07/02/14	56695	10		y
24/06/14	56832	3	1	y
25/06/14	56833	4	2	y
26/06/14	56834	6	3	y
22/07/14	56860	4		
23/07/14	56861	6		
24/07/14	56862	7		
16/12/14	57007	8	1	y
17/12/14	57008	6	1	y
20/04/15	57132	1		
21/04/15	57133	11		
22/04/15	57134	7		
23/04/15	57135	6		
06/02/16	57424	3	7	
07/02/16	57425	3	5	
08/02/16	57426	2	10	
30/05/16	57538	7	3	
31/05/16	57539	4	5	
09/07/16	57578	8	1	
10/07/16	57579	7	2	
22/10/16	57683	4	1	y
24/10/16	57685	1	1	y
17/02/17	57440	8	2	
18/02/17	57441	8	1	
	Total	217	115	

Table 2.2 *Spectroscopic epochs for the PS1-A sample currently available from SDSS/BOSS.*

Target	MJD	Date
J014139	56902	02/09/14
J081916	52325	20/02/02
J084626	56363	12/03/13
J103511	56783	06/05/14
J105040	53035	31/01/04
J152844	56091	13/06/12
J154404	55333	17/05/10
J163528	52144	23/08/01
J164740	55691	10/05/11

Table 2.2 and will be incorporated in subsequent analyses.

2.3 Spectroscopic reduction pipeline

2.3.1 Pipeline overview

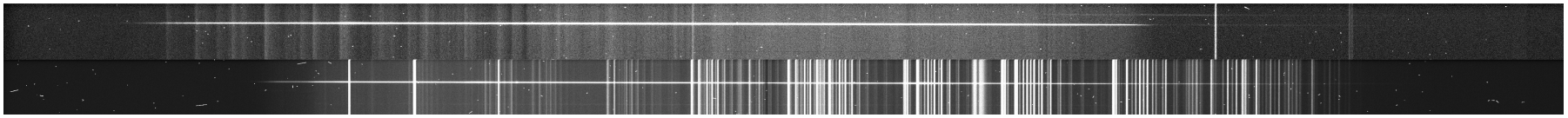

Figure 2.1 *Raw, full-length images obtained for target J223210 on 9/9/13. Blue arm on top, red arm below.*

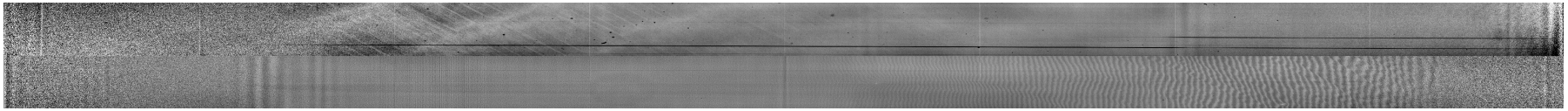

Figure 2.2 *Normalized flat fields generated from the calibration observations on 9/9/13. Blue arm on top, red arm below.*

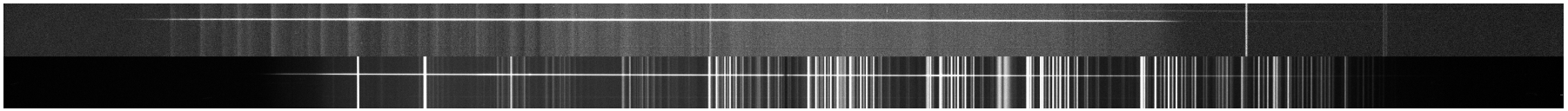

Figure 2.3 *Bias-corrected, flat-fielded, cosmic-ray subtracted images for target J223210 on 9/9/13. Blue arm on top, red arm below.*

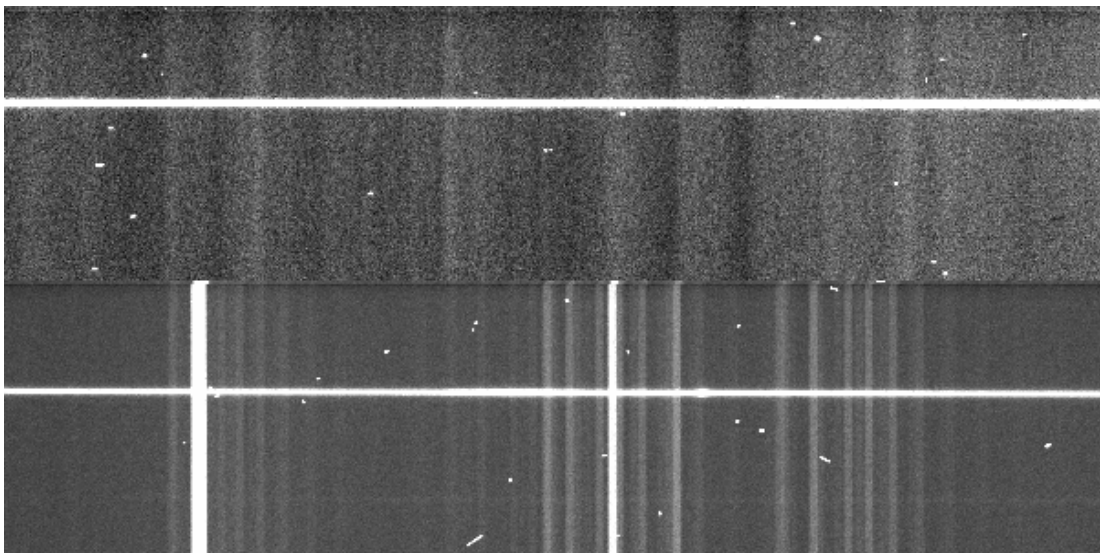

Figure 2.4 *Zoomed portion of the raw spectra obtained for target J223210 on 9/9/13. Blue arm on top, red arm below. Note the sky lines, cosmic ray hits and evidence for narrow-line emission in the red-arm AGN trace (right of center).*

The spectroscopic reduction pipeline I have developed for this project consists primarily of custom-made PYRAF scripts. PYRAF is a Python package which provides a straightforward interface for interacting with the National Optical Astronomy Observatories (NOAO) Image Reduction and Analysis Facility (IRAF) software. This software is powerful but occasionally suffers due to a dated user interface and lack of supporting documentation. The custom-made scripts I have developed include many of the key parameter settings used in the IRAF tasks and are designed to automate as many steps in the reduction process as possible. In general, default IRAF parameter values are used though some have been adjusted to match specific WHT header information and to take account of some suggested guidelines as per Massey & Jacoby (1992). One cannot remove the human element completely when using IRAF tools to reduce long-slit spectra and, in fact, one may not want to. However, the time saved in implementing the pipeline has proven invaluable as it allows one to reduce an entire nights telescope data in a matter of hours. It was also important for the project that all of the spectroscopic data were reduced homogeneously. As such, all of the data used in this work have been reduced by myself using this pipeline. An example of raw science data from the WHT is shown in Fig. 2.4.

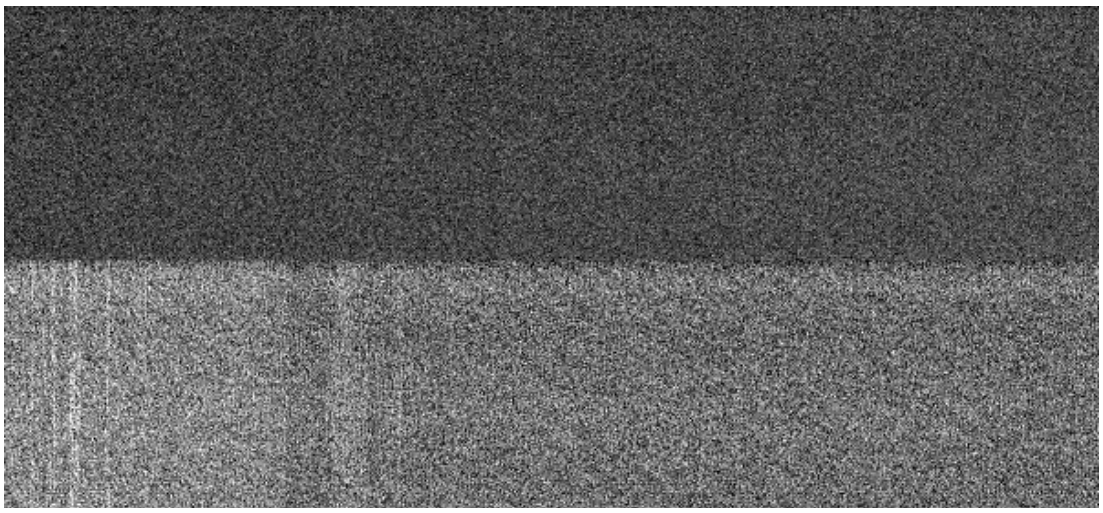

Figure 2.5 *Zoomed portion of the master bias frames generated from the calibration images obtained on 9/9/13. Blue arm on top, red arm below. Note the additional structure in the red arm bias, the result of a problematic bias frame in this region which was not excluded before combining. With a combined total of 20 bias frames, the overall effect is very slight.*

2.3.2 Bias correction and flat-fielding

The first step in the pipeline is the generation of lists of observation files that can be used in the various IRAF scripts. To accomplish this, a script scans an edited version of the WHT-generated 'runlog' file for certain key phrases or values, such as *'isis red bias'* and separates them according to their type. The next step is to generate a master bias for each arm using the `zerocombine` function. Next, the images are trimmed and bias-corrected, including an overscan correction, using `ccdproc`. This step also allows for interpolation over a small number of bad pixel columns which are defined in a separate file. A section of example master bias frames is displayed in Fig. 2.5.

Next, the master flats are generated for each arm using `flatcombine`, and are then normalized using `response` by fitting a smooth function through the data to better highlight the pixel-to-pixel variations. A section of the resulting flats in displayed in Fig. 2.6 and the full images are displayed in Fig. 2.2. The science images are then flat-fielded using these masters with the `ccdproc` function.

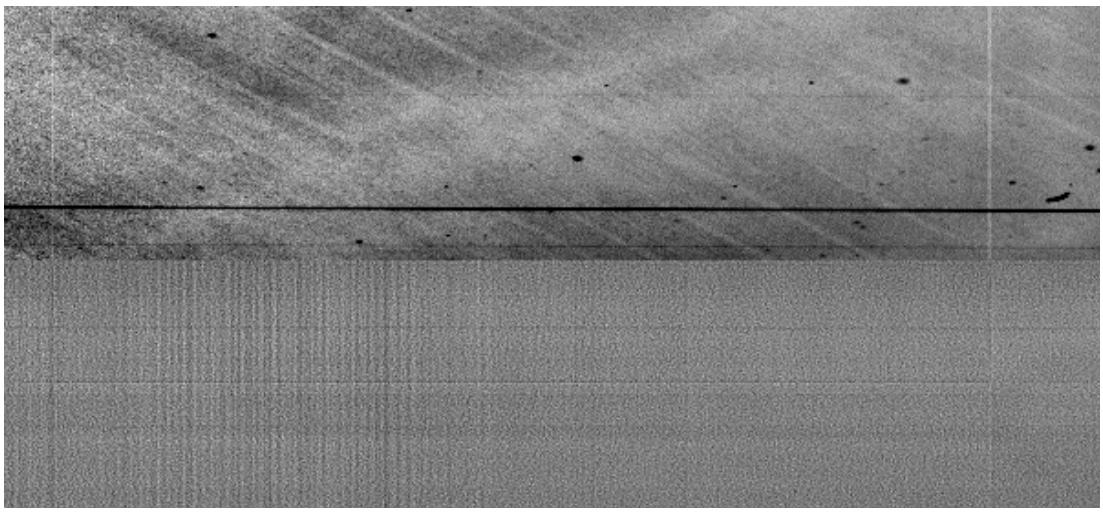

Figure 2.6 *Zoomed portion of the normalized flat fields generated from the observations on 9/9/13. Blue arm on top, red arm below. In this region of the spectra, the red arm is relatively featureless whereas there is some notable structure in the blue.*

2.3.3 Cosmic-ray removal

The next step in the reduction pipeline is the removal of any cosmic rays which have affected each image. A very useful tool for this task is the LACOS_SPEC script (van Dokkum, 2001) which attempts to fit the target spectra and sky lines with a smooth function and then scans the image iteratively in order to identify any cosmic rays and interpolate over them using the nearest non-contaminated pixels. The script generates a bad pixel mask which, when blinked together with the original and cosmic-ray-subtracted images, allows one to determine if the cosmic rays have been removed cleanly. This is the first time-consuming aspect of the pipeline as, occasionally, the extraction would fail, requiring an adjustment of the sigma-clipping parameters used in the script. A section of a bias-corrected, flat-fielded, cosmic-ray subtracted image is displayed in fig. 2.7, for the same target as displayed in 2.4.

For some of the early observations on the WHT, there have been header issues which meant that for some pairs of red/blue images, the header of one of them would not reflect the correct mean airmass value at the time of observation. As this may affect the flux calibration step, albeit slightly, a supplementary script was written which corrects for this problem. This header issue was reported to the ING and has since been addressed.

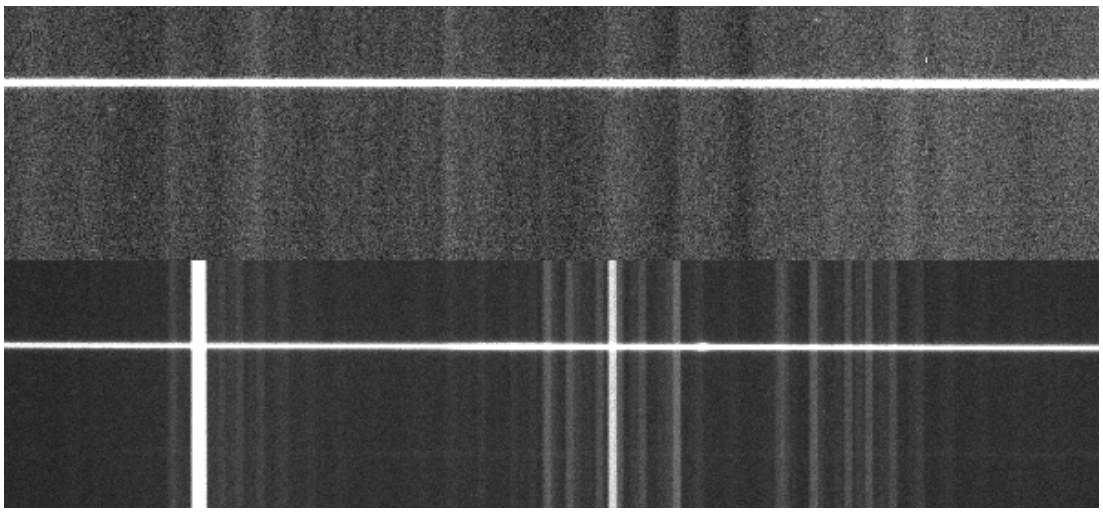

Figure 2.7 *Zoomed portion of the bias-corrected, flat-fielded, cosmic-ray extracted images for target J223210 on 9/9/13. Blue arm on top, red arm below.*

2.3.4 Aperture extraction

The 2D images are now ready for aperture extraction. That is, the reduction to a 1D spectrum by defining an aperture which encompasses the majority of the light from the target and simultaneously defining regions from which to estimate the contribution from the sky background. This task is accomplished using the `apall` function. This is quite a time-intensive process. To ensure an appropriate aperture size, I would measure the FWHM of the target trace at three equally spaced points along the dispersion axis. Typically the FWHM would increase towards the blueward end of the trace. To minimise the loss of target flux, whilst avoiding an unnecessary reduction in SNR from an arbitrarily large aperture, as per Horne (1986), the width of the target aperture was set to be 3x the measured FWHM at the blue end, rounded up to the nearest pixel. For faint targets, up to 200 columns were summed to ensure a cleaner measurement of the true FWHM.

In addition to extracting the aperture for the science target, an additional step was to then extract the same aperture from the arc-lamp calibration image at the start of the night, for use in the next section.

Once the aperture was defined, the next step in the `apall` package is to ensure that the fit of a smooth function through the trace adequately accounts for the changing target centroid along the dispersion axis, primarily due to atmospheric refraction and instrument flexure. This process can be helped by defining the 'good' regions of the trace, where the software reliably finds the centroid, and

excluding noisy regions or areas with sharp changes. The resulting extracted spectrum is then output to file, along with the sky subtraction and error maps.

2.3.5 Wavelength calibration

There are four steps to the wavelength calibration process. The first is to use the arc-lamp images taken at the start of the night to define a wavelength calibration function which can then be applied to every science image throughout the night. This is achieved through the use of the `identify` and `reidentify` functions. The first extracted science arc-lamp spectrum for the night is displayed, and the user then identifies three known lines, from comparison with the published arc-lamp maps, across the full range of the spectrum. Once these wavelengths have been entered, it is possible to then load in the full catalogue of lines from a separate file. This ensures that as many lines as possible are identified and should increase the accuracy of the wavelength calibration function. The next step is to visually confirm that the tool has successfully identified each line. If not, perhaps due to a blend or excessive noise, they can be excluded. The remaining lines are then used to define a smooth function that allows a pixel to wavelength conversion across the entire spectrum.

The second step is to use the `reidentify` task to automatically perform this step for the remaining science arc-lamp images. This extra step ensures that each extracted science spectrum has a corresponding arc-lamp calibration function specific to the extracted aperture. This should minimise any problems relating to changes in the position of the trace relative to the original arc-lamp image. The third step is to simply use the `dispcor` task to apply the wavelength calibration to each science spectrum. In general, the wavelength calibrations have an rms of ~ 0.1 Å, though this increases as the slit width is increased. As the arc-lamps are also taken using the increased slit-width, this results in fewer clean line identifications.

The fourth step is to make a correction for instrument flexure since the original arc-lamp image. This is possible by measuring the position of a known atmospheric line in both the red/blue extracted sky maps, and using this to apply a linear shift to the data so that these match. This assumes that the shift due to flexure is, to first order, a linear effect. To achieve this, using the `splot` function, I fit a guassian to measure the centroid of the prominent atmospheric atomic oxygen line at 5577.338 Å. This is clearly visible in both red/blue science

images. I then run `specshift` to correct the spectra so that these values match. Typically, the shift is less than ~ 3 Å. This additional change limits my confidence in the global wavelength calibration to $\pm \sim 0.5$ Å.

2.3.6 Flux calibration and combining

Prior to flux calibration, the spectra are trimmed, using `scopy`, to remove the outer-most regions where the signal is negligible. At the same time, the inner 'wings' of each red/blue pair, where the response of the instrument declines very steeply, are isolated. This allows for a more accurate sensitivity function fit in the next step. The wavelength ranges were chosen to be as follows: blue arm (3100–5100 Å); blue wing (4900–5350 Å); red wing (5250–5700 Å) and red arm (5500–10600 Å). These numbers were chosen, after some testing, to provide enough overlap between the various regions whilst avoiding those with a very poor sensitivity. After flux calibration, the spectra are recombined to produce a single optical spectrum. In cases with multiple shots, all arm/wing spectra are combined at the same time.

Flux calibration is an involved step and revolves around using standard star spectra, with known spectral information, to produce a sensitivity function for the instrument. At the same time, additional extinction due to changes in airmass must also be taken into account. If the observing conditions are good, this is a relatively straightforward process but transparency issues, during either the standard or science observation, can skew the derived flux values. Transparency issues are usually assumed to be a grey-shift but colour changes can be seen if there are pointing issues, or a spike in the seeing, which can result in differential light loss along the slit. Observations are usually taken at, or near, the parallactic angle to help minimise atmospheric refraction effects, which also increase with airmass.

During the majority of our WHT observation runs, we attempted to keep the cadence on standard star visits to approximately 2h. In addition, it was beneficial to have science observations bracketed by pairs of observations of the same standard, as this can help to highlight issues with transparency during the flux calibration stage, as will be detailed below.

The first step in the flux calibration process is defining the spectral bandpasses to be used when measuring the standard star spectrum. This is done using the

`standard` function and a copy of the file containing the published data on the spectrophotometric standard star. The key part of this step is to remove any bandpasses covering spectral features which are not intrinsic to the standard star, but are instead caused by telluric absorption, particularly the oxygen A and B bands and a number of lesser H_2O bands. At this stage, it is also possible to define additional bandpasses outwith those provided by the standard star file. Frequently, the standard star files are only provided in the range 3200–9200 Å. These new regions do not have a corresponding flux value but can be useful in helping to manually constrain the far ends of the sensitivity function in the next step. The flux calibration outwith this wavelength range must necessarily be treated with caution.

The second step is to make use of the `sensfunc` function. This takes the standard star information provided in the previous section, the mean extinction curve for the La Palma observatory, the airmass of the standard observations, and computes a smooth function through the data that converts from pixel counts to a specific spectral flux density. This should ensure that the chosen standard star spectrum closely matches the published version. It is at this stage that the most appropriate choice of standard star must be made. Usually, this will be a choice between two pointings on the same standard, one imaged before, one after the science target. In excellent conditions, both standards will provide for a very similar sensitivity function. This is rarely the case, as one will usually appear to have a poorer response, perhaps because of a transparency problem, slit-loss effects, or the limitations of using a mean extinction curve. In these cases, to minimise transparency issues, the standard with the superior response function, i.e. the one least affected by transparency issues, is used to fit the sensitivity function.

It is also possible to derive a residual extinction function from pairs of standards. This attempts to make a correction with airmass that brings both standard stars into line. In theory, this will remove problems when relying on the mean extinction curve by accounting for any additional colour/extinction effects on the night. In practice, I felt that by ascribing any transparency effects to additional extinction, this may introduce spurious colour changes. It also had a tendency to over/underestimate the flux calibration as a result. After some testing, I decided that the safest course of action was to choose the most appropriate single standard epoch, and make use of the mean extinction curve for the observatory in lieu of a residual extinction. This may leave the spectra vulnerable to a variable extinction

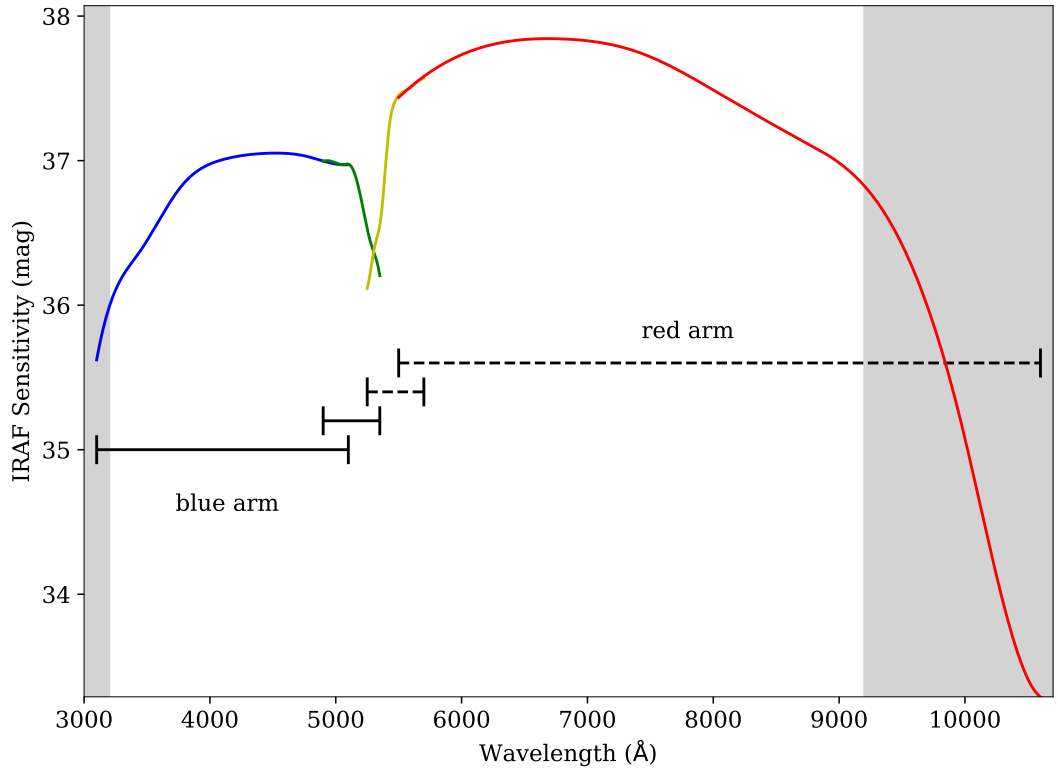

Figure 2.8 *Sensfunc produced for one of the standards on 9/9/13. Note the sharp decline in the function at the inner 'wings'. The wavelength ranges used for the red/blue arms and inner wings are as follows: 3100-5100Å (blue curve); 4900-5350Å (green); 5250-5700Å (yellow); 5500-10600Å (red). The grey shaded areas are less certain due to the lack of available standard star data in this region.*

curve but provides for more stable absolute flux estimates.

The last step in the flux calibration process is to use the `calibrate` function to apply each sensitivity function, including the mean extinction curve for the observatory, to all of the science images covered by that particular standard observation. Fig. 2.8 shows an example of the sensfunc obtained for the four different calibration regions. Note the sharp drop-off seen at the inner wings of the red/blue arms. This is the reason they were flux calibrated separately.

The next step in the pipeline is to combine all individual red/blue/wing spectra into the final science spectrum. This is achieved using the `scombine` function. This produces an average over all epochs, weighted by exposure time if necessary, and rebins to a linear wavelength scale. Fig. 2.9 shows the final spectrum obtained for target J223210 on 9/9/13. Unfortunately, the scombine function in IRAF does not simultaneously provide for the combination of error maps, meaning they need

to be constructed manually, as will be detailed in the next section.

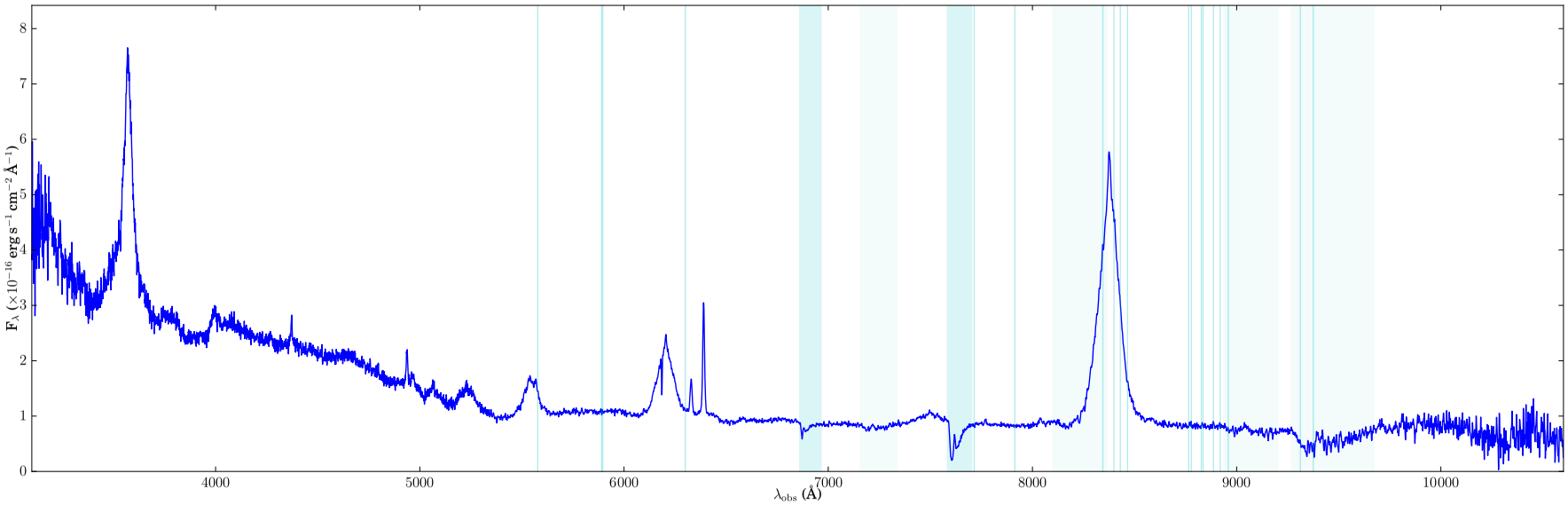

Figure 2.9 *Final combined spectrum for target J223210 on 9/9/13. The vertical lines indicate the location of prominent telluric features. The dip seen in Hβ is due to a cosmic ray hit that has not been subtracted particularly well.*

2.3.7 Error-map generation

It is simple to average error maps using the `scombine` function but it does not have a provision for the propagation of errors over multiple exposures. Thus, to produce more reasonable error maps in these cases, it was necessary to write an additional script which attempts to sum the errors in quadrature whilst being careful not to count overlapping wing regions as independent exposures. One drawback of this procedure is that it requires an interpolation of the error maps due to the non-uniform sampling of the individual epochs before combination. While not ideal, a linear interpolation was adopted and should provide a reasonable approximation. The new error maps, when compared with estimates of the standard deviation from featureless regions of the spectra, appear to agree well (see Fig. 2.10). There are also suggestions that the IRAF pipeline itself may be overestimating the errors slightly but these error maps should be sufficient for now.

2.4 PS1-A AGN transient sample

The AGN transient sample that I will be referring to throughout the remainder of this thesis comprises those AGN flagged up as part of the PS1/FGSS transient identification programme described above. This includes the initial AGN reported in Section 2.1.6 and any additional AGN which were subsequently spectroscopically confirmed. No new targets have been added to the sample since July 2014. Thus, the 'PS1-A' AGN transient sample comprises 64 AGN and, as of Sep 2017, a total of 235 individual spectroscopic epochs (217 WHT, 18 MMT). As these reduced spectra are key to the work contained herein, some additional details relating to the measurement procedures are detailed below.

Of the 64 targets in the sample, this includes one blazar candidate with no confirmed redshift as yet (J025633), and an AGN not technically flagged as a transient (J084626). These objects are included for completeness. In terms of baselines between repeat visits, at time of writing (Mar 2017), 47 have a separation greater than 1yr, 38 $>$ 2yr, 25 $>$ 3yr, 6 $>$ 4yr and 1 $>$ 5yr. Four targets have not been revisited and several are no longer being actively monitored. The two principal reasons for this are that they have either become too faint, or have been ranked as a very low priority for follow-up based on the available

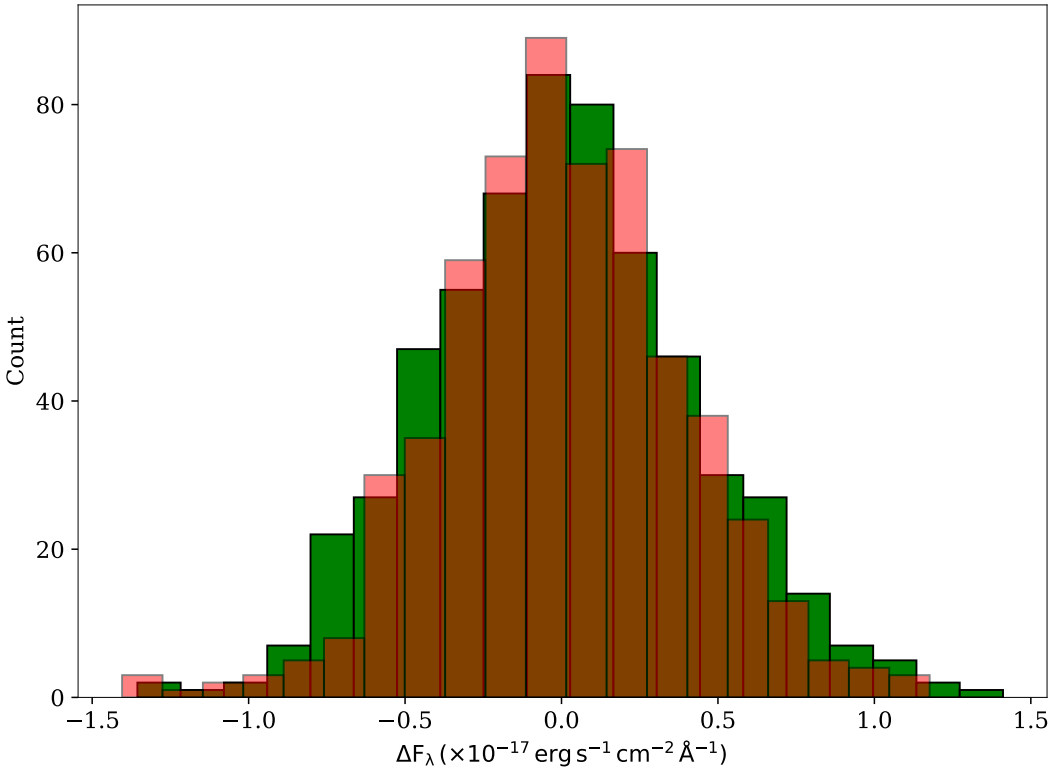

Figure 2.10 *A test of the validity of an error map produced using the error combination script. Plotted in red are the residuals to a continuum-subtracted region of featureless spectrum for target J142232 on 23/4/15 (average of 4x1800s exposures). In green is a normal distribution with a width equal to the mean sigma in the generated error map for this same region. The two appear to agree well.*

photometry.

2.4.1 Re-scaling spectroscopic epochs

Due to its nature, long-slit spectroscopy frequently suffers from transparency problems. If the standard star has been affected, this can lead to an overestimate of the true flux of any science images. In these cases, it may be possible to make use of another standard observation on the same night. However, this may then lead to additional calibration issues if observing conditions on the night have changed appreciably since that standard observation was taken. If the target is affected by transparency issues, then this will present as a total reduction in flux after calibration. As this work is concerned with how these transients are evolving over time, this requires that an attempt is made to quantify the target flux at each epoch to ascertain if there may be calibration issues and, if required, take steps to correct it.

In order to achieve this, I was able to make use of the LT photometry for these events. The IRAF function `bands` can be used to estimate the spectral magnitude for a given bandpass and filter profile. I made use of a filter transmission curve for the LT g band[1] to ensure that these results would be as accurate as possible. The possibility of broad line contamination is worth noting but the estimates should at least be consistent with the LT photometry. With these magnitude estimates in hand, it is possible to fit a smooth function through the LT light curve data which allows one to see if a) there are any epochs which are likely to have suffered from transparency effects and b) provide a scaling correction factor if desired. The correction factor assumes that the transparency problems can be considered a grey shift. As mentioned above, this will not correct for any differential light loss from the slit or additional colour effects, but will at least serve as useful starting point.

As a useful check on the validity of this method, the scaling correction factors should be centered around a value of 1 and the distribution should be approximately symmetric about this value. This is indeed the case. The main drawback is that, if the LT light curve is sparsely sampled, the smooth fit may not perform well. It does at least allow for an objective rescaling, regardless of the true underlying AGN activity. An example of this method is shown in Fig.

[1] http://telescope.livjm.ac.uk/TelInst/Inst/IOO/

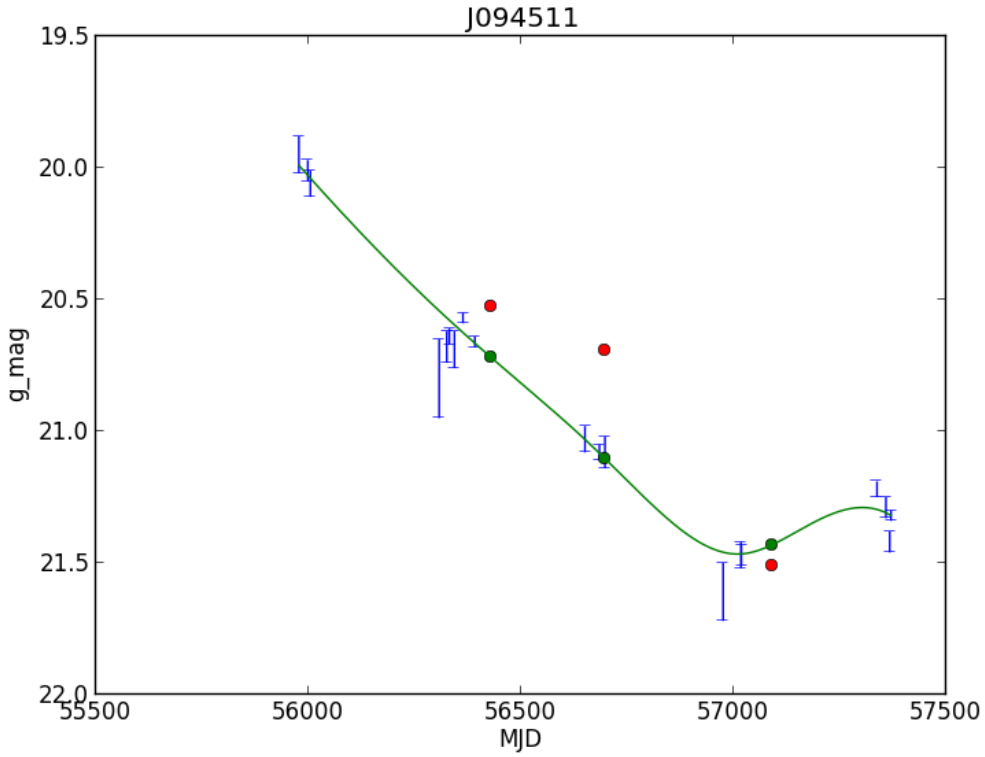

Figure 2.11 *Example scaling fit to target J094511. The spectral epochs in red are the estimated LT g-band magnitudes. Those in green are the rescaling points to the cubic spline fit to the LT light curve shown.*

2.11. It is also possible to rescale according to specific model light curves and it will be noted where appropriate if/how the scaling has been applied.

2.4.2 De-reddening and composite model fitting

For the spectral fitting process, a PYTHON package, LMFIT, was used. This is a non-linear optimization and curve-fitting tool that builds on a Levenberg–Marquardt algorithm. It is used to fit single or multiple Gaussian components to the emission lines and provide a power-law fit to approximate the local continuum. The power law used in the fitting routine takes the form

$$F_\lambda = A(\lambda/5100\,\text{Å})^\beta, \tag{2.1}$$

where A is the normalization and β is the power-law slope. In addition to the above components, a template fit was used to estimate the Fe contribution. In the UV, the empirical template is that from Vestergaard & Wilkes (2001), and

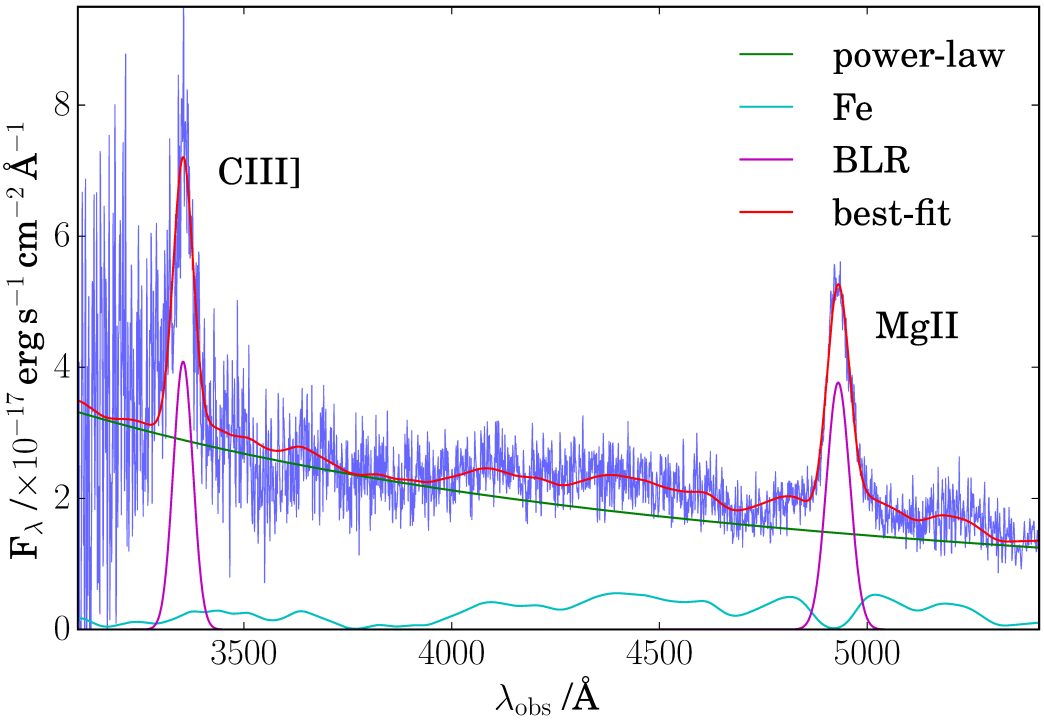

Figure 2.12 *Example of the fitting process for target J094511. The components include the following: power-law (green), Gaussian line fits (magenta), convolved iron template (cyan) and overall best fit (red).*

in the optical, where possible, that of Véron-Cetty et al. (2004). These regions are defined in greater detail in Section 3.2. The Fe template is convolved with a Gaussian in order to better approximate the true blended Fe emission. The width of the convolving Gaussian was set to match that of the broad MgII/H β components in the UV/optical, respectively.

Before performing any fits the spectra are first corrected for Milky Way extinction using the A_V values provided by Schlafly et al. (2012) (via the NASA/IPAC database) and the extinction law in the optical from Cardelli et al. (1989). No attempt has been made to correct for host galaxy reddening at this stage. The most prominent telluric features above 6860 Å were masked out during the fitting process. When fitting H β the narrow line widths and centres were tied to that of [OIII]5007. An example fit is shown in Fig. 2.12.

2.5 Microlensing models and analysis techniques

This section will summarize the methods used for exploring the suggestion that the slow-blue PS1 transients may be due to microlensing events. That is, the bulk of the observed variability is due to an intervening stellar-mass object passing near the line of sight to the distant AGN. This lens object may be also belong to an intervening galaxy. This section contains many technical details which pertain to the work carried out in Chapter 4.

Initially, I will concentrate on modelling events due to single isolated lensing stars, rather than the complex magnification maps due to multiple stars in the line of sight normally considered in quasar microlensing studies (e.g. Wambsganss 1992; Lewis & Irwin 1995; Vernardos & Fluke 2013). This is justified because we are dealing with random sightlines rather than objects pre-selected as multiply imaged quasars. For example, a sight line through the Milky Way at the solar radius, with an assumed stellar surface mass density of $\sim 40\,\mathrm{M}_\odot\,\mathrm{pc}^{-2}$ (Bovy & Rix, 2013), would result in an optical depth to microlensing of ~ 0.01 if placed at $z = 0.2$ with the quasar at $z = 1.0$. We will also usually be looking through a galaxy well below L_*.

On the other hand, the effect of shear caused by the overall potential of the lensing galaxy containing the microlensing star will often be significant, so that in general we will be dealing with 'Chang–Refsdal' (CR) lenses (Chang & Refsdal, 1984). Some of the more complex and/or multiply-peaked light curves in the sample may be a result of this. There are other events which are generally smooth and single peaked, so I will start with the simplest model ignoring shear and using a simple point lens. In later sections I will examine the effect of varying that assumption.

2.5.1 Point-source point-lens model

This model is likely an oversimplification but will nevertheless prove useful. In this model the magnification is given by:

$$\mu = \frac{y^2 + 2}{y\sqrt{y^2 + 4}}, \quad y := \beta/\theta_\mathrm{E}. \tag{2.2}$$

Here, y is the normalized source position in units of the Einstein radius of the

Table 2.3 *Free parameters in the simple microlensing model.*

Parameter	Description
M_l	Lens mass
$v_\perp$	Transverse velocity
t_0	Mid-point epoch
z_d	Lens redshift
y_0	Impact parameter
F_s	Source flux (pre-lensing)
F_b	Background flux (unlensed)

lens, which is given by:

$$\theta_\mathrm{E} = \left(\frac{4GM}{c^2} \frac{D_\mathrm{ds}}{D_\mathrm{d} D_\mathrm{s}} \right)^{1/2}. \tag{2.3}$$

D_d, D_s and D_ds are the angular diameter distances for the lens, source and between the lens and source, respectively. To compute the light curve $F(t) = \mu(t) F_\mathrm{s}$ requires the formula for the trajectory of the source, as in Wambsganss (2006):

$$y(t) = \sqrt{y_0^2 + \left(\frac{t - t_0}{t_\mathrm{E}} \right)^2}, \quad t_\mathrm{E} := \frac{D_\mathrm{d} \theta_\mathrm{E}}{v_\perp}, \tag{2.4}$$

where y_0 is the impact parameter at t_0 and $v_\perp$ is the transverse velocity of the lens relative to the observer/source line of sight. The Einstein time-scale, t_E defines a characteristic time-scale for the lensing event. Figure 2.13 shows some example light curve for various impact parameters. If one includes an additional background flux contribution from the host/lens galaxy, this particular model has seven parameters. These are listed in Table 2.3. It should be noted that, due to the degeneracies inherent to t_E, there are technically only five free parameters but it is instructive to include the additional parameters, particularly if one wishes to say anything about the lens object.

In order to explore this model in more detail, EMCEE, a Bayesian model fitting package that uses a Markov chain Monte Carlo (MCMC) method to explore parameter space, was used (Foreman-Mackey et al., 2013). Gaussian errors are assumed and the parameters constrained to remain physical. In order to deal with the mass/velocity degeneracy in the model, a lognormal prior on the expected lens mass was used. This takes the form of a Chabrier IMF (Chabrier, 2003)

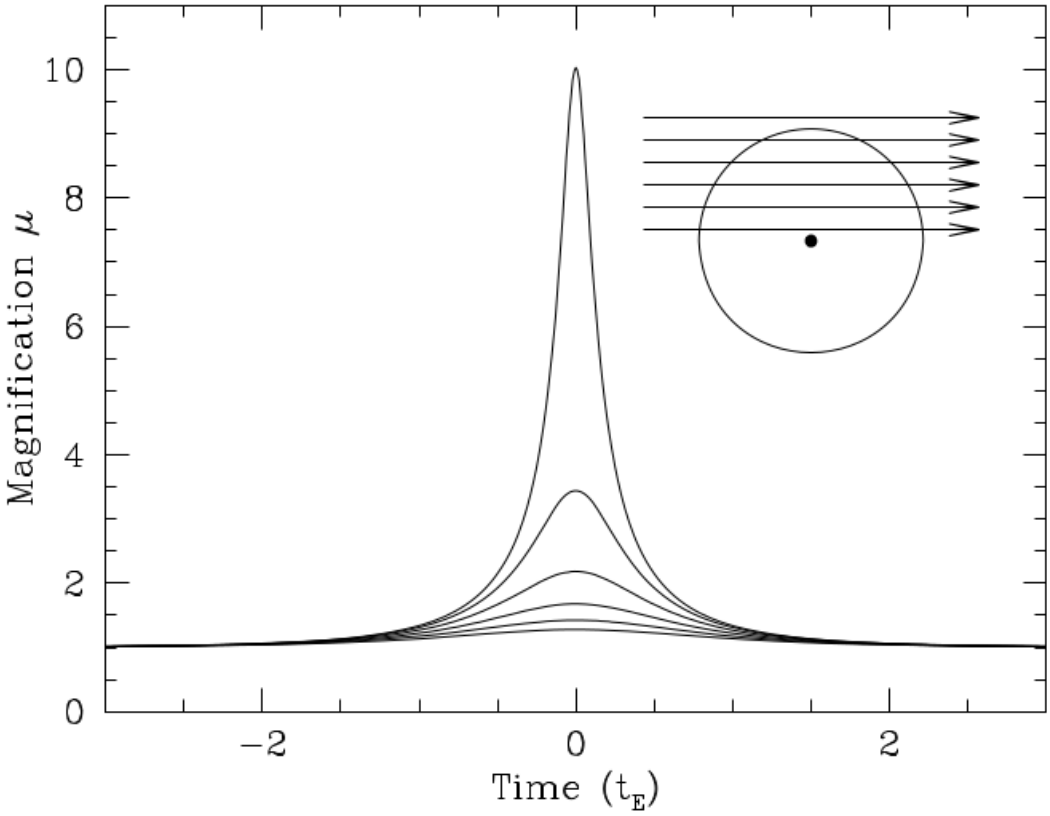

Figure 2.13 *Example simple microlensing light curves showing the expected magnification vs timescale for various impact parameters. Reproduced from Wambsganss (2006).*

with an additional weighting factor M to account for the increase in lensing cross-section with mass. The lower limit for the lens mass was set at $10^{-3}\mathrm{M}_{\odot}$ and the transverse velocity of the lens was left free. This is the configuration used for the work in Chapter 4. Chapter 5 uses a different prior configuration to address shortcomings with the earlier work and will be discussed therein. Over the course of a lensing event, an AGN will also have some level of, as yet unknown, intrinsic variability. A simple approach that attempts to allow for this was to increase the errors on the photometry by an additional 10% of the flux level at each epoch, a fairly conservative estimate for typical AGN variability. The CRTS data were not used in this analysis due to concerns over colour effects resulting from the clear filter used.

The likelihood function is formed from the product of the sequence of Gaussian PDFs for each data point with respect to the model. The MCMC program takes the natural log of this so it has the following form:

$$-0.5 \sum \ln(2\pi\sigma_i^2) + \frac{(y_{\mathrm{obs},i} - y_{\mathrm{model},i})^2}{\sigma_i^2} \tag{2.5}$$

In Chapter 4, parameter constraints from the MCMC analysis are obtained using the marginalized posterior probability distributions. For each, the peak value was determined by fitting a polynomial through the maximum of the distribution using a coarse sampling (logarithmic bins for M_{l} and $v_{\perp}$). A finer sampling of the distribution was used to determine the narrowest allowable range, which encompassed > 68 per cent of the data about this peak. In addition, values for r_{E}, the Einstein radius in the source plane, were calculated from the MCMC trace output. This distribution (logarithmic bins) was then used to produce constraints in the same manner as for the other parameters. Some results from this MCMC analysis will be displayed in Section 4.5.1.

2.5.2 Extended sources

The assumption of the AGN as a point-source will not always be valid, so it is necessary to consider extended source models. Indeed, this fact can potentially be exploited to yield additional information regarding the accretion disc and broad line region (BLR) structure. In order to explore extended source models in more detail, an inverse-ray-shooting code technique (Jiménez-Vicente, 2016) was used

to construct magnification maps, initially for a point-lens model. The maps that have been constructed are normalized in units of the Einstein radius, have a pixel scale of $1/800\,\theta_{\rm E}$ and side length of $4\,\theta_{\rm E}$. A simplifying assumption is that the accretion disc and BLR sources are Gaussian. This should be reasonable for low inclinations ($\phi < 45°$) and disc-like morphologies, when projected along the line of sight (Mortonson et al., 2005; Sluse et al., 2011). For a given set of lens/source parameters, the light curve for the event is obtained by varying the source position under the magnification map as a function of time and integrating to find the total amplification at each epoch.

A detailed MCMC analysis of extended sources under a point-mass lens, as we have done for the point-source model, is computationally expensive and still in the preliminary stage. Therefore, I have deferred some of these results to Chapter 5. Nevertheless, for this current work I am able to use this extended model in a qualitative fashion to determine whether or not the point-source approximation remains valid when estimates for the true disc size are used. My starting point for this testing was first to derive estimates for the expected accretion-disc size. For this, I make use of the simplified thin-disc model from Morgan et al. (2010). This provides a simple formula for the effective disc size:

$$\log_{10}\left(\frac{R_{2500}}{\rm cm}\right) = 15.184 + \frac{2}{3}\log_{10}\left(\frac{M_{\rm BH}}{10^9 {\rm M}_\odot}\right) + \frac{1}{3}\log_{10}\left(\frac{L_{\rm bol}}{\eta L_{\rm E}}\right), \tag{2.6}$$

where $L_{\rm bol}$ is the bolometric luminosity, η the accretion efficiency and $L_{\rm E}$ the Eddington luminosity. However, from the study of differential microlensing of components of strongly lensed quasars, Morgan et al. (2010) also found evidence that the accretion disc may in fact be around four times larger than this relationship implies. They derive the following empirical relationship:

$$\log_{10}\left(\frac{R_{2500}}{\rm cm}\right) = 15.78 + 0.8\log_{10}\left(\frac{M_{\rm BH}}{10^9 {\rm M}_\odot}\right). \tag{2.7}$$

Both of these relationships require an estimate for the mass of the black hole. For this, I make use of the McLure & Dunlop (2004) single epoch relation:

$$\frac{M_{\rm BH}}{{\rm M}_\odot} = 3.2\left(\frac{\lambda L_{3000}}{10^{37}{\rm W}}\right)^{0.62}\left[\frac{{\rm FWHM_{MgII}}}{{\rm km\,s^{-1}}}\right]^2. \tag{2.8}$$

This gives the black hole mass as a function of MgII line width and luminosity at 3000 Å. This relationship depends on accurate estimates of the monochromatic continuum luminosity and MgII width. Both may be overestimated if there is an ongoing microlensing event. In the absence of a confirmed AGN baseline luminosity, I make use of the faintest(latest) spectral epoch for these calculations. The black hole mass estimates for each epoch are noted in Chapter 3. For equation (2.6), the bolometric luminosity was calculated using the monochromatic luminosity (λL_{2500}), from the same epoch as the black hole mass estimate, along with a bolometric correction factor of 5.6 (Elvis et al., 1994). The accretion efficiency was assumed to be 0.1. Finally, the Gaussian sources for testing with the magnification maps are generated with a 2σ radius equivalent to the accretion-disc size estimates obtained above.

An important test of this extended source model is to see if it can reproduce the analytic light curve from the point-source model in the limit when the source size is very small. This is achieved by setting the size of the source to a single pixel and testing a wide range of impact parameters. The results are in excellent agreement, even for very small impact parameters, and implies that pixel/resolution effects should be minimal as long as source sizes larger than the pixel scale are used.

Sources larger than the accretion-disc estimates, which are more appropriate when considering BLR emission, are also considered. The results of an extended source analysis for some objects are displayed in Section 4.5.2.

2.5.3 Chang-Refsdal models and beyond

For the models I have discussed so far, the assumption of a point-mass lens is reasonable as it is assumed the microlensing is caused by a single star. However, this neglects the presence of an external shear due to the lens-host galaxy or additional stars along the line of sight, which can have significant consequences. This background perturbation breaks the circular symmetry of the point-mass lens and results in the degenerate point in the source plane unfolding into a caustic pattern of varying complexity. The corresponding light curve may exhibit double peaks or more complex structure as a result, particularly if the size of the source is small enough relative to the caustic network.

In multiply imaged quasars, it is possible to use the positions of the quasar images and lens galaxy to estimate the convergence and shear parameters (κ,γ)

for each image. This also encapsulates the expected macromagnification before any microlensing perturbations are taken into account. However, in my case, I frequently do not have an unambiguous detection of the position/redshift of any lens galaxy or multiple images, which may be going unresolved in the photometry. With this in mind, the point-lens models mentioned previously have the implicit working assumption that the convergence and shear, and hence macromagnification, are small enough to be neglected. This is likely to be an oversimplification but should be sufficient to demonstrate the feasibility of the microlensing scenario for the single-peaked objects.

For the multiply peaked objects, a more complex lensing model is required. The model which describes the effect of microlensing plus an external shear, is that of the CR lens (Chang & Refsdal, 1984). This is a useful starting point as it treats the lens-host galaxy as an additional point mass nearby. Here, the shear parameter is defined as the ratio of the Einstein radius of the galaxy to the distance of the stellar lens from the galaxy centre, all squared. If this ratio is greater than unity, there can be strongly demagnified regions in the lens map. This adds a further layer of complexity when considering the light curves. For very small shear values, the magnification map is essentially the same as for an isolated point lens.

Fig. 2.14 shows how the shear varies in relation to the lens galaxy mass for selected star–galaxy separations. This assumes a lens redshift of 0.2 and source redshift of 1.0. Lawrence et al. (2016) estimates that an AGN will have a foreground galaxy present in perhaps 0.2% of cases but only a small fraction of these will have an ongoing high-amplitude microlensing event at any one time. We appear to be in a regime where some events will be well approximated by a point lens and others will require a more detailed treatment of the perturbing lens galaxy.

The use of a CR magnification map allows a qualitative explanation for the double-peaked light curve seen in some of the slow-blue transients and some early results are displayed for J142232 in Chapter 4. A thorough analysis of these more complex lensing models is still required and will be the subject of future work.

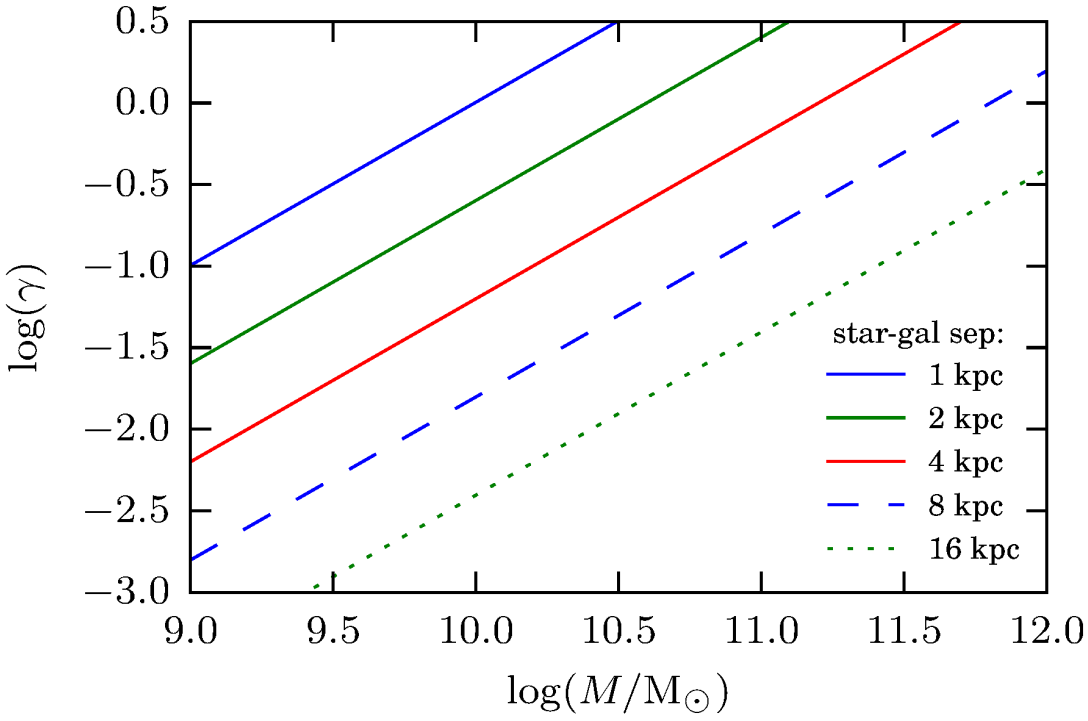

Figure 2.14 *Plot of the Chang-Refsdal shear parameter, γ, against total galaxy mass for selected star-galaxy distances. Here, the lens redshift is assumed to be 0.2 and the source redshift 1.*

Chapter 3

Spectral evolution of 64 long-term AGN transients

3.1 Introduction

The focus of this chapter is on a summary of the main observations and results from the comprehensive spectroscopic monitoring campaign of the PS1-A AGN transient sample. The purpose is to distill the large amount of spectroscopic data into a range of quantifiable parameters to allow a detailed examination, both of the sample as a whole and of the evolution seen in individual objects. This dataset offers a unique opportunity to probe these long-term AGN transients in context and offers us clues as to the underlying physical mechanisms at work.

3.2 Outline

The PS1-A AGN transient sample comprises a total of 64 objects and 235 individual spectral epochs. This includes one observed AGN, J084626, which was not technically flagged as a transient but is nevertheless included for completeness. Five objects from the sample only have a single spectral epoch though 48 have three or more. The construction of the sample and photometric/spectroscopic monitoring procedures are detailed in Chapter 2.

To compare and contrast the observations across this sample requires the

extraction of information from the spectra in a uniform manner. The procedures for reducing the spectroscopic data have been outlined in detail in Section 2.3 and will not be repeated here. The final step in this process is to fit multiple components to the data (after correcting for Milky Way reddening), typically a power-law to approximate the continuum, a convolved Fe template and Gaussian components for the broad/narrow lines. With the measured parameters for these components, it is then possible to derive other parameters such as redshift, monochromatic luminosity, line equivalent width etc. For the work in this chapter, I have chosen to focus on three key regions of the spectra for measurement purposes: i) the rest-frame UV; ii) the [OII]3727 region; iii) Hβ/[OIII] complex (including Hγ). In the WHT spectra, the rest-frame UV region will consist of everything from 3100Å (observer frame, the blue arm limit) up to 3080Å $\times$(1+z) as this is the limit of the FeUV template (see Chapter 2). The [OII]3727 region fit consists of a much simpler local power-law fit and Gaussian component for the line across a $\sim$200Å window. The Hβ fit, hereafter the 'optical', extends from 4200Å $\times$(1+z) to 5300Å $\times$(1+z) and includes an estimate of the FeOpt contribution using the Veron-Cetty iron template and, where possible, also attempts to fit HeII4686. Hα is visible in only a few low redshift cases and typically suffers from significant telluric absorption so has not been measured for this current work. Strong telluric lines are masked out during the fitting process but these masks are occasionally relaxed in cases where a prominent line is present near one of the edges. In addition to the WHT spectra, 18 spectral epochs were taken using the blue arm spectrograph on the MMT. In these cases the lower wavelength cutoff is at the higher value of 3200Å, meaning that the rest-frame UV measurements may not be directly comparable with those from the WHT.

Given the range of redshifts for these AGN, the fitted UV region can sometimes be extensive, including multiple broad lines, up to Lyman alpha, or may simply include MgII, which is present for every object in this sample. This should be kept in mind when comparing the evolution of the UV power-law slopes across the sample. Where possible, any clearly identifiable absorption lines were also fitted with Gaussian components. The profile of some broad lines, namely MgII/CIV/Hβ, would occasionally warrant a double-Gaussian fit to the line, particularly if the signal-to-noise allowed, as long as there was an improvement in the reduced chi-squared value for the resulting fit. With these double-component fits, the FWHM of the line was measured by taking a similar approach to Vestergaard & Osmer (2009) that is, the FWHM is computed for the composite line profile. In my case the errors are computed via a Monte Carlo method using

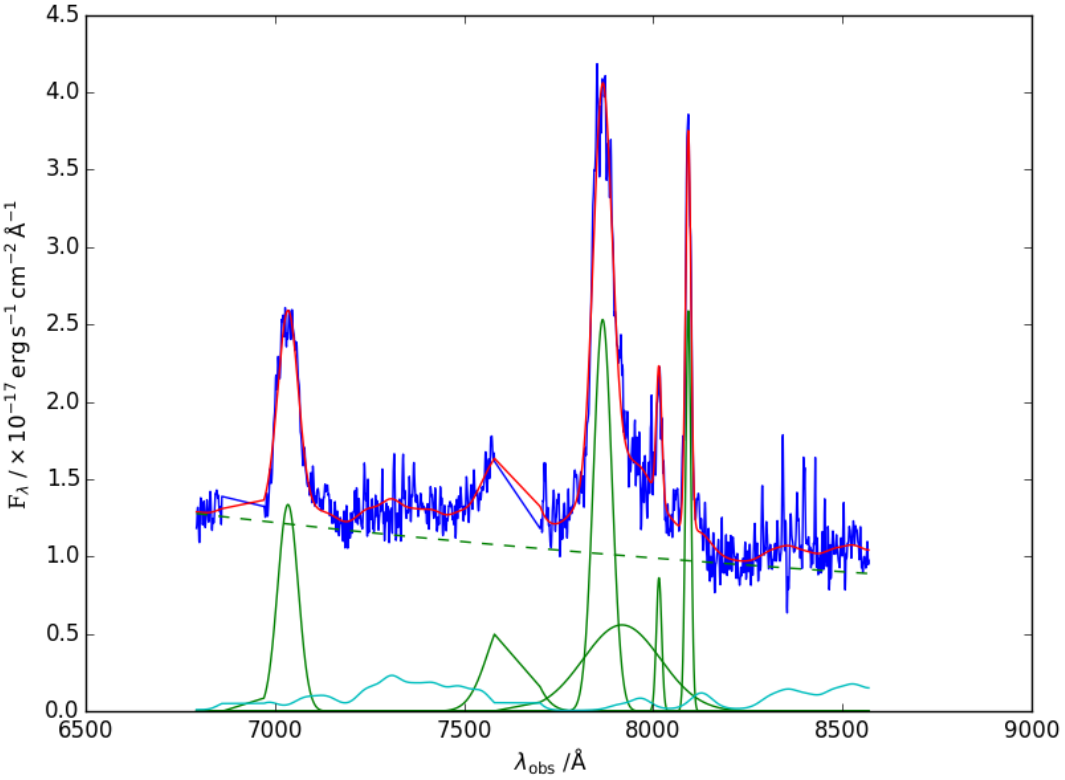

Figure 3.1 *Example of fit to the Hβ region obtained for target J014139 on 22/10/16. Line and continuum components are shown as green solid/dashed lines respectively, the Fe contribution is in cyan and the complete fit is shown in red. This includes a two-component fit for the Hβ line and the discontinuity near $HeII_{4686}$ at ∼ 7600Å is due to a telluric mask.*

the single-component parameter constraints. An example of a fit which includes a double-component for Hβ is shown in Figure 3.1.

The most common parameters used for comparison in large spectroscopic AGN samples tend to be line equivalent width and continuum luminosity. The local power-law fit in each spectrum provides the means for deriving each. Unless otherwise noted, monochromatic luminosities are computed in the AGN rest-frame, assuming spherical symmetry, and using a Planck13 cosmology (Planck Collaboration et al. (2014); $H_0 = 67.8, \Omega_\Lambda = 0.693$) for luminosity distance calculations. The line flux can be taken directly from the Gaussian fit(s) to the data as this is one of the three fitted parameters, in addition to line sigma and centre, used in the pipeline. The equivalent width is then simply the total observed line flux divided by the continuum flux at line centre, divided by an additional factor (1+z) to shift to rest-frame. The redshift is determined from [OIII]/[OII] narrow-line components, where possible, and from the narrower MgII component if not. One object, J025633, displays a featureless spectrum and as such has no defined redshift as yet. Because of this, it will be excluded from the remainder of this analysis. One AGN, J154404, is the most distant in the sample and in this case the redshift has been determined using CIV rather than MgII.

Given that I am also interested in the evolution of these objects, I must also take into account the possibility of line profile changes and/or continuum/colour changes. The UV and optical power-law slopes can serve as a proxy for any colour changes in these objects. Any observed changes may represent intrinsic color changes in the AGN or perhaps present as a contrast effect between a fading AGN component and a static host galaxy contribution. Similarly, any evolution in the line profiles may be revealed by monitoring the widths/centroids of the line though it is possible that small profile changes may be overlooked in this manner. The signal-to-noise ratio of individual epochs is likely to be the limiting factor in confirming profile changes in any case.

Other derived parameters which I have included are the bolometric luminosity and black-hole mass which, in turn, allow an estimate for the Eddington fraction in these objects. The bolometric luminosity has been estimated using the empirical relationship from Krawczyk et al. (2013):

$$\log(\mathrm{L_{bol}}) = (0.9869 \pm 0.0003)\log(\nu_{2500} L_{2500}) + (1.051 \pm 0.014) \qquad (3.1)$$

though these estimates should necessarily be treated with a degree of caution, primarily due to the fact that the transients are still evolving. The black-hole mass is derived from the luminosity and MgII FWHM, in this case using the Vestergaard et al relation (Vestergaard & Osmer, 2009)[1]

$$\log\left(\frac{\mathrm{M_{BH}}}{\mathrm{M_{\odot}}}\right) = 0.86 + 0.5\log\left(\frac{\mathrm{L_{3000}}}{10^{44}\mathrm{ergs^{-1}}}\right) + 2\log\left(\frac{\mathrm{MgII_{FWHM}}}{\mathrm{kms^{-1}}}\right) \tag{3.2}$$

which again should be treated with caution. This caution is warranted given the fact that the majority of these objects are brighter now than at the Sloan epoch. This raises the possibility that the derived bolometric luminosities and black-hole masses may be overestimated. Rather than make any further assumptions at this stage, I simply derive these parameters at each epoch and include them in the master table.

The results of the parameter estimation/derivation process for this spectroscopic sample are presented in the following section(s). A caveat which should be noted is that the uncertainties on many parameters represent the uncertainty from the spectroscopic fitting process only. There will be an additional systematic uncertainty present regarding the absolute flux calibration at each spectral epoch. As noted in Chapter 2, I have attempted to reduce these transparency effects by rescaling the spectral epochs to that of a smoothed fit through the LT light curve for each object. In objects with an erratic or poorly sampled LT light curve this may introduce, or fail to correct for, spuriously high/low data points. Scaling-independent parameters, such as the line equivalent width, will not be subject to the same degree of uncertainty.

3.3 Global results

This section will focus on the full spectroscopic sample. In later sections, subsets will be defined which will allow a closer look at the evolutionary trends seen in these objects. Initial results for a selection of parameters can found in Table 3.1. This includes the number of spectral epochs, the observed change in magnitude seen from SDSS to peak, a selection of key max/min parameters derived from

[1]This relationship is an update on the mass-scaling relationship used in Chapters 2/4. In this chapter, in contrast to the others, I make use of multi-component MgII fits and have adopted a similar technique for determining the composite FWHM as the work referenced here. It was felt that this should improve the reliability of the mass estimates reported herein.

the data and an estimate of the maximum Eddington fraction seen in any epoch for each target. For this sample all of the objects remain sub-Eddington with only a few rising above ∼10%. Given that there are a large number of both measured and derived parameters which may prove useful, all of the data has been tabulated with the intention of being made available online.

Figure 3.2 shows the distribution in redshift, luminosity, MgII FWHM and black-hole mass for every object in the sample (with the exception of J025633). The black-hole mass is derived as noted in the previous section. These histograms represent the weighted means across all epochs. A quick glance shows that there is one object with an anomalously high MgII FWHM. This is due to a problem obtaining a reliable fit to the MgII region in this object and also results in a spuriously high black-hole mass. The total range in redshift is from 0.276 to 2.146 though approximately two-thirds of the sample are below a redshift of 1. The conversion to bolometric luminosity results in an observed range spanning two orders of magnitude from $44.3 < \log(L_{\rm bol}) < 46.1$ erg/s. The observed black-hole mass ranges from $7.8 < \log(M_{\rm BH}) < 10.1$ $M_{\odot}$. For the MgII FWHM the observed values range from $2400 < {\rm MgII}_{\rm FWHM} < 10900$ km/s, excluding the spurious outlier.

Figure 3.3 shows the relationship between derived black-hole mass and bolometric luminosity for every spectral epoch, that is, each target appears multiple times in the figure. The points are coloured to reflect the UV power-law slope. In general, redder objects appear to exhibit a higher black hole mass for a given luminosity but the slope is shallower than for the bluest objects in the sample. Readily apparent is the correlation between luminosity and black-hole mass, as would be expected, though there are some interesting outliers. Note in particular the five points corresponding to the bluest object in the sample, J150210 which has shown an achromatic decrease of ∼0.5 dex in luminosity since observations began. This object will be discussed in greater detail in the following sections. Given that this sample has been selected due to their transient nature, one must be careful when interpreting some of the values noted above.

Comparison of Figure 3.2 with the quasar catalogue from Shen et al. (2011, Fig. 13) shows that the AGN in the PS1-A sample display typical MgII FWHM values and continuum slopes. It is worth noting that this sample also contains proportionately more low luminosity objects and higher MgII EW values relative to the Shen catalogue. This may not be immediately surprising given that the majority of AGN in this sample are at relatively low redshifts and were not

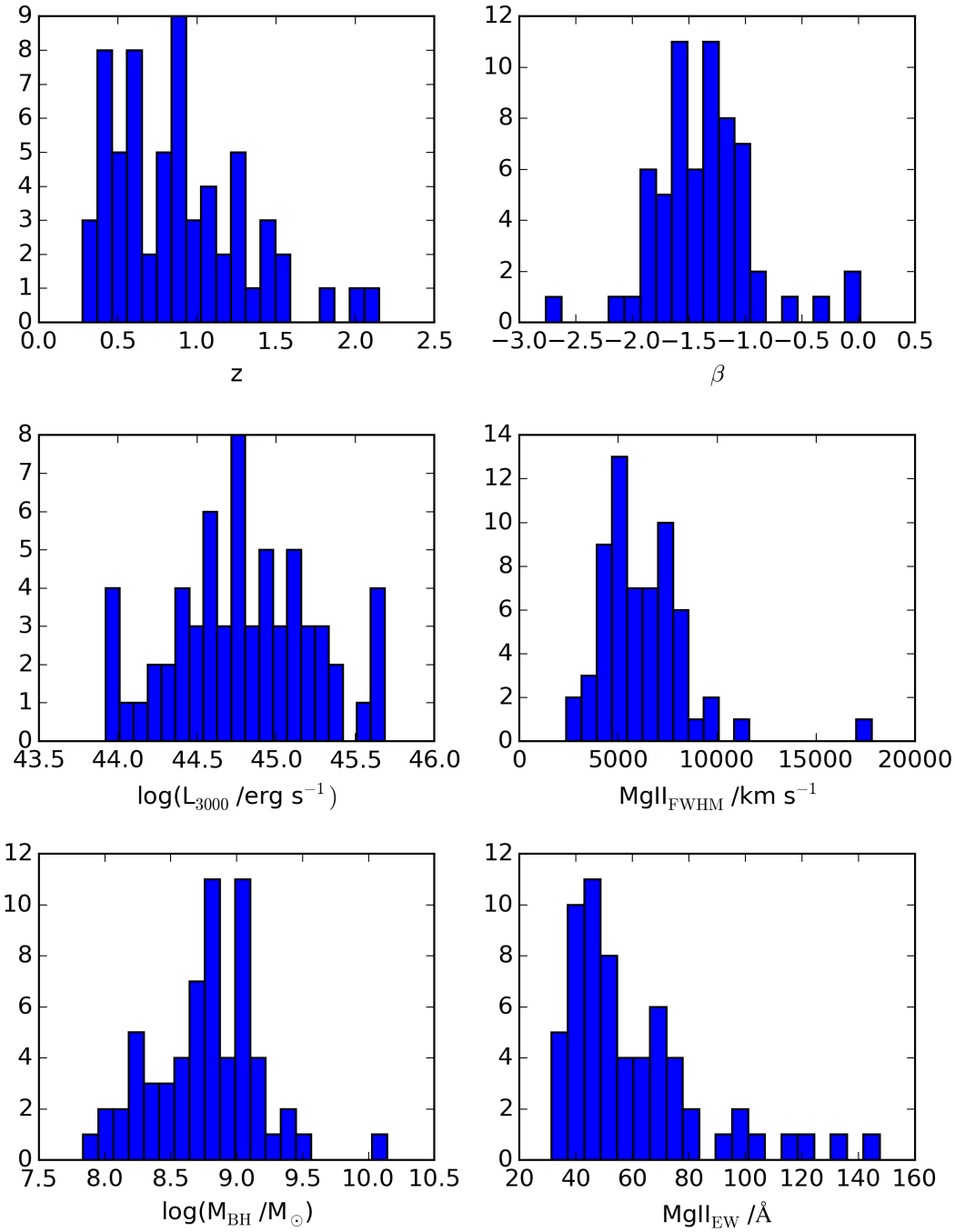

Figure 3.2 *Distribution of various parameters for the PS1 AGN transient sample. See Section 3.2 for more information.*

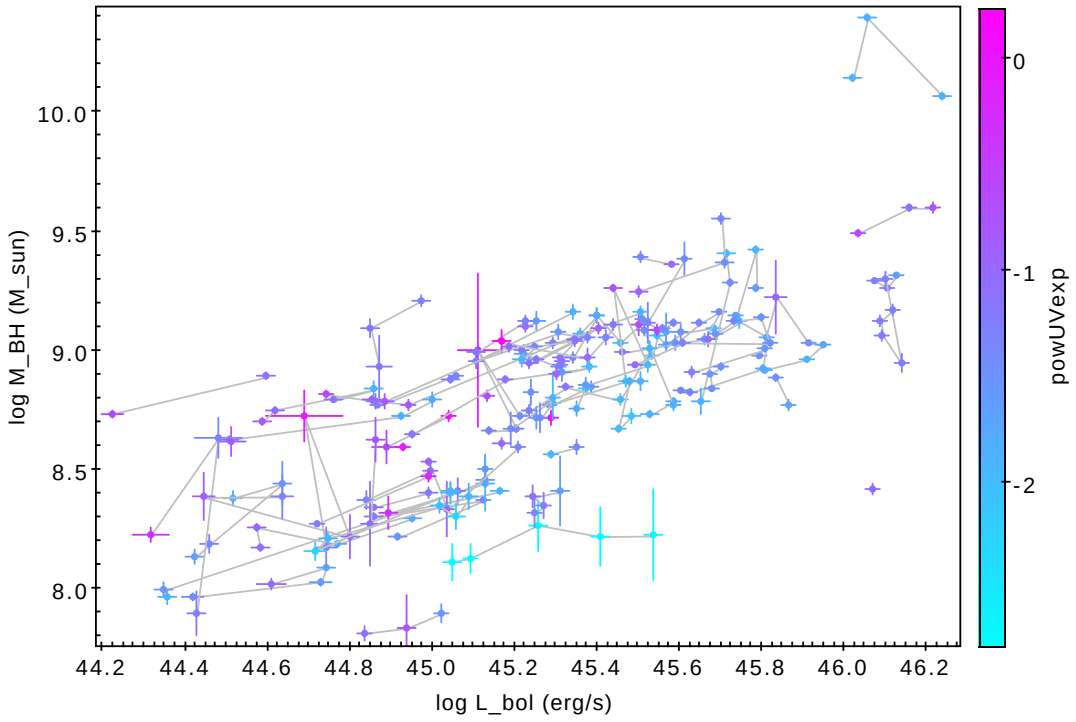

Figure 3.3 *Derived black-hole mass vs bolometric luminosity for the entire sample. The points are coloured to reflect the slope of the measured power-law fit in the UV. Every spectral epoch is plotted and data for individual AGN are linked via a grey line.*

previously classified as AGN. It is less clear if the black-hole masses in this sample are lower relative to the Shen catalogue but given that some of these transients are still ongoing there may be some erroneously high black-hole masses here. This assumes that the low state is the default or 'quiescent' state of course. This simple static catalogue comparison shows that, to first order, there is nothing immediately unusual about the AGN in this sample. That is, given a single spectroscopic observation, they might be considered normal with respect to the wider AGN/quasar population. What makes them unusual is the knowledge that the majority of these AGN light curves are evolving, sometimes significantly, with respect to the more typical 0.2 mag fluctuations seen in AGN. With this in mind, the next sections will shift the focus onto the spectroscopic evolution of these objects to see what else might be learned.

Table 3.1 *A selection of observed and derived parameters for all targets. (1-4) Target Identifier, position and no. of spectral epochs. (5) Milky Way extinction values. (6) Mean redshift. (7) SDSS earliest g-band epoch minus the LT peak g-band epoch. (8)/(9) Max/min values for the monochromatic luminosity. (10)/(11) Max/min values for MgII rest-frame equivalent width. (12) Minimum black hole mass. (13) Minimum bolometric luminosity. (14) Maximum Eddington fraction ($L_{\rm bol}/L_{\rm Edd}$). Two targets are missing data, J025633, which has a near-featureless spectrum and J154404, the highest redshift target in the sample, with no reliable MgII detection.*

Target	RA	Dec	#	A_V	z	Δg	$L_{3000,\rm min}$	$L_{3000,\rm max}$	$\rm MgII_{EW,lo}$	$\rm MgII_{EW,hi}$	$M_{\rm BH,min}$	$L_{\rm bol,min}$	$\rm EddFrac_{max}$
				mag		mag	$\log(\rm erg\,s^{-1})$	$\log(\rm erg\,s^{-1})$	(Å)	(Å)	$\log(M_\odot)$	$\log(\rm erg\,s^{-1})$	$L_{\rm bol}/L_{\rm Edd}$
J003545	00 35 45.85	-22 51 17.9	1	0.0548	1.167	1.76 ± 0.19	44.91 ± 0.01	44.91 ± 0.01	44.3 ± 1.3	44.3 ± 1.3	8.72 ± 0.03	45.29 ± 0.02	0.030 ± 0.002
J011356	01 13 56.51	+06 36 03.0	1	0.1157	0.825	1.69 ± 0.06	44.70 ± 0.00	44.70 ± 0.00	73.8 ± 1.8	73.8 ± 1.8	8.81 ± 0.03	45.13 ± 0.02	0.017 ± 0.001
J011635	01 16 35.54	+22 08 10.4	3	0.1178	1.796	2.21 ± 0.07	45.50 ± 0.01	45.72 ± 0.00	56.0 ± 1.2	118.8 ± 3.4	10.06 ± 0.02	46.02 ± 0.02	0.012 ± 0.001
J014139	01 41 39.25	-00 57 04.4	3	0.0759	0.616	2.92 ± 0.31	44.36 ± 0.00	44.52 ± 0.00	44.5 ± 10.9	61.8 ± 2.2	7.81 ± 0.03	44.84 ± 0.02	0.107 ± 0.011
J025633	02 56 33.77	+37 07 12.4	5	0.3009		2.82 ± 0.06	±	±	±	±	±	±	±
J031240	03 12 40.87	+18 36 41.1	10	0.237	0.895	2.20 ± 0.07	44.85 ± 0.00	45.15 ± 0.00	50.3 ± 0.9	88.5 ± 2.1	8.96 ± 0.02	45.34 ± 0.02	0.031 ± 0.002
J081445	08 14 45.09	+23 26 30.4	5	0.1085	1.170	2.34 ± 0.10	44.99 ± 0.00	45.21 ± 0.00	41.7 ± 1.3	58.2 ± 0.6	8.99 ± 0.01	45.46 ± 0.02	0.033 ± 0.002
J081916	08 19 16.20	+33 14 05.9	4	0.1323	0.426	1.80 ± 0.08	43.90 ± 0.01	44.12 ± 0.01	91.5 ± 9.8	144.6 ± 4.2	8.13 ± 0.03	44.43 ± 0.02	0.016 ± 0.001
J083544	08 35 44.41	+10 08 01.3	6	0.0881	1.325	1.77 ± 0.06	45.29 ± 0.00	45.44 ± 0.00	41.0 ± 0.4	64.7 ± 0.5	8.92 ± 0.01	45.80 ± 0.02	0.071 ± 0.004
J083714	08 37 14.14	+26 09 32.6	2	0.0985	1.280	1.53 ± 0.09	44.71 ± 0.01	44.81 ± 0.01	77.3 ± 1.9	100.1 ± 4.2	8.93 ± 0.02	45.22 ± 0.02	0.019 ± 0.001
J084305	08 43 05.55	+55 03 51.4	5	0.0824	0.895	1.46 ± 0.12	44.30 ± 0.00	44.87 ± 0.00	39.3 ± 1.3	154.1 ± 3.6	8.77 ± 0.02	44.74 ± 0.02	0.015 ± 0.001
J084626	08 46 26.97	+43 13 55.3	2	0.0654	0.576	±	45.00 ± 0.00	45.07 ± 0.00	37.8 ± 0.7	42.4 ± 0.9	8.73 ± 0.02	45.53 ± 0.02	0.051 ± 0.003
J085220	08 52 20.12	+25 57 01.4	3	0.0975	0.855	1.44 ± 0.04	45.03 ± 0.00	45.12 ± 0.00	48.3 ± 2.4	51.3 ± 3.9	9.08 ± 0.08	45.52 ± 0.02	0.025 ± 0.005
J085759	08 57 59.89	+25 54 54.5	3	0.1009	0.746	1.86 ± 0.06	44.81 ± 0.00	45.01 ± 0.00	34.5 ± 1.0	51.5 ± 1.1	9.03 ± 0.02	45.30 ± 0.02	0.019 ± 0.001
J090244	09 02 44.51	+04 52 10.9	2	0.0984	0.437	1.56 ± 0.06	43.77 ± 0.01	44.12 ± 0.01	143.0 ± 3.5	162.7 ± 6.2	8.73 ± 0.02	44.22 ± 0.03	0.004 ± 0.000
J090514	09 05 14.13	+50 36 28.5	3	0.0607	1.288	2.27 ± 0.14	45.20 ± 0.01	45.30 ± 0.00	41.5 ± 1.2	57.5 ± 1.7	9.04 ± 0.03	45.67 ± 0.02	0.046 ± 0.003
J092635	09 26 35.70	+07 25 32.6	3	0.1381	0.465	2.04 ± 0.08	44.37 ± 0.01	44.48 ± 0.00	28.7 ± 4.4	45.4 ± 1.3	8.93 ± 0.13	44.85 ± 0.02	0.007 ± 0.002
J094309	09 43 09.97	+28 35 08.4	3	0.0565	1.271	1.04 ± 0.03	45.60 ± 0.00	45.63 ± 0.00	29.3 ± 0.3	33.6 ± 0.4	9.26 ± 0.01	46.08 ± 0.02	0.055 ± 0.003
J094511	09 45 11.08	+17 45 44.7	4	0.0718	0.757	2.30 ± 0.12	44.10 ± 0.01	44.42 ± 0.01	69.0 ± 1.5	220.8 ± 6.4	8.17 ± 0.02	44.57 ± 0.02	0.036 ± 0.002
J103511	10 35 11.67	+46 04 46.9	1	0.0679	0.941	1.89 ± 0.10	44.90 ± 0.00	44.90 ± 0.00	54.5 ± 1.2	54.5 ± 1.2	8.84 ± 0.02	45.39 ± 0.02	0.028 ± 0.002
J103726	10 37 26.93	-00 38 52.4	1	0.1619	0.993	1.92 ± 0.13	44.70 ± 0.01	44.70 ± 0.01	69.8 ± 1.7	69.8 ± 1.7	8.61 ± 0.02	45.17 ± 0.02	0.029 ± 0.002
J103837	10 38 37.09	+02 11 19.7	4	0.0877	0.620	1.84 ± 0.09	44.37 ± 0.01	44.63 ± 0.00	45.9 ± 0.5	131.9 ± 3.4	8.21 ± 0.01	44.86 ± 0.02	0.046 ± 0.003
J104556	10 45 56.48	+05 26 56.2	5	0.0658	0.994	2.15 ± 0.06	45.12 ± 0.00	45.31 ± 0.00	26.9 ± 0.4	52.9 ± 0.7	8.82 ± 0.01	45.60 ± 0.02	0.060 ± 0.003
J105040	10 50 40.83	+39 17 35.6	4	0.038	0.306	1.61 ± 0.03	43.91 ± 0.01	44.21 ± 0.01	47.5 ± 1.0	77.5 ± 2.5	7.96 ± 0.01	44.42 ± 0.02	0.040 ± 0.003
J105502	10 55 02.00	+33 00 02.5	4	0.0551	0.417	1.75 ± 0.04	43.81 ± 0.01	44.61 ± 0.00	38.0 ± 1.5	161.6 ± 4.2	7.96 ± 0.03	44.35 ± 0.02	0.039 ± 0.010

J110805	11 08 05.80	+62 15 00.8	4	0.027	0.532	2.48 ± 0.12	44.04 ± 0.01	44.47 ± 0.01	49.2 ± 1.7	105.6 ± 1.9	8.61 ± 0.06	44.51 ± 0.02	0.013 ± 0.001
J111547	11 15 47.78	+65 20 25.9	3	0.0322	0.410	1.57 ± 0.04	43.89 ± 0.03	43.98 ± 0.04	60.0 ± 8.1	133.5 ± 9.7	7.89 ± 0.09	44.32 ± 0.04	0.027 ± 0.006
J113309	11 33 09.68	-03 39 09.5	2	0.1233	0.460	2.11 ± 0.05	44.38 ± 0.01	44.51 ± 0.01	58.5 ± 2.0	111.1 ± 2.3	8.34 ± 0.01	44.86 ± 0.02	0.031 ± 0.002
J114742	11 47 42.78	+65 05 54.8	3	0.0503	0.896	1.51 ± 0.07	44.45 ± 0.03	44.65 ± 0.00	100.0 ± 2.4	128.3 ± 2.2	8.59 ± 0.02	44.89 ± 0.03	0.017 ± 0.001
J115553	11 55 53.06	+39 36 42.1	2	0.0567	0.853	2.17 ± 0.14	44.75 ± 0.00	44.86 ± 0.00	58.3 ± 0.8	63.7 ± 1.9	8.56 ± 0.01	45.29 ± 0.02	0.046 ± 0.004
J124728	12 47 28.03	+24 56 53.8	3	0.0405	0.447	2.12 ± 0.04	44.48 ± 0.01	44.62 ± 0.01	40.1 ± 1.5	66.1 ± 3.5	8.31 ± 0.07	44.89 ± 0.02	0.038 ± 0.003
J132958	13 29 58.39	+03 40 07.7	2	0.0634	1.117	3.35 ± 0.57	44.75 ± 0.00	44.81 ± 0.00	26.9 ± 0.5	40.2 ± 0.6	8.77 ± 0.01	45.30 ± 0.02	0.027 ± 0.002
J133004	13 30 04.98	+15 22 30.8	7	0.0568	0.357	2.73 ± 0.24	43.98 ± 0.01	44.41 ± 0.00	37.1 ± 1.7	100.5 ± 4.9	8.17 ± 0.09	44.45 ± 0.03	0.031 ± 0.007
J135846	13 58 46.66	+61 54 09.1	6	0.0389	0.849	2.52 ± 0.08	44.78 ± 0.00	45.00 ± 0.01	30.6 ± 0.9	63.4 ± 1.9	8.76 ± 0.03	45.28 ± 0.02	0.032 ± 0.002
J141056	14 10 56.35	+59 30 31.6	5	0.0222	0.675	1.75 ± 0.17	44.77 ± 0.00	44.95 ± 0.00	52.0 ± 1.1	68.1 ± 1.5	8.94 ± 0.02	45.24 ± 0.02	0.017 ± 0.001
J142232	14 22 32.45	+01 40 26.7	8	0.09	1.075	3.24 ± 0.33	44.65 ± 0.00	45.06 ± 0.00	25.0 ± 0.5	66.3 ± 1.0	8.66 ± 0.01	45.11 ± 0.05	0.052 ± 0.003
J142902	14 29 02.69	+16 24 29.9	4	0.07	0.439	1.57 ± 0.04	44.13 ± 0.01	44.32 ± 0.01	65.5 ± 2.8	117.5 ± 2.0	8.70 ± 0.01	44.59 ± 0.02	0.008 ± 0.001
J143531	14 35 31.51	+07 13 32.7	2	0.0733	1.571	1.84 ± 0.09	45.02 ± 0.01	45.12 ± 0.00	102.5 ± 1.4	118.8 ± 3.4	9.36 ± 0.01	45.51 ± 0.02	0.013 ± 0.001
J150042	15 00 42.64	+52 42 38.5	3	0.0448	0.752	2.31 ± 0.11	44.53 ± 0.00	44.72 ± 0.00	38.1 ± 0.9	62.1 ± 3.3	8.33 ± 0.11	44.99 ± 0.02	0.041 ± 0.011
J150210	15 02 10.46	+23 09 15.3	5	0.1271	0.630	2.78 ± 0.10	44.44 ± 0.01	44.94 ± 0.01	33.9 ± 3.7	103.6 ± 3.8	8.11 ± 0.08	45.05 ± 0.02	0.166 ± 0.073
J151201	15 12 01.72	+05 00 56.2	4	0.1369	0.930	1.94 ± 0.07	44.91 ± 0.00	44.98 ± 0.00	42.1 ± 0.6	55.2 ± 1.7	8.67 ± 0.01	45.45 ± 0.02	0.049 ± 0.003
J151234	15 12 34.96	+55 34 25.5	3	0.0415	0.554	2.18 ± 0.10	44.38 ± 0.00	44.56 ± 0.00	58.5 ± 0.9	90.1 ± 1.2	8.76 ± 0.01	44.87 ± 0.02	0.012 ± 0.001
J151944	15 19 44.00	+00 11 47.4	4	0.1689	0.534	2.34 ± 0.08	44.63 ± 0.00	44.76 ± 0.00	38.8 ± 1.0	77.5 ± 1.3	8.99 ± 0.02	45.11 ± 0.02	0.011 ± 0.001
J152238	15 22 38.66	+39 23 42.8	3	0.0651	1.566	2.12 ± 0.14	45.13 ± 0.01	45.23 ± 0.01	38.0 ± 2.5	88.9 ± 2.1	8.79 ± 0.05	45.65 ± 0.02	0.058 ± 0.007
J152844	15 28 44.18	+42 57 22.6	4	0.0797	0.773	1.75 ± 0.06	44.62 ± 0.00	44.89 ± 0.00	32.7 ± 1.0	49.9 ± 1.2	8.95 ± 0.03	45.11 ± 0.02	0.017 ± 0.001
J154404	15 44 04.39	+14 49 29.2	2	0.1157	2.151	-0.22 ± 0.07	45.00 ± 0.13	45.28 ± 0.02	±	±	±	45.48 ± 0.09	±
J154445	15 44 45.52	+27 29 14.4	4	0.0887	0.548	2.08 ± 0.05	44.76 ± 0.00	44.80 ± 0.01	39.6 ± 2.0	52.0 ± 3.0	8.32 ± 0.06	45.25 ± 0.02	0.068 ± 0.010
J155427	15 54 27.16	+52 35 13.9	6	0.0297	0.572	2.52 ± 0.07	44.70 ± 0.00	44.77 ± 0.00	36.8 ± 2.5	44.7 ± 9.3	8.67 ± 0.07	45.19 ± 0.02	0.028 ± 0.004
J160329	16 03 29.42	+06 05 05.8	2	0.1375	1.410	2.81 ± 0.22	45.34 ± 0.00	45.35 ± 0.00	25.2 ± 0.7	34.1 ± 0.5	8.77 ± 0.02	45.83 ± 0.02	0.099 ± 0.007
J160332	16 03 32.98	+58 03 05.9	4	0.0507	1.038	1.79 ± 0.11	44.68 ± 0.01	44.88 ± 0.00	98.3 ± 0.9	138.7 ± 1.1	8.96 ± 0.03	45.22 ± 0.02	0.016 ± 0.001
J160414	16 04 14.08	+09 13 54.2	4	0.1218	0.437	1.92 ± 0.03	44.80 ± 0.00	44.96 ± 0.00	67.2 ± 2.5	100.1 ± 12.6	8.96 ± 0.03	45.17 ± 0.02	0.021 ± 0.002
J161022	16 10 22.86	+08 38 46.2	5	0.1065	1.975	1.33 ± 0.09	45.59 ± 0.02	45.67 ± 0.00	26.5 ± 1.1	54.6 ± 1.0	8.94 ± 0.03	46.07 ± 0.02	0.125 ± 0.012
J162849	16 28 49.02	+33 30 24.4	3	0.0603	0.581	2.34 ± 0.07	44.39 ± 0.01	44.72 ± 0.00	36.6 ± 0.7	74.7 ± 2.2	8.78 ± 0.03	44.86 ± 0.02	0.012 ± 0.001
J163528	16 35 28.65	+46 35 31.6	3	0.0561	1.454	0.03 ± 0.02	45.61 ± 0.00	45.79 ± 0.00	45.1 ± 1.0	71.7 ± 1.1	9.49 ± 0.02	46.04 ± 0.02	0.033 ± 0.002
J164740	16 47 40.41	+24 17 48.9	3	0.2061	0.845	1.47 ± 0.03	45.05 ± 0.01	45.22 ± 0.01	35.6 ± 0.7	55.5 ± 1.3	9.25 ± 0.02	45.50 ± 0.02	0.017 ± 0.001
J170845	17 08 45.13	+19 05 11.7	2	0.1639	0.585	1.92 ± 0.05	44.35 ± 0.01	44.52 ± 0.00	64.0 ± 4.9	94.6 ± 9.0	8.37 ± 0.04	44.84 ± 0.02	0.025 ± 0.002
J174101	17 41 01.68	+26 54 00.7	1	0.1161	1.103	0.64 ± 0.04	45.61 ± 0.00	45.61 ± 0.00	39.5 ± 1.2	39.5 ± 1.2	8.41 ± 0.02	46.07 ± 0.02	0.361 ± 0.026
J175610	17 56 10.00	+46 39 58.7	7	0.1133	0.676	1.91 ± 0.05	44.47 ± 0.01	44.84 ± 0.00	38.5 ± 1.3	82.2 ± 1.7	8.65 ± 0.02	44.95 ± 0.02	0.023 ± 0.002
J212547	21 25 47.51	+05 02 19.7	3	0.2089	1.263	1.91 ± 0.07	45.23 ± 0.00	45.29 ± 0.00	31.5 ± 0.4	35.5 ± 0.4	9.14 ± 0.01	45.74 ± 0.02	0.032 ± 0.002

J214006	21 40 06.26	+10 47 37.7	2	0.1678	0.621	2.67 ± 0.15	44.23 ± 0.00	44.58 ± 0.00	48.9 ± 1.3	85.2 ± 1.4	8.27 ± 0.01	44.72 ± 0.02	0.026 ± 0.002
J223210	22 32 10.51	-08 06 21.2	7	0.1251	0.276	1.87 ± 0.03	44.14 ± 0.01	44.55 ± 0.01	50.4 ± 3.5	128.6 ± 5.7	8.16 ± 0.04	44.72 ± 0.03	0.046 ± 0.006
J233237	23 32 37.52	-10 04 44.0	6	0.0674	1.456	2.20 ± 0.16	45.03 ± 0.00	45.33 ± 0.00	54.4 ± 1.2	90.1 ± 1.0	8.94 ± 0.01	45.49 ± 0.02	0.049 ± 0.003
J234953	23 49 53.52	-09 16 06.9	3	0.0845	1.272	1.87 ± 0.20	45.17 ± 0.00	45.21 ± 0.00	43.1 ± 0.6	47.1 ± 0.5	8.84 ± 0.01	45.67 ± 0.02	0.055 ± 0.003
J235635	23 56 35.25	+13 56 15.9	3	0.1533	0.932	1.83 ± 0.08	45.07 ± 0.00	45.12 ± 0.00	51.2 ± 0.7	72.5 ± 1.4	9.08 ± 0.02	45.55 ± 0.02	0.024 ± 0.001

3.4 Subsample definitions

In order to identify the 'most variable' objects in the PS1-A sample it is relatively straightforward to make a selection based on the fractional change in the continuum or the strength of the broad lines relative to this. This selection is shown in Figure 3.4. It plots the relative change in MgII rest-frame equivalent width against change in bolometric luminosity. A factor > 2.5 change in continuum or > 2.5 in equivalent width warrants immediate selection as a significantly variable object. The exact cut is somewhat arbitrary but the ten objects selected in this way are hereby denoted the 'Prime' subsample for later discussion. It should be noted that this selection is based only on the spectroscopic monitoring and will therefore neglect objects with large photometric changes prior to any spectroscopic observations.

In addition to the 'Prime' selection, it is also useful to define subsets based on the characteristics of the entire light curve. The reasons for this are twofold: first, this should allow for a general comparison between objects with similar light curve profiles and second, this selection should be less sensitive to the cadence of the spectroscopy which may not have sampled the peak(s) or could otherwise be missing longer-term trends. Below, I define four subsets based on the approximate shape of the light curve since the SDSS epoch. As each classification is somewhat subjective the targets selected for the following subsets will represent the stronger candidates for each type, with the weaker or harder to define objects being excluded. In cases where more than one classification may be appropriate I have attempted to select the most dominant feature in describing the light curve. The subsets are defined as follows:

'Simple': This light curve shows a rise to a single identifiable peak and then subsequent decline. The peak can appear cuspy or 'table-top' in nature with a relatively rapid rise/fall. Example: J105502 (Fig. 3.5)

'Rounded': Similar to the Simple case but the light curve shows a broader, more gradual evolution on a longer timescale and the peak is less well defined. May also show some additional structure on top of the long-term trend. Example: J155427 (Fig. 3.6)

'Dipper': Displays signs of fairly rapid decreases in brightness, potentially in a quasi-periodic manner. Example: J223210 (Fig. 3.7)

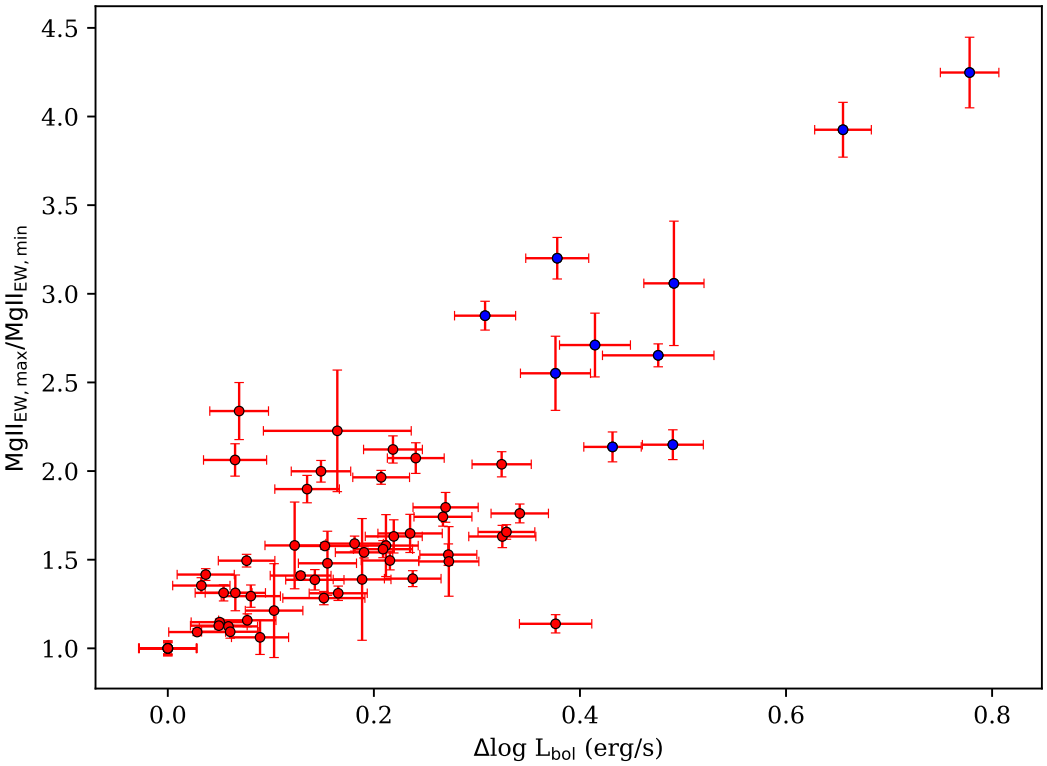

Figure 3.4 *Selection of the 'Prime' subsample based on significant spectroscopic changes over the duration of the observing campaign.*

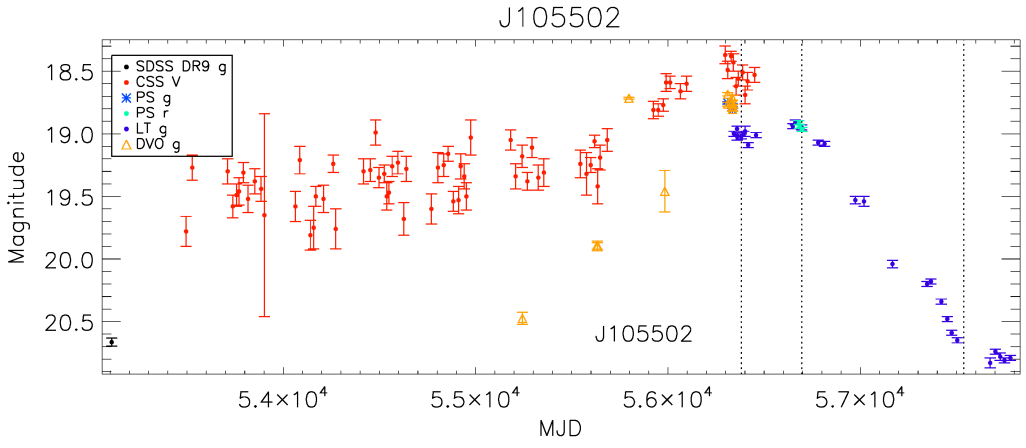

Figure 3.5 *Light curve for J105502 including SDSS, CRTS, DVO, LT data. An example of the 'Simple' subsample. Figure credit: CM*

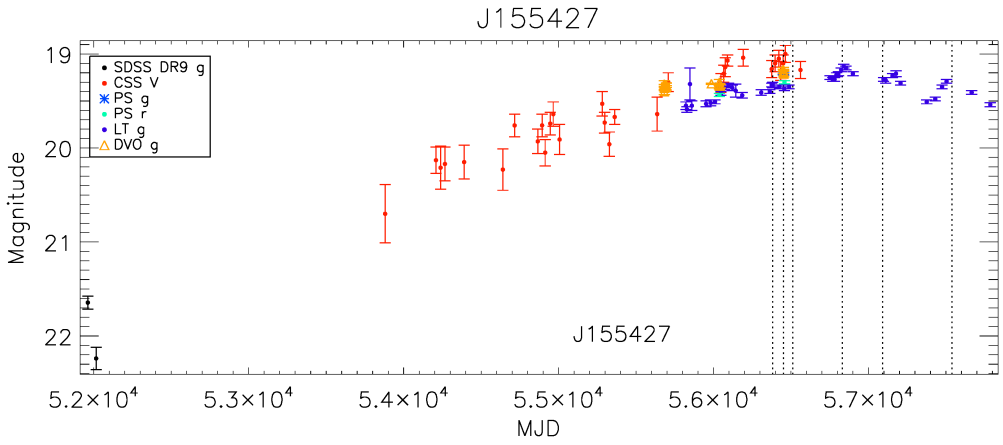

Figure 3.6 *Light curve for J155427 including SDSS, CRTS, DVO, LT data. An example of the 'Rounded' subsample. Figure credit: CM*

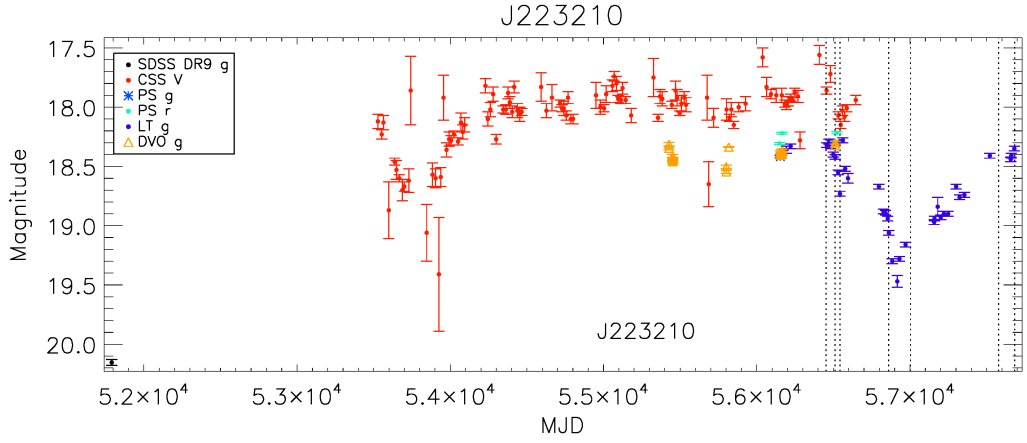

Figure 3.7 *Light curve for J223210 including SDSS, CRTS, DVO, LT data. An example of the 'Dipper' subsample. Figure credit: CM*

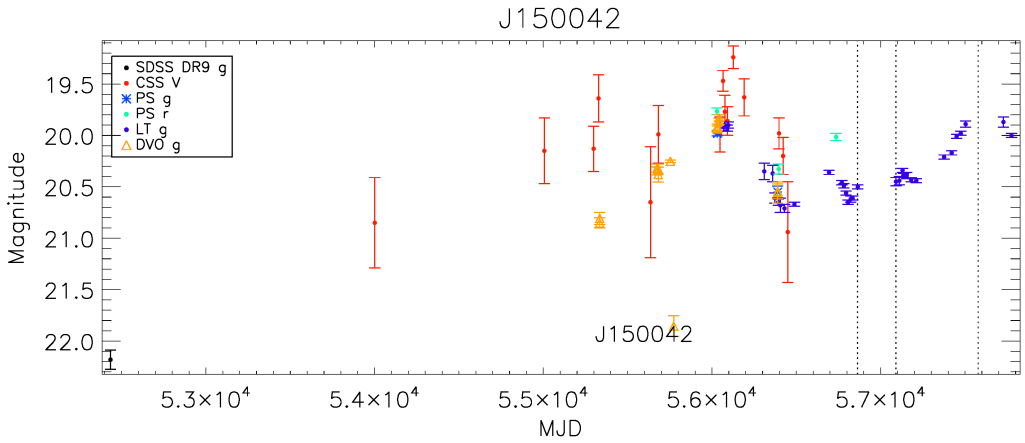

Figure 3.8 *Light curve for J150042 including SDSS, CRTS, DVO, LT data. An example of the 'Double' subsample. Figure credit: CM*

'Double': Displays evidence of two separate peaks in the light curve in addition to a general rise/fall in magnitude. Example: J150042 (Fig. 3.8)

3.5 Subsample spectral evolution

I will now discuss each of these subsets in turn, with a particular focus on their evolution. The prime subset will be discussed last, with a separate treatment on each individual object. For each of the four broad subsets defined above, there will follow a scatter plot of log equivalent width vs L_{1450} for three lines: MgII, $[OII]_{3727}$ and $[OIII]_{5007}$. This style of plot has been chosen to allow comparison with other similar works (eg. Dietrich et al. (2002); Zhang et al. (2013)). Using equivalent widths instead of line fluxes should also minimise rescaling issues relating to the spectra but note that the derived L_{1450} measurements may be subject to additional systematic uncertainty. The power-law slopes, measured in the rest-frame UV and the Hβ region, hereafter simply referred to as the optical slope, are also plotted relative to L_{1450}. The scaling of the x/y axes are consistent between subsets to allow easier comparison. On each of the equivalent width plots, three trend lines have been added as a guide as to the expected changes if $f_{\rm line} \propto f_{\rm cont}^{\alpha}$ for various values of α. These represent cases where the line tracks the continuum ($\alpha = 1$), the line remains unchanged ($\alpha = 0$) and the line tracks the continuum but to a lesser extent ($\alpha = 0.5$). The [OIII] equivalent widths include the flux from any additional intermediate-width components from the fitting process.

3.5.1 Spectral evolution: 'Simple'

Figure 3.9 shows the evolution of equivalent widths for this subset which consists of 10 objects in total. As might be expected from their light curves, there are significant changes in both equivalent width and luminosity. For MgII, the general trend appears consistent with the line fluxes changing less than the continuum and in some cases not at all. J150210 is a notable example of this and will be discussed further as part of the 'Prime' subsample. The narrow lines show a considerable degree of scatter in their tracks. Some of this scatter is likely due to rescaling problems and slit losses rather than intrinsic changes in the host objects. This is more likely the case with J142902. In the case of J090244 on the other hand, there is a noticeable change in the structure of the Hβ/[OIII] region which may indicate real changes or perhaps problems with the fit. Here, an intermediate-width [OIII] component has been used in fitting both epochs but it is possible the Hβ emission is double-peaked and this change in flux has incorrectly been attributed to an [OIII] component.

Comparison with Dietrich et al. (2002) shows that the MgII EW in these objects straddles the typical value of $\sim$ 1.8 at these luminosities. Thus, from this plot alone, it is difficult to ascertain whether or not these objects are returning to quiescence or are instead undergoing an extinction/obscuration event. Similarly, comparison with the [OII]/[OIII] values from Zhang et al. (2013) seem to indicate that the [OII] EW is higher than average for these luminosities.

The power-law slopes for the UV and optical region are shown in Fig. 3.10. J150210 is immediately noticeable for being the bluest object, which stays fixed at this slope as the optical undergoes a significant change. This may be a good example of the host galaxy being seen in contrast against the fading of the AGN component. This would require that the AGN itself is not undergoing any intrinsic colour change. A lesser example of this type of trend is seen in J105502. In general, the evolution of the optical slopes tends to be steeper than that seen in the UV.

3.5.2 Spectral evolution: 'Rounded'

The Rounded subset, which consists of 8 targets, stands apart from the Simple objects, particularly with regard to the MgII EW. In general these objects are of

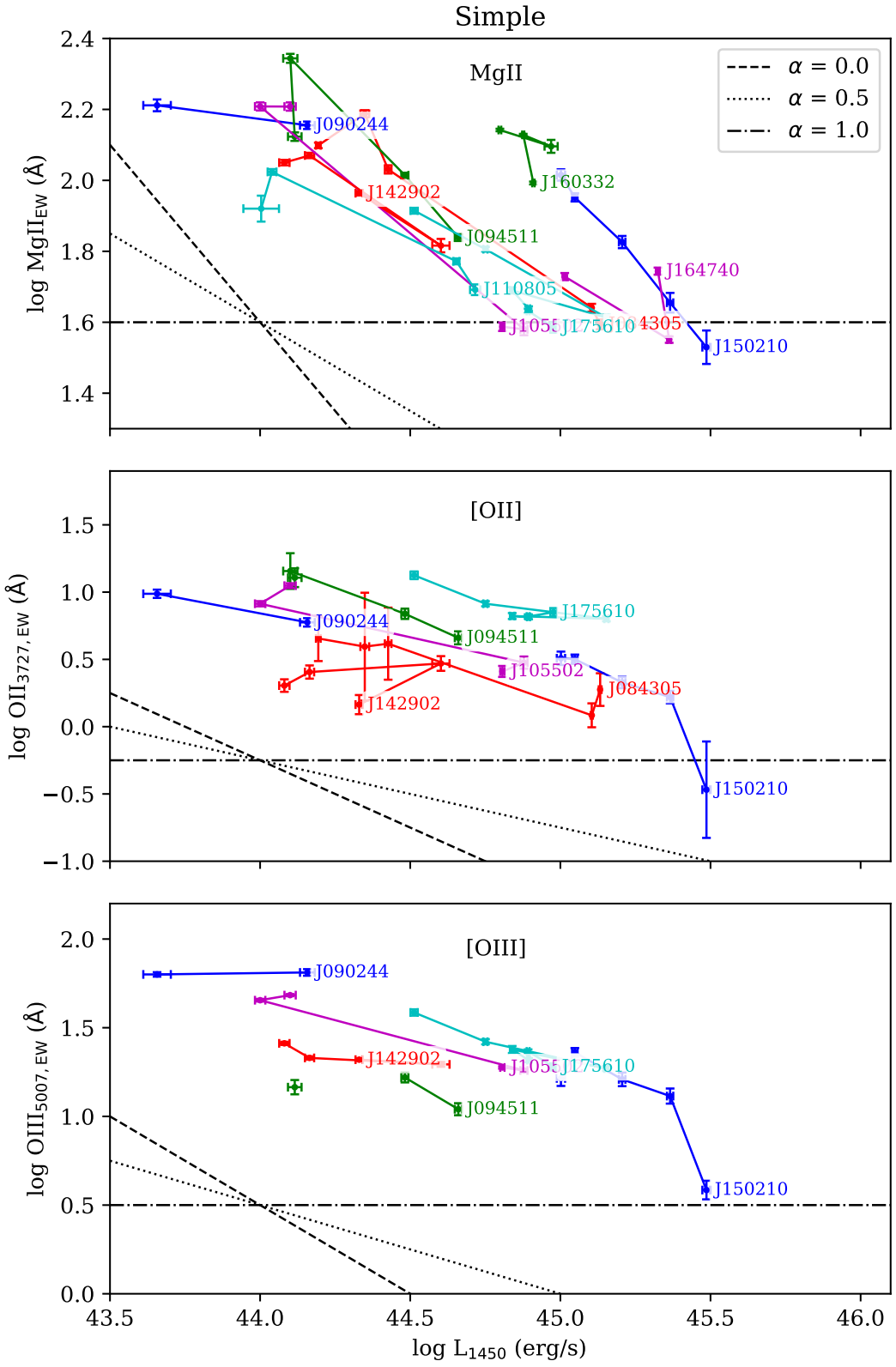

Figure 3.9 *Rest-frame equivalent widths plotted against the monochromatic continuum luminosity at 1450Å. Trend lines are shown for* $f_{line} \propto f_{cont}^{\alpha}$ *for given values of* α.

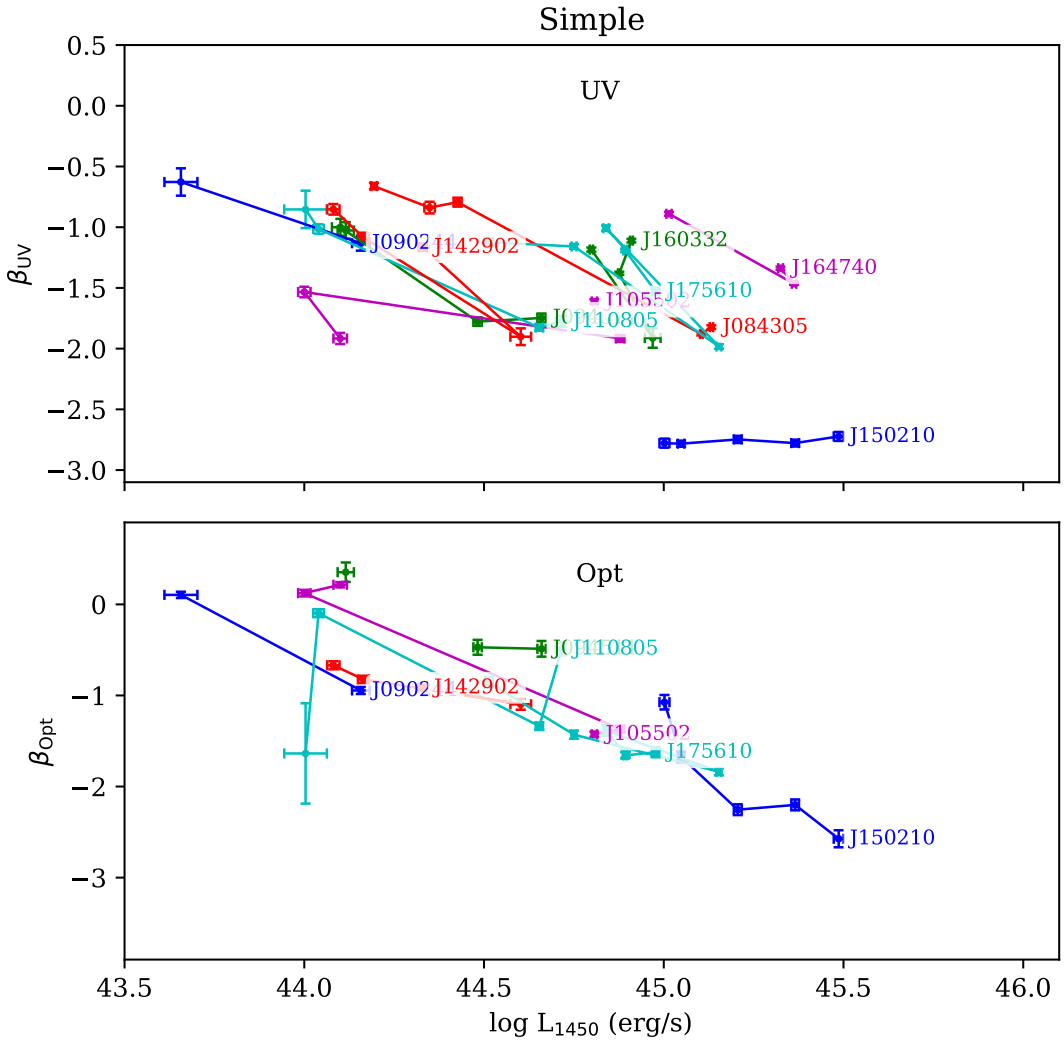

Figure 3.10 *Power-law slopes from the UV and optical regions plotted against the monochromatic continuum luminosity at 1450Å .*

a higher luminosity (and redshift) and lower equivalent width. The scatter is also greater in these objects. In the case of J011635, the MgII fit is unsatisfactory and likely an overestimate, which also leads to a spuriously large black-hole mass as noted earlier. One of the clearest trends is for J142232, which starts with a comparatively low equivalent width but has since evolved to a more typical value which may be an indication that the low state can be considered 'normal'. This object also shows signs of modest evolution in the line flux during this time. It should be noted that, in addition to fitting the criteria for a rounded light curve, this object shows additional structure, with identifiable peaks/plateaus, making it a possible candidate for the 'Double' subset. J031240 appears to be behaving in a similar fashion as it draws closer to the SDSS magnitudes though still has some way to go.

The narrow line fluxes are less illuminating here as there were fewer reliable detections in these objects. The second epoch for J014139 is not reliable and for J155427 they should also be treated with caution. For the latter, a good fit to [OIII] required a second component but this was not possible at every epoch. In the case of J124728, telluric absorption may be the cause of the extra scatter seen.

The power-law slopes, Fig. 3.10, for this subset are also interesting. Again the increased scatter is apparent but in general the trends appear to be steeper than that seen in the Simple subset and with most objects tending to be redder when fainter. There are one or two exceptions to this which have a flatter trend.

3.5.3 Spectral evolution: 'Dipper'

The exact definition for this subset is somewhat vague but it is possible that some of these transients are due to obscuration of some kind, leading to relatively rapid, sometimes erratic dips in the light curve. Five objects currently fit this description. The equivalent widths in Figure 3.13 show some interesting behavior. Most notable is J223210, which has undergone a full dip of ~ 1 magnitude and has now returned to the high state. Consequently, the evolutionary tracks have evolved in an interesting fashion. Generally, the line fluxes appear to be relatively constant though there are indications of additional changes. [OII] is very low in this object and may not be reliably detected at every epoch. Conversely, there are indications that an extended component for [OIII] may be changing. This object will be discussed further in the Prime section.

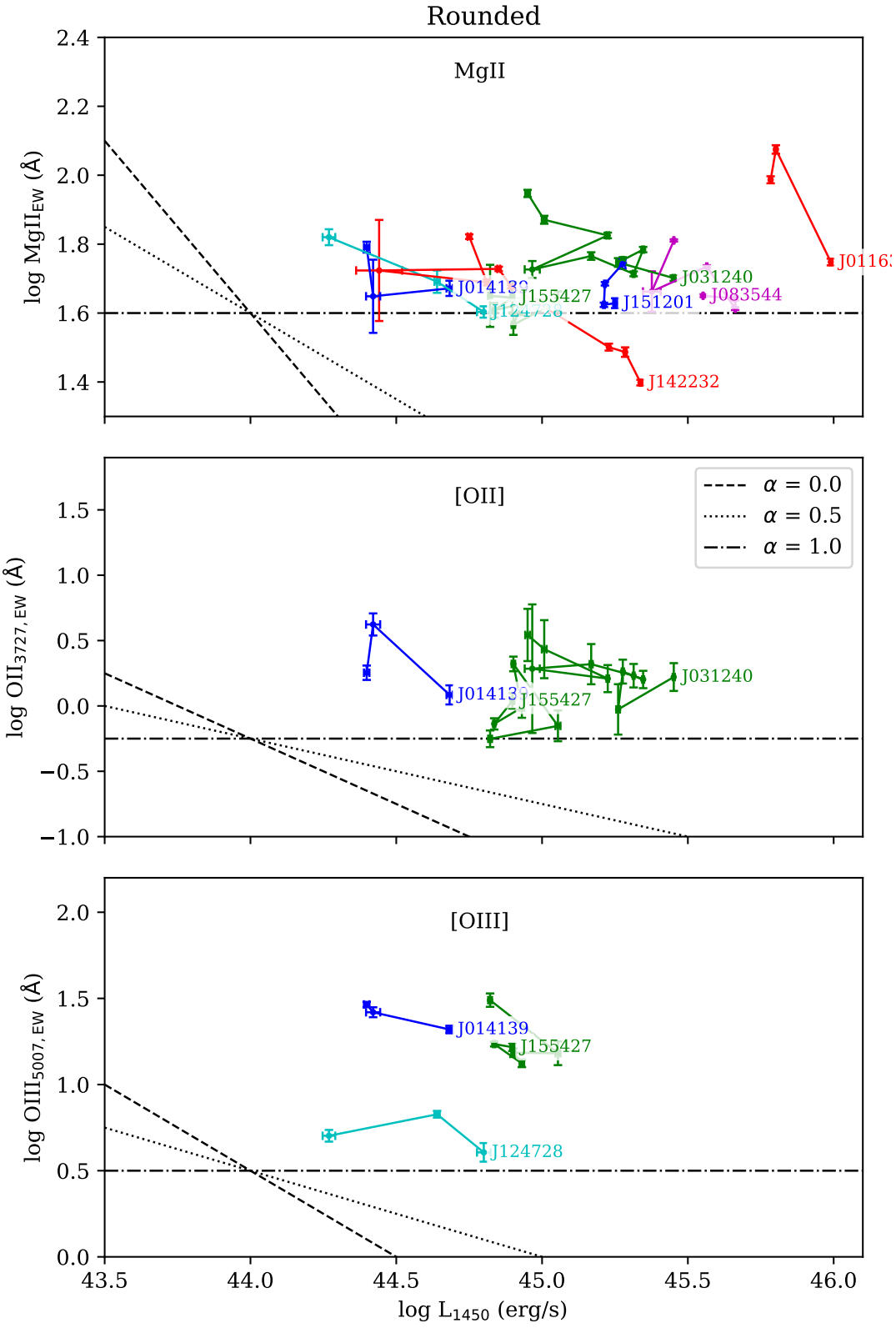

Figure 3.11 *Rest-frame equivalent widths plotted against the monochromatic continuum luminosity at 1450Å. Trend lines are shown for* $f_{line} \propto f_{cont}^{\alpha}$ *for given values of* α.

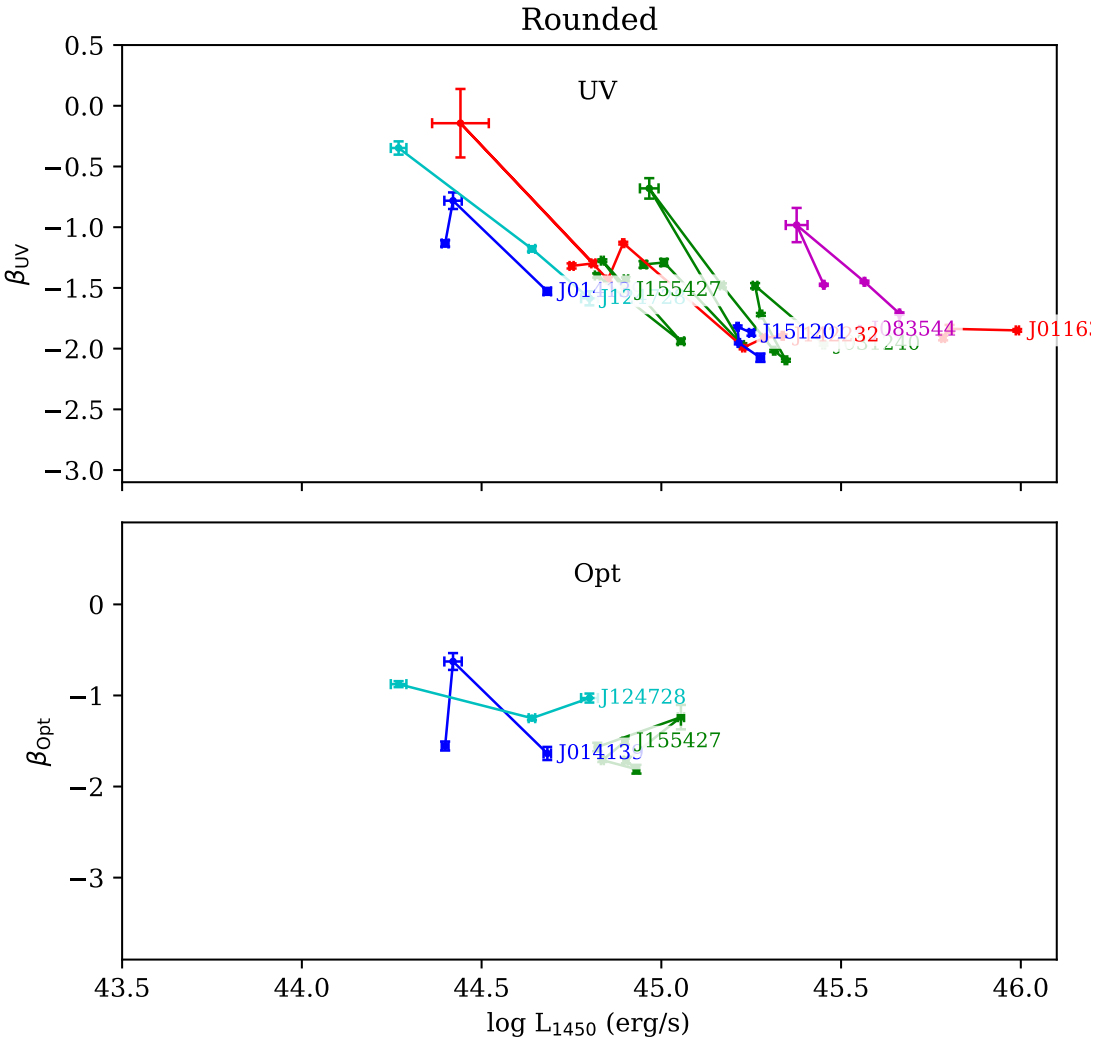

Figure 3.12 *Power-law slopes from the UV and optical regions plotted against the monochromatic continuum luminosity at 1450Å .*

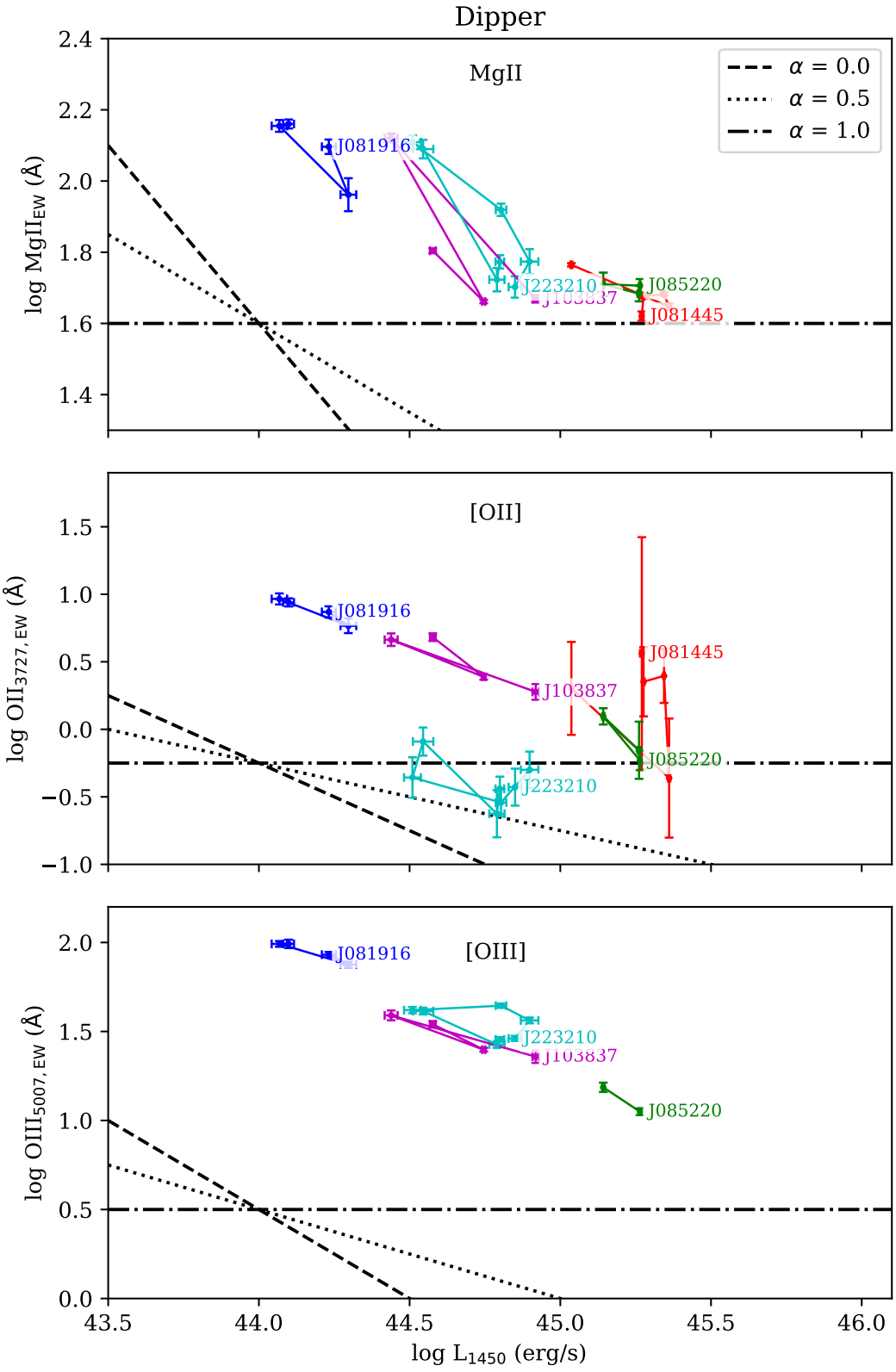

Figure 3.13 *Rest-frame equivalent widths plotted against the monochromatic continuum luminosity at 1450Å . Trend lines are shown for $f_{line} \propto f_{cont}^{\alpha}$ for given values of α.*

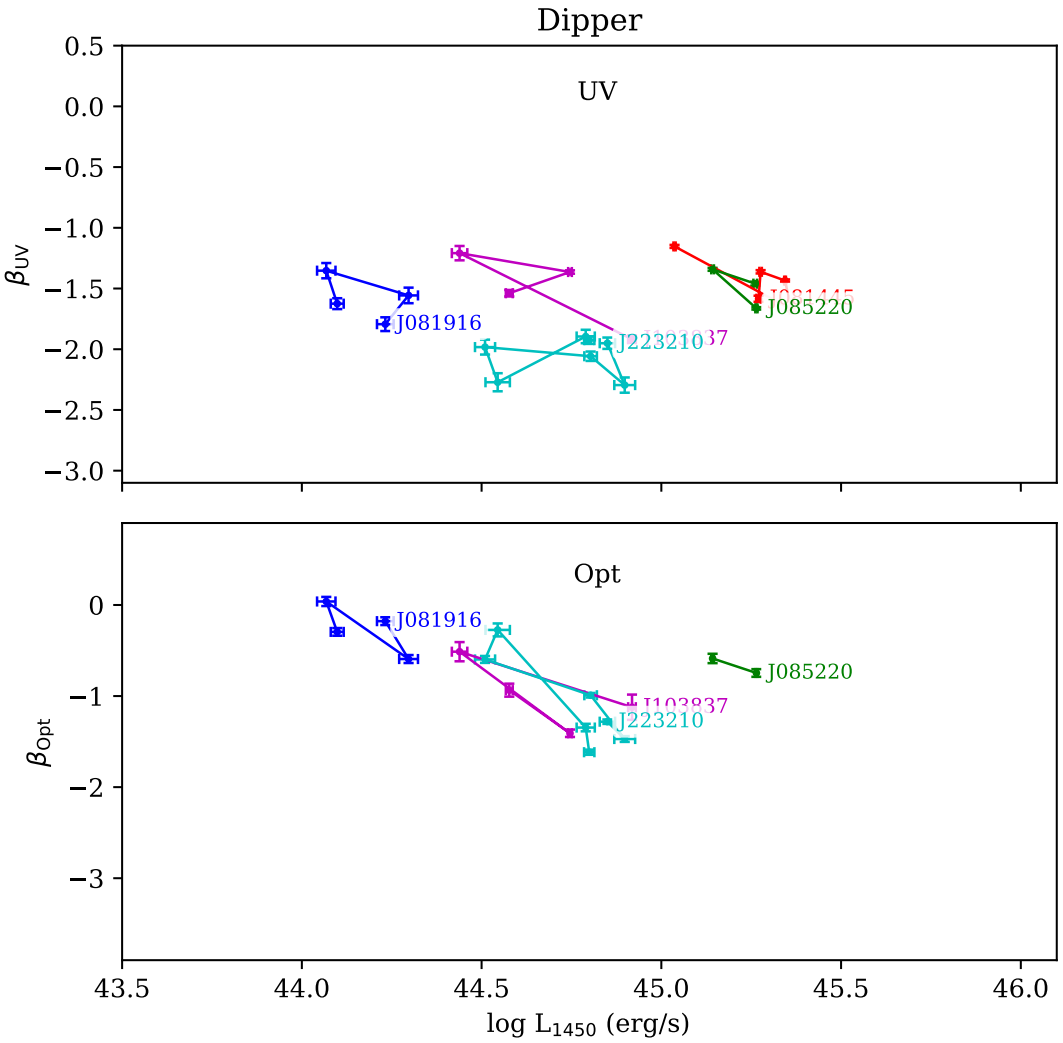

Figure 3.14 *Power-law slopes from the UV and optical regions plotted against the monochromatic continuum luminosity at 1450Å .*

The power-law slopes in Fig. 3.14 are also fairly typical to within the scatter seen. J223210 sees a relatively stable UV slope but changes in the optical which again imply that we are seeing more of the host galaxy intruding into the mix as the AGN component fades.

3.5.4 Spectral evolution: 'Double'

The intention with this subset was to try and identify those light curves with at least two definable peaks in addition to any bulk changes. This is a somewhat subjective criterion, particularly in poorly sampled light curves but may prove instructive. Others objects with more erratic light curves or multiple peaks have

not been included at this stage. Fig. 3.15 shows the equivalent widths which, in general, imply that the line fluxes are changing to a lesser extent than the continuum. There are some objects with notable scatter. In the case of J092635 and J133004 this is likely due to rescaling issues. For J152238 a major telluric feature was present at MgII.

Again, the additional scatter is seen in the power-law slope evolution tracks in Fig. 3.16. These appear consistent with the other subsets, perhaps most closely related to the Simple subset in terms of the general trends seen.

3.6 Detailed spectral evolution: 'Prime'

This section will detail observations regarding each object in the highly spectroscopically variable 'Prime' subsample with a particular attention to the evolution of various parameters over the spectroscopic observation campaign. For each object a number of parameters will be plotted. To aid comparison between each, they will typically be presented relative to the observed maximum in lieu of absolute units. The raw light curves for each of these objects can be found in Appendix B.

3.6.1 J084305

This object (Fig. 3.17), part of the Simple subset, displays a marked decline in the continuum of ~ 1.5 mag in the g-band. The 4th epoch may be problematic due to this being taken with the MMT. As a result, a smaller portion of the UV region was visible which may have adversely affected the fit in this region. This may explain the jump in the Fe component at this epoch. There is a notable decline in CIII] flux which appears to track the continuum relatively closely. This is in contrast to MgII which, if one ignores the 4th epoch, is consistent with being relatively stable over this period with perhaps a late decline.

It remains to be seen how this object continues to evolve. It is now at a level consistent with the brightest of three SDSS epochs ($g \sim 21.6$) but may yet decline further. As evidenced in the UV power-law slope there appears to have been a detectable colour change in this object, with it becoming redder as it fades. Sadly there is no CRTS data available to allow a determination of the pre-PanSTARRS

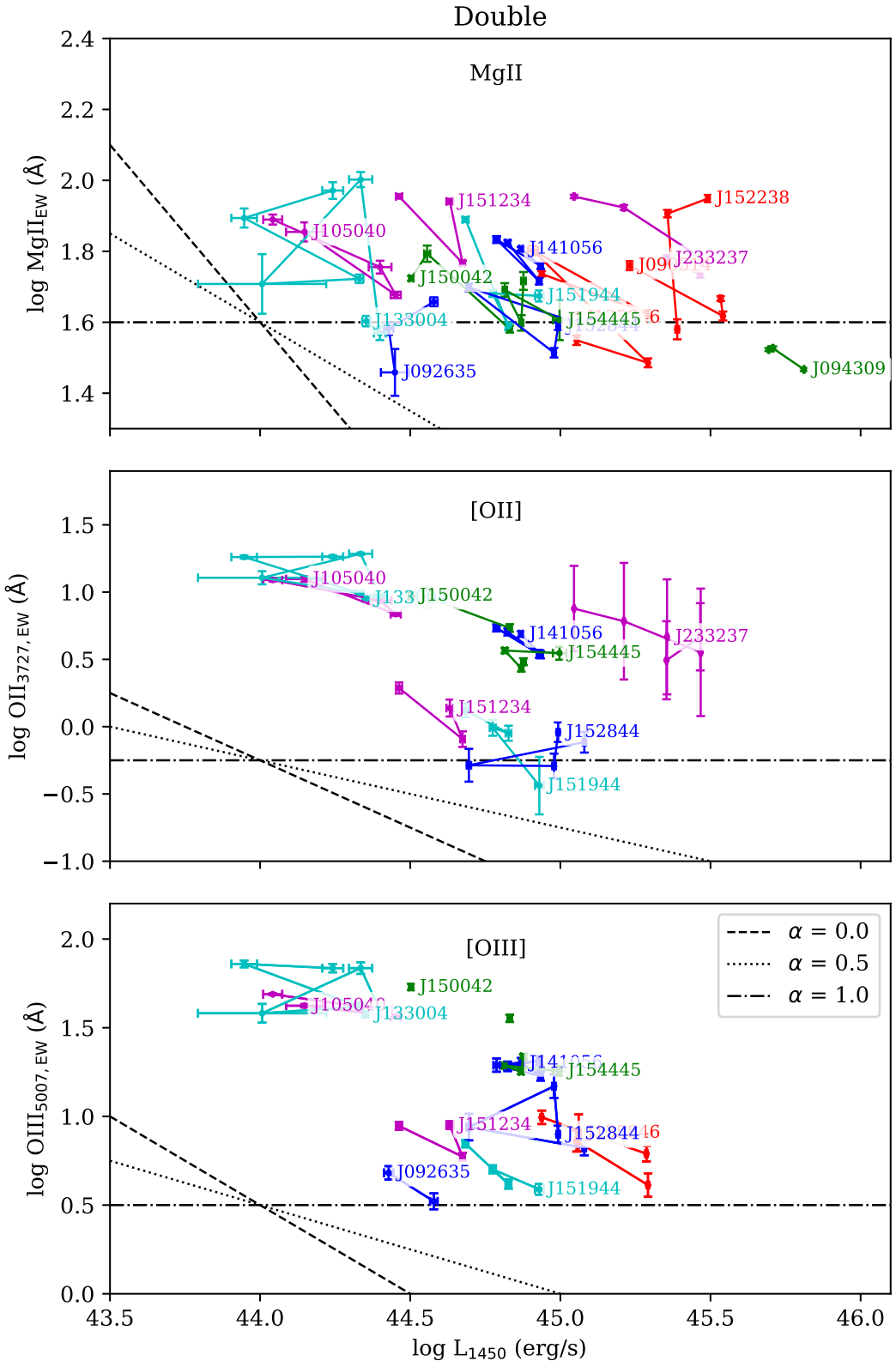

Figure 3.15 *Rest-frame equivalent widths plotted against the monochromatic continuum luminosity at 1450Å. Trend lines are shown for* $f_{line} \propto f_{cont}^{\alpha}$ *for given values of* α.

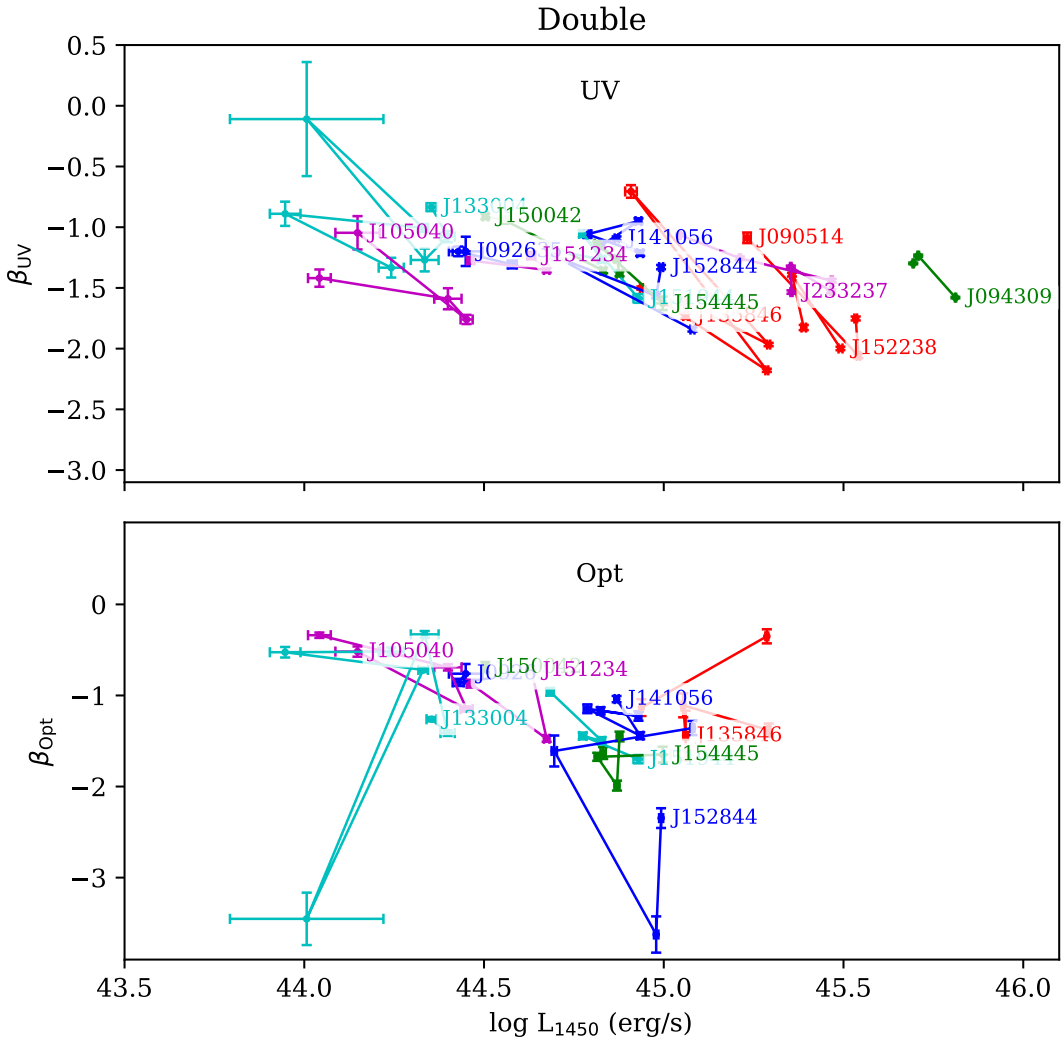

Figure 3.16 *Power-law slopes from the UV and optical regions plotted against the monochromatic continuum luminosity at 1450Å .*

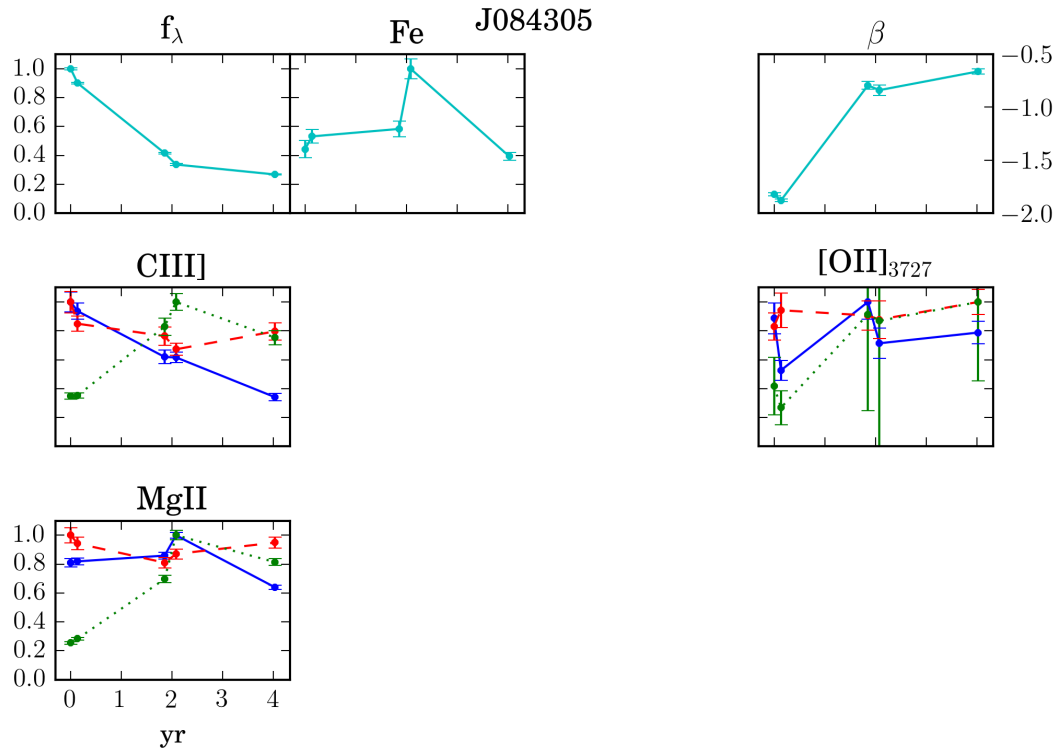

Figure 3.17 *Evolution of various parameters in the 'Prime' subsample. Top row: continuum values (f_{3000}, f_{5000}) and Fe template scaling relative to the maximum epoch and power-law slopes - cyan: UV, magenta: Optical. Bottom/middle rows: Line fluxes/FWHM/EW (blue/red/green) relative to the maximum epoch.*

era behavior.

3.6.2 J094511

This object (Fig. 3.18), another 'Simple' object, shows many similarities with J084305. This time, there are CRTS data which allow us to see a near-symmetrical, smooth light curve which rises at least two magnitudes from the SDSS epoch and is now returning to this level. The spectral epochs do not directly sample the peak but begin perhaps a third of the way down. The third epoch was from the MMT and should be treated with caution as the UV fit is not over exactly the same wavelength region as for the WHT epochs. This may explain why the Fe and MgII components are up in this epoch.

Generally there has been a significant decline in CIII] which appears to have stabilised. MgII also appears to be declining, if one is cautious of the MMT

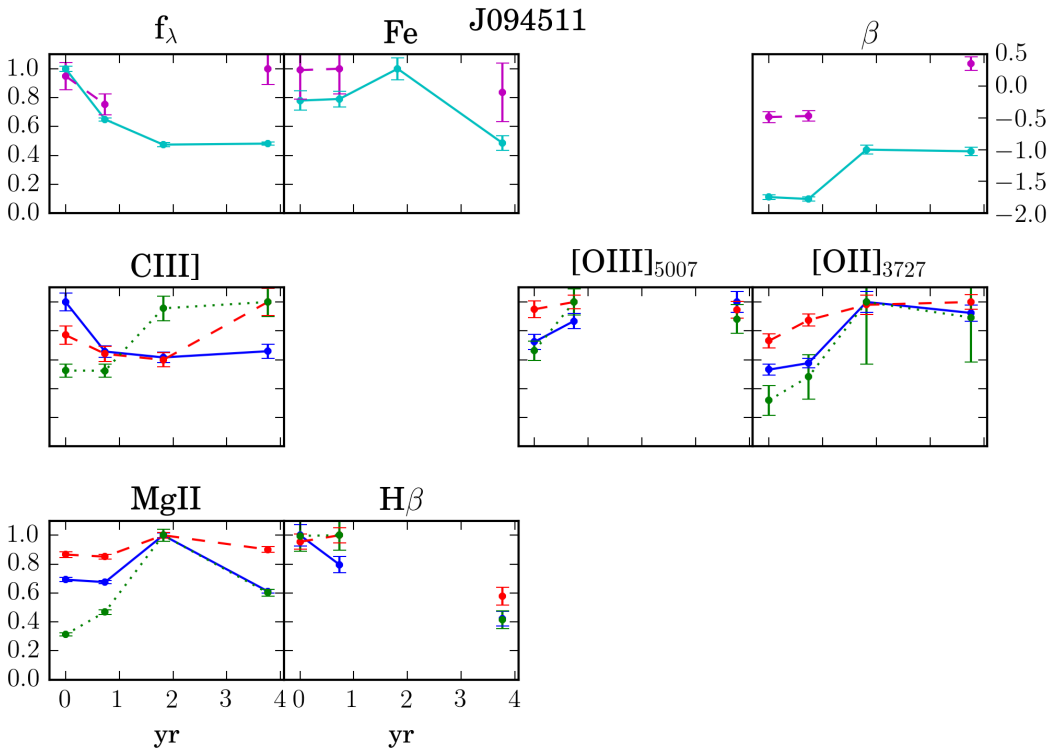

Figure 3.18 *Evolution of various parameters in the 'Prime' subsample. Top row: continuum values (f_{3000}, f_{5000}) and Fe template scaling relative to the maximum epoch and power-law slopes - cyan: UV, magenta: Optical. Bottom/middle rows: Line fluxes/FWHM/EW (blue/red/green) relative to the maximum epoch.*

epoch measurement, though at a slower rate. There also appears to have been a marked decrease in Hβ flux which does appear real though this region of the spectrum is fairly noisy. If this is accurate it implies that this line has tracked the continuum changes very closely. There are also signs of the host galaxy contrast increasing at this last epoch.

The [OII] detection here is strong and possibly indicates that the spectral scaling is not adequate, perhaps at the final epoch if the third epoch is incorrect. Alternatively, there may have been a slight increase in this line. On this sort of timescale this may not be considered very likely.

3.6.3 J103837

This object (Fig. 3.19) is currently part of the 'Dipper' subset, though one may also consider this multiply peaked or even erratic. The rescaling for the second

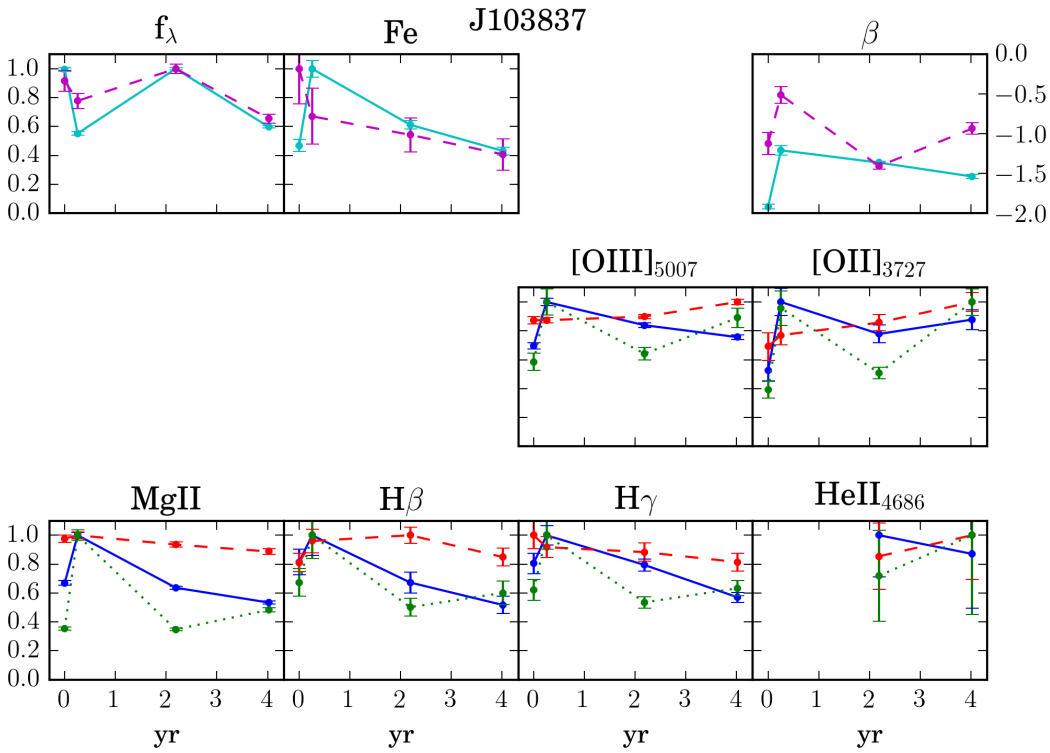

Figure 3.19 *Evolution of various parameters in the 'Prime' subsample. Top row: continuum values (f_{3000}, f_{5000}) and Fe template scaling relative to the maximum epoch and power-law slopes - cyan: UV, magenta: Optical. Bottom/middle rows: Line fluxes/FWHM/EW (blue/red/green) relative to the maximum epoch.*

epoch has almost certainly been overestimated due to a lack of LT data at this point. This was likely a sharp drop in the continuum, as evidenced by the spike in equivalent widths for all lines and change in UV slope.

The final two epochs have reliable detections of HeII and a redshifted second component to Hβ. The second epoch has no reliable HeII and the first epoch is noisy resulting in a wide Hβ component which looks spurious. This region suffers due to telluric features present at HeII and on the redward side of the [OIII] lines.

Given the erratic nature of this object, it is difficult to draw any conclusions as to trends seen here. It may be prudent to rescale according to the narrow lines to attempt to correct for the rescaling problem. Regardless, the colour change at the 'Dip' remains interesting.

3.6.4 J105502

This object (Fig. 3.20) is part of the 'Simple' subset and displays some interesting trends. The light curve displays a notable, slightly extended peak of more than ~ 1 magnitude above the SDSS epoch and has now returned to this level. The spectral epochs have also sampled the peak twice and twice again at quiescence. The rescaling at the last two epochs is in doubt due to the changes apparent in [OII] but there are some striking trends. Most notable is the large drop in continuum flux, accompanied by a colour change which is significant in the optical. This is an indication of the host galaxy becoming more apparent as the AGN component fades whilst remaining relatively blue.

The line fluxes also show a decline in MgII that is significantly less than that seen in the other broad lines. Here, the fit is improved with the addition of a second redshifted $H\beta$ component, which may instead be related to a wider [OIII] component but there is a telluric absorption feature on top of the $H\beta$ line which hampers this measurement.

3.6.5 J110805

This object (Fig. 3.21) is currently in the 'Simple' subset but displays a fair amount of structure in the light curve after the main peak, possibly evidence of it being a 'Dipper' or erratic in general. With no reliable detections of [OII] and the loss of the [OIII] region to a strong telluric absorption feature there is no check on the validity of the spectral scaling. The final epoch is a noisy MMT spectrum and should also be treated with caution.

The main conclusions that can be drawn from this object are that there has been a decline of approximately ~ 1.5 magnitudes from the main peak and ~ 1 mag between the 2nd and 4th spectral epochs. This appears to have coincided with a decline in broad line strength as well.

3.6.6 J133004

This object (3.22) is part of the 'Double' subset. That is, there are two clearly defined peaks superimposed on a change of more than two magnitudes since the SDSS epoch and it is still some way from returning to this value. The fourth

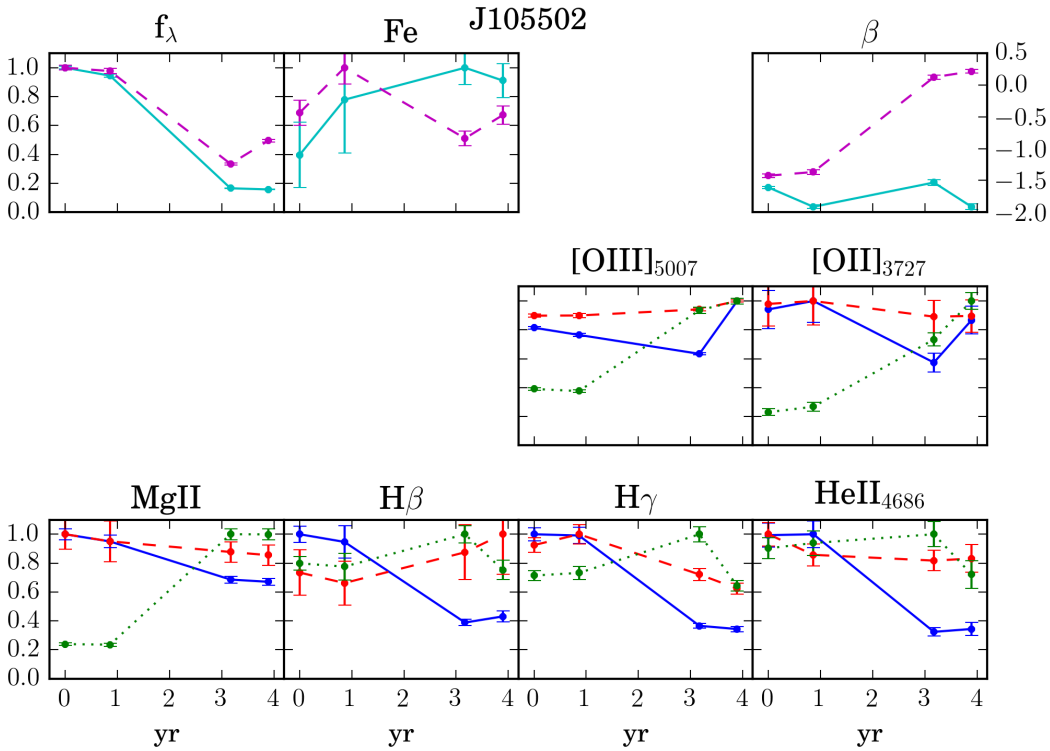

Figure 3.20 *Evolution of various parameters in the 'Prime' subsample. Top row: continuum values (f_{3000}, f_{5000}) and Fe template scaling relative to the maximum epoch and power-law slopes - cyan: UV, magenta: Optical. Bottom/middle rows: Line fluxes/FWHM/EW (blue/red/green) relative to the maximum epoch.*

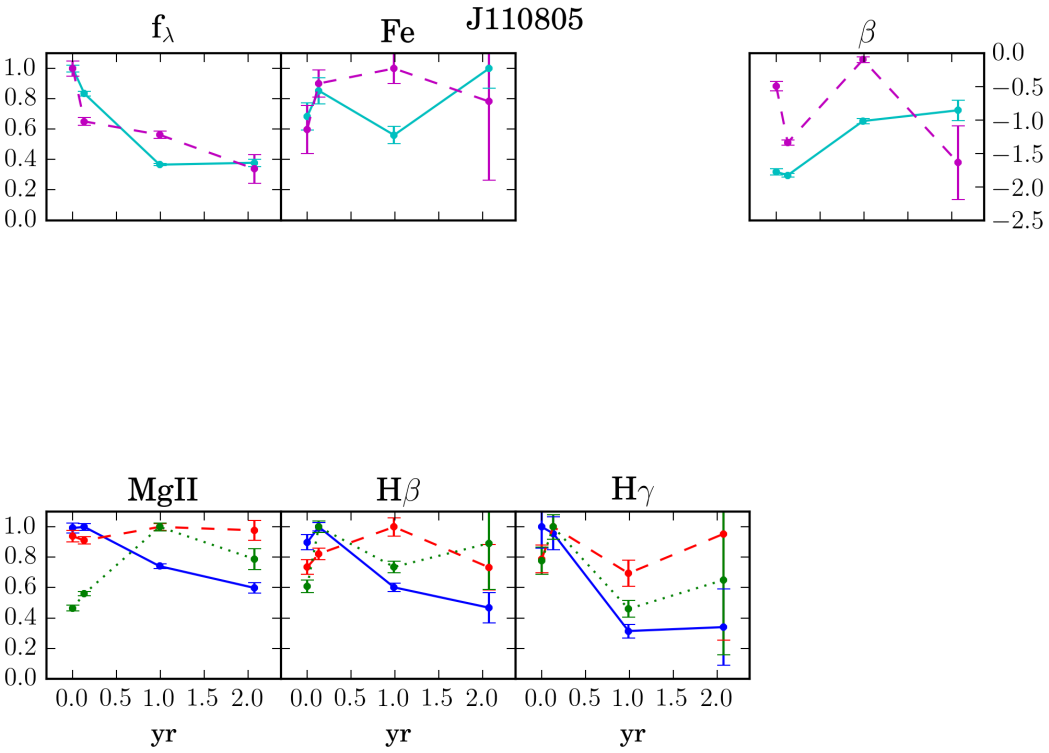

Figure 3.21 *Evolution of various parameters in the 'Prime' subsample. Top row: continuum values (f_{3000}, f_{5000}) and Fe template scaling relative to the maximum epoch and power-law slopes - cyan: UV, magenta: Optical. Bottom/middle rows: Line fluxes/FWHM/EW (blue/red/green) relative to the maximum epoch.*

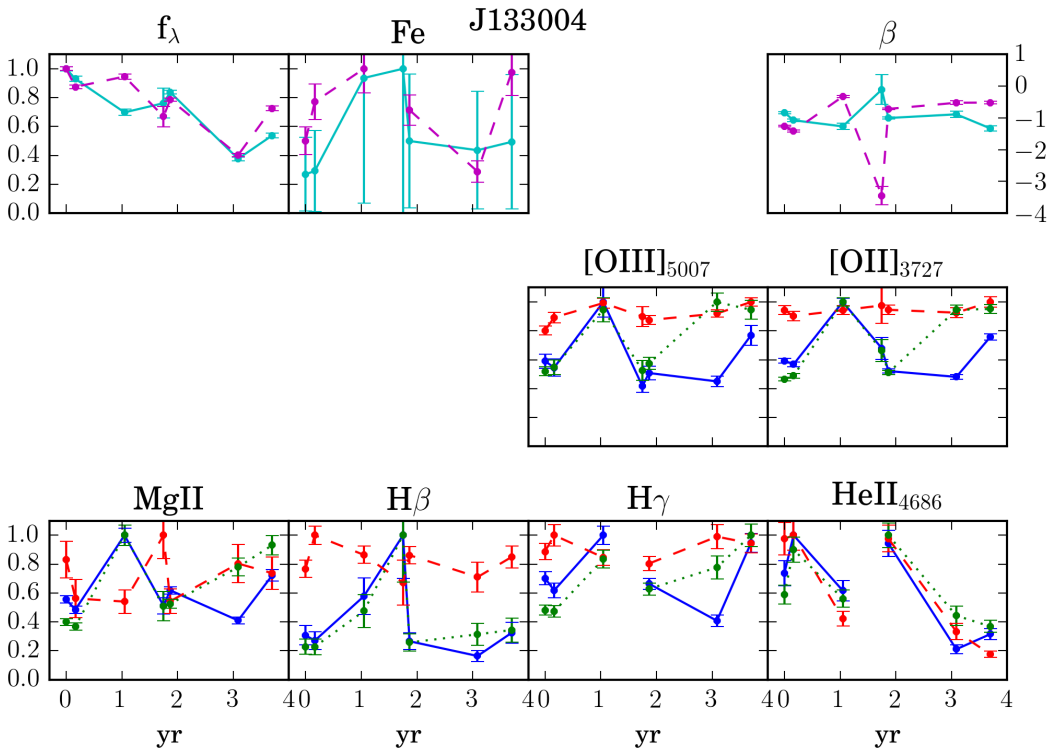

Figure 3.22 *Evolution of various parameters in the 'Prime' subsample. Top row: continuum values (f_{3000}, f_{5000}) and Fe template scaling relative to the maximum epoch and power-law slopes - cyan: UV, magenta: Optical. Bottom/middle rows: Line fluxes/FWHM/EW (blue/red/green) relative to the maximum epoch.*

epoch is a relatively poor MMT spectrum and should be treated with caution. A quick glance at the [OII] line, which is strong in this object, shows that the rescaling at the third epoch is likely poor. Interestingly this corresponds to the dip in-between peaks in the light curve, with signs of a colour change. The final epoch also looks to be overestimated. Taking this into account, it appears as if the MgII/Hβ flux has been relatively stable throughout but HeII has responded more strongly to the continuum changes, as might be expected with this line.

3.6.7 J142232

This object (Fig. 3.23) has been placed into the 'Rounded' subset due to a long-term gradual trend in the light curve though there are additional structures present meaning it could also have been classed as a multiply-peaked event. Nevertheless, over the period of the spectral observations there has been a drop in the continuum of over ~ 1 magnitude though this object still has some way to

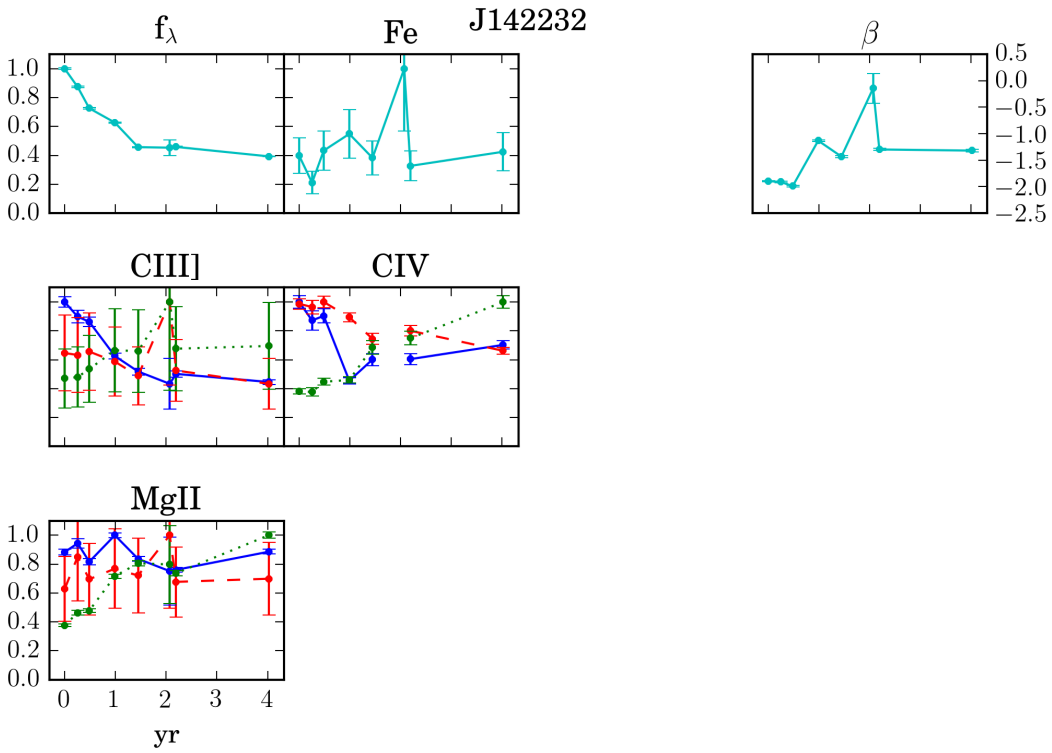

Figure 3.23 *Evolution of various parameters in the 'Prime' subsample. Top row: continuum values (f_{3000}, f_{5000}) and Fe template scaling relative to the maximum epoch and power-law slopes - cyan: UV, magenta: Optical. Bottom/middle rows: Line fluxes/FWHM/EW (blue/red/green) relative to the maximum epoch.*

go before reaching the magnitude of the SDSS epoch. The 6th epoch is a very poor MMT spectrum and should be treated with caution. The CIV measurement should likewise be treated with caution as this line was near the blue wing and was constrained to match the width of the CIII] component in order to provide a reasonable fit.

What is most apparent is that CIII] appears to be tracking the continuum changes closely with MgII changing only weakly in response to this. This may also be true of CIV. There is also a slight change in the UV power-law slope, becoming slightly redder at later epochs. Unfortunately there are no reliable narrow-line detections.

3.6.8 J150210

This object (Fig. 3.24), part of the 'Simple' subset, is notable for a number of reasons. There is a marked drop in continuum flux with little to no change in the MgII flux. This also happens to be the bluest object in the sample, with a relatively steep power-law slope in the UV and an appreciable Eddington fraction ranging from approximately 0.07 to 0.17 in the low-state and high-state respectively. The light curve is also almost unique amongst the PS1 sample. It is very smooth, has a clearly defined peak after a rapid rise and has since been declining slowly, with perhaps a plateau before continuing to decline. This could even be considered to be a longer-lived version of a type II-P supernova light curve.

The initial [OII] detection is not reliable and the [OIII] region suffers due to telluric absorption features but the trends in the line fluxes appear to be well defined. MgII is static throughout with $H\beta$ changing only slightly, if at all. The low Hγ point is likely unreliable. There is also a marked increase in the power-law slope in the optical but the UV remains fixed. It should be noted that the UV fit does not perform as well for this object as it does for others in the PS1 sample, particularly for the brightest epochs. There are indications of problems with the UV Fe template fit and the possible need for additional emission/absorption components which are as yet unidentified.

3.6.9 J175610

This object (Fig. 3.25) is part of the 'Simple' subset. There are arguably two peaks to this light curve but these are barely resolved with the available photometry. The object has only recently begun to decline sharply and is now trending towards the SDSS era magnitude at ~ 21.3 mag. The first four epochs are sampled before the peak at ~ 19.5 mag though there was not much evolution in the photometry over this period. The CIII] measurements were very close to the blue edge of the spectra and should be treated with a degree of caution.

There are signs of changes in the MgII flux relative to Hβ. The narrow-line fluxes indicate there may be scaling issues at early epochs though it is interesting that the [OII]/[OIII] fluxes do not correlate with one another. There is an interesting amount of scatter in both UV/optical power-law slopes which might not have

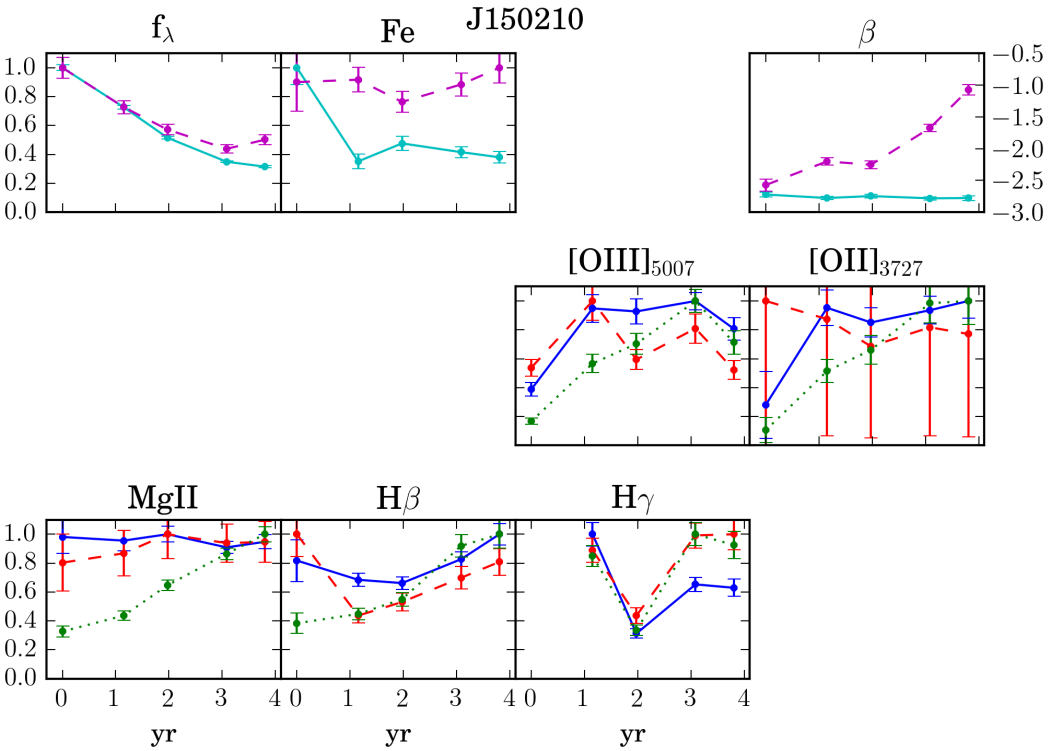

Figure 3.24 *Evolution of various parameters in the 'Prime' subsample. Top row: continuum values (f_{3000}, f_{5000}) and Fe template scaling relative to the maximum epoch and power-law slopes - cyan: UV, magenta: Optical. Bottom/middle rows: Line fluxes/FWHM/EW (blue/red/green) relative to the maximum epoch.*

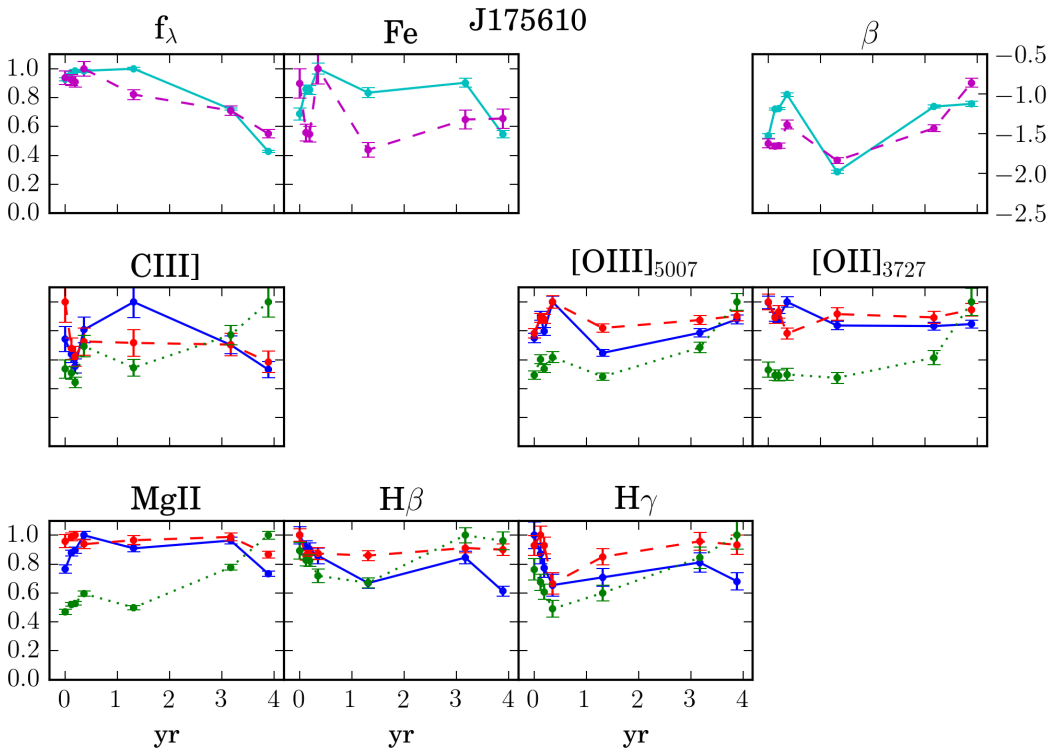

Figure 3.25 *Evolution of various parameters in the 'Prime' subsample. Top row: continuum values (f_{3000}, f_{5000}) and Fe template scaling relative to the maximum epoch and power-law slopes - cyan: UV, magenta: Optical. Bottom/middle rows: Line fluxes/FWHM/EW (blue/red/green) relative to the maximum epoch.*

been expected given the rather modest continuum changes for the early epochs. This may be an indication that the CIII] fit has performed poorly.

3.6.10 J223210

The best example of a 'Dipper'. This object (Fig. 3.26) is the lowest redshift object in the sample and also has evolved from high state to low and has since returned to normal. The high state is assumed to be normal given that the light curve is very flat-topped. The CRTS data also shows evidence of at least one earlier dip which was similar to that which was observed in this campaign. The SDSS epoch may also indicate an even earlier dipping event. This object is relatively blue and stayed this way in the dip as seen in the UV power-law slope but the change in the optical may be attributed to the host galaxy becoming more apparent in the low state.

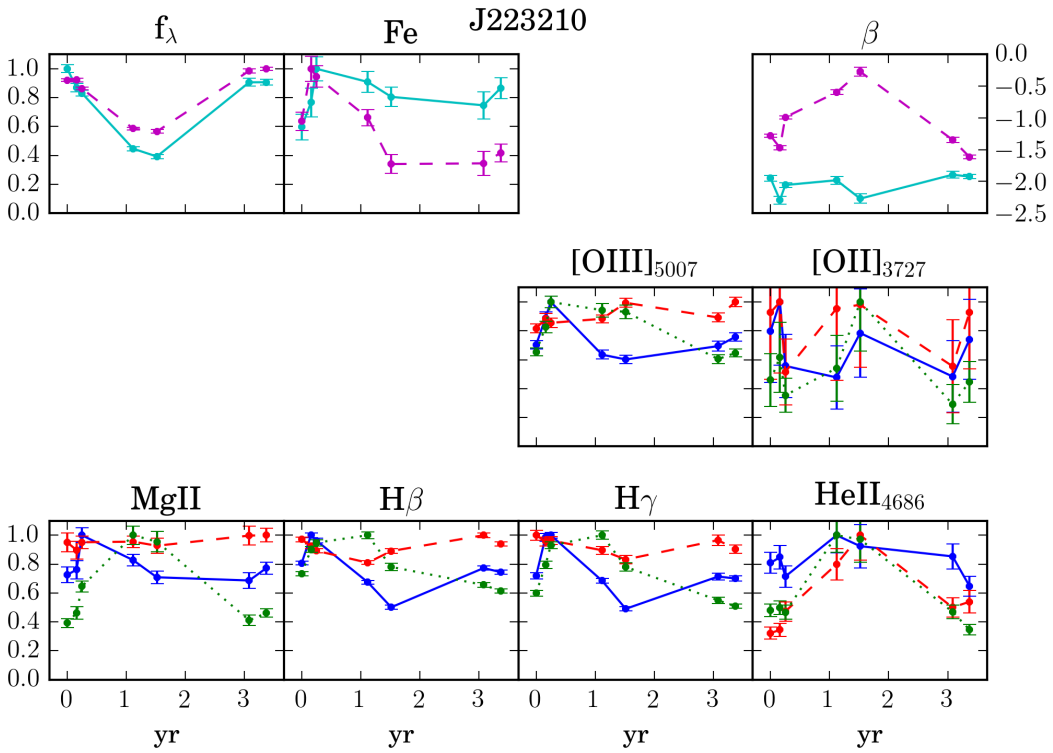

Figure 3.26 *Evolution of various parameters in the 'Prime' subsample. Top row: continuum values (f_{3000}, f_{5000}) and Fe template scaling relative to the maximum epoch and power-law slopes - cyan: UV, magenta: Optical. Bottom/middle rows: Line fluxes/FWHM/EW (blue/red/green) relative to the maximum epoch.*

The [OII] detections are weak and should be treated with caution, as should the HeII measurements in the low state as it became indistinct in the spectra for these epochs. The [OIII] measurements also imply that the rescaling on the 2nd/3rd epochs is not ideal. If so, this implies that MgII has remained relatively unchanged throughout the dip and Hβ has evolved slightly. The equivalent width trends do not match the MgII line well so this would appear to be accurate. There is also an interesting trend in the optical Fe which may be real.

3.6.11 Summary

What has been learned from the information presented here? One of the key challenges is to ascertain the underlying physical mechanisms responsible for these transient events. Possible scenarios, mentioned in Chapter 1, include: intrinsic AGN variability from accretion disc instabilities or other suitable mechanism; tidal disruption flares; orbital/dynamical effects such as obscuration; microlensing

due to an intervening stellar-mass object(s) or perhaps superluminous supernovae. It is also likely, given that these objects have been selected due to their extreme variability, we are seeing a mixture of all of these. The decision to divide these events into subsets has allowed a uniform spectroscopic comparison between similar events. Care must be taken with the rescaling and measurement uncertainties but some conclusions can be made.

1) Based on any individual spectral epoch, there is little to distinguish these AGN from their less variable counterparts. Possible exceptions to this are objects like J150210, where the UV/Fe pseudo-continuum fit is markedly poor at certain epochs.

2) The 'Rounded' subset may be a longer-duration and/or higher-luminosity equivalent of the 'Simple' subset. This is evident from the trends seen for the MgII equivalent width. Many of the 'Simple' subset objects see a significant change in EW as the light curves are beginning to return the levels seen in the SDSS era. In contrast, the majority of 'Rounded' objects are still some way off returning to these levels but appear to be following a similar trend. Conversely, the colour changes seen in the latter objects appear to be stronger in the UV. As will be talked about in the next chapter, it is possible that these may all be microlensing events. In the 'Simple' microlensing cases the accretion disc may go largely unresolved whereas in the 'Rounded' subsample this is not the case, leading to a less cuspy light curve and possible colour changes as the event unfolds. Distinguishing true intrinsic colour changes from a simpler change in AGN/host contrast will also be an important next step. The changes seen in the BLR fluxes for these objects will also shed more light on these events as they continue to evolve.

3) The 'Dipper' objects are good candidates for an obscuration event of some kind. In contrast to the other AGN in this chapter, the normal state for these objects would appear to be the high state. Particularly in the case of J223210 where the flat-topped light-curve, plus dipping events, are hard to explain via any other mechanism. Early testing does appear to rule out the possibility that the changes seen in this object can be explained with an increase in intrinsic reddening, rather requiring a dense object to obscure the central engine.

4) Many of these events display differential changes in the BLR fluxes. In some cases line changes track those of the continuum, see CIII] in J142232, and typically MgII is the least responsive, if indeed it moves at all. Unfortunately the scatter

and cadence in the spectral observations for many objects does not allow firm conclusions on differential BLR changes to be made. An observation campaign designed with a high spectroscopic cadence, in order to better sample the changes over the peak, for one of these transients would be a worthy enterprise.

5) Tidal disruption events do not appear to be the favoured option for many of these events. There are a three reasons for this. Firstly, the timescales involved are typically much longer than those reported in the literature. This causes issues relating to the energy budget and efficiency of any accretion event, perhaps requiring very massive stars as disruption candidates. Secondly the presence of He lines in TDEs is well established but it is not clear that broad MgII, or indeed other line species, would also be produced in these events. Thus, it becomes necessary to have an extant accretion disc, with BLR established, before the disruption event takes place. Thirdly, many of the light curves show a gradual increase in flux rather than a sharp initial increase and gradual decline more typical of TDE candidates. J150210, with it's very blue colour, relatively rapid rise to peak and low MgII FWHM relative to the rest of the sample may be a possible exception to this.

As many of these events are still evolving, it is hoped that this observational campaign will continue beyond the scope of this thesis. At time of writing there are six more nights of WHT observations scheduled for the remainder of 2017. In future I hope to keep the data tables presented here concurrent with the latest spectroscopy so that they remain a complete record of observations.

With the broad classification scheme for these transients defined, I will now turn my attention to the underlying cause of the variability, particularly the microlensing hypothesis. Chapter 4 will focus on a small subset of candidate objects, including two from the 'Simple' subset, which should prove to host the most likely candidates for microlensing. Indeed, for the two objects mentioned, the microlensing model appears to work well, even allowing for moderate constraints on the size of the BLR region. The analysis in Chapter 5 will revisit the classification scheme defined here, a key result appears to be that the 'Rounded' objects are not simply longer-lived 'Simple' events but rather cases where the accretion disc may be getting resolved by the lens.

Chapter 4

Spectroscopic analysis of four 'hypervariable' AGN: A microneedle in the haystack?

This chapter details the spectroscopic analysis of four microlensing candidates from the PS1-A AGN transient sample. The results are presented in Bruce et al. (2017). The photometric and spectroscopic data for this work comprises all observations taken prior to the beginning of 2016. To remain consistent with the published work, additional observations since that time are not included. In Chapter 5 I will re-visit these objects as part of a microlensing analysis for the full AGN transient sample. This will also allow me to address an issue concerning the implementation of the priors used in the MCMC analysis but this discussion is deferred until the next chapter. For this publication I have undertaken the majority of the work. A number of technical details have already been covered in Chapter 2 and the reader will be referred back to these sections where appropriate.

In this work I analyse four extreme active galactic nuclei (AGN) transients to explore the possibility that they are caused by rare, high-amplitude microlensing events. These previously unknown type-I AGN are located in the redshift range 0.6–1.1 and show changes of > 1.5 mag in the g band on a time-scale of $\sim$years. Multi-epoch optical spectroscopy, from the William Herschel Telescope, shows clear differential variability in the broad line fluxes with respect to the continuum changes and also evolution in the line profiles. In two cases, a simple point-source, point-lens microlensing model provides an excellent match to the long-

term variability seen in these objects. For both models, the parameter constraints are consistent with the microlensing being due to an intervening stellar mass object but as yet there is no confirmation of the presence of an intervening galaxy. The models predict a peak amplification of 10.3/13.5 and an Einstein time-scale of 7.5/10.8 yr, respectively. In one case, the data also allow constraints on the size of the CIII] emitting region, with some simplifying assumptions, to be $\sim$ 1.0–6.5 light-days and a lower limit on the size of the MgII emitting region to be $>$ 9 light-days (half-light radii). This CIII] radius is perhaps surprisingly small. In the remaining two objects, there is spectroscopic evidence for an intervening absorber but the extra structure seen in the light curves requires a more complex lensing scenario to adequately explain.

4.1 Introduction

The identification of a class of active galactic nuclei (AGN) transients that are smoothly evolving, by factors of several, on year-long time-scales (Lawrence 2012; Lawrence et al. 2016, hereafter L16) has raised a number of interesting questions regarding the underlying cause. These 'hypervariable' AGN may simply be at the extreme end of the tail of typical AGN variability(MacLeod et al., 2010, 2012) or, perhaps more interestingly, there may be an extrinsic cause. Plausible mechanisms for these transients include the following: accretion events/instabilities; tidal disruption events (TDEs) or extinction events. A fourth possibility, and the focus for this particular work, is that some of these AGN transients are actually rare, high-amplitude microlensing events. If this is the case, through analysis of multi-epoch spectroscopy and simple lensing models, we have the potential to uncover valuable information on the innermost regions of these enigmatic objects.

Observational studies of the microlensing seen in multiply imaged AGN are well established and provide the means with which one can ascertain properties intrinsic to those objects (Irwin et al., 1989; Eigenbrod et al., 2008; Morgan et al., 2010; Blackburne et al., 2011; Mosquera & Kochanek, 2011; Jiménez-Vicente et al., 2012, 2014; Sluse et al., 2012; MacLeod et al., 2015). This involves a monitoring of the AGN components in order to ascertain both the level of variability intrinsic to the AGN and that due to microlensing, typically a low-level 'flickering', in one or more of these components. In contrast, the AGN here exhibit no clear sign of strong lensing effects and are varying significantly

and smoothly (relative to typical AGN behaviour). If a rare, high-amplitude microlensing event is the cause of this variability, this places these previously unknown AGN in a different regime to their multiply imaged counterparts.

Here, four promising AGN transients are selected as candidates for an exploration of the microlensing scenario and its consequences. That is, the hypothesis that an intervening stellar mass object is responsible for the bulk variability seen in these objects. It should be noted that microlensing events will not explain all hypervariable AGN activity; rather, they likely describe a subset of this interesting population. In the interest of brevity, I will focus entirely on the microlensing scenario but alternative variability scenarios are considered in L16.

Section 4.2 describes the sample selection, observational data and reduction pipeline. Spectroscopic results are detailed in Section 4.3. Section 4.4 outlines the procedures used for exploring different lensing models with results detailed in Section 4.5. In Section 4.6, the implications for future work and the advantages/disadvantages over existing microlensing studies involving multiply imaged AGN are discussed. As in Chapter 3, cosmological calculations for this work make use of Planck13 values.

4.2 Observations

4.2.1 Target selection criteria

The four objects here were selected from the PS1-A AGN transient sample, discovered as part of a wider transient search initially designed to look for TDEs around quiescent black holes. The full sample is described in Chapter 2.

To explore the microlensing hypothesis, objects were selected from the PS1-A sample based on the following criteria. First, that the photometry displays signs of smooth evolution on long time-scales with a change in magnitude of $\Delta g > 0.5$ mag over the period of spectral observations. Secondly, that there are a minimum of two spectral observations separated by at least one year (observed frame). The former favours microlensing events over intrinsic variability and the latter increases the chance of observing spectroscopic trends, allowing further testing of the microlensing hypothesis.

Table 4.1 *Summary of the target selection criteria noted in Section 4.2.1*

Short ID	SDSS ID	Single-peak?	Double-peak?	Int-gal?
J084305	J084305.54+550351.3	Yes	No	No
J094511	J094511.08+174544.7	Yes	No	No
J142232	J142232.45+014026.8	No	Yes	Yes
J103837	J103837.08+021119.6	No	No	Yes

Additional factors that favour a microlensing scenario are summarized in Table 4.1. Here, the presence of a near-symmetric single- or double-peaked structure in the light curve, or evidence for an intervening galaxy, and hence lens repository, are noted. At least one of these additional factors was required in the target selection process leaving a total of four microlensing candidates for consideration. Any evidence for an intervening galaxy will be discussed as part of the spectroscopic results for that target (Section 4.3).

4.2.2 Photometry

The photometric data used for these targets comes from several sources: SDSS, Pan-STARRS, The Liverpool Telescope and CRTS survey. More detail on the photometry is provided in Chapter 2.

SDSS data

In the SDSS data for these targets not all bands are best fit with extended models, as might be expected with the presence of an AGN component. Also, from DR7 to DR9, J103837 has had the classification changed to stellar. The least reliable data is that for J142232, which, in addition to being faint, is flagged as having been affected by a cosmic ray hit.

Pan-STARRS data

Here the Pan-STARRS 1 3π $g_{\rm P1}$ data are from the PV1.2 data release (Schlafly et al., 2012; Tonry et al., 2012; Magnier et al., 2013) and magnitudes have been calculated from the PSF fluxes and associated zero-points.

Liverpool Telescope data

The transients were initially monitored every few days in $u_{\rm LT}$, $g_{\rm LT}$ and $r_{\rm LT}$ to determine how fast they were evolving and then roughly every few weeks. Scheduling and weather constraints sometimes meant that there was not always the desired cadence on some targets. Only the $g_{\rm LT}$ data is utilized here.

CRTS data

This survey makes use of three different telescopes and allows me to recover pre-Pan-STARRS era light curves for some of the objects. A note of caution is that this survey uses clear filters calibrated to a V-band zero-point, so colour effects may be significant. An approximate magnitude offset has been applied so that the light curve appears consistent with the other data sets for each target and the data have also been seasonally averaged for clarity. Due to the uncertainty regarding colour effects, the CRTS data is used for illustrative purposes but not used in the modelling process.

4.2.3 Spectroscopy

WHT data

Technical information regarding the configuration of the ISIS spectrograph is provided in Chapter 2. Additional observational details for each target are given in Table 4.2.

Table 4.2 *Details of the spectral observations carried out for the objects listed here. The airmass values reflect the mean airmass over the duration of the observation(s). Magnitudes estimates are approximations based on the LT photometry. Seeing estimates reflect the range in measured full width at half maximum (FWHM) of the central region of the blue arm trace for each image.*

Target	Scope	Date	Exposures	g_{mag}	Slit	Seeing	Airmass	Notes
J084305–1	WHT	2013-02-09	$1 \times 1800\,\mathrm{s}$	20.0	2 arcsec	2.2 arcsec	1.74	Dark, patchy cloud, variable seeing
–2	WHT	2013-03-31	$2 \times 1800\,\mathrm{s}$	20.2	1 arcsec	1.1–1.2 arcsec	1.12–1.14	Moon 73%(sep 122°), stable
–3	WHT	2014-12-17	$4 \times 1800\,\mathrm{s}$	21.1	2 arcsec	2.0–2.7 arcsec	1.51–1.24	Dark, variable seeing
–4	MMT	2015-03-10	$2 \times 1800\,\mathrm{s}$	21.3	1.5 arcsec	0.8–1.1 arcsec	1.1–1.09	Moon 82%(sep 96°), variable seeing
J094511–1	WHT	2013-05-15	$2 \times 1800\,\mathrm{s}$	20.7	1 arcsec	1.3 arcsec	1.18–1.28	Moon 30%(sep 24°), stable
–2	WHT	2014-02-07	$4 \times 1800\,\mathrm{s}$	21.1	1 arcsec	1.0–1.4 arcsec	1.34–1.08	Moon 63%(sep 80°), light cloud
–3	MMT	2015-03-09	$2 \times 1800\,\mathrm{s}$	21.5	1.5 arcsec	0.8–0.9 arcsec	1.06–1.04	Moon 89%(sep 63°), variable seeing
J142232–1	WHT	2013-02-11	$2 \times 1800\,\mathrm{s}$	20.0	1.5 arcsec	1.8–2.0 arcsec	1.24–1.18	Dark, variable seeing
–2	WHT	2013-05-15	$1 \times 1800\,\mathrm{s}$	20.1	1 arcsec	1.8 arcsec	1.34	Dark, stable
–3	WHT	2013-08-07	$1 \times 1800\,\mathrm{s}$	20.2	1 arcsec	1.1 arcsec	1.58	Dark, stable
–4	WHT	2014-02-07	$2 \times 1800\,\mathrm{s}$	20.6	1 arcsec	1.1–1.2 arcsec	1.14–1.13	Dark, stable
–5	WHT	2014-07-24	$4 \times 1800\,\mathrm{s}$	21.0	1 arcsec	1.6–2.1 arcsec	1.25–1.93	Dark, stable
			$1 \times 900\,\mathrm{s}$					
(unused) –6	MMT	2015-03-09	$2 \times 1800\,\mathrm{s}$	21.0	1 arcsec	–	1.38–1.28	Moon 89%(sep 14°), variable, v. poor
–7	WHT	2015-04-23	$4 \times 1800\,\mathrm{s}$	21.0	1 arcsec	1.6–1.9 arcsec	1.25–1.68	Dark, stable
J103837–1	WHT	2013-02-11	$1 \times 1800\,\mathrm{s}$	19.7	1.5 arcsec	1.9 arcsec	1.13	Dark, variable seeing
–2	WHT	2013-05-15	$1 \times 1800\,\mathrm{s}$	20.2	1 arcsec	1.3 arcsec	1.38	Moon 30%(sep 40°), stable
–3	WHT	2015-04-21	$2 \times 1800\,\mathrm{s}$	19.8	1 arcsec	0.8–0.9 arcsec	1.13–1.12	Dark, stable

Table 4.3 *Information on the targets in this section. The A_V values are those obtained from Schlafly & Finkbeiner (2011) assuming an R_V of 3.1.*

Target	RA	Dec	z	A_V
J084305	08 43 05.55	+55 03 51.4	0.8955	0.0824
J094511	09 45 11.08	+17 45 44.7	0.758	0.0718
J103837	10 38 37.09	+02 11 19.7	0.620	0.0877
J142232	14 22 32.45	+01 40 26.7	1.076	0.09

MMT data

A small number of observations were made with the blue arm spectrograph on the 6.5m MMT situated on Mount Hopkins, Arizona. Here, the $300\,\mathrm{g\,mm^{-1}}$ grating was used with 2× binning in the spatial direction. A filter wheel issue meant that no order-sorting filter was used. This may affect the third epoch for target J094511 and fourth epoch for J084305. Due to variable conditions and a nearby bright Moon, the sixth epoch for J142232 was very poor and will not be used in the analysis.

Spectroscopic reduction pipeline and modelling

Chapter 2 provides a thorough outline of the reduction pipeline and composite model fitting procedures for the spectra and will not be detailed further here. Before performing any fits the spectra are first corrected for Milky Way extinction using the A_V values in Table 4.3 and the extinction law in the optical from Cardelli et al. (1989). No attempt has been made to correct for host galaxy reddening at this stage. The most prominent telluric features above 6860 Å were masked out during the fitting process. When fitting H β the narrow line widths and centres were tied to that of $[\mathrm{OIII}]_{5007}$.

4.3 Spectroscopic results

The results from the spectroscopic analysis are presented in three key figures. Fig. 4.1 shows the target light curves and line flux evolution. The line fluxes have been plotted relative to the first epoch to allow quick comparison. Fig. 4.2 shows the evolution of the systemic velocity offsets and emission line widths. Fig. 4.3 shows the evolution of the spectral profiles after continuum and Fe template

subtraction. For clarity, a median filter has been applied to the broad lines. Additional measurements can also be found in Table 4.11. The observed spectra are shown in Figs. 4.10, 4.11, 4.12, 4.13.

Three of the four targets, J084305, J094511 and J142232, show clear evidence for a differential evolution of the continuum with respect to the line fluxes. In general, the continuum decreases by a factor ~ 4 and, to a lesser degree, the CIII] flux tracks this change. The MgII flux either tracks the continuum change weakly or is consistent with no change at all. The photometry indicates that the targets have been evolving smoothly over this period. A more detailed summary of each object now follows and the reader should refer back to the figures mentioned in the previous paragraph.

Any evidence for an intervening galaxy, which would lend weight to the microlensing scenario, will be presented on a per target basis.

4.3.1 J084305

The light curve of this target shows a smooth decline of $\sim 0.6\,\mathrm{mag\,yr^{-1}}$ from a peak more than two magnitudes brighter than the SDSS observations 16 years ago. There are no CRTS data that allow us to see the pre-Pan-STARRS evolution. There are two spectral epochs near the observed maximum around 56100 MJD and a further two after a decline of at least one magnitude. The most recent photometry suggests the target is now returning to the level of the Sloan era. Of the three SDSS epochs, two are at $g \simeq 22.25$ mag and the third has the higher value of $g = 21.56$ mag, which may indicate a problem with the Sloan *cmodel* fit(s). The microlensing model shown, to which the spectra have been rescaled, does a good job of reproducing the large amplitude changes. Further details on the model are in Section 4.5.1.

As to the spectral evolution, the continuum is seen to drop by a factor of 5 over the period spanned by the observations. The CIII] flux shows a corresponding drop by a factor of ~ 2. In contrast, the MgII and Fe fluxes are consistent with no change or perhaps even a late increase. Both the MgII and CIII] lines get narrower during the decline. In addition, both lines appear blueshifted relative to the systemic velocity, CIII] more so than MgII. There are intriguing but inconclusive signs of an evolution of the offsets, which shift bluewards by $500\,\mathrm{km\,s^{-1}}$ or so and then recover. There are also apparent changes in the red wing of the MgII profile and

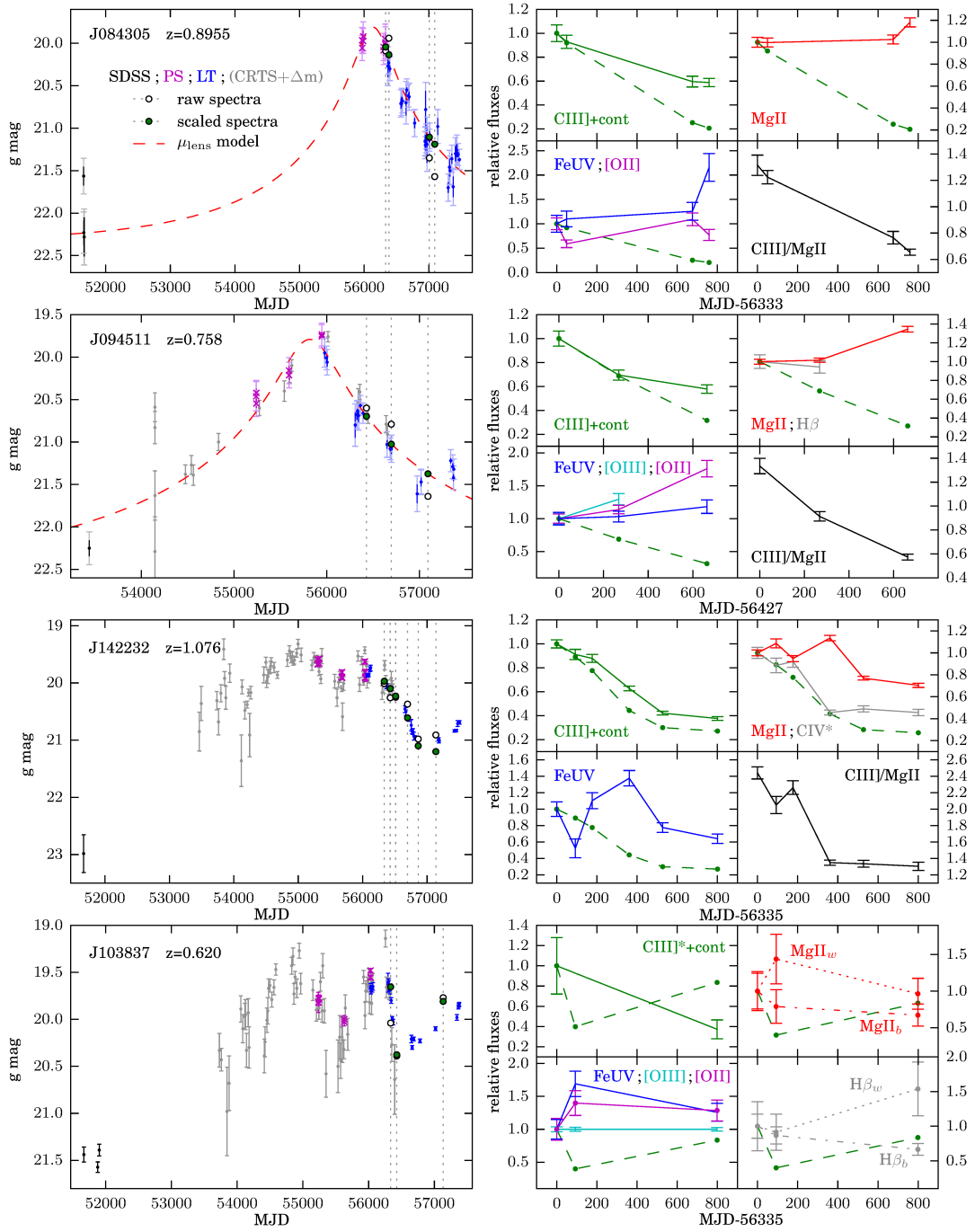

Figure 4.1 *Left-hand panels: composite light curves for each target including spectral epochs. The open circles show the raw spectral magnitudes before rescaling as per Section 4.2.3 and the green circles show the rescaled values. CRTS data have offsets of +0.1/0.1/0.4/0.2 mag, respectively. The extended tails on the error bars for J084305 and J094511 reflect the errors used in the microlensing analysis. Right-hand panels: relative fluxes of the various measured spectral components. For the first three targets, the fourth panel shows the CIII]/MgII ratio. For J103837, the two Gaussian components used in the fit (broad and wide) are displayed. Asterisks denote less reliable values as noted in the text. The green dashed line reflects the continuum under CIII] in each case.*

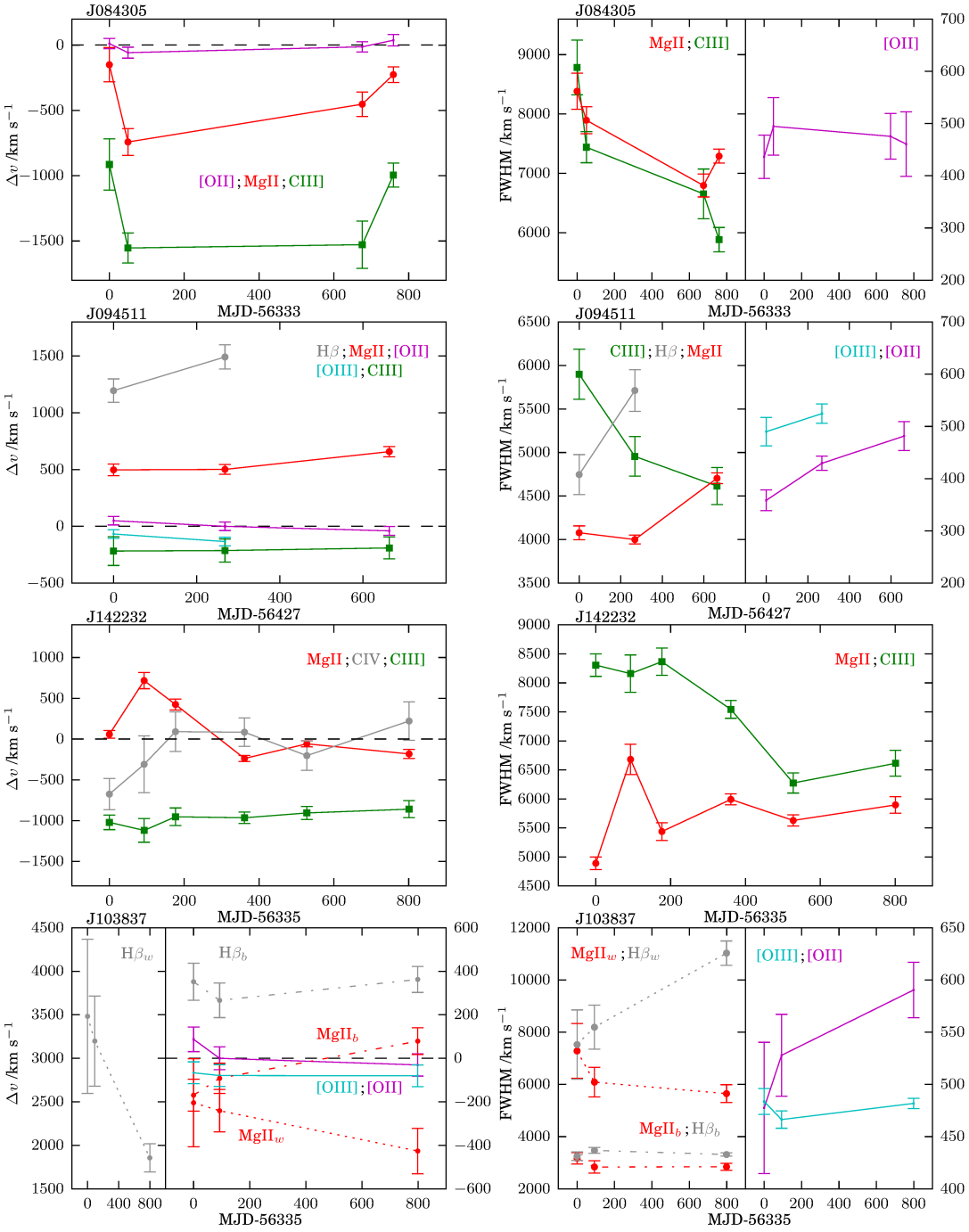

Figure 4.2 *Left-hand panels: velocity offsets for the centre of the measured line profiles for each target assuming rest-frame wavelengths, in Å, of the following: CIV(1549); CIII](1909); MgII(2800); [OII](3727); Hβ/[OIII](4861/5007). The AGN systemic redshift/velocity is determined from the median of the [OII] centres. In the case of J142232, due to a lack of observed narrow lines, MgII has been used. The error bars in this case only reflect the uncertainty in the measured line centre and omit the additional systemic velocity uncertainty. The FWHM of CIV for J142232 is not shown as this value was tied to that of CIII] in the fitting process. Right-hand panels: FWHM of the measured line profiles for each target.*

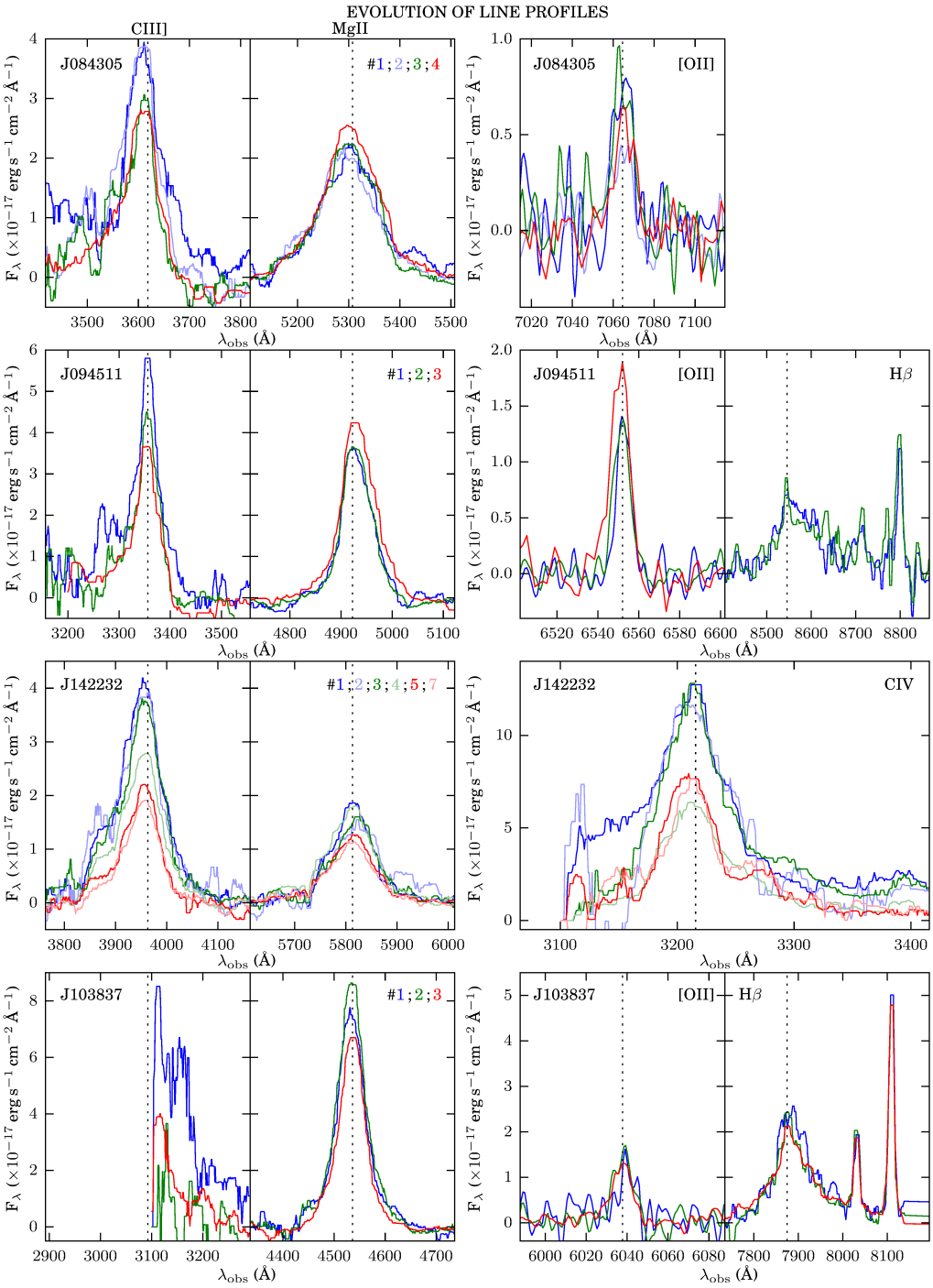

Figure 4.3 *Left-hand panels: CIII] and MgII profiles for each object. For J103837, the profile is truncated due to the blue arm cut-off. Right-hand panels: additional emission line profiles measured in the fitting process. For clarity, all plots, barring those for [OII], have had a median filter applied.*

both wings of CIII], most notably around the expected position of the fainter AlIII component. The scatter seen in the [OII] flux may be due to slit-width changes.

There are no clear spectral features suggestive of an intervening galaxy but this possibility cannot yet be ruled out. The microlensing model for this target shows that any intervening galaxy flux will be at least a factor of 2 below the AGN/host baseline flux in the g band, making spectroscopic detection during an ongoing event difficult. In addition, two of the three SDSS epochs are flagged as having issues with the Petrosian radii. This may simply be due to noise or is perhaps an indicator of morphological issues.

4.3.2 J094511

Since the SDSS epoch some 11 years ago, this target has been evolving at around $\sim 0.4\,\mathrm{mag\,yr^{-1}}$ and displays an approximately symmetric light curve about a peak around 56000 MJD, with an apparent dip/rise after the 57000 MJD mark. There are three spectral epochs for this object spread over two years, after the maximum, with a factor ~ 2 decrease in flux over this period. As with J084305, the spectra have been scaled to the microlensing model (Section 4.5), though the accuracy of the third epoch scaling is less certain due to the additional structure in the light curve at this point.

As with J084305, there is a marked difference between the evolution of MgII and CIII] fluxes. CIII] drops to $\sim 60\%$ of the initial value while MgII is consistent with no change and possibly an increase of $\sim 30\%$ if the third epoch scaling is correct. This increase is also seen for [OII], though a larger slit width was used at the third epoch. At this epoch, the MMT spectrum did not have sufficient wavelength coverage to catch H β/[OIII], so it is harder to draw firm conclusions on any trends here. The H β broad component is redshifted by $\sim 1300\,\mathrm{km\,s^{-1}}$ and MgII shows a smaller $\sim 500\,\mathrm{km\,s^{-1}}$ redshift. CIII] shows a modest blueshift of $\sim 250\,\mathrm{km\,s^{-1}}$. There is no sign of an evolution in velocity offsets as seen for J084305. The CIII] and MgII line widths show the same trend as their amplitudes, as do the narrow lines, though H β only shows an increase in width. Looking at the line profiles, CIII] shows a significant blue wing change whereas MgII sees a change on the red wing. It is perhaps interesting that [OII] sees an enhancement primarily on the blue wing. No clear spectral signature of a possible intervening galaxy has been detected.

4.3.3 J142232

The light curve for this target shows there has been a rise of approximately three magnitudes since the SDSS epoch and $|\Delta g| \simeq 1.22$ mag over the six spectral epochs as estimated from interpolation of the LT light curve. The SDSS epoch is faint and should therefore be treated with caution. The photometry shows this target to be evolving smoothly but there is a notable dip around 55500 MJD, this is after the assumed 'peak' around 55000 MJD. An earlier dip around 54200 MJD is also visible though the CRTS data show considerable scatter here. After the 56500 mark, there is a rapid drop of $\sim 1.1\,\mathrm{mag\,yr^{-1}}$, the time of the spectral observations, but the most recent photometry shows this levelling off. The cadence of the LT observations is not always ideal, which may affect the spectral scaling corrections (Sec. 4.2.3).

For this target, outside of the rest-frame UV ($\lambda_{\mathrm{obs}} > 6400\,\text{Å}$), no other spectral features or narrow emission lines were detected. Given a lack of detected narrow lines, the systemic velocity/redshift has been determined from the median MgII line centre. For clarity, the corresponding increase in uncertainty has been omitted from the plot in Fig. 4.2. Also, at this redshift the CIV line is seen, albeit very near the blue cut-off. Shortward of $\sim 3200\,\text{Å}$, the flux calibration is less reliable due to the lack of calibration points for the chosen standard stars. [1]

The spectroscopic results for J142232 are broadly similar to that seen in J084305/J094511. There is a factor ~ 4 drop in the continuum and the CIII]/CIV fluxes appear to track this change quite closely, dropping by a factor ~ 3. The MgII flux also tracks the continuum to a lesser extent, dropping by a factor ~ 2. The Fe component behaves similarly, though there is a higher degree of scatter. The CIII] centre shows a blueshift of $\sim 1000\,\mathrm{km\,s^{-1}}$, which does not evolve, and the line gets narrower in decline. In contrast, MgII shows a higher degree of scatter in the velocity offset and an increase in line width of $\sim 1000\,\mathrm{km\,s^{-1}}$ over this period. There is evidence for evolution of the line profiles, most notably on the CIII] blue wing MgII/CIV red wing.

In addition, there is also a set of strong narrow absorption features present, possibly evidence for an intervening galaxy. These features are consistent with MgII/Fe absorption at $z = 0.855$ and are highlighted in Fig. 4.4. The AGN is

[1] The fitting pipeline would occasionally fail to fit CIV and instead add an additional continuum component. To prevent this, the width of CIV was constrained to be the same as CIII], so the CIV results should be treated with caution.

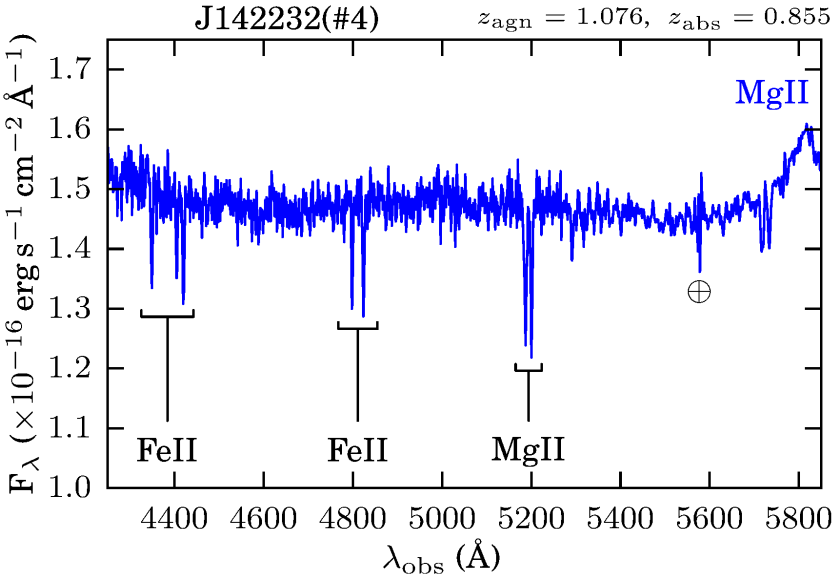

Figure 4.4 *Fourth spectral epoch for J142232 highlighting the narrow absorption features seen. These are consistent with MgII/FeII absorption at a lower redshift or possibly an outflow intrinsic to the AGN. A similar MgII/FeII feature is seen nearer the blue wing of the MgII broad line though in this case only the MgII doublet is readily visible.*

at $z = 1.076$. Alternatively, this feature may be the result of an outflow intrinsic to the AGN. However, this Δv is close to $0.1c$, much greater than the value of $0.01c$ typically used to distinguish between associated and intervening systems (York et al., 2006) making an outflow unlikely in this case. There is also a second similar but fainter feature, seen nearer the blue wing of the MgII broad line. In addition, the SDSS epoch for this target is flagged as a possible blend, i.e. more than one peak was detected in a given filter. Given that the target was faint at this epoch, this may not be reliable but lends further weight to the possible presence of an intervening galaxy.

4.3.4 J103837

This object exhibits the most complex light curve and the spectra have been scaled relative to the $[\mathrm{OIII}]_{5007}$ flux (Section 4.2.3). There is evidence of at least three peaks with occasional rapid changes in brightness, particularly around 56300 MJD, which shows a drop of ~ 0.4 mag over 2.5 months. Here, the cadence of the LT photometry is less than ideal. It is possible the drop was larger than observed. After the drop, it appears to rise more gradually at $\sim 0.2\,\mathrm{mag\,yr^{-1}}$ though there is a spike in the data ($g = 19.79$ mag) at the third spectral epoch

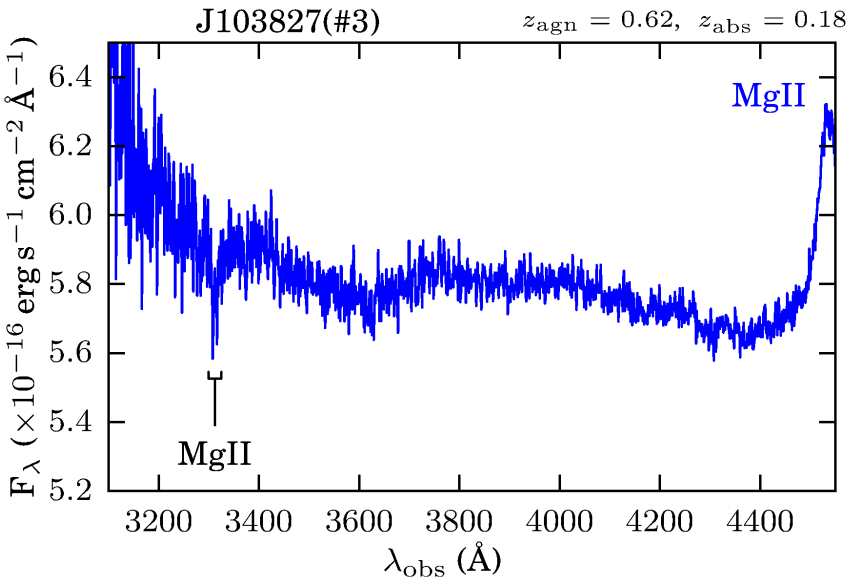

Figure 4.5 *Third spectral epoch for J103837 highlighting the narrow absorption feature. It is consistent with an MgII doublet at a lower redshift than the AGN.*

at 57137 MJD. There is a peak-to-peak change from the Sloan era of at least two magnitudes. The increase in complexity, coupled with the lack of LT data at the second spectral epoch causes a problem when attempting to correct the spectral data for transparency effects (Section 4.2.3). For this object, the [OIII] flux was used to rescale the data as the interpolation using the LT data was poor. This may introduce additional errors if the line flux varies either intrinsically over this time-scale or due to aperture/seeing effects.

Given that in this case the second spectral epoch represents the minimum, it is harder to draw conclusions regarding any spectroscopic trends. The SNR of the third epoch was sufficient to allow a more complex fit for the H β/MgII lines. In this case, two Gaussian profiles were used simultaneously. The CIII] results should be treated with caution as the bulk of the line was beyond the blue cutoff requiring that the line centre and width be fixed relative to that of MgII. It was not reliably detected at the second epoch. Both of the wider Gaussian components for H β/MgII appear to undergo a blueshift over the period of observations and H β shows evidence of an increase in FWHM also.

For this target, an absorption doublet was seen that may indicate the presence of an intervening galaxy. It is consistent with MgII at a low redshift and is highlighted in Fig. 4.5. This feature has only been reliably detected in the third epoch, likely due to the higher SNR achieved in the blue. Here, the suspected

absorber lies at $z = 0.18$ and is far less likely to be an outflow intrinsic to the AGN ($z = 0.62$) as might be the case for the absorption seen in J142232. If in outflow, the velocity would be in excess of $0.25c$ (i.e. $>> 0.01c$). This is seen in some high-ionization species but is perhaps implausibly high for these low-ionization lines.

4.4 Microlensing models: techniques

The microlensing models used in this work are detailed in Chapter 2 and in the interest of brevity will not be repeated here. The first part of the analysis in this work is for the simple point-source/point-lens case and the MCMC techniques used for parameter estimation. Extended sources are then considered. Finally, more complex lensing models are considered in a qualitative manner.

4.5 Microlensing models: results

In this section, the results from the analysis of the various microlensing models are presented. First is the point-source point-lens model MCMC analysis. This performs well for the two single-peaked targets, J084305 and J094511. Secondly, extended source models are applied to the same targets. I find it is not possible to differentiate between extended accretion-disc models and the point-source approximation, suggesting the disc may be only marginally resolved in these cases. Also, while not a full exploration of parameter space, I am able to place some constraints on the size of the emitting region for CIII], particularly for J084305. Finally, an initial exploration into the more complex case of microlensing with an external shear is made for J142232 and J103837.

4.5.1 Point-source point-lens model

J084305

The microlensing parameter estimates for J084305 are shown in Table 4.4 and the marginalized parameter model fit to the data is shown in Fig. 4.1. The full MCMC results are displayed in Fig. 4.14. Here, one can see that there is a strong

Table 4.4 *Parameter estimates obtained from the MCMC analysis, including the Einstein radius in the source plane, for J084305. The model using these marginalized parameters, assuming a negligible background flux, produces a fit to the data with a reduced chi-squared value of 0.69 and has an Einstein radius of 12.1 light-days. Parameter definitions are as per Table 2.3.*

J084305		$z_{\rm agn} = 0.8955$
parameter	value	unit
z_d	$0.34\,^{+0.27}_{-0.21}$	
M_l	$0.37\,^{+1.19}_{-0.29}$	$\mathrm{M}_\odot$
$v_\perp$	$830\,^{+1080}_{-510}$	$\mathrm{km\,s^{-1}}$
y_0	$0.097\,^{+0.026}_{-0.031}$	θ_E
t_0	$56137\,^{+23}_{-23}$	MJD
F_s	$5.5\,^{+1.5}_{-1.6}$	$\times 10^{-18}\mathrm{erg\,s^{-1}cm^{-2}\AA^{-1}}$
F_b	< 1.8	$\times 10^{-18}\mathrm{erg\,s^{-1}cm^{-2}\AA^{-1}}$
r_E	$10.5\,^{+17.0}_{-6.3}$	light-days
	$r_{E,\rm mp} = 12.1$ l.d.	$\chi^2_\nu = 0.69$

correlation of lens mass with transverse velocity, as expected, and also with impact parameter versus the pre-lensed AGN (or 'source') flux. An anticorrelation is seen for the background flux with respect to both impact parameter and source flux. The model light curve produces a fit to the data with a reduced chi-squared value of 0.69. This assumes a negligible background component and has been calculated using the same photometric errors as that for the MCMC analysis. Given the good fit to the data, this model was used to scale the spectra. This specific model has an Einstein radius of 12.1 light-days, Einstein time-scale of 7.5 yr and a peak amplification of 10.3.

Though poorly constrained, the values obtained for the lens mass (0.37 $\mathrm{M}_\odot$), transverse velocity ($830\,\mathrm{km\,s^{-1}}$) and redshift (0.34 as compared to 0.895 for the AGN) are all physically reasonable. The estimate for the background flux from the host/lens galaxies is consistent with an upper limit ($g \leq 23.6$ mag assuming a simple conversion from the value obtained for $F_{\rm b}$, in this case the 68th percentile from the MCMC trace) and the AGN would have an unlensed magnitude of $g \simeq 22.3$ mag.

J094511

The microlensing parameter estimates for J094511 are shown in Table 4.5 and the marginalized parameter model fit to the data is shown in Fig. 4.1. The model

Table 4.5 *Parameter estimates obtained from the MCMC analysis, including the Einstein radius in the source plane, for J094511. The model using these marginalised parameters, assuming a negligible background flux, produces a fit to the data with a reduced chi-squared value of 1.14 and has an Einstein radius of 12.8 light-days. Parameter definitions are as per Table 2.3.*

J094511		$z_{\rm agn} = 0.758$
Parameter	Value	Unit
$z_{\rm d}$	$0.29\,^{+0.24}_{-0.18}$	
$M_{\rm l}$	$0.40\,^{+1.47}_{-0.32}$	$\mathrm{M}_{\odot}$
$v_{\perp}$	$580\,^{+950}_{-360}$	$\mathrm{km\,s^{-1}}$
y_0	$0.074\,^{+0.033}_{-0.029}$	$\theta_{\rm E}$
t_0	$55816\,^{+26}_{-26}$	MJD
$F_{\rm s}$	$4.3\,^{+1.8}_{-1.8}$	$\times 10^{-18}\mathrm{erg\,s^{-1}cm^{-2}\,\AA^{-1}}$
$F_{\rm b}$	< 1.8	$\times 10^{-18}\mathrm{erg\,s^{-1}cm^{-2}\,\AA^{-1}}$
$r_{\rm E}$	$11.9\,^{+18.9}_{-7.2}$	Light-days
	$r_{\rm E,mp} = 12.8$ l.d.	$\chi^2_{\nu} = 1.14$

light curve produces a fit to the data with a reduced chi-squared value of 1.14. This specific model has an Einstein radius of 12.8 light-days, Einstein time-scale of 10.8 yr and a peak amplification of 13.5. The CRTS data was not used in the analysis but is in broad agreement with the model. The accuracy of the model may be adversely affected due to the extra structure seen in the light curve at later epochs (MJD>57000).

Similarly to J084305, the same correlations are seen and the parameter estimates are physically reasonable. In this case, the transverse velocity and impact parameter are lower. Using these parameter estimates, the Einstein time-scale is 10.8 yr, Einstein radius 12.8 light-days and the peak amplification factor is 13.5. The estimate for the unlensed flux level from the host/lens galaxies is consistent with an upper limit ($g \leq 23.6$ mag) and the AGN would have an unlensed magnitude of $g \simeq 22.6$ mag.

4.5.2 Extended source models

The preceding section provides good evidence that the point-source, point-lens microlensing model is a reasonable approximation for the continuum changes seen in J084305 and J094511. I now explore these lensing models in the regime where the point-source approximation no longer applies. This is particularly important with regards to the size of the BLR. The spectroscopic analysis shows there is

Table 4.6 *Empirical estimates for the accretion-disc sizes for J084305, calculated as per Section 2.5.2.*

Source	Size (light-days)	($\theta_{\rm E}$)
Thin disc	0.19	0.016
Morgan disc	0.91	0.075

evidence for the differential evolution of the BLR fluxes, namely MgII and CIII], with respect to the continuum. If these lines are partially resolved by the lens, then it allows constraints to be placed on the size of the emitting region. Indeed, in the case of J084305 in particular, there is evidence to suggest that the CIII] region is compact enough to undergo significant changes in amplification as the lensing event unfolds.

J084305

In order to test the validity of the point-source model, I compare extended accretion-disc models using empirical estimates for the disc size and contrast with the point-source approximation. The lens model parameters and accretion-disc size estimates are listed in Tables 4.4 and 4.6 respectively. The results are shown in Fig. 4.6. It is clear from the figure that there is little separation between the models except perhaps during the midpoint of the event. Here, the increased amplification seen at the peak for the larger Morgan disc is likely a result of the source being of a suitable size to have significant flux overlapping the regions of highest magnification for the given impact parameter. The fit to the light curve for the thin-disc model has $\chi^2_\nu = 0.70$ and for the Morgan disc $\chi^2_\nu = 0.88$. For lensing models with a smaller projected Einstein radius (varying $z_{\rm d}$, $M_{\rm l}$, $v_\perp$ within the derived parameter constraints), the distinction between the models becomes more apparent, favouring the smaller thin-disc and point-source models. Conversely, for larger Einstein radii, both extended models converge to the point-source solution.

The fact that both the point-source and extended accretion-disc models perform well suggests that, within the constraints imposed by the light curve, the point-source approximation is reasonable, at least in the g band. However, the possibility that the disc is being resolved, if only marginally, still exists. This does not rule out chromatic effects due to microlensing but makes it harder to draw any conclusions as to the true thermal profile of the disc.

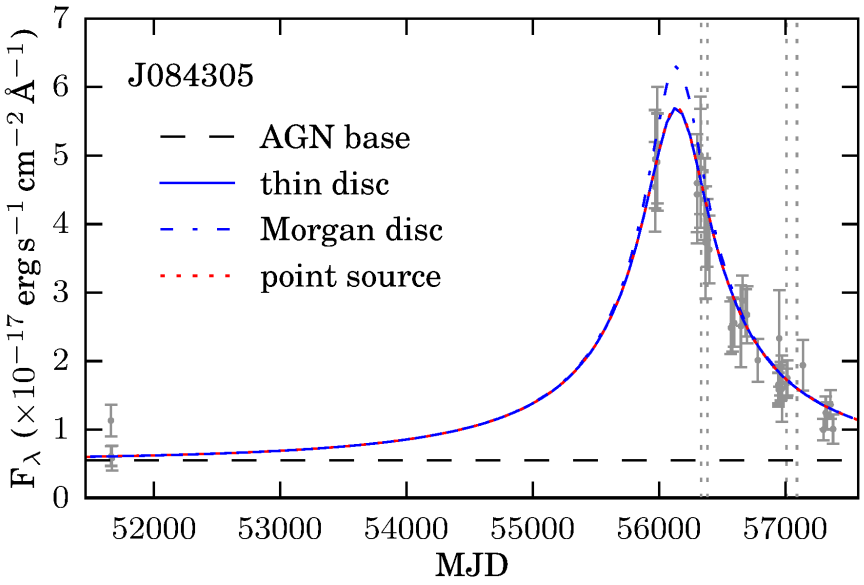

Figure 4.6 *Extended source model light curves for J084305. The grey data are the original photometry points and the vertical lines are the spectral epochs. The source sizes are listed in Table 4.6. The dashed line represents the AGN base flux.*

Table 4.7 *Estimated CIII] and MgII sizes for J084305. They have been determined from the spectroscopic data as per Section 4.5.2. The errors here reflect the fitting process only.*

Source	Size (light-days)	($\theta_{\rm E}$)
CIII]	4.8 ± 0.2	0.40 ± 0.02
MgII	> 15	> 1.24

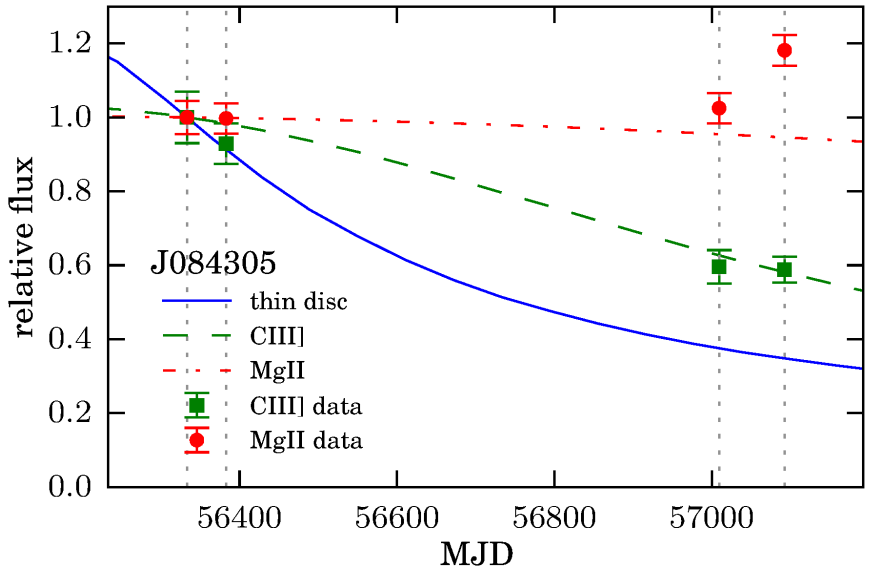

Figure 4.7 *Evolution of extended model fluxes relative to the first spectral epoch. Overplotted are the spectroscopic measurements of CIII] and MgII. The source sizes are listed in Table 4.7.*

There are indications that the BLR is being partially resolved by the lens. Fig. 4.7 shows the flux evolution for selected source models, relative to the first spectroscopic epoch, against the observed data for CIII] and MgII. Again, note the differential evolution of the lines with respect to the continuum. If one assumes that this is a lensing effect, the data for CIII] is sufficient to allow a determination of the size of the emitting region using a χ^2 distribution, assuming Gaussian errors. The values are noted in Table 4.7. Given the uncertainty in the Einstein radius of the lens, the relative size of 0.4 θ_{E} should prove more robust than the absolute size. For this particular lens model, the absolute size of the CIII] emitting region is 4.8 ± 0.2 light-days. The true value is likely to be in the range $\sim$ 2–11 light-days when the uncertainties in the lens model parameters are taken into account. In the case of MgII, the data is consistent with no change or perhaps a late increase in flux. A source size greater than approximately 15 light-days (or $> 1.2\ \theta_{\mathrm{E}}$) would see little evolution in flux over this period. This provides a lower limit to the size of the MgII emitting region. It does not explain the jump in flux seen for the fourth epoch. However, this could be due to a scaling problem. As will be discussed below, the estimate for the size of the CIII] emitting region is relatively compact when compared with size predictions for the CIV and H β regions.

Table 4.8 *Empirical estimates for the accretion-disc sizes for J094511, calculated as per Section 2.5.2.*

Source	Size (light-days)	($\theta_{\rm E}$)
Thin disc	0.097	0.0076
Morgan disc	0.31	0.024

J094511

J094511 shows similarities to that of J084305. The empirical accretion-disc size estimates are listed in Table 4.8. Using the lensing model parameters in Table 4.5, these provide light curves that are nearly indistinguishable from the point-source case. Again, this suggests that the point-source approximation is reasonable but does not rule out the possibility that the disc is being resolved. For this target, the uncertainty on the scaling of the third epoch means that it is not yet possible to place reasonable constraints on BLR sizes. What can be said for this object is that if the observed changes are due to microlensing, then the size of the CIII] region again has to be small, perhaps of the order of ∼1 light-day as this line appears to track the continuum closely.

4.5.3 Lensing plus external shear

J142232

A detailed analysis of more complex lensing morphologies is beyond the scope of this chapter, but an exploratory analysis is presented here in order to address the question of whether or not the double- or indeed multiply peaked light curves seen in this sample can also be due to microlensing.

J142232 exhibits a clear double-peak in the light curve, which requires the use of a more complicated magnification map in order to try and reproduce this. For this test, a CR lens (Sec. 2.5.3) with the external shear parameter set to 0.05 was used. With reference to Fig. 2.14, this value is reasonable for smaller galaxies with a star–galaxy separation ∼4 kpc. It is enough to unfold the central degenerate point into a diamond-like caustic region. For this target, there is also a possible lens redshift due to the presence of absorption features in the spectrum. Using this and an assumed lens mass of 0.5 $M_{\odot}$ gives this particular lens model an Einstein radius at source of ∼6.24 light-days. As for J084305, two empirical

Table 4.9 *Empirical estimates for the accretion-disc sizes for J142232, calculated as per Section 2.5.2.*

Source	Size (light-days)	($\theta_{\rm E}$)
Thin disc	0.23	0.036
Morgan disc	0.83	0.13

accretion-disc size estimates were used and these sizes noted in Table 4.9. Next, the source track and intrinsic flux were varied to provide the qualitative light curves seen in Fig. 4.8. The magnification map and source/track used in this model are shown in Fig. 4.9.

It is worth noting that the larger Morgan disc does not resolve the double-peak structure that is seen for the thin disc. The thin-disc model fit to the data is poor around 54000 MJD but the CRTS data (points prior to $\sim$ 56000 MJD) are less reliable at these fainter magnitudes. It is also possible that the single Sloan epoch of $g = 23$ mag is not reliable and that the clear CRTS filter will introduce colour effects. These caveats aside, this lens model does provide a plausible explanation for the double-peaked structure seen in J142232 but requires refinement before any further conclusions can be drawn. As with J084305 and J094511, there is evidence to suggest that the BLR emission regions, particularly CIII] but also MgII in this case, are compact enough to show significant amplification changes on these time-scales.

J103837

In the case of J103837 there is even more complexity in the light curve. The CR lens example used for J142232 allows a comparison with double-peaked light curves, but to explain the three peaks seen for this object requires a more complex/realistic model. There is also spectroscopic evidence for an intervening system at $z = 0.18$, which, if confirmed, would help reduce the model uncertainties. Assuming a lens mass of $0.1{\rm M}_{\odot}$, this projects to an Einstein radius of $\sim$ 8 light-days. The thin-disc size estimate, based on the faintest of the three observed epochs is $\sim$ 0.1 light-days. The presence of an external shear with additional lens masses could provide an adequate explanation for the variability seen in this object. It will be the focus of future work.

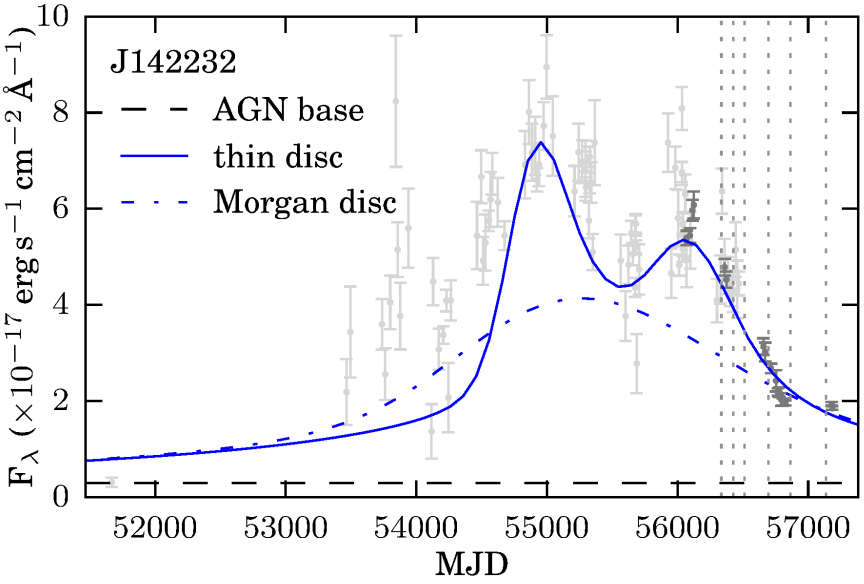

Figure 4.8 *Chang-Refsdal lens model light curves for J142232. The grey data are the original photometry points, the darker points are the LT epochs. The source sizes are listed in Table 4.9. The dashed line represents the AGN base flux.*

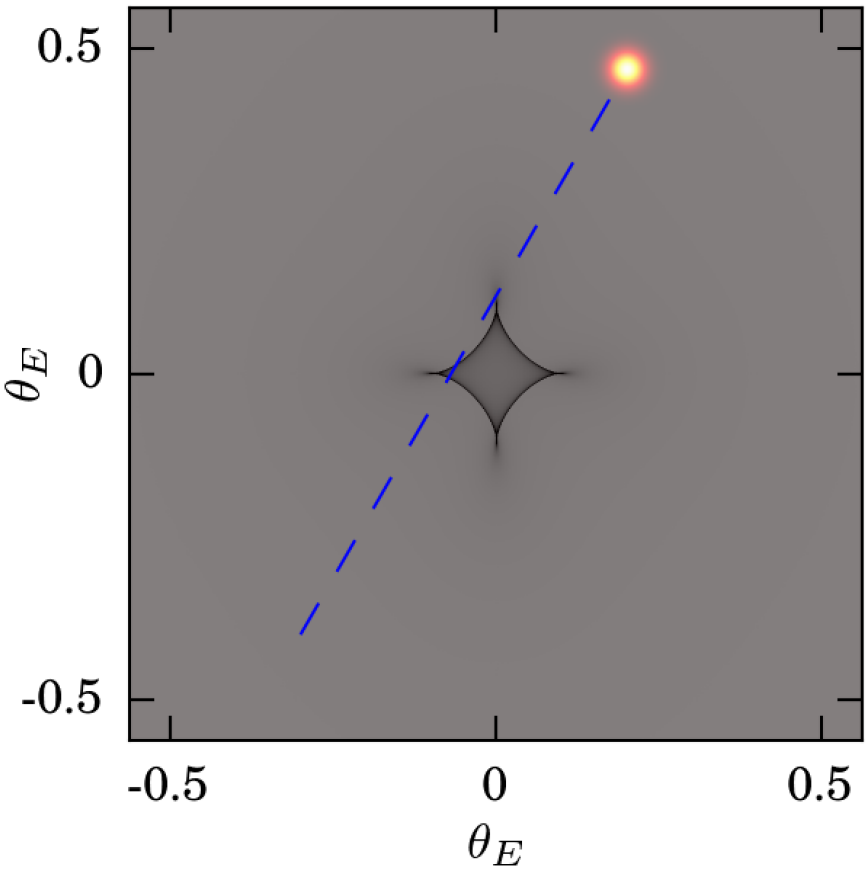

Figure 4.9 *Magnification map and source/track to produce the thin-disc light curve shown in Fig. 4.8.*

4.6 Discussion

The AGN transients in this paper have been selected because they are candidates for microlensing events. The photometry shows a minimum of a factor 5 increase in flux and a smooth evolution on year-long time-scales. For three of the objects, the spectroscopy reveals differential evolution in the broad line fluxes with respect to the continuum. In particular, CIII] is seen to track the changes in the continuum more closely than that of MgII. Two objects also show spectroscopic signatures indicating the possible presence of an intervening galaxy. A simple point-source/point-lens model produces a reasonable fit to the bulk continuum changes seen for the single-peaked events. The testing of extended accretion-disc models with these lens configurations, given the parameter uncertainties, suggests the point-source approximation is reasonable but does not allow me to rule out the possibility that the accretion discs are being resolved, if only marginally. When extended source models are included for the BLR, the differential changes seen in the broad lines can be interpreted as the BLR being partially resolved by the lens. This implies that the CIII] emitting region is smaller than that for MgII and the data for J084305 allows size constraints for these regions of the order $\sim$ 2–11 light-days. More complex lensing models are required to produce light curves displaying multiple peaks.

Having summarized my results so far, I now put them into context of what we know about AGN, discuss whether they make sense and what we might learn from them. The focus for this discussion will be on the microlensing hypothesis. Other plausible scenarios include the following: TDEs; accretion-disc instabilities; and extinction events. These are considered in more detail in L16. Target J142232 also has X-ray data available. Collinson (2016) shows that this object can be considered X-ray loud for its peak luminosity but not for its pre-outburst luminosity, i.e. the low state seems to be the normal one. This is consistent with the microlensing scenario.

4.6.1 Continuum variability

Can the variability of the AGN in this paper be described as typical? In the context of the wider AGN population, long-term optical variability is commonly described in terms of a damped-random-walk (DRW) model (Kelly et al., 2009;

Table 4.10 *Damped-random-walk parameters obtained for J084305 and J094511. The values have been computed for the observed data and the residuals after subtraction of the microlensing model.*

	J084305		J094511	
	Observed	Residual	Observed	Residual
SF_∞	1.62	0.21	2.19	0.26
$\log(\tau)$	3.72	1.96	3.94	2.28

MacLeod et al., 2010, 2012). It quantifies the variability using a structure function, which gives the rms magnitude difference as a function of time lag between different epochs. This model performs well when applied to large quasar samples. The two key parameters are the damping or characteristic time-scale, τ, and the asymptotic rms magnitude difference at the longest time-scales, SF_∞. Chelsea MacLeod computed the DRW parameters for J084305 and J094511 in two situations. First, for the original light curve and second, for the residual light curve after taking the microlensing model into account. The values obtained are displayed in Table 4.10.

With reference to MacLeod et al. (2010, Table 2), it is clear the DRW parameter values for the observed data are atypical for quasars and may even be biased due to a different underlying process describing the observed variability (Kozłowski, 2016). However, after taking the microlensing models into account, the parameters $[\log(\tau) \sim 2, SF_\infty \sim 0.2]$ are much more typical for quasars. A typical DRW origin for the bulk variability in these objects cannot be conclusively ruled out but this does lend further credence to the microlensing hypothesis. Regardless of the physical model it is notable that, after removing the trend, they look normal.

The underlying mechanism responsible for typical AGN variability is thought to be related to accretion-disc thermal instabilities and/or reprocessing of X-ray/UV emission (Kelly et al., 2011; Shappee et al., 2014; Edelson et al., 2015). There may also be reprocessing of FUV emission due to optically thick clouds on the inner edge of the BLR. This can reproduce some of the observed UV/optical lags (Gardner & Done, 2017) and can also address issues in relation to observations of the UV bump (Lawrence, 2012). In effect, these clouds would give rise to a 'pseudo-continuum' component, which may prove important when testing various surface brightness profiles relating to the accretion disc and BLR. It has been suggested that the variability seen in luminous quasars on long time-scales may be primarily due to ongoing microlensing (Hawkins, 2002). This work makes use of a

structure function analysis to quantify the timescales for variability seen in both low- and high-luminosity AGN. The results suggest a two-component model for AGN variability. At low luminosities/redshifts, AGN variations are dominated by intrinsic variability but at high luminosities/redshifts a cosmologically distributed population of compact lenses may be provide a more adequate explanation for the bulk variability seen in these objects.

4.6.2 Accretion disc: point-source or extended?

Is the point-source/point-lens model an oversimplification? To first order, the model produces a reasonable fit to the bulk continuum changes in J084305/J094511 and also allows constraints on the lens parameters, which are reasonable given that there is currently no confirmed lens redshift. In addition, the testing of extended accretion discs with these lens parameters, using two different estimates for the true disc size, also produces reasonable fits to the data. The thin-disc prediction is broadly consistent but we can rule out the Morgan et al. (2010) model for some lens configurations. Thus, I can be reasonably confident in the validity of the point-source approximation but note that it is still possible that the disc is being resolved by the lens. Broadly speaking, for an accretion disc of approximately $\sim 0.1\,\theta_{\rm E}$ or greater, it becomes possible to differentiate from the point-source solution using our data. Early further testing using MCMC models and extended sources shows tentative evidence that the disc is being resolved, but, given the large uncertainties on the Einstein radius of the lens, I am not yet able to place meaningful constraints on the absolute size of the accretion disc in these objects. In this work, I have also made the simplifying assumption that the accretion-disc surface brightness profile can be treated as a Gaussian, with a 2σ radius equivalent to the radii calculated in Equations 2.6 & 2.7. This should prove reasonable as Mortonson et al. (2005) state that microlensing fluctuations are relatively insensitive to all circular disc model properties with the exception of the half-light radius.

The colour changes seen in the UV power-law slopes for these objects at later epochs (Table 4.11) are an indication that the disc is at least partially resolved by the lens. These changes would be sensitive to the temperature profile of the disc and also the presence of any caustic structure in the lens configuration. For the reasons outlined above, I have not attempted to constrain the disc profile but hope to explore this in a follow-up paper. Alternatively, changes in amplification

between the disc and a more extended 'pseudo-continuum' cloud component could also produce the observed colour change though this possibility has not been fully explored (Lawrence, 2012). At later epochs, host/lens galaxy contamination may also need to be accounted for. For J084305/J094511, the estimate for the expected host/lens galaxy contribution is at least a factor of 2–3 below the AGN base level in the g band. This goes some way in explaining why the detection of lens galaxy signatures in the spectra for these objects has proven difficult.

A further consideration is the effect of any broad line flux intruding into the filters used in the observations, particularly with respect to MgII in the g band. In the MCMC modelling for J084305/J094511, this extra flux component should be accounted for within the unlensed flux parameter, which is not currently well constrained, but should not invalidate the results. The spectra have also been scaled to the microlensing model, using an LT g-band transmission function to measure the flux, in order to keep the spectral measurements consistent with the photometry. A sign that the microlensing model for J094511 performs less well than expected is the resulting significant flux increase seen in the third epoch for MgII/[OII]. The additional structure in the light curve at late epochs is the likely cause for this discrepancy. As the event continues to evolve/fade, it will be interesting to note whether or not this discrepancy is resolved with further modelling.

4.6.3 BLR

With the simplifying assumption that the variability in the broad lines is entirely due to lensing, the differential changes between the continuum, CIII] and MgII fluxes seen in three of the targets suggest that the BLR is at least partially resolved. Indeed, for J084305 the data is sufficient to allow constraints on the size of the CIII] emitting region. These measurements are made with the assumption that the simplified lens model is appropriate but should necessarily be treated with a degree of caution. The size estimate from the model is ~ 5 light-days with an expected range of ~ 1.7–11 light-days when taking account the uncertainty in the Einstein radius of the lens. These sizes reflect the 2σ radii used in the extended source modelling. Converting to half-light radii yields ~ 1.0–6.5 light-days, which is surprisingly small when compared with BLR radius estimators. One example is from Bentz et al. (2009) for H β and another from Kaspi et al. (2007) for CIV. Using these, after obtaining a continuum luminosity for J084305

from the fourth epoch UV power-law and correcting for the lensing amplification, I obtain a radius of 34 and 31 light-days for H β and CIV respectively. Given these values, one would expect CIII] to perhaps be at least comparable in size, if not a factor of up to 2 larger than that seen for CIV. It is possible that the size estimate suffers due to the fact that the lens model is an oversimplification. This will be discussed in the next section.

For comparison with other observations, there are a handful of published lags for CIII] that have been determined from reverberation mapping. These serve as a proxy for BLR radius and some notable results include Peterson & Wandel (1999); Onken & Peterson (2002); Metzroth et al. (2006) and Trevese et al. (2014). Most are for low-redshift/luminosity targets and show CIII] to be of the order of 3.5–30 light-days for these objects, with a considerable degree of uncertainty. The high-luminosity quasar in Trevese et al. (2014) has a much larger radius of the order of 270 light-days. For J084305, we estimate, after correcting for the lensing amplification, a bolometric luminosity for the AGN of $\log(L_{\rm bol}) \sim 44.7$. This is at the lower luminosity end of published lags but again suggests that our estimate is intriguingly small. Of particular interest is the result from Sluse et al. (2011), where a radius for CIII] has been estimated based on the microlensing of a multiply imaged quasar. Here, a multicomponent fit to the CIII] profile provided evidence that the broadest components lie closer to the accretion disc and are therefore more affected by microlensing. In relative terms, their broadest component (for CIII] and CIV) is around four times larger than the continuum emitting region. The narrowest component is around a factor of 25 larger. Thus, the estimate for the CIII] region in J084305, though small, may in fact be dominated by the changes in the inner component. Thus far, I have only used a single component for the CIII] region, primarily due to SNR issues. An analysis of spectral ratios for J084305/J094511 shows tentative evidence for a changing very broad component redwards of the broad CIII] line, though one must be careful not to over interpret the data. A further consideration is the true morphology of the CIII] region. Reverberation mapping is sampling in the radial direction whereas microlensing provides a transverse sampling. Perhaps the CIII] region is more compact along certain lines of sight than reverberation mapping implies.

For J084305, in contrast to CIII], the MgII flux is consistent with no change. This implies that this region is more extended and therefore will not exhibit significant changes over the time-scale of our observations. The lower size limit obtained is

based on a single component to the line. Limited testing with the use of a double Gaussian component to the line does not significantly affect the single component measurements or the Fe template fit. Sluse et al. (2012) show that both CIII] and MgII exhibit changes due to microlensing in a sample of multiply imaged quasars. They see evidence that the BLR is in general not spherically symmetric and that a bi-conical outflow model may not be appropriate in these cases. These systems benefit from the additional information supplied by the resolvable quasar images.

Thus far it has been assumed that the variability seen in the broad lines is entirely due to lensing but a more realistic scenario must include some intrinsic variability over the period of our observations. It may also be possible that, rather than being resolved by the lens, the observed broad line changes are entirely intrinsic to the AGN. Taking the MgII line as an example, Sun et al. (2015) see significant variability in this line ($\sim 10\%$) on ~ 100 d time-scales. The amplitude of light-curve variability seen in MgII also correlates with that seen in the continuum. Some reliable reverberation lags for MgII are reported in Shen et al. (2016), but a clear correlation with luminosity is not always apparent. In other cases, MgII is unresponsive to continuum changes (Cackett et al., 2015) but on longer time-scales MgII does appear to respond to large changes in continuum flux (MacLeod et al., 2016). In the case of J084305 and J094511, the MgII line does not seem to respond to the continuum drop even on these long time-scales. Given that the MgII line should be at least partially dependent on the ionizing continuum, this is perhaps surprising. Lensing as an extrinsic cause for the continuum variability provides a natural solution however.

4.6.4 Lensing system

For the two objects where the simple lensing model performs well, it is unfortunate that, as yet, there are no confirmed signatures of the presence of a lensing galaxy. This confirmation would allow a move beyond the simple lensing models detailed here. At present, I am assuming that the convergence/shear (and hence macromagnification) are small enough to be neglected. Without confirmation of the presence of any multiple images or a reliable lens galaxy detection/redshift, the true lens parameters are very difficult to pin down and thus the results reported here should necessarily be treated with caution. However, there are two points worth considering, particularly in the context of J084305/J094511, which help to put the assumption of a minimal convergence/shear on surer footing.

Each will be discussed in turn.

First, the light curves are evolving smoothly. This is straightforward to do in the point-lens case but, in the presence of extended regions of caustic structure, one might expect more variation/asymmetry in the light curves. One solution is that the accretion disc is extended enough such that any caustic structure is poorly resolved. This could easily give rise to a single-peaked event without revealing the extra structure present in the magnification map. Preliminary testing of a more advanced MCMC approach has allowed me to make use of extended sources using a lower-resolution version of the CR magnification map ($\gamma = 0.05$) used in the qualitative analysis for J142232. I add an eighth parameter for the source radius and the impact parameter is treated in the same way as for the point-lens case, i.e. an offset in the y-axis. Early results show that, with a good fit to the J084305 light curve, the most probable 2σ radius for the accretion disc is ~ 3 light-days or $\sim 0.2R_{\rm E}$. While, as expected, the effect of the additional shear was to increase the size of the accretion disc, this value is now larger than both empirical estimates for the disc size listed in Table 4.6.

Secondly, there is a large change in amplification of $\sim 2\,$mag and the light curves are approximately symmetric. It is relatively straightforward to achieve light curves of this nature in low-kappa/gamma regimes (below ~ 0.1), as there will likely be isolated regions of high amplification in the magnification map. However, if the magnification map is a complex caustic network with many overlapping regions, it becomes more difficult to reproduce such light curves. As discussed in L16, a random foreground galaxy need not be particularly massive and it may be that these targets are not multiply imaged at all. Singly imaged sources are more likely to have an optical depth to microlensing below 0.1 than their multiply imaged counterparts (Wyithe & Turner, 2002).

Short of the confirmation of a lens galaxy, one way of improving the constraints on the lens parameters would be to include a prior on the transverse velocity of the lens in the MCMC analysis. For now, this parameter has been left free as a useful check on the validity of the results. The predicted values for the velocity are reasonable though perhaps a little high, particularly for J084305 with $v_{\perp} = 830\,^{+1080}_{-510}$ km s^{-1}. If the lens is at a low redshift, then the transverse velocity for this target can be dominated by the peculiar velocity component of the lens galaxy, and values this high are not completely unreasonable (Mosquera & Kochanek, 2011). It also possible, though perhaps less likely, that some of these lensing events are due to isolated extragalactic point-masses.

4.6.5 Future work

One major drawback of this sample is that it is currently very difficult to remove any intrinsic AGN variability, preventing tighter constraints on the lensing parameters. This is possible for a number of multiply imaged quasars, where the time delays between images are short enough that intrinsic variations can be corrected for. For these, there is also a known lens galaxy. In contrast, these objects are among the lowest luminosity and lowest redshift AGN lensing candidates known. The SDSS i-band magnitudes for J084305/J094511 are 20.98/21.11 mag (DR12 cModelMag), respectively; comparison with Mosquera & Kochanek (2011) shows that there are only four targets at $z < 1$ and 10/87 with $i > 20$ mag. Whilst it may not be possible to disentangle the intrinsic AGN variability from the observations, these low-luminosity targets do allow for a greater chance of observing larger amplitude changes in the BLR. In addition, the lensing models used for these objects may prove to be comparatively simple when compared to those involving massive elliptical lensing galaxies.

A priority for the future is to obtain high-resolution imaging of these targets in order to ascertain if there is evidence of any strong lensing or indeed the lens galaxy itself. There is also a good prospect of detecting many more lensed AGN candidates from long-baseline photometry. In addition, the slow evolution and high amplitude maximize the chances for obtaining follow-up observations of each event. For J084305/J094511, the models give an Einstein time of 7.5/10.8 yr and peak magnification factor for the continuum of 10.3/13.5, respectively. Long-term surveys should provide the opportunity to select targets on the slow rise to a high-amplitude microlensing event and allow ample time to plan follow-up observations accordingly. It would prove invaluable to monitor one of these microlensing events with a cadence that allows reverberation mapping to be performed simultaneously.

It is likely that more of the objects in the full PS1-A AGN sample are also undergoing microlensing events. For some, the simple model again provides a good fit to the data though their slow evolution meant that they were not included in this chapter. Other targets are excellent candidates for microlensing events in which the accretion disc may be well resolved by the lens. These, as with J142232/J103837, require a more thorough analysis in order to fully address these questions. More complex magnification maps, such as those available through the `GERLUMPH` data base (Vernardos et al., 2015) are also being considered. In

addition, incorporating all available photometry bands into the analysis is a high priority for future work.

If the microlensing interpretation is correct, this provides a valuable way of probing the inner regions of AGN. This technique is already being used for strong-lensed, multiply imaged quasars (Sluse et al., 2012, 2015). If the lens-host galaxy is small and the event is due to a single stellar lens, these objects will be in a different regime to their multiply imaged cousins. This, coupled with the fact that they are high-amplification events evolving over year-long time-scales, also allows a coordinated observational strategy. As the microlensing event unfolds, it can provide a transverse sampling of the BLR, perhaps even the accretion disc. The shorter time-scale variability allows a probe of the radial structure via reverberation mapping. These high-amplitude microlensing events may be unique opportunities for mapping the inner structure of an AGN.

4.7 Conclusions

In summary, I have analysed four extreme AGN transients, selected as candidates for rare, high-amplitude microlensing events. The light-curve information, primarily from the LT and supplemented by data from Pan-STARRS and SDSS has allowed a detailed MCMC analysis of a simple point-lens point-source model. This model has proven to be an excellent fit to the data in the two single-peaked cases, J084305 and J094511. After removing the signal due to microlensing, the long-term variability in these objects appears much more typical of the wider AGN population.

The multi-epoch spectroscopy from the WHT has also provided valuable insight into these events. All four targets display differential variability of the broad line fluxes with respect to the continuum. In three objects, the CIII] flux is seen to track the continuum closely whereas the MgII flux is less responsive to these changes or shows signs of no change at all. Using the working lensing models and the simplifying assumption of Gaussian surface brightness profiles, the changes can be interpreted as being due to regions of differing size being affected by the lensing event to a different extent. The continuum emission in the g band can be reasonably treated as a point-source and the CIII] region is more compact than for MgII. In the case of J084305, the data also allows size constraints to be placed on these regions.

The two objects not well described by the simple lensing models are J142232 and J103837. In both cases, there is evidence for an intervening absorber, suggestive of the presence of a lensing galaxy. It is clear that the extra structure in the light curve for these double- or multiply peaked events, requires a more complex lensing scenario to describe the event. This will likely involve the presence of additional lens masses and/or external shear with the resulting caustic network giving rise to the features seen in the light curves. Any thorough analysis of these more complex models will also require consideration of extended sources, both for the accretion disc and BLR. Current limitations have meant that this will be left for future work, but microlensing is still the favoured scenario for the long-term variability seen in these objects.

Future time-domain surveys will be an invaluable source of microlensing events of this type. A challenge to overcome will be in identifying the gradual trends over a year or more that might indicate a high-amplitude event is imminent. If possible, this may allow sufficient time to coordinate an observing strategy, particularly with regard to reverberation mapping. The amplification, by an order of magnitude or more, of a higher redshift, lower luminosity AGN would be an ideal candidate for a reverberation mapping (RM) study. This, combined with a detailed lensing analysis, allows an unprecedented opportunity for probing the inner regions of these AGN. They are in a different regime, but wholly complimentary, to the microlensing studies in more luminous, multiply imaged AGN. We must make the most of these opportunities whenever they arise.

4.8 Supplementary data

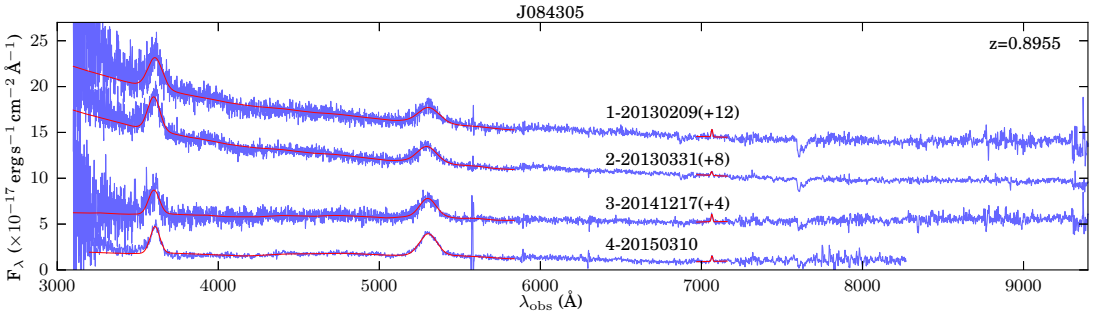

Figure 4.10 *Spectra for J084305 as produced by my reduction pipeline. They have been scaled to our microlensing model (4.5.1) and are corrected for Milky Way reddening. The red lines show the best-fitting models from the fitting process.*

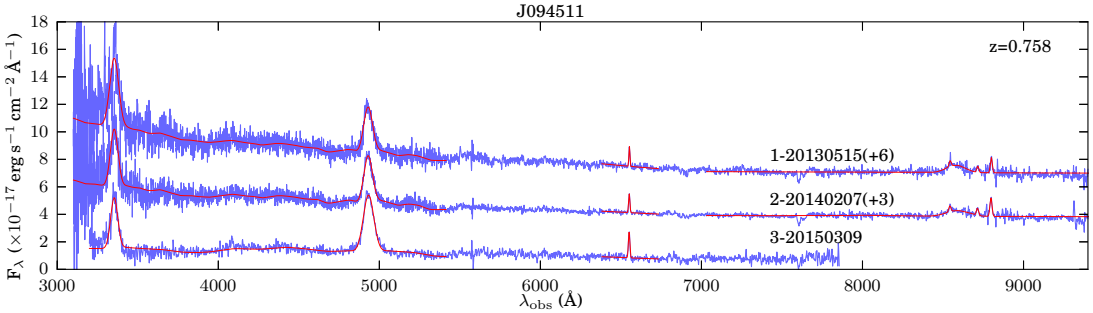

Figure 4.11 *Spectra for J094511 as produced by my reduction pipeline. They have been scaled to our microlensing model (4.5.1) and are corrected for Milky Way reddening. The red lines show the best-fitting models from the fitting process.*

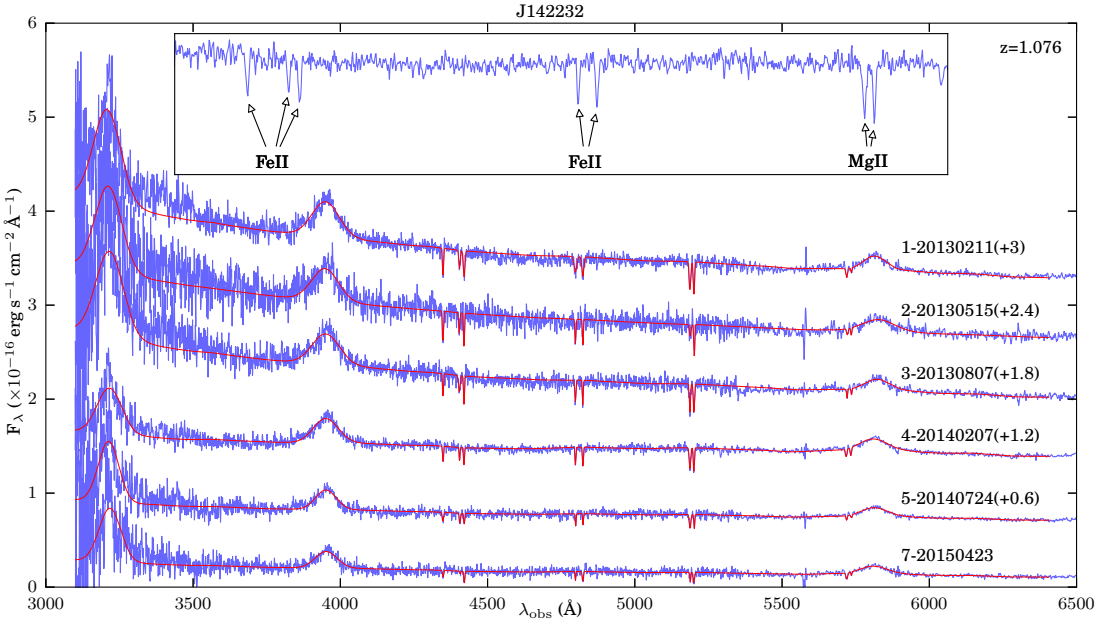

Figure 4.12 *Spectra for J142232 as produced by my reduction pipeline. They have been scaled to our LT data (4.2.3) and are corrected for Milky Way reddening. The red lines show the best-fitting models from the fitting process. Inset is a zoomed region of the central portion of the fourth epoch to highlight the absorption complex.*

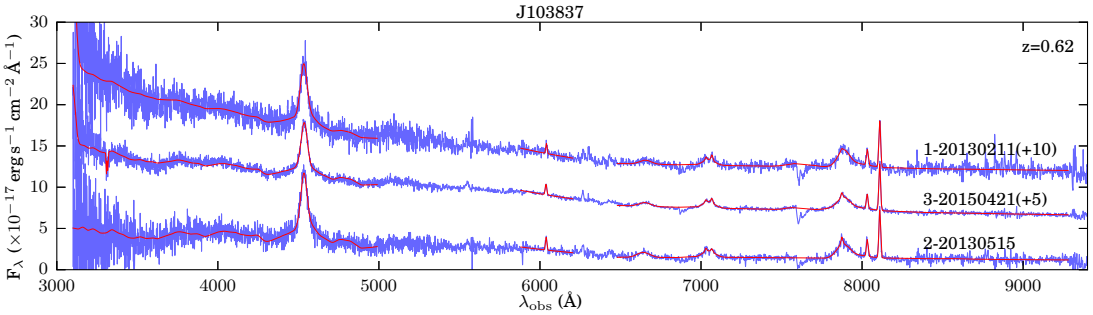

Figure 4.13 *Spectra for J103837 as produced by my reduction pipeline. They have been scaled to our LT data (4.2.3) and are corrected for Milky Way reddening. The red lines show the best-fitting models from the fitting process.*

Table 4.11 *Data table. (1) Scaling correction factor applied to the spectrum as described in 4.2.3. (2) Power law slope from the fit given by Eq. 2.1. (3) Observed AGN monochromatic continuum flux at rest-frame 3000Å calculated from the power-law fit to the UV region. (4) AGN monochromatic continuum luminosity derived from (2). (5)/(6)/(7) Line centre, sigma and total line flux from the Gaussian fit to MgII in the observed frame. For J103837 the values are from the narrower of the two broad MgII components. (8) Black hole mass calculated using the McLure & Dunlop (2004) relation. Errors are from the fitting process only.*

Target	MJD	Scale	β	f_{3000}	L_{3000}	$\lambda_{\rm MgII}$	$\sigma_{\rm MgII}$	$A_{\rm MgII}$	$M_{\rm BH}$
				$\rm erg\,s^{-1}cm^{-2}Å^{-1}$	$\log_{10}(\rm erg\,s^{-1})$	Å	Å	$\rm erg\,s^{-1}\,cm^{-2}$	$\log_{10}(\rm M_\odot)$
		(1)	(2)	$\times10^{-17}$ (3)	(4)	(5)	(6)	$\times10^{-15}$ (7)	(8)
J084305-1	56333.2	1.04	-1.82±0.02	3.378±0.026	44.907±0.002	5304.9±2.2	63.0±2.3	2.84±0.09	8.91±0.03
J084305-2	56382.9	0.83	-1.86±0.01	3.035±0.018	44.861±0.002	5294.4±1.7	59.2±1.7	2.83±0.07	8.83±0.02
J084305-3	57009.0	1.25	-0.78±0.04	1.368±0.024	44.515±0.005	5299.5±1.5	51.0±1.5	2.91±0.07	8.49±0.02
J084305-4	57092.2	1.42	-0.82±0.05	1.099±0.029	44.420±0.008	5303.5±0.9	54.8±0.9	3.36±0.05	8.49±0.01
J094511-1	56427.9	0.91	-1.75±0.04	1.899±0.036	44.446±0.006	4930.3±0.6	28.5±0.6	2.60±0.05	8.00±0.02
J094511-2	56695.9	0.80	-1.75±0.03	1.308±0.023	44.284±0.005	4930.3±0.4	27.9±0.4	2.64±0.03	7.89±0.01
J094511-3	57091.2	1.28	-0.99±0.07	0.848±0.034	44.096±0.012	4932.9±0.4	32.9±0.4	3.50±0.04	7.91±0.01
J142232-1	56335.2	1.04	-1.90±0.01	3.008±0.017	45.093±0.002	5813.2±0.9	40.3±0.9	1.78±0.03	8.56±0.02
J142232-2	56428.1	1.17	-1.91±0.02	2.664±0.028	45.040±0.003	5825.9±1.9	55.1±2.2	1.93±0.06	8.80±0.03
J142232-3	56511.9	1.02	-1.99±0.02	2.238±0.018	44.964±0.002	5820.3±1.3	44.8±1.3	1.69±0.04	8.57±0.02
J142232-4	56696.2	0.80	-1.13±0.01	1.892±0.011	44.891±0.002	5807.5±0.7	49.3±0.8	2.02±0.02	8.61±0.01
J142232-5	56862.9	0.89	-1.43±0.02	1.116±0.010	44.662±0.003	5810.9±0.7	46.3±0.8	1.37±0.02	8.42±0.01
J142232-7	57136.1	0.77	-1.32±0.02	1.061±0.012	44.640±0.003	5808.5±1.1	48.5±1.2	1.25±0.02	8.44±0.02
J103837-1	56335.1	1.42	-1.92±0.03	6.016±0.095	44.699±0.005	4533.6±0.8	20.3±1.4	3.00±0.52	7.94±0.06
J103837-2	56427.9	1.01	-1.24±0.06	2.515±0.073	44.320±0.008	4534.8±0.7	18.2±1.5	2.37±0.55	7.61±0.07
J103837-3	57133.9	0.96	-1.38±0.01	5.227±0.037	44.638±0.002	4537.4±0.5	18.3±0.9	2.01±0.29	7.81±0.04

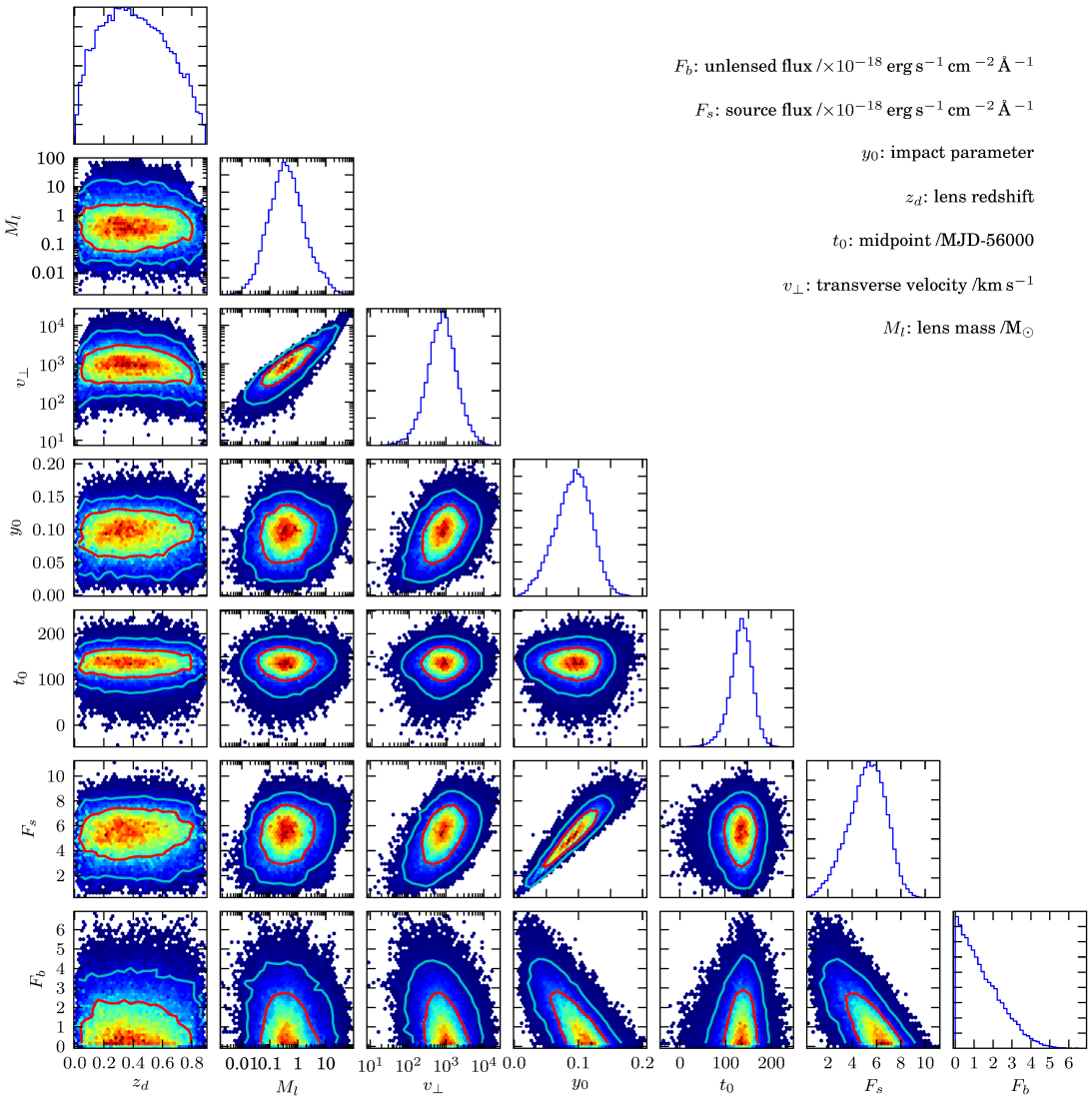

Figure 4.14 *Corner plot from the MCMC analysis showing the one- and two-dimensional posterior probability distributions for J084305.*

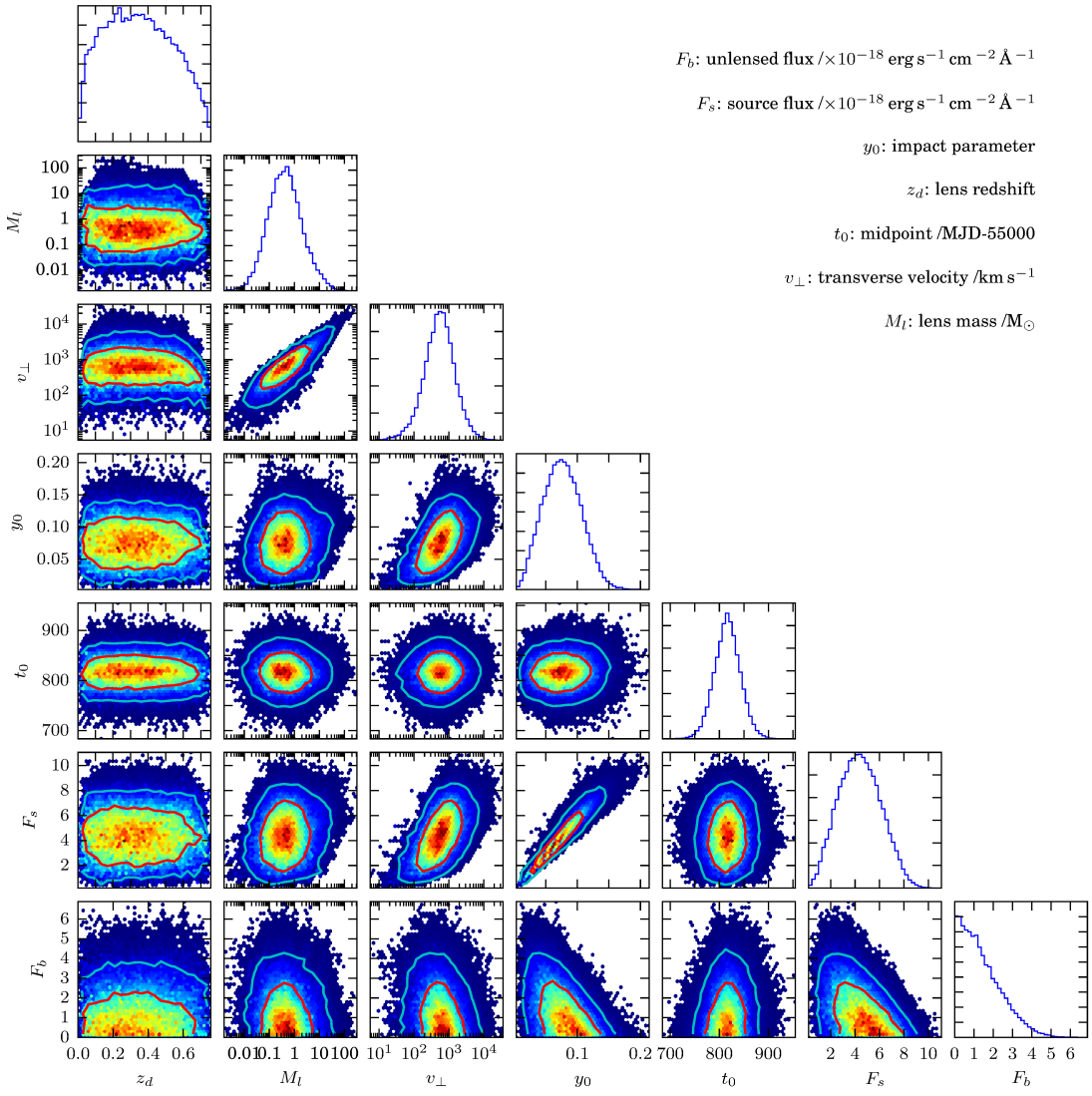

Figure 4.15 *Corner plot from the MCMC analysis showing the one- and two-dimensional posterior probability distributions for J094511.*

Chapter 5

AGN transients under a simple lens: full sample analysis

5.1 Introduction

The AGN transients described thus far have continued to evolve as the work on the previous chapters was carried out. At time of writing (Sep 2017), the Liverpool Telescope continues to provide low-cadence photometry on these objects and there have been further spectroscopic observations with the William Herschel Telescope. While microlensing is unlikely to be the sole cause for the observed variability in all of these objects, it is nevertheless useful to re-visit the MCMC analysis used to explore the simple point-lens, point-source microlensing model (Chapter 4) in the context of the entire sample. The first half of this chapter will detail the pertinent results from this comprehensive approach. For those targets which are not well-described by this model, I will detail preliminary results from a more realistic microlensing modelling approach which can take into account the possibility that the AGN accretion disc may be resolved by the lens. One point to note is that the SDSS magnitudes used here are PSF magnitudes rather than cmodel magnitudes as previous, a result of the cross-matching algorithm used when producing the up-to-date light curves.

5.2 Refining the simple microlensing analysis

As detailed in Chapter 4, the point-lens, point-source analysis involved using an MCMC approach to ascertain the plausibility of this microlensing scenario. In the interest of brevity the technical aspects will not be repeated here but I will comment on some modifications to the priors used. Previously in the 7-parameter model, the redshift and transverse velocity of the lens, $v_{\perp}$ were left free and a prior was placed on the lens mass, $M_{\rm L}$. This prior took the form of a Chabrier IMF with a mass-weighting to attempt to allow for the increase in lensing cross-section with mass. Since this work was carried out, I have felt it necessary to revisit this choice of prior for two reasons. The first concerns the implementation of the mass-weighting. The earlier work suffered due to a problem in the code which inadvertently applied an *inverse* mass-weighting, contrary to what was required. As it transpires, this single prior was still sufficient to allow the MCMC analysis to converge. Testing with corrected variations of the mass-weighted prior revealed a loss of stability, with a tendency to struggle to converge and/or result in spuriously high lens masses and transverse velocities. This is not unexpected due to the fact that there is a mass/velocity degeneracy in the model . A further complication is that the Einstein timescale, $t_{\rm E}$ is also proportional to the square root of the product of the lens distance and lens-source distance. This can also allow for arbitrarily high lens masses, even with constraints on the lens velocity, if the lens is located near to the observer or AGN host. With this in mind, the second reason to revisit the choice of priors was to place an additional prior on the transverse velocity of the lens which would help to stabilise the analysis and allow for results which remained physically reasonable.

In order to produce a more refined version of the MCMC analysis for this current work, I have elected to place a prior on both the lens mass and transverse velocity while allowing the lens redshift to remain free. For now, the lens mass prior takes the simpler form of a log-normal distribution with $\mu = 0$ and $\sigma = 1$ $\ln(\mathrm{M}_{\odot})$. This particular distribution peaks at $0.37\mathrm{M}_{\odot}$ and has a median value of $1\mathrm{M}_{\odot}$. For the transverse velocity a Gaussian prior with mean 400 and sigma 200 km/s was used. Granted, these are likely an oversimplification but for the purposes of this chapter they should suffice. My principal aim is simply to ascertain which light-curves can be reasonably approximated with the point-lens, point-source microlensing model. The derived parameter constraints reported here will reflect the median values and one sigma percentile range from the MCMC trace.

Table 5.1 *Comparison between parameter estimates from the simple microlensing MCMC results for target J084305. The analysis for this chapter included the latest photometry and updated priors as detailed in Section 5.2*

J084305		$z_{\rm agn} = 0.8952$	
Parameter	Ch4 Value	Ch5 Value	Unit
$z_{\rm d}$	$0.40^{+0.25}_{-0.23}$	$0.39^{+0.26}_{-0.25}$	
$M_{\rm l}$	$0.39^{+1.37}_{-0.30}$	$0.73^{+0.79}_{-0.37}$	$\rm M_{\odot}$
$v_{\perp}$	800^{+1080}_{-470}	490^{+180}_{-170}	$\rm km\,s^{-1}$
y_0	$0.093^{+0.026}_{-0.031}$	$0.046^{+0.022}_{-0.018}$	$\theta_{\rm E}$
t_0	56135^{+22}_{-24}	56135^{+24}_{-26}	MJD
$F_{\rm s}$	$5.30^{+1.43}_{-1.69}$	$2.37^{+1.13}_{-0.90}$	$\times 10^{-18}\rm erg\,s^{-1}cm^{-2}\AA^{-1}$
$F_{\rm b}$	≤ 2.55	$2.05^{+0.77}_{-0.91}$	$\times 10^{-18}\rm erg\,s^{-1}cm^{-2}\AA^{-1}$

The earlier results from Chapter 4, which may have been biased towards smaller lens masses, do still remain valid as can be seen in Table 5.1. Here, the parameter constraints obtained for target J084305 are compared with those from the previous chapter. The results using the refined MCMC analysis also make use of the latest available photometry. Of the seven available parameters, only the source flux, F_s, has decreased by more than the one sigma limit from the earlier estimates. This is likely due to the fact the updated photometry has also allowed for better constraints on the unlensed flux component, F_b which went unconstrained in the previous analysis. Given a well-sampled light curve it appears that the posterior is not too sensitive to the exact choice of prior.

Of the available photometry, the MCMC analysis makes use of g-band data from SDSS, Pan-STARRS(DVO), and LT. In addition, I have also included g-band data from the Palomar Transient Factory (PTF) survey (Law et al., 2009) where available. Data from CRTS and also the SuperCOSMOS catalogue, derived from scans of the Schmidt survey photographic plates (Hambly et al., 2001), are not used in this analysis. This is primarily due to concerns about the reliability of the data and/or filter effects, but the complete light curves can be found in Appendix B. This chapter will primarily focus on the photometric data only. Work to re-evaluate the spectroscopic data in light of this analysis is currently ongoing. For clarity, the light curves presented here display the photometry used in the analysis as a uniform data set. The complete light curves for these objects, highlighting individual data sources, are displayed in Appendix B.

5.3 Results of comprehensive analysis

In order to present the most promising candidates for a point-source, point-lens microlensing transient I have used three parameters to rank the quality of each fit. The first is to compute the reduced chi squared for the best-fit parameters obtained from the MCMC analysis, here defined at the peak of the posterior distribution. For this, the errors on the photometry, as in the MCMC analysis, have been increased to allow for some intrinsic AGN variation. The increased errors are given by: $\sigma^2 = \sigma^2_{\rm phot} + \sigma^2_{\rm AGN}$ where $\sigma_{\rm AGN} = 0.1$. For clarity, the original photometric errors are displayed in the following plots, along with the corresponding best-fit model light curve. The second parameter used is $\sigma^*_{\rm AGN}$, defined as the level of intrinsic AGN variability which would be required to produce a reduced chi squared value of 1.00. This should allow for microlensing candidates with a higher degree of intrinsic variability than assumed above. The third parameter is a proxy for determining the presence of significant structure in the residuals to the microlensing fit. From the residuals I compute the longest sequential run of points either above/below zero and denote this value as r. A good fit to the macro-behavior of the light curve would expect this number to remain relatively low. If high, it suggests that there is a significant amount of structure in the residuals which the model is failing to account for.

Armed with these three objective ranking parameters I then determined the most promising microlensing candidates using the following criteria: $\chi^2_\nu \leq 1.5$ `OR` $\sigma_{\rm AGN} \leq 0.15$ `AND` $r \leq 8$. The exact choice of values is somewhat arbitrary but this results in six high priority objects which will be discussed below. Table 5.2, sorted in order of ascending χ^2_ν, shows the values of the ranking parameters for every object in the sample. The table also shows the classification of each object as per Chapter 3. After discussing the best microlensing candidates, I will also highlight a number of objects which are not convincing simple lens candidates but are nonetheless worthy of discussion. Many targets in this sample display similar features to these, which can be thought of as representing the most common failure modes of the simple model. In the figures shown below, the residuals plot also highlights the region corresponding to the ranking parameter r in green ($r \leq 8$), yellow ($8 < r \leq 16$) or red ($r > 16$). In targets where there are multiple sequential runs of the same length, only the first instance is displayed.

Table 5.2 *Parameters used for ranking the resulting MCMC best-fit simple microlensing models for the entire AGN transient sample, sorted by χ^2_ν. This includes J025633 with no confirmed redshift (assumed $z = 1$ in the analysis). Parameter definition as per Section 5.3 with favoured simple microlensing candidates in bold.* [1]*Objects originally classified as per Chapter 3 but excluded from that analysis due to an insufficient sampling of spectroscopic epochs.* [2]*NVSS detections, i.e. radio-loud objects.*

Target	χ^2_ν	$\sigma^*_{\rm AGN}$	r	class
J083714	**0.78**	**0.09**	**5**	Simple[1]
J083544	**0.84**	**0.09**	**6**	Rounded
J084305	**1.03**	**0.10**	**5**	Simple
J114742	1.15	0.11	9	
J235635	**1.49**	**0.12**	**4**	
J103511	1.69	0.13	11	Dipper[1]
J175610	1.71	0.13	10	Simple
J164740	1.71	**0.15**	**7**	Simple
J143531	1.99	**0.14**	**8**	Simple[1]
J234953	1.99	0.14	11	
J103726	2.08	0.16	4	Simple[1]
J141056	2.19	0.16	13	Double
J135846	2.31	0.16	12	Double
J111547	2.38	0.16	7	Simple[1]
J160332	2.38	0.16	12	Simple
J104556	2.48	0.17	10	
J094309	2.54	0.16	10	Double
J003545	2.76	0.21	7	Simple[1]
J094511	2.96	0.20	15	Simple
J212547	3.01	0.21	16	
J085220	3.06	0.18	11	Dipper
J113309	3.10	0.18	7	Dipper[1]
J163528	3.13	0.18	8	
J151944	3.21	0.18	8	Double
J011356	3.52	0.22	10	Dipper[1]
J174101	3.53	0.21	5	[2]
J081445	3.61	0.21	18	Dipper
J214006	3.66	0.22	7	Simple[1 2]
J090244	3.72	0.21	13	Simple[2]
J152238	3.79	0.21	9	Double
J161022	3.88	0.20	20	
J151234	3.88	0.22	10	Double
J011635	4.00	0.21	17	Rounded
J105502	4.18	0.22	13	Simple
J151201	4.42	0.22	17	Rounded
J233237	4.56	0.24	19	Double
J170845	4.87	0.23	10	
J090514	5.06	0.26	13	Double
J103837	5.18	0.24	10	Dipper
J031240	5.19	0.24	23	Rounded
J085759	5.33	0.24	13	
J154445	5.37	0.25	29	Double
J155427	5.42	0.27	19	Rounded
J115553	5.51	0.26	7	
J081916	5.94	0.28	9	Dipper
J105040	5.97	0.25	11	Double

J160329	6.04	0.31	14	[2]
J152844	6.35	0.26	6	Double
J142902	6.40	0.33	15	Simple
J124728	6.44	0.27	10	Rounded
J092635	6.70	0.28	8	Double
J223210	7.07	0.28	16	Dipper
J142232	7.20	0.54	10	Rounded
J133004	8.27	0.31	9	Double
J160414	8.36	0.29	6	
J162849	8.85	0.32	15	
J110805	10.24	0.38	20	Simple
J150042	10.38	0.36	14	Double
J025633	12.53	0.41	15	[2]
J154404	14.05	0.69	9	[2]
J132958	15.67	1.31	8	
J150210	15.88	0.44	16	Simple
J014139	25.97	1.14	23	Rounded

The results can be summarised as follows. Of the 63 AGN listed here, six ($\sim 10\%$) meet the criteria for a convincing simple microlensing event. As suspected, the subset of targets classed as 'Simple' in Chapter 3 have provided the best matches in this analysis. It is notable that J083544, classed as a 'Rounded', appears to be the only object with this classification for which the model performs well. This is an indication that J083544 may have been misclassified. It appears as if the 'Rounded' objects are not simply longer-lived manifestations of those in the 'Simple' category. In these and a number of other objects, the failure of the simple microlensing model does not rule out the possibility that these are still microlensing events. Rather, they provide insight as to the more complex models which will be required to provide a more satisfactory match to the data. Some notable failures will be discussed following an overview of the six best-performing events.

5.4 Discussion of the six best performing simple objects

5.4.1 J083714

This object (Fig. 5.1, Table 5.3) could be considered the 'smoking-gun' simple microlensing candidate. It has formally the best fit of any target in the sample

Figure 5.1 *Top: Simple microlensing model for J083714. Full parameter constraints are displayed in Table 5.3. Also displayed are the ranking parameters described in Section 5.3. Bottom: Residuals to the fit with the highlighted region reflecting the location of the data points corresponding to the ranking parameter r.*

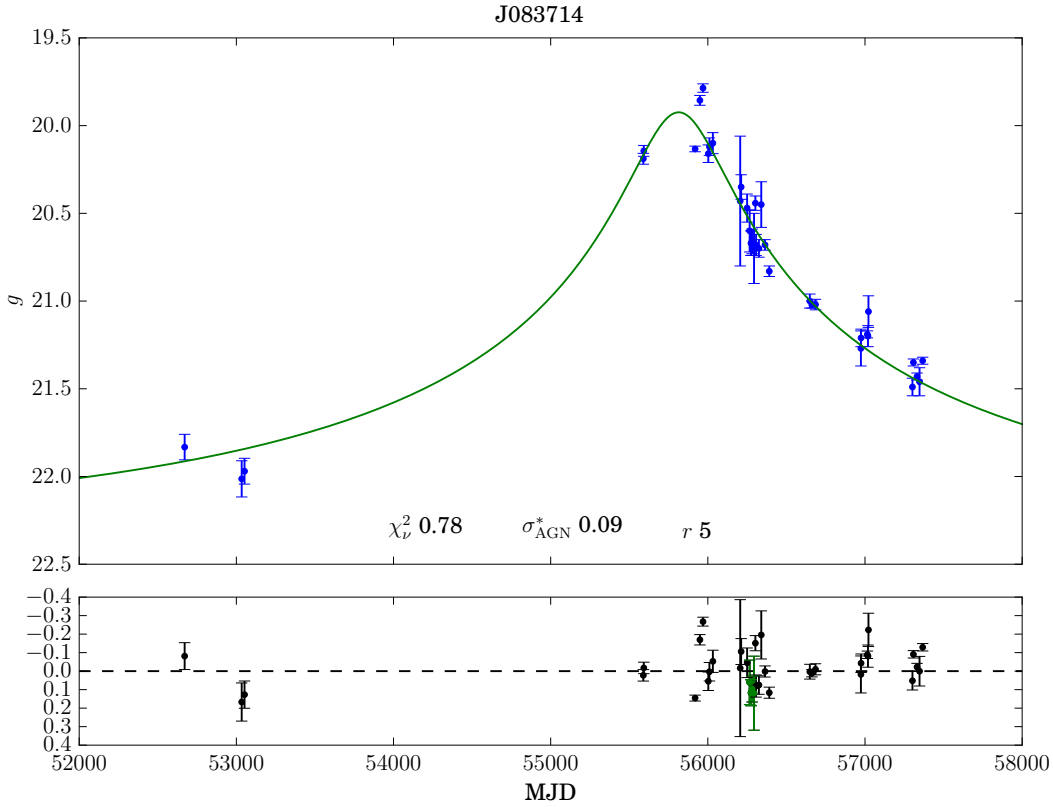

and the CRTS photometry also appears to suggest a single-peaked light curve. Unfortunately for this target, the spectroscopic sampling is less than ideal. The target is now returning to quiescence from a peak delta-mag of ~ 2.2.

5.4.2 J083544

This object (Fig. 5.2, Table 5.4) has a very well sampled light-curve and the simple model provides an excellent match to the data. The transient is still evolving and has some way to go before returning to the assumed quiescence of the Sloan epoch. Currently, the background or 'unlensed' flux parameter is consistent only with an upper limit. The CRTS data also agrees well with this object. One possible cause for concern is the anomalously high SuperCOSMOS data point. As can be seen in Table 5.2, this object is the only 'Rounded' object which displays a convincing fit. This strongly suggests that the classification

Table 5.3 *Parameter constraints from the MCMC analysis for J083714.*

J083714		$z_{\rm agn} = 1.2798$
Parameter	Value	Unit
$z_{\rm d}$	$0.55^{+0.38}_{-0.37}$	
$M_{\rm l}$	$0.77^{+0.88}_{-0.41}$	$\mathrm{M}_{\odot}$
$v_{\perp}$	480^{+190}_{-170}	$\mathrm{km\,s^{-1}}$
y_0	$0.048^{+0.025}_{-0.019}$	$\theta_{\rm E}$
t_0	55813^{+26}_{-27}	MJD
$F_{\rm s}$	$2.28^{+1.20}_{-0.89}$	$\times 10^{-18}\mathrm{erg\,s^{-1}cm^{-2}\AA^{-1}}$
$F_{\rm b}$	$3.23^{+0.93}_{-1.08}$	$\times 10^{-18}\mathrm{erg\,s^{-1}cm^{-2}\AA^{-1}}$

Table 5.4 *Parameter constraints from the MCMC analysis for J083544.*

J083544		$z_{\rm agn} = 1.3254$
Parameter	Value	Unit
$z_{\rm d}$	$0.54^{+0.36}_{-0.33}$	
$M_{\rm l}$	$1.48^{+1.63}_{-0.82}$	$\mathrm{M}_{\odot}$
$v_{\perp}$	340^{+170}_{-140}	$\mathrm{km\,s^{-1}}$
y_0	$0.046^{+0.018}_{-0.015}$	$\theta_{\rm E}$
t_0	56999^{+25}_{-24}	MJD
$F_{\rm s}$	$3.51^{+1.38}_{-1.17}$	$\times 10^{-18}\mathrm{erg\,s^{-1}cm^{-2}\AA^{-1}}$
$F_{\rm b}$	≤ 8.03	$\times 10^{-19}\mathrm{erg\,s^{-1}cm^{-2}\AA^{-1}}$

should be updated to 'Simple'. The failure of the simple model to reproduce the rounded light curves will be described with respect to object J155427 below.

5.4.3 J084305

This object (Fig. 5.3, Table 5.5) has already been the subject of a detailed microlensing analysis as part of Chapter 4. Using the most recent LT data and updated priors still produces an excellent fit to the data and also tightens the constraints on all parameters. Most significantly, the unlensed flux is now constrained.

5.4.4 J235635

This particular object (Fig. 5.4, Table 5.6) has a fairly erratic light curve but manages to score well in terms of the three ranking criteria defined above. Currently there are no constraints on the unlensed flux but this is likely to improve as this transient still has some way to evolve. Given that this event

Figure 5.2 *Top: Simple microlensing model for J083544. Full parameter constraints are displayed in Table 5.4. Also displayed are the ranking parameters described in Section 5.3. Bottom: Residuals to the fit with the highlighted region reflecting the location of the data points corresponding to the ranking parameter r.*

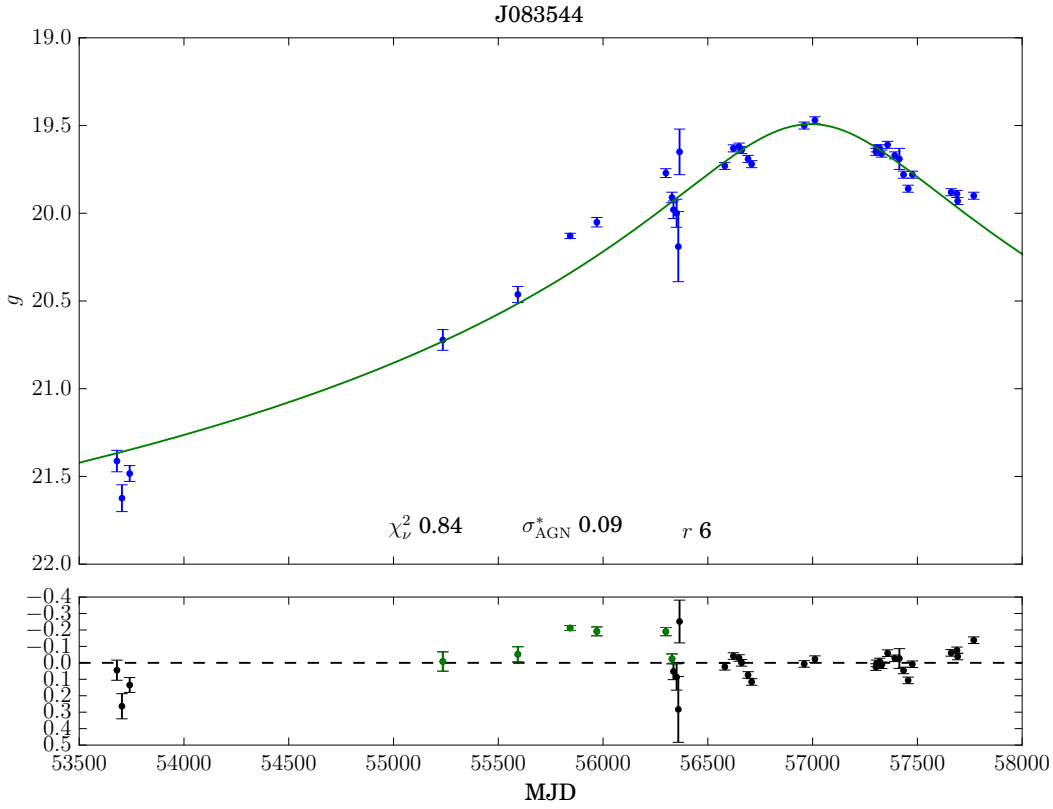

Table 5.5 *Parameter constraints from the MCMC analysis for J084305.*

J084305		$z_{\rm agn} = 0.8952$
Parameter	Value	Unit
$z_{\rm d}$	$0.39^{+0.26}_{-0.25}$	
$M_{\rm l}$	$0.73^{+0.79}_{-0.37}$	$\mathrm{M}_\odot$
$v_\perp$	490^{+180}_{-170}	$\mathrm{km\,s^{-1}}$
y_0	$0.046^{+0.022}_{-0.018}$	$\theta_{\rm E}$
t_0	56135^{+24}_{-26}	MJD
$F_{\rm s}$	$2.37^{+1.13}_{-0.90}$	$\times 10^{-18}\mathrm{erg\,s^{-1}cm^{-2}\AA^{-1}}$
$F_{\rm b}$	$2.05^{+0.77}_{-0.91}$	$\times 10^{-18}\mathrm{erg\,s^{-1}cm^{-2}\AA^{-1}}$

Figure 5.3 *Top: Simple microlensing model for J084305. Full parameter constraints are displayed in Table 5.5. Also displayed are the ranking parameters described in Section 5.3. Bottom: Residuals to the fit with the highlighted region reflecting the location of the data points corresponding to the ranking parameter r.*

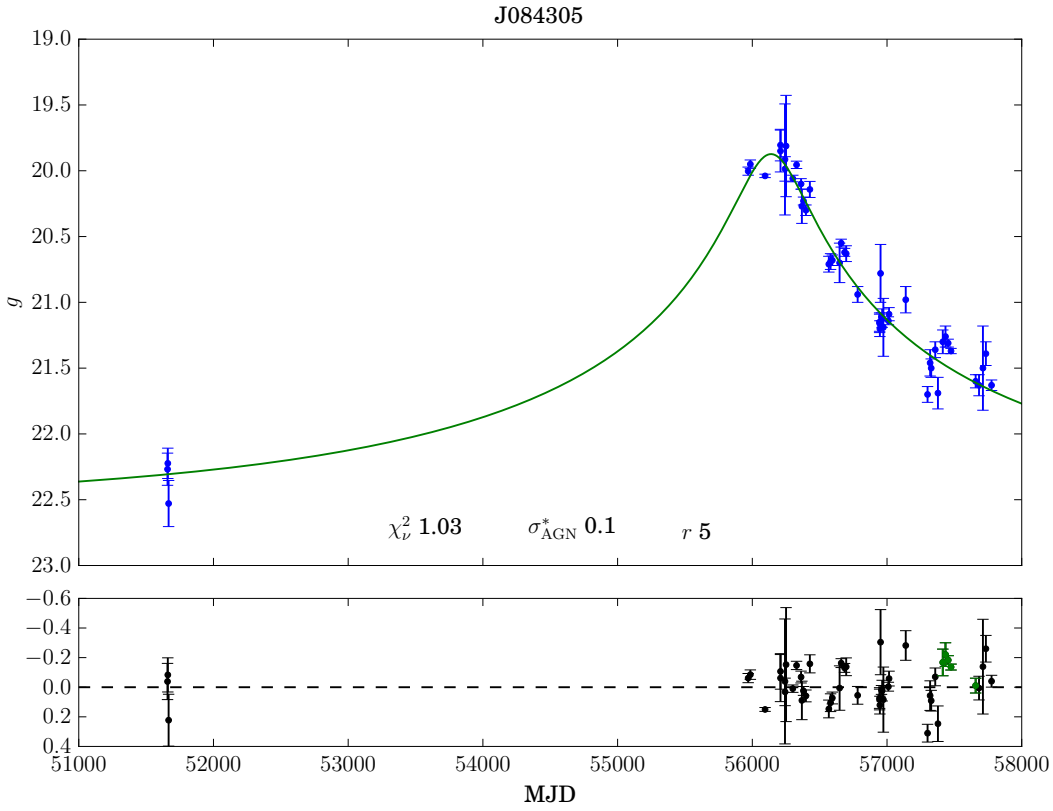

Figure 5.4 *Top: Simple microlensing model for J235635. Full parameter constraints are displayed in Table 5.6. Also displayed are the ranking parameters described in Section 5.3. Bottom: Residuals to the fit with the highlighted region reflecting the location of the data points corresponding to the ranking parameter r.*

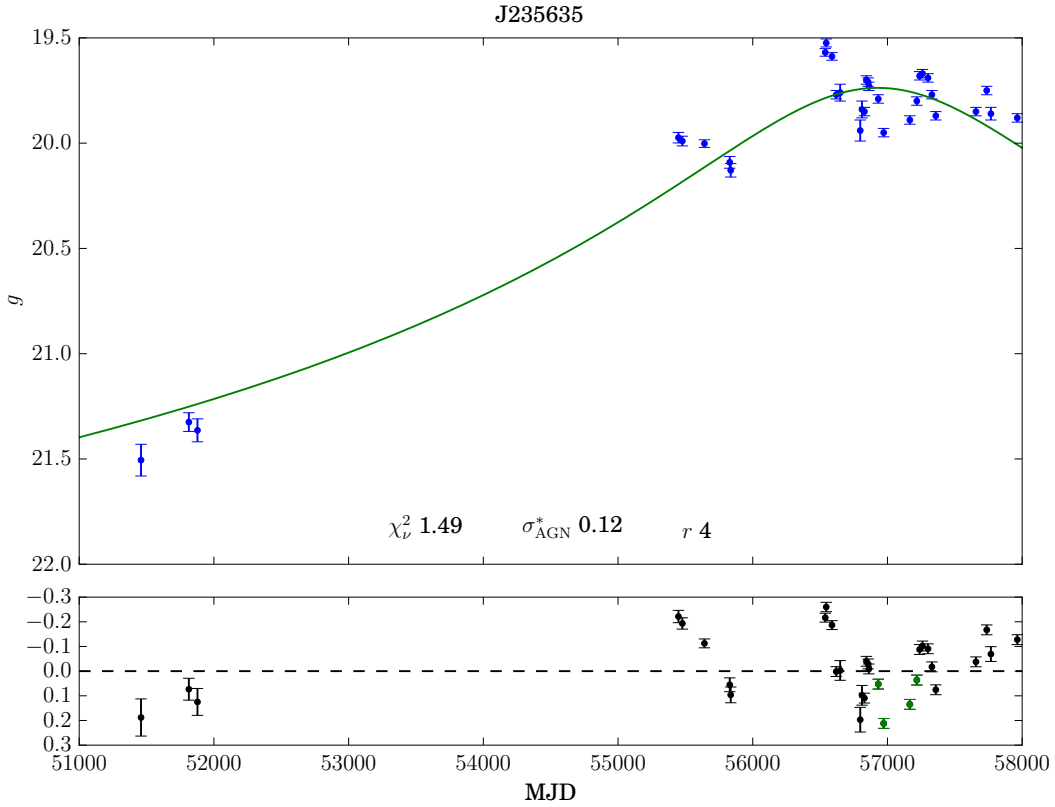

is still relatively near the peak it remains to be seen if this will remain a viable simple microlensing candidate.

5.4.5 J164740

This object (Fig. 5.5, Table 5.7) has a well-sampled light curve over the assumed single-peak and agrees well with the CRTS data. Again, there appears to be a higher-than-assumed level of intrinsic variation as evidenced from the shorter time-scale variations. In this object the unlensed flux is not well constrained. As this target continues to evolve, additional light curve data at or near quiescence should allow for tighter constraints.

Table 5.6 *Parameter constraints from the MCMC analysis for J235635*

J235635		$z_{\rm agn} = 0.9319$
Parameter	Value	Unit
$z_{\rm d}$	$0.41^{+0.25}_{-0.23}$	
$M_{\rm l}$	$1.90^{+2.44}_{-1.12}$	$\mathrm{M}_\odot$
$v_\perp$	280^{+160}_{-120}	$\mathrm{km\,s^{-1}}$
y_0	$0.076^{+0.028}_{-0.025}$	$\theta_{\rm E}$
t_0	56934^{+89}_{-86}	MJD
$F_{\rm s}$	$4.57^{+1.69}_{-1.53}$	$\times 10^{-18}\mathrm{erg\,s^{-1}cm^{-2}\AA^{-1}}$
$F_{\rm b}$	≤ 1.03	$\times 10^{-18}\mathrm{erg\,s^{-1}cm^{-2}\AA^{-1}}$

Figure 5.5 *Top: Simple microlensing model for J164740. Full parameter constraints are displayed in Table 5.7. Also displayed are the ranking parameters described in Section 5.3. Bottom: Residuals to the fit with the highlighted region reflecting the location of the data points corresponding to the ranking parameter r.*

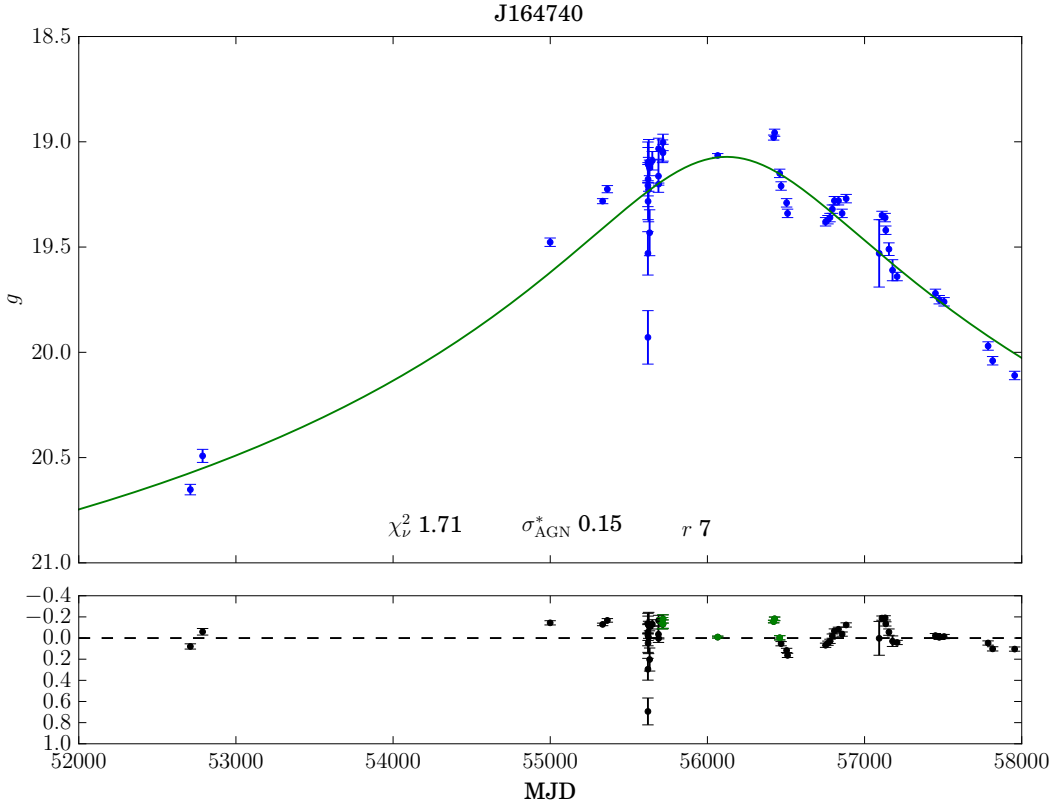

Table 5.7 *Parameter constraints from the MCMC analysis for J164740.*

J164740		$z_{\rm agn} = 0.8448$
Parameter	Value	Unit
$z_{\rm d}$	$0.40^{+0.22}_{-0.22}$	
$M_{\rm l}$	$1.50^{+1.88}_{-0.80}$	$\mathrm{M}_{\odot}$
$v_{\perp}$	410^{+170}_{-160}	$\mathrm{km\,s^{-1}}$
y_0	$0.084^{+0.035}_{-0.030}$	$\theta_{\rm E}$
t_0	56131^{+30}_{-33}	MJD
$F_{\rm s}$	$9.27^{+3.93}_{-3.38}$	$\times 10^{-18}\mathrm{erg\,s^{-1}cm^{-2}\AA^{-1}}$
$F_{\rm b}$	≤ 4.25	$\times 10^{-18}\mathrm{erg\,s^{-1}cm^{-2}\AA^{-1}}$

Table 5.8 *Parameter constraints from the MCMC analysis for J143531.*

J143531		$z_{\rm agn} = 1.5706$
Parameter	Value	Unit
$z_{\rm d}$	$0.67^{+0.46}_{-0.43}$	
$M_{\rm l}$	$0.85^{+1.05}_{-0.45}$	$\mathrm{M}_{\odot}$
$v_{\perp}$	470^{+180}_{-170}	$\mathrm{km\,s^{-1}}$
y_0	$0.076^{+0.037}_{-0.030}$	$\theta_{\rm E}$
t_0	55592^{+48}_{-52}	MJD
$F_{\rm s}$	$3.55^{+1.71}_{-1.42}$	$\times 10^{-18}\mathrm{erg\,s^{-1}cm^{-2}\AA^{-1}}$
$F_{\rm b}$	$2.44^{+1.62}_{-1.48}$	$\times 10^{-18}\mathrm{erg\,s^{-1}cm^{-2}\AA^{-1}}$

5.4.6 J143531

This object (Fig. 5.6, Table 5.8) sees a reasonable fit to the data and appears to also agree with the CRTS data. In this case there appears to be a higher degree of intrinsic scatter but otherwise the fit performs well. It will be interesting to see if target returns to the level of the Sloan era in the coming years. Similar to J083714, the spectroscopic sampling is less than ideal for this object.

5.5 Simple microlensing: notable failures

There are a number of objects which failed to make the cut for a convincing point-lens, point-source microlensing fit. The principal reason for this is usually evidence for a second distinct peak in the data or notable failure in the model at certain epochs. The possibility for two (or more) peaks in the data is always present. This should also be borne in mind for the previous section. There, even though the simple model is performing very well, some targets do not have sufficient photometry detailing the ingress of the event. In those cases we may be

Figure 5.6 *Top: Simple microlensing model for J143531. Full parameter constraints are displayed in Table 5.8. Also displayed are the ranking parameters described in Section 5.3. Bottom: Residuals to the fit with the highlighted region reflecting the location of the data points corresponding to the ranking parameter r.*

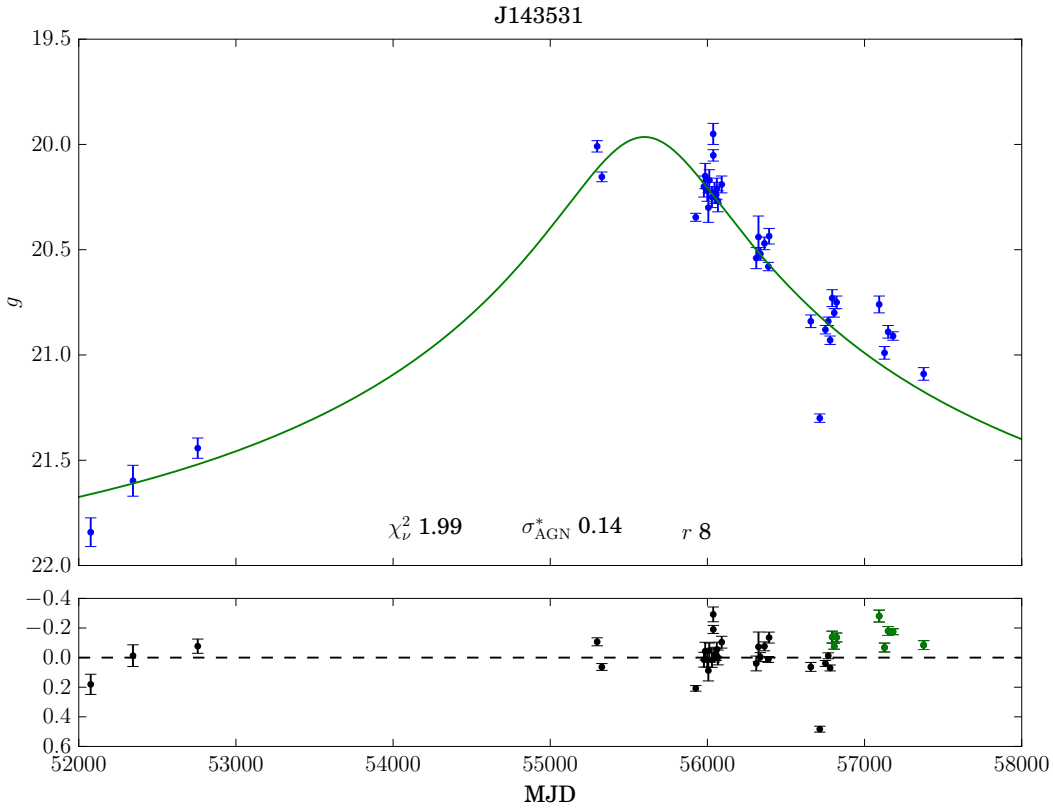

seeing only one peak from a true double though this is perhaps a fairly remote possibility in these cases. Differentiating between peaks and erratic variability becomes trickier if the cadence of the photometry is not sufficient to give a general idea of the short-term intrinsic variability over the long-term trend.

In this section I will describe three objects which are not convincing 'simple' microlensing events but are nevertheless excellent candidates for more complex lensing behaviour. Though the simple microlensing model is disfavoured, lensing remains a likely explanation for these events. The issues with the simple model fit thus point the way towards more realistic lensing models. In the next section I will detail the current progress in producing more realistic lensing models to adequately explain these events.

5.5.1 J105502

The simple fit for this object (Fig. 5.7, Table 5.9) performs well on the rise but less so on the decline. This object is in fact a prime candidate for a closely-separated caustic-crossing lensing event. This requires that the source moves through a small caustic region in the magnification map, perhaps caused by external shear or a binary lens, leading to two distinct peaks in the light curve. This would allow for a more rapid rise/decline and, in this case, requires the target track to pass near a region of higher magnification on the ingress. The discrepant DVO point at MJD$\sim$ 55800 is almost certainly in error as the target was below the horizon at this epoch. From this data, the MCMC failed to constrain the unlensed flux. The CRTS data broadly agrees with the photometry but the colour correction estimate does not seem to agree at all epochs. Target J114742, which was narrowly excluded from the high priority candidates listed above, is another example of this type of residual structure in the light curve.

5.5.2 J111547

This object (Fig. 5.8, Table 5.10) is notable for two reasons. The first is that this is potentially the highest amplification event in the entire sample. In fact, the MCMC failed to adequately constrain the impact parameter, in-part due to the lack of photometric data across the peak. The best fitting model in this case produces a $\sim$ 5 magnitude flare. The second notable feature is that even

Figure 5.7 *Top: Simple microlensing model for J105502. Full parameter constraints are displayed in Table 5.9. Also displayed are the ranking parameters described in Section 5.3. Bottom: Residuals to the fit with the highlighted region reflecting the location of the data points corresponding to the ranking parameter r.*

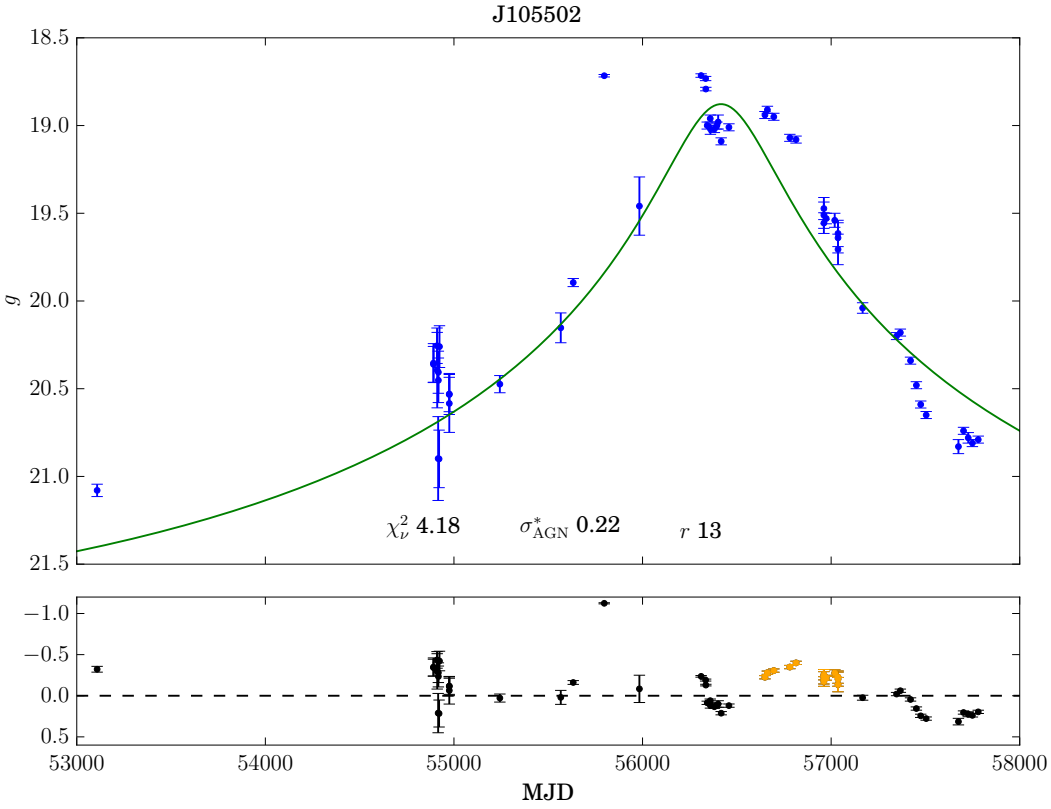

Table 5.9 *Parameter constraints from the MCMC analysis for J105502.*

J105502		$z_{\rm agn} = 0.4168$
Parameter	Value	Unit
$z_{\rm d}$	$0.20^{+0.10}_{-0.10}$	
$M_{\rm l}$	$1.49^{+1.94}_{0.76}$	$\mathrm{M}_\odot$
$v_\perp$	470^{+190}_{-180}	$\mathrm{km\,s^{-1}}$
y_0	$0.040^{+0.017}_{-0.015}$	$\theta_{\rm E}$
t_0	56416^{+32}_{-31}	MJD
$F_{\rm s}$	$5.35^{+2.35}_{-2.04}$	$\times 10^{-18}\mathrm{erg\,s^{-1}cm^{-2}\AA^{-1}}$
$F_{\rm b}$	≤ 1.26	$\times 10^{-18}\mathrm{erg\,s^{-1}cm^{-2}\AA^{-1}}$

Figure 5.8 *Top: Simple microlensing model for J111547. Full parameter constraints are displayed in Table 5.10. Also displayed are the ranking parameters described in Section 5.3. Bottom: Residuals to the fit with the highlighted region reflecting the location of the data points corresponding to the ranking parameter r.*

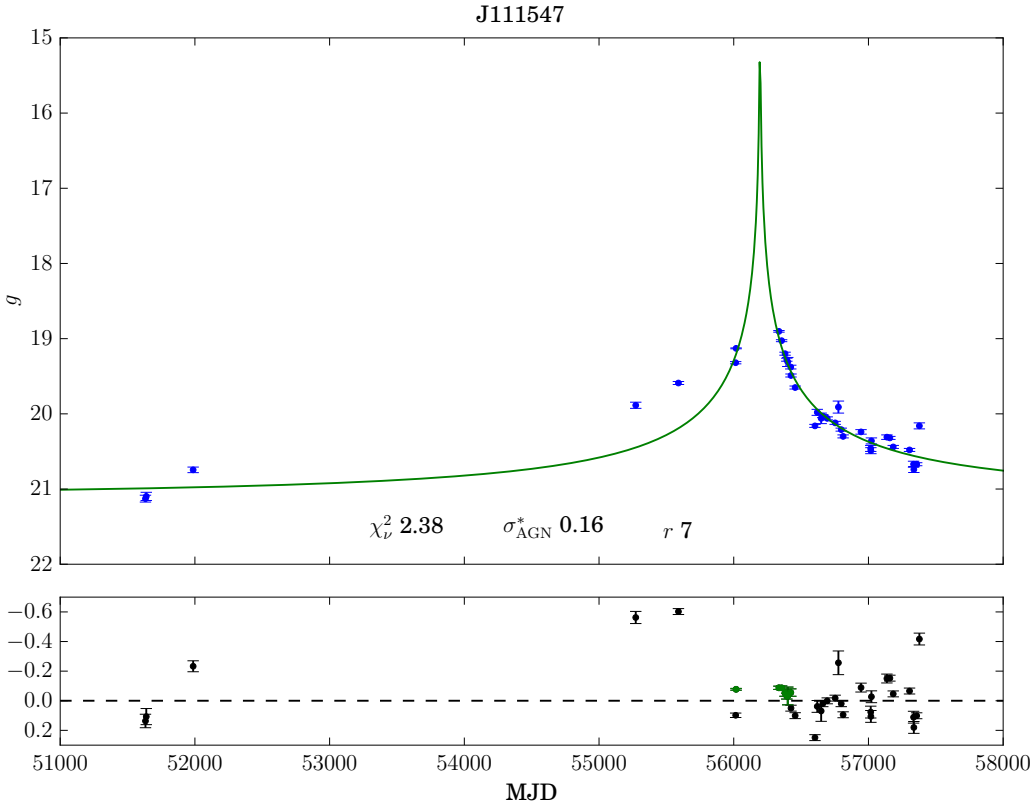

though the fit to the egress appears to perform very well, the early photometry is suggestive of additional structure. This is borne out by sparse CRTS data, suggestive of a second peak which may have occurred at some point around MJD$\sim$ 53000. In contrast to the previous target, this light curve could then be considered a more classic example of a two-horned microlensing event.

5.5.3 J155427

This object (Fig. 5.9, Table 5.11) is one of the sub-class of transient light curves which have been termed 'rounded' and the reason for this is clear when looking at the best-fitting simple model. The cuspy nature of the simple microlensing light curve does not allow for an adequate fit to the data. The CRTS data in this case provides a very clear picture of the post-Sloan era, confirming a single rounded peak for this event. The reason this object may prove to be very interesting is that

Table 5.10 *Parameter constraints from the MCMC analysis for J111547.*

J111547		$z_{\rm agn} = 0.4100$
Parameter	Value	Unit
$z_{\rm d}$	$0.23^{+0.10}_{-0.12}$	
$M_{\rm l}$	$0.84^{+0.87}_{0.44}$	$\mathrm{M}_{\odot}$
$v_{\perp}$	470^{+180}_{-170}	$\mathrm{km\,s^{-1}}$
y_0	≤ 0.016	$\theta_{\rm E}$
t_0	56193^{+9}_{-9}	MJD
$F_{\rm s}$	$3.17^{+1.57}_{-1.17}$	$\times 10^{-18}\mathrm{erg\,s^{-1}cm^{-2}\AA^{-1}}$
$F_{\rm b}$	$1.46^{+0.11}_{-0.13}$	$\times 10^{-17}\mathrm{erg\,s^{-1}cm^{-2}\AA^{-1}}$

Table 5.11 *Parameter constraints from the MCMC analysis for J155427.*

J155427		$z_{\rm agn} = 0.5722$
Parameter	Value	Unit
$z_{\rm d}$	$0.26^{+0.15}_{-0.13}$	
$M_{\rm l}$	$1.93^{+2.80}_{1.22}$	$\mathrm{M}_{\odot}$
$v_{\perp}$	110^{+100}_{-60}	$\mathrm{km\,s^{-1}}$
y_0	$0.017^{+0.007}_{-0.006}$	$\theta_{\rm E}$
t_0	56741^{+28}_{-28}	MJD
$F_{\rm s}$	$1.80^{+0.74}_{-0.68}$	$\times 10^{-18}\mathrm{erg\,s^{-1}cm^{-2}\AA^{-1}}$
$F_{\rm b}$	≤ 1.33	$\times 10^{-19}\mathrm{erg\,s^{-1}cm^{-2}\AA^{-1}}$

a partially-resolved accretion disc under a point-lens may provide an adequate description for this event, allowing for a more rounded light-curve profile across the peak (see next section). This hypothesis is backed up by the fact that the u-band light curve for this target, while not as well sampled, shows a narrower peak than for either g/r. With the assumption that the u-band emission peaks at smaller radii this may even allow for a determination of the temperature profile of the disc. In the simple model fit, the unlensed flux is unconstrained. One possible problem is seen in the SuperCOSMOS data point. If accurate, this suggests that the target was actually in a bright state in the pre-Sloan era.

5.5.4 J094511: not as simple as first thought

This object (Fig. 5.10, Table 5.12) has been included as a notable example of a target which was previously thought to be an excellent simple microlensing candidate. It was covered as part of the work in Chapter 4. The most recent photometry for this object, which confirms a suspected plateau in the data, has made the simple lensing scenario less likely. As this target continues to evolve, it is possible that it will still return to the level seen in the Sloan era. It is also

Figure 5.9 *Top: Simple microlensing model for J155427. Full parameter constraints are displayed in Table 5.11. Also displayed are the ranking parameters described in Section 5.3. Bottom: Residuals to the fit with the highlighted region reflecting the location of the data points corresponding to the ranking parameter r.*

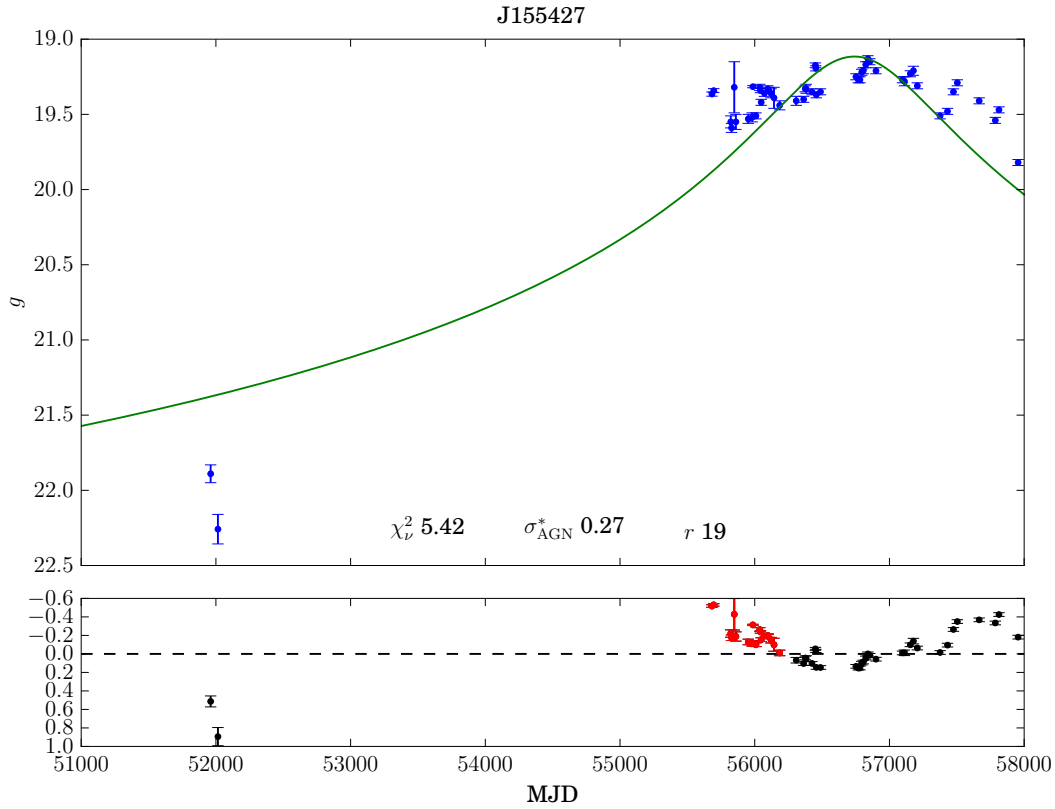

Figure 5.10 *Top: Simple microlensing model for J094511. Full parameter constraints are displayed in Table 5.12. Also displayed are the ranking parameters described in Section 5.3. Bottom: Residuals to the fit with the highlighted region reflecting the location of the data points corresponding to the ranking parameter r.*

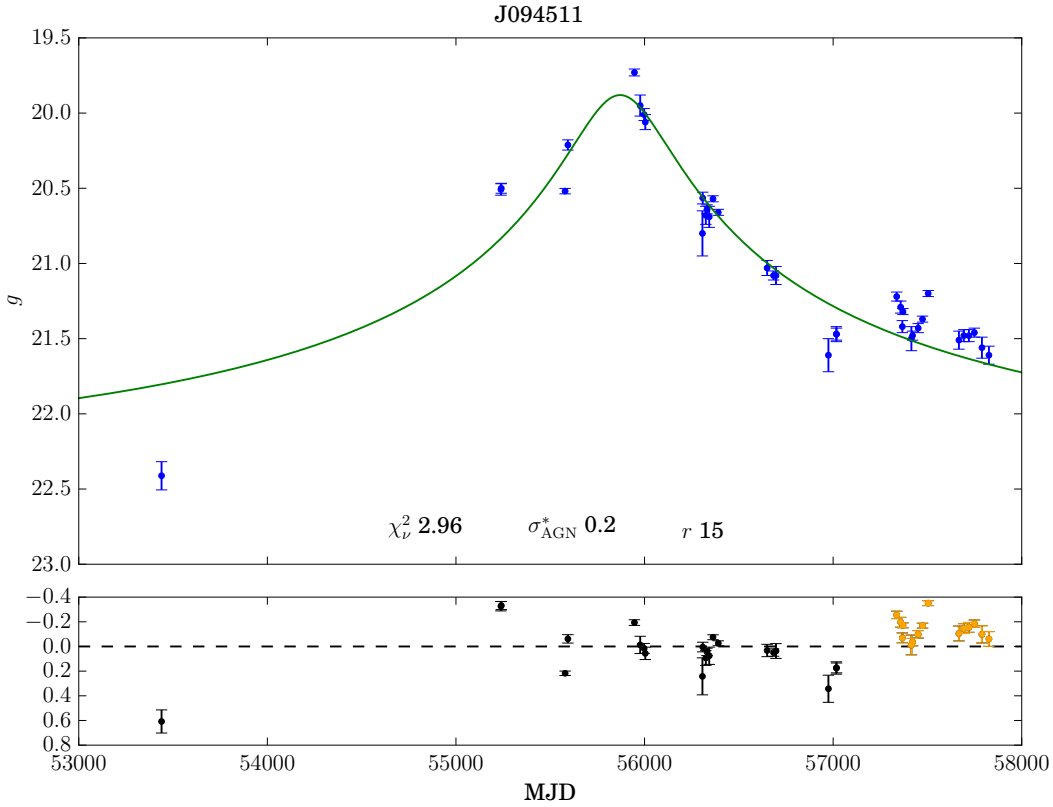

possible that the Sloan data point is erroneous. One further intriguing possibility is that this object was seen during an ingress into a caustic region and will undergo a further flare-up at some point in the future on the egress.

5.6 Extended source under a point-lens: J155427 case study

Once the point-source and/or simple-lens approximation breaks down, the range of parameter space for these microlensing models which needs to be explored increases dramatically. This requires a move beyond an analytical light curve to the convolution of a magnification map and extended source, with a given profile, to produce light curves. Unfortunately, this also becomes computationally expensive. Some of my early extended-source testing has been discussed for

Table 5.12 *Parameter constraints from the MCMC analysis for J094511.*

J094511		$z_{\rm agn} = 0.7573$
Parameter	Value	Unit
$z_{\rm d}$	$0.36^{+0.21}_{-0.22}$	
$M_{\rm l}$	$0.85^{+0.94}_{0.44}$	$\rm M_\odot$
$v_\perp$	460^{+180}_{-170}	$\rm km\,s^{-1}$
y_0	$0.043^{+0.023}_{-0.017}$	$\theta_{\rm E}$
t_0	55869^{+20}_{-20}	MJD
$F_{\rm s}$	$2.09^{+1.10}_{-0.79}$	$\times 10^{-18}\rm erg\,s^{-1}cm^{-2}\AA^{-1}$
$F_{\rm b}$	$3.35^{+0.84}_{-0.97}$	$\times 10^{-18}\rm erg\,s^{-1}cm^{-2}\AA^{-1}$

J084305 in Chapter 4 but I have been working towards producing an MCMC-derived fit to light curve data to robustly explore the available parameter space. Here, I will note the progress in this area with a focus on a relatively simple model: an extended source under a point-lens, in particular for J155427.

For this I began by adapting the extended source code, originally from Jiménez-Vicente (2016), which had been used as part of my work for Bruce et al. (2017). The radial extent of the magnification maps was two Einstein radii and I began by creating a low-resolution point-lens magnification map, 401 pixels across, giving a resolution of 0.01 Einstein radii per pixel. The generation of a light curve by convolving this map with a Gaussian source at every epoch for a given set of lensing parameters typically takes less than a second, making this a viable time-frame for, say, an MCMC run of 200,000 iterations on a single PC for early testing. For comparison, my original point-source, point-lens MCMC code was capable of two million iterations in $\sim$ 5 minutes. Thus, the principal drawbacks of this more complex model are that there may be pixel-rounding errors due to the low resolution and that the ability to run more than 200k iterations is prohibitively expensive computationally. I am still looking into how to make the code more efficient, particularly with a view to multi-threaded applications and scalability. Nonetheless, the early results from this process are presented in Figures 5.11 and 5.12 which show the best-fit model light curve and MCMC corner plot.

The low resolution of the model gives the stepped appearance of the light curve but a first glance shows that this fit clearly performs better than the simplest microlensing model shown earlier. It still struggles to reach the depths of the Sloan epoch but does provide a natural explanation for the rounded-top nature of this light curve. The new parameter of interest to us in this case is $S_{\rm S}$, the Gaussian sigma of the source profile used, in units of the Einstein radius of

Figure 5.11 *Light curve for J155427 and model fit obtained from the low-resolution MCMC microlensing analysis.*

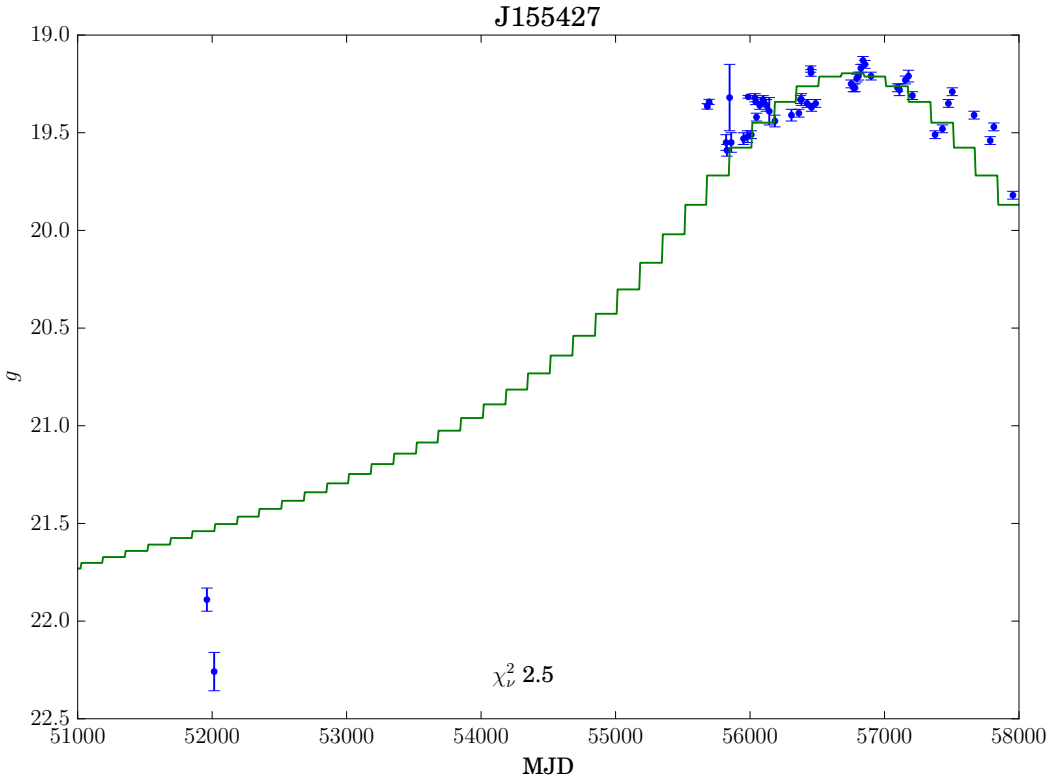

Figure 5.12 *Corner plot from the low-resolution MCMC microlensing analysis for J155427.*

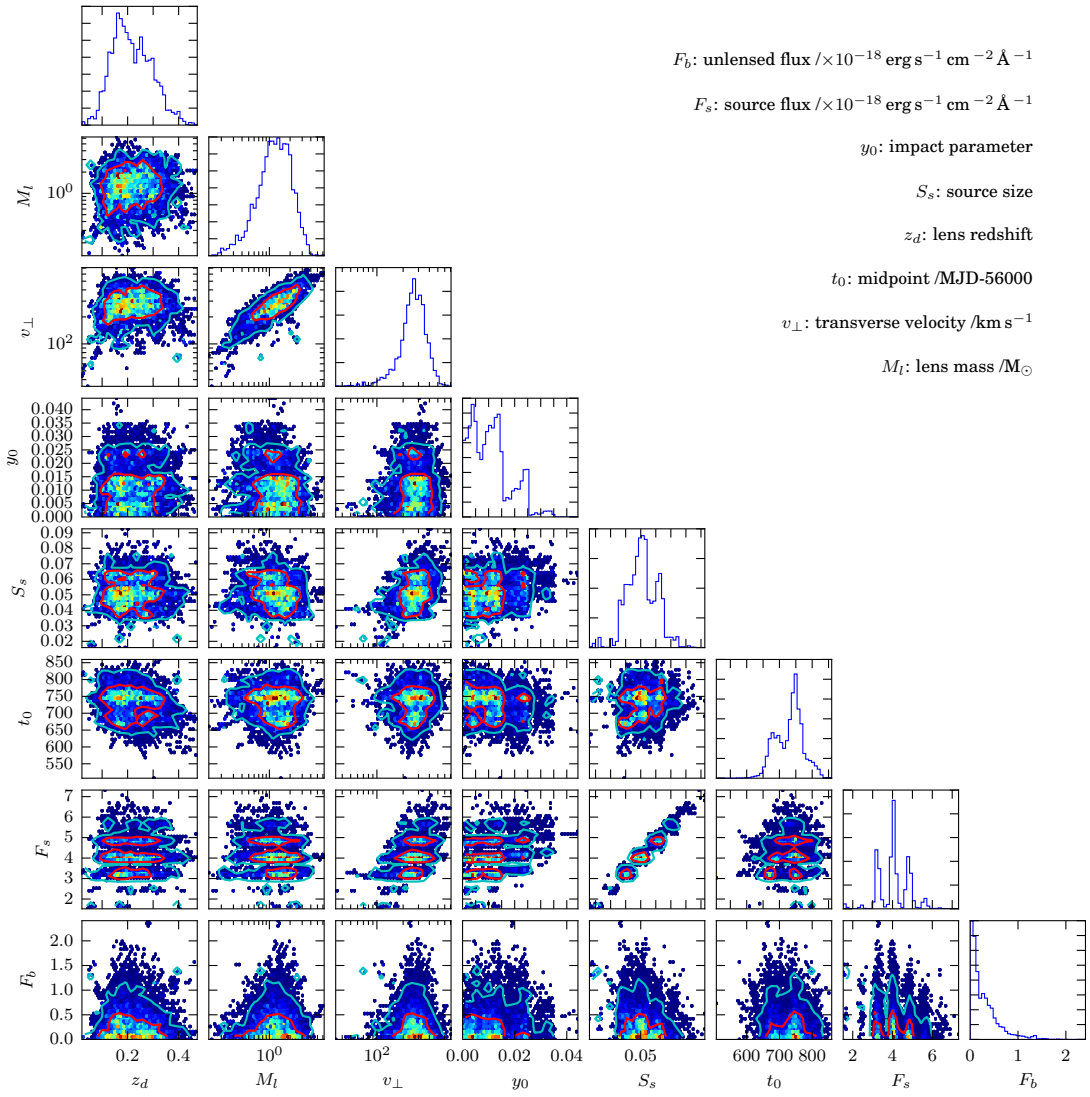

the lens. Given that this is a function of the other lens parameters one must be careful when inferring an absolute size. For the best-fit model shown, the value of $0.045\,\theta_{\rm E}$ corresponds to a one-sigma radius of ~ 11 light-hours, or ~ 40 Schwarschild radii for a $10^8\,{\rm M}_\odot$ black hole. A higher-resolution run should yield more accurate results as, for example, the predicted impact parameter is very near to the resolution limit of the current run. These resolution effects are clearly visible in the corner plot where there are isolated peaks of higher probability, likely caused by pixel-rounding when rendering the extended source map.

The size estimates above are perfectly plausible and indicate there is merit to the resolved accretion disc hypothesis. In the wider context, it appears that for some microlensing candidates the lens configuration is such that the accretion disc can be safely approximated as a point-source whereas in cases such as this, resolution effects become important. For this object, there is also tentative evidence in the u-band photometry for a less-rounded peak which would lend further credence to this idea. Future work will need to incorporate all available photometry and this may even allow the temperature gradient of the disc to be probed.

As an early foray into the realm of more complex microlensing models this has proved invaluable in probing the limits of my current method. In principle it is relatively straightforward to replace the point-lens magnification map with any other chosen lensing configuration. If the lens parameters could be constrained easily this would be more straightforward but with an unknown lens redshift and source track, and the possibility of adding additional masses and/or external shear, this results in a rapidly increasing number of possible magnification maps required for testing.

5.7 Extended source under a complex lens

There are a number of targets which exhibit multiple, or asymmetric peaks in the light curve. If microlensing is still the cause of this variability this will require, in addition to using an extended source profile as per the previous section, the use of a more sophisticated magnification map than that of a point lens. A relatively simple example of this would be a Chang Refsdal lens (Chang & Refsdal, 1984), or perhaps a binary lens scenario. In the former case the presence of external shear due to a lens galaxy produces caustic structure in the magnification map whereas in the latter case the presence of a second mass in close proximity is

sufficient to do the same.

The principle problem in modelling these more realistic lensing scenarios is that the available parameter space increases dramatically. Instead of a simple impact parameter, one must now calculate the trajectory of the source relative to any additional structure in the magnification map. There are also a large number of possible lens configurations which may give rise to similar magnification maps. As in the case of most of the targets in the AGN transient sample, there is rarely definitive evidence for the redshift of the lens which makes this problem particularly intractable. Thus, the approach to modelling used in many multiply-imaged lensed quasar studies, where the lens-galaxy redshift and mass can be reasonably constrained, is not yet possible for the AGN described here.

An example of a qualitative 'complex' microlensing fit to a target with a suspected lens redshift has already been seen in Chapter 4. To be able to perform this type of fit in an objective and efficient fashion will require considerable computational effort. Some parameter constraints will be possible, such as placing upper limits on the mass of any (unseen) lens galaxy. The various parameter degeneracies involved will likely require further assumptions and simplifications before making this a feasible enterprise.

5.8 Next steps

It may never be proven conclusively that microlensing is the cause for the AGN transients described thus far but there is further work which is now being carried out to ensure that the model remains plausible when taking into account all available data. This will follow on from the work in Chapter 4 and requires a careful analysis of the most recent spectroscopic data. A key factor will be to empirically estimate the size of the accretion disc from the spectroscopy. The size of the disc in relation to the Einstein radius of the lens is crucial as the point-source approximation begins to break down, leading to chromatic effects and less-cuspy light curve profiles, if the disc is greater than approximately 5% θ_{E}. In addition, the possibility for observing BLR changes due to microlensing is also increased if the disc size is small relative to the lens footprint. This will be more likely for low-luminosity AGN.

In the cases where the accretion disc is being resolved, a higher-resolution

magnification map should allow for a robust, independent accretion disc size estimate to compare with that estimated from the spectroscopy. Though the complexity would increase, this work could also be performed using simultaneous fits to all available photometric bands. This should allow for tighter constraints as naively one would expect the bluer bands to originate from smaller radii. Accurate modelling of BLR contamination in some bands, not currently accounted for, may also prove to be of importance. Any further observations of differential BLR variability will also require consideration under the microlensing scenario. As for J084305 and the CIII] line in Chapter 4, it may be possible to derive a simple estimate for the radii of one or more BLR line species.

Chapter 6

Sharov 21: the remarkable AGN flare

6.1 Introduction

The outburst seen in Sharov21 was an exceptional event. Originally interpreted as a nova in M31 (Nedialkov et al., 1996; Sharov et al., 1998) it was later discovered to be an AGN at the much greater redshift of 2.1 (Meusinger et al., 2010). The flare was relatively short-lived in relation to the majority of transients in this thesis but was a high-amplification event. Meusinger et al. (2010) reasoned that the event was most likely to be caused by either microlensing, due to a star in M31, or a tidal disruption event. They favoured the latter explanation as the probability of a high-amplitude lensing event seemed remote. However, the tidal disruption scenario requires that a $\sim 10\,\mathrm{M}_{\odot}$ star be disrupted at or near to an extant accretion disc, the effects of which are not well understood. As a further test of the ideas outlined in this thesis, I thought it would be interesting to re-visit this object to see if anything new can be learned.

The Meusinger et al. (2010) paper has an excellent light curve for Sharov21 that stretches over several decades. To date, there have been no other observed high amplitude events in this object. The authors kindly made available this data set and, as an initial foray, I elected to put this object through my MCMC code to see how the simplest point-lens, point-source model performed.

6.2 Sharov 21: simple microlensing MCMC results

As a first test, I conducted this analysis using exactly the same initial guesses for each parameter as for every other AGN transient in this thesis. This included setting the initial guess at the lens redshift to 0.2 despite it being likely that the lens should reside in M31. The key here was to remain objective with respect to the lensing parameters. As before, the main assumption being made is for a stellar-mass lens and here I am making use of the refined MCMC priors as detailed in Chapter 5. The light curve data here are B-band magnitudes so the effective wavelength for magnitude to flux conversions was adjusted to 4420 Å .

This first attempt failed to converge, as seen in Fig. 6.1. This figure shows the walkers in the MCMC code for each parameter. If all goes well the walkers should quickly spread out to map the available parameter space and then settle into a quasi-stable block thereafter. In this case this does not happen, particularly for the source flux and lens flux indicating that the walkers did not have enough time to converge and/or that there is a problem with the model. It is interesting to note that in this first run, the suspected lens redshift was found to be high, i.e. near to Sharov21 itself but did not find a higher likelihood region in opposite sense, i.e. near M31. I believe this is a sign that the code was not able to efficiently map the lens redshift parameter space, currently constrained to be > 0 and $< z_{\rm AGN}$ and with a uniform prior. Given that the effective cosmological redshift for M31 would be on the order 10^{-4}, I reasoned that the code did not have sufficient scope for mapping this many orders of magnitude in the time alloted.

In an attempt to correct for this I began another run but this time using a search on $\log(z_{\rm d})$ rather than linear $z_{\rm d}$ as previous. Given the decades-long light-curve, I also placed a constraint that the peak be within $\pm$400 days of the main event to ensure the run spent less time in low-likelihood regions.

The second run performed very well. The associated walker plot is shown is Fig. 6.2. After the initial spread-out, the walkers settle into a sensible range with only a few getting stuck in regions of very low likelihood. Note that the 'burn-in' period was set as the first 1000 iterations ie. the parameter constraints are derived from the second-half of the trace, and are listed in Table 6.1. The corner plot for this run is shown in Fig. 6.3. In this instance, with the initial redshift parameter still set to $\log(0.2)$, there is a clear preference for very low redshift values. Given the parameter constraints, this places the lens within ~ 3.4 Mpc

Figure 6.1 *MCMC walker plot for Sharov21 which failed to converge. Each panel shows one of the parameters used in the model. Left, from top to bottom: z_d, M_l, $v \perp$, y_0. Right, from top to bottom: t_0, F_s, F_b. Units as per Table 6.1*

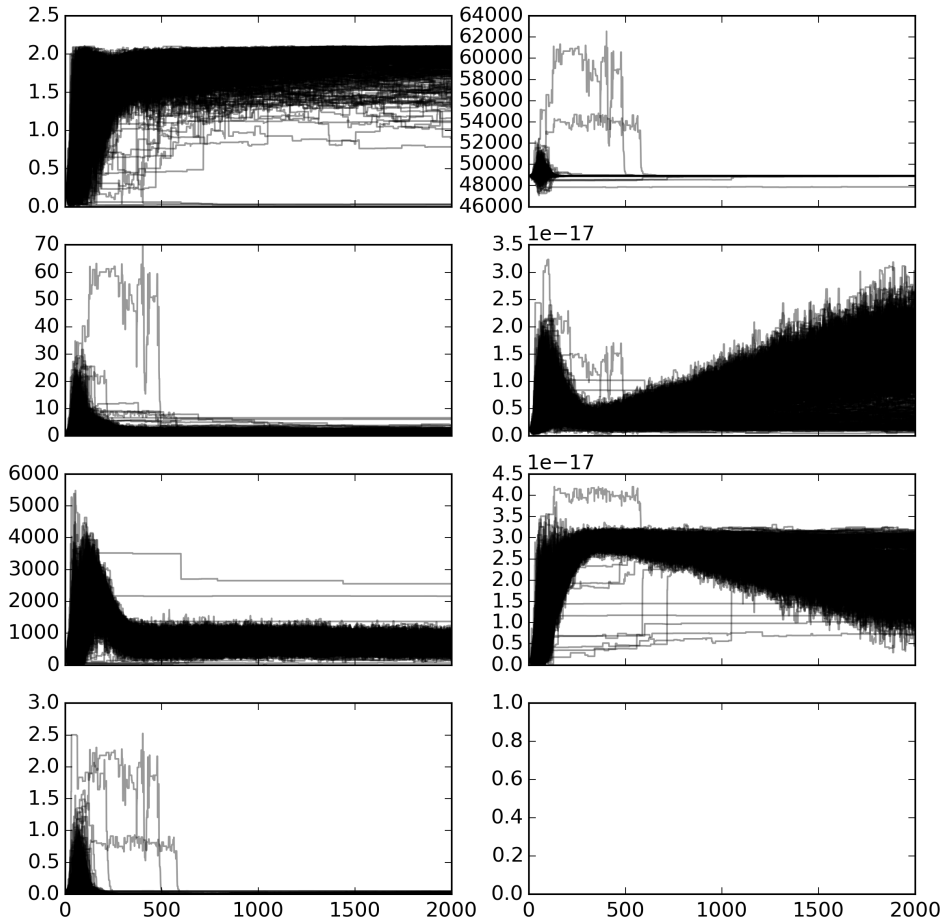

Table 6.1 *Parameter constraints for the Sharov21 event from the simple microlensing MCMC analysis.*

Sharov21		$z_{\rm agn} = 2.109$
Parameter	Value	Unit
$\log(z_{\rm d})$	$-3.72^{+0.60}_{-0.69}$	
$M_{\rm l}$	$1.19^{+2.09}_{-0.75}$	$\mathrm{M}_{\odot}$
$v_{\perp}$	420^{+200}_{-190}	$\mathrm{km\,s^{-1}}$
y_0	$0.029^{+0.008}_{-0.007}$	$\theta_{\rm E}$
t_0	48913^{+1}_{-1}	MJD
$F_{\rm s}$	$2.18^{+0.57}_{-0.50}$	$\times 10^{-17}\mathrm{erg\,s^{-1}cm^{-2}\AA^{-1}}$
$F_{\rm b}$	$1.26^{+0.47}_{-0.55}$	$\times 10^{-17}\mathrm{erg\,s^{-1}cm^{-2}\AA^{-1}}$

of Earth. The best-fit model in this case has a lens redshift corresponding to a distance of 2.35 Mpc. However, the median lens redshift value corresponds to 0.85 Mpc, ie. within 10% of the true distance of M31. This is a significant result. With the only assumption being that of a stellar-mass lens, the simple model analysis provides an independent estimate that the lens is most likely to be located within M31. This lends additional weight to the microlensing hypothesis.

There are two light curve plots for this target. The first (Fig. 6.4) shows the long-term light curve. The second (Fig. 6.5) shows a zoomed-in view of the main event. The fit performs relatively well but is not an exact match to the data. A better fit would require a more rapid rise to peak and more gradual decline. Thus, while the simple microlensing model cannot easily be ruled out, this event may require a caustic crossing ingress to adequately explain. The expected egress may have gone unnoticed in the photometry. On the other hand, the intrinsic variability seen in Sharov 21 during quiescence may be enough to explain the discrepancies.

6.3 Discussion

The results presented here are still preliminary but it is very interesting that the MCMC analysis provides an objective way of constraining the lens redshift to the approximate distance of M31. It is also interesting to note that when the lens redshift is low the Einstein radius, when projected at the distance of the source, can be quite large. In the case of the best-fit model reported above, this distance corresponds to $\sim$ 1 light-year at the redshift of Sharov21, with the full range constrained to $\sim 1 - 10$ light-years. Contrast this with the results from Chapter

Figure 6.2 *MCMC walker plot for Sharov21 which performs better than the previous attempt. Each panel shows one of the parameters used in the model. Left, from top to bottom: log(z_d), M_l, $v \perp$, y_0. Right, from top to bottom: t_0, F_s, F_b. Units as per Table 6.1*

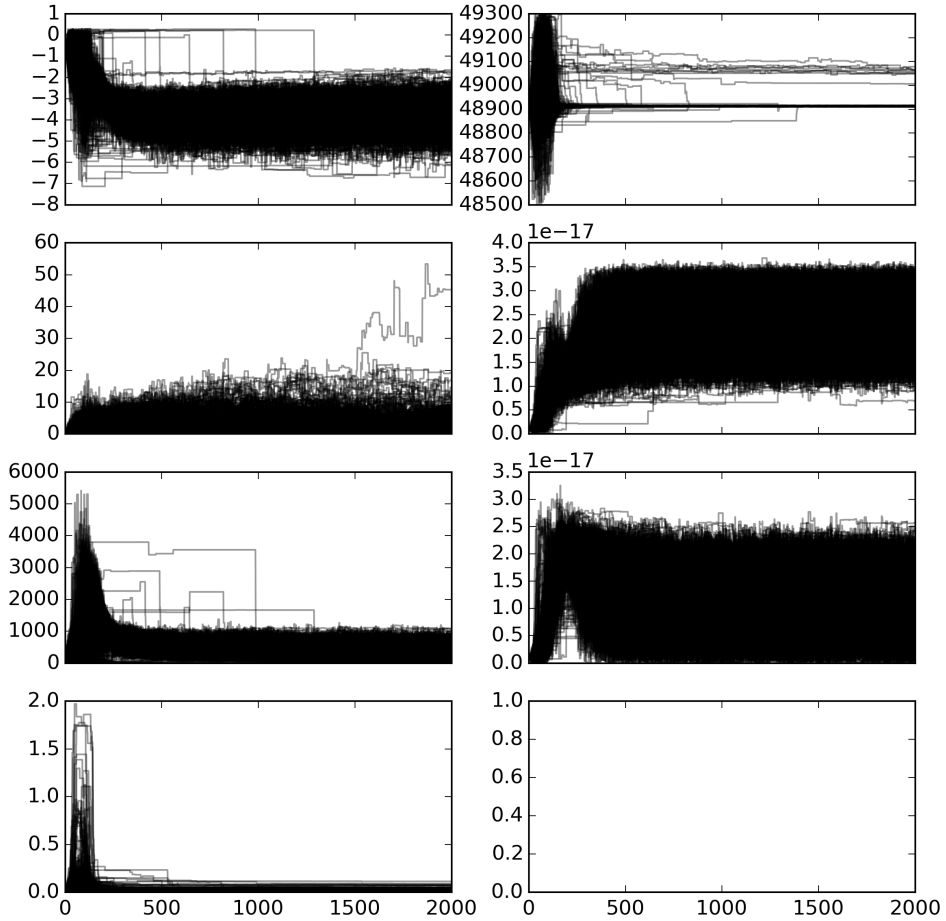

Figure 6.3 *Corner plot for the successful MCMC run for Sharov21. Note that the values for the lens redshift are in log(z_d).*

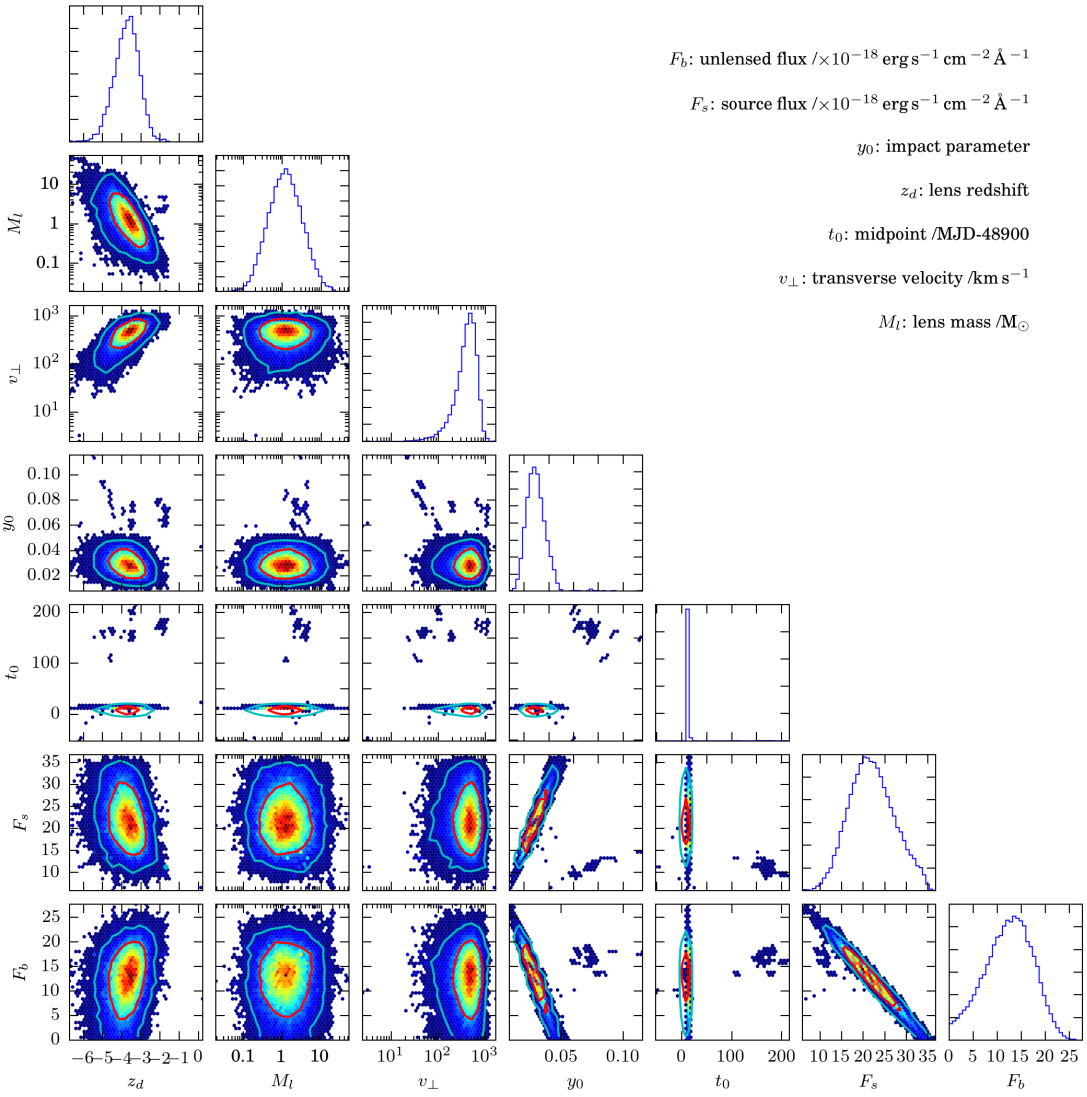

Figure 6.4 *Full light curve and residuals to the microlensing fit for Sharov 21, using the data supplied by Meusinger et al. (2010). Fit parameters, as defined in Chapter 5, are also displayed.*

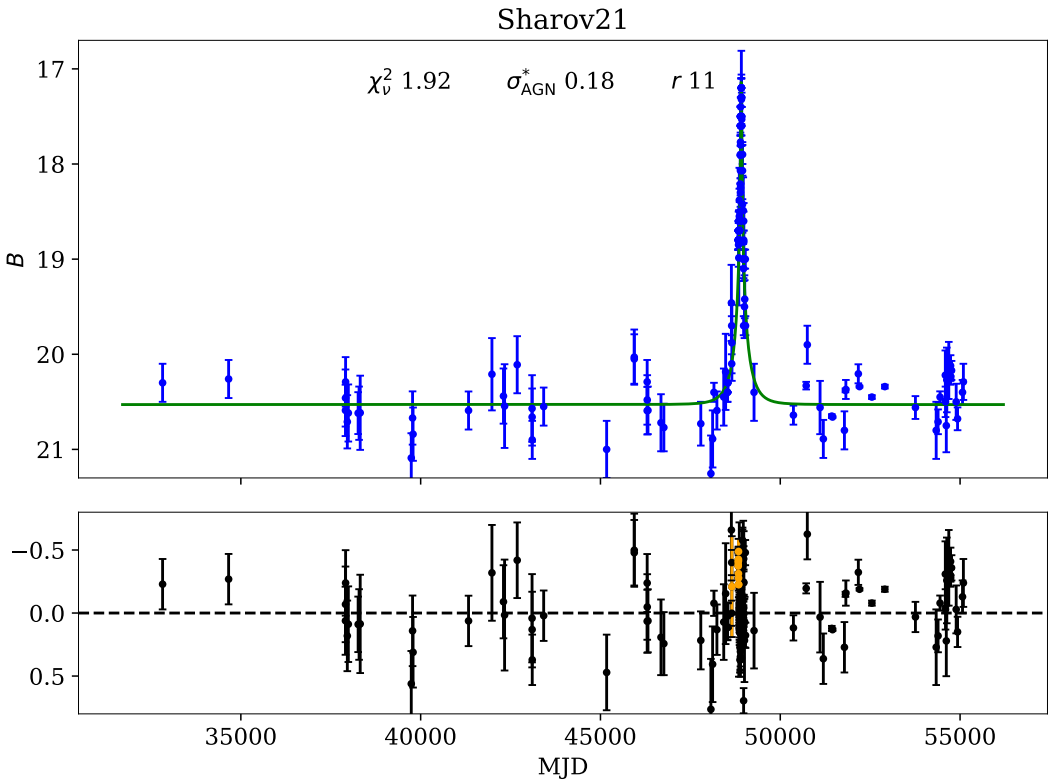

Figure 6.5 *Zoomed-in portion of the light curve for Sharov 21 showing the main transient event and residuals to the microlensing fit. Fit parameters, as defined in Chapter 5, are also displayed.*

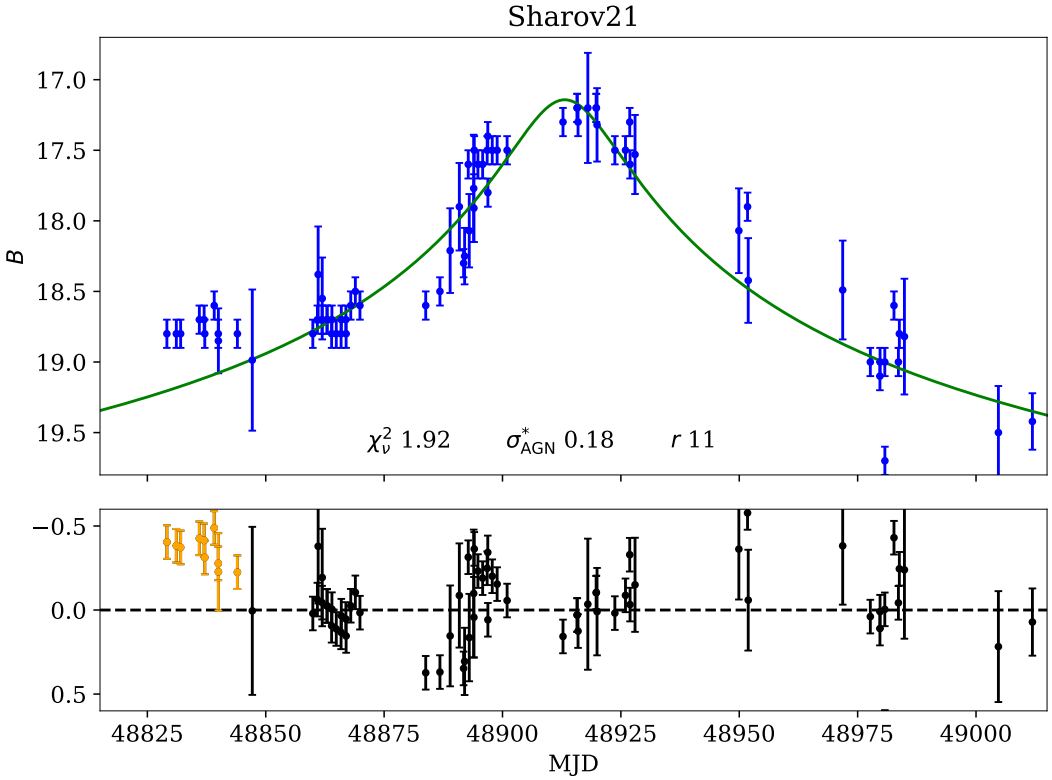

Figure 6.6 *PHAT colour composites for Sharov21, highlighted with a red cross. Left: ACS/WFC F814W/F475W; right: ACS/WFC F160W/F110W. The cutouts are approximately 10 arcseconds across.*

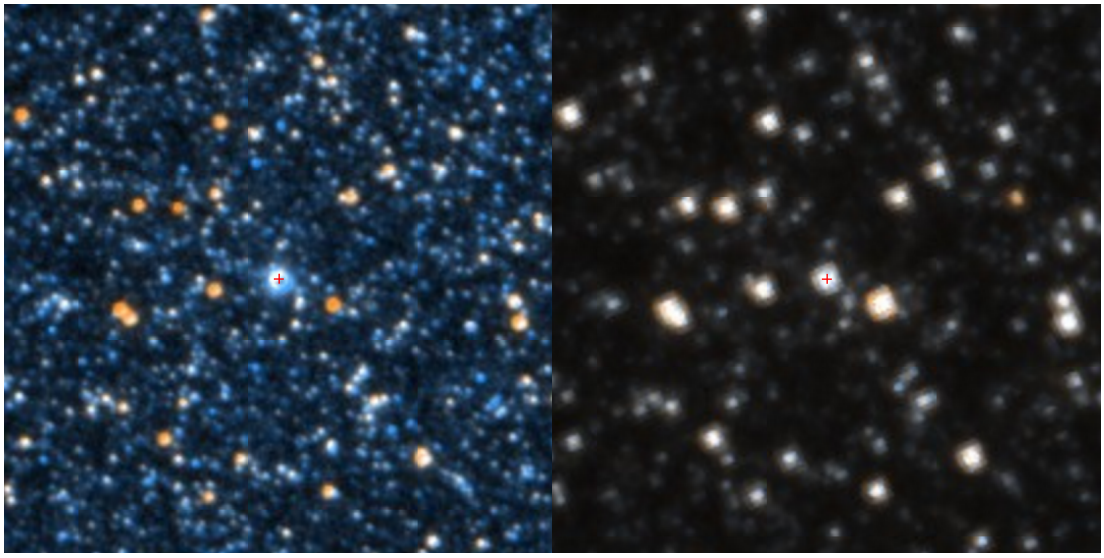

4 which correspond to radii on the order of tens of light-days for J084305 and J094511. This makes it very likely that the accretion disc can be assumed safely to be a point-source in this case but also increases the chance that the BLR will have also undergone significant amplification during the event. Depending on the full extent and morphology of the BLR, this amplification may have matched that seen for the accretion disc or it may have only been partially resolved. If partially resolved, some of the tentative colour changes reported in Meusinger et al. (2010) may be the result of differential changes in BLR contamination for one or more of the filters used.

Since the publication of Meusinger et al. (2010), Sharov21 has fortuitously been observed in multiple filters during 2011/12 as part of the Panchromatic Hubble Andromeda Treasury (PHAT, Williams et al. (2014)). The survey is divided into various bricks/fields. Sharov21 appears in: brick 08, field 14 [F275W/F336W/F475W/F814W/F110W/F160W]; brick 08, field 15 [F275W/F336W/F475W/F814W] and brick 06, field 02 [F475W/F814W]. The optical and infra-red filter composites are displayed in Figure 6.6 along with a zoomed-out view of 'Brick 08' in Figure 6.7 to show where this object sits in relation to the stellar disc of M31. A cursory glance at the images shows that Sharov21 does not appear to be near any bright contaminants but does lie in a crowded star field as might be expected.

Figure 6.7 *Sharov 21 location, with respect to 'Brick 08' in the PHAT survey, marked with a red cross. North is up, East is left. The projected size is* $\sim 1.5\,\mathrm{kpc} \times 3\,\mathrm{kpc}$ *(*$\sim 6.6' \times 13'$*).*

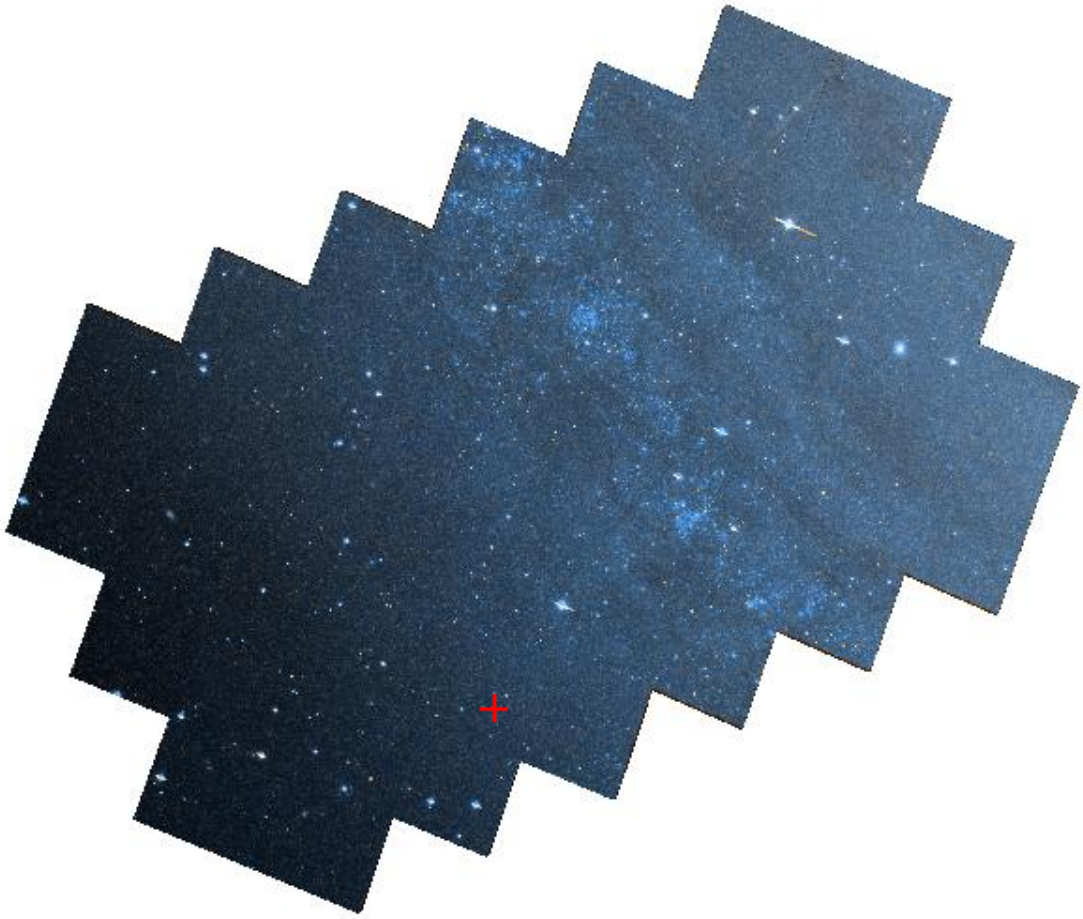

As mentioned in the previous chapter, the prospect for performing more realistic microlensing model fits is improved with a well-sampled light curve and a known lens redshift. Thus this target provides an excellent opportunity to work on developing an approach to fitting these models. This will require an estimate for the significance of any external shear caused by the mass distribution of M31 and exploration of a binary lens configuration. Both scenarios could provide a natural explanation for the asymmetry seen in the transient profile but for now the simple microlensing case performs relatively well. Given that mass profiles for M31 are available, an estimate for the significance of any external shear will be a key area for future work. It remains to be seen if the optical depth to microlensing in this part of M31 matches the estimate quoted in Meusinger et al. (2010). The probability was expected to be low but in a wider context, the possibility of observing other quasars being microlensed by stars in M31 would very valuable indeed.

Chapter 7

Summary and conclusion

I will now summarise the progress which has been made thus far. This will include a discussion on the direction of future work concerning these long-lived AGN transients and any others which are yet to be detected.

7.1 PS1 'slow-blue' AGN transient sample

The PS1 'slow-blue' AGN transient sample currently consists of 64 targets and a total of 235 spectroscopic epochs charting the evolution of these events. The transients were originally identified by cross-matching Pan-STARRS sources with those in the Sloan footprint. In addition to finding supernovae and TDE candidates, this produced a significant number of slowly-evolving type-I AGN, exhibiting changes greater than 1.5 magnitudes over long timescales. These have since been monitored, photometrically and spectroscopically, over a number of years. The spectra and light curves for the sample are shown in Appendices A and B respectively.

I have developed a reduction pipeline for the spectroscopic data taken, primarily, using the William Herschel Telescope. Using this, all spectroscopic data has since been reduced in a homogeneous manner. A spectral fitting routine has also been applied at every epoch to provide a large data set comprising, among others, line fluxes, widths, spectral indices and numerous derived parameters. This has allowed me to chart the spectroscopic evolution of the entire sample. A key priority for future work will be to incorporate any additional spectroscopic

observations prior to making the data set available for online access.

It has become apparent that the majority of objects in this sample, when considering any individual spectral epoch, are not markedly different to the typical AGN population. They are distributed across a fairly broad range of redshifts ($\sim 0.2 \lesssim z \lesssim 2$) and luminosities ($10^{44} \lesssim \mathrm{L}_{3000} \lesssim 10^{45.5}$ erg/s). Estimates for the black hole mass (using the MgII line width), bolometric luminosity and Eddington fraction have also been calculated at each epoch. As many of these objects are still evolving these parameter estimates may be subject to additional systematic uncertainty.

When the spectroscopic evolution is taken into account some trends in the sample do emerge. A general light curve classification scheme can sub-divide this sample into 'simple' objects (cuspy, single-peaked), 'rounded' objects (slow-rollers), 'dippers' and double- or multiply-peaked events. The simple objects are generally lower luminosity and display higher MgII equivalent widths than the rounded subset. The rounded objects also appear to exhibit a greater degree of colour change, as evidenced from the UV power-law slope evolution. In many objects, the data shows that there is a differential evolution in some BLR line species with respect to the continuum. This effect is typically weaker in MgII than in other line species. In some cases the MgII flux is consistent with no change at all even after a substantial drop in the continuum.

The simplest microlensing model, the point-lens, point-source approximation, has provided a good match to $\sim$10% of the transient events in the sample. With the assumption of a stellar-mass lens, and later an additional lens transverse velocity constraint, the MCMC analysis provides useful parameter constraints for each event. In some cases the background, or unlensed flux, is unconstrained, likely due to a lack of data at or near quiescence. As many events are continuing to evolve, the additional light curve information will help to improve these parameter constraints. This analysis has also provided evidence that the 'rounded' light curves described above are not simply longer-lived instances of the 'simple' events. This is a strong indication that the point-source approximation is not appropriate for modelling these events, which may instead be examples of an accretion disc being partially resolved by the lens.

Using the simple microlensing model parameters for J084305, which provides an excellent match to the light curve, has also allowed a test of extended sources as an explanation of the differential variability seen in the BLR for this object.

With some simplifying assumptions this has allowed me to place constraints on the size of the CIII] emitting region and an upper lower limit on the size for MgII. Since this work was carried out this object has continued to evolve as predicted and now has additional photometric and spectroscopic observations. Revisiting this object in the light of the new data will be an important future step.

I have begun adapting the MCMC analysis to allow parameter constraints to be determined in cases where the accretion disc is possibly being resolved by the lens. In the first case study, J155427, this was shown to be a much better match to the data than the point-source model but will require a higher resolution treatment before any firm conclusions can be made.

In several notable objects, the point-lens, point-source microlensing model works relatively well but fails to reproduce additional structure seen in the light curves. These cases are strong candidates for testing lensing models which incorporate additional point masses, or the presence of external shear, in order to better reproduce the light curves.

So far, no convincing explanation has been provided for the 'dipper' objects which may be due to obscuration events. This work is in a preliminary stage and is currently with collaborators in Durham, with a particular focus on the prototype dipper, J223210. Thus far it appears as if a simple reddening event is insufficient to explain observations.

Other objects, for example, J150210, stand out from the rest of the sample for different reasons. In this case the light curve profile is akin to that of a long-lived TDE, or possibly super-luminous supernova, and displays zero colour change in the UV throughout. This may still prove to be a complex microlensing event. It will be very interesting to see how events such as this continue to evolve.

7.1.1 Sharov 21

While not part of the AGN transient sample this event has proven to be a very important with regard to the testing of the microlensing hypothesis. With a slight refinement to the MCMC analysis, the point-source, point-lens microlensing model provides a very reasonable fit to the bulk changes seen in this object. Perhaps more importantly, this analysis has also provided an independent check that the most likely location of the lens is indeed in M31. It may be possible

to provide a better match to the structure in the light curve at the main event by incorporating a more complex lens and the information now available to us through the PHAT M31 HST survey. This work is a high priority for the future.

7.2 Future work

I am now confident that microlensing is the correct explanation for at least $\sim 10 - 20\%$ of the targets in this sample. In future, I would like to make use of all of the data available to me in this 'mu-lens' subset of objects. This will include incorporating any subsequent photometry/spectroscopy into the analysis. But perhaps more importantly, I also plan to incorporate the other photometric bands (from the various surveys) into the MCMC analysis. In order to do this effectively, I will need to ensure that any discrepancies between bandpasses, and the possibility of broad line flux intruding into some, are properly accounted for. This will also require a method for constraining the suspected host/lens galaxy contributions with better precision, most likely involving template-fitting as part of the process. It may also be beneficial to be more quantitative in my approach to the intrinsic AGN variability, perhaps by incorporating DRW parameters into the analysis as well. The end result should allow a comprehensive look at the colour changes evidenced in some of these objects. This should prove very useful in differentiating between cases where the point-source approximation succeeds or fails. In the former case, observed colour changes may be adequately explained by, say, an achromatic AGN transient and changing contrast between host/lens galaxy and/or BLR contributions. In the latter case, definitive evidence that the accretion disc is being resolved would prove invaluable.

The work outlined in the previous paragraph can also evolve in parallel with the improvement of the extended-source and complex-lens light curve fitting routines. In part, this will require a higher-resolution treatment with respect to the magnification maps used in my existing code in addition to increasing the efficiency/computing power used. However, it may prove beneficial to make use of magnification maps which are already available such as this provided by the GERLUMPH database (Vernardos et al., 2015). Much of this work would be simplified if a known or suspected redshift for the lens was available as this would simplify the selection of the most likely lens configurations. As noted in Chapter 4, a number of spectra display signs of an intervening absorber. A careful fitting/stacking analysis of the spectra for each object may allow more detections

of this nature to be made.

Finally, the prospect for detecting new, slowly-evolving AGN transients should not be overlooked. The evolution in temporal coverage from SDSS to Pan-STARRS to LSST will allow many more of these objects to be discovered in future. Given that they take a number of years to evolve, it should also be possible to flag up those which are only just on the rise to a suspected microlensing peak. This opens up the possibility of obtaining high-cadence spectroscopy and photometry 'over the top'. This would effectively be a reverberation mapping campaign of an AGN microlensing event. This could allow an unprecedented glimpse into the morphology of the inner-most regions of these objects, where RM provides a radial sampling and the lens a transverse sampling. A valuable data set indeed.

Appendix A

Spectra

This appendix contains every spectral epoch for the targets discussed in this paper. Each figure includes the best-fit templates from the UV/[OII]/Hβ regions and the errormap. A fixed offset has been applied.

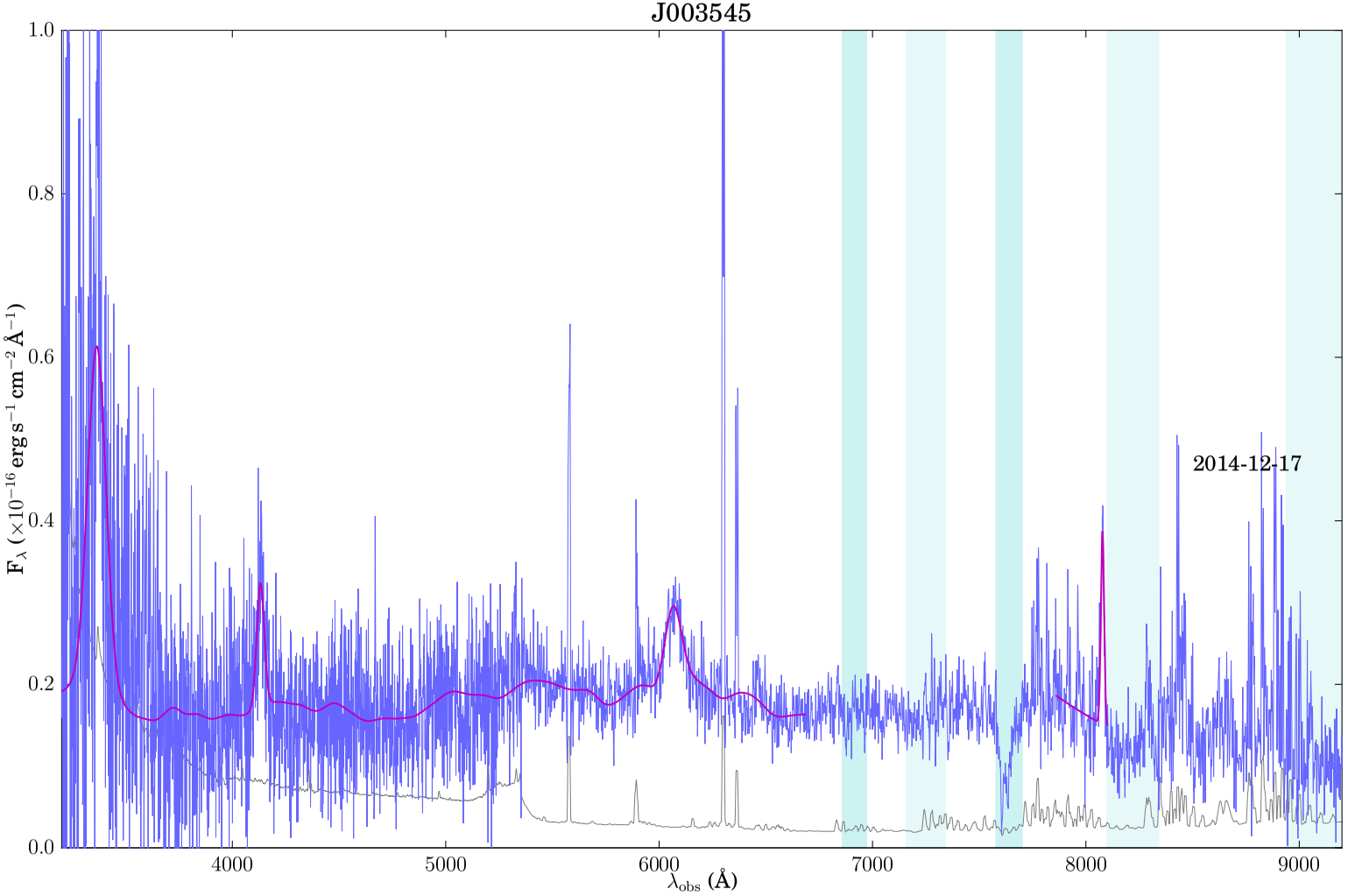
J003545
2014-12-17
F_λ ($\times 10^{-16}$ erg s^{-1} cm^{-2} Å^{-1})
λ_{obs} (Å)
0.0
0.2
0.4
0.6
0.8
1.0
4000
5000
6000
7000
8000
9000

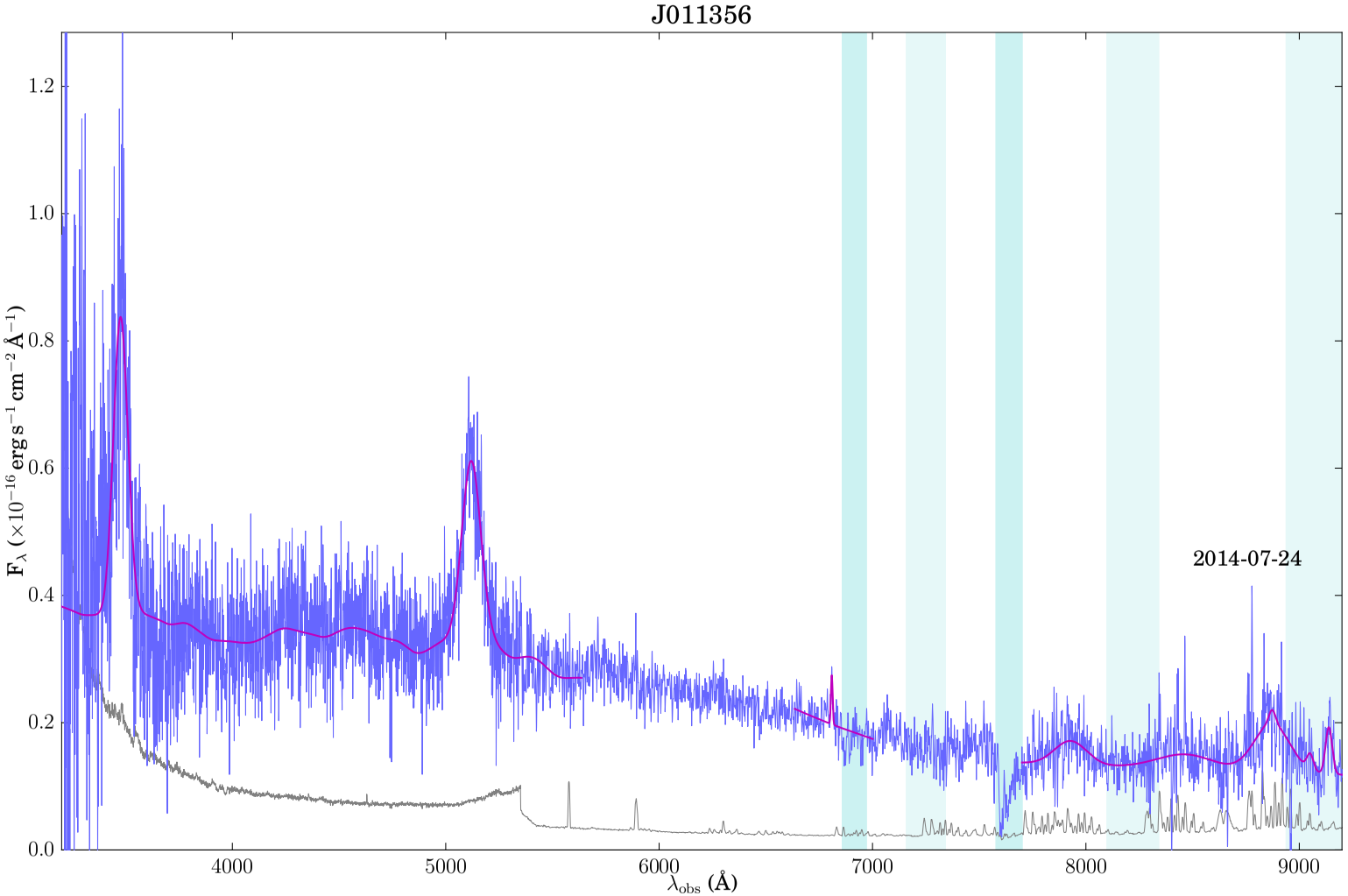
J011356
2014-07-24
F_λ ($\times 10^{-16}$ erg s^{-1} cm^{-2} Å^{-1})
λ_{obs} (Å)
0.0
0.2
0.4
0.6
0.8
1.0
1.2
4000
5000
6000
7000
8000
9000

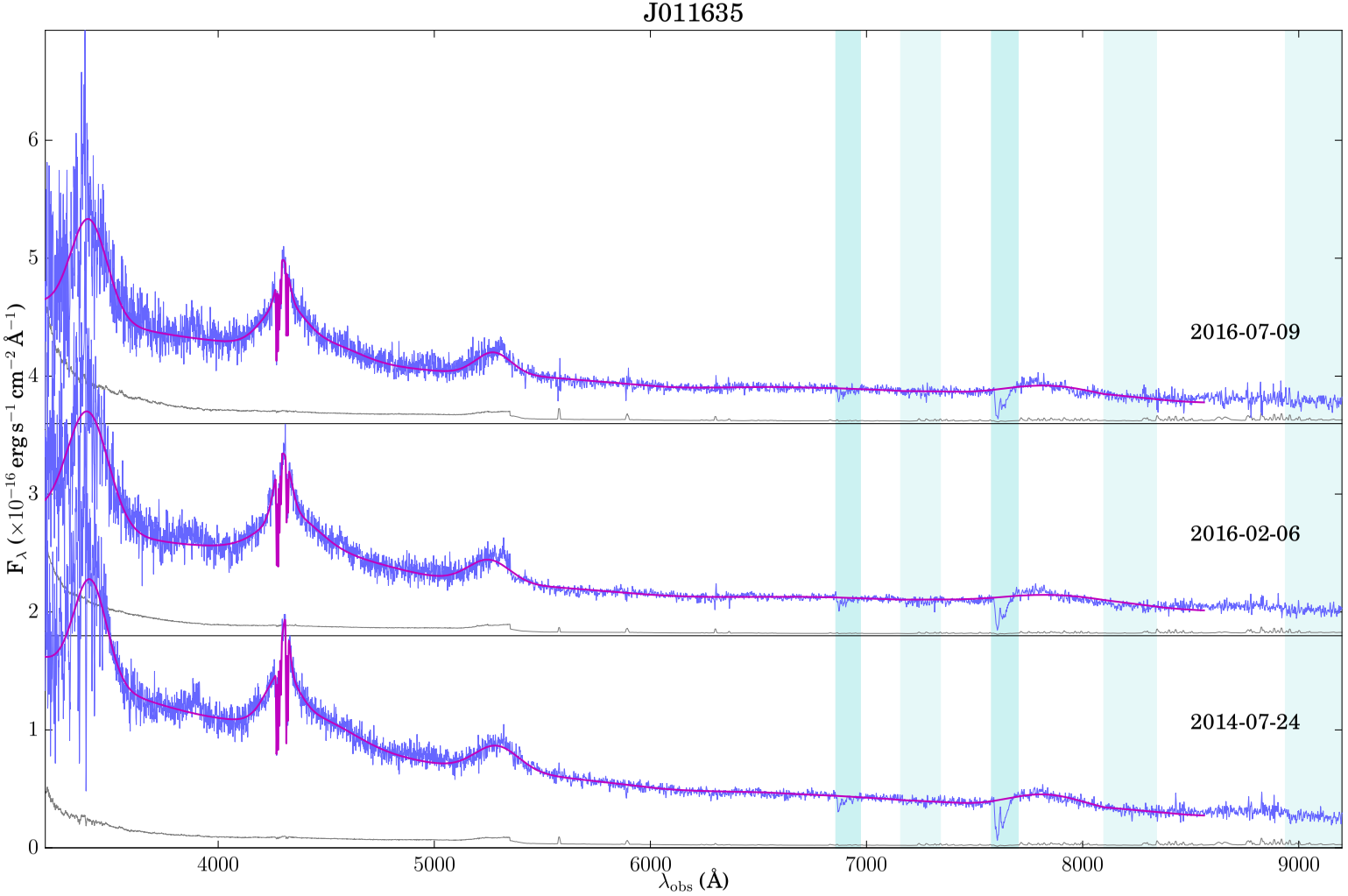
J011635
2016-07-09
2016-02-06
2014-07-24
F_λ ($\times 10^{-16}$ erg s^{-1} cm^{-2} Å^{-1})
λ_{obs} (Å)
0
1
2
3
4
5
6
4000
5000
6000
7000
8000
9000

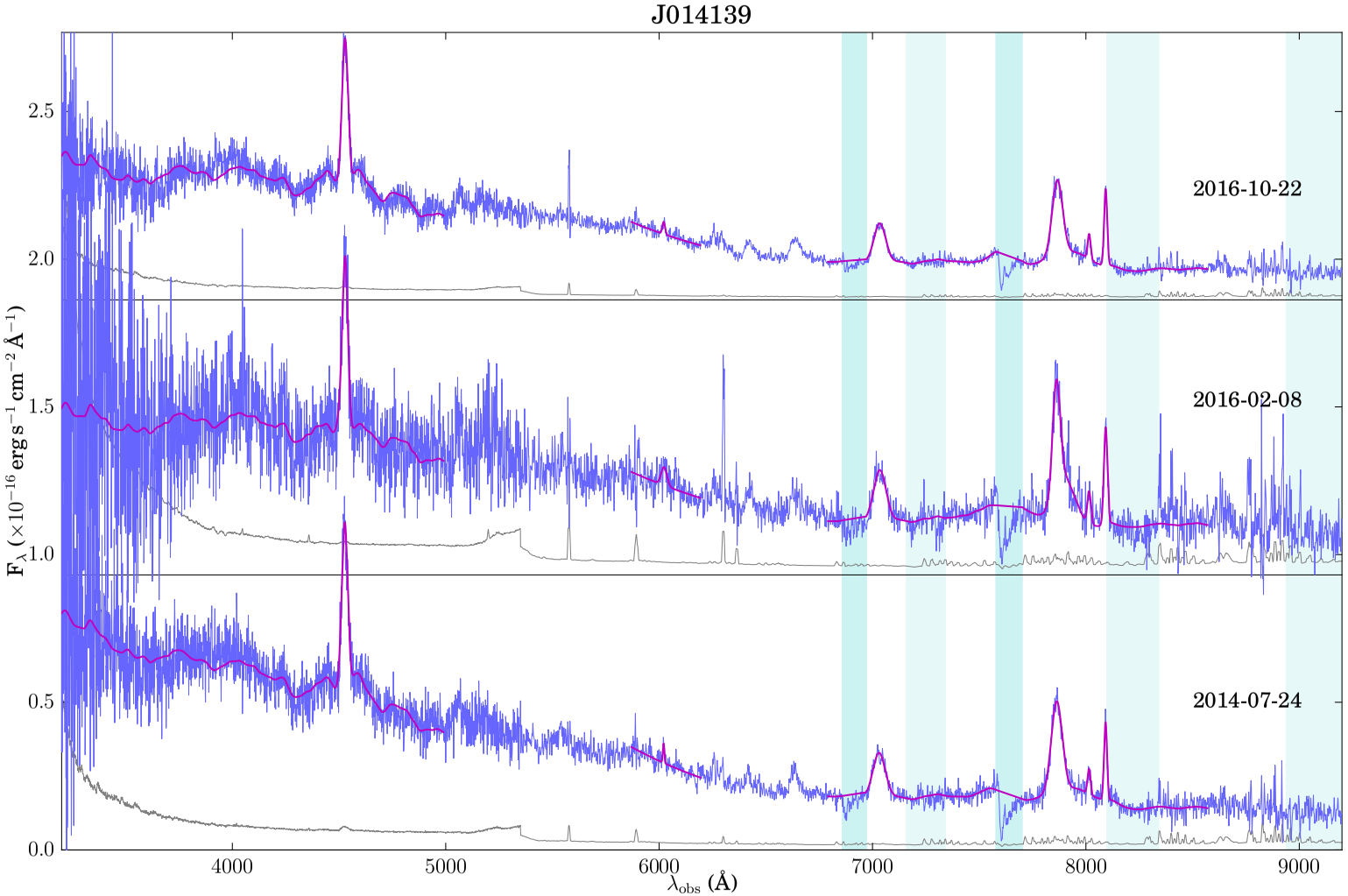
J014139
2016-10-22
2016-02-08
2014-07-24
F_λ ($\times 10^{-16}$ erg s^{-1} cm^{-2} Å^{-1})
λ_{obs} (Å)
0.0
0.5
1.0
1.5
2.0
2.5
4000
5000
6000
7000
8000
9000

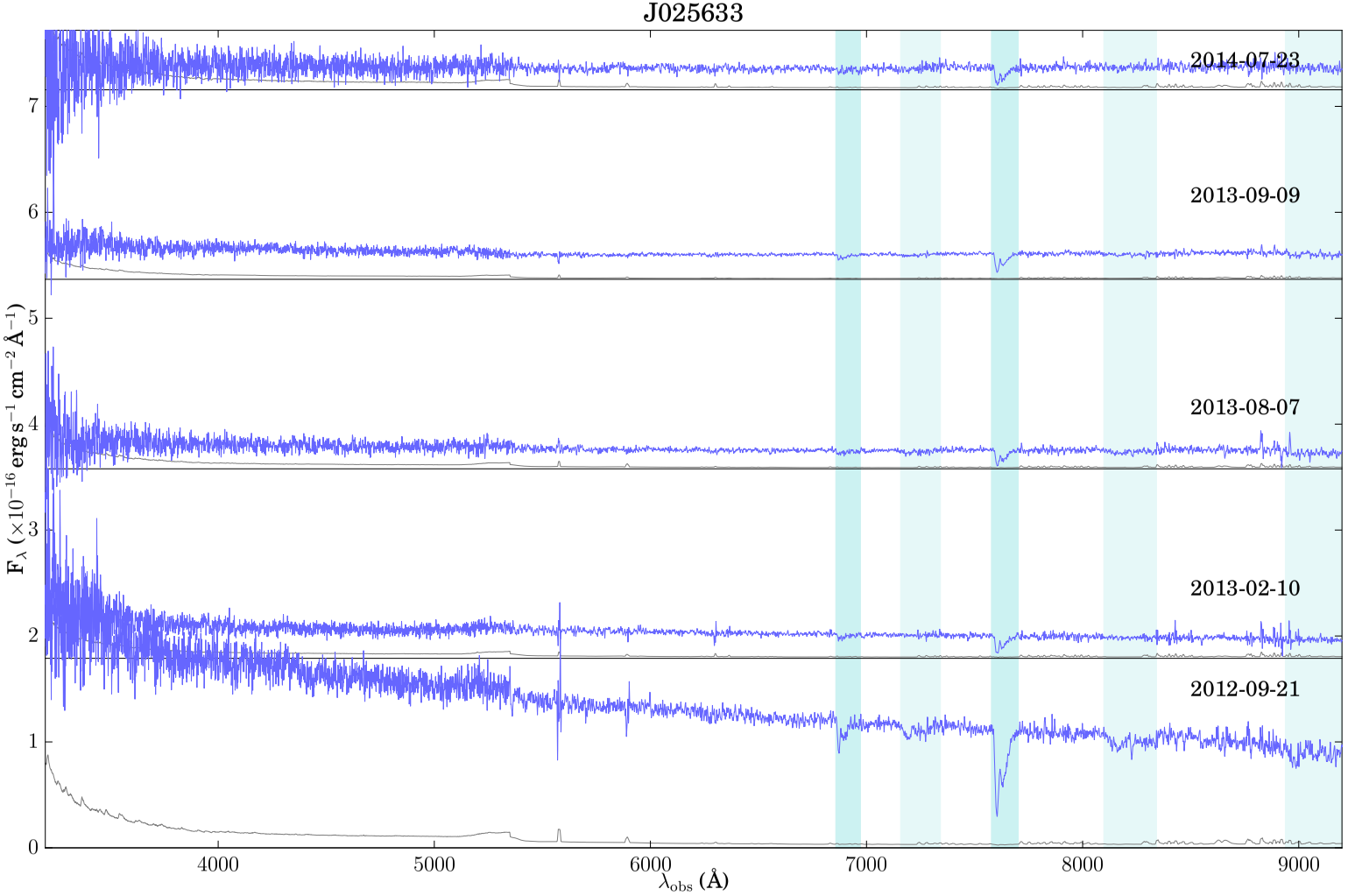
J025633
2014-07-23
2013-09-09
2013-08-07
2013-02-10
2012-09-21
F_λ ($\times 10^{-16}$ erg s^{-1} cm^{-2} Å^{-1})
λ_{obs} (Å)
0
1
2
3
4
5
6
7
4000
5000
6000
7000
8000
9000

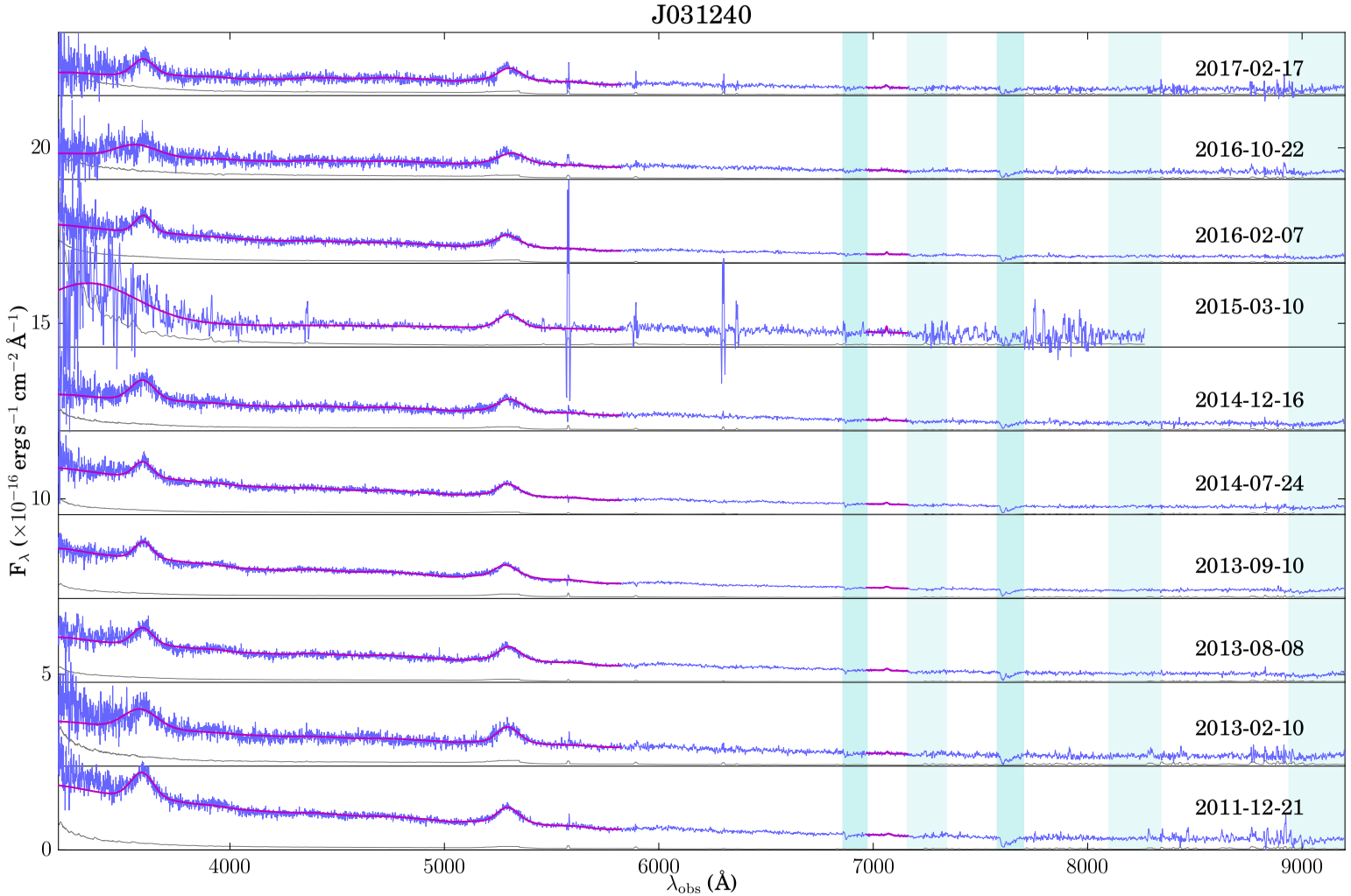
J031240
2017-02-17
2016-10-22
2016-02-07
2015-03-10
2014-12-16
2014-07-24
2013-09-10
2013-08-08
2013-02-10
2011-12-21
0
5
10
15
20
4000
5000
6000
7000
8000
9000
F_λ ($\times 10^{-16}$ erg s^{-1} cm^{-2} Å^{-1})
λ_{obs} (Å)

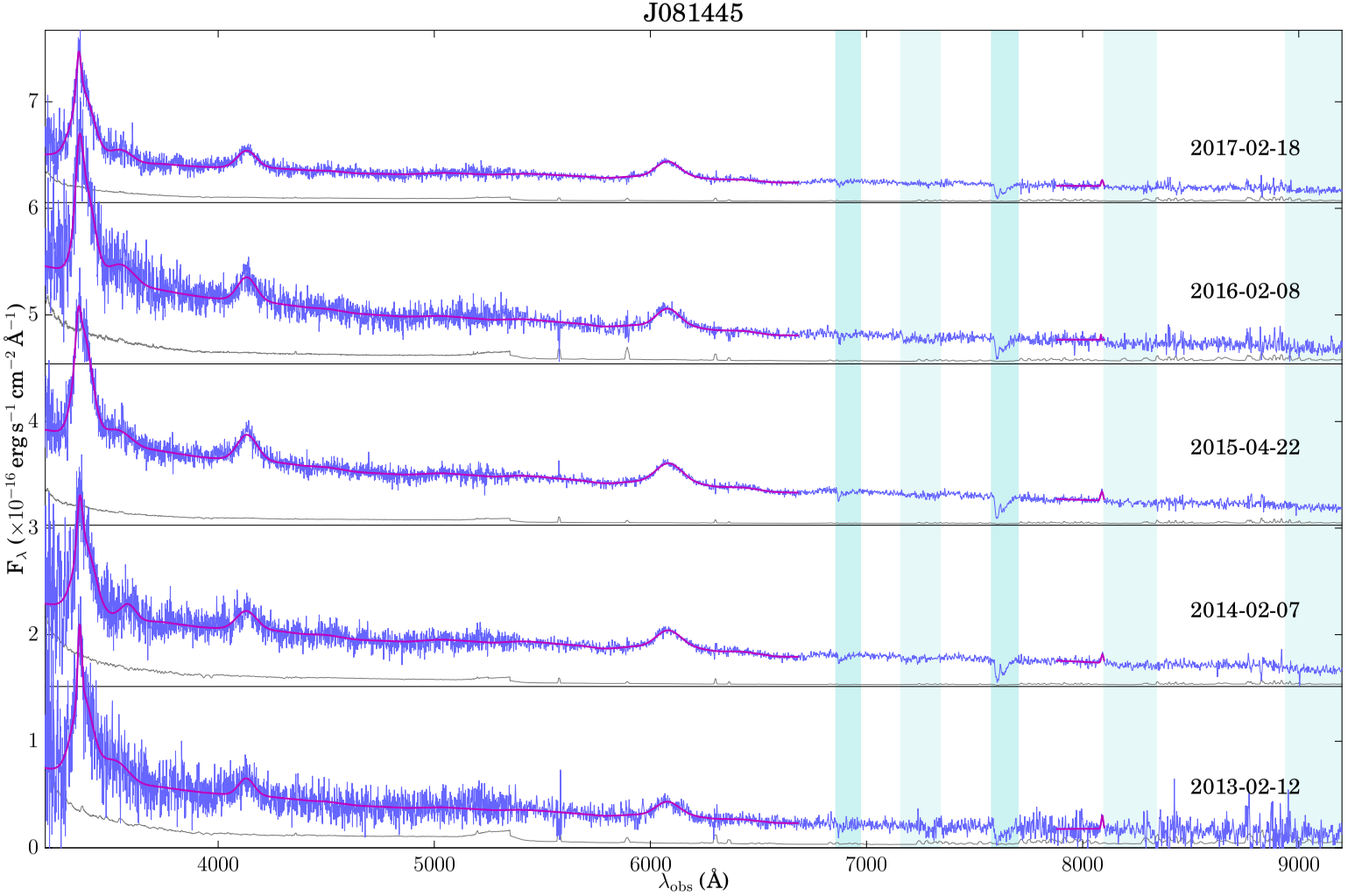
J081445
2017-02-18
2016-02-08
2015-04-22
2014-02-07
2013-02-12
F_λ ($\times 10^{-16}$ erg s^{-1} cm^{-2} Å^{-1})
λ_{obs} (Å)
0
1
2
3
4
5
6
7
4000
5000
6000
7000
8000
9000

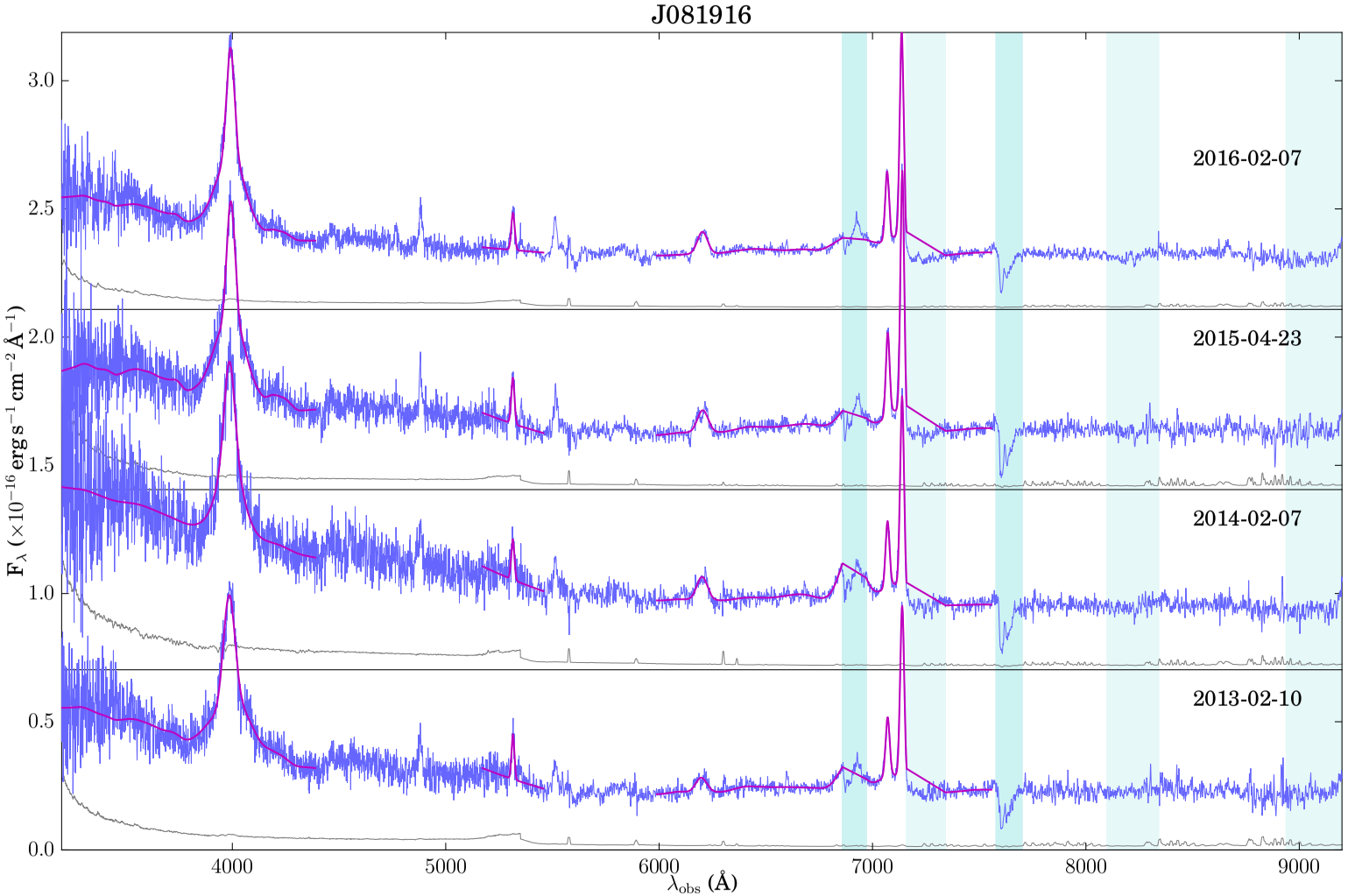
J081916
2016-02-07
2015-04-23
2014-02-07
2013-02-10
F_λ ($\times 10^{-16}$ erg s^{-1} cm^{-2} Å^{-1})
λ_{obs} (Å)
0.0
0.5
1.0
1.5
2.0
2.5
3.0
4000
5000
6000
7000
8000
9000

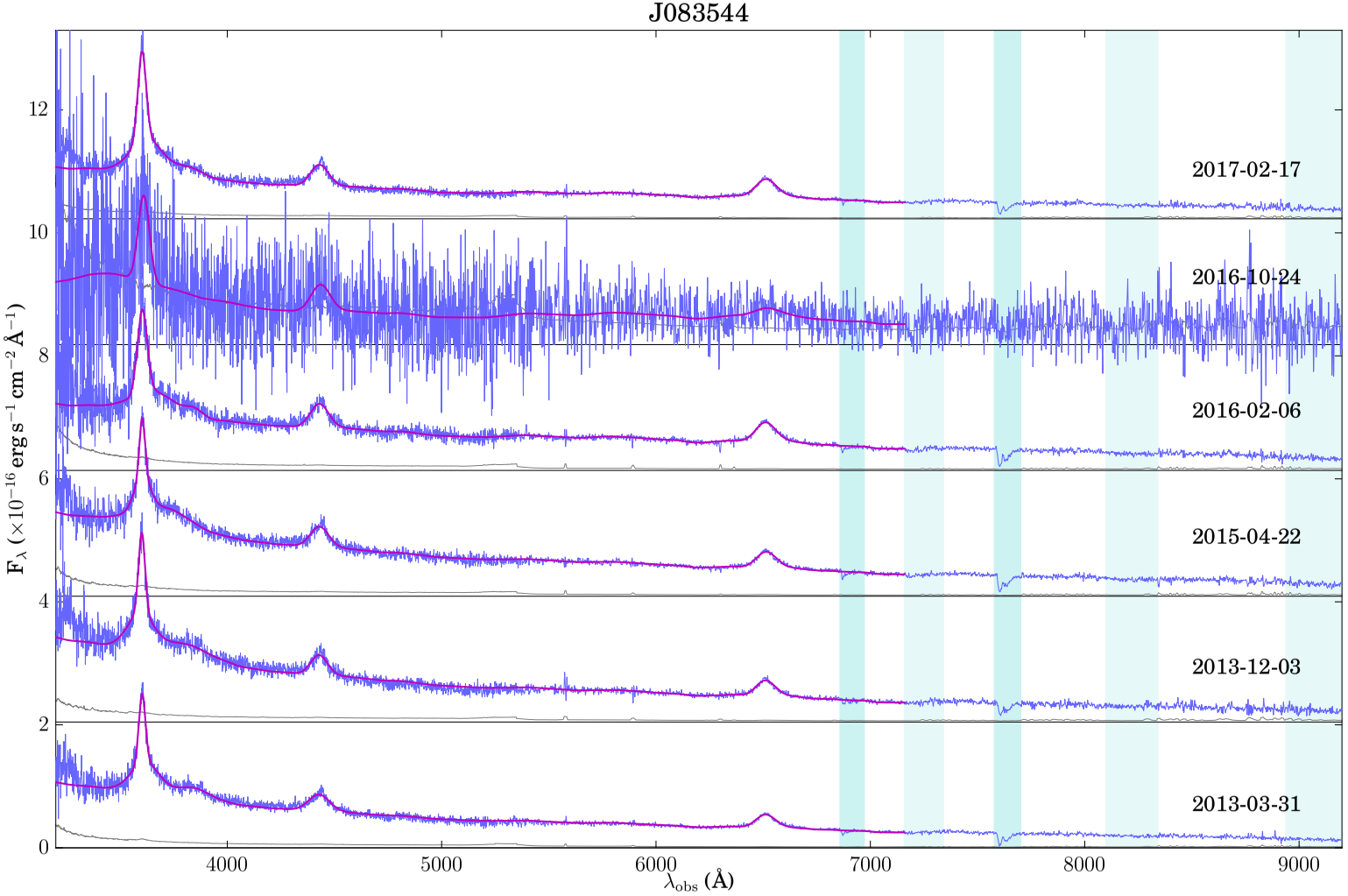
J083544
2017-02-17
2016-10-24
2016-02-06
2015-04-22
2013-12-03
2013-03-31
F_λ ($\times 10^{-16}$ erg s^{-1} cm^{-2} Å^{-1})
λ_{obs} (Å)
0
2
4
6
8
10
12
4000
5000
6000
7000
8000
9000

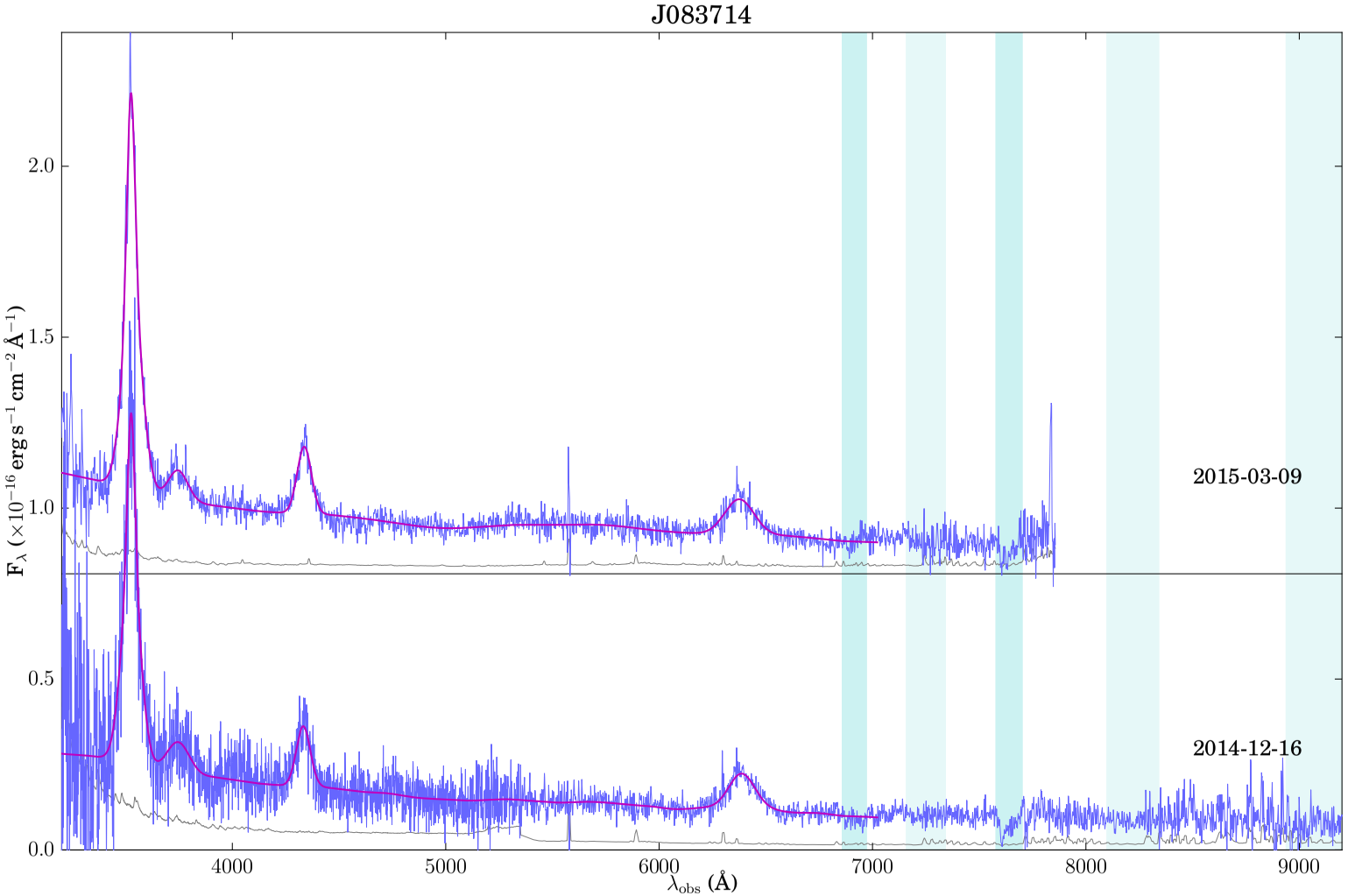
J083714
2015-03-09
2014-12-16
F_λ ($\times 10^{-16}$ erg s^{-1} cm^{-2} Å^{-1})
λ_{obs} (Å)
0.0
0.5
1.0
1.5
2.0
4000
5000
6000
7000
8000
9000

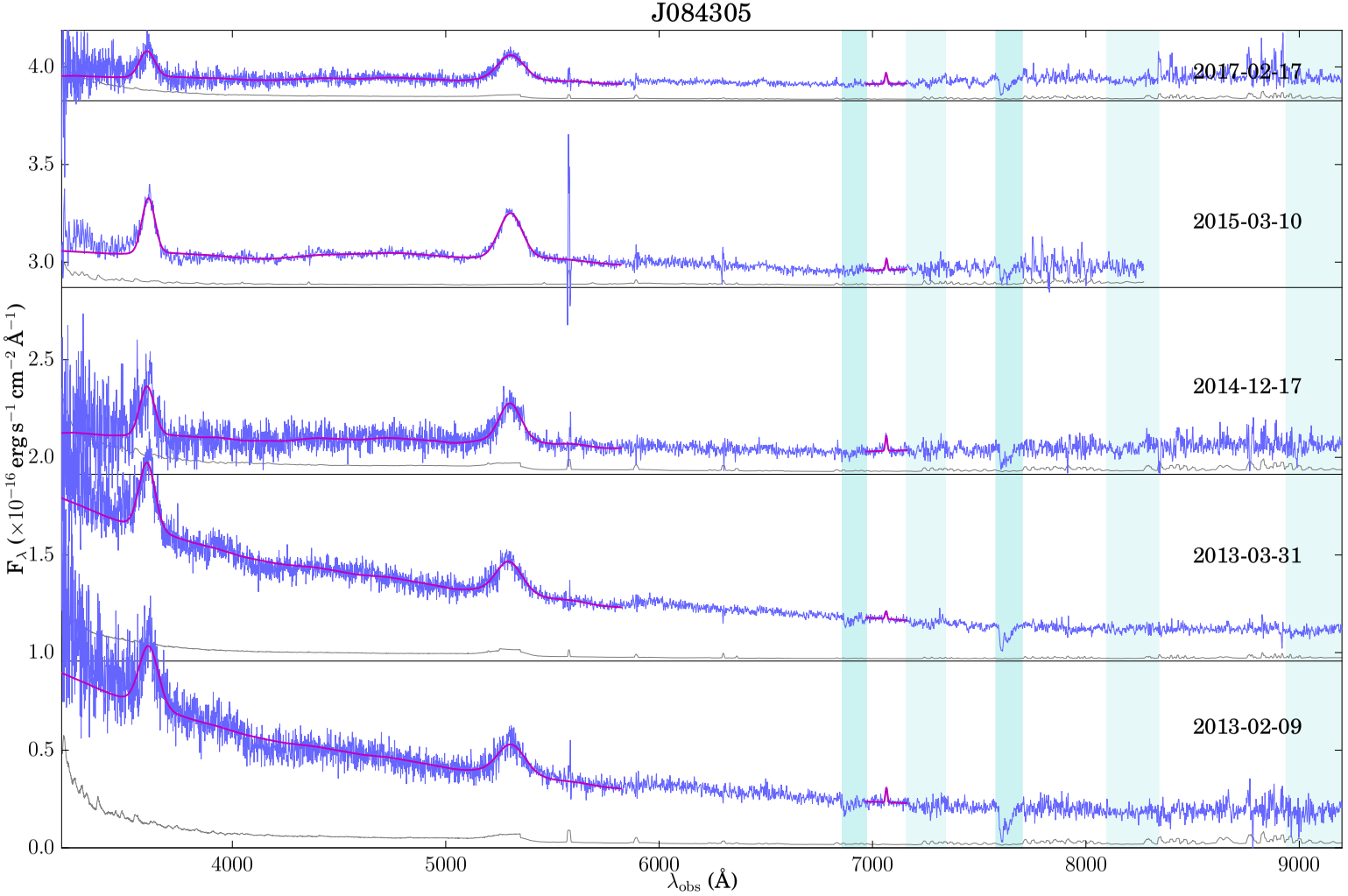
J084305
2017-02-17
2015-03-10
2014-12-17
2013-03-31
2013-02-09
F_λ ($\times 10^{-16}$ erg s^{-1} cm^{-2} Å^{-1})
λ_{obs} (Å)
0.0
0.5
1.0
1.5
2.0
2.5
3.0
3.5
4.0
4000
5000
6000
7000
8000
9000

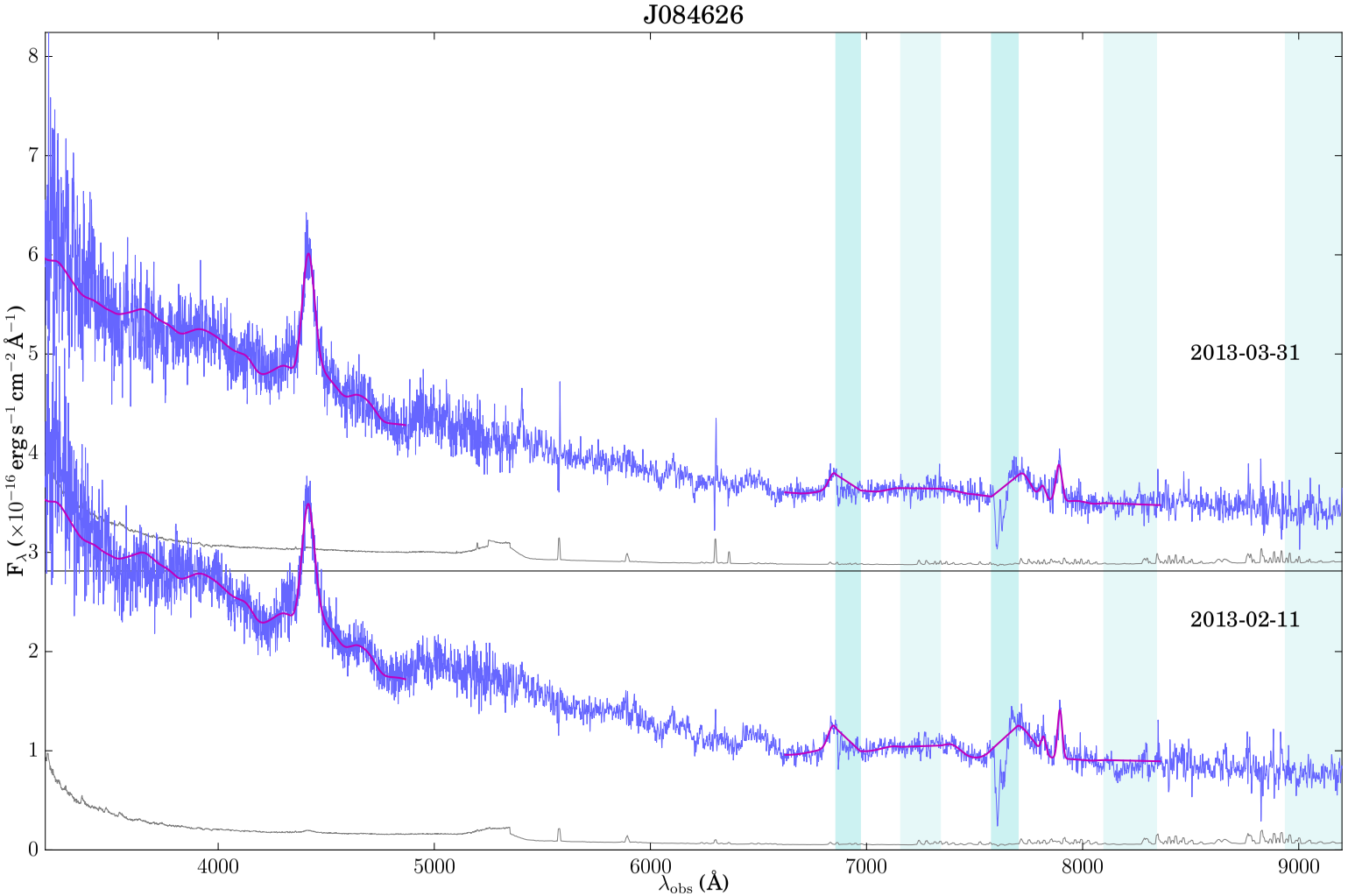
J084626
2013-03-31
2013-02-11
F_λ ($\times 10^{-16}$ erg s^{-1} cm^{-2} Å^{-1})
λ_{obs} (Å)
0
1
2
3
4
5
6
7
8
4000
5000
6000
7000
8000
9000

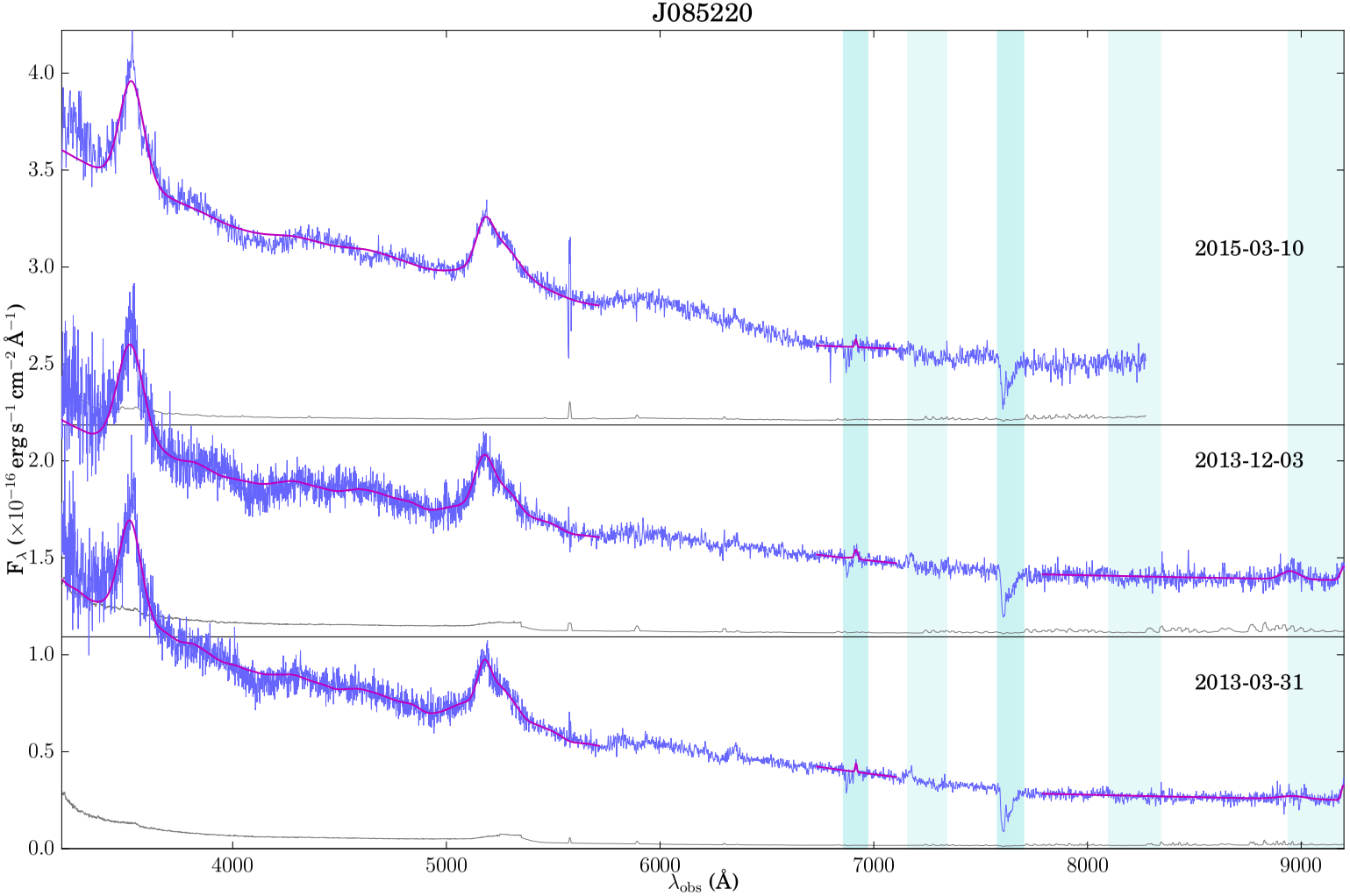
J085220
2015-03-10
2013-12-03
2013-03-31
F_λ ($\times 10^{-16}$ erg s^{-1} cm^{-2} Å^{-1})
λ_{obs} (Å)
0.0
0.5
1.0
1.5
2.0
2.5
3.0
3.5
4.0
4000
5000
6000
7000
8000
9000

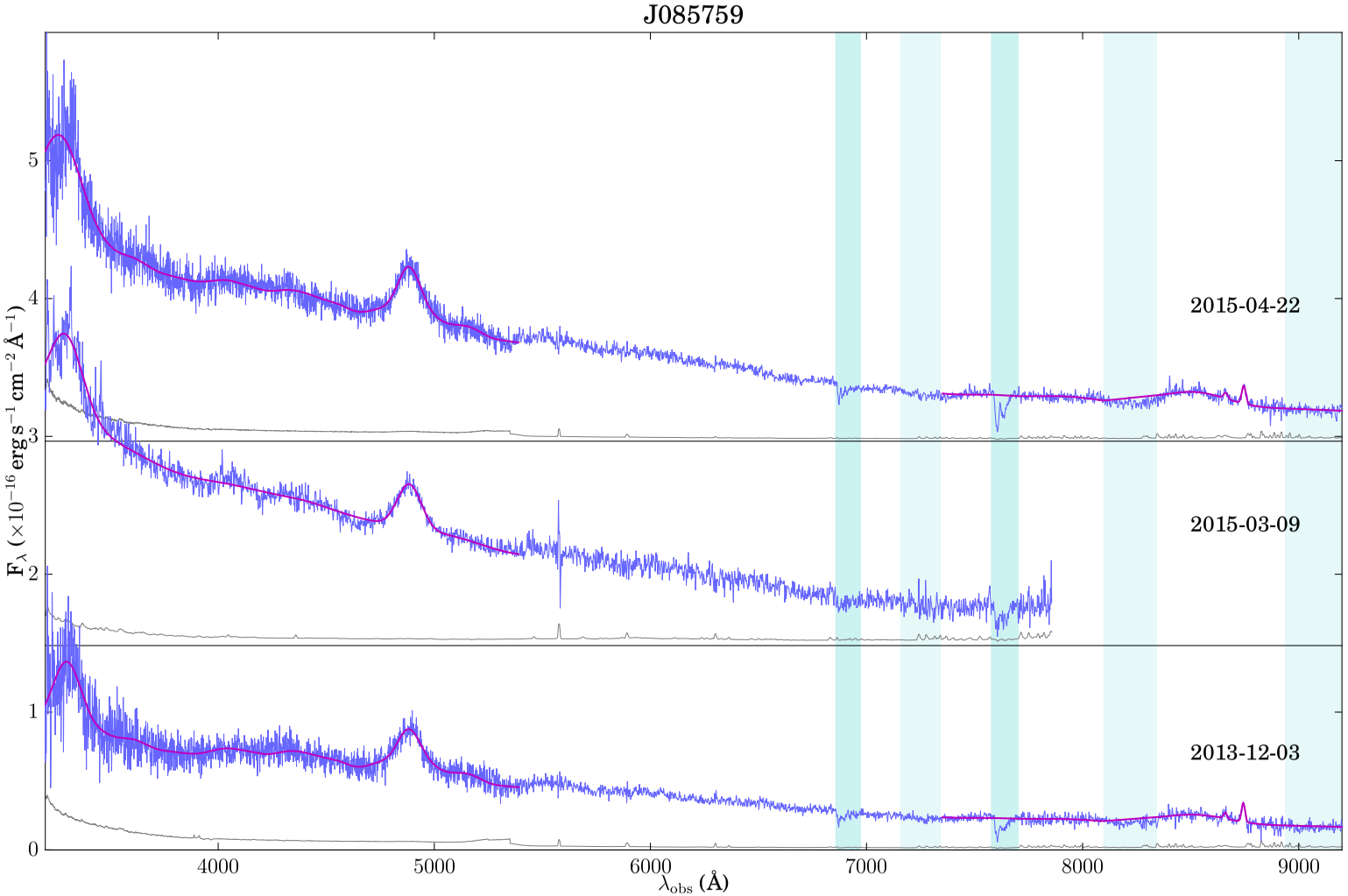
J085759
2015-04-22
2015-03-09
2013-12-03
F_λ ($\times 10^{-16}$ erg s^{-1} cm^{-2} Å^{-1})
λ_{obs} (Å)
0
1
2
3
4
5
4000
5000
6000
7000
8000
9000

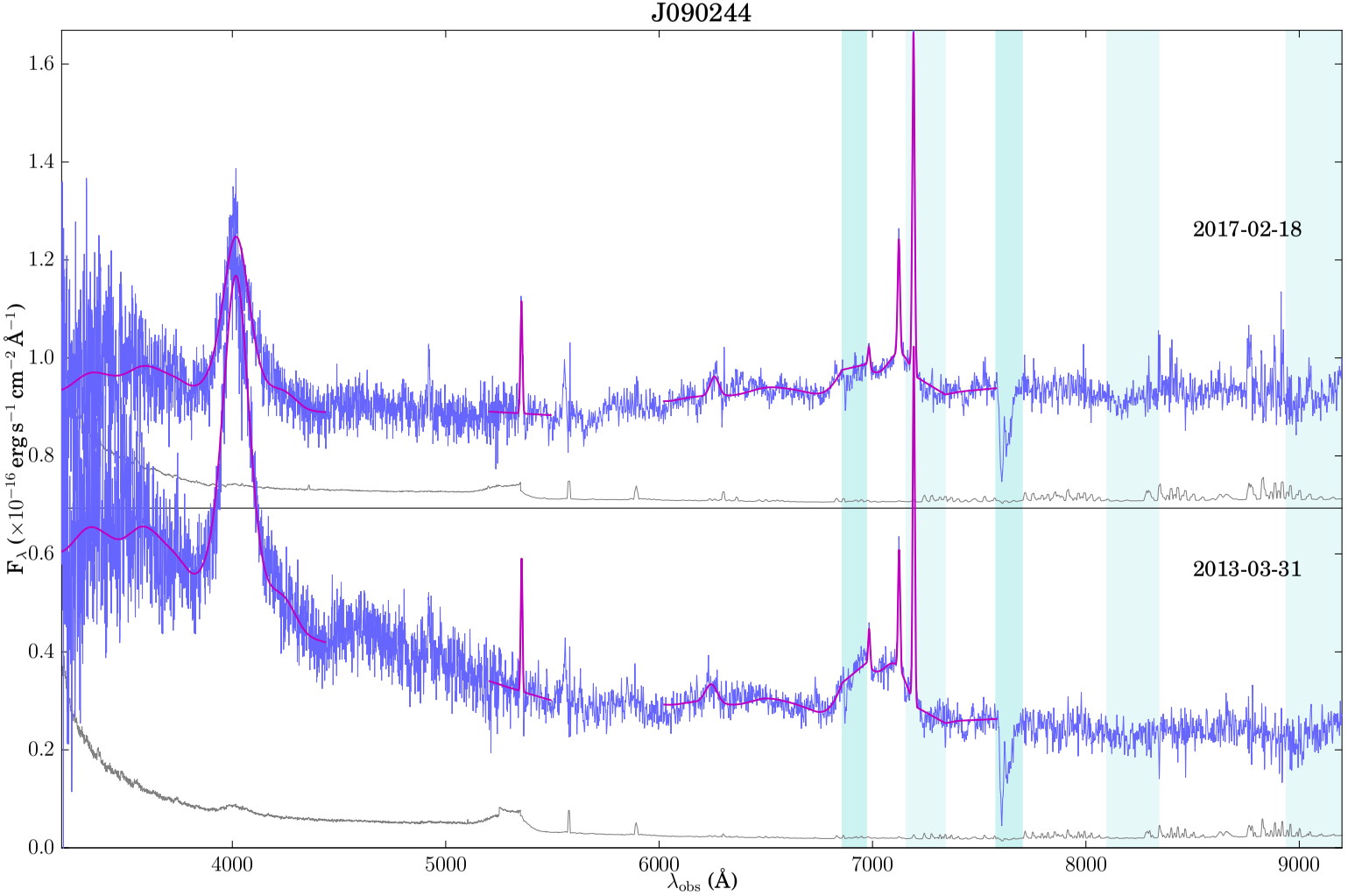
J090244
2017-02-18
2013-03-31
F_λ ($\times 10^{-16}$ erg s^{-1} cm^{-2} Å^{-1})
λ_{obs} (Å)
0.0
0.2
0.4
0.6
0.8
1.0
1.2
1.4
1.6
4000
5000
6000
7000
8000
9000

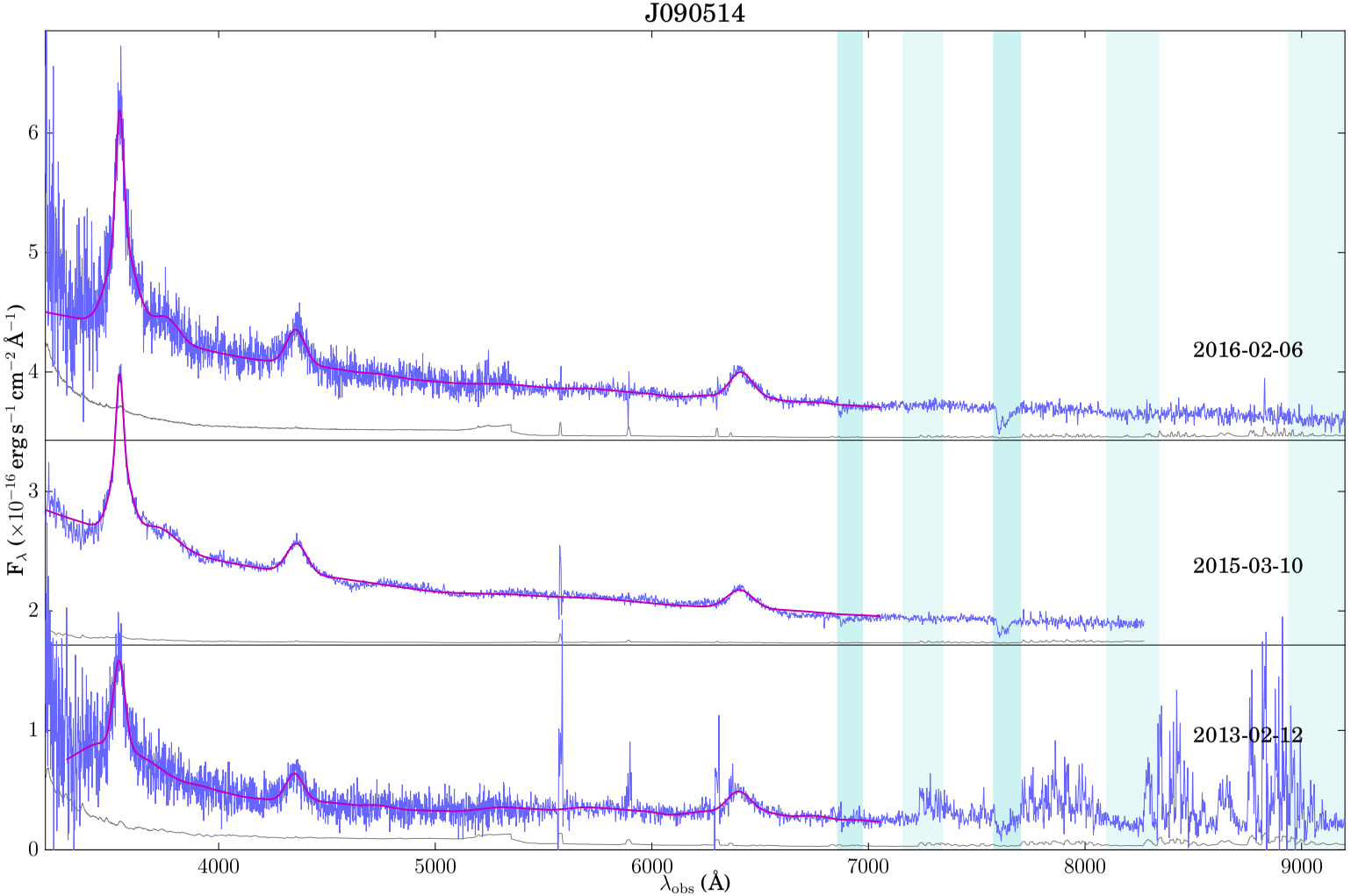
J090514
2016-02-06
2015-03-10
2013-02-12
F_λ ($\times 10^{-16}$ erg s^{-1} cm^{-2} Å^{-1})
λ_{obs} (Å)
0
1
2
3
4
5
6
4000
5000
6000
7000
8000
9000

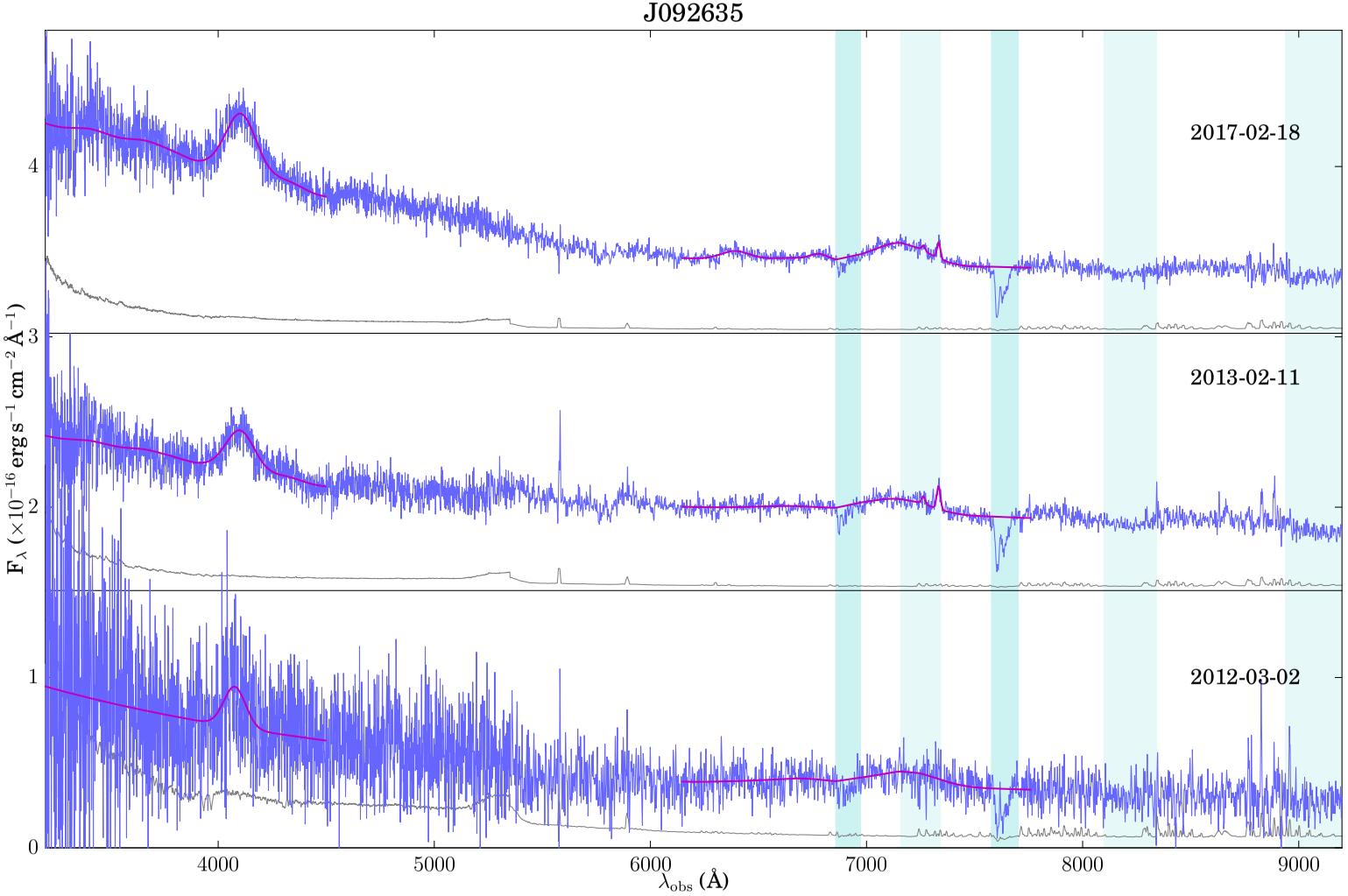
J092635
2017-02-18
2013-02-11
2012-03-02
F_λ ($\times 10^{-16}$ erg s^{-1} cm^{-2} Å^{-1})
λ_{obs} (Å)
0
1
2
3
4
4000
5000
6000
7000
8000
9000

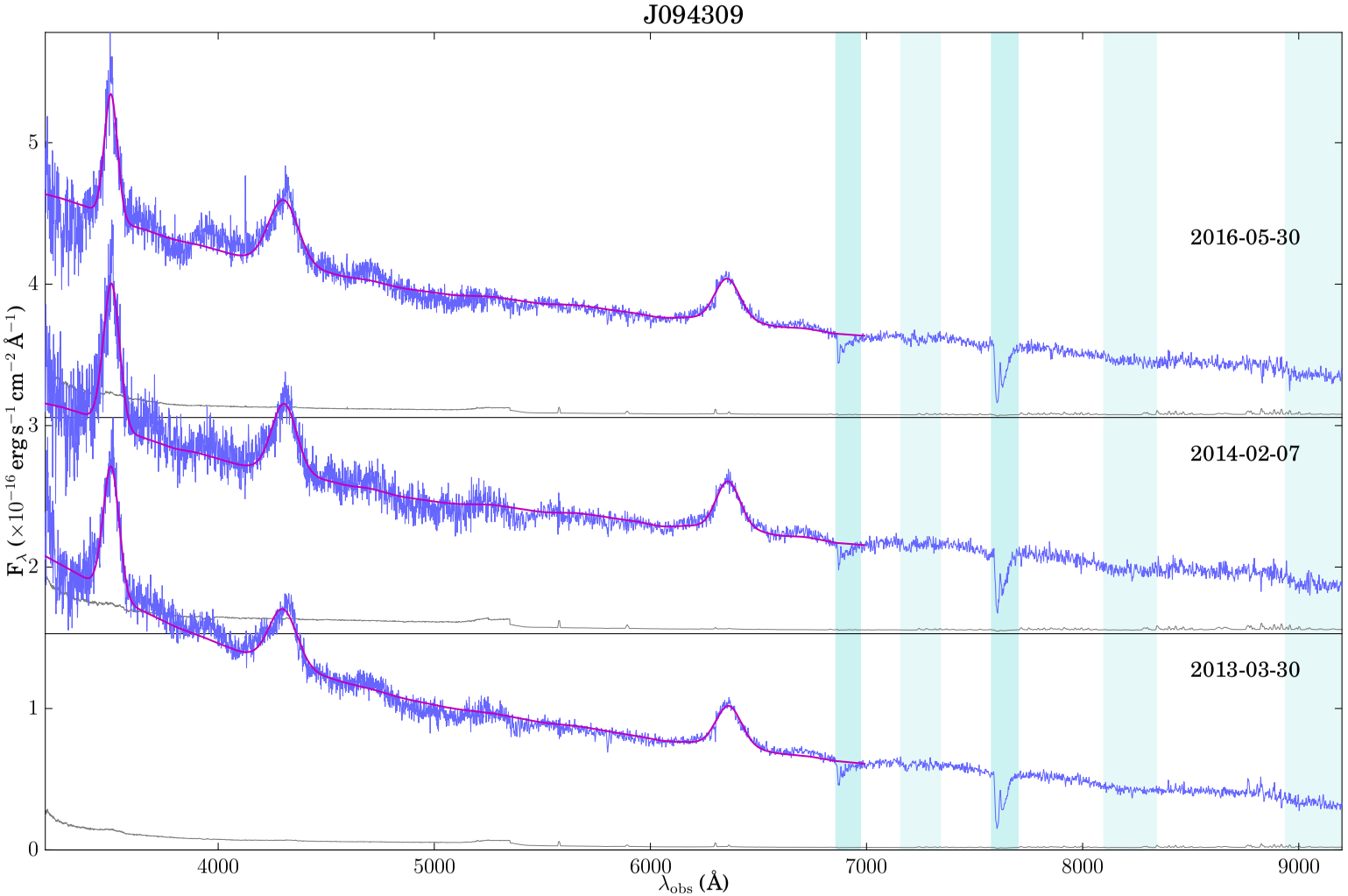
J094309
2016-05-30
2014-02-07
2013-03-30
F_λ ($\times 10^{-16}$ erg s^{-1} cm^{-2} Å^{-1})
λ_{obs} (Å)
0
1
2
3
4
5
4000
5000
6000
7000
8000
9000

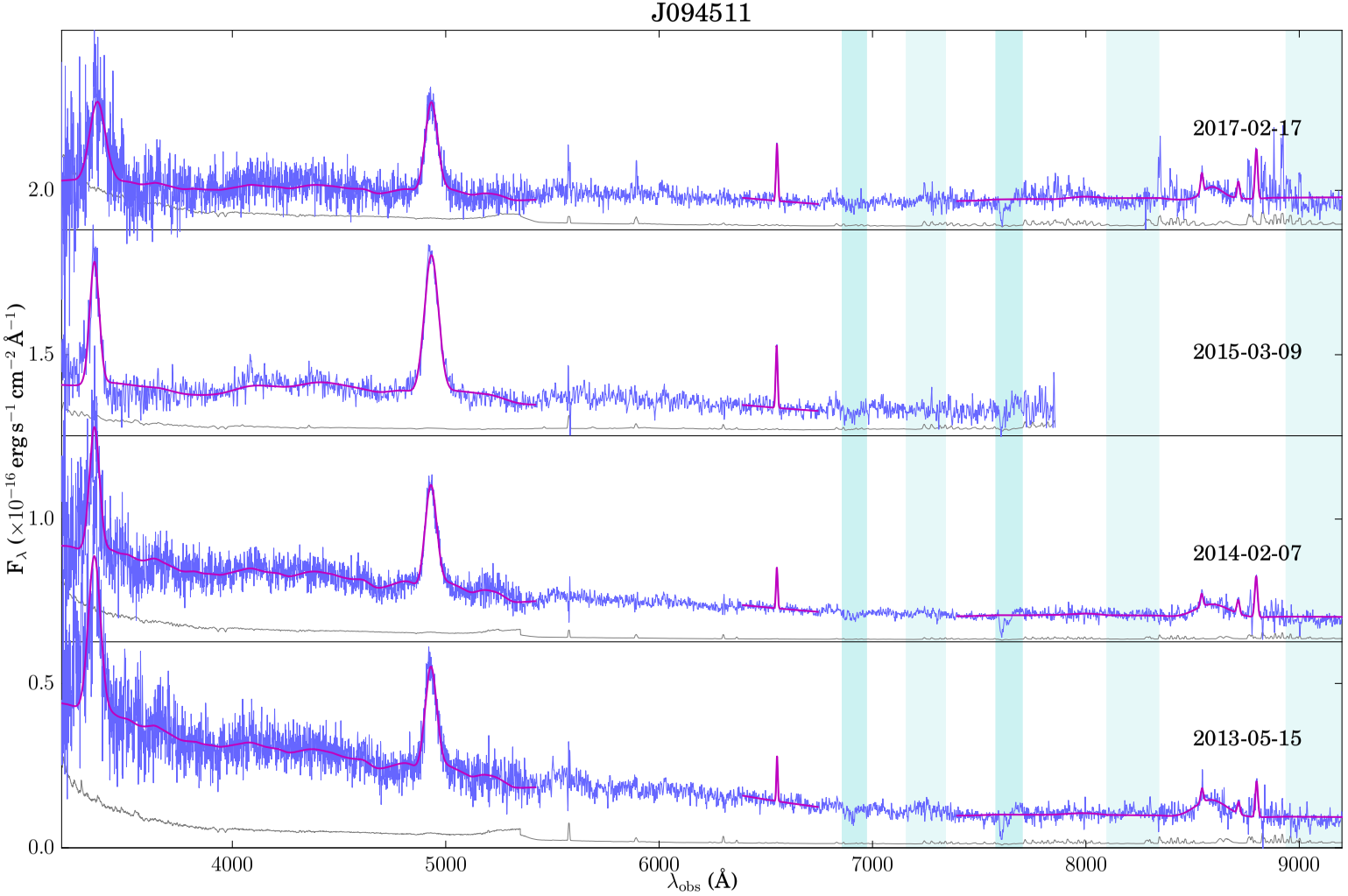
J094511
2017-02-17
2015-03-09
2014-02-07
2013-05-15
F_λ ($\times 10^{-16}$ erg s^{-1} cm^{-2} Å^{-1})
λ_{obs} (Å)
0.0
0.5
1.0
1.5
2.0
4000
5000
6000
7000
8000
9000

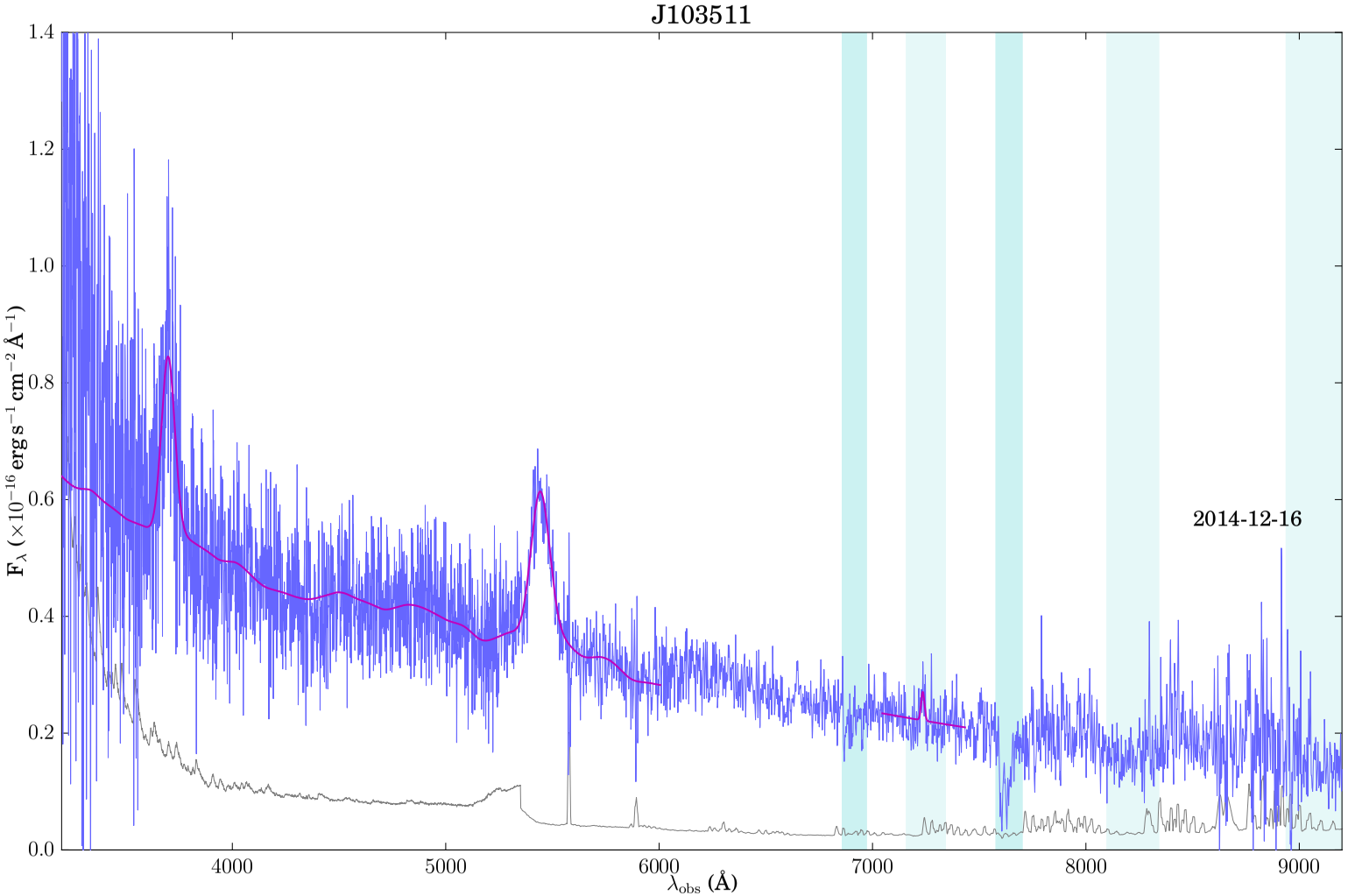
J103511
2014-12-16
F_λ ($\times 10^{-16}$ erg s^{-1} cm^{-2} Å^{-1})
λ_{obs} (Å)
0.0
0.2
0.4
0.6
0.8
1.0
1.2
1.4
4000
5000
6000
7000
8000
9000

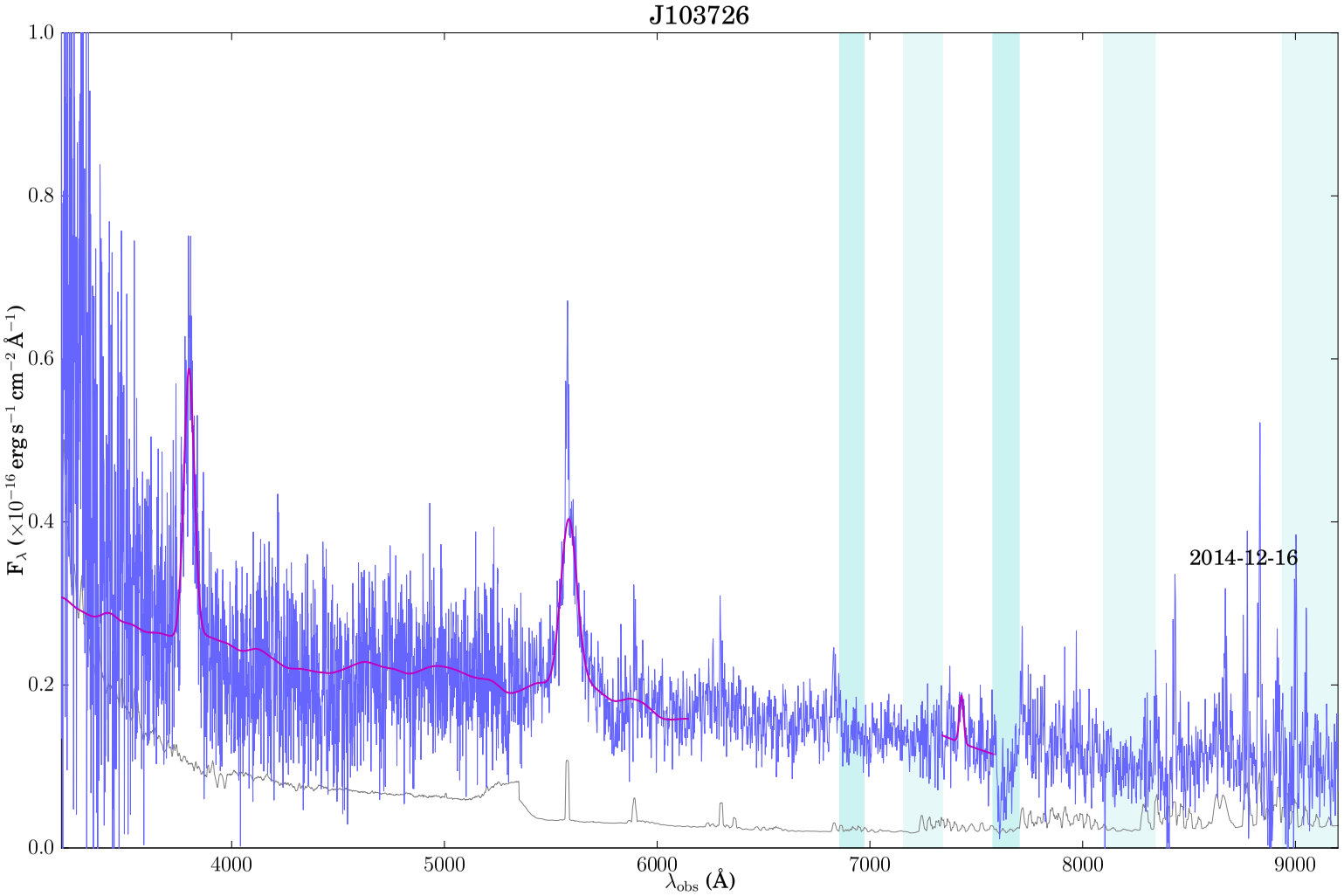
J103726
2014-12-16
F_λ ($\times 10^{-16}$ erg s^{-1} cm^{-2} Å^{-1})
λ_{obs} (Å)
0.0
0.2
0.4
0.6
0.8
1.0
4000
5000
6000
7000
8000
9000

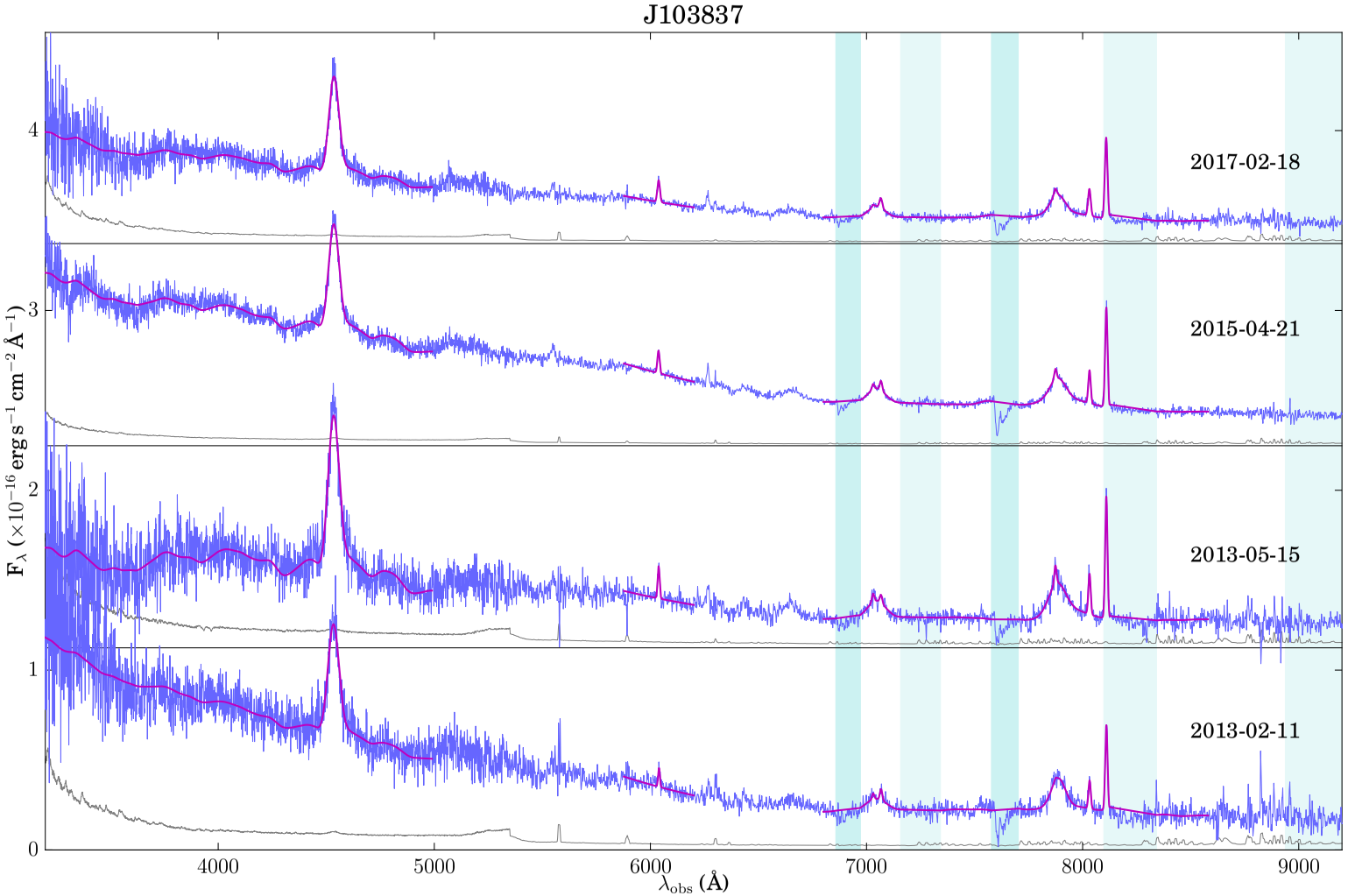
J103837
2017-02-18
2015-04-21
2013-05-15
2013-02-11
F_λ ($\times 10^{-16}$ erg s^{-1} cm^{-2} Å^{-1})
λ_{obs} (Å)
0
1
2
3
4
4000
5000
6000
7000
8000
9000

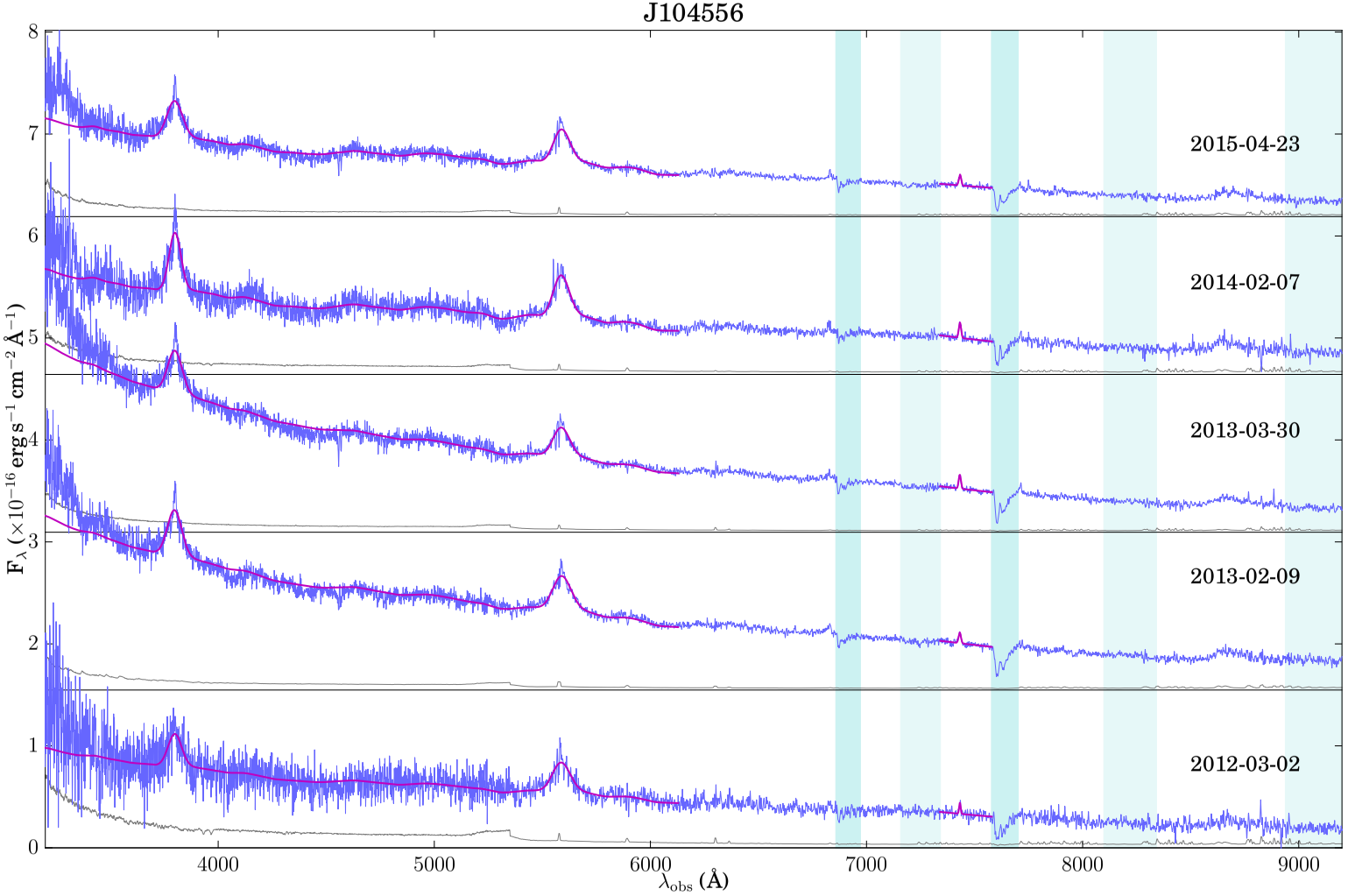
J104556
2015-04-23
2014-02-07
2013-03-30
2013-02-09
2012-03-02
F_λ ($\times 10^{-16}$ erg s^{-1} cm^{-2} Å^{-1})
λ_{obs} (Å)
0
1
2
3
4
5
6
7
8
4000
5000
6000
7000
8000
9000

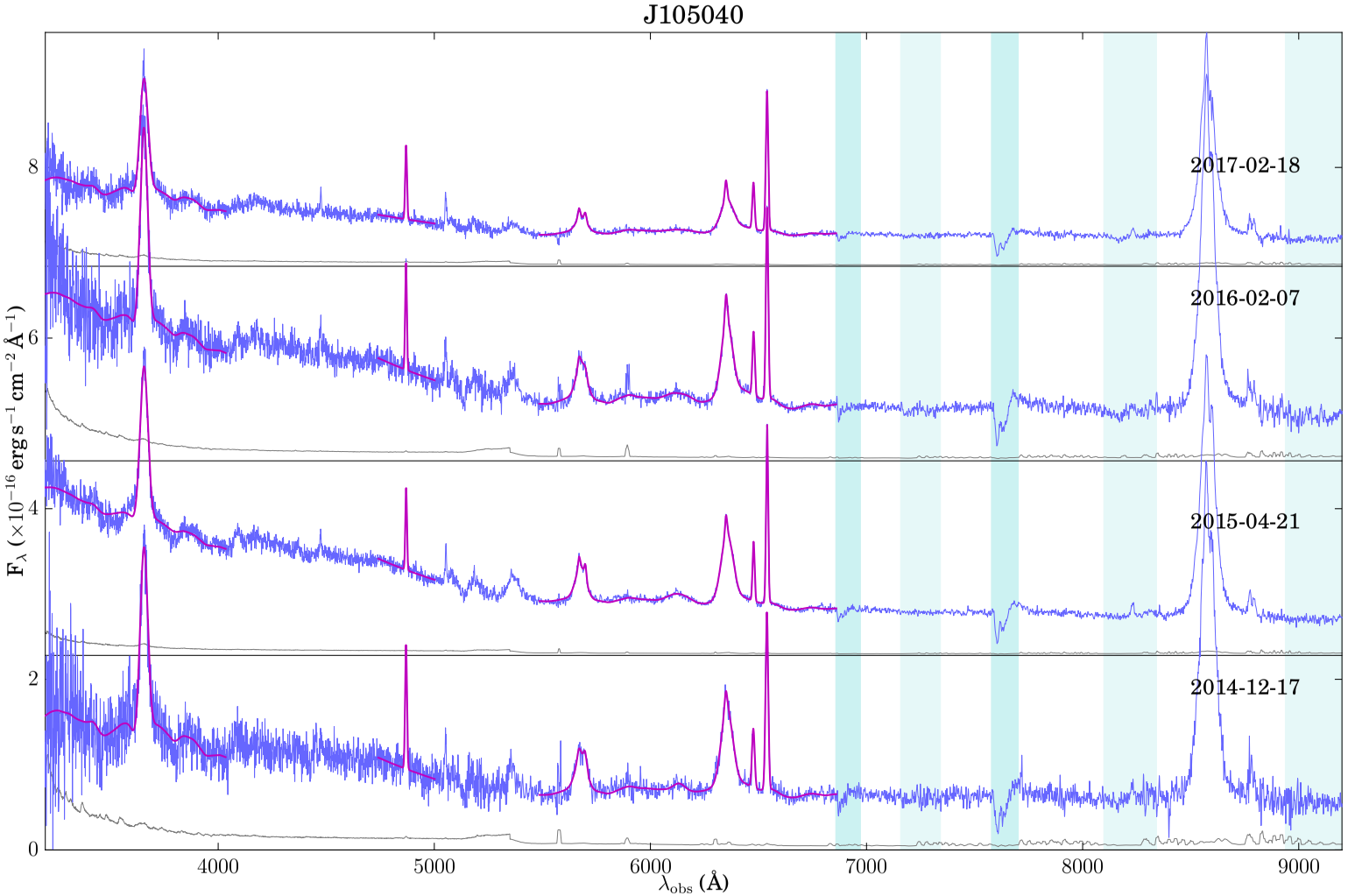
J105040
2017-02-18
2016-02-07
2015-04-21
2014-12-17
F_λ ($\times 10^{-16}$ erg s^{-1} cm^{-2} Å^{-1})
λ_{obs} (Å)
0
2
4
6
8
4000
5000
6000
7000
8000
9000

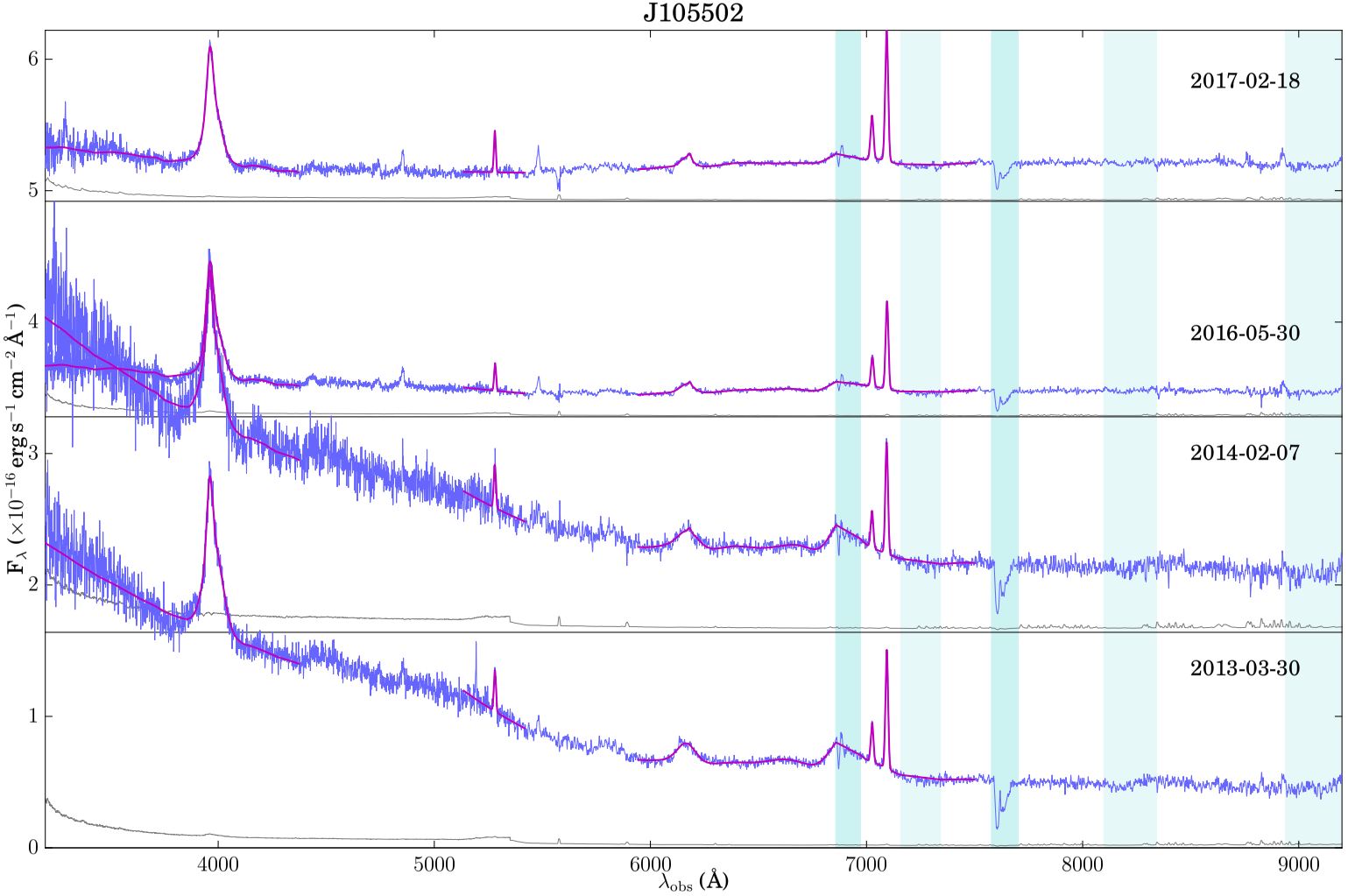
J105502
2017-02-18
2016-05-30
2014-02-07
2013-03-30
F_λ ($\times 10^{-16}$ erg s^{-1} cm^{-2} Å^{-1})
λ_{obs} (Å)
0
1
2
3
4
5
6
4000
5000
6000
7000
8000
9000

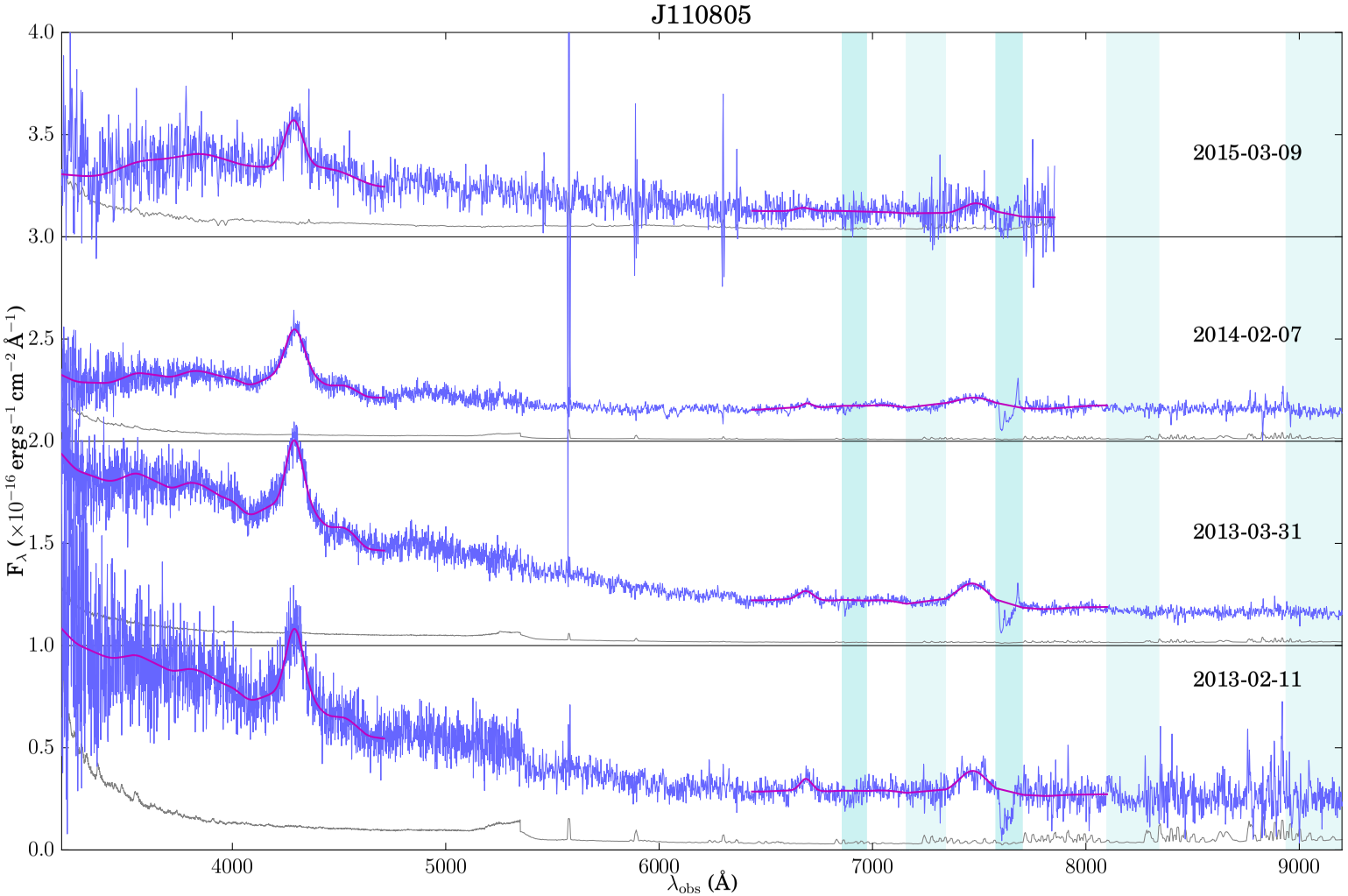
J110805
2015-03-09
2014-02-07
2013-03-31
2013-02-11
F_λ ($\times 10^{-16}$ ergs s^{-1} cm^{-2} Å^{-1})
λ_{obs} (Å)
4.0
3.5
3.0
2.5
2.0
1.5
1.0
0.5
0.0
4000
5000
6000
7000
8000
9000

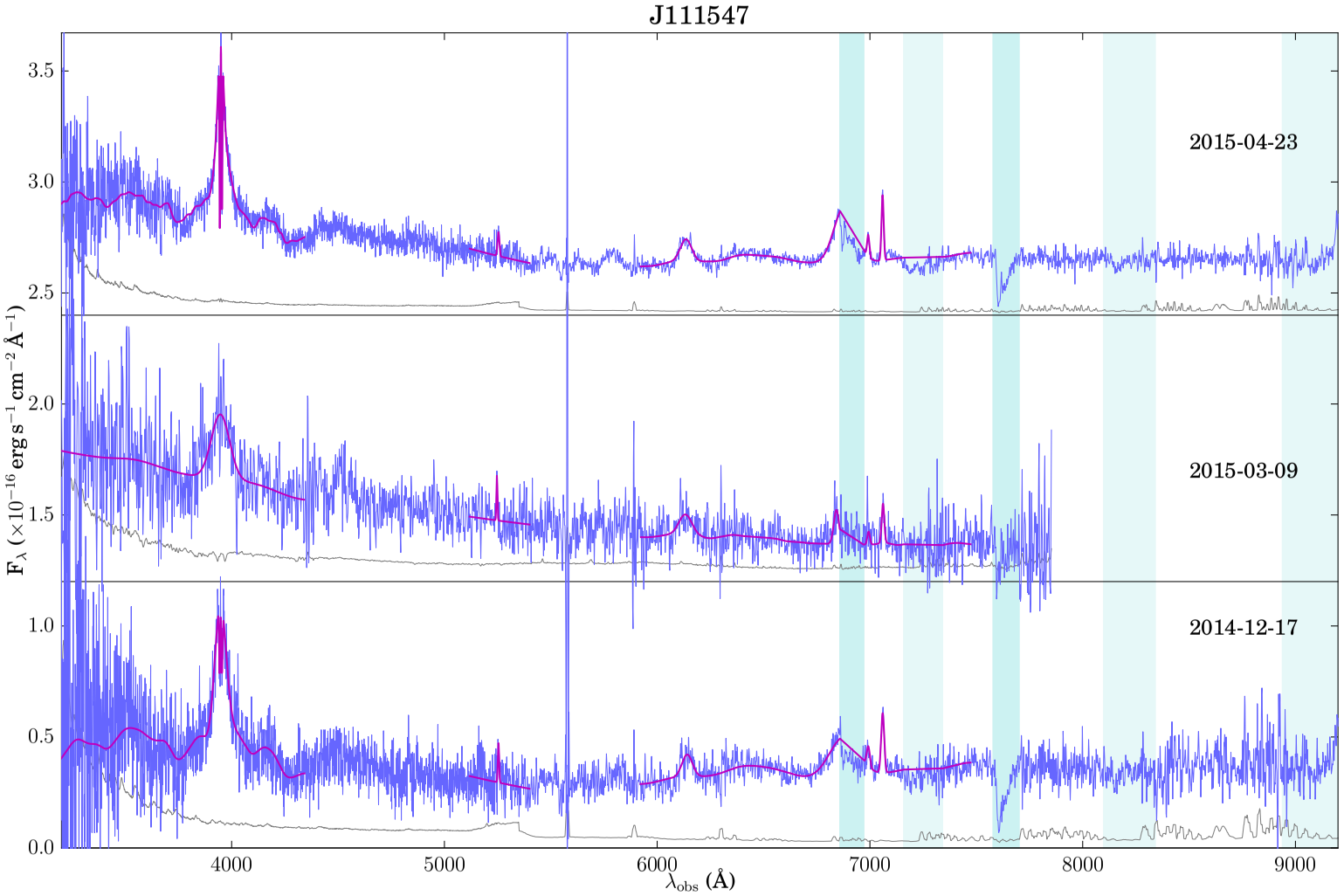
J111547
2015-04-23
2015-03-09
2014-12-17
F_λ ($\times 10^{-16}$ erg s^{-1} cm^{-2} Å^{-1})
λ_{obs} (Å)
0.0
0.5
1.0
1.5
2.0
2.5
3.0
3.5
4000
5000
6000
7000
8000
9000

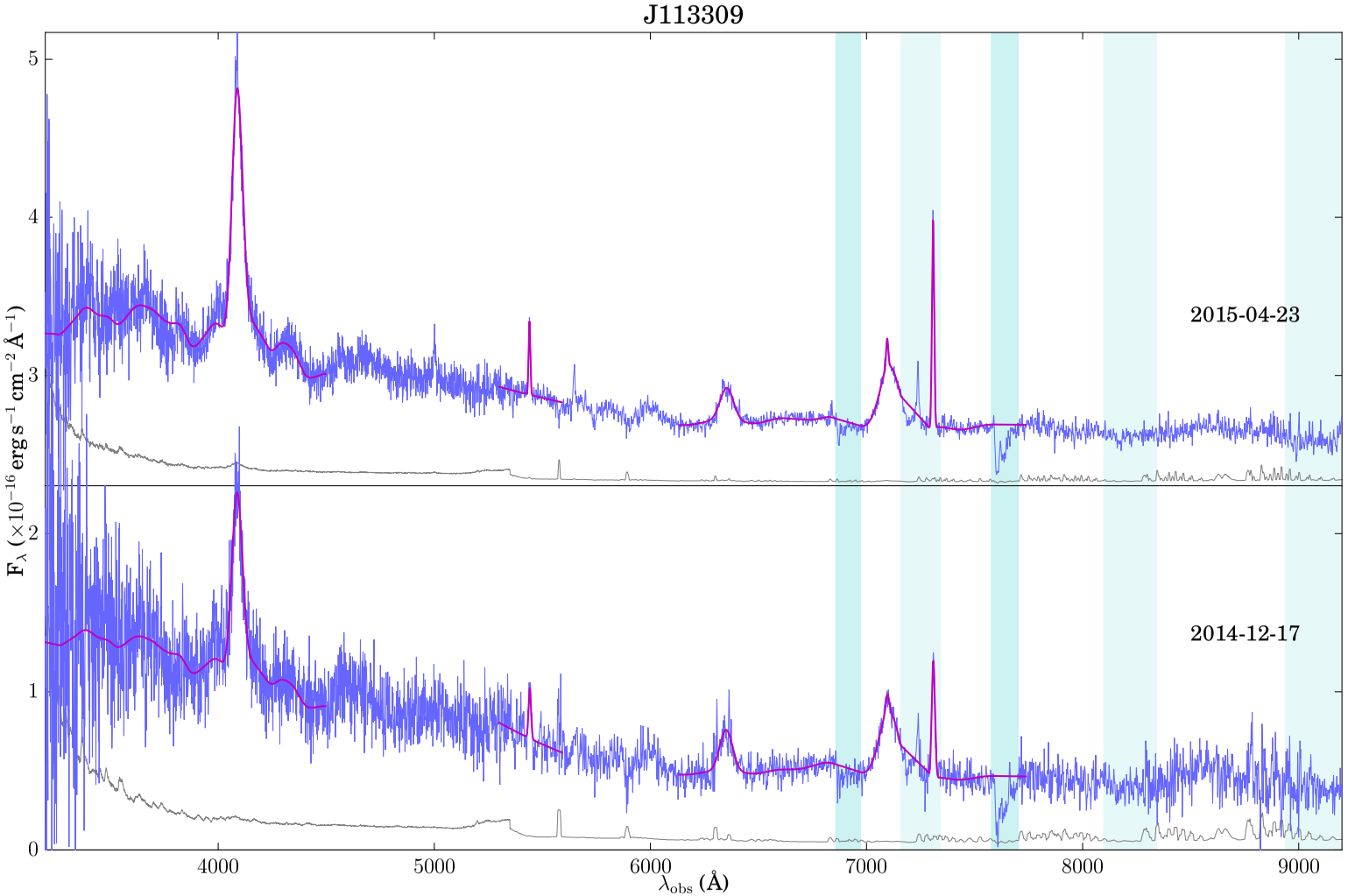
J113309
2015-04-23
2014-12-17
F_λ ($\times 10^{-16}$ erg s^{-1} cm^{-2} Å^{-1})
λ_{obs} (Å)
0
1
2
3
4
5
4000
5000
6000
7000
8000
9000

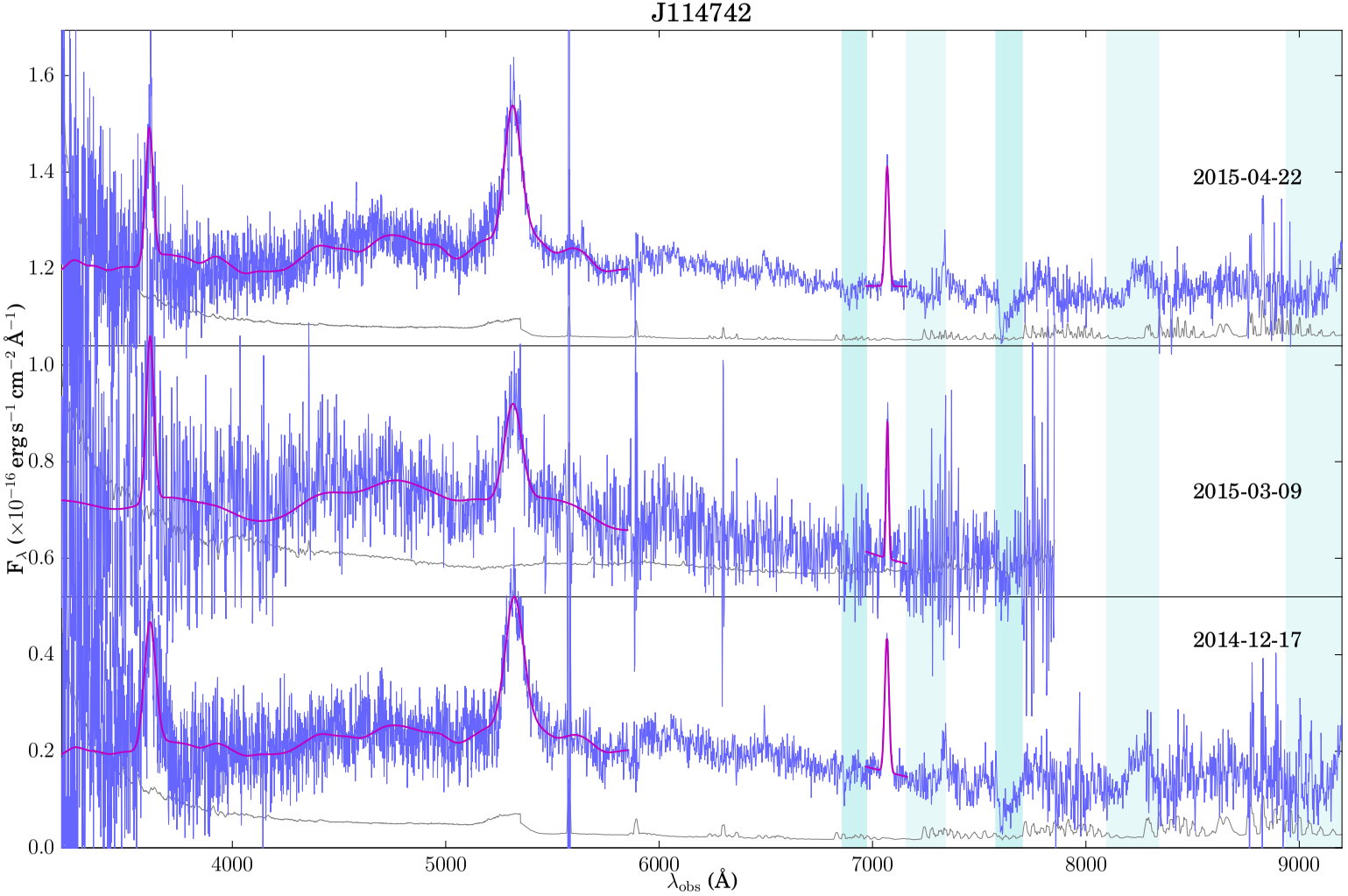
J114742
2015-04-22
2015-03-09
2014-12-17
F_λ ($\times 10^{-16}$ erg s^{-1} cm^{-2} Å^{-1})
λ_{obs} (Å)
0.0
0.2
0.4
0.6
0.8
1.0
1.2
1.4
1.6
4000
5000
6000
7000
8000
9000

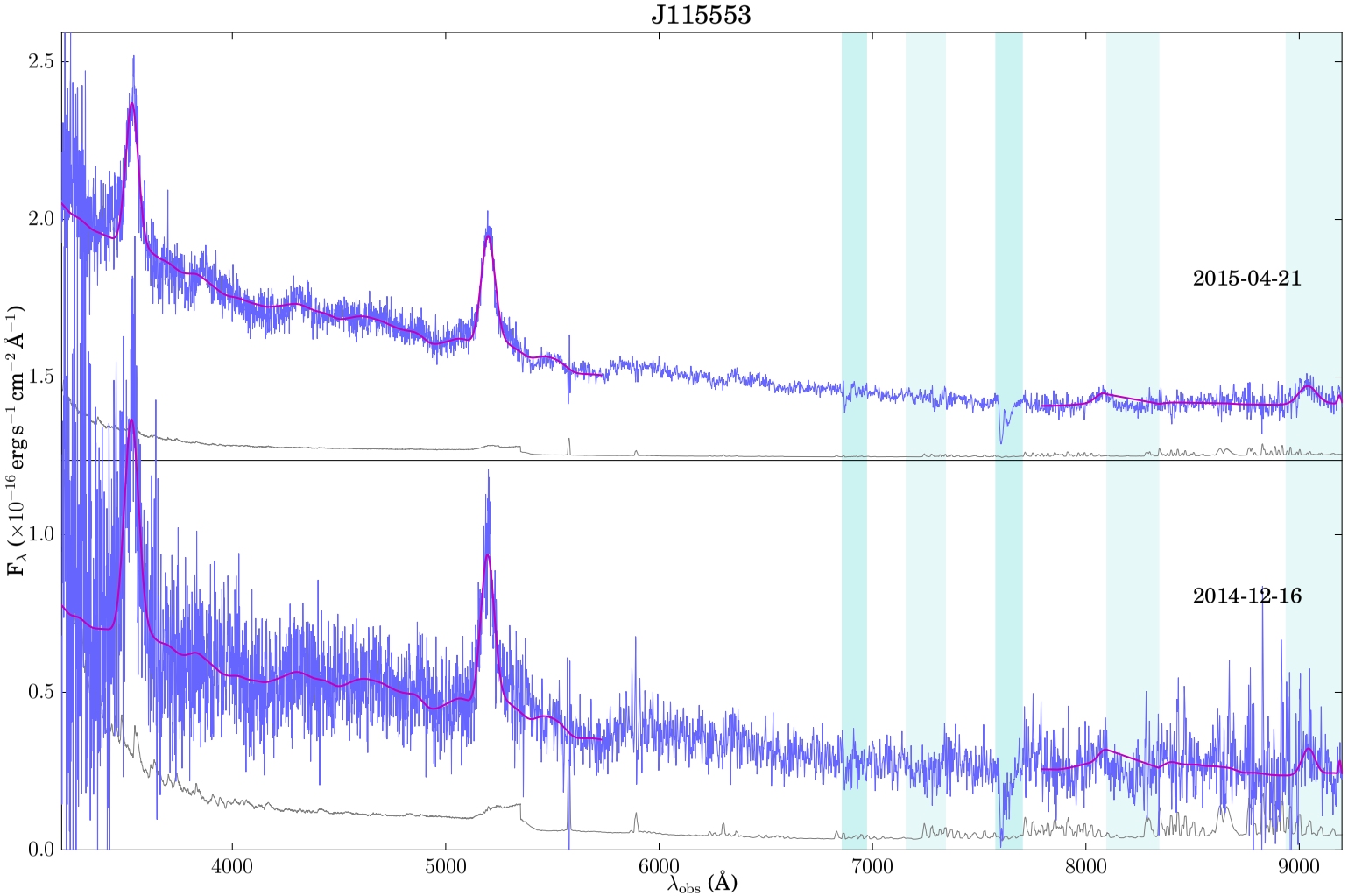
J115553
2015-04-21
2014-12-16
F_λ ($\times 10^{-16}$ erg s^{-1} cm^{-2} Å^{-1})
λ_{obs} (Å)
0.0
0.5
1.0
1.5
2.0
2.5
4000
5000
6000
7000
8000
9000

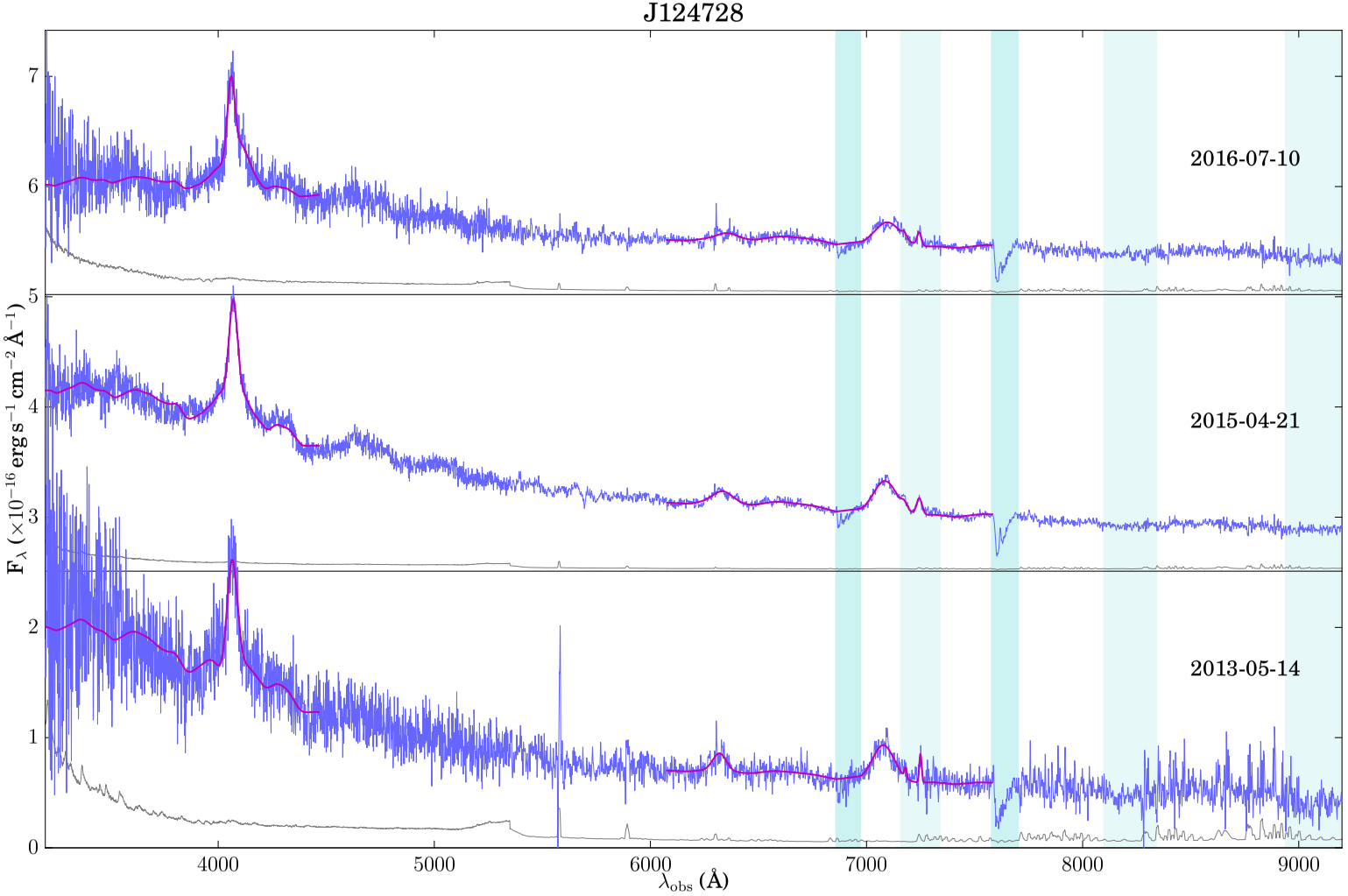
J124728
2016-07-10
2015-04-21
2013-05-14
F_λ ($\times 10^{-16}$ erg s^{-1} cm^{-2} Å^{-1})
λ_{obs} (Å)
0
1
2
3
4
5
6
7
4000
5000
6000
7000
8000
9000

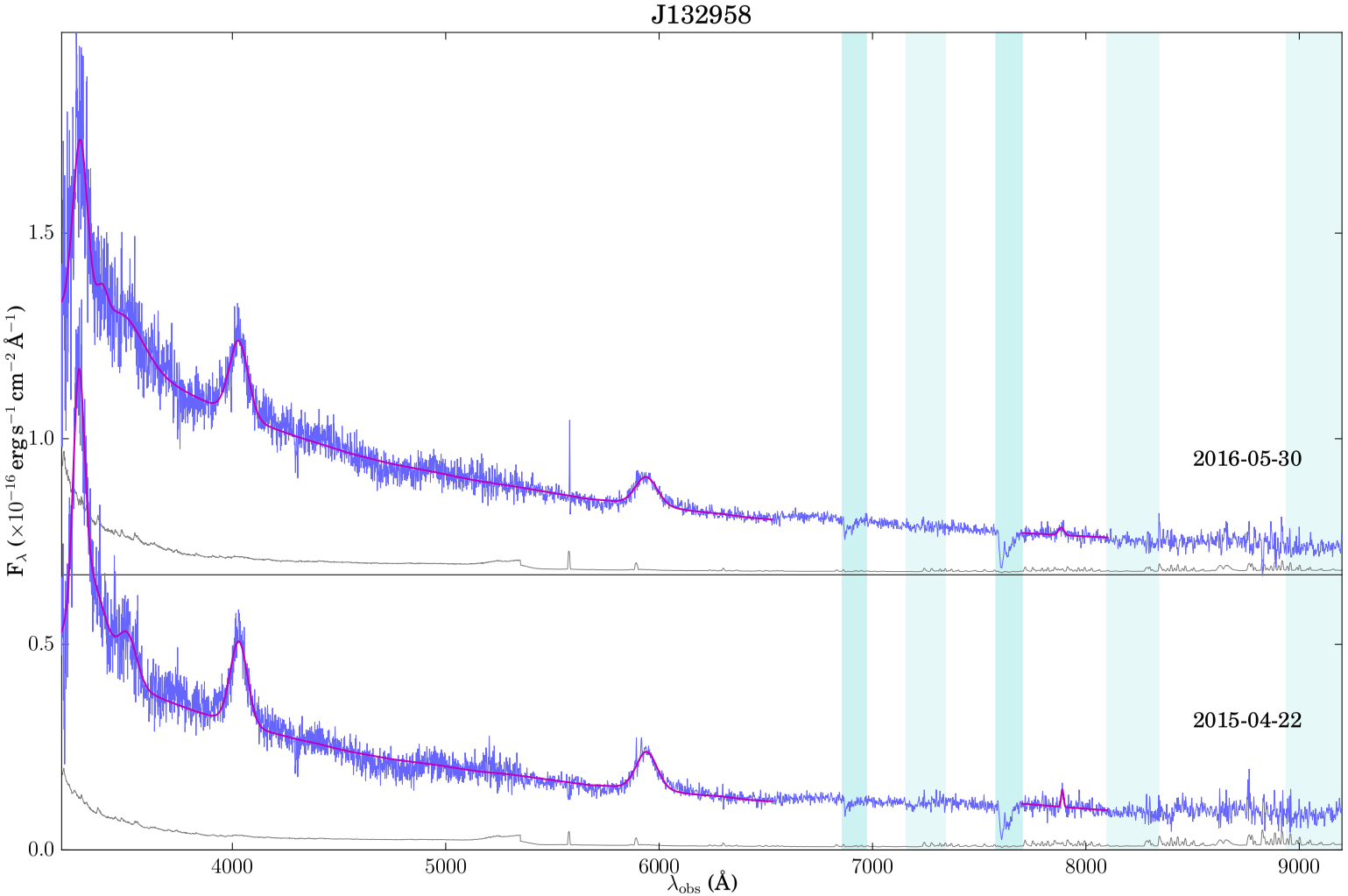
J132958
2016-05-30
2015-04-22
F_λ ($\times 10^{-16}$ ergs^{-1} cm^{-2} Å^{-1})
λ_{obs} (Å)
0.0
0.5
1.0
1.5
4000
5000
6000
7000
8000
9000

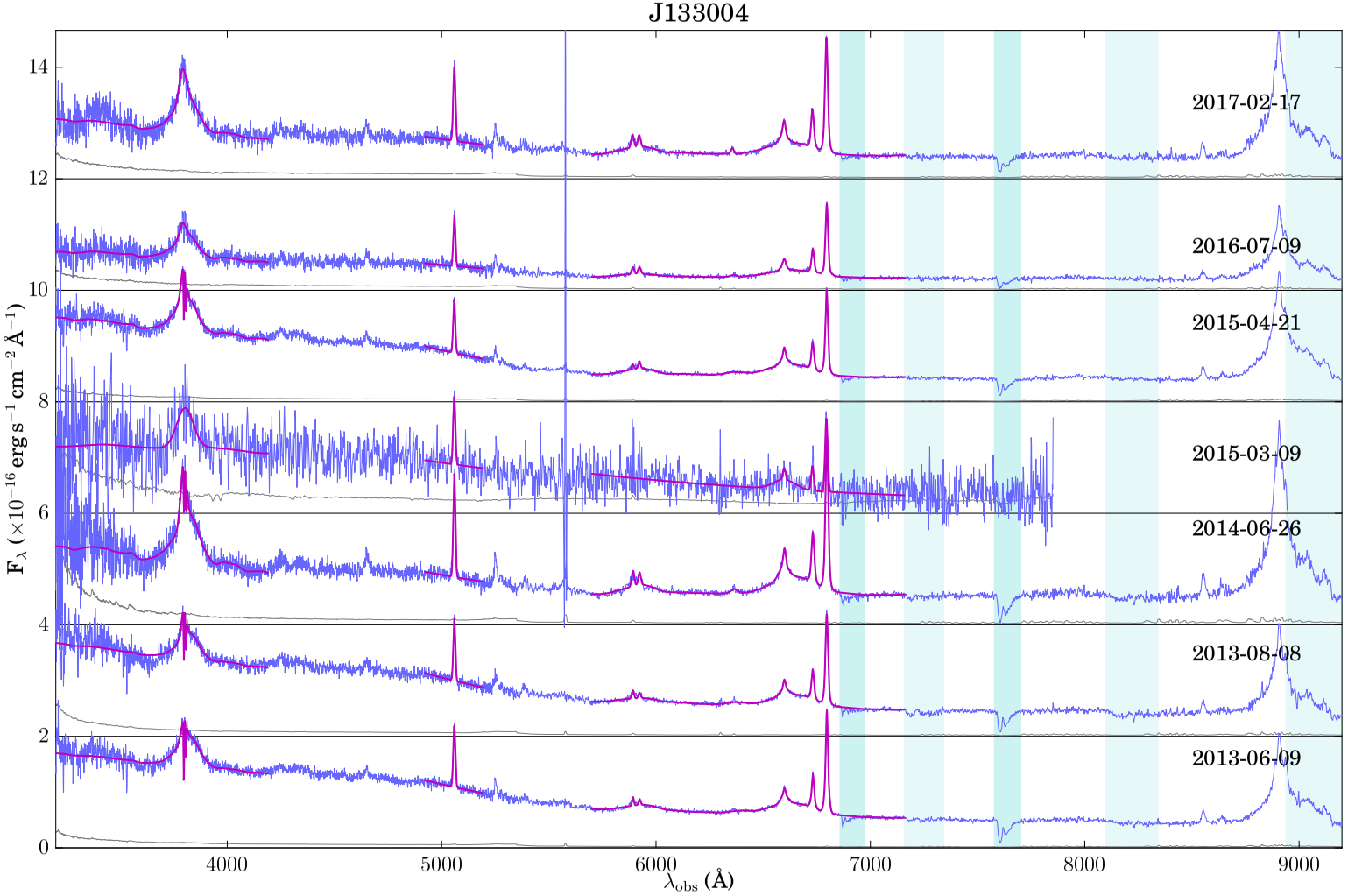
J133004
2017-02-17
2016-07-09
2015-04-21
2015-03-09
2014-06-26
2013-08-08
2013-06-09
F_λ ($\times 10^{-16}$ erg s^{-1} cm^{-2} Å^{-1})
λ_{obs} (Å)
0
2
4
6
8
10
12
14
4000
5000
6000
7000
8000
9000

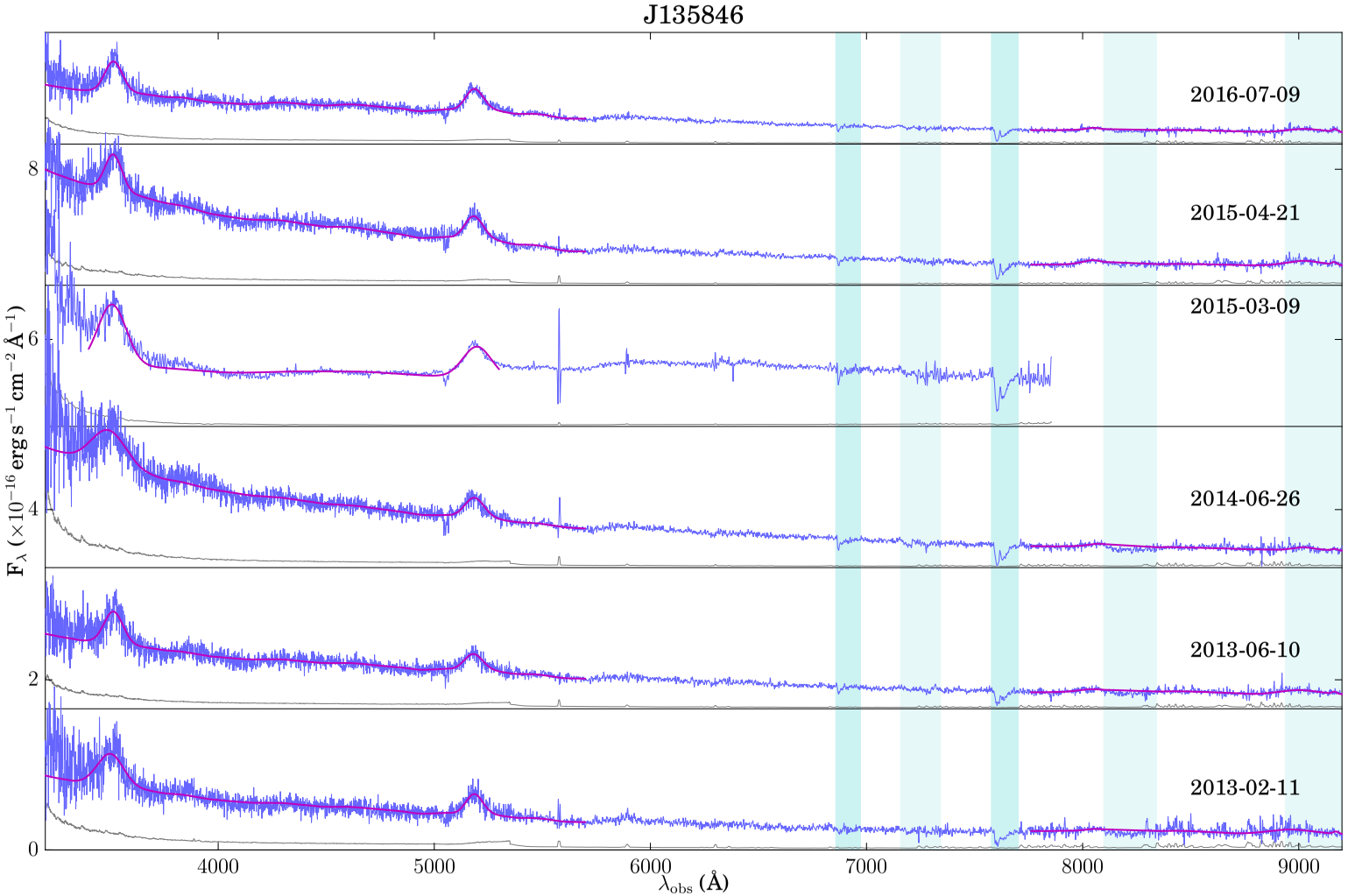
J135846
2016-07-09
2015-04-21
2015-03-09
2014-06-26
2013-06-10
2013-02-11
F_λ ($\times 10^{-16}$ erg s^{-1} cm^{-2} Å^{-1})
λ_{obs} (Å)
0
2
4
6
8
4000
5000
6000
7000
8000
9000

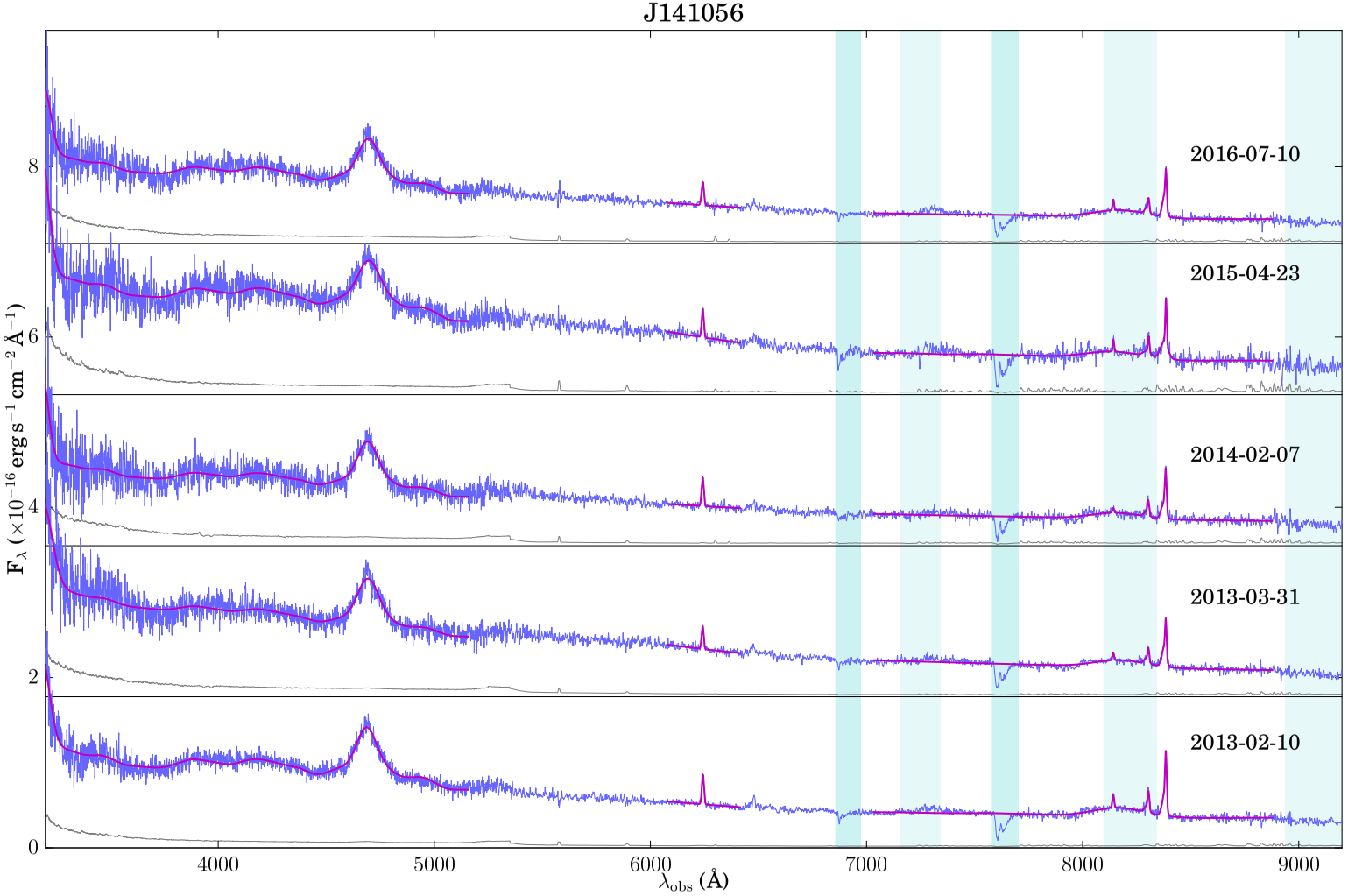
J141056
2016-07-10
2015-04-23
2014-02-07
2013-03-31
2013-02-10
F_λ ($\times 10^{-16}$ erg s^{-1} cm^{-2} Å^{-1})
λ_{obs} (Å)
0
2
4
6
8
4000
5000
6000
7000
8000
9000

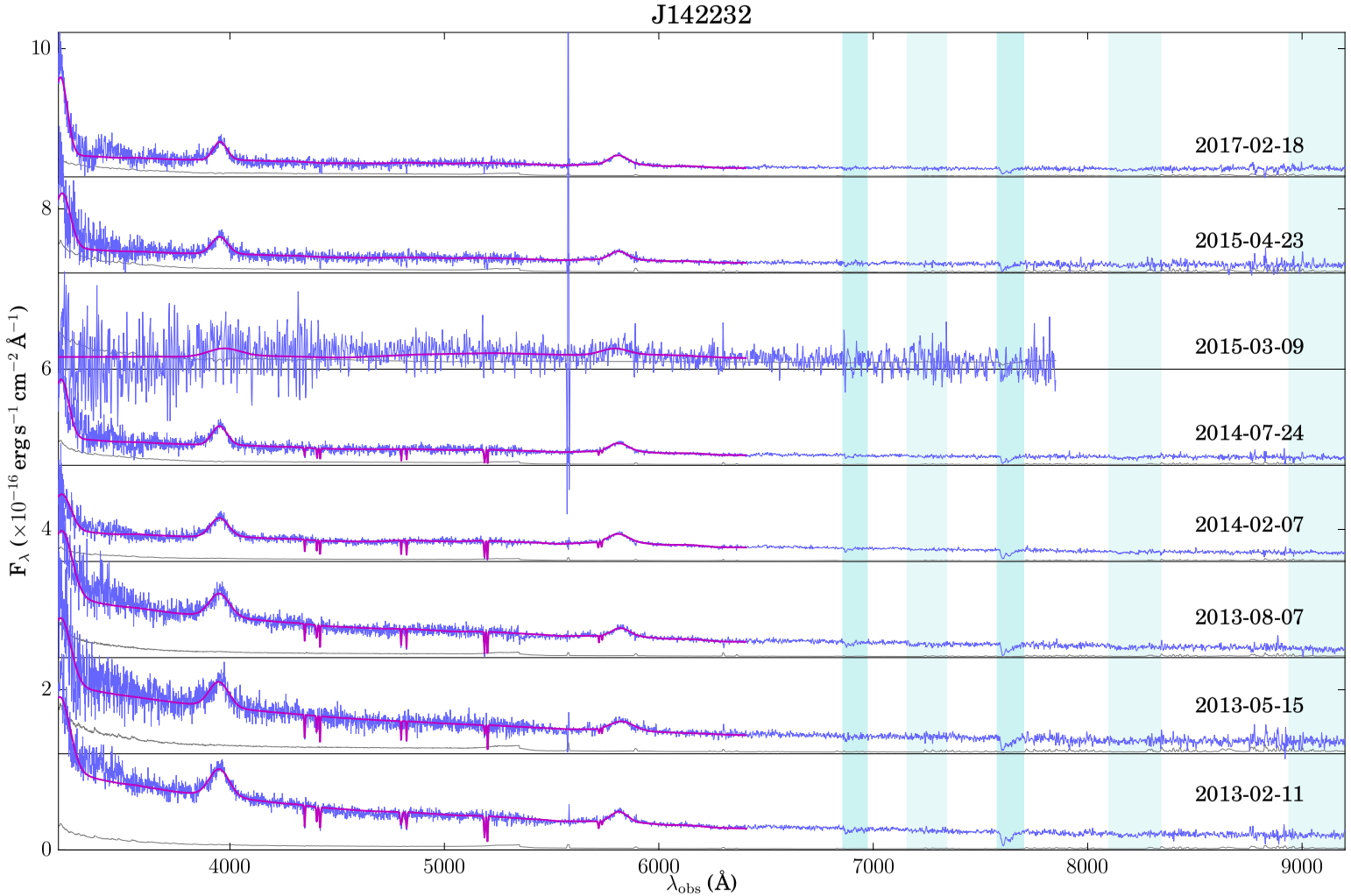
J142232
2017-02-18
2015-04-23
2015-03-09
2014-07-24
2014-02-07
2013-08-07
2013-05-15
2013-02-11
F_λ ($\times 10^{-16}$ erg s^{-1} cm^{-2} Å^{-1})
λ_{obs} (Å)
0
2
4
6
8
10
4000
5000
6000
7000
8000
9000

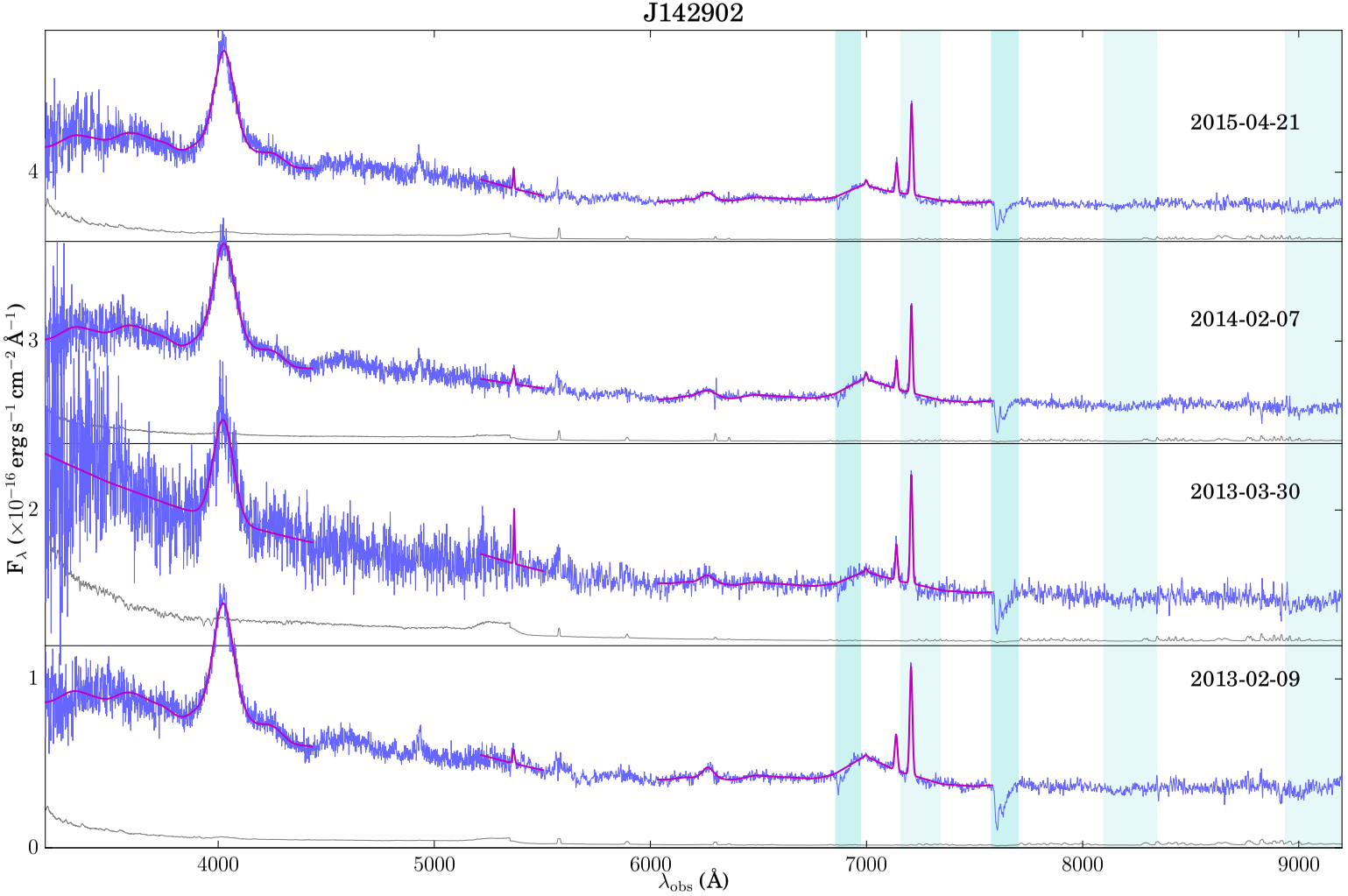
J142902
2015-04-21
2014-02-07
2013-03-30
2013-02-09
F_λ ($\times 10^{-16}$ erg s^{-1} cm^{-2} Å^{-1})
λ_{obs} (Å)
0
1
2
3
4
4000
5000
6000
7000
8000
9000

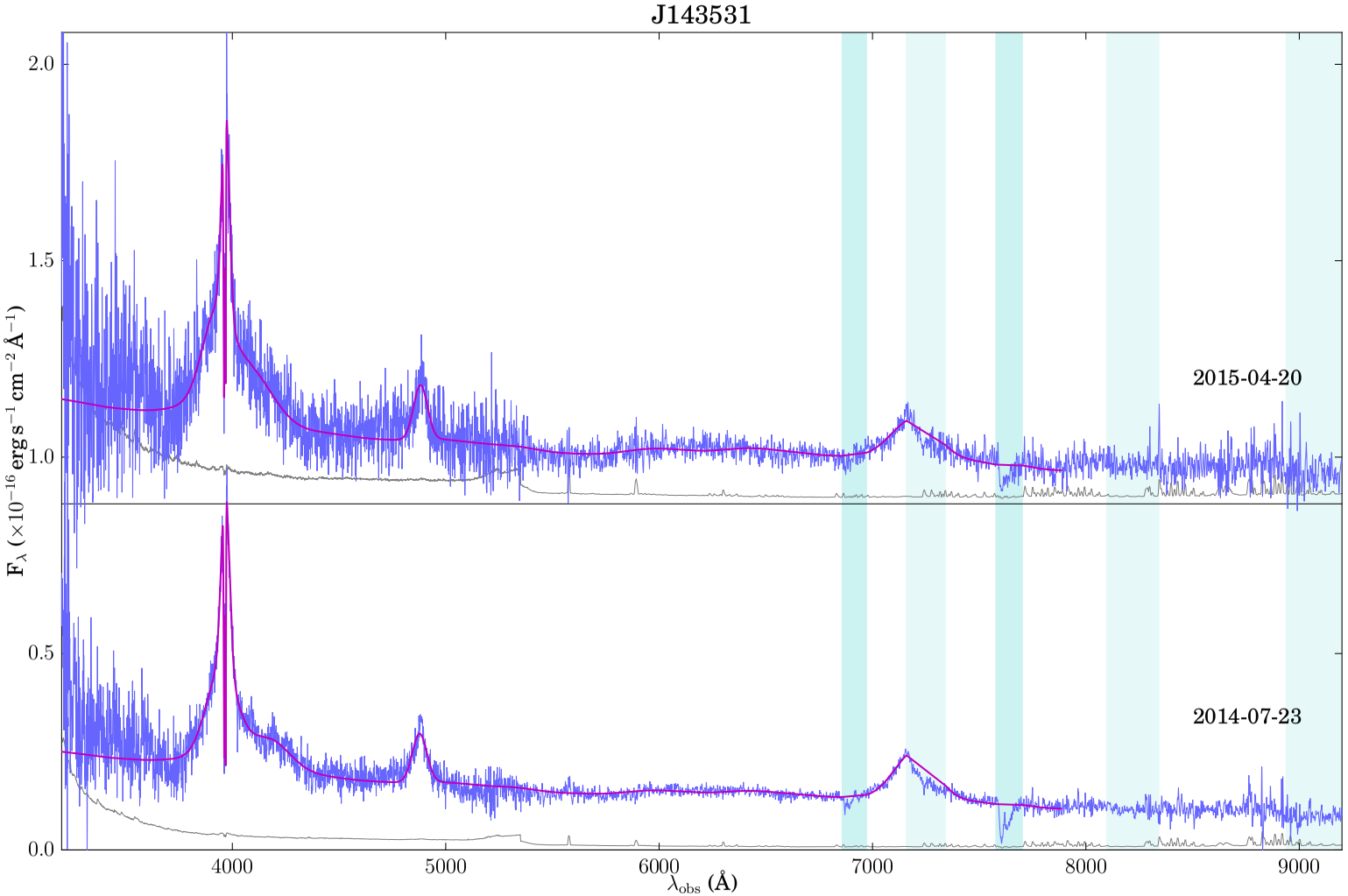
J143531
2015-04-20
2014-07-23
F_λ ($\times 10^{-16}$ erg s^{-1} cm^{-2} Å^{-1})
λ_{obs} (Å)
0.0
0.5
1.0
1.5
2.0
4000
5000
6000
7000
8000
9000

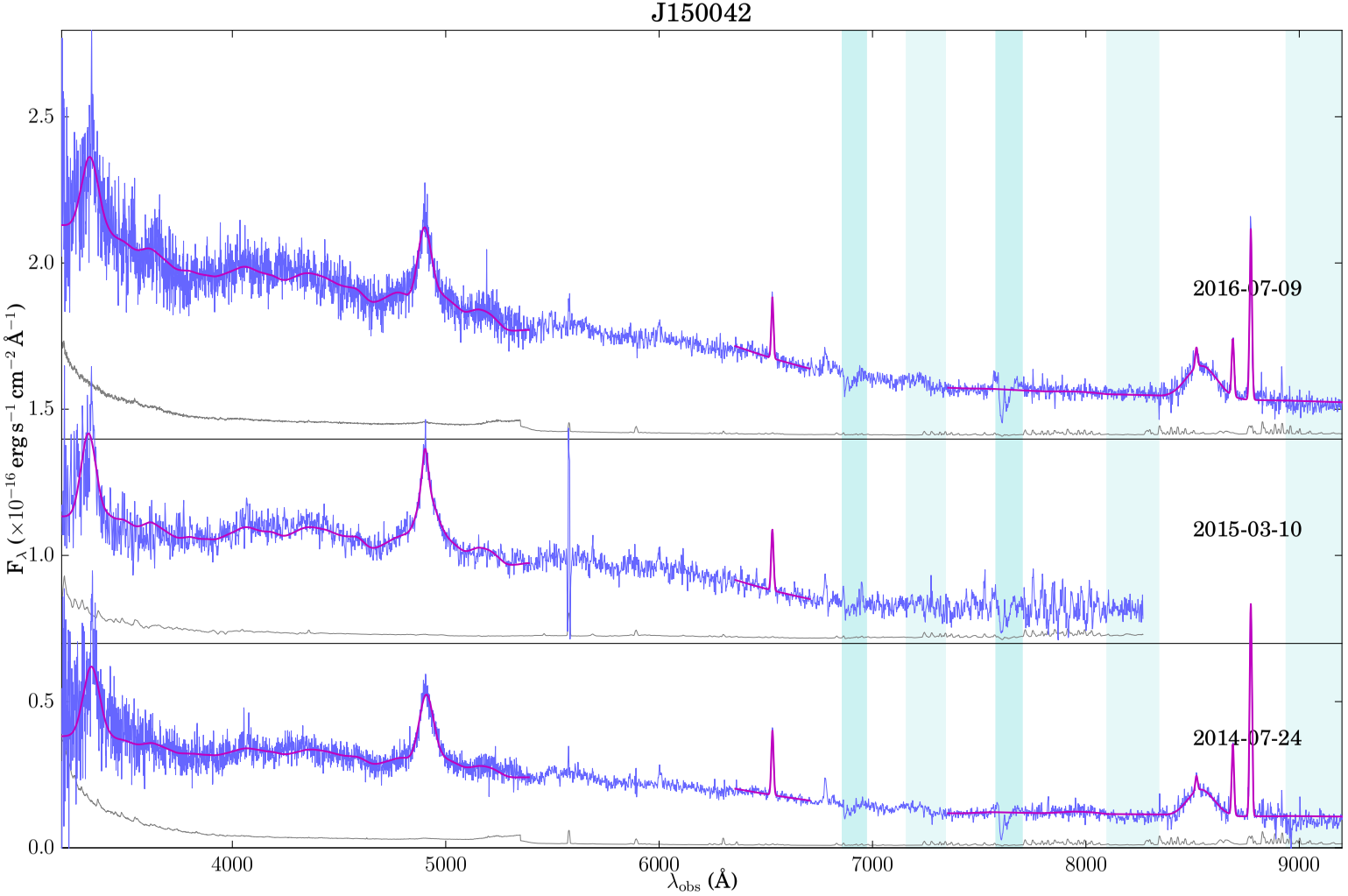
J150042
2016-07-09
2015-03-10
2014-07-24
F_λ ($\times 10^{-16}$ erg s^{-1} cm^{-2} Å^{-1})
λ_{obs} (Å)
0.0
0.5
1.0
1.5
2.0
2.5
4000
5000
6000
7000
8000
9000

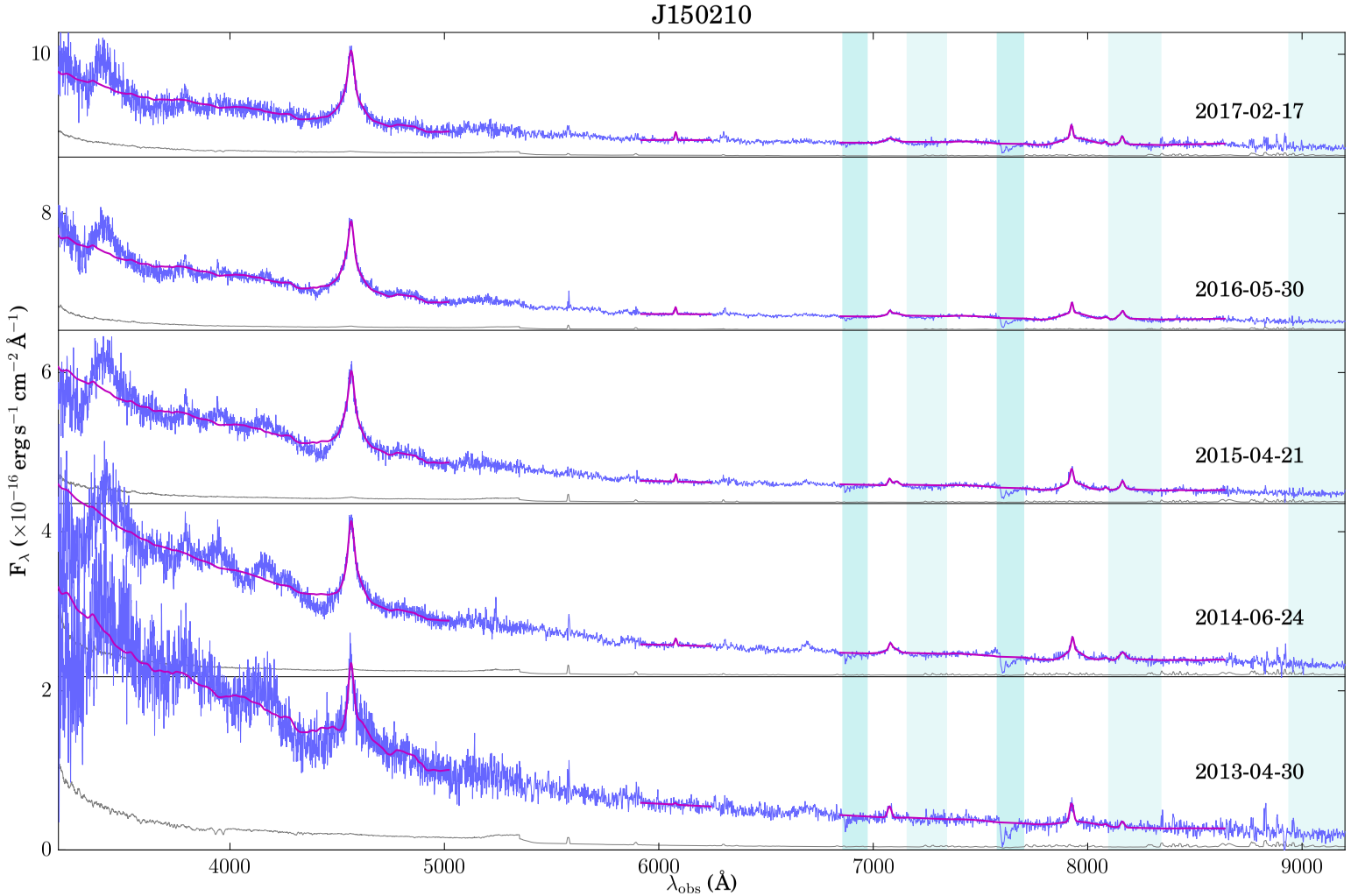
J150210
2017-02-17
2016-05-30
2015-04-21
2014-06-24
2013-04-30
F_λ ($\times 10^{-16}$ erg s^{-1} cm^{-2} Å^{-1})
λ_{obs} (Å)
0
2
4
6
8
10
4000
5000
6000
7000
8000
9000

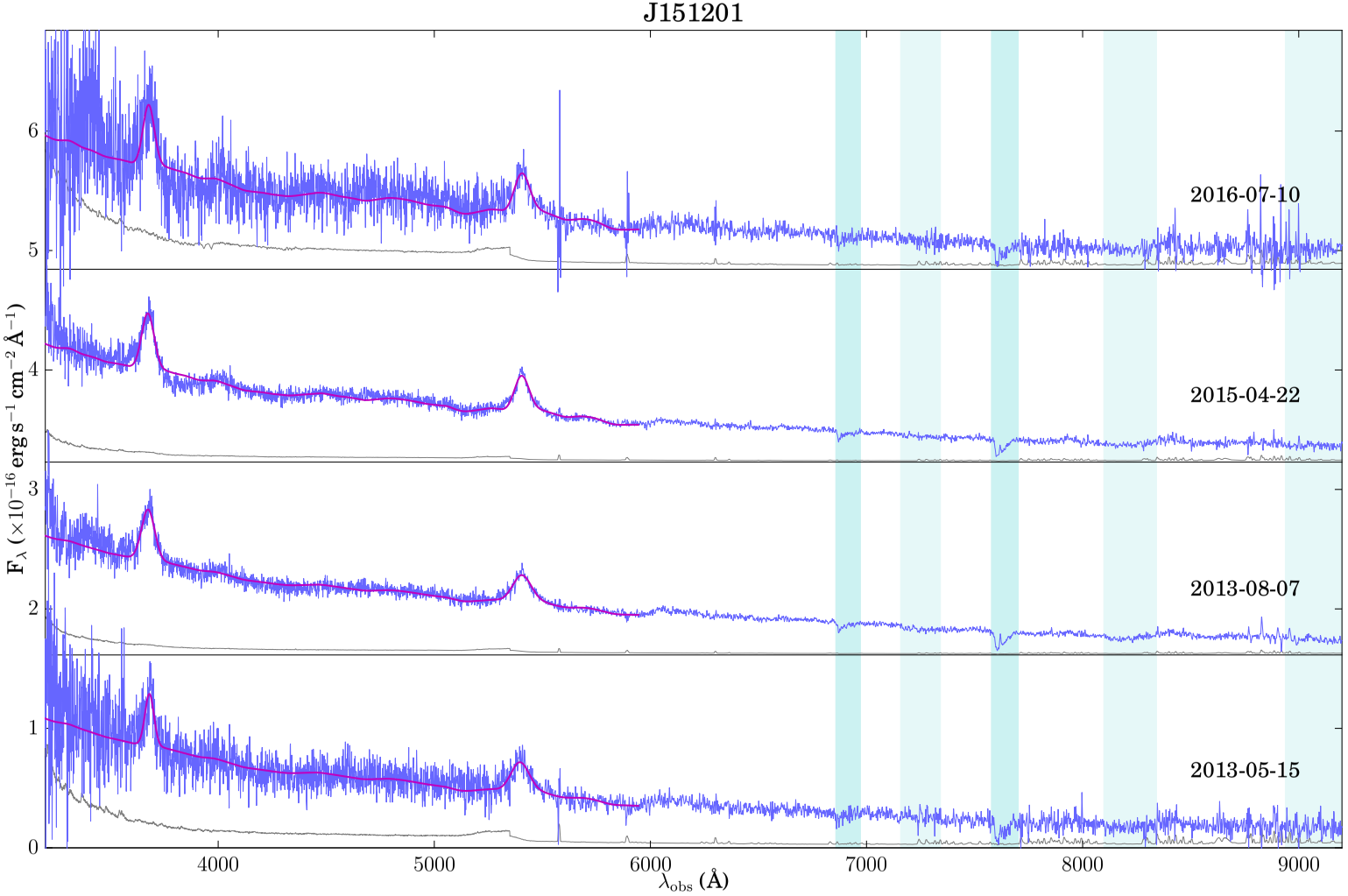
J151201
2016-07-10
2015-04-22
2013-08-07
2013-05-15
F_λ ($\times 10^{-16}$ erg s^{-1} cm^{-2} Å^{-1})
λ_{obs} (Å)
0
1
2
3
4
5
6
4000
5000
6000
7000
8000
9000

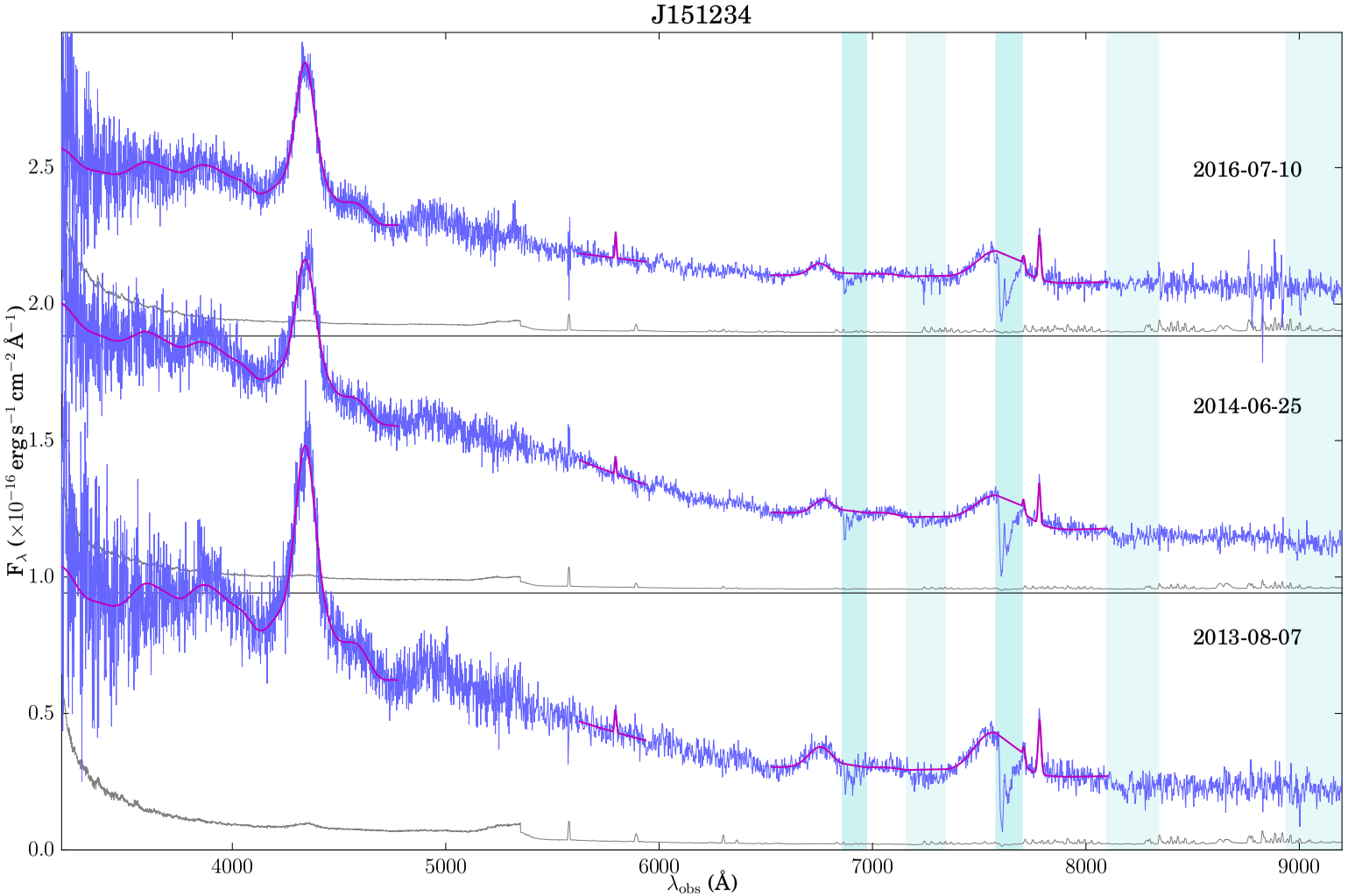
J151234
2016-07-10
2014-06-25
2013-08-07
F_λ ($\times 10^{-16}$ erg s^{-1} cm^{-2} Å^{-1})
λ_{obs} (Å)
0.0
0.5
1.0
1.5
2.0
2.5
4000
5000
6000
7000
8000
9000

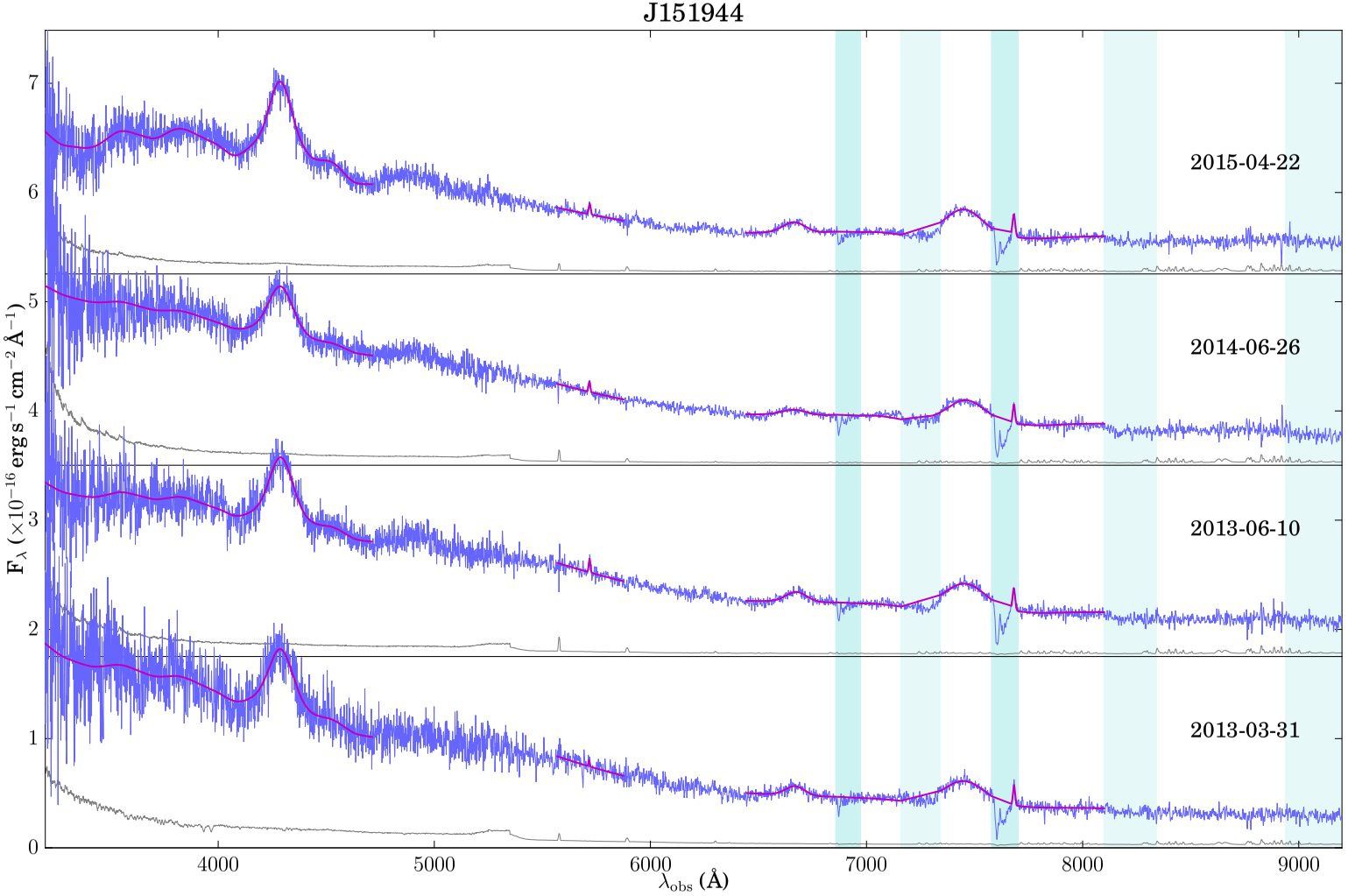
J151944
2015-04-22
2014-06-26
2013-06-10
2013-03-31
F_λ ($\times 10^{-16}$ erg s^{-1} cm^{-2} Å^{-1})
λ_{obs} (Å)
0
1
2
3
4
5
6
7
4000
5000
6000
7000
8000
9000

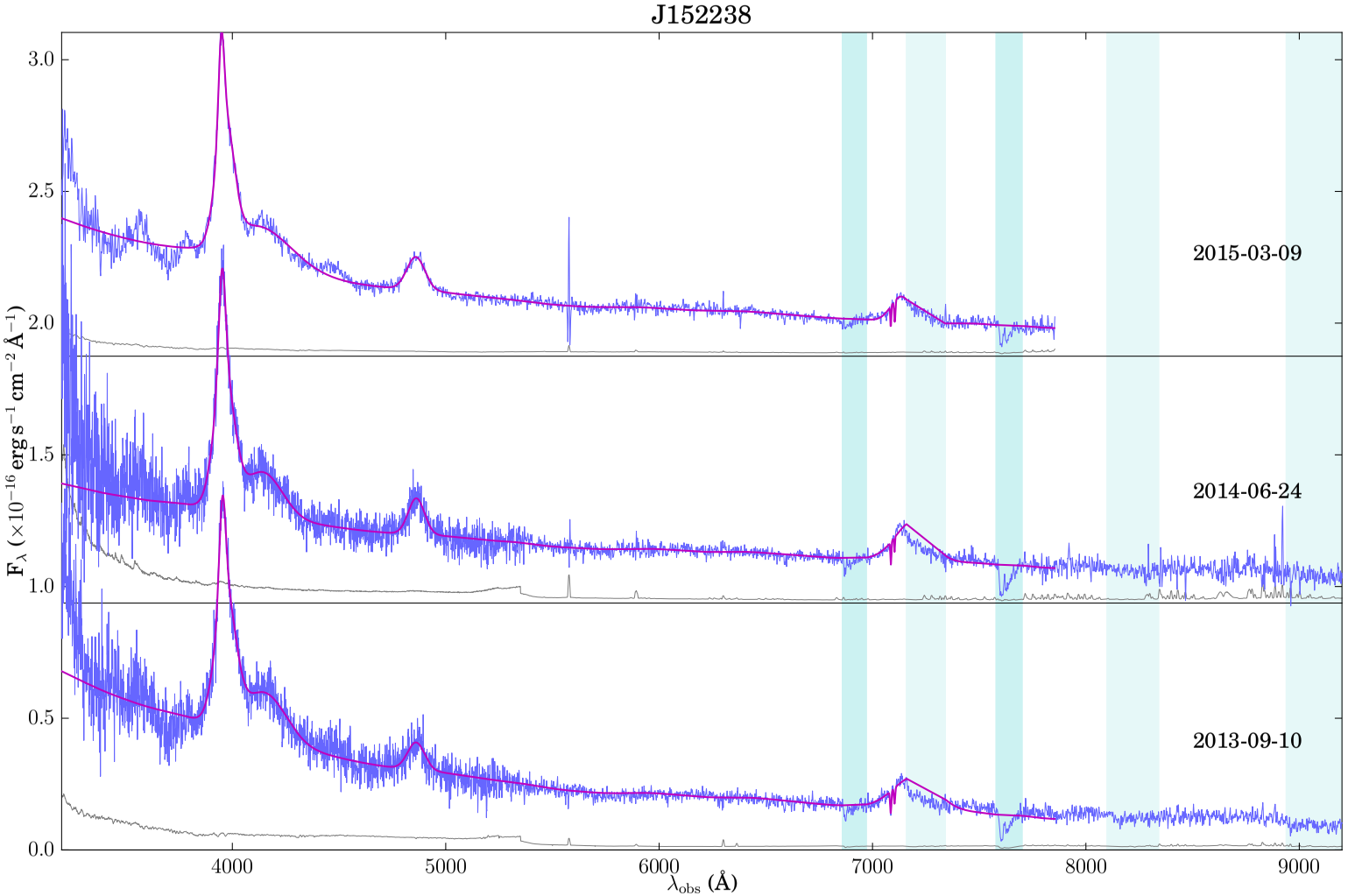
J152238
2015-03-09
2014-06-24
2013-09-10
F_λ ($\times 10^{-16}$ erg s^{-1} cm^{-2} Å^{-1})
λ_{obs} (Å)
0.0
0.5
1.0
1.5
2.0
2.5
3.0
4000
5000
6000
7000
8000
9000

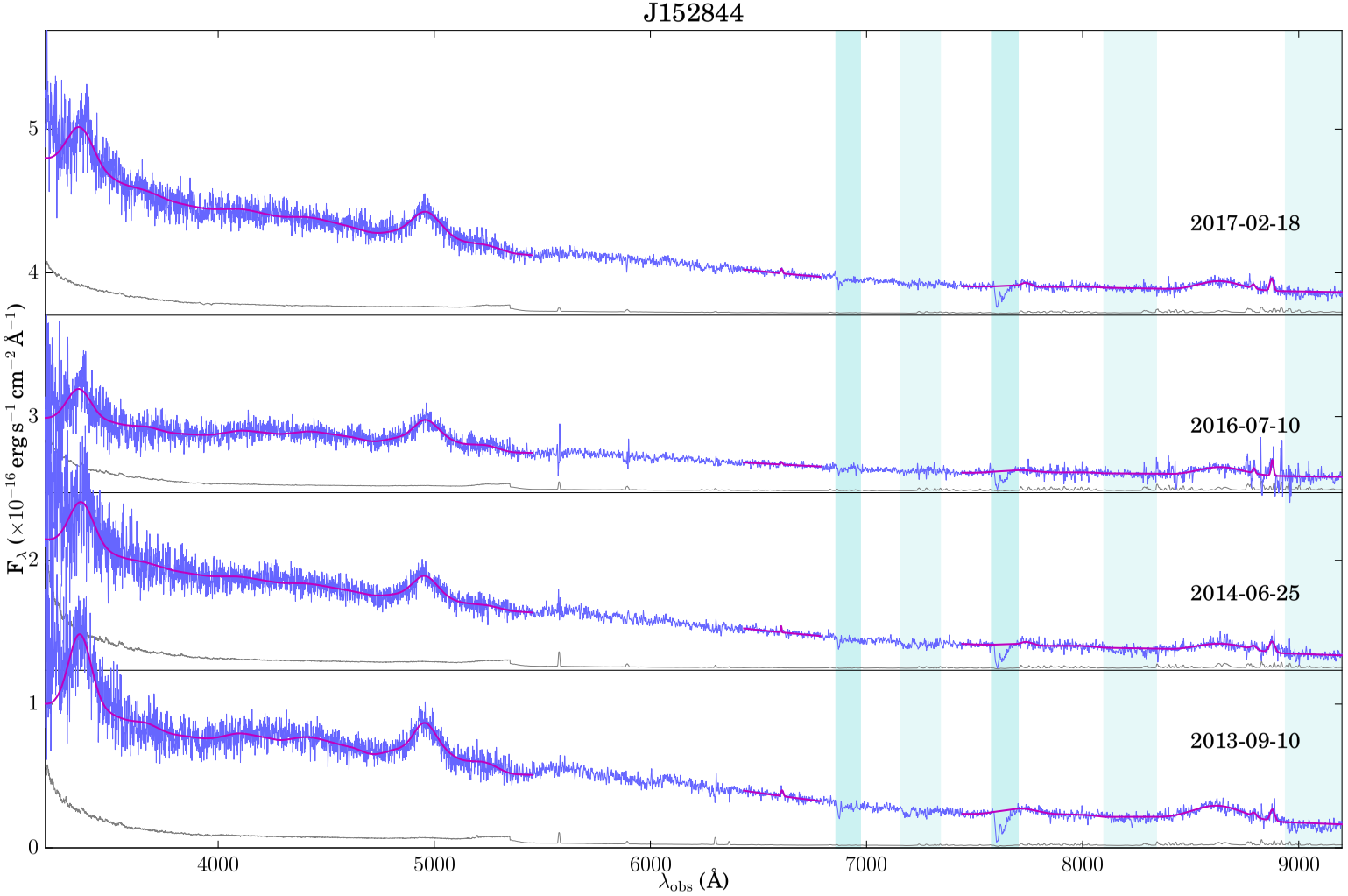
J152844
2017-02-18
2016-07-10
2014-06-25
2013-09-10
F_λ ($\times 10^{-16}$ erg s^{-1} cm^{-2} Å^{-1})
λ_{obs} (Å)
0
1
2
3
4
5
4000
5000
6000
7000
8000
9000

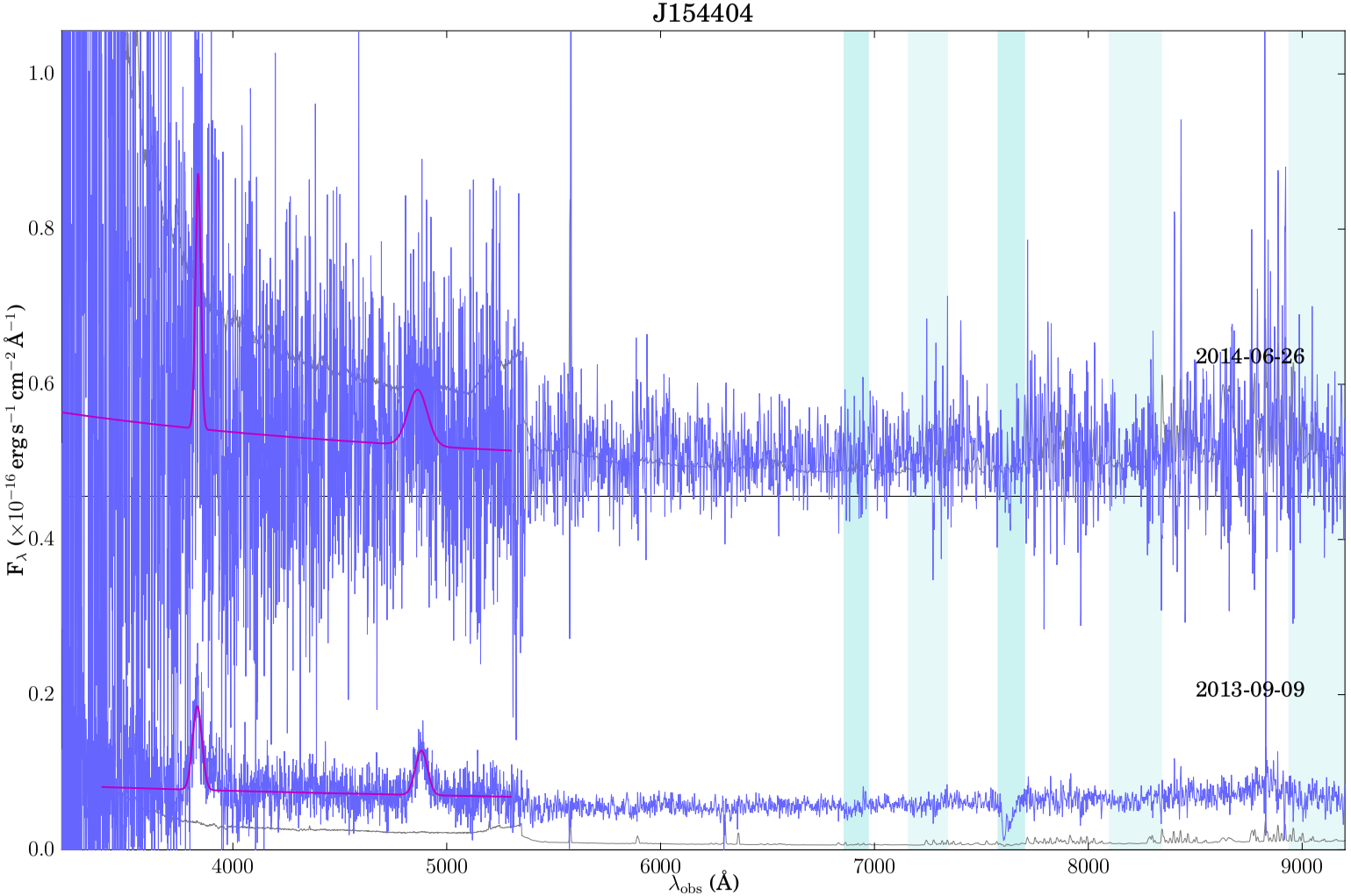
J154404
2014-06-26
2013-09-09
F_λ ($\times 10^{-16}$ erg s^{-1} cm^{-2} Å^{-1})
λ_{obs} (Å)
0.0
0.2
0.4
0.6
0.8
1.0
4000
5000
6000
7000
8000
9000

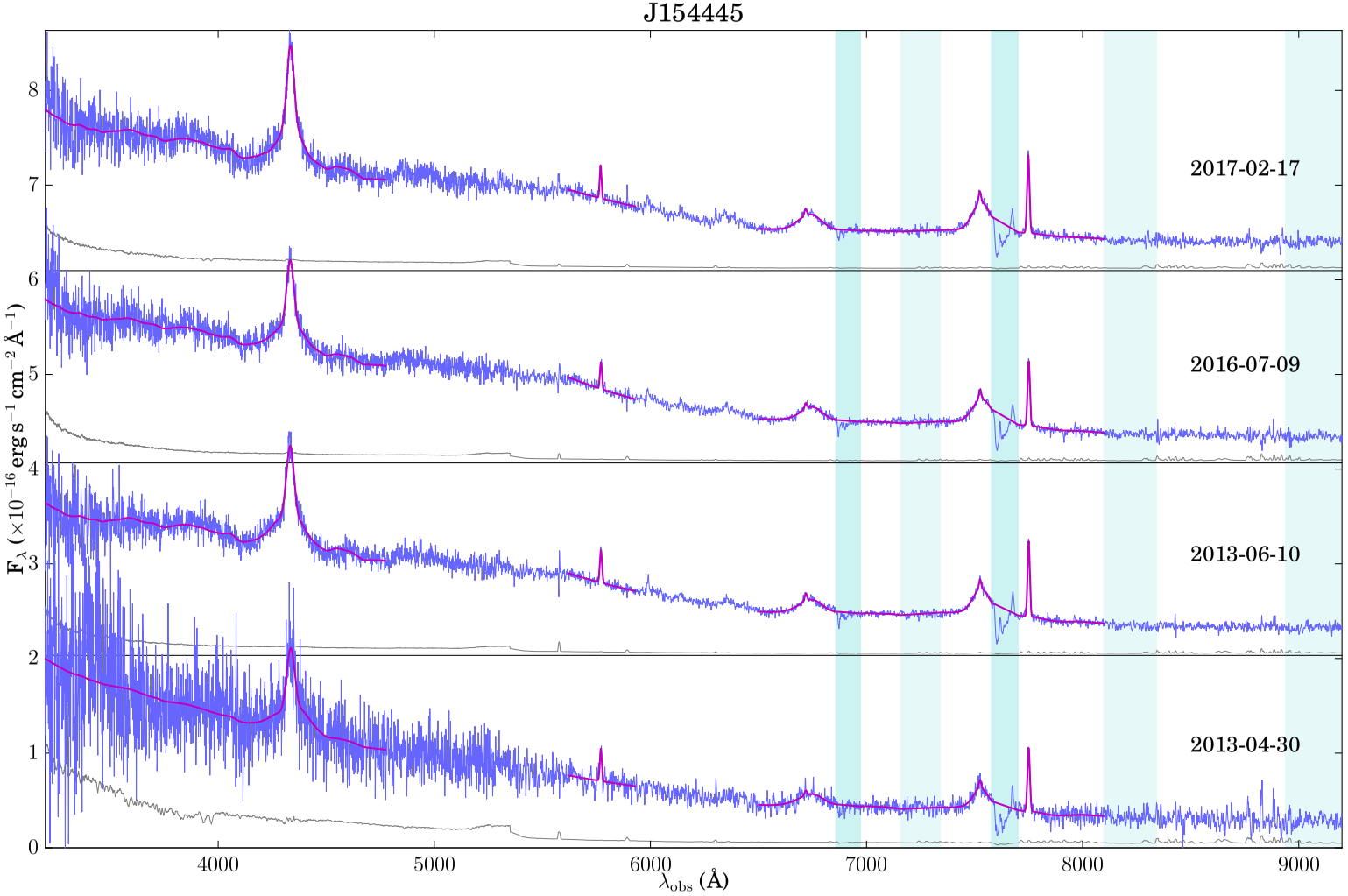
J154445
2017-02-17
2016-07-09
2013-06-10
2013-04-30
F_λ ($\times 10^{-16}$ erg s^{-1} cm^{-2} Å^{-1})
λ_{obs} (Å)
0
1
2
3
4
5
6
7
8
4000
5000
6000
7000
8000
9000

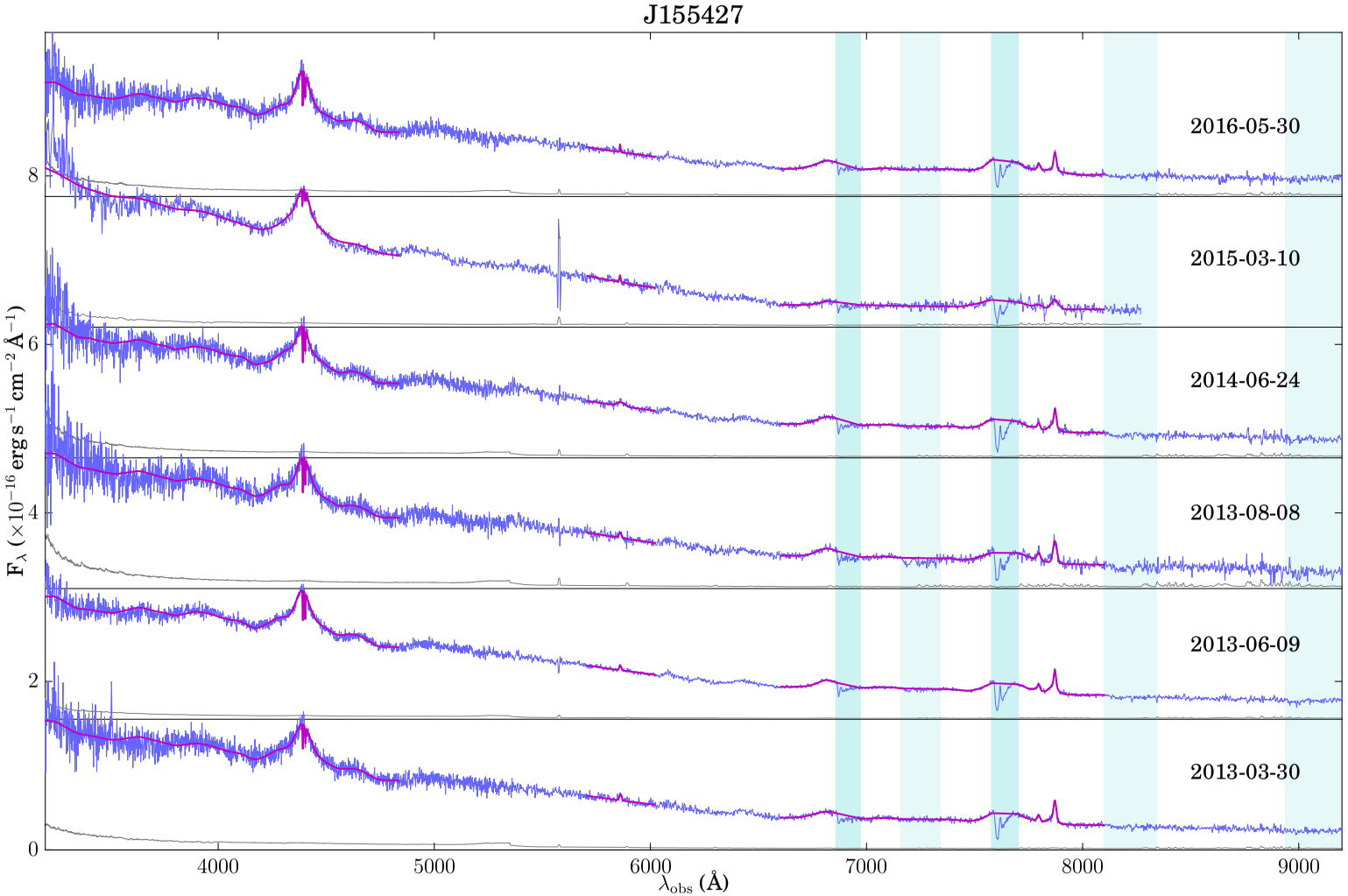
J155427
2016-05-30
2015-03-10
2014-06-24
2013-08-08
2013-06-09
2013-03-30
F_λ ($\times 10^{-16}$ erg s^{-1} cm^{-2} Å^{-1})
λ_{obs} (Å)
0
2
4
6
8
4000
5000
6000
7000
8000
9000

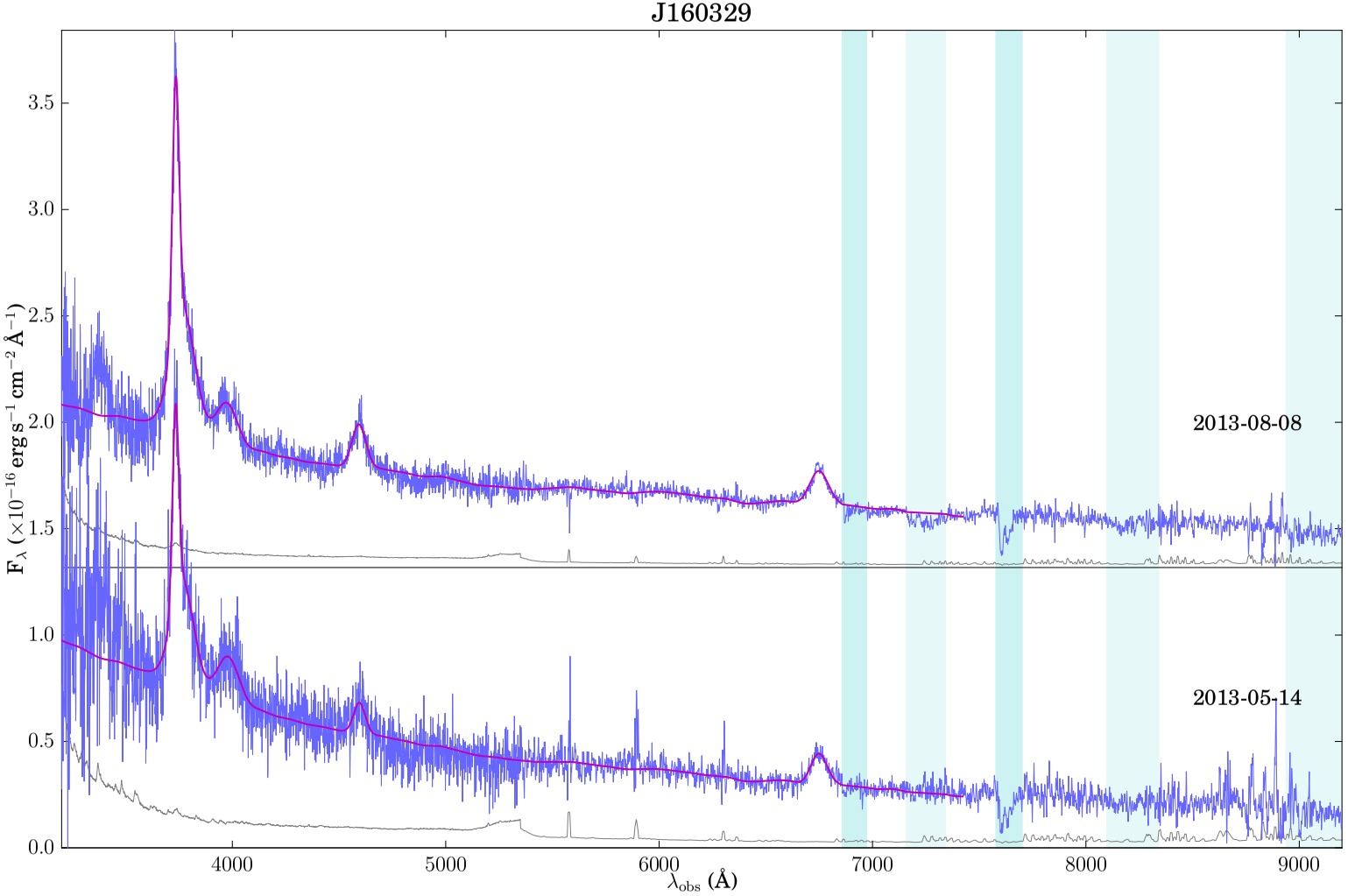
J160329
2013-08-08
2013-05-14
F_λ ($\times 10^{-16}$ erg s^{-1} cm^{-2} Å^{-1})
λ_{obs} (Å)
0.0
0.5
1.0
1.5
2.0
2.5
3.0
3.5
4000
5000
6000
7000
8000
9000

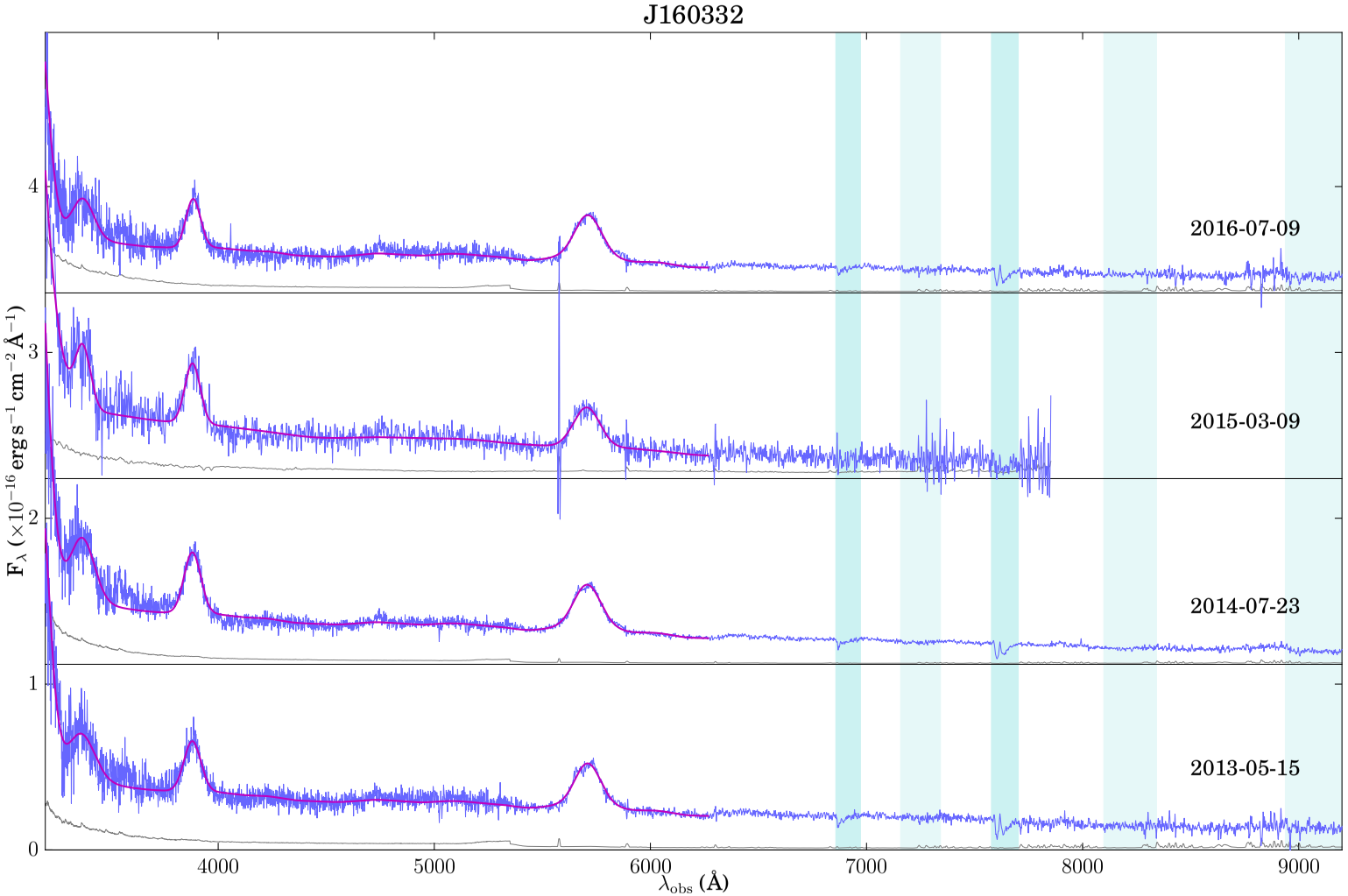
J160332
2016-07-09
2015-03-09
2014-07-23
2013-05-15
F_λ ($\times 10^{-16}$ erg s^{-1} cm^{-2} Å^{-1})
λ_{obs} (Å)
0
1
2
3
4
4000
5000
6000
7000
8000
9000

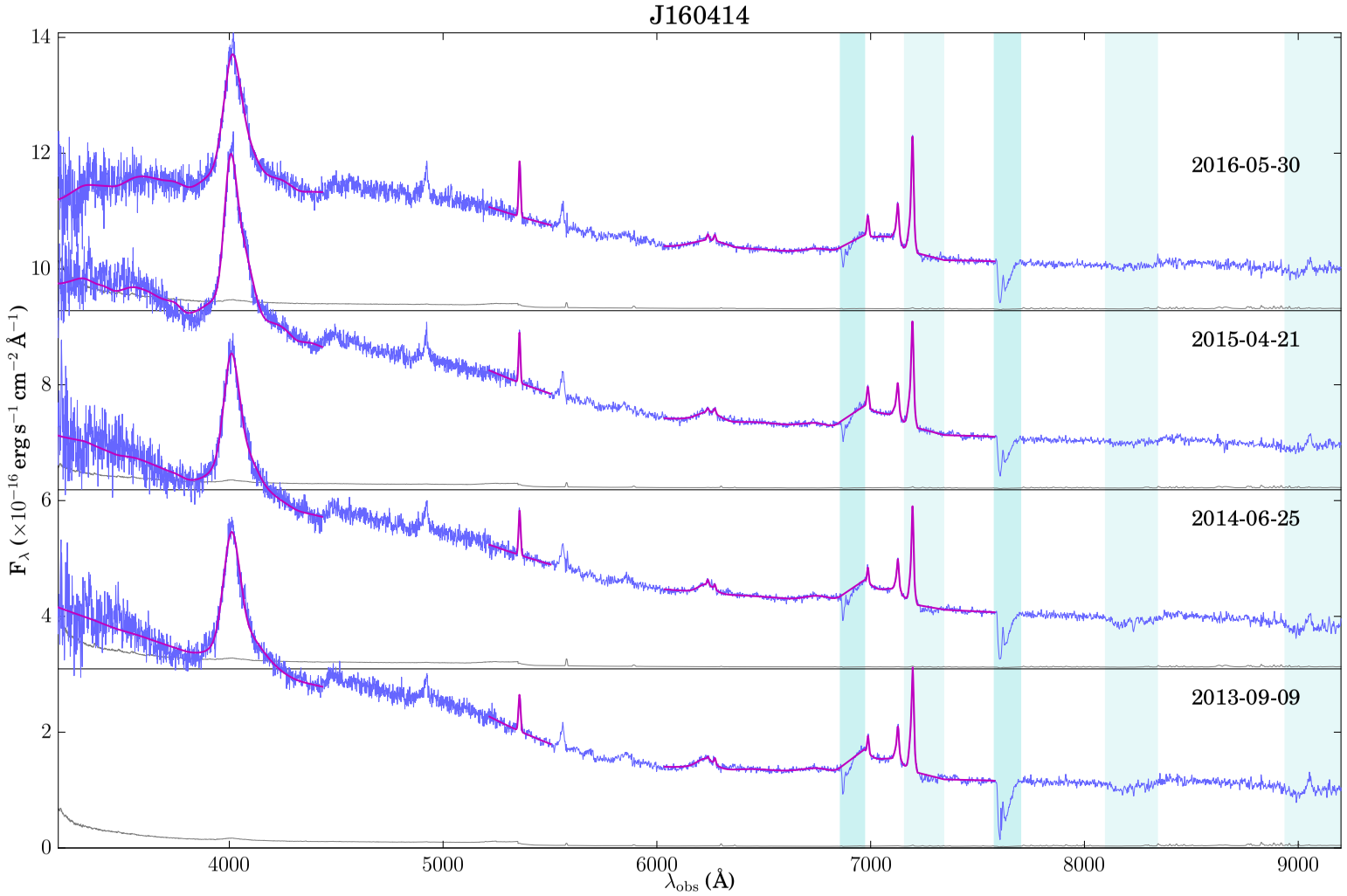
J160414
2016-05-30
2015-04-21
2014-06-25
2013-09-09
F_λ ($\times 10^{-16}$ erg s^{-1} cm^{-2} Å^{-1})
λ_{obs} (Å)
0
2
4
6
8
10
12
14
4000
5000
6000
7000
8000
9000

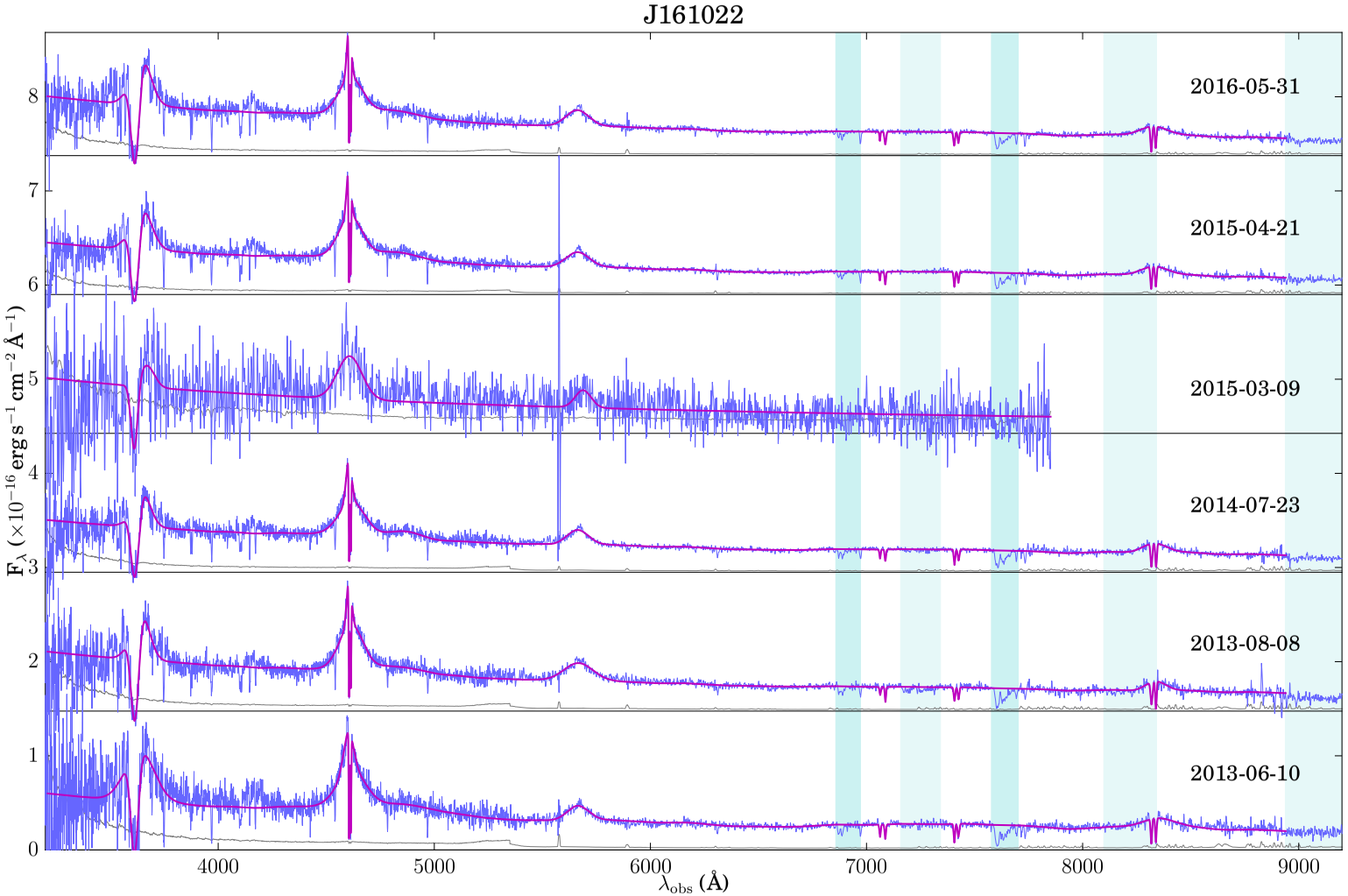
J161022
2016-05-31
2015-04-21
2015-03-09
2014-07-23
2013-08-08
2013-06-10
F_λ ($\times 10^{-16}$ erg s^{-1} cm^{-2} Å^{-1})
λ_{obs} (Å)
0
1
2
3
4
5
6
7
8
4000
5000
6000
7000
8000
9000

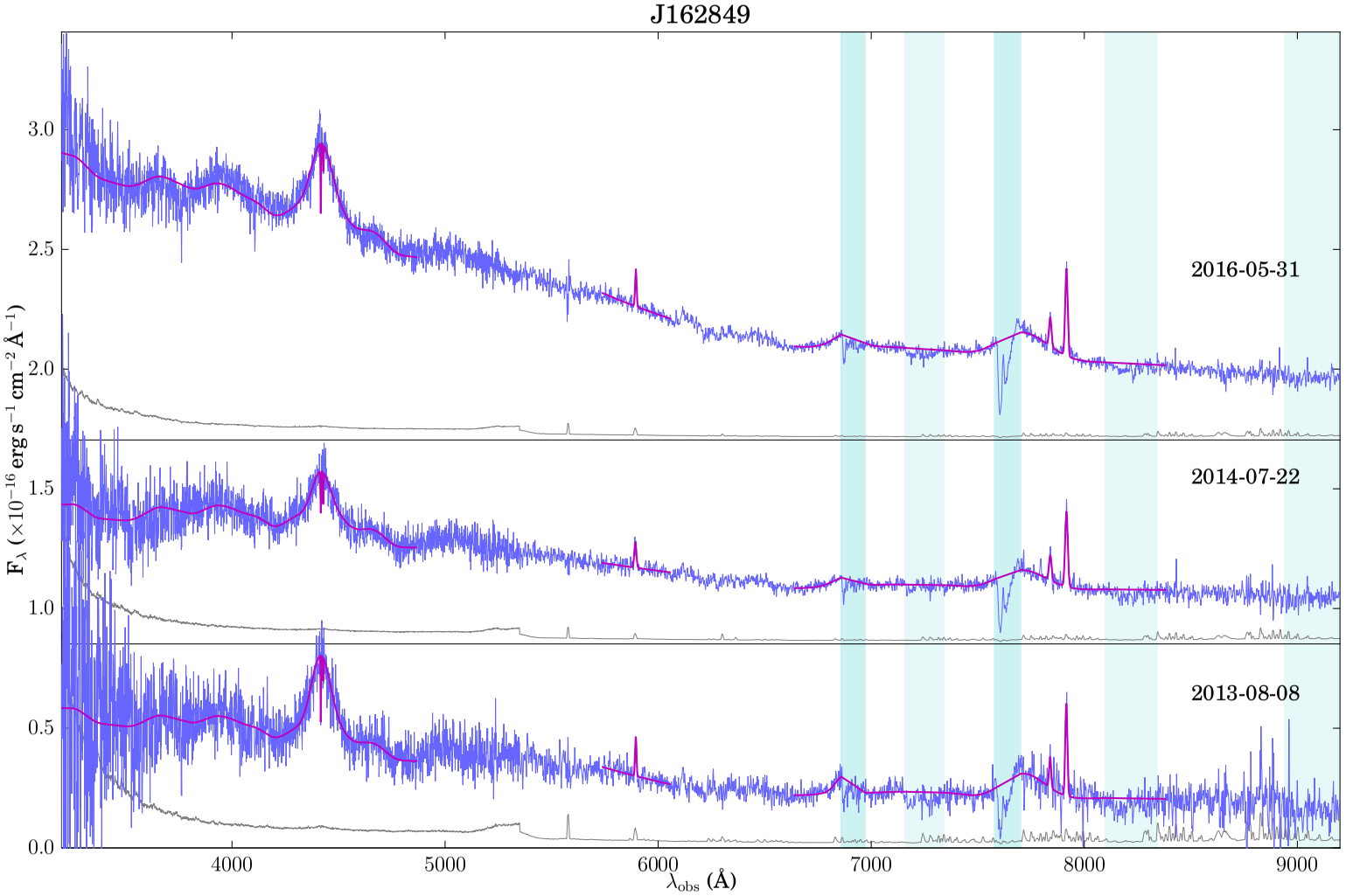
J162849
2016-05-31
2014-07-22
2013-08-08
F_λ ($\times 10^{-16}$ erg s^{-1} cm^{-2} Å^{-1})
λ_{obs} (Å)
0.0
0.5
1.0
1.5
2.0
2.5
3.0
4000
5000
6000
7000
8000
9000

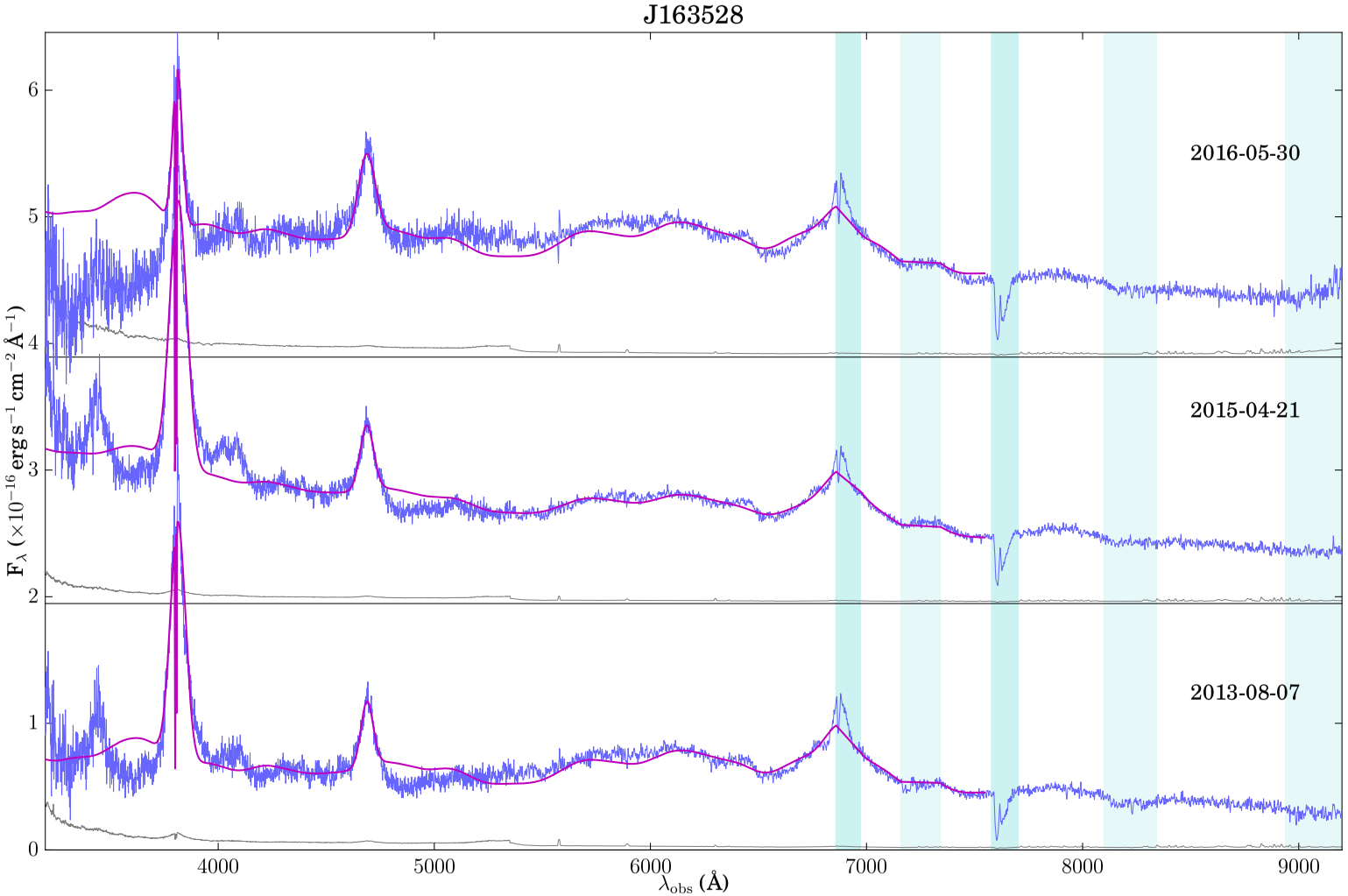
J163528
2016-05-30
2015-04-21
2013-08-07
F_λ ($\times 10^{-16}$ erg s^{-1} cm^{-2} Å^{-1})
λ_{obs} (Å)
0
1
2
3
4
5
6
4000
5000
6000
7000
8000
9000

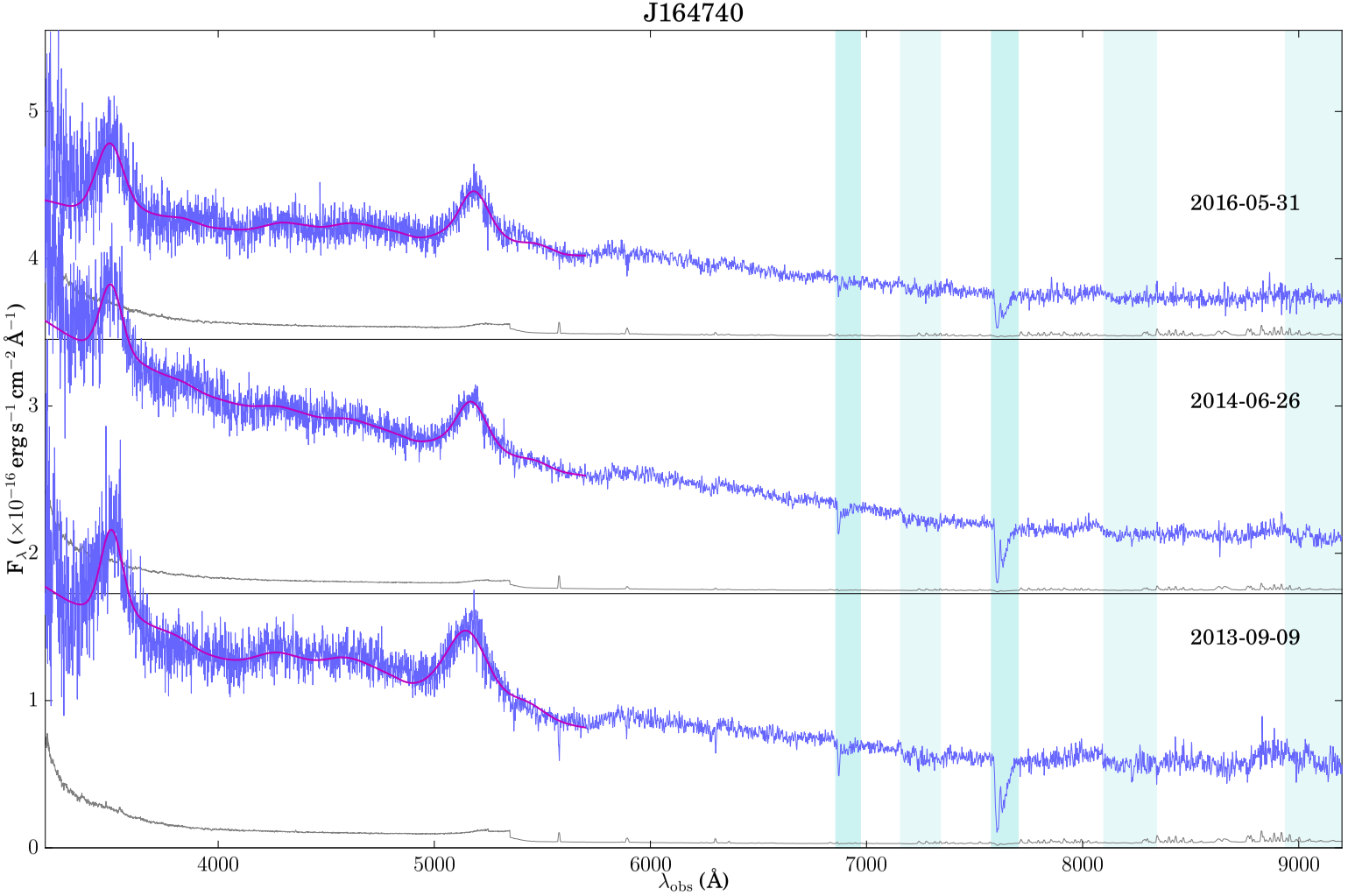
J164740
2016-05-31
2014-06-26
2013-09-09
F_λ ($\times 10^{-16}$ erg s^{-1} cm^{-2} Å^{-1})
λ_{obs} (Å)
0
1
2
3
4
5
4000
5000
6000
7000
8000
9000

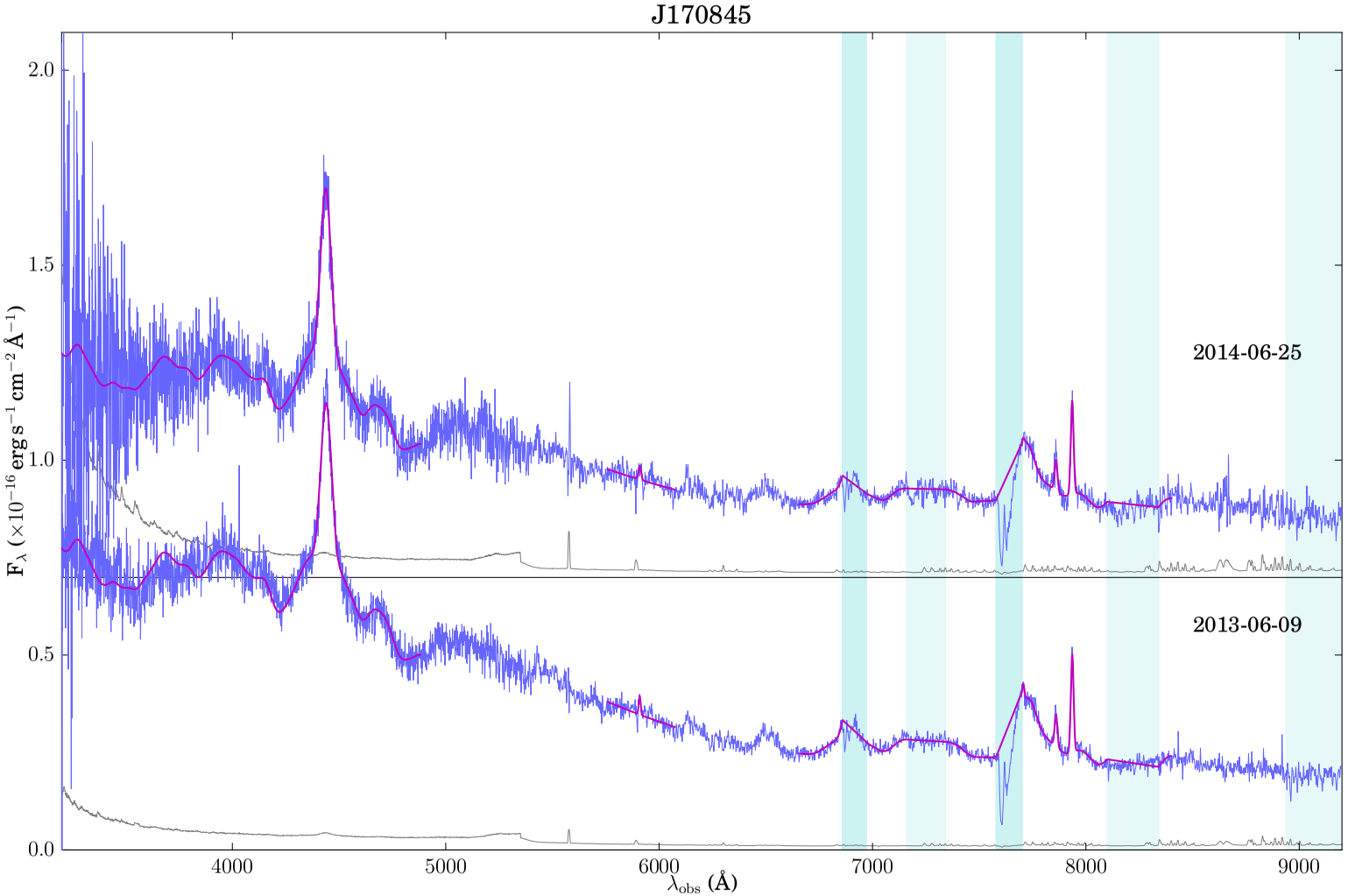
J170845
2014-06-25
2013-06-09
F_λ ($\times 10^{-16}$ erg s^{-1} cm^{-2} Å^{-1})
λ_{obs} (Å)
0.0
0.5
1.0
1.5
2.0
4000
5000
6000
7000
8000
9000

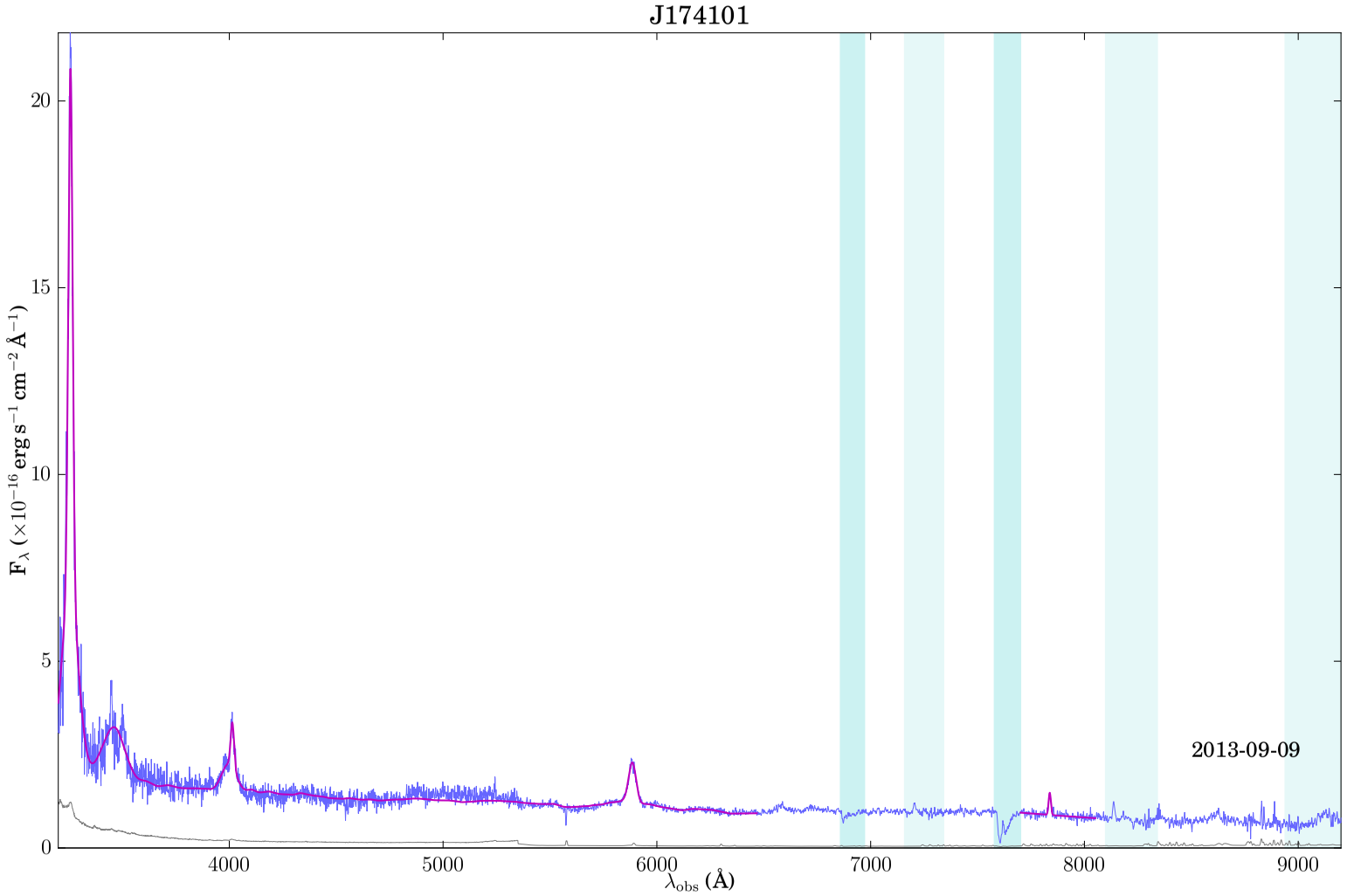
J174101
2013-09-09
F_λ ($\times 10^{-16}$ erg s^{-1} cm^{-2} Å^{-1})
λ_{obs} (Å)
0
5
10
15
20
4000
5000
6000
7000
8000
9000

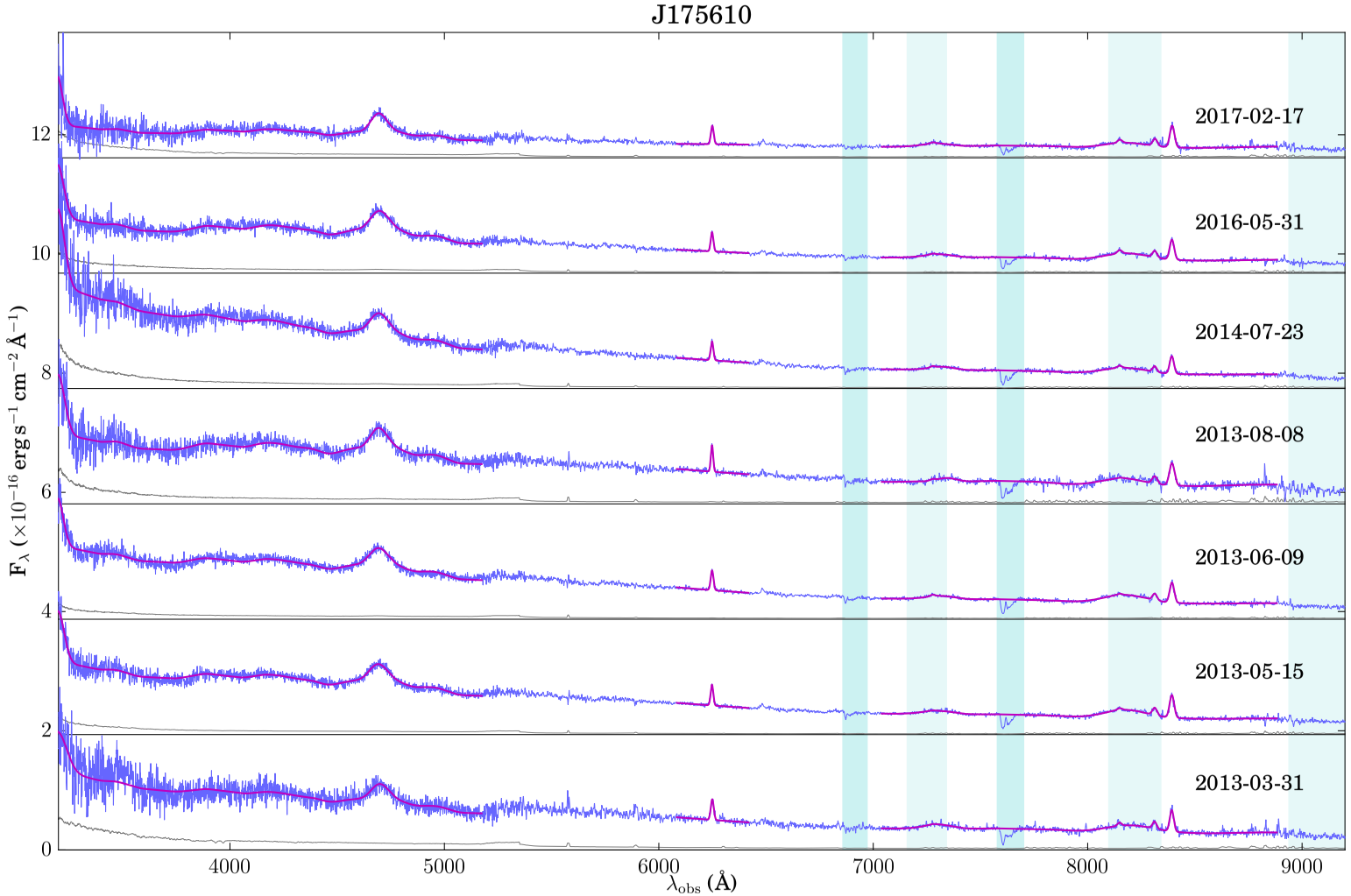
J175610
2017-02-17
2016-05-31
2014-07-23
2013-08-08
2013-06-09
2013-05-15
2013-03-31
F_λ ($\times 10^{-16}$ erg s^{-1} cm^{-2} Å^{-1})
λ_{obs} (Å)
0
2
4
6
8
10
12
4000
5000
6000
7000
8000
9000

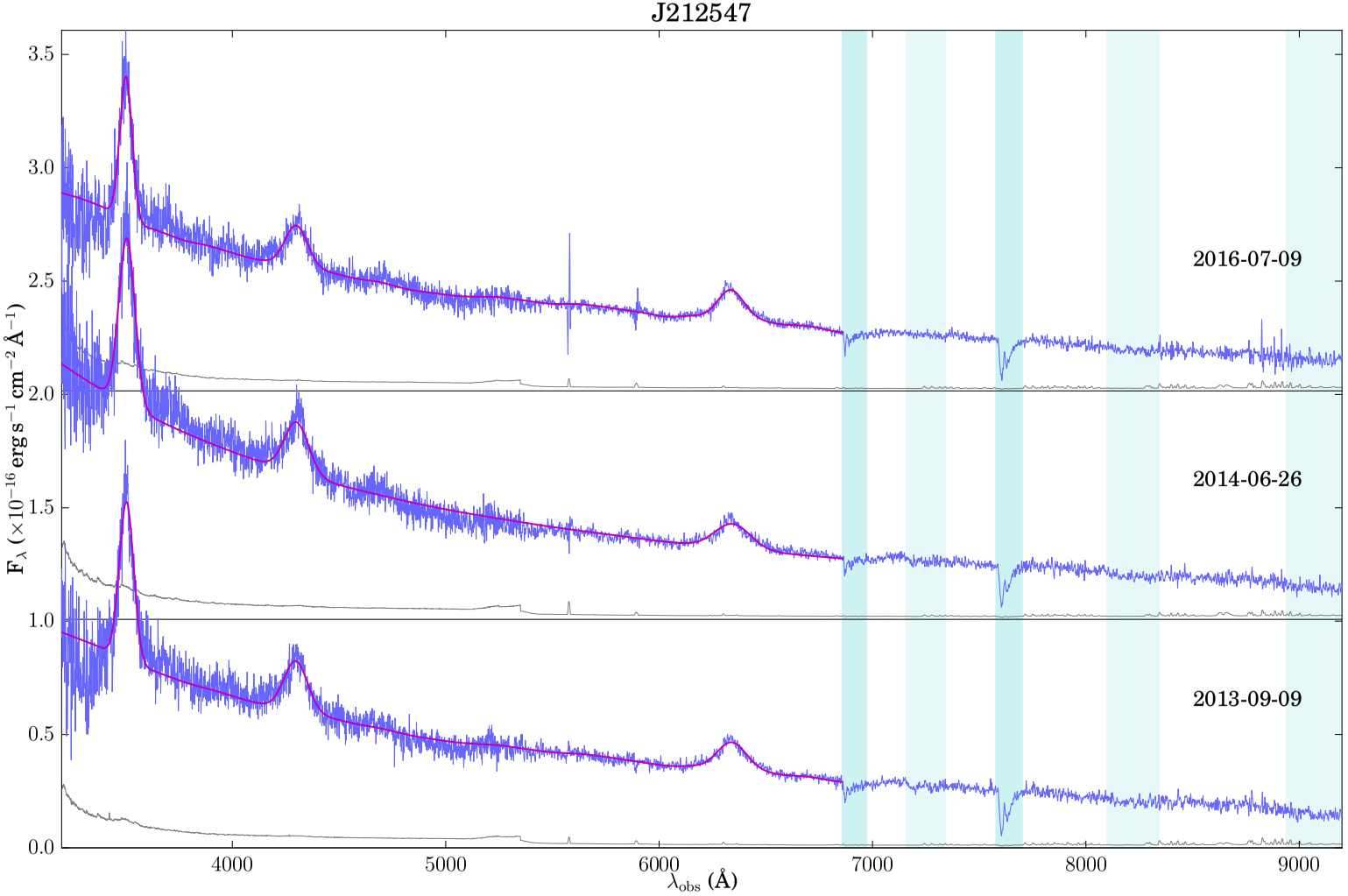
J212547
2016-07-09
2014-06-26
2013-09-09
F_λ ($\times 10^{-16}$ erg s^{-1} cm^{-2} Å^{-1})
λ_{obs} (Å)
0.0
0.5
1.0
1.5
2.0
2.5
3.0
3.5
4000
5000
6000
7000
8000
9000

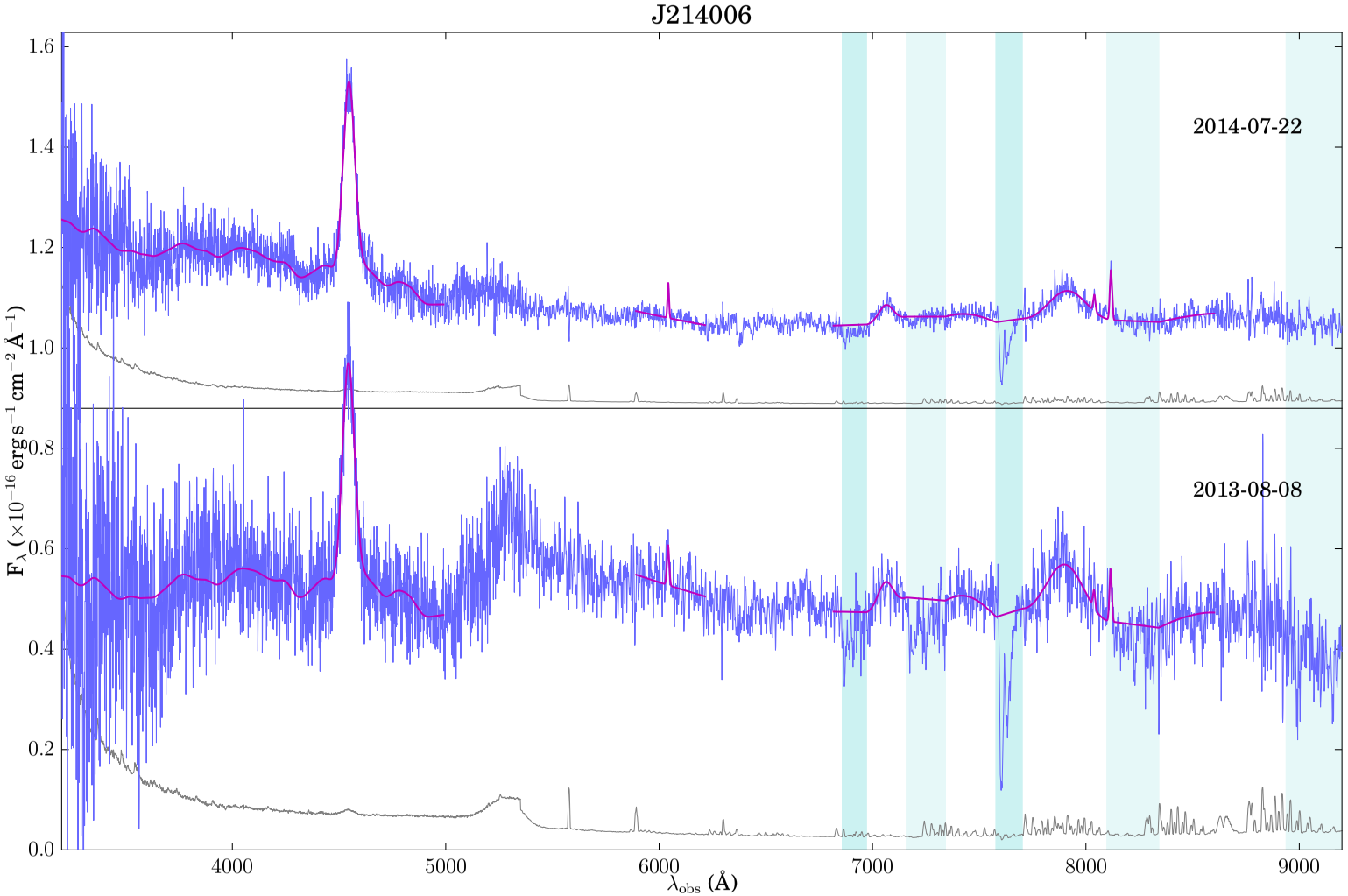
J214006
2014-07-22
2013-08-08
F_λ ($\times 10^{-16}$ erg s^{-1} cm^{-2} Å^{-1})
λ_{obs} (Å)
0.0
0.2
0.4
0.6
0.8
1.0
1.2
1.4
1.6
4000
5000
6000
7000
8000
9000

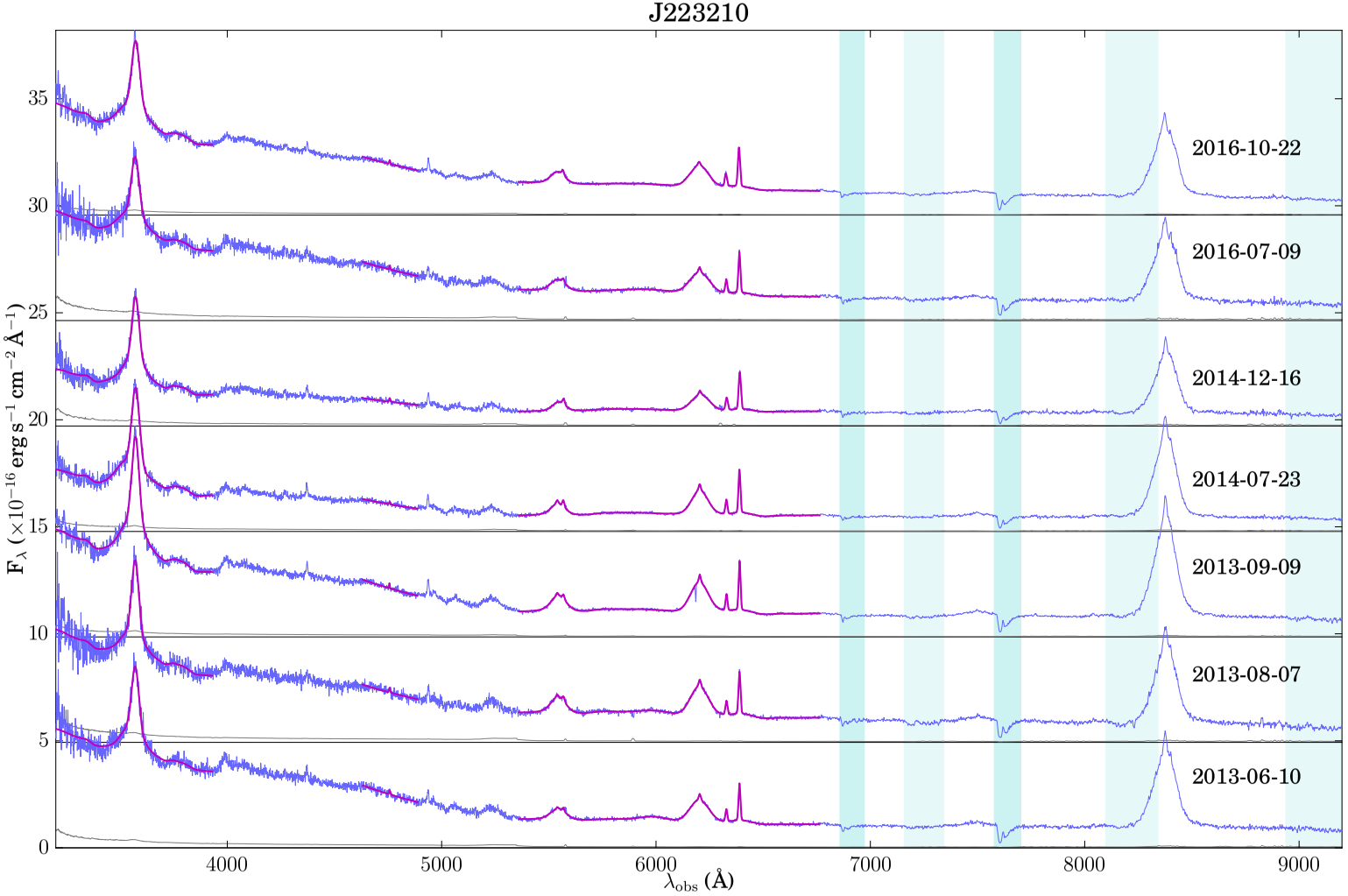
J223210
2016-10-22
2016-07-09
2014-12-16
2014-07-23
2013-09-09
2013-08-07
2013-06-10
F_λ ($\times 10^{-16}$ erg s^{-1} cm^{-2} Å^{-1})
λ_{obs} (Å)
0
5
10
15
20
25
30
35
4000
5000
6000
7000
8000
9000

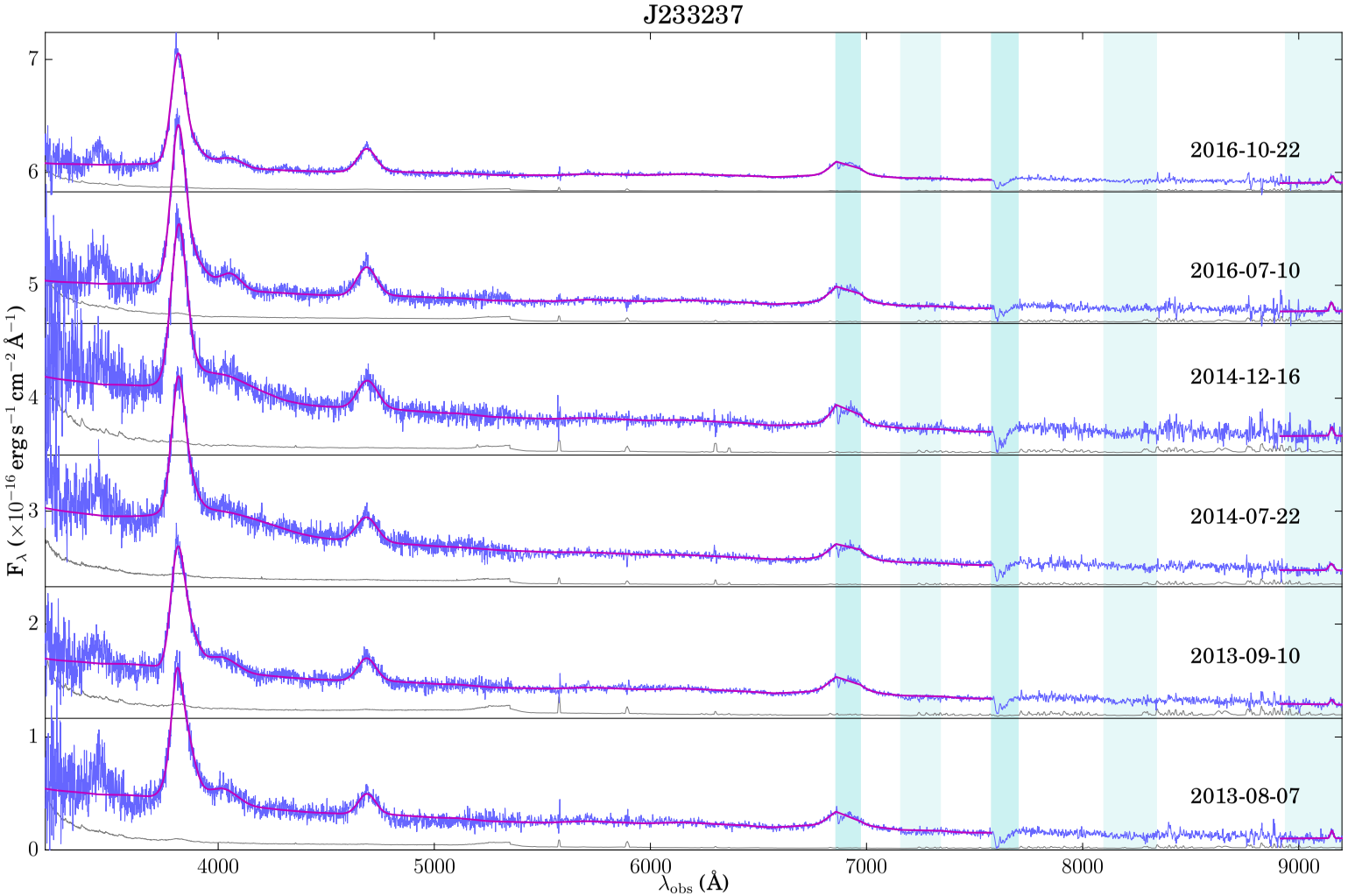
J233237
2016-10-22
2016-07-10
2014-12-16
2014-07-22
2013-09-10
2013-08-07
F_λ ($\times 10^{-16}$ erg s^{-1} cm^{-2} Å^{-1})
λ_{obs} (Å)
0
1
2
3
4
5
6
7
4000
5000
6000
7000
8000
9000

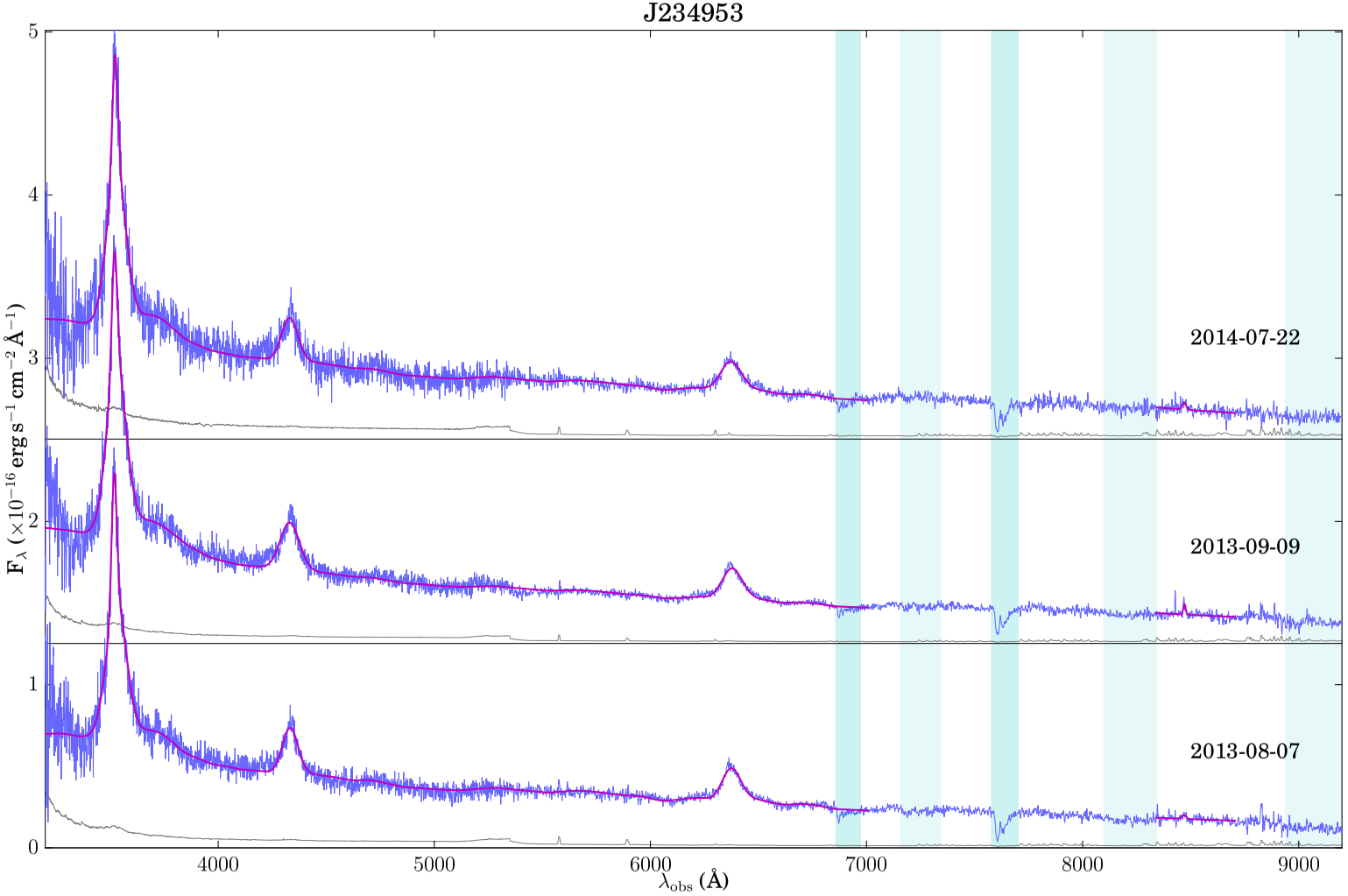
J234953
2014-07-22
2013-09-09
2013-08-07
F_λ ($\times 10^{-16}$ erg s^{-1} cm^{-2} Å^{-1})
λ_{obs} (Å)
0
1
2
3
4
5
4000
5000
6000
7000
8000
9000

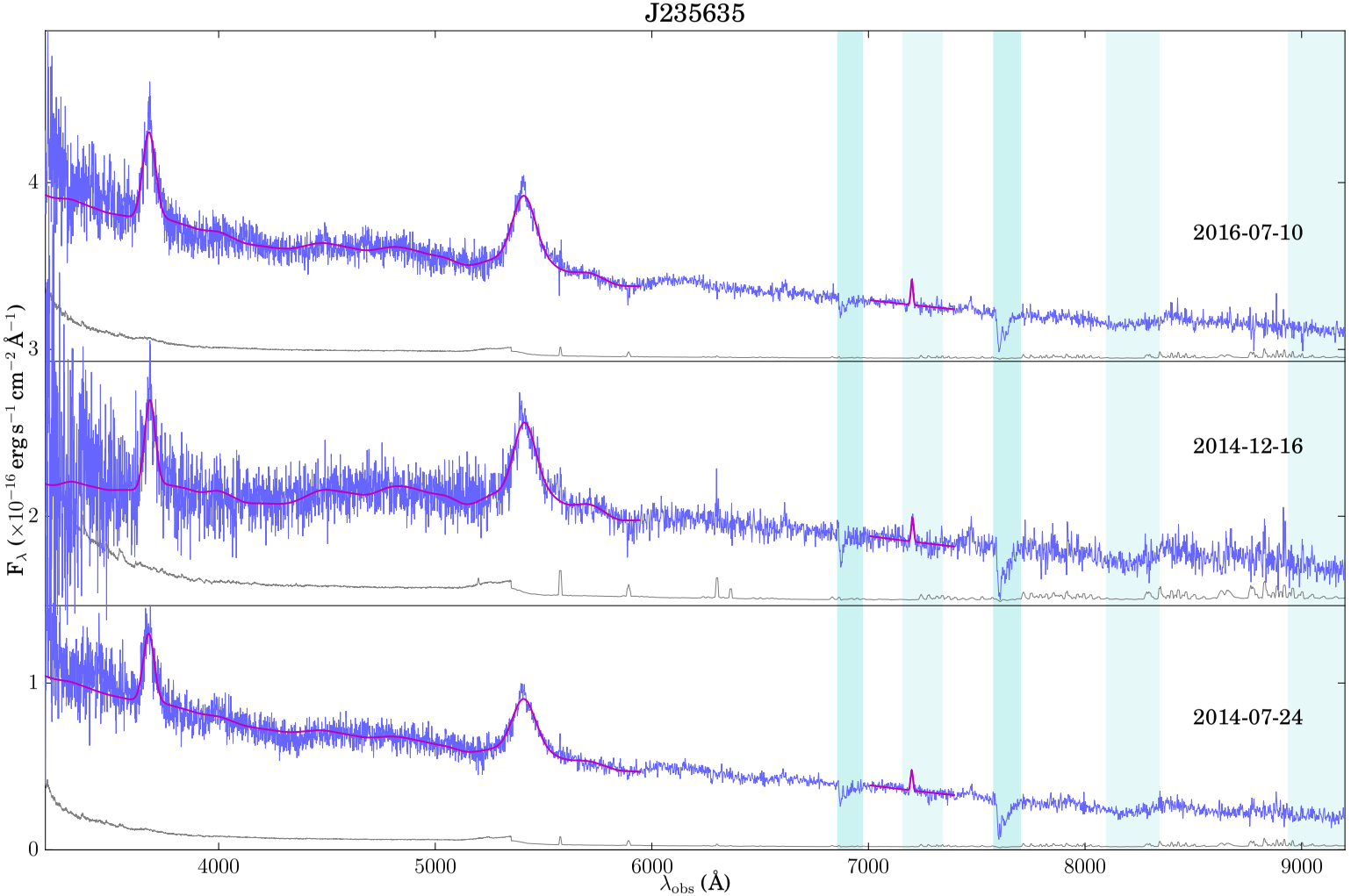
J235635
2016-07-10
2014-12-16
2014-07-24
F_λ ($\times 10^{-16}$ erg s^{-1} cm^{-2} Å^{-1})
λ_{obs} (Å)
0
1
2
3
4
4000
5000
6000
7000
8000
9000

Appendix B

Light curves

This appendix contains all of the g-band photometry for the targets discussed in this paper. Each figure shows: LT data (blue); DVO data (red); PTF data (green); SDSS data (PSF magnitudes, black); SuperCOSMOS data (magenta, Hambly et al. (2001)) and CRTS data (grey). Given the clear filter used in the CRTS survey, an approximate correction has been made using two relations. The first is a correction from V_{CSS} to V[1] and the second is a correction from V to $g_{\rm SDSS}$ (and estimate for $B-V$) for quasars at $z \leq 2.1$ (Jester et al., 2005). I have chosen to apply this correction using the observed colour at the SDSS epoch. Any intrinsic colour changes will increase the probability for a mismatch at later epochs. Note that the SuperCOSMOS data are point source B magnitudes but no corrections have been applied at this stage.

[1] http://nesssi.cacr.caltech.edu/DataRelease/FAQ2.html

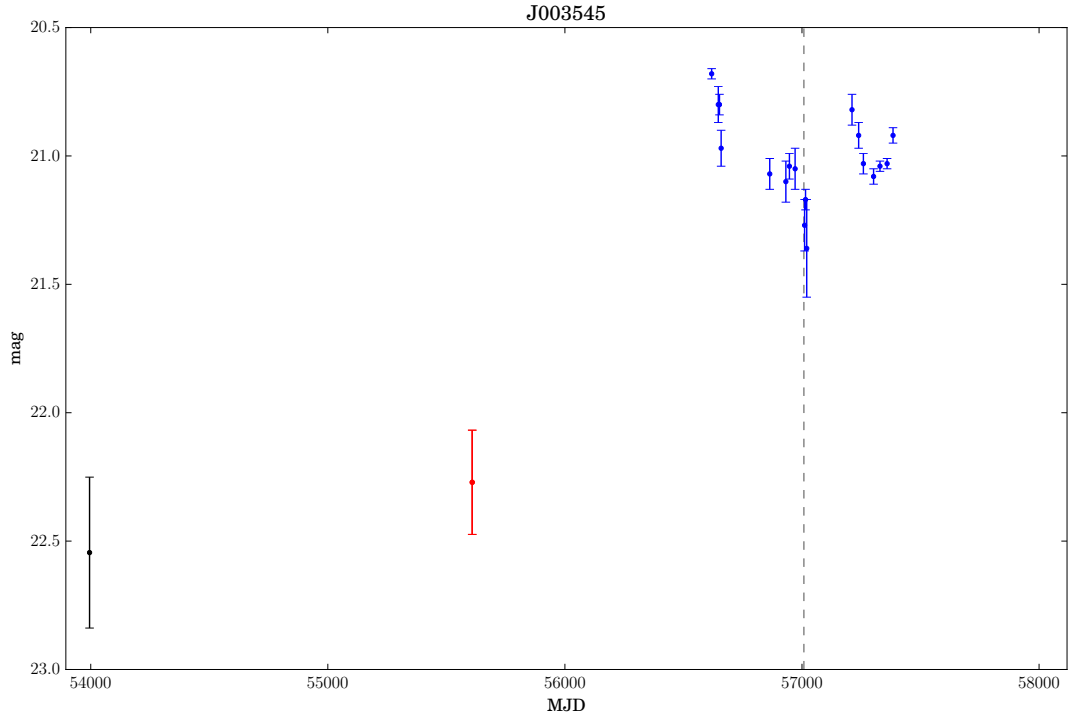
J003545
20.5
21.0
21.5
22.0
22.5
23.0
mag
54000
55000
56000
57000
58000
MJD

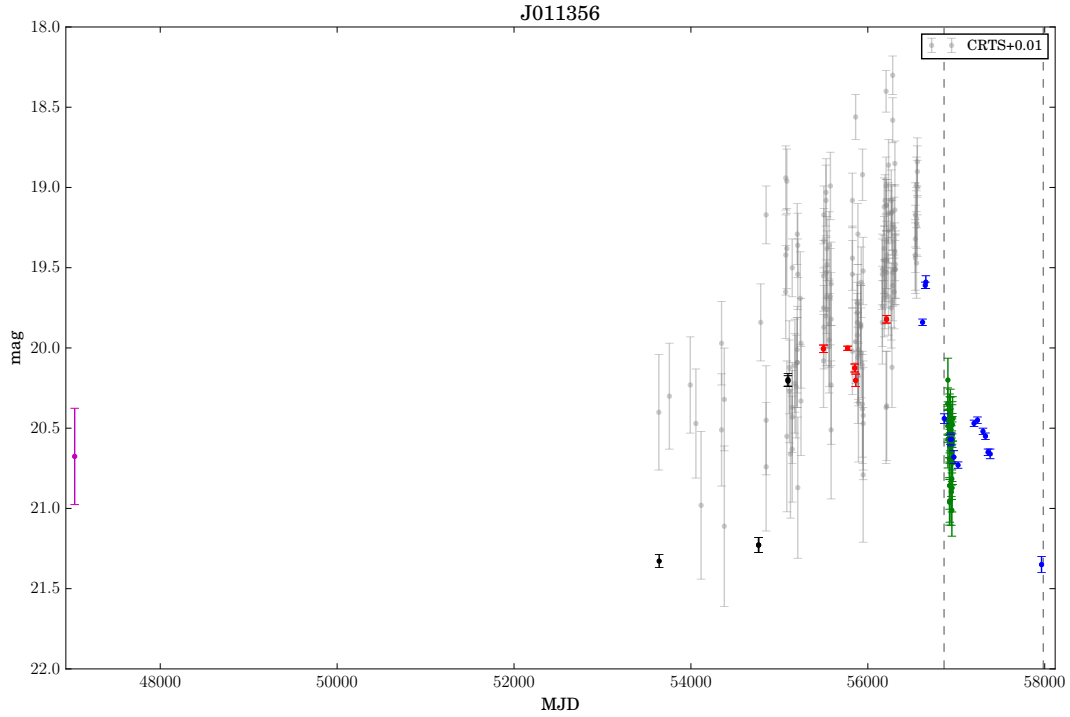
J011356
CRTS+0.01
18.0
18.5
19.0
19.5
20.0
20.5
21.0
21.5
22.0
mag
48000
50000
52000
54000
56000
58000
MJD

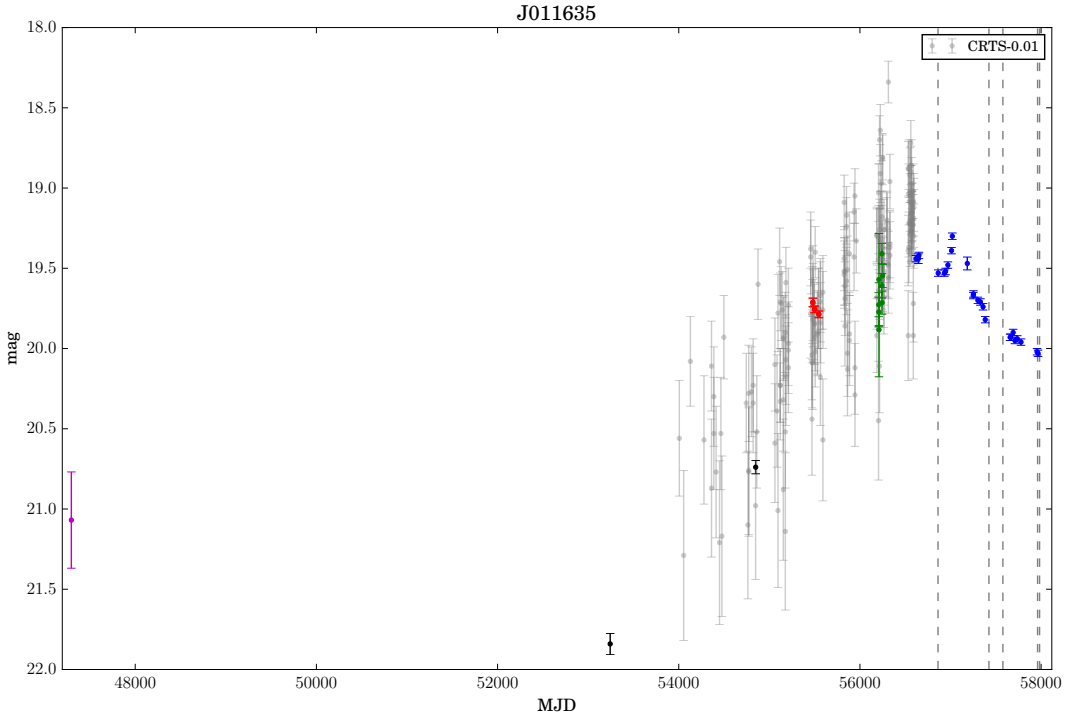
J011635
CRTS-0.01
mag
MJD
18.0
18.5
19.0
19.5
20.0
20.5
21.0
21.5
22.0
48000
50000
52000
54000
56000
58000

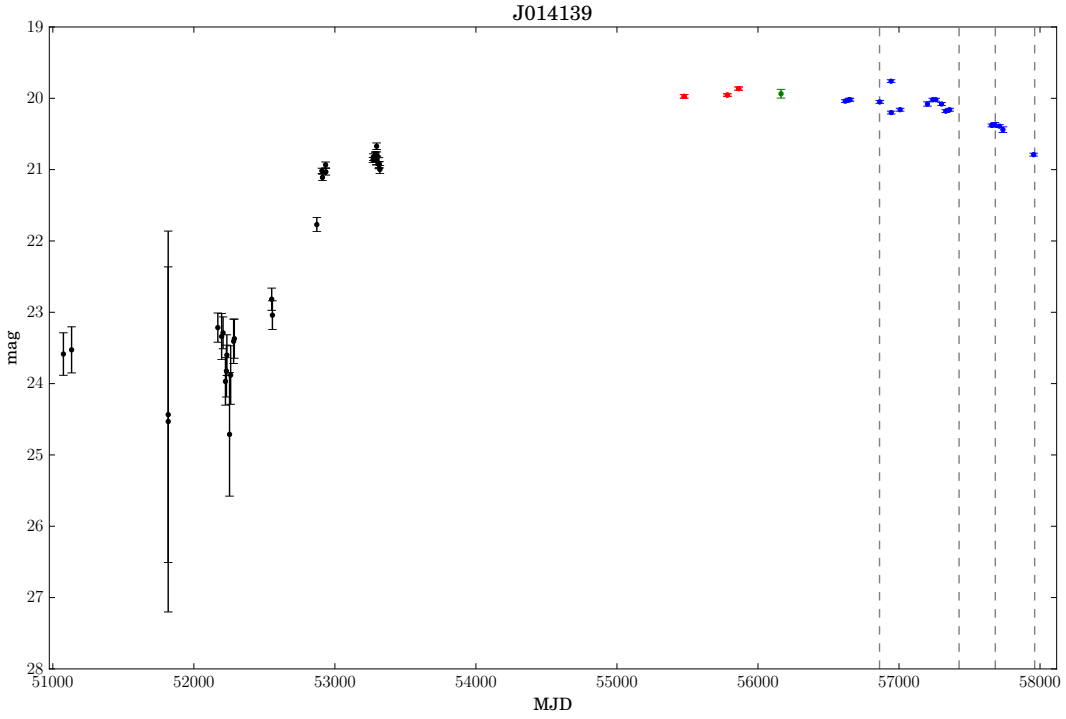
J014139
mag
MJD
19
20
21
22
23
24
25
26
27
28
51000
52000
53000
54000
55000
56000
57000
58000

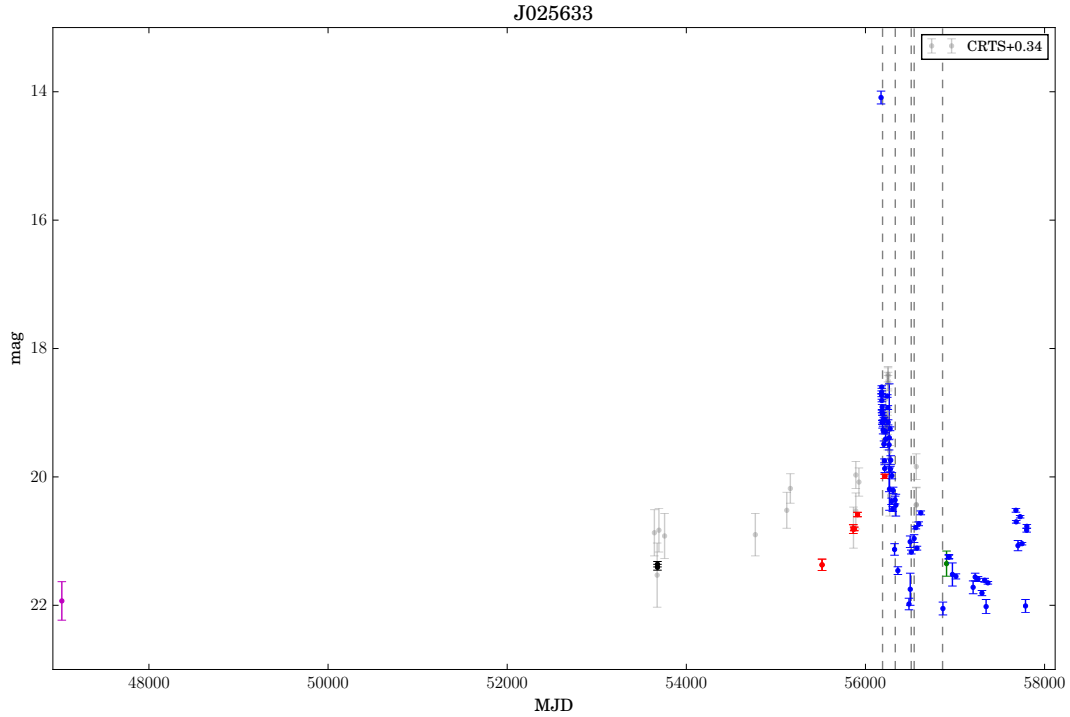
J025633
CRTS+0.34
mag
MJD
14
16
18
20
22
48000
50000
52000
54000
56000
58000

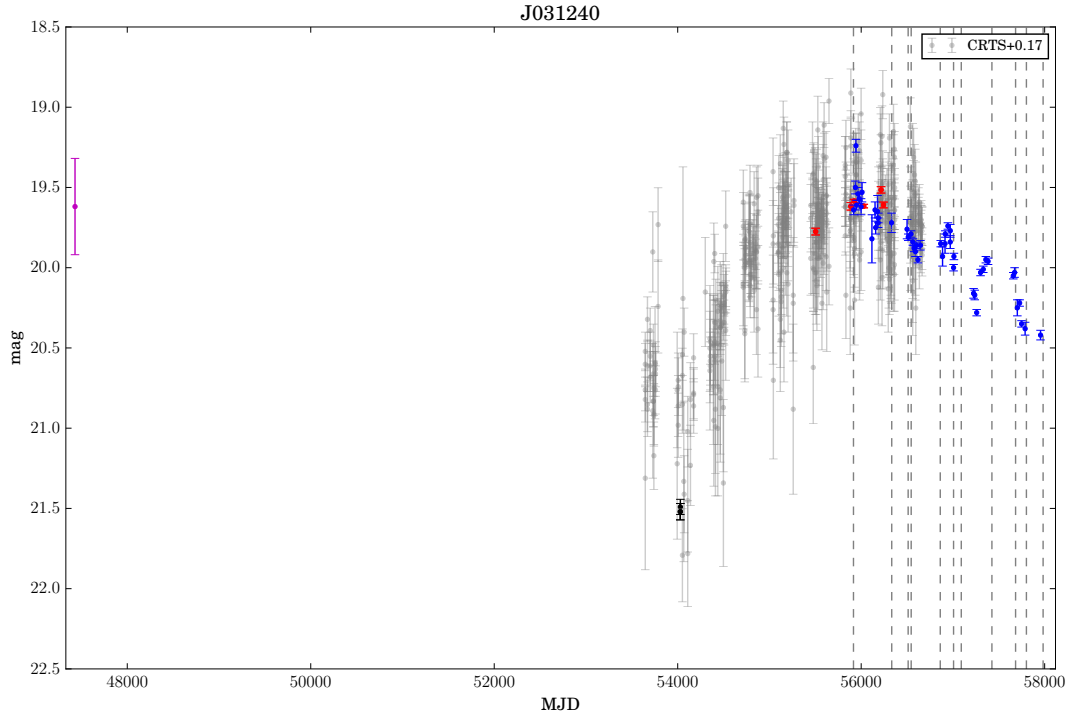
J031240
CRTS+0.17
mag
MJD
18.5
19.0
19.5
20.0
20.5
21.0
21.5
22.0
22.5
48000
50000
52000
54000
56000
58000

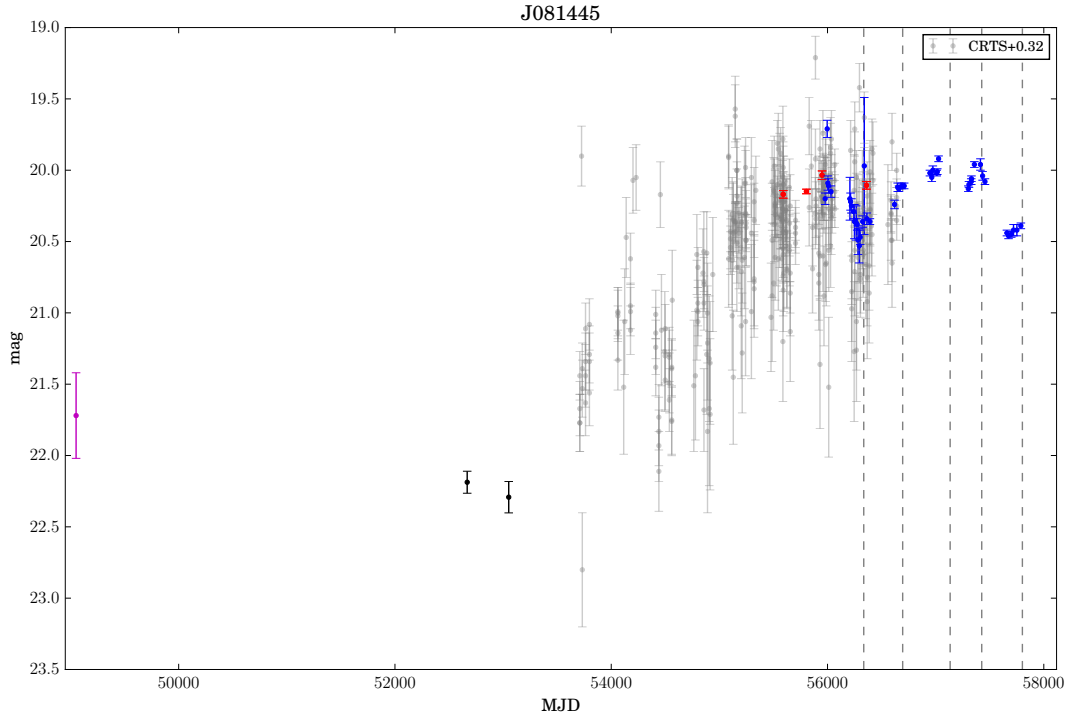
J081445
CRTS+0.32
mag
MJD
19.0
19.5
20.0
20.5
21.0
21.5
22.0
22.5
23.0
23.5
50000
52000
54000
56000
58000

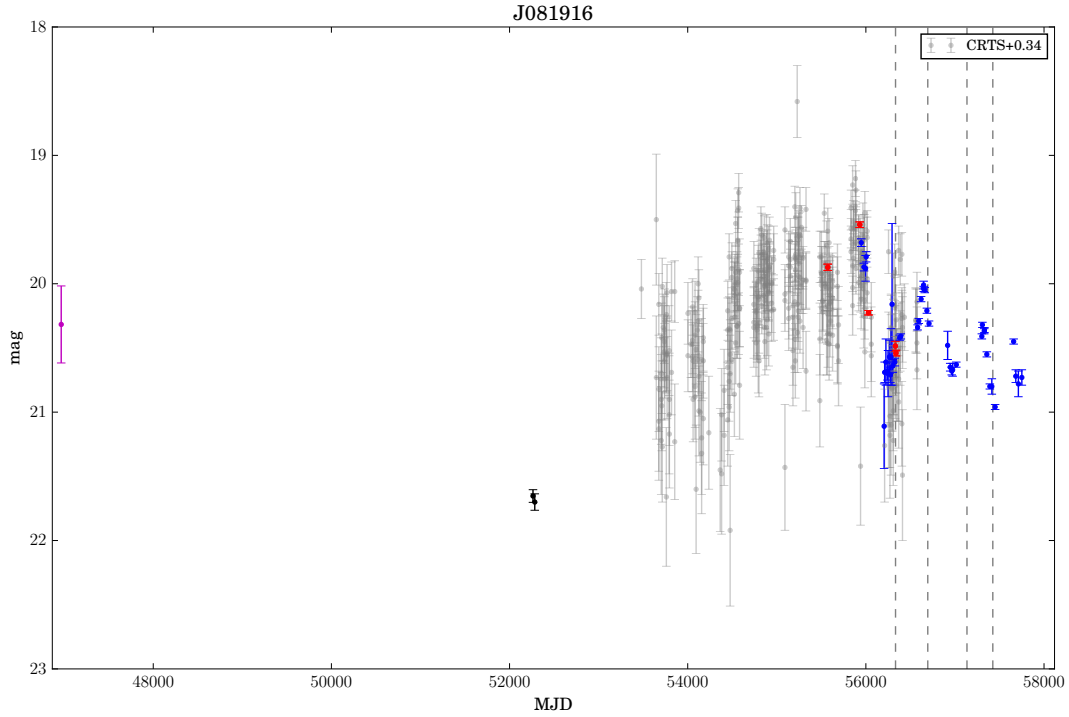
J081916
CRTS+0.34
mag
MJD
18
19
20
21
22
23
48000
50000
52000
54000
56000
58000

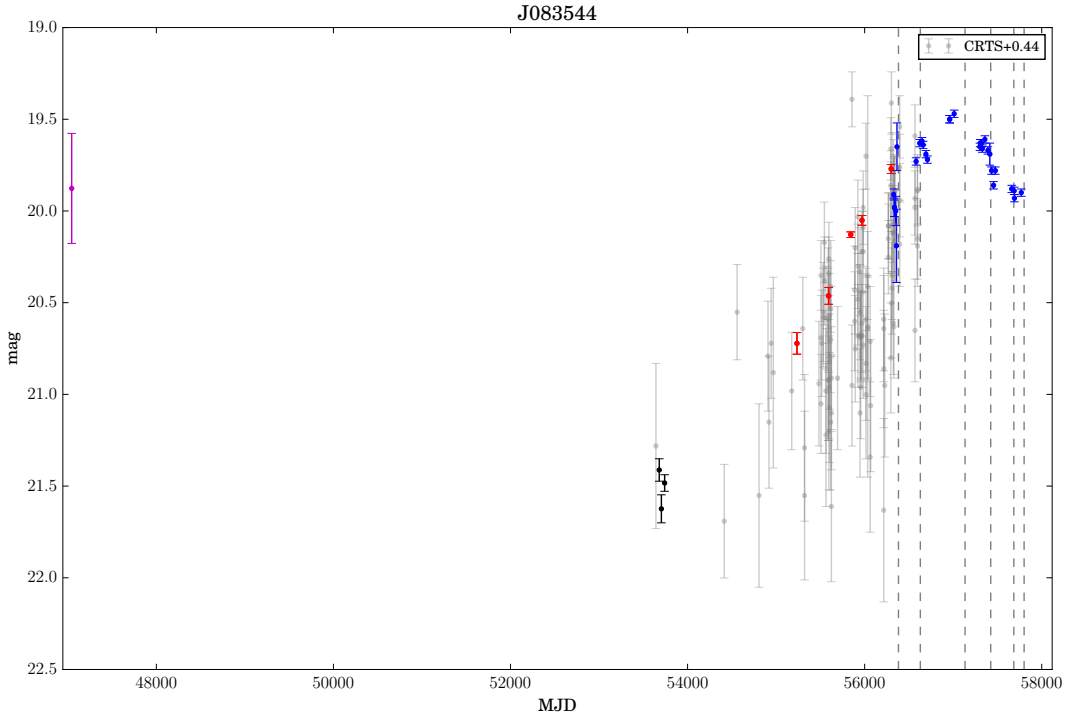
J083544
CRTS+0.44
mag
MJD
19.0
19.5
20.0
20.5
21.0
21.5
22.0
22.5
48000
50000
52000
54000
56000
58000

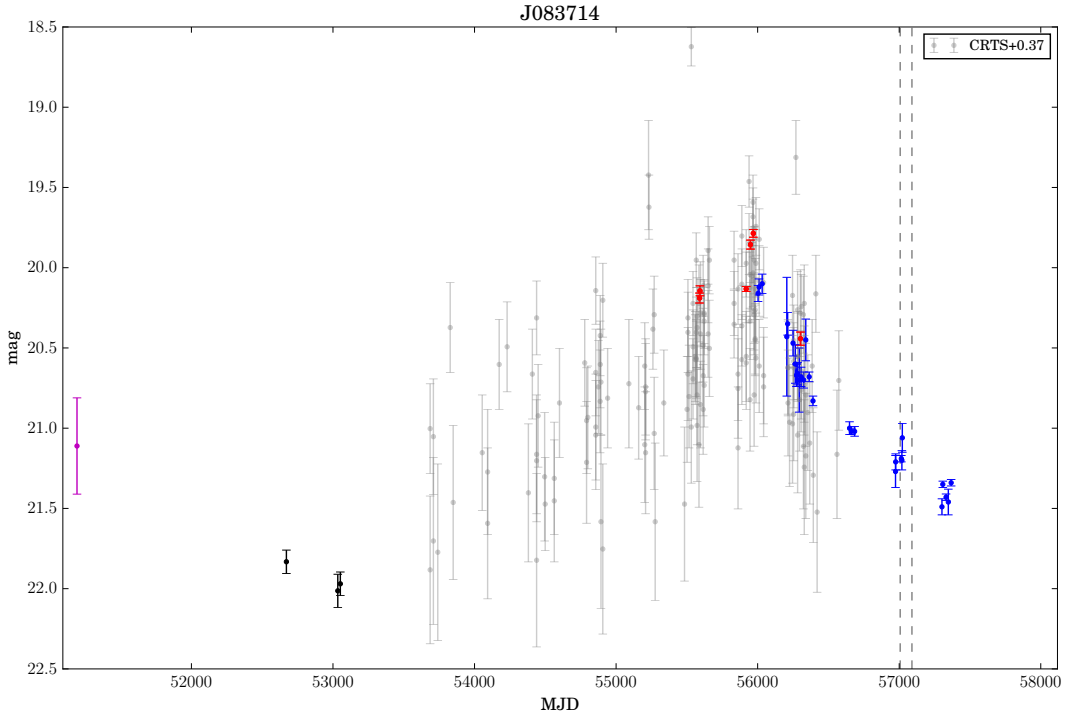
J083714
CRTS+0.37
mag
MJD
18.5
19.0
19.5
20.0
20.5
21.0
21.5
22.0
22.5
52000
53000
54000
55000
56000
57000
58000

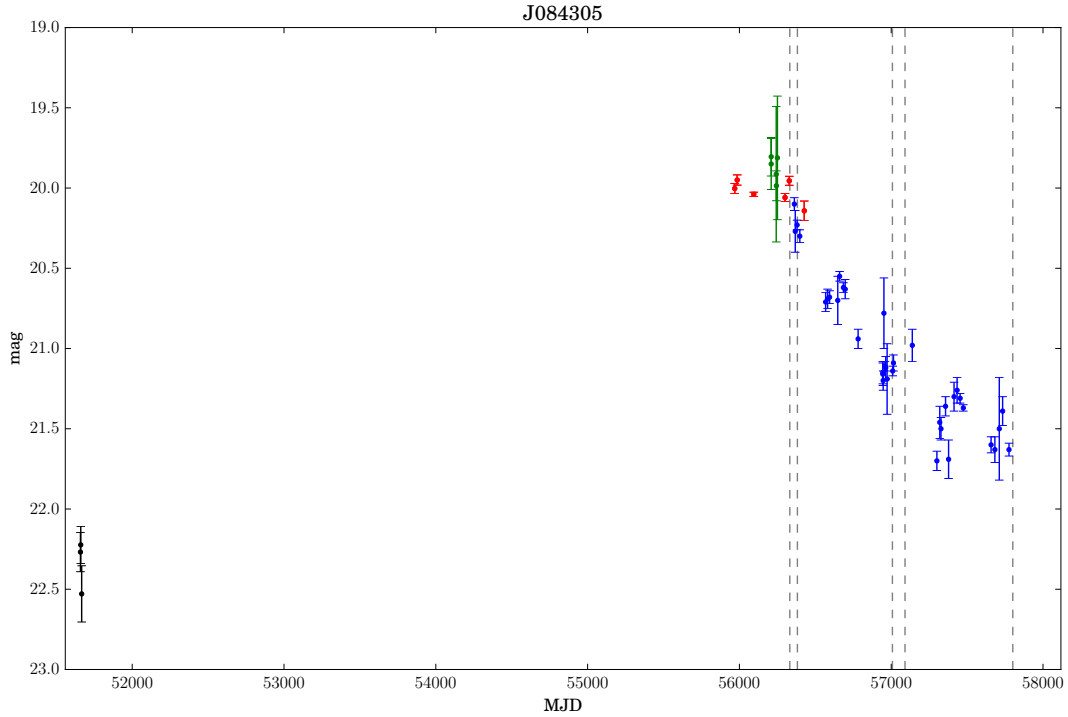
J084305
mag
MJD
19.0
19.5
20.0
20.5
21.0
21.5
22.0
22.5
23.0
52000
53000
54000
55000
56000
57000
58000

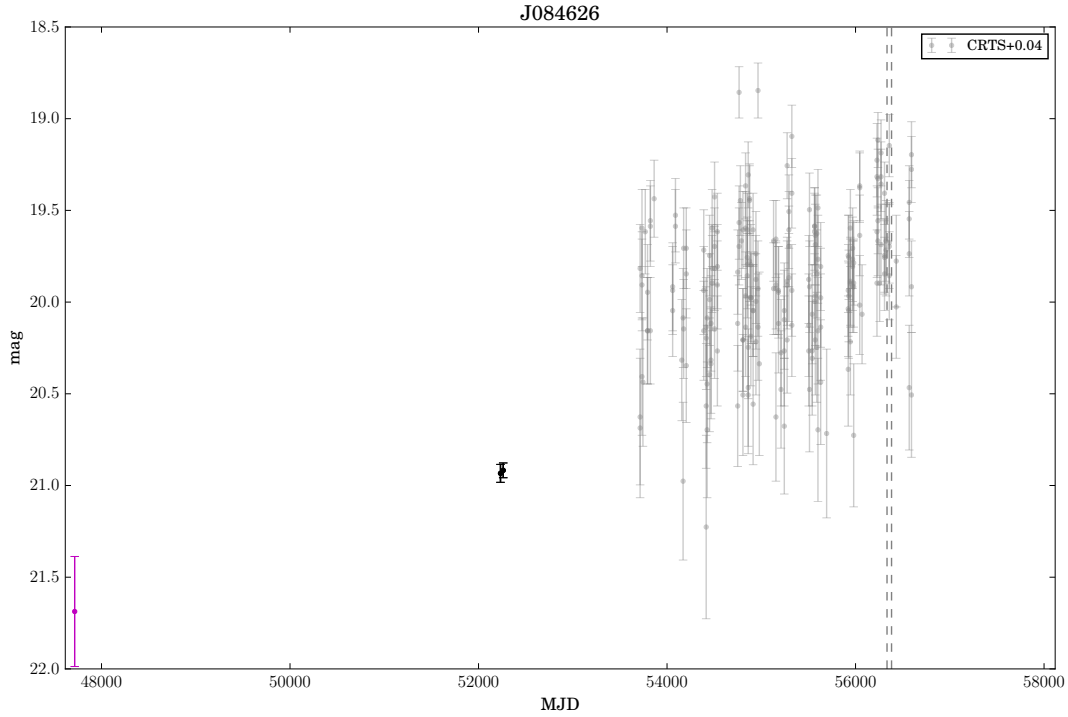
J084626
CRTS+0.04
mag
MJD
18.5
19.0
19.5
20.0
20.5
21.0
21.5
22.0
48000
50000
52000
54000
56000
58000

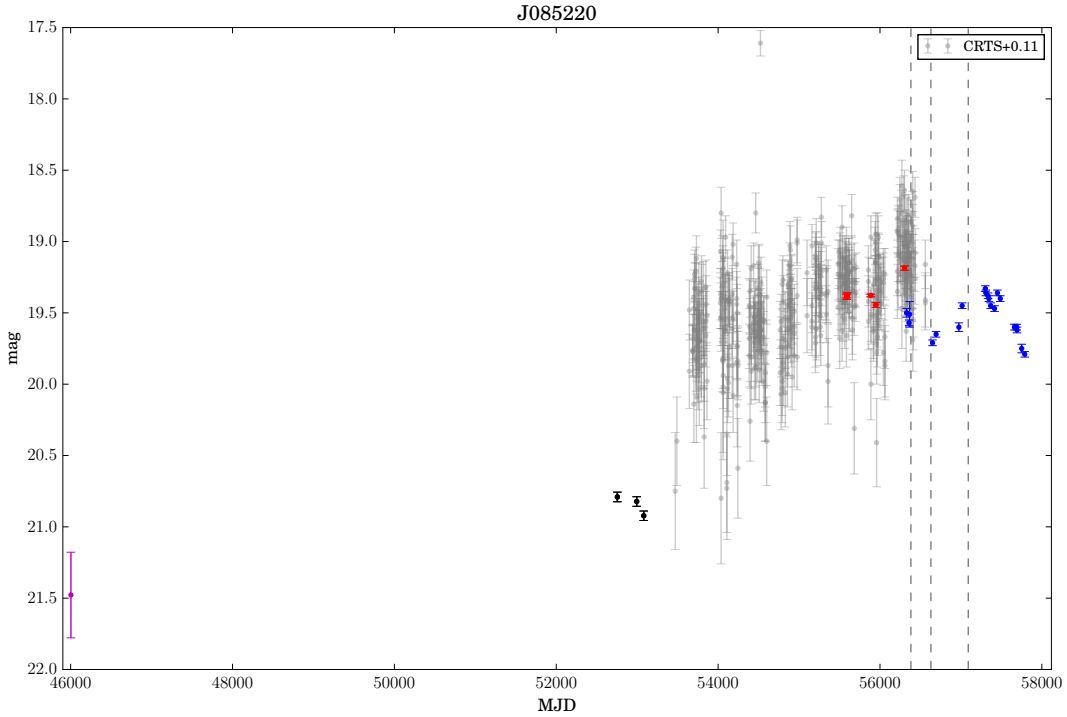
J085220
CRTS+0.11
mag
MJD
17.5
18.0
18.5
19.0
19.5
20.0
20.5
21.0
21.5
22.0
46000
48000
50000
52000
54000
56000
58000

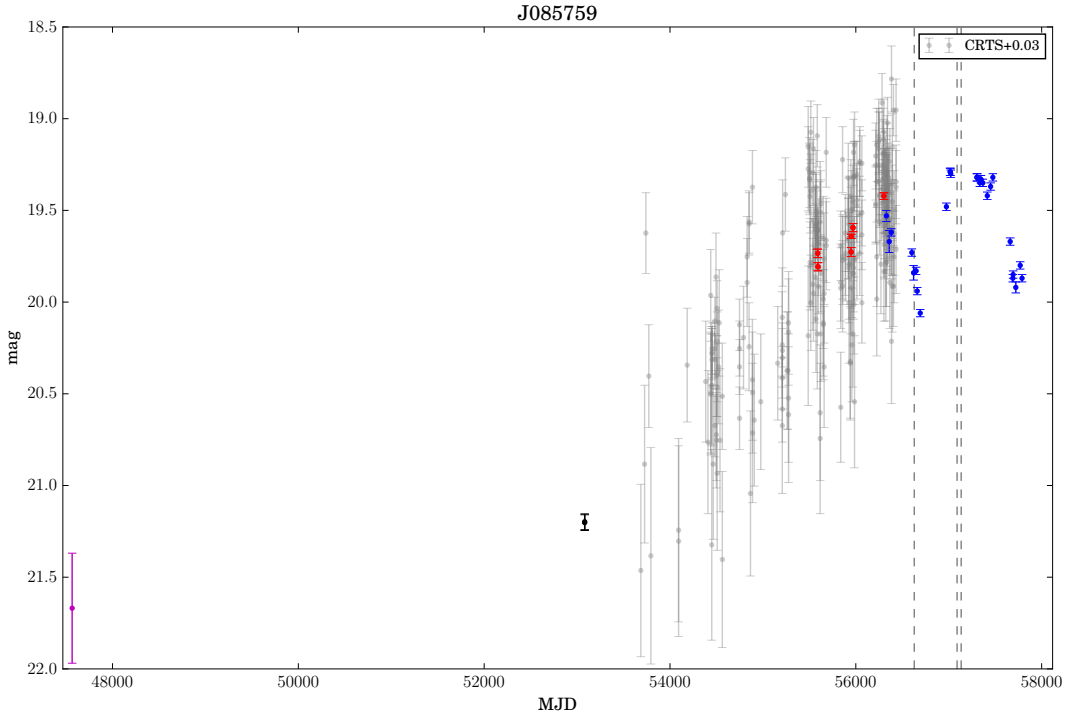
J085759
CRTS+0.03
mag
MJD
18.5
19.0
19.5
20.0
20.5
21.0
21.5
22.0
48000
50000
52000
54000
56000
58000

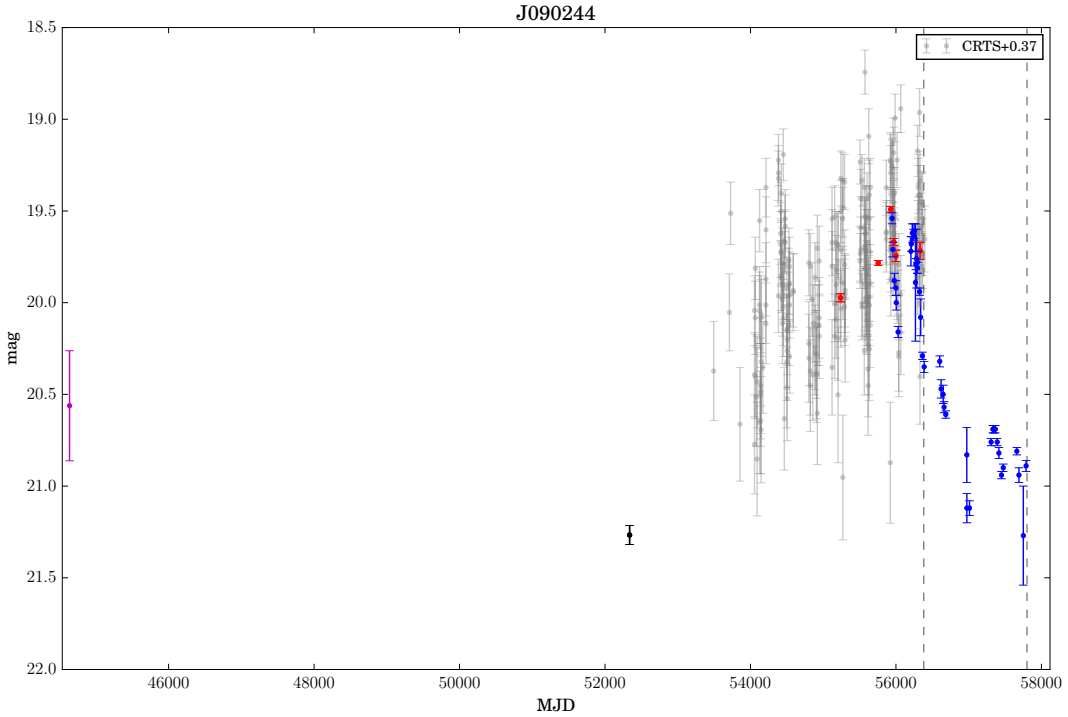
J090244
CRTS+0.37
mag
MJD
18.5
19.0
19.5
20.0
20.5
21.0
21.5
22.0
46000
48000
50000
52000
54000
56000
58000

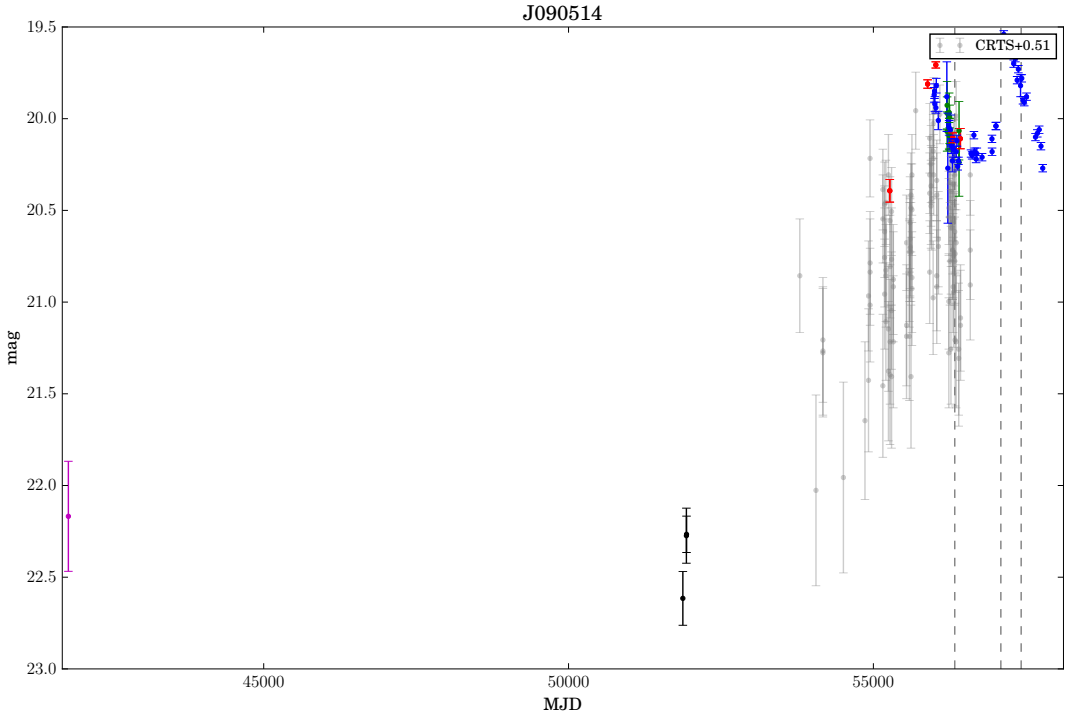
J090514
CRTS+0.51
mag
MJD
19.5
20.0
20.5
21.0
21.5
22.0
22.5
23.0
45000
50000
55000

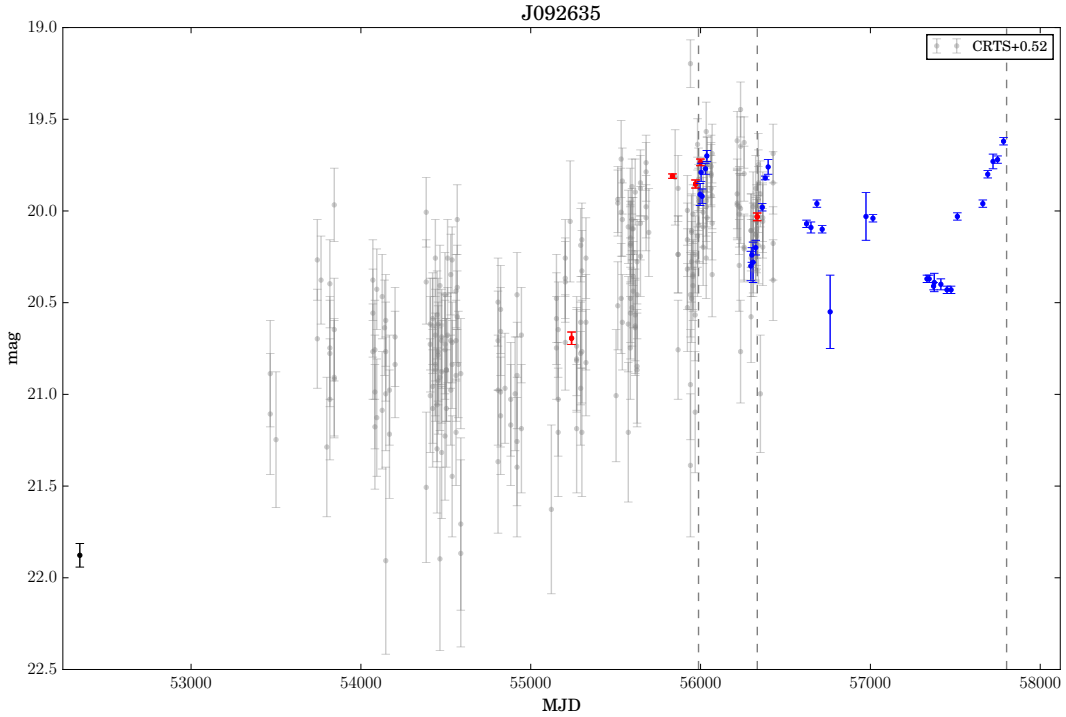
J092635
CRTS+0.52
mag
MJD
19.0
19.5
20.0
20.5
21.0
21.5
22.0
22.5
53000
54000
55000
56000
57000
58000

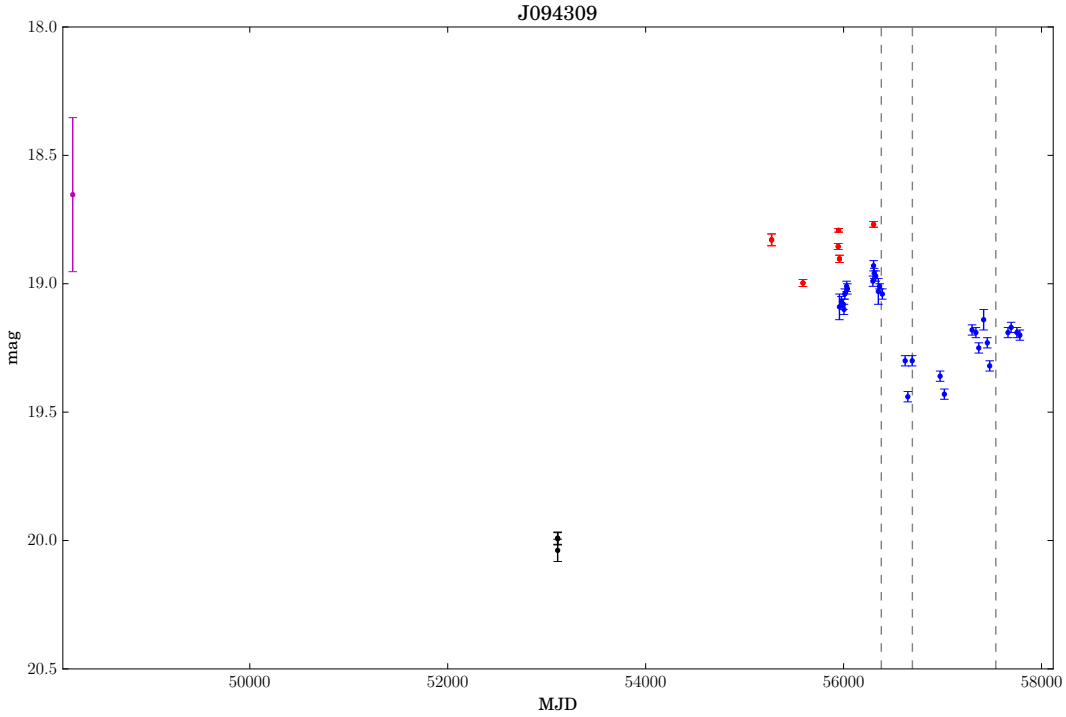
J094309
mag
MJD
18.0
18.5
19.0
19.5
20.0
20.5
50000
52000
54000
56000
58000

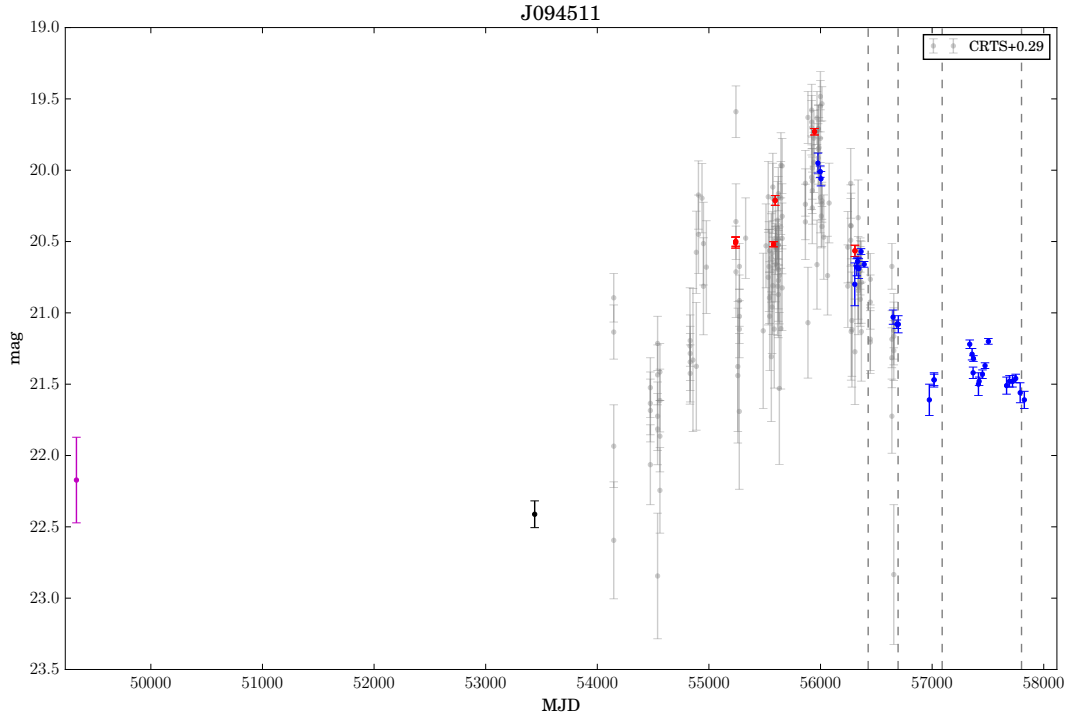
J094511
CRTS+0.29
mag
MJD
19.0
19.5
20.0
20.5
21.0
21.5
22.0
22.5
23.0
23.5
50000
51000
52000
53000
54000
55000
56000
57000
58000

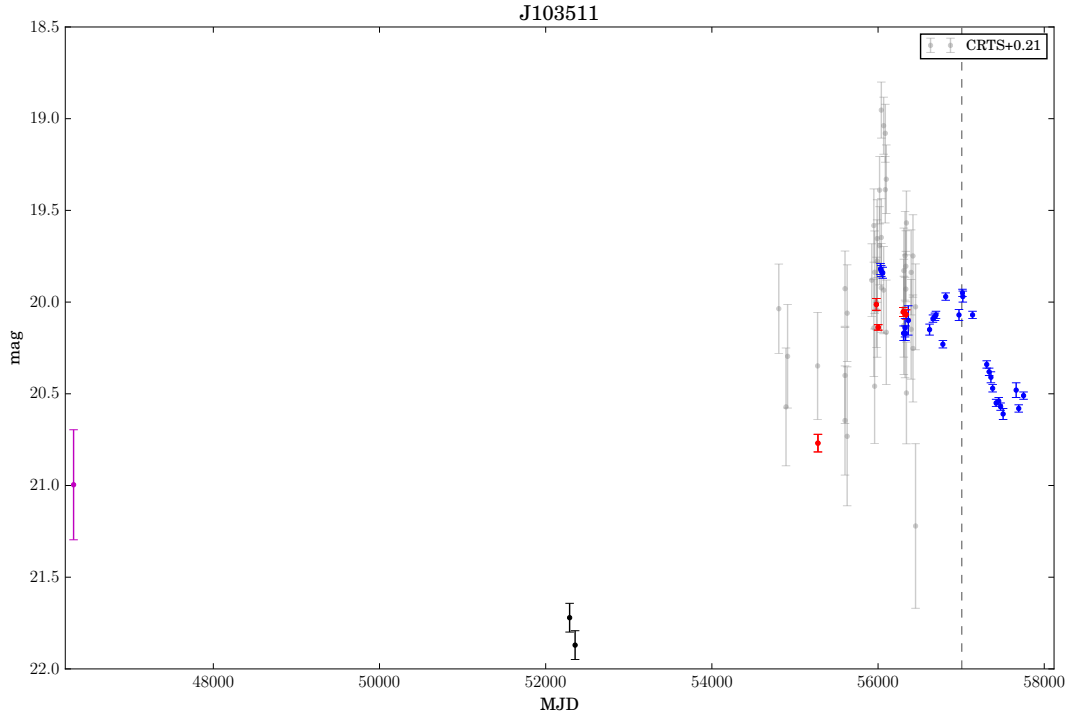
J103511
CRTS+0.21
mag
MJD
18.5
19.0
19.5
20.0
20.5
21.0
21.5
22.0
48000
50000
52000
54000
56000
58000

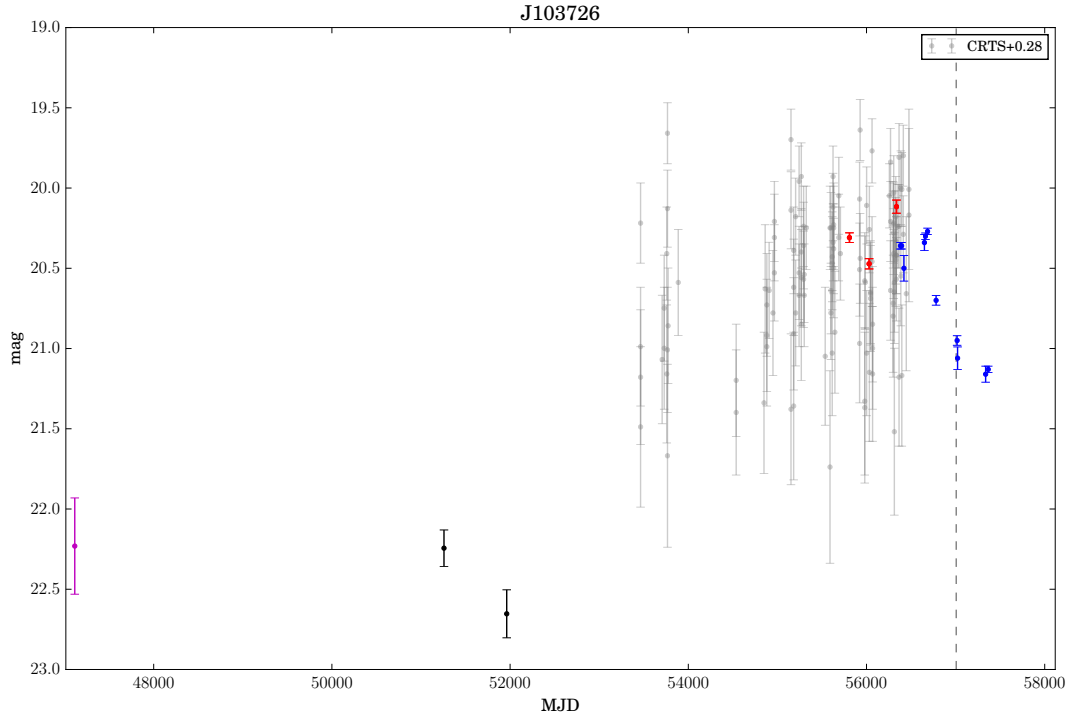
J103726
CRTS+0.28
mag
MJD
19.0
19.5
20.0
20.5
21.0
21.5
22.0
22.5
23.0
48000
50000
52000
54000
56000
58000

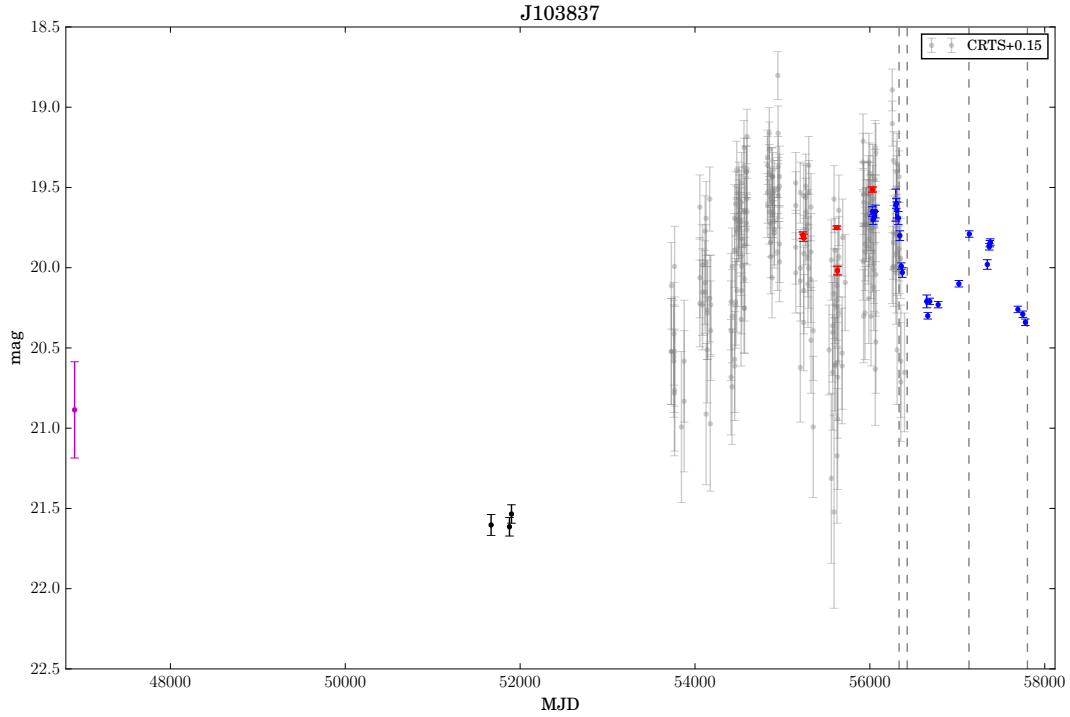
J103837
CRTS+0.15
mag
MJD
18.5
19.0
19.5
20.0
20.5
21.0
21.5
22.0
22.5
48000
50000
52000
54000
56000
58000

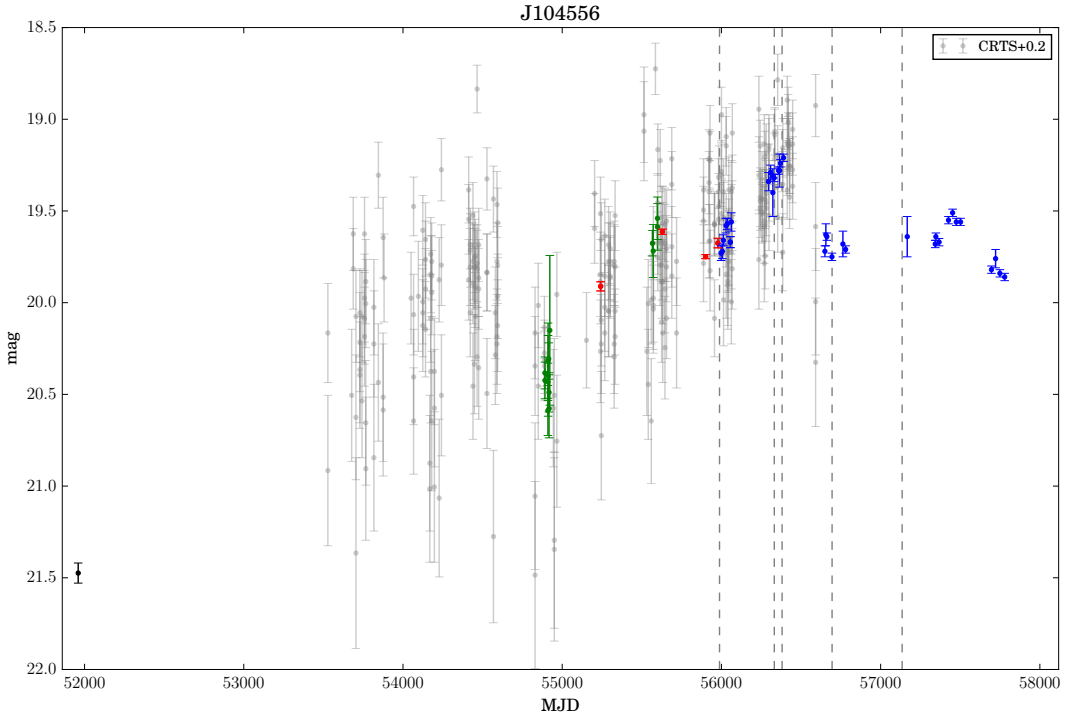
J104556
CRTS+0.2
mag
MJD
18.5
19.0
19.5
20.0
20.5
21.0
21.5
22.0
52000
53000
54000
55000
56000
57000
58000

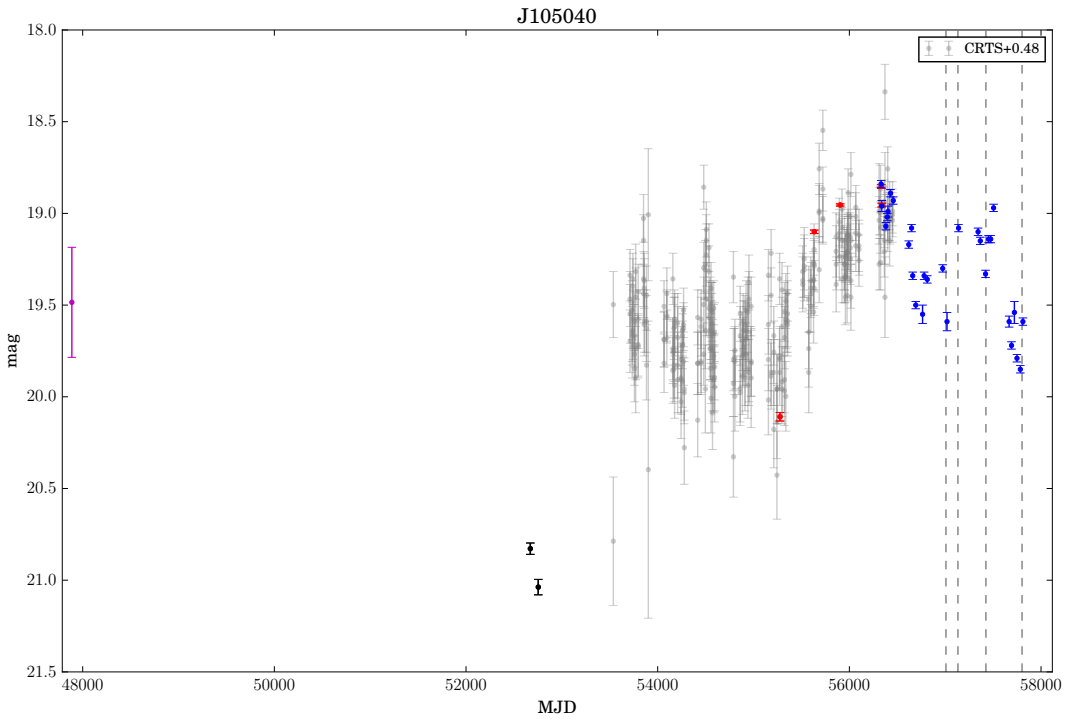
J105040
CRTS+0.48
mag
MJD
18.0
18.5
19.0
19.5
20.0
20.5
21.0
21.5
48000
50000
52000
54000
56000
58000

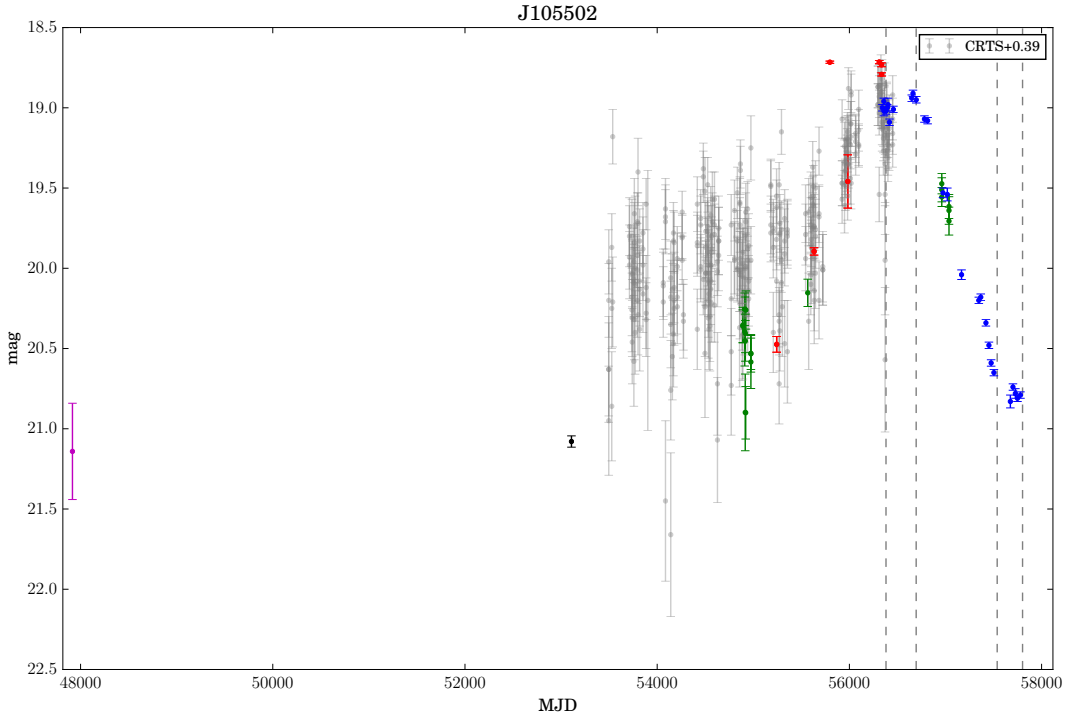
J105502
CRTS+0.39
mag
MJD
18.5
19.0
19.5
20.0
20.5
21.0
21.5
22.0
22.5
48000
50000
52000
54000
56000
58000

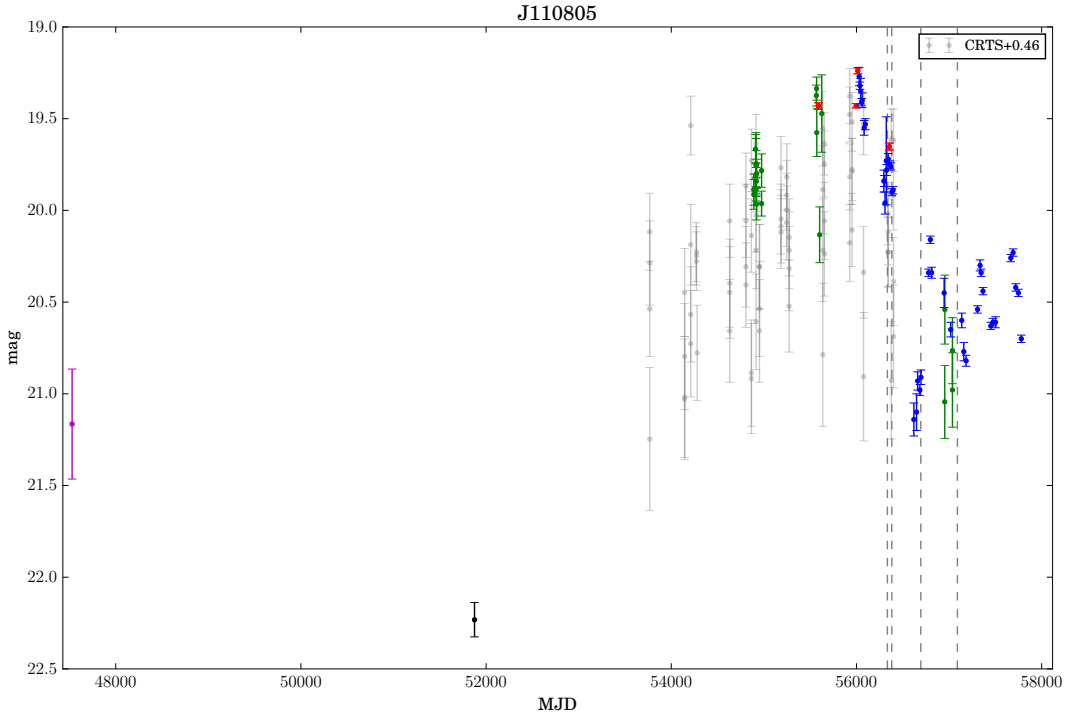
J110805
CRTS+0.46
mag
MJD
19.0
19.5
20.0
20.5
21.0
21.5
22.0
22.5
48000
50000
52000
54000
56000
58000

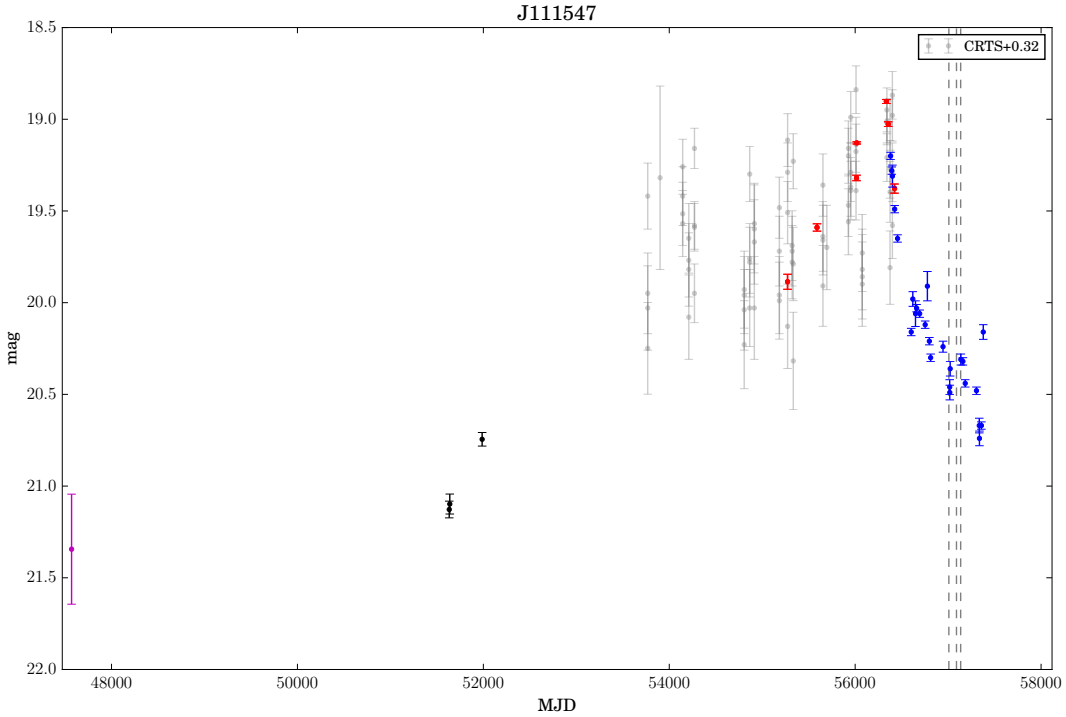
J111547
CRTS+0.32
mag
MJD
18.5
19.0
19.5
20.0
20.5
21.0
21.5
22.0
48000
50000
52000
54000
56000
58000

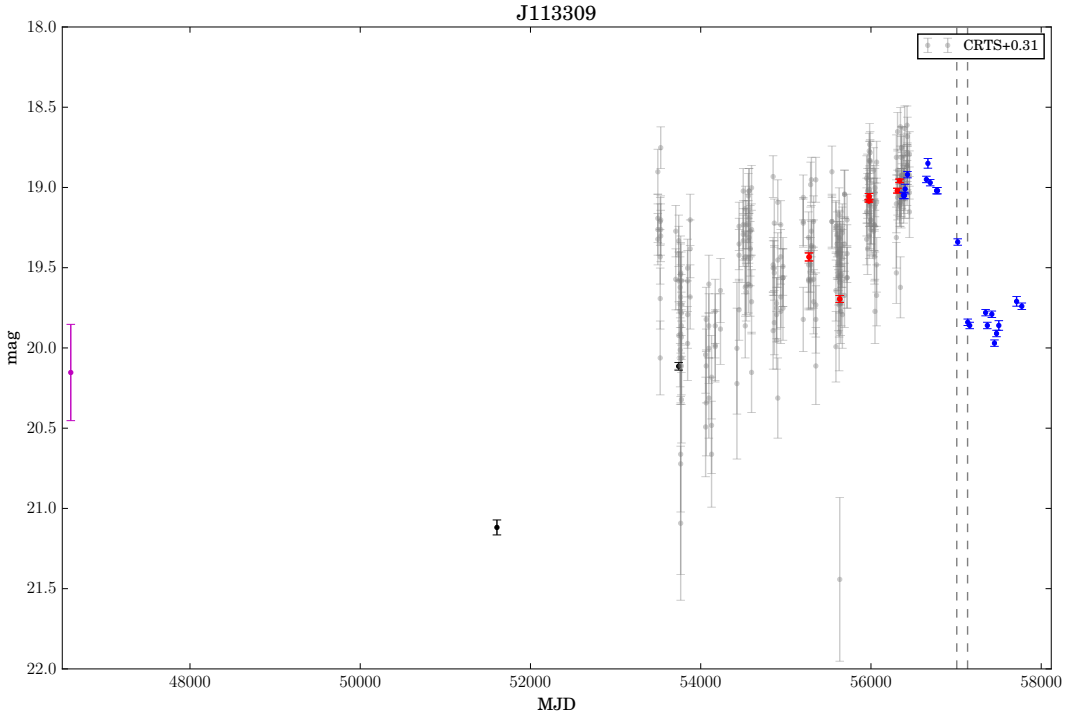
J113309
CRTS+0.31
mag
MJD
18.0
18.5
19.0
19.5
20.0
20.5
21.0
21.5
22.0
48000
50000
52000
54000
56000
58000

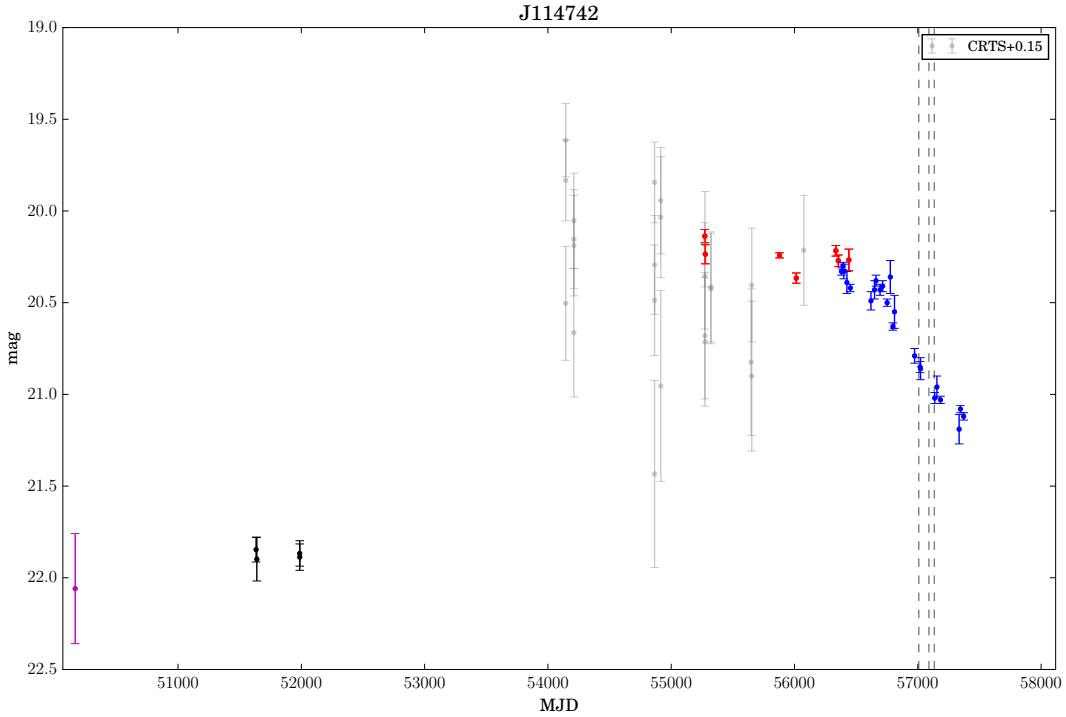
J114742
CRTS+0.15
mag
MJD
19.0
19.5
20.0
20.5
21.0
21.5
22.0
22.5
51000
52000
53000
54000
55000
56000
57000
58000

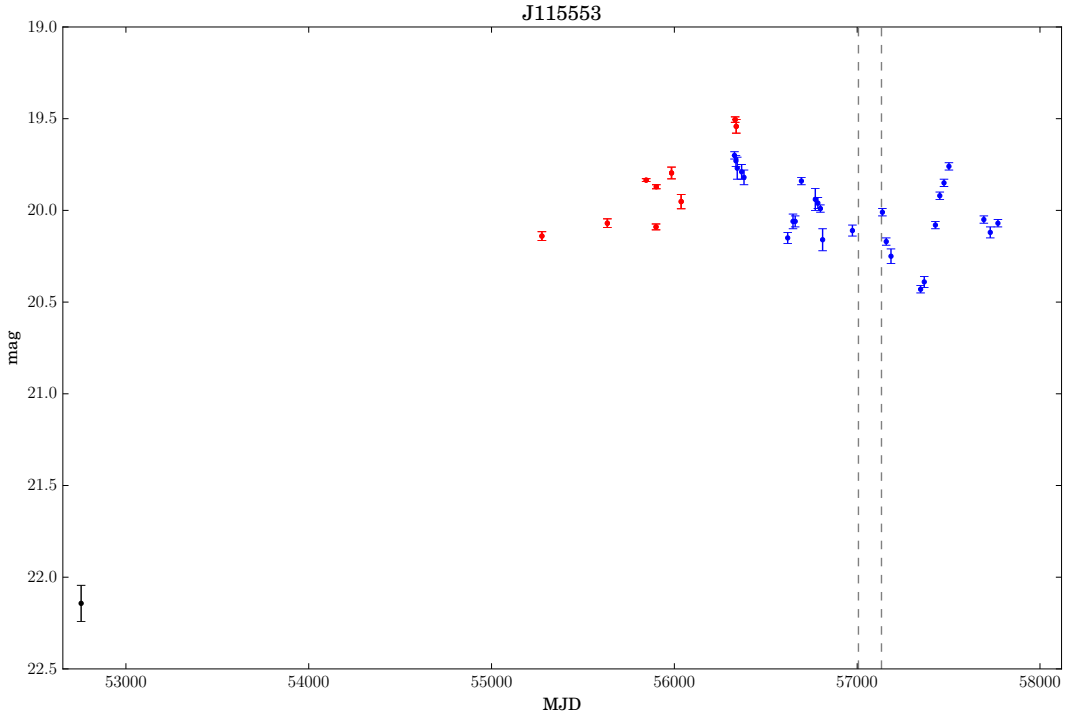
J115553
mag
MJD
19.0
19.5
20.0
20.5
21.0
21.5
22.0
22.5
53000
54000
55000
56000
57000
58000

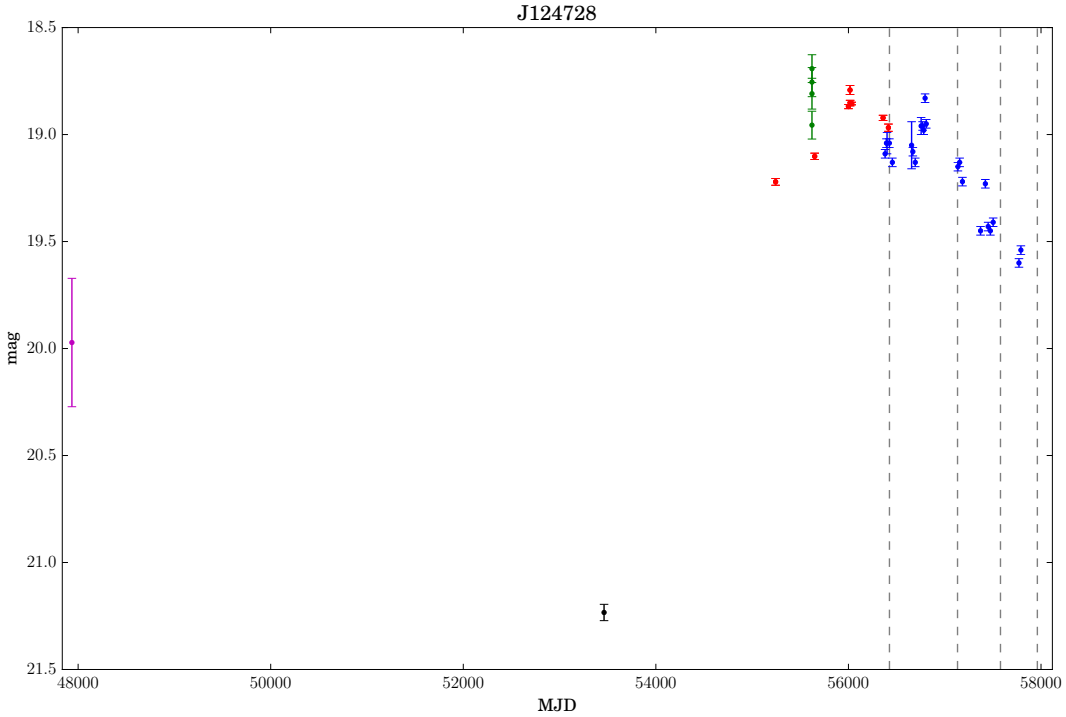
J124728
18.5
19.0
19.5
20.0
20.5
21.0
21.5
mag
48000
50000
52000
54000
56000
58000
MJD

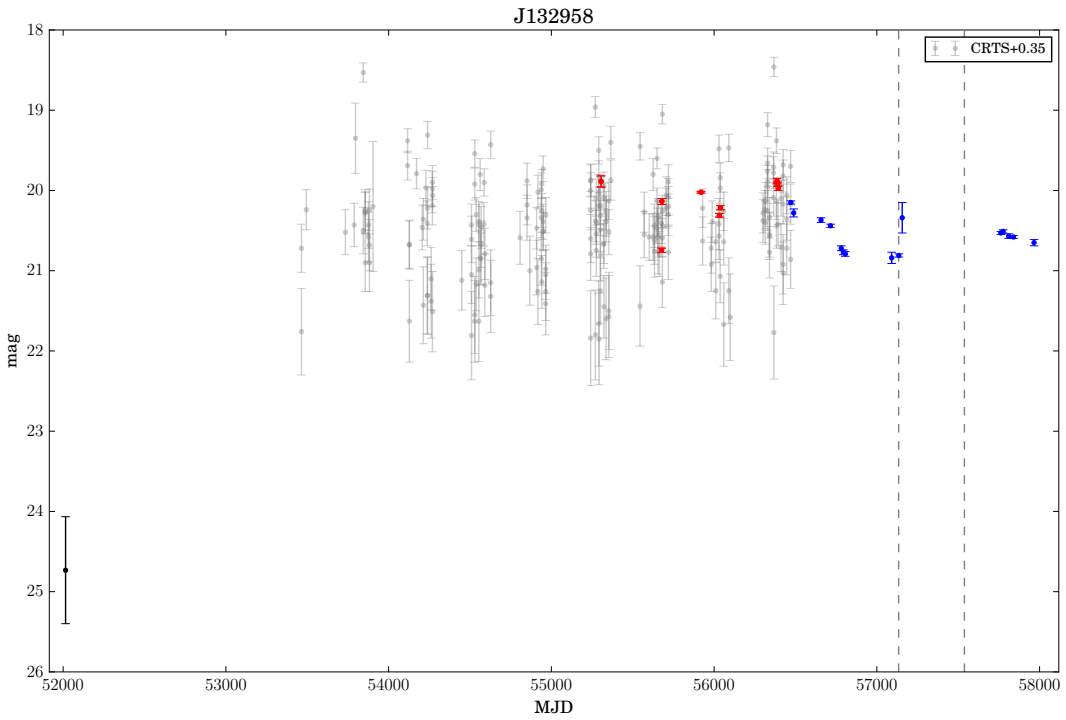
J132958
CRTS+0.35
18
19
20
21
22
23
24
25
26
mag
52000
53000
54000
55000
56000
57000
58000
MJD

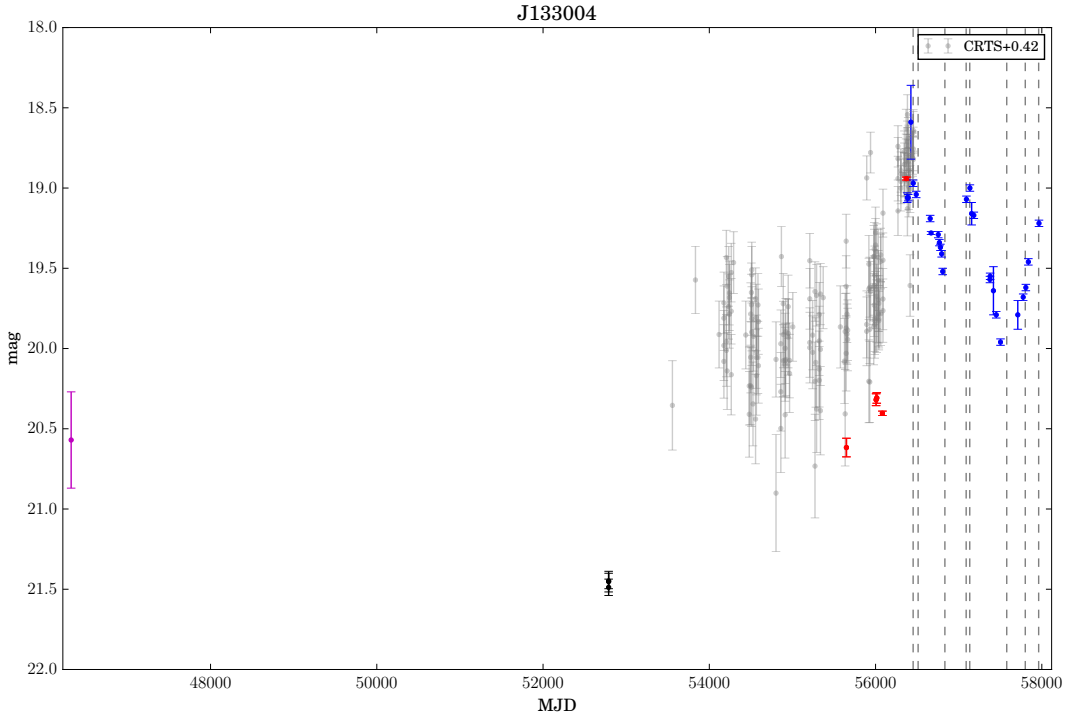
J133004
CRTS+0.42
mag
MJD
18.0
18.5
19.0
19.5
20.0
20.5
21.0
21.5
22.0
48000
50000
52000
54000
56000
58000

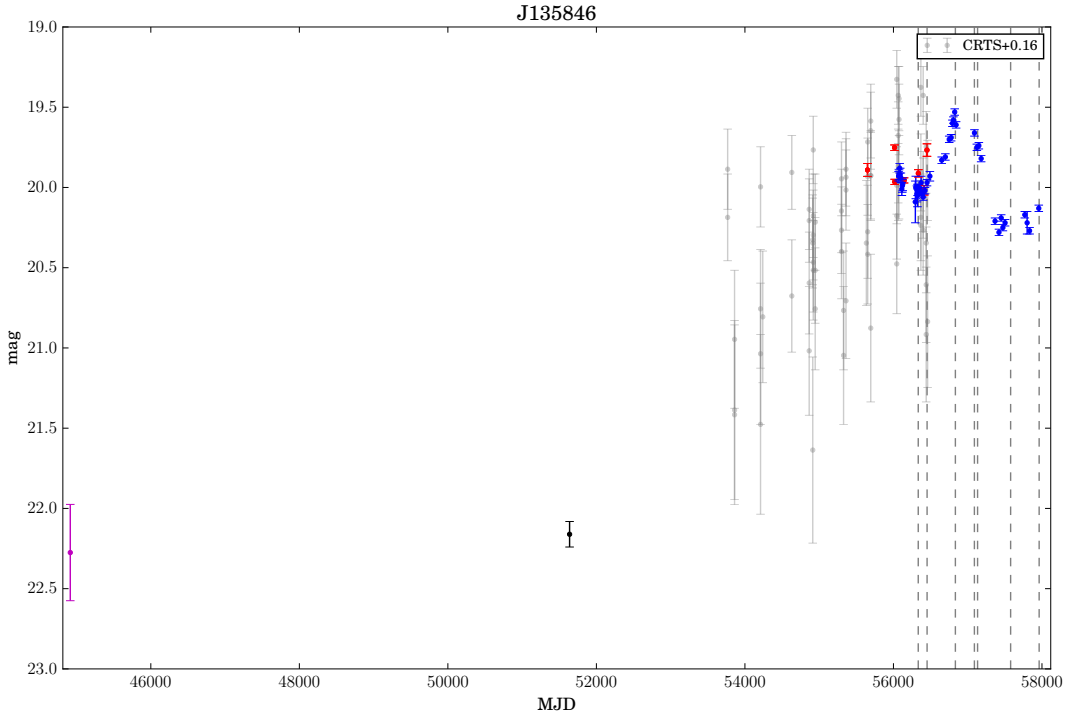
J135846
CRTS+0.16
mag
MJD
19.0
19.5
20.0
20.5
21.0
21.5
22.0
22.5
23.0
46000
48000
50000
52000
54000
56000
58000

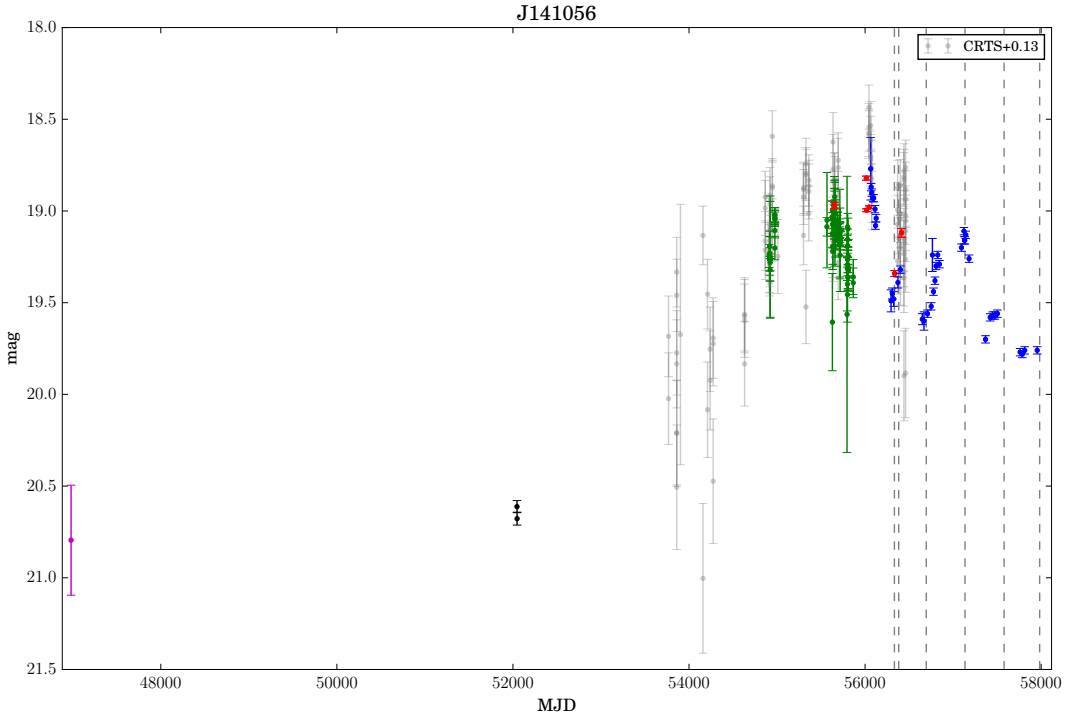
J141056
CRTS+0.13
mag
MJD
18.0
18.5
19.0
19.5
20.0
20.5
21.0
21.5
48000
50000
52000
54000
56000
58000

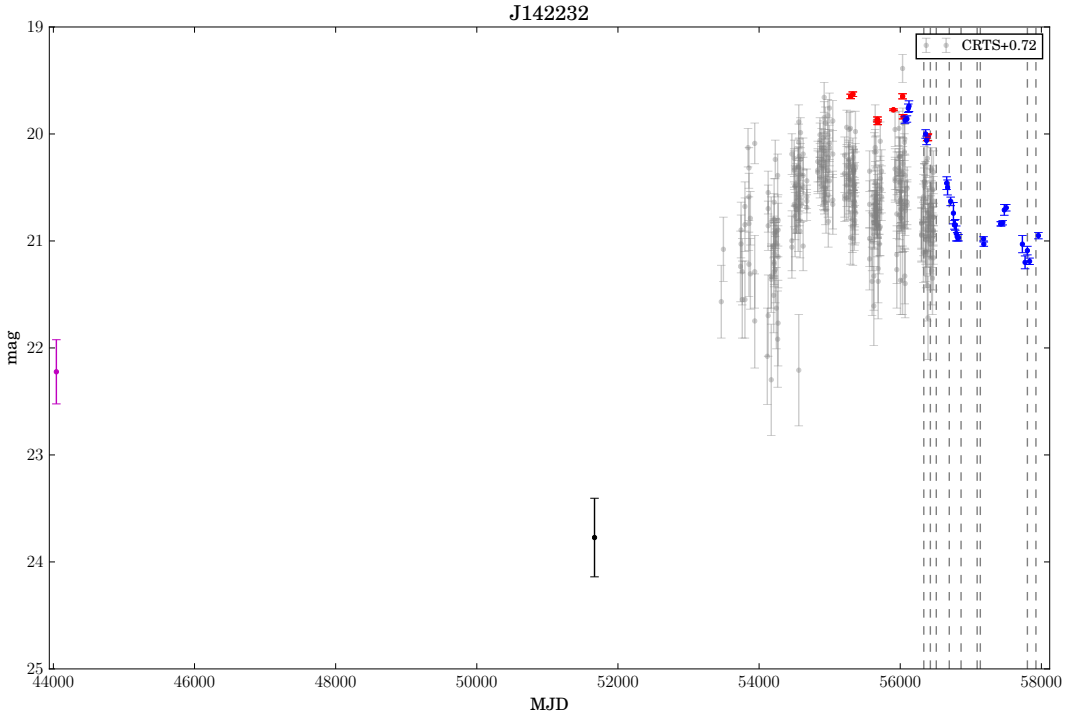
J142232
CRTS+0.72
mag
MJD
19
20
21
22
23
24
25
44000
46000
48000
50000
52000
54000
56000
58000

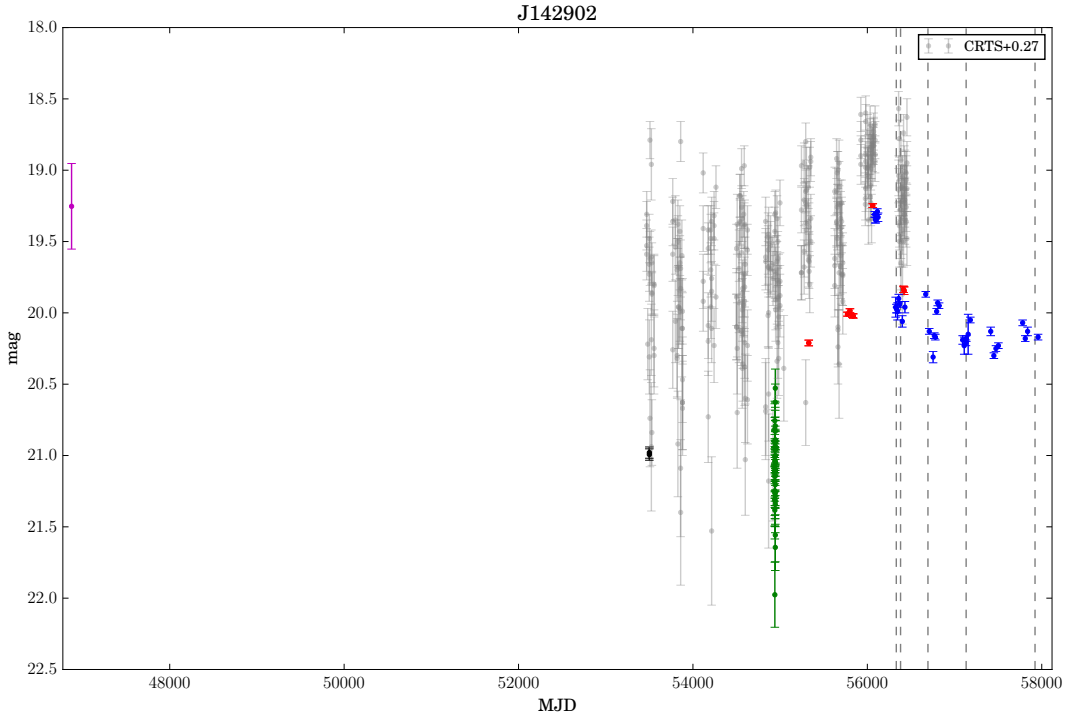
J142902
CRTS+0.27
mag
MJD
18.0
18.5
19.0
19.5
20.0
20.5
21.0
21.5
22.0
22.5
48000
50000
52000
54000
56000
58000

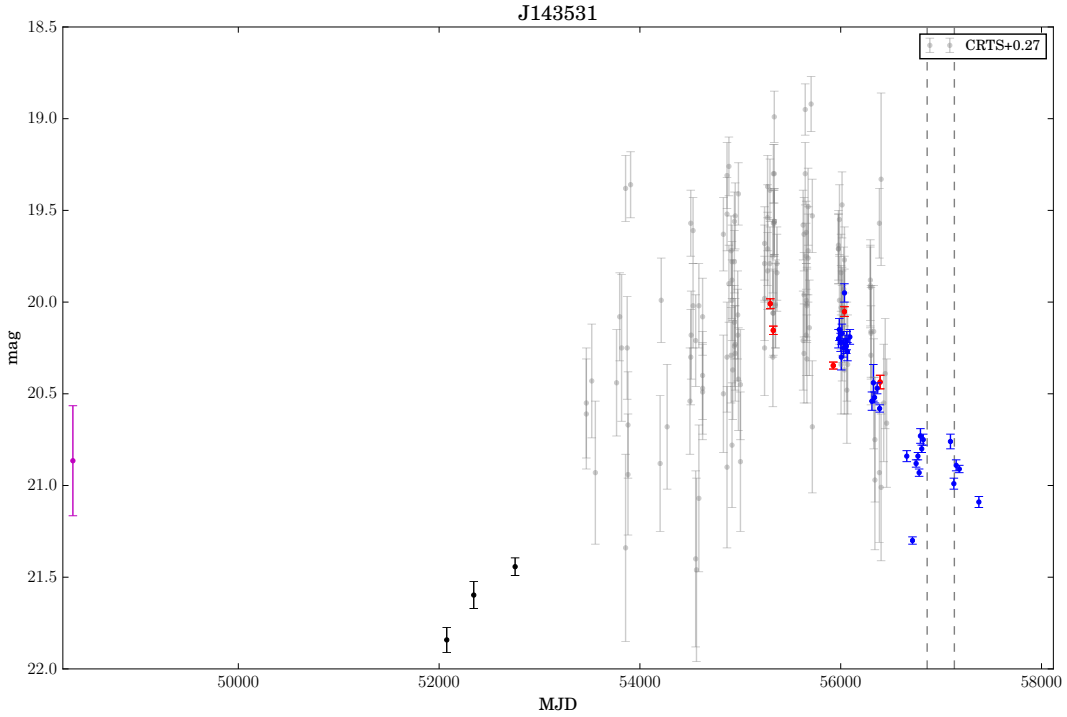
J143531
CRTS+0.27
mag
MJD
18.5
19.0
19.5
20.0
20.5
21.0
21.5
22.0
50000
52000
54000
56000
58000

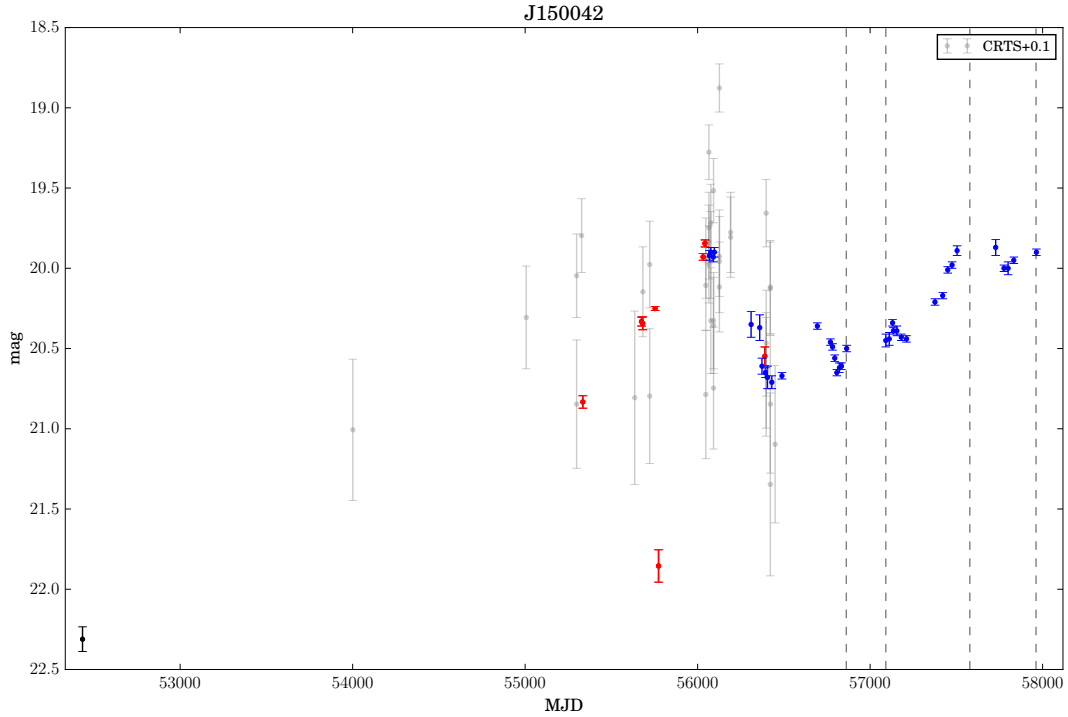
J150042
CRTS+0.1
mag
MJD
18.5
19.0
19.5
20.0
20.5
21.0
21.5
22.0
22.5
53000
54000
55000
56000
57000
58000

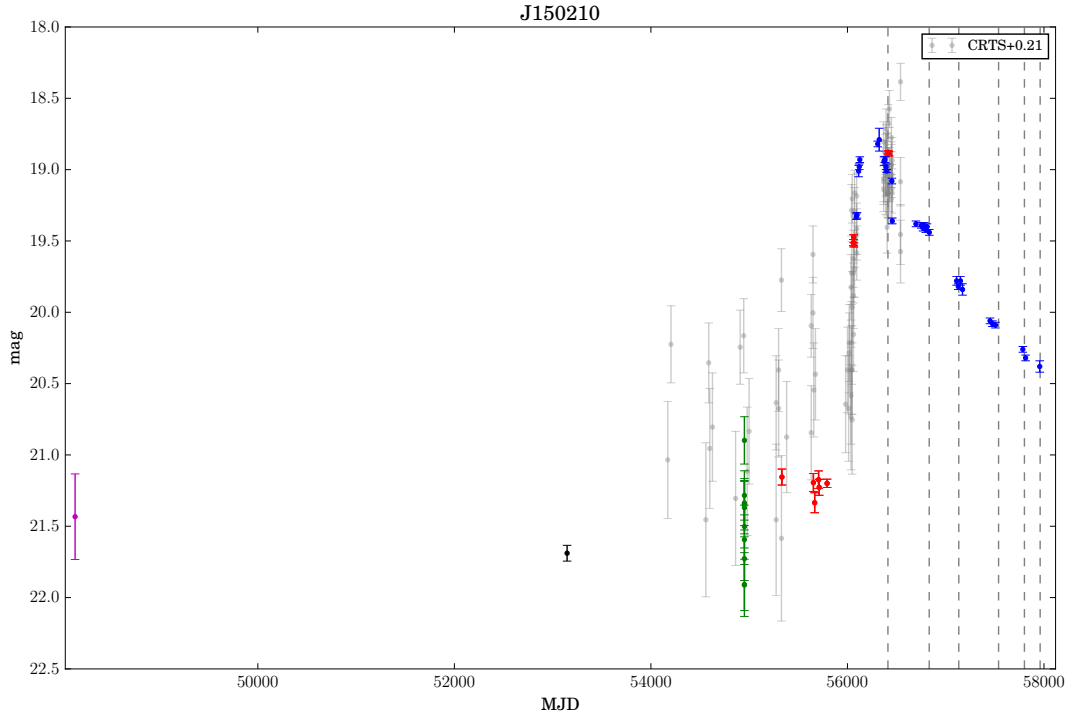
J150210
CRTS+0.21
mag
MJD
18.0
18.5
19.0
19.5
20.0
20.5
21.0
21.5
22.0
22.5
50000
52000
54000
56000
58000

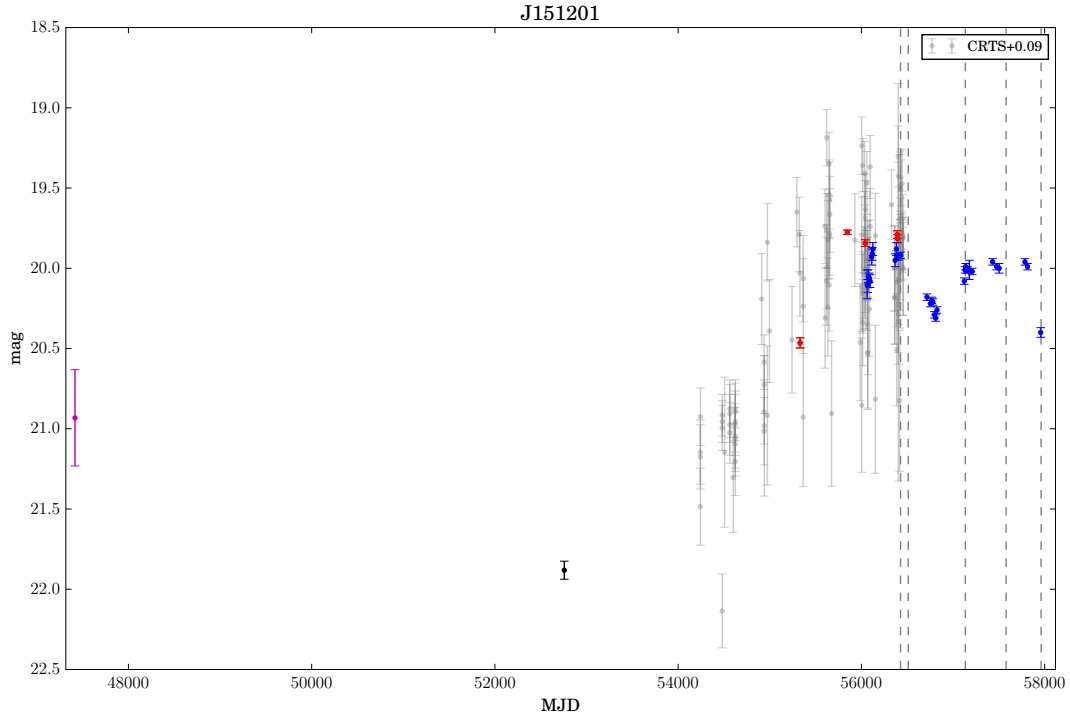
J151201
CRTS+0.09
mag
MJD
18.5
19.0
19.5
20.0
20.5
21.0
21.5
22.0
22.5
48000
50000
52000
54000
56000
58000

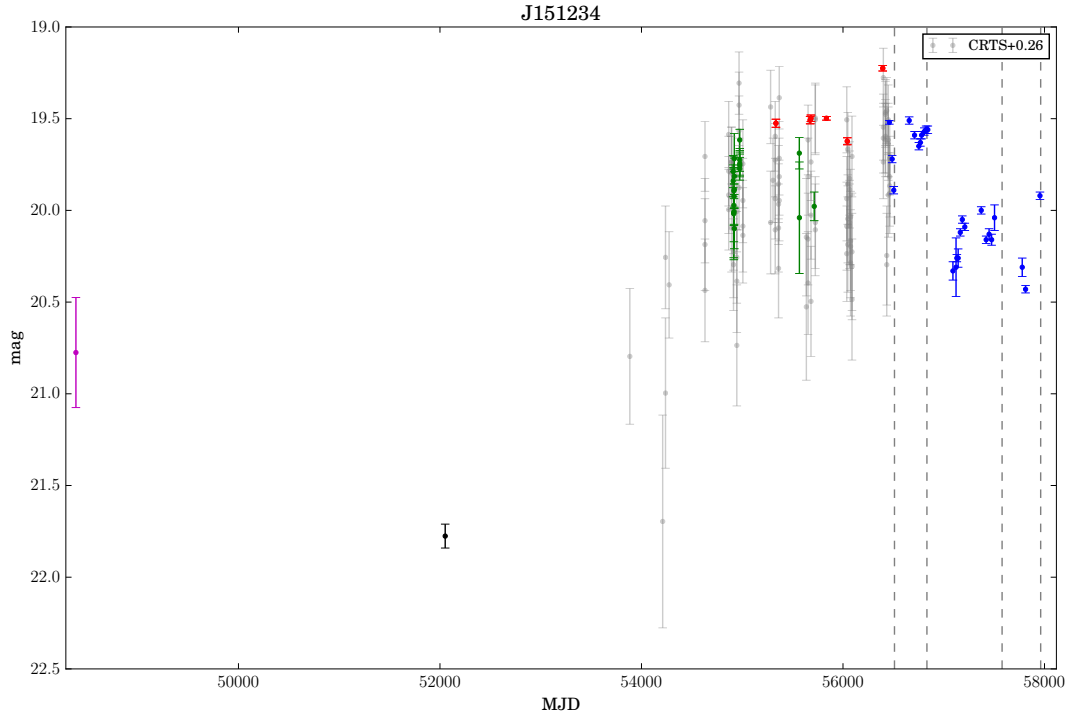
J151234
CRTS+0.26
mag
MJD
19.0
19.5
20.0
20.5
21.0
21.5
22.0
22.5
50000
52000
54000
56000
58000

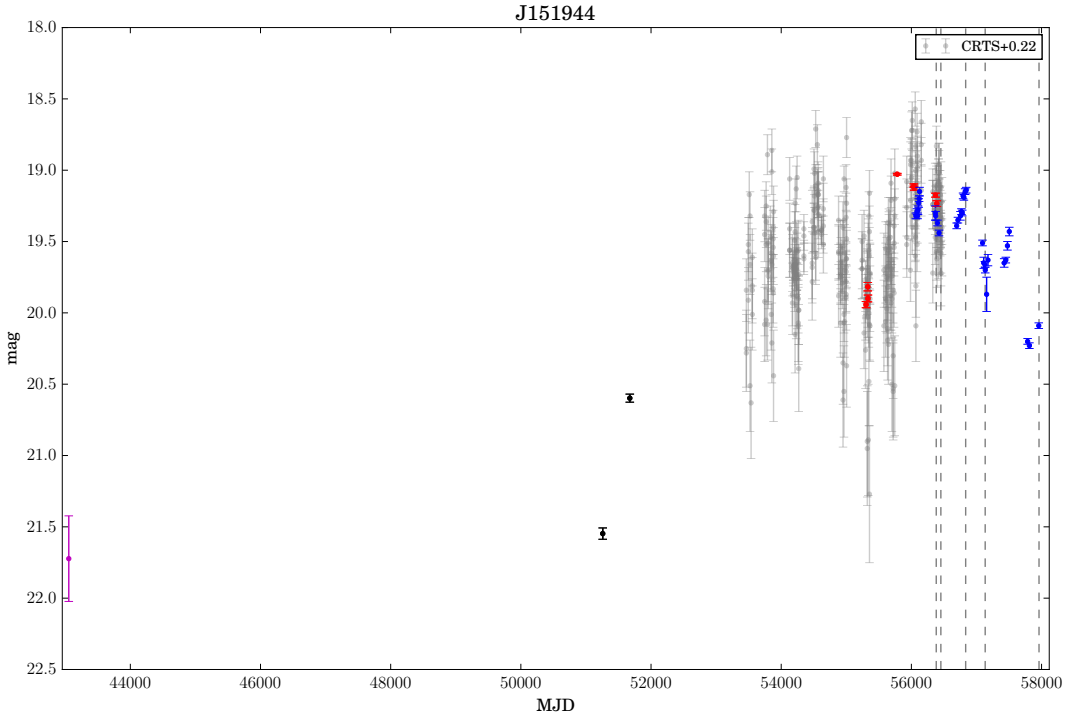
J151944
CRTS+0.22
mag
MJD
18.0
18.5
19.0
19.5
20.0
20.5
21.0
21.5
22.0
22.5
44000
46000
48000
50000
52000
54000
56000
58000

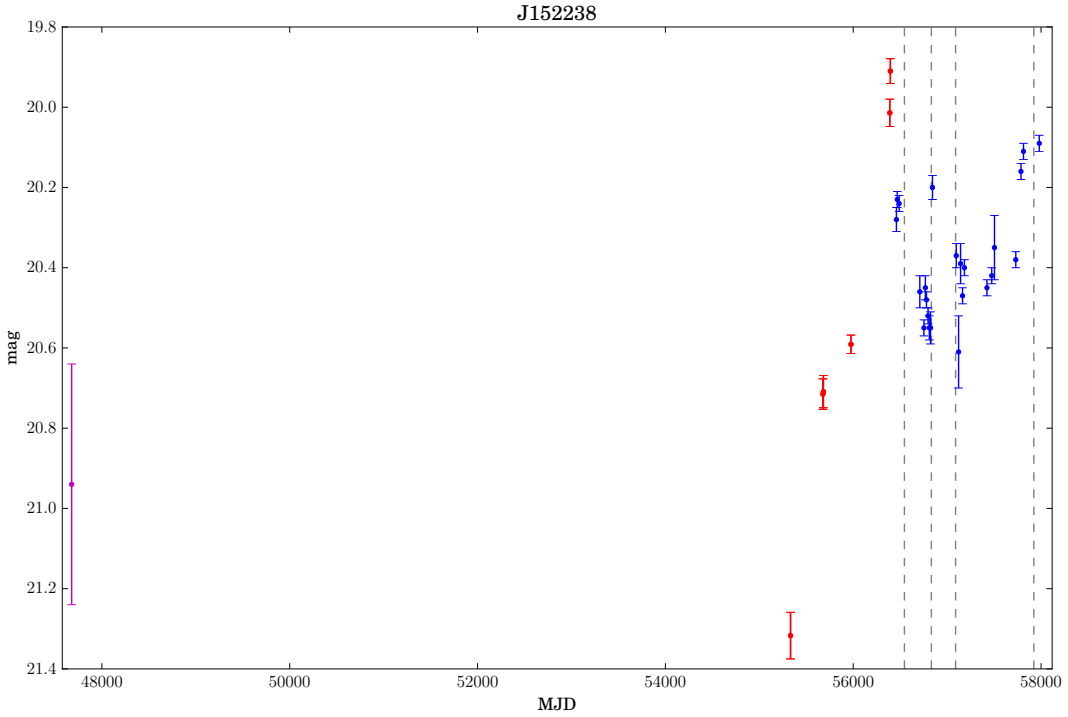
J152238
mag
MJD
19.8
20.0
20.2
20.4
20.6
20.8
21.0
21.2
21.4
48000
50000
52000
54000
56000
58000

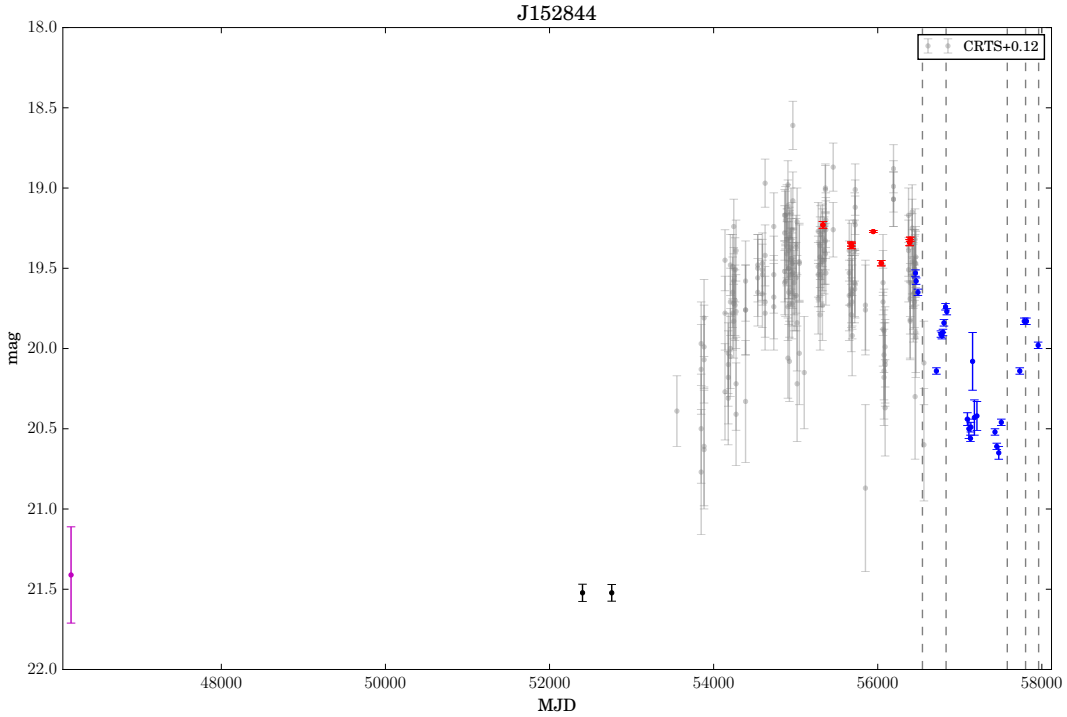
J152844
CRTS+0.12
mag
MJD
18.0
18.5
19.0
19.5
20.0
20.5
21.0
21.5
22.0
48000
50000
52000
54000
56000
58000

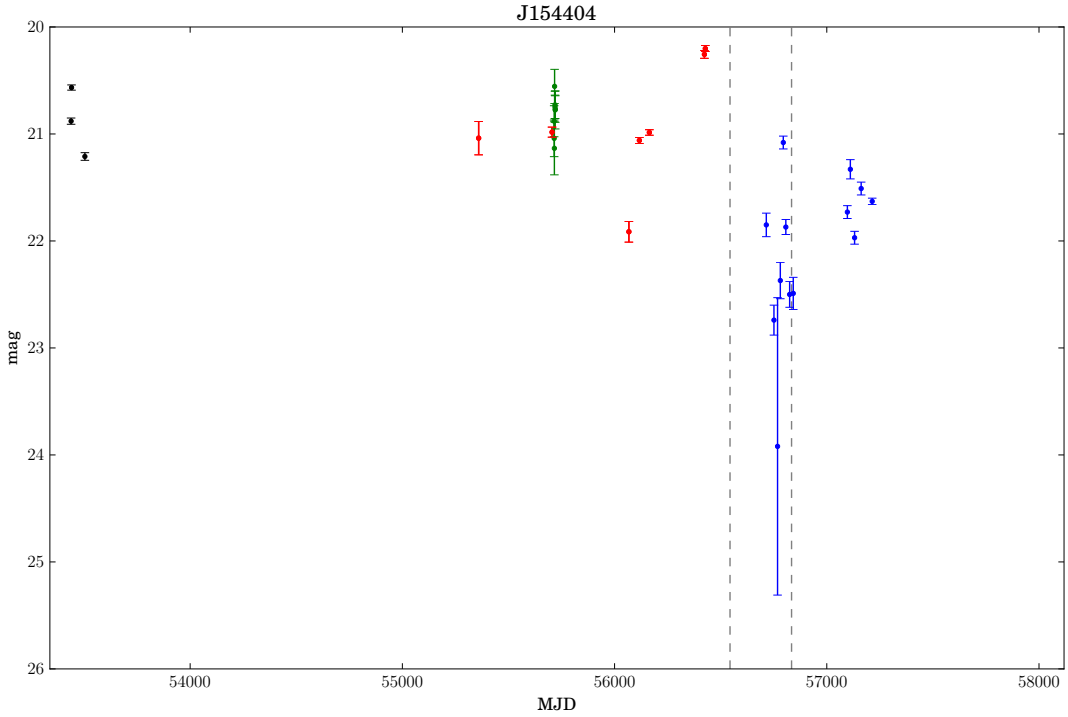
J154404
mag
MJD
20
21
22
23
24
25
26
54000
55000
56000
57000
58000

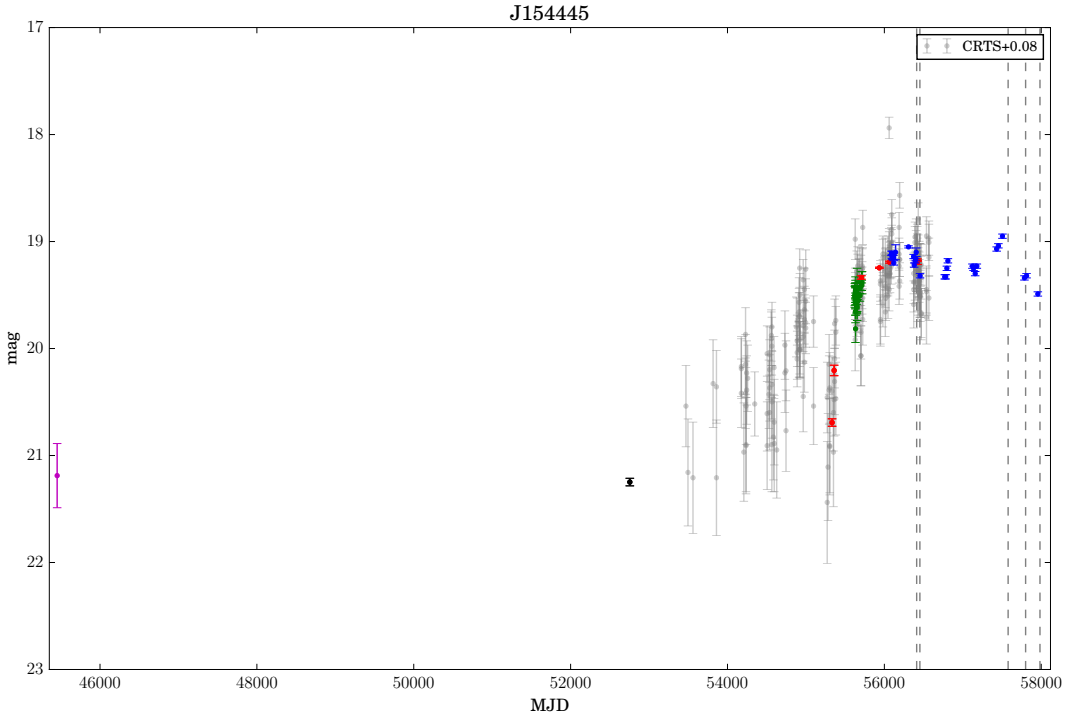
J154445
CRTS+0.08
mag
MJD
17
18
19
20
21
22
23
46000
48000
50000
52000
54000
56000
58000

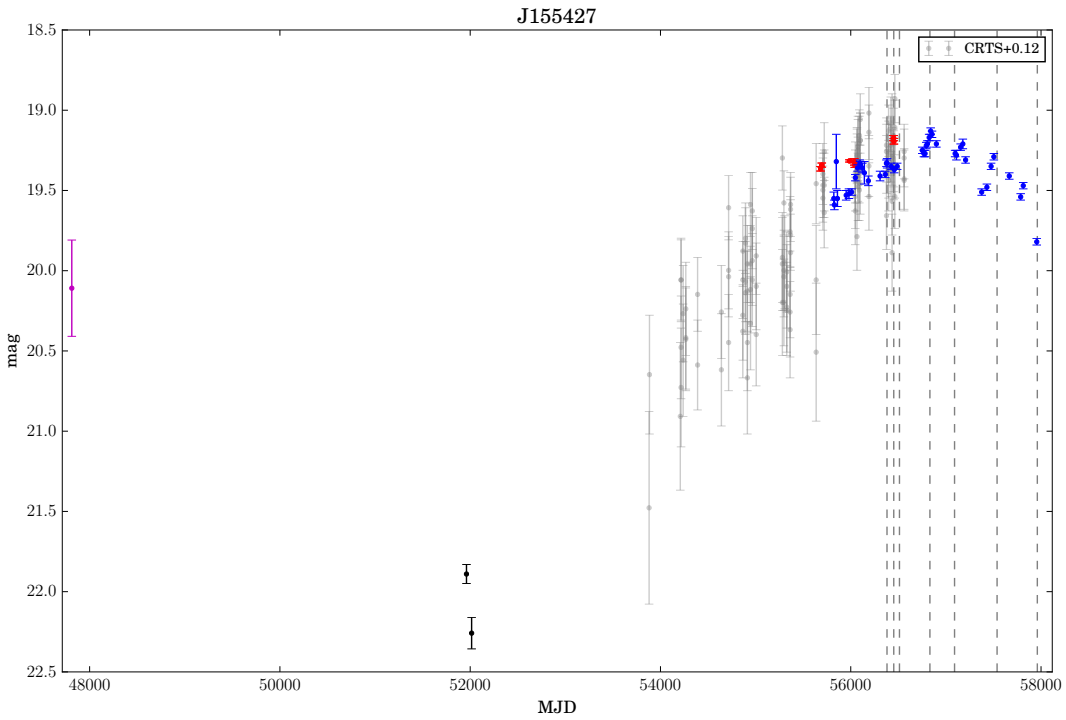
J155427
CRTS+0.12
mag
MJD
18.5
19.0
19.5
20.0
20.5
21.0
21.5
22.0
22.5
48000
50000
52000
54000
56000
58000

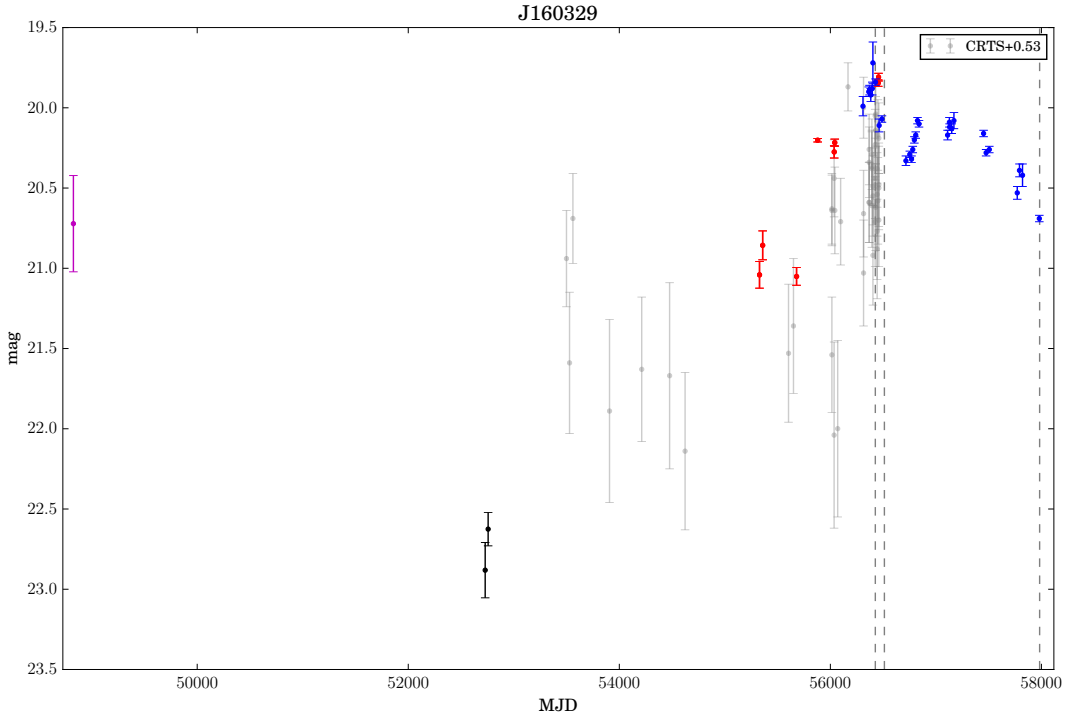
J160329
CRTS+0.53
mag
MJD
19.5
20.0
20.5
21.0
21.5
22.0
22.5
23.0
23.5
50000
52000
54000
56000
58000

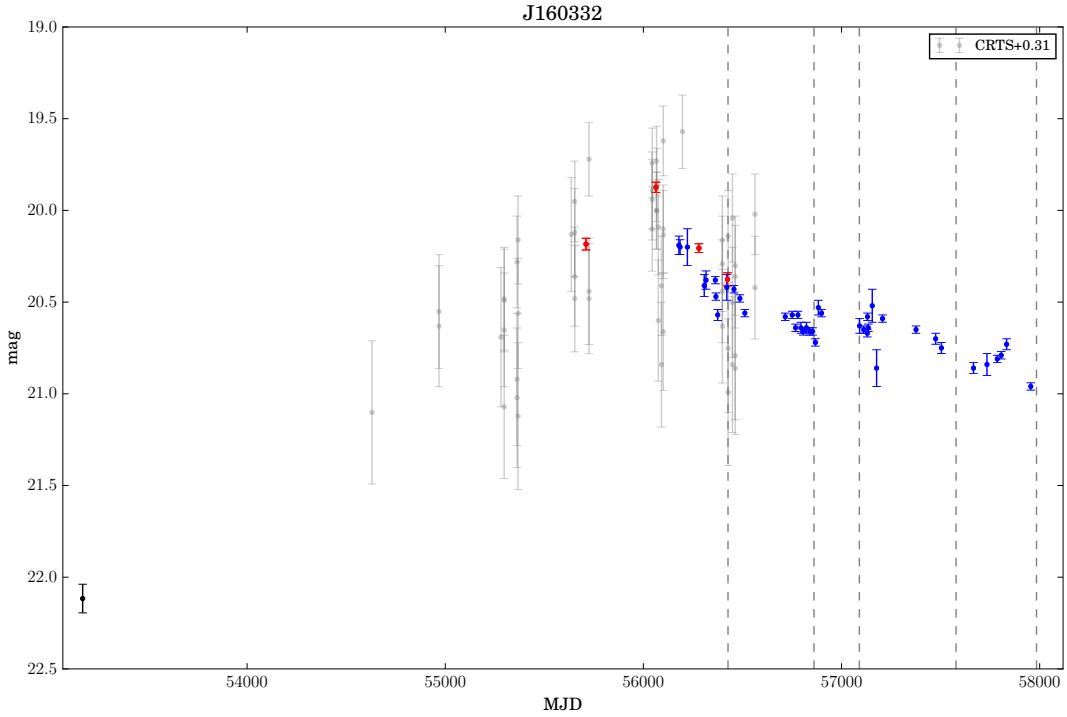
J160332
CRTS+0.31
mag
MJD
19.0
19.5
20.0
20.5
21.0
21.5
22.0
22.5
54000
55000
56000
57000
58000

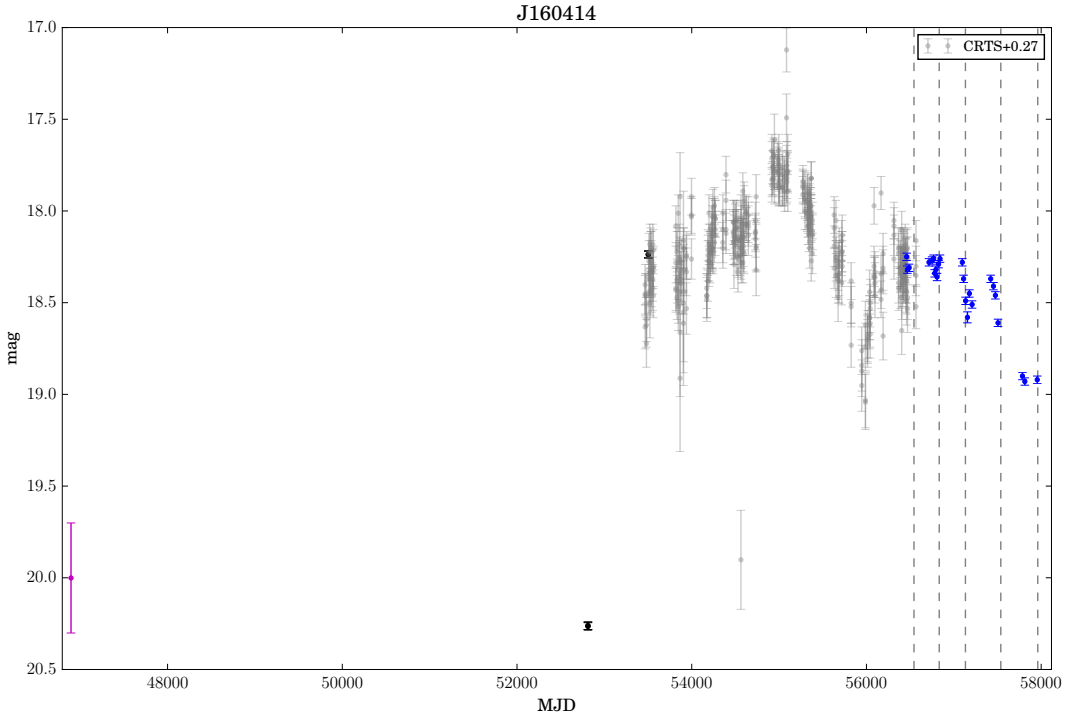
J160414
CRTS+0.27
mag
MJD
17.0
17.5
18.0
18.5
19.0
19.5
20.0
20.5
48000
50000
52000
54000
56000
58000

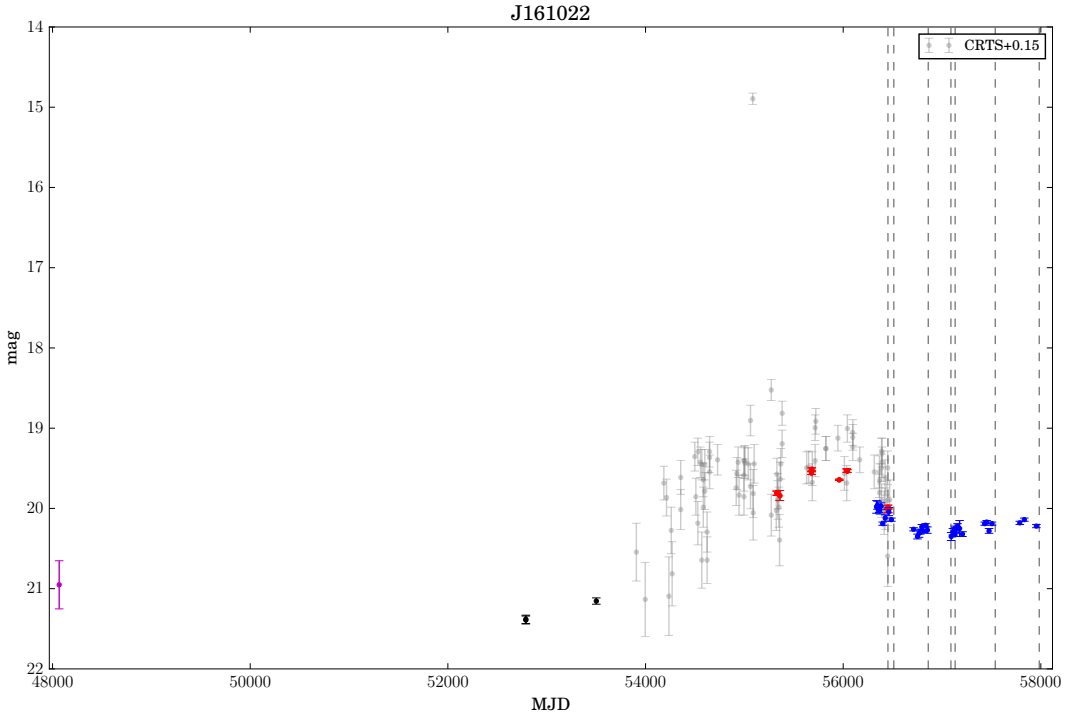
J161022
CRTS+0.15
mag
MJD
14
15
16
17
18
19
20
21
22
48000
50000
52000
54000
56000
58000

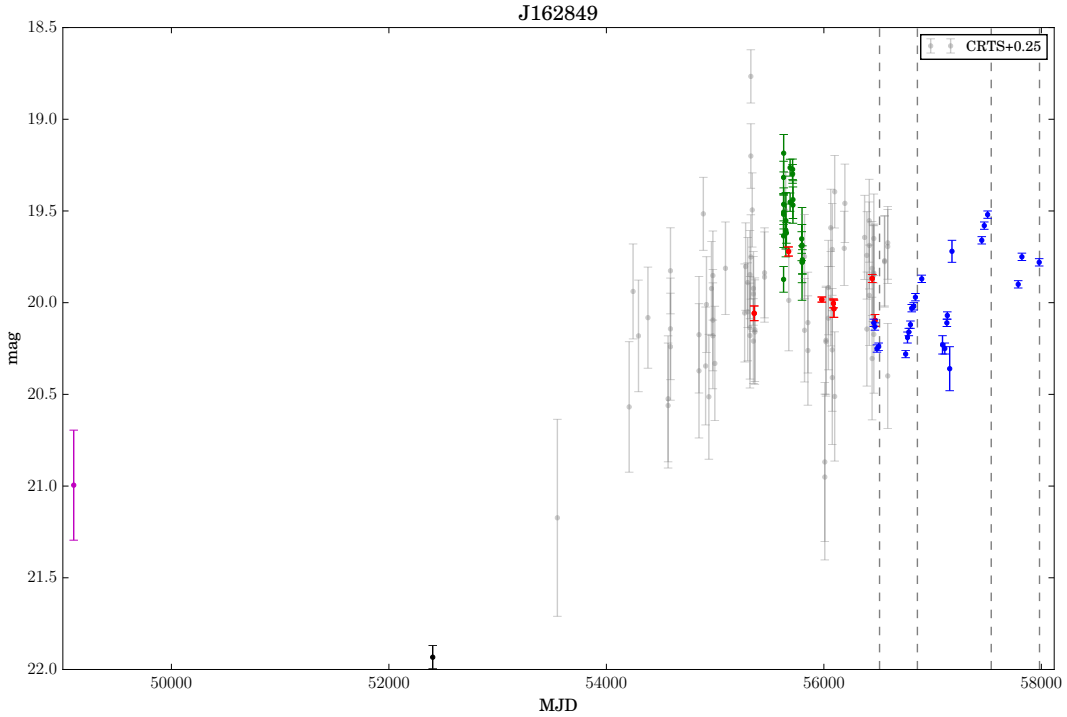
J162849
CRTS+0.25
mag
MJD
18.5
19.0
19.5
20.0
20.5
21.0
21.5
22.0
50000
52000
54000
56000
58000

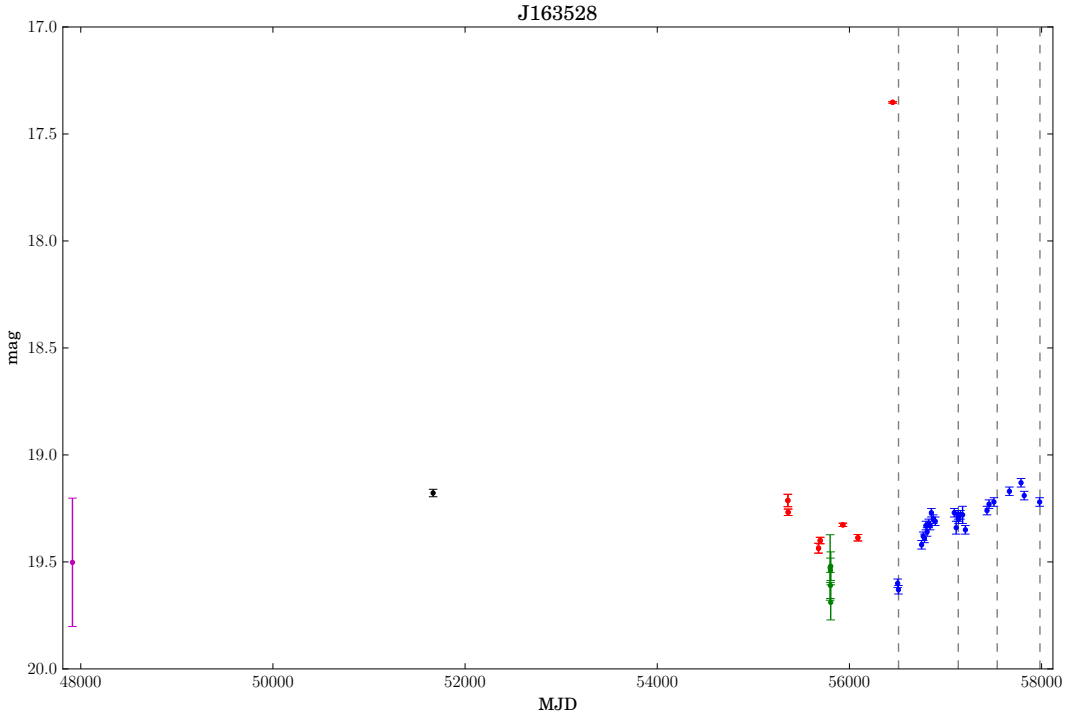
J163528
mag
MJD
17.0
17.5
18.0
18.5
19.0
19.5
20.0
48000
50000
52000
54000
56000
58000

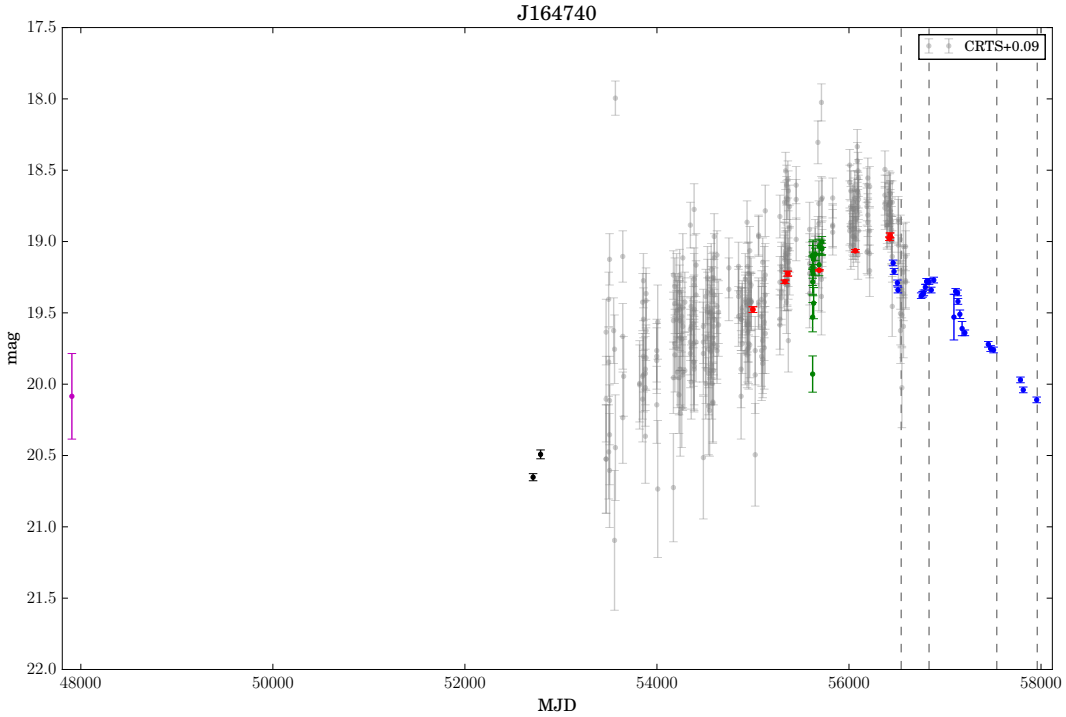
J164740
CRTS+0.09
mag
MJD
17.5
18.0
18.5
19.0
19.5
20.0
20.5
21.0
21.5
22.0
48000
50000
52000
54000
56000
58000

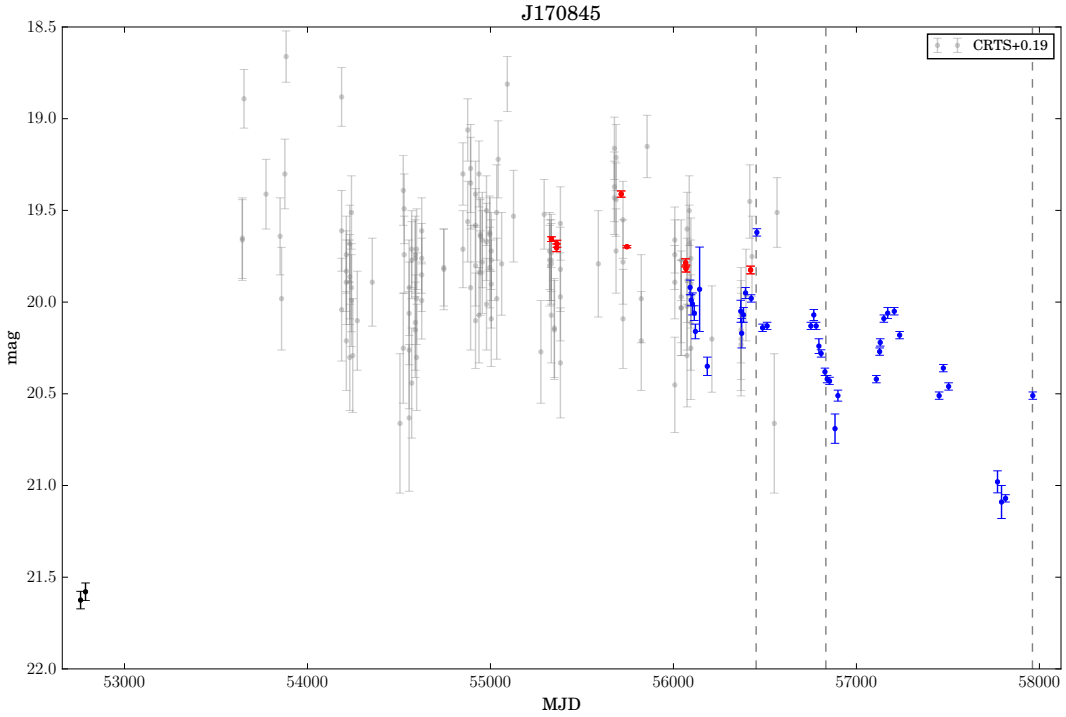
J170845
CRTS+0.19
mag
MJD
18.5
19.0
19.5
20.0
20.5
21.0
21.5
22.0
53000
54000
55000
56000
57000
58000

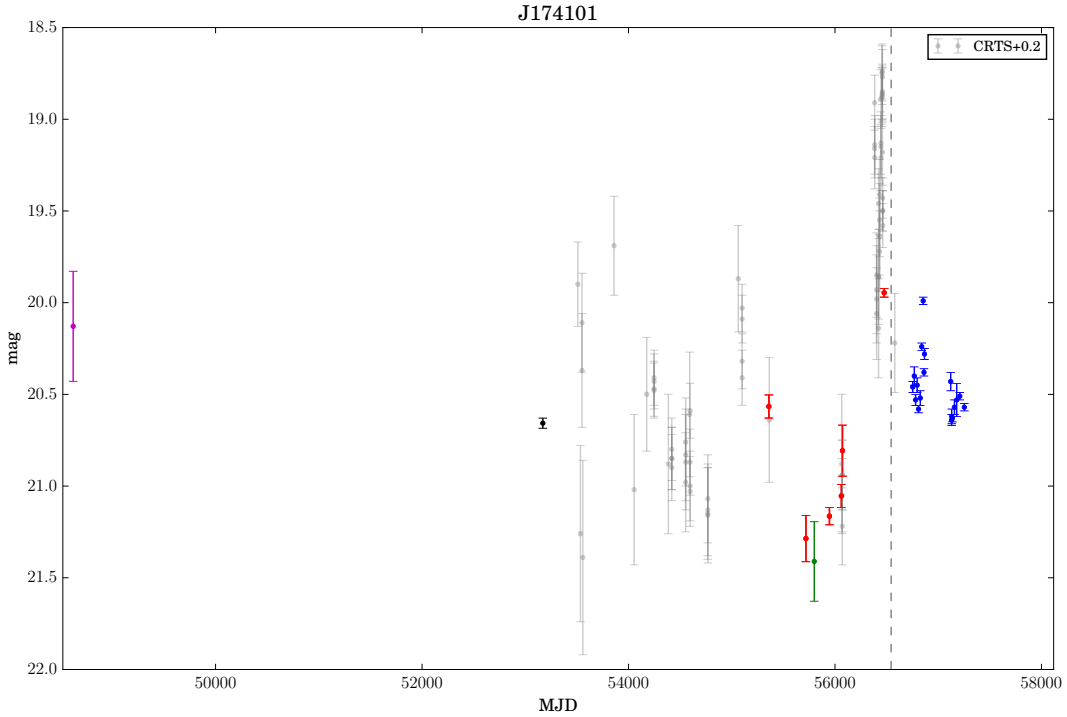
J174101
CRTS+0.2
mag
MJD
18.5
19.0
19.5
20.0
20.5
21.0
21.5
22.0
50000
52000
54000
56000
58000

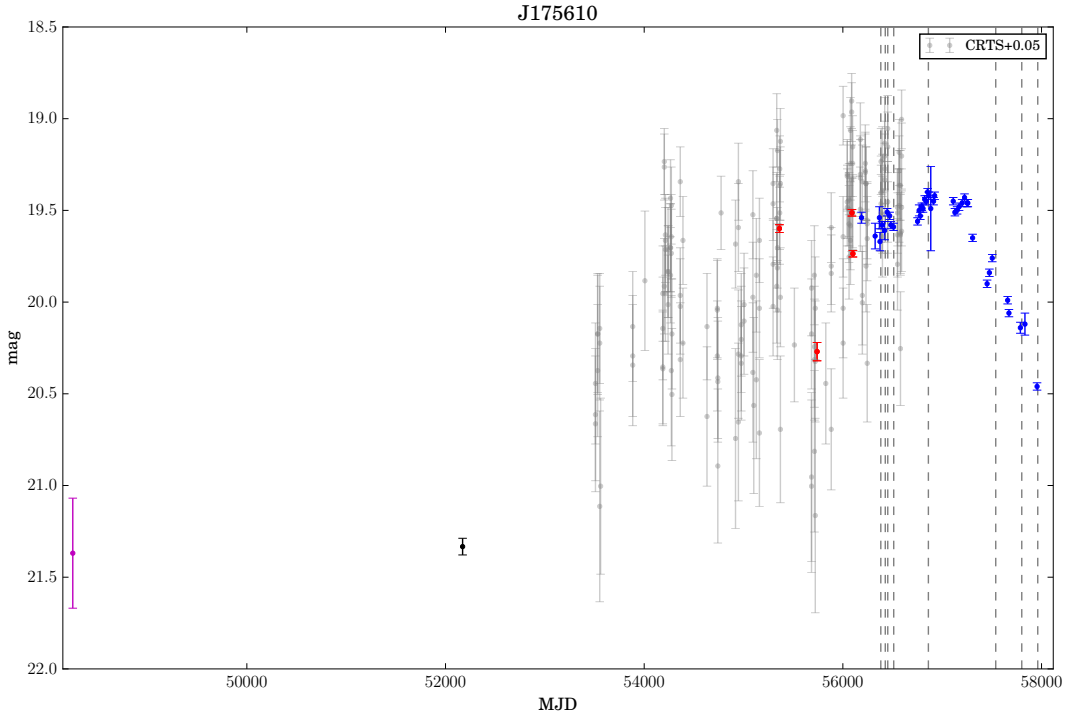
J175610
CRTS+0.05
mag
MJD
18.5
19.0
19.5
20.0
20.5
21.0
21.5
22.0
50000
52000
54000
56000
58000

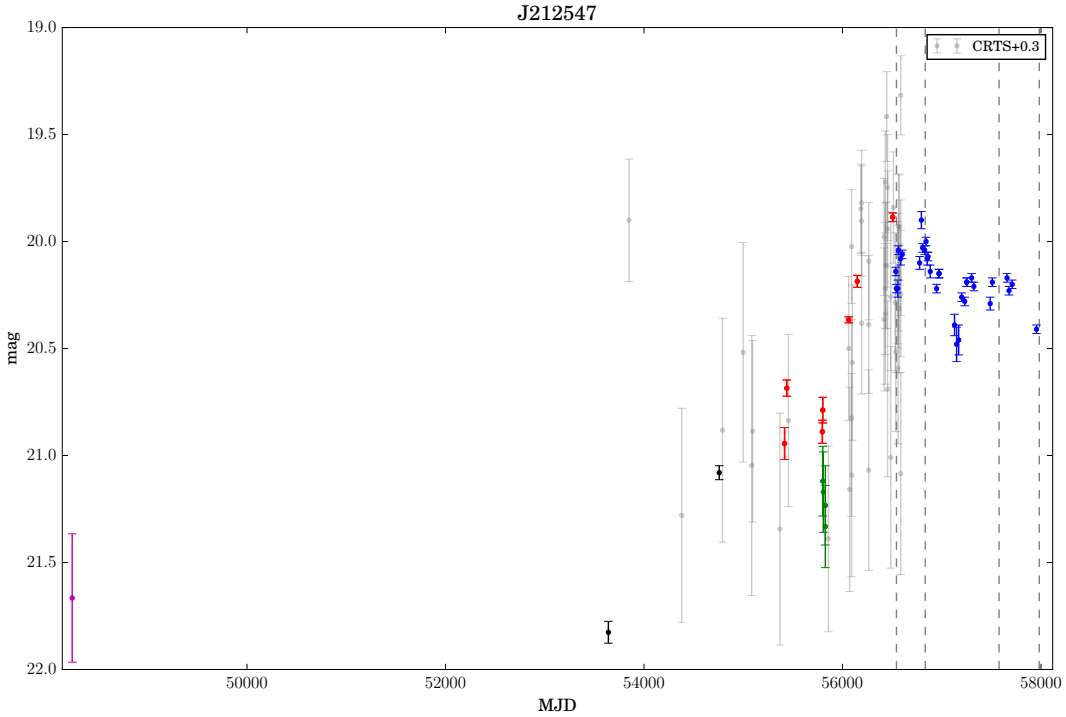
J212547
CRTS+0.3
mag
MJD
19.0
19.5
20.0
20.5
21.0
21.5
22.0
50000
52000
54000
56000
58000

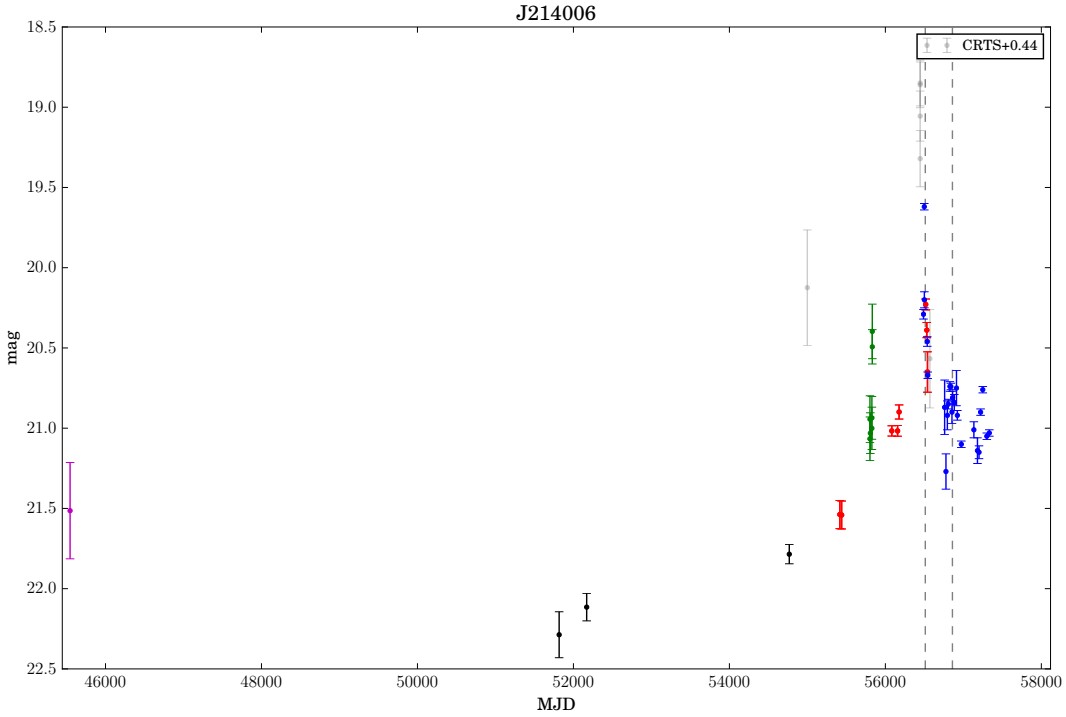
J214006
CRTS+0.44
mag
MJD
18.5
19.0
19.5
20.0
20.5
21.0
21.5
22.0
22.5
46000
48000
50000
52000
54000
56000
58000

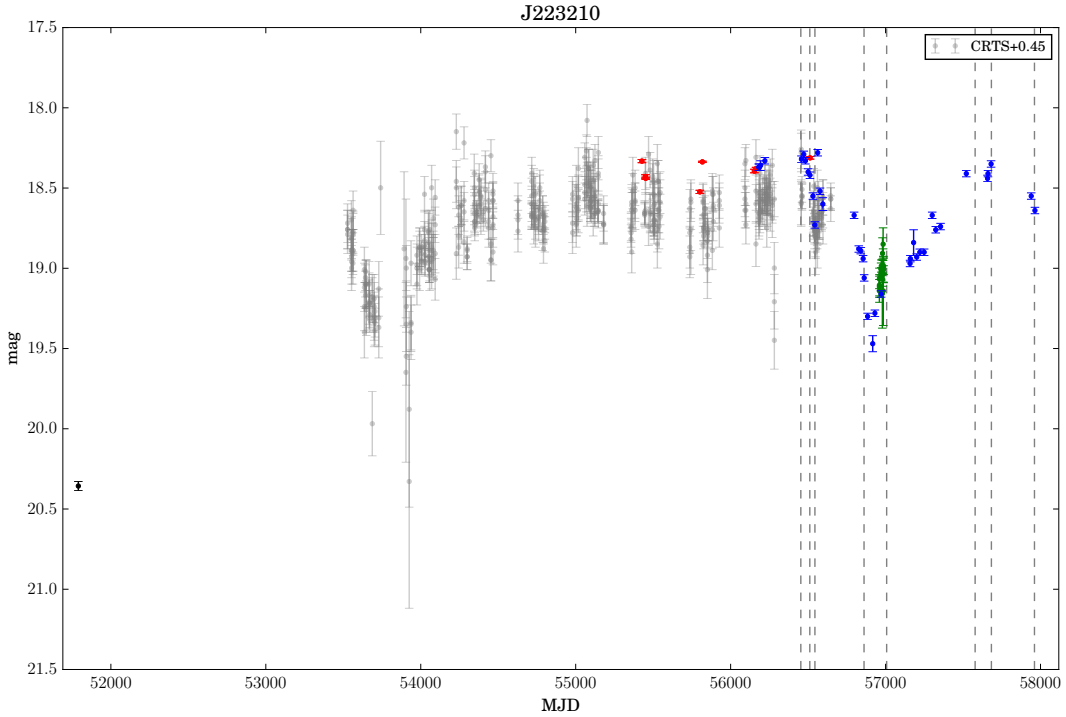
J223210
CRTS+0.45
mag
MJD
17.5
18.0
18.5
19.0
19.5
20.0
20.5
21.0
21.5
52000
53000
54000
55000
56000
57000
58000

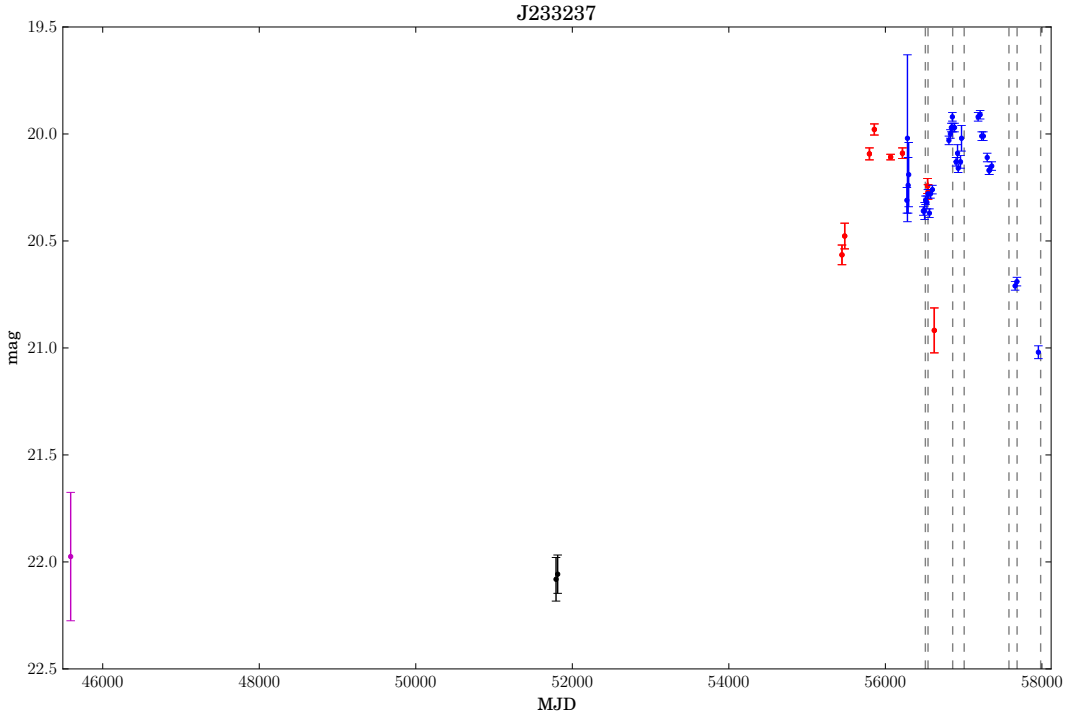
J233237
mag
MJD
19.5
20.0
20.5
21.0
21.5
22.0
22.5
46000
48000
50000
52000
54000
56000
58000

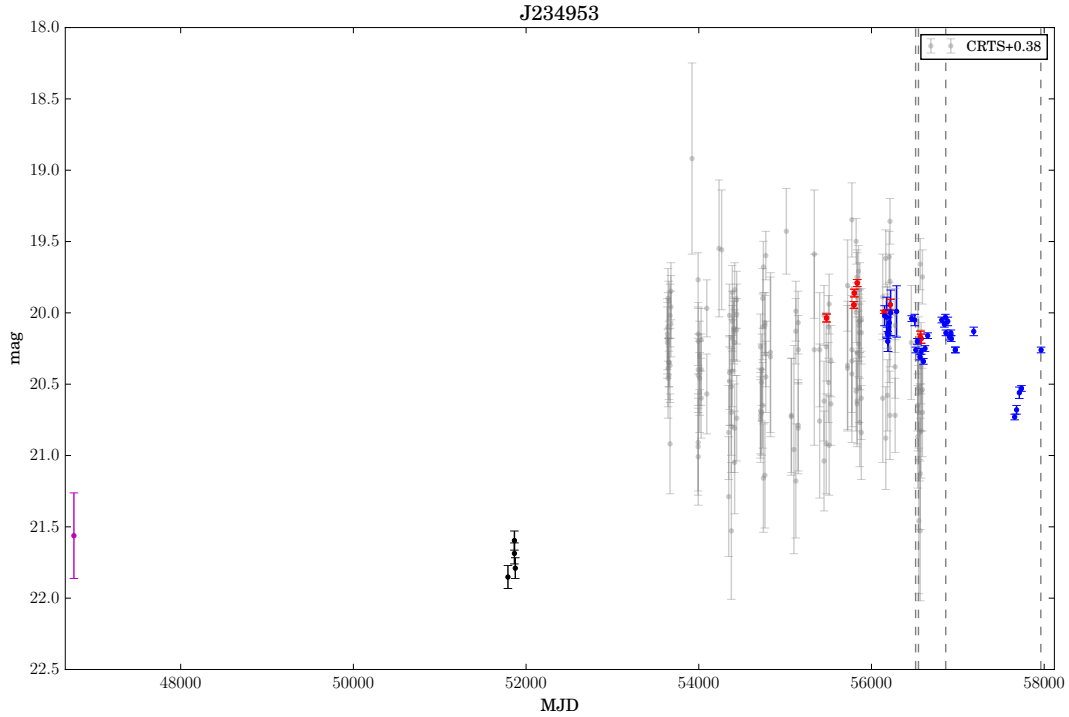
J234953
CRTS+0.38
mag
MJD
18.0
18.5
19.0
19.5
20.0
20.5
21.0
21.5
22.0
22.5
48000
50000
52000
54000
56000
58000

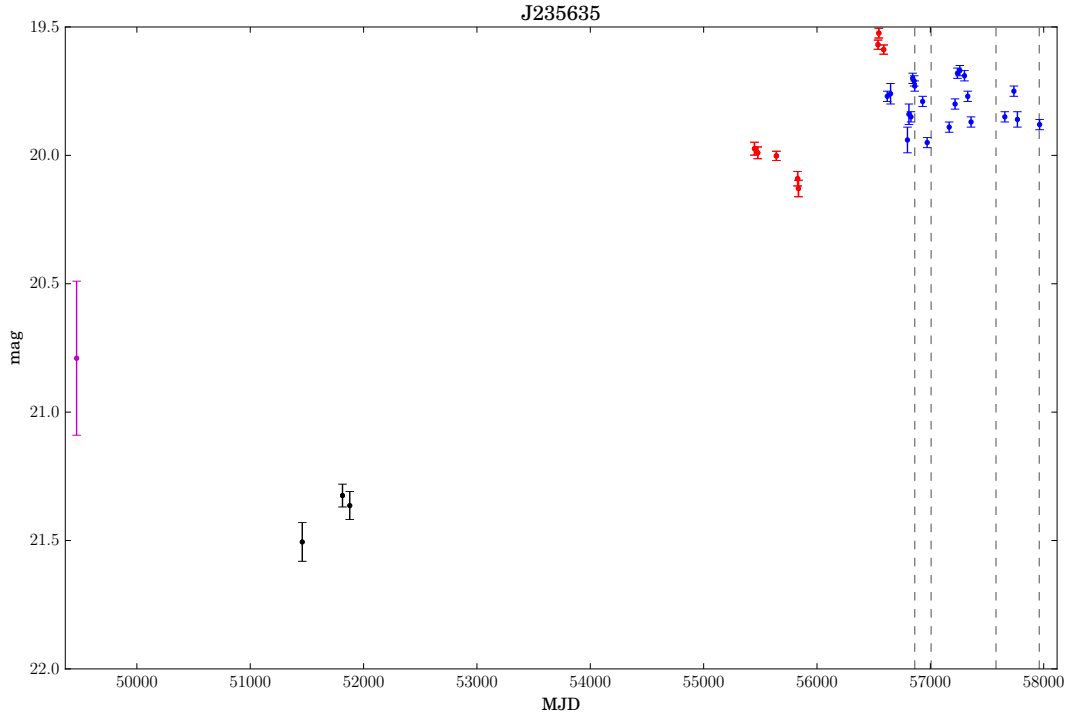
J235635
mag
MJD
19.5
20.0
20.5
21.0
21.5
22.0
50000
51000
52000
53000
54000
55000
56000
57000
58000

Appendix C

StarsightVR

C.1 Introduction

As part of my commitment to the public engagement remit of the Principals Career Development Scholarship I took the lead on a project designed to explore the possibility of taking groups of people stargazing using virtual reality (VR) headsets. This project was a resounding success. The following summary is adapted from text submitted by myself for the ninth conference proceedings of The Inspiration of Astronomical Phenomena in 2015 (INSAP IX, in press).

C.2 'StarsightVR'

The Oculus Rift Planetarium Project was a pilot-scheme, funded by a Science and Technology Facilities Council (STFC) small-project public engagement award in 2015. The main aim was to explore the possibility of integrating planetarium software with the Oculus Rift virtual reality development headset (DK2). The initial project was deemed a success and work continues on the project under the name StarsightVR[1]. The software allows multiple machines to connect to a stargazing host whilst allowing users an independent view of the night sky, with or without a VR headset. The software is open-source and has been designed with the capability for live internet-based stargazing talks thus providing a useful

[1] starsightvr.org.uk

Figure C.1 *A single Oculus Rift DK2 headset running StarsightVR.*

new tool for astronomical outreach.

Virtual reality headsets for use in the home have long been sought after but only in recent years have they begun to reach the level of sophistication or pricing required to be viable. One of the first companies to make waves in this market was Oculus[2]. The company's initial development work, crowd-funded through a kickstarter campaign, created a prototype headset that showed that a home-VR experience was within reach. The second iteration, the Oculus Rift DK2, improved on the original prototype and started shipping to developers in July 2015.

The idea behind StarsightVR was simple: adapt planetarium software to display with the Oculus Rift headset and so give the wearer the ability to look anywhere they liked on a simulated night sky. Given that the Scottish weather and light summer skies frequently hamper live stargazing sessions at the Royal Observatory Edinburgh (ROE), such a tool would prove invaluable, both as a poor weather backup and as an educational tool, allowing full use of the planetarium software and its features.

In addition to a single-user VR stargazing experience, it was also desirable to

[2]www.oculus.com

include the capability for group experiences. Stargazing with the benefit of an expert can be very rewarding and this became a key component of the project. The planetarium software selected for the project was Stellarium[3], a popular open-source package and an ideal place to begin testing these ideas.

With the basic idea in hand, a proposal was made to the STFC Public Engagement Small Awards Scheme. Alastair Bruce, an astronomy PhD student, took the role of project leader with Professor Andy Lawrence as formal principal investigator. The project was selected for full funding, totalling £9,150, and work began towards the end of 2014. The software developer engaged to work on the project, Guillaume Chereau[4], is part of the Stellarium development team and was fortunately already very familiar with the base code.

After purchase of three DK2 headsets and hardware for testing, the rest of the funds were used to buy the software development time required. Early tests were promising and allowed the addition of extra functionality to help improve the overall experience. A key aspect of StarsightVR is that it does not make use of a fully 3D rendered environment. Given the distances involved in astronomical observations, 3D rendering provides little extra depth at the cost of more processing power required for the headset, so the decision was made to keep the overhead as small as possible.

Integration of Stellarium with the DK2 headset is achieved by performing the required colour-correction and image distortion in Stellarium so that the image displayed by the headset is as desired. Updates on the position/orientation of the headset allow Stellarium to render the appropriate portion of sky. If no headset is present, the user will see a default Stellarium projection and can enable VR-mode with a simple toggle. Feedback from VR testing has proven very positive and as long as the hardware is providing a smooth frame rate the experience is very rewarding, particularly if there is someone on hand to guide the person wearing the headset around the sky. Simply turning off the ground for VR users is a memorable event indeed! One current caveat is that the colour correction is not always ideal, partly exacerbated by stars being rendered as point-like white objects using r/g/b pixels.

The remote control aspect in StarsightVR is achieved using a handler for key events triggered on the host machine, such as turning on constellation lines,

[3] www.stellarium.org
[4] noctua-software.com/about

which are then broadcast to connected clients for replication. This ensures that connected machines are synchronised with the host but are also running independently, allowing each user the freedom to look wherever they wish. This works regardless of the presence of a VR headset. Users can enable the remote control through a standard Stellarium plugin interface.

In order to help provide a live, multi-user connected stargazing tour (with or without a headset), additional features have been added. The first is the addition of an arrow alerting users as to the direction of the host's selected target. This ensures that navigating around the sky is very straightforward. A second feature is the ability to replace the Moon with any of the solar system planets. This was done for the benefit of headset users as it was felt that many people would find attempting to 'zoom in' to an object disorienting. The added benefit of these features is that they provide a memorable view of these objects. Similarly, some deep-sky objects have had a toggle added to make them larger on the sky. Not yet included is built-in audio support for the host astronomer, allowing talks to be heard by connected users. However, there are many suitable third-party apps available, so this extension could easily be added in future.

With the original project funding spent, the proof-of-concept build of StarsightVR has managed to achieve all of the goals set out in the project proposal. In order to continue development, two further avenues of funding have been donations, via the ROE Trust[5], together with a modest crowdfunder campaign. Monies raised are being directed towards improving and maintaining the current build;, for more information see the StarsightVR website. For future work, we hope to begin scheduling live stargazing shows and, when funding permits, integrating different operating systems and the latest VR headsets. This market is evolving quickly, as is the software, and it remains to be seen which vendor(s) will stand the test of time.

The current generation of VR headsets were designed primarily for gaming but they are clearly well suited as educational tools. StarsightVR is not a full-blown 3D package as its main purpose was to be an immersive stargazing experience only. Consequently, it should prove less demanding than some other VR applications. Also, it is freely available. For those that have no easy access to a full dome planetarium, StarsightVR fills the void between these and the clouds...

[5] roetrust.org.uk

C.3 Update: September 2017

Since the time of writing the above text, StarsightVR has continued to evolve. An attempt at establishing more secure funding, in the form of an STFC Large Project Award, was sadly unsuccessful. It is likely that another attempt will be made in the future. Having made it to the final selection stage on this occasion gives me confidence that the StarsightVR concept has merit. The software development is on hiatus until more funding can be secured but the most recent prototype build features support for the most recent consumer release version of the Oculus Rift headset, the CV1.

As of September 2017, hundreds of people in and around the Edinburgh area have been able to experience StarsightVR, many as part of the ROE open days and various public engagement events. If I am able to secure further funding, my first aim will be to design a fully portable setup for the system which will allow me to travel further afield. I am particularly keen that StarsightVR should be experienced by anyone without easy access to a truly dark night sky. While not as good as the real thing, it can provide a valuable experience for many.

Bibliography

Abazajian K. N., et al., 2009, ApJS, 182, 543

Ahn C. P., et al., 2012, ApJS, 203, 21

Antonucci R., 1993, Annual Review of Astron and Astrophys, 31, 473

Antonucci R. R. J., Miller J. S., 1985, ApJ, 297, 621

Arcavi I., et al., 2014, ApJ, 793, 38

Aretxaga I., Joguet B., Kunth D., Melnick J., Terlevich R. J., 1999, ApJl, 519, L123

Bahcall J. N., Kozlovsky B.-Z., 1969, ApJ, 155, 1077

Baldwin J. A., 1977, ApJ, 214, 679

Baldwin J., Ferland G., Korista K., Verner D., 1995, ApJl, 455, L119

Bentz M. C., et al., 2009, ApJ, 705, 199

Blackburne J. A., Pooley D., Rappaport S., Schechter P. L., 2011, ApJ, 729, 34

Blackburne J. A., Kochanek C. S., Chen B., Dai X., Chartas G., 2014, ApJ, 789, 125

Blackburne J. A., Kochanek C. S., Chen B., Dai X., Chartas G., 2015, ApJ, 798, 95

Blaes O., 2007, in Ho L. C., Wang J.-W., eds, Astronomical Society of the Pacific Conference Series Vol. 373, The Central Engine of Active Galactic Nuclei. p. 75 (arXiv:astro-ph/0703589)

Blandford R. D., McKee C. F., 1982, ApJ, 255, 419

Bovy J., Rix H.-W., 2013, ApJ, 779, 115

Bruce A., et al., 2017, MNRAS, 467, 1259

Burbidge G. R., Burbidge E. M., Sandage A. R., 1963, Reviews of Modern Physics, 35, 947

Cackett E. M., Gültekin K., Bentz M. C., Fausnaugh M. M., Peterson B. M., Troyer J., Vestergaard M., 2015, ApJ, 810, 86

Cardelli J. A., Clayton G. C., Mathis J. S., 1989, ApJ, 345, 245

Chabrier G., 2003, PASP, 115, 763

Chang K., Refsdal S., 1984, A&A, 132, 168

Chartas G., et al., 2016, Astronomische Nachrichten, 337, 356

Chornock R., et al., 2014, ApJ, 780, 44

Clavel J., et al., 1991, ApJ, 366, 64

Collinson J., 2016, MNRAS, submitted

Condon J. J., Cotton W. D., Greisen E. W., Yin Q. F., Perley R. A., Taylor G. B., Broderick J. J., 1998, AJ, 115, 1693

Dai X., Kochanek C. S., Chartas G., Kozłowski S., Morgan C. W., Garmire G., Agol E., 2010, ApJ, 709, 278

De Rosa G., et al., 2015, ApJ, 806, 128

Dietrich M., Hamann F., Shields J. C., Constantin A., Vestergaard M., Chaffee F., Foltz C. B., Junkkarinen V. T., 2002, ApJ, 581, 912

Done C., Davis S. W., Jin C., Blaes O., Ward M., 2012, MNRAS, 420, 1848

Drake A. J., et al., 2009, ApJ, 696, 870

Edelson R., et al., 2015, ApJ, 806, 129

Edelson R., et al., 2017, ApJ, 840, 41

Eigenbrod A., Courbin F., Sluse D., Meylan G., Agol E., 2008, A&A, 480, 647

Elvis M., et al., 1994, ApJS, 95, 1

Elvis M., Risaliti G., Zamorani G., 2002, ApJl, 565, L75

Fausnaugh M. M., et al., 2016, ApJ, 821, 56

Finkbeiner D. P., et al., 2016, ApJ, 822, 66

Floyd D. J. E., Bate N. F., Webster R. L., 2009, MNRAS, 398, 233

Foreman-Mackey D., Hogg D. W., Lang D., Goodman J., 2013, PASP, 125, 306

Francis P. J., Hewett P. C., Foltz C. B., Chaffee F. H., Weymann R. J., Morris S. L., 1991, ApJ, 373, 465

Frank J., King A., Raine D. J., 2002, Accretion Power in Astrophysics: Third Edition

Fraser M., et al., 2014, MNRAS, 439, L56

Gardner E., Done C., 2017, MNRAS, 470, 3591

Gaskell C. M., 2008, in Revista Mexicana de Astronomia y Astrofisica Conference Series. pp 1–11 (arXiv:0711.2113)

Gezari S., et al., 2012, Nature, 485, 217

Graham M. J., Djorgovski S. G., Drake A. J., Stern D., Mahabal A. A., Glikman E., Larson S., Christensen E., 2017, MNRAS, 470, 4112

Greenstein J. L., 1963, Nature, 197, 1041

Grier C. J., et al., 2013, ApJ, 764, 47

Guillochon J., Ramirez-Ruiz E., 2013, ApJ, 767, 25

Hambly N. C., et al., 2001, MNRAS, 326, 1279

Hawkins M. R. S., 2002, MNRAS, 329, 76

Hazard C., Mackey M. B., Shimmins A. J., 1963, Nature, 197, 1037

Heckman T. M., Best P. N., 2014, Annual Review of Astron and Astrophys, 52, 589

Holoien T. W.-S., et al., 2017, MNRAS, 464, 2672

Horne K., 1986, PASP, 98, 609

Inserra C., et al., 2013, ApJ, 770, 128

Irwin M. J., Webster R. L., Hewett P. C., Corrigan R. T., Jedrzejewski R. I., 1989, AJ, 98, 1989

Jester S., et al., 2005, AJ, 130, 873

Jiang Y.-F., et al., 2017, ApJ, 836, 186

Jiménez-Vicente J., 2016, Astrophysical Applications of Gravitational Lensing. Cambridge University Press, Cambridge, p. 251

Jiménez-Vicente J., Mediavilla E., Muñoz J. A., Kochanek C. S., 2012, ApJ, 751, 106

Jiménez-Vicente J., Mediavilla E., Kochanek C. S., Muñoz J. A., Motta V., Falco E., Mosquera A. M., 2014, ApJ, 783, 47

Kankare E., 2017, Nature, accepted

Kankare E., et al., 2015, Astronomy and Astrophysics, 581, L4

Kaspi S., Brandt W. N., Maoz D., Netzer H., Schneider D. P., Shemmer O., 2007, ApJ, 659, 997

Kelly B. C., Bechtold J., Siemiginowska A., 2009, ApJ, 698, 895

Kelly B. C., Sobolewska M., Siemiginowska A., 2011, ApJ, 730, 52

Khachikian E. Y., Weedman D. W., 1971, ApJl, 164, L109

Kochanek C. S., 2004, ApJ, 605, 58

Koratkar A., Blaes O., 1999, PASP, 111, 1

Korista K. T., Goad M. R., 2000, ApJ, 536, 284

Korista K. T., et al., 1995, ApJS, 97, 285

Kozłowski S., 2016, MNRAS, 459, 2787

Kozłowski S., 2017, Astronomy and Astrophysics, 597, A128

Krawczyk C. M., Richards G. T., Mehta S. S., Vogeley M. S., Gallagher S. C., Leighly K. M., Ross N. P., Schneider D. P., 2013, ApJS, 206, 4

LaMassa S. M., et al., 2015, ApJ, 800, 144

Law N. M., et al., 2009, PASP, 121, 1395

Lawrence A., 1987, PASP, 99, 309

Lawrence A., 2012, MNRAS, 423, 451

Lawrence A., et al., 2016, MNRAS, 463, 296

Lewis G. F., Irwin M. J., 1995, MNRAS, 276, 103

Lin D., et al., 2017, Nature Astronomy, 1, 0033

MacLeod C. L., et al., 2010, ApJ, 721, 1014

MacLeod C. L., et al., 2012, ApJ, 753, 106

MacLeod C. L., et al., 2015, ApJ, 806, 258

MacLeod C. L., et al., 2016, MNRAS, 457, 389

Magnier E. A., et al., 2013, ApJS, 205, 20

Malkan M. A., 1983, ApJ, 268, 582

Massey P., Jacoby G. H., 1992, in Howell S. B., ed., Astronomical Society of the Pacific Conference Series Vol. 23, Astronomical CCD Observing and Reduction Techniques. p. 240

McLure R. J., Dunlop J. S., 2004, MNRAS, 352, 1390

Metzroth K. G., Onken C. A., Peterson B. M., 2006, ApJ, 647, 901

Meusinger H., et al., 2010, Astronomy and Astrophysics, 512, A1

Meylan G., Jetzer P., North P., Schneider P., Kochanek C. S., Wambsganss J., eds, 2006, Gravitational Lensing: Strong, Weak and Micro (arXiv:astro-ph/0407232)

Morgan C. W., Kochanek C. S., Morgan N. D., Falco E. E., 2010, ApJ, 712, 1129

Morganson E., et al., 2014, ApJ, 784, 92

Mortonson M. J., Schechter P. L., Wambsganss J., 2005, ApJ, 628, 594

Mosquera A. M., Kochanek C. S., 2011, ApJ, 738, 96

Mosquera A. M., Muñoz J. A., Mediavilla E., 2009, ApJ, 691, 1292

Mosquera A. M., Kochanek C. S., Chen B., Dai X., Blackburne J. A., Chartas G., 2013, ApJ, 769, 53

Nedialkov P. L., Tikhonov N. A., Kurtev R. G., Ivanov G. R., 1996, Information Bulletin on Variable Stars, 4411

Netzer H., 2013, The Physics and Evolution of Active Galactic Nuclei

Netzer H., 2015, Annual Review of Astron and Astrophys, 53, 365

Novikov I. D., Thorne K. S., 1973, in Dewitt C., Dewitt B. S., eds, Black Holes (Les Astres Occlus). pp 343–450

Oke J. B., 1963, Nature, 197, 1040

Onken C. A., Peterson B. M., 2002, ApJ, 572, 746

Paczynski B., 1986, ApJ, 304, 1

Peterson B. M., 1997, An Introduction to Active Galactic Nuclei

Peterson B. M., 2008, New Astronomy Review, 52, 240

Peterson B. M., Wandel A., 1999, ApJl, 521, L95

Peterson B. M., Meyers K. A., Carpriotti E. R., Foltz C. B., Wilkes B. J., Miller H. R., 1985, ApJ, 292, 164

Planck Collaboration et al., 2014, Astronomy and Astrophysics, 571, A16

Poindexter S., Morgan N., Kochanek C. S., 2008, ApJ, 673, 34

Pooley D., Blackburne J. A., Rappaport S., Schechter P. L., 2007, ApJ, 661, 19

Pringle J. E., Rees M. J., 1972, Astronomy and Astrophysics, 21, 1

Richards G. T., et al., 2006, ApJS, 166, 470

Ruan J. J., et al., 2016, in American Astronomical Society Meeting Abstracts. p. 421.06

Runnoe J. C., et al., 2016, MNRAS, 455, 1691

Schlafly E. F., Finkbeiner D. P., 2011, ApJ, 737, 103

Schlafly E. F., et al., 2012, ApJ, 756, 158

Schmidt M., 1963, Nature, 197, 1040

Seyfert C. K., 1943, ApJ, 97, 28

Shakura N. I., Sunyaev R. A., 1973, A&A, 24, 337

Shappee B. J., et al., 2014, ApJ, 788, 48

Sharov A. S., Alksnis A., Nedialkov P. L., Shokin Y. A., Kurtev R. G., Ivanov V. D., 1998, Astronomy Letters, 24, 445

Shen Y., Liu X., 2012, ApJ, 753, 125

Shen Y., et al., 2011, ApJS, 194, 45

Shen Y., et al., 2016, ApJ, 818, 30

Sluse D., et al., 2011, A&A, 528, A100

Sluse D., Hutsemékers D., Courbin F., Meylan G., Wambsganss J., 2012, A&A, 544, A62

Sluse D., Hutsemékers D., Anguita T., Braibant L., Riaud P., 2015, A&A, 582, A109

Soltan A., 1982, MNRAS, 200, 115

Steele I. A., et al., 2004, in Oschmann Jr. J. M., ed., Proc. SPIE Conf. Ser. Vol. 5489, Ground-based Telescopes. SPIE, Bellingham. p. 679

Sun M., et al., 2015, ApJ, 811, 42

Tonry J. L., et al., 2012, ApJ, 750, 99

Tran H. D., 2003, ApJ, 583, 632

Trevese D., Perna M., Vagnetti F., Saturni F. G., Dadina M., 2014, ApJ, 795, 164

Vernardos G., Fluke C. J., 2013, MNRAS, 434, 832

Vernardos G., Fluke C. J., Bate N. F., Croton D., Vohl D., 2015, ApJS, 217, 23

Véron-Cetty M.-P., Joly M., Véron P., 2004, A&A, 417, 515

Vestergaard M., Osmer P. S., 2009, ApJ, 699, 800

Vestergaard M., Wilkes B. J., 2001, ApJS, 134, 1

Wambsganss J., 1992, ApJ, 386, 19

Wambsganss J., 2006, in Meylan G., Jetzer P., North P., Schneider P., Kochanek C. S., Wambsganss J., eds, Saas-Fee Advanced Course 33: Gravitational Lensing: Strong, Weak and Micro. Springer, Berlin. p. 453

Wambsganss J., Paczynski B., Schneider P., 1990, ApJl, 358, L33

Watson M. G., Bruce A., MacLeod C., Osborne J. P., Schwope A. D., 2016, MNRAS, 460, 4282

Williams B. F., et al., 2014, ApJS, 215, 9

Wyithe J. S. B., Turner E. L., 2002, ApJ, 567, 18

York D. G., et al., 2006, MNRAS, 367, 945

Yu Q., Tremaine S., 2002, MNRAS, 335, 965

Zhang K., Wang T.-G., Gaskell C. M., Dong X.-B., 2013, ApJ, 762, 51

de Vries W. H., Becker R. H., White R. L., Loomis C., 2005, AJ, 129, 615

van Dokkum P. G., 2001, PASP, 113, 1420